UNIVERSITY OF SOUTHAMPTON

FACULTY OF PHYSICAL AND APPLIED SCIENCES

School of Physics and Astronomy

Optical Cooling Using the Dipole Force

by

André Xuereb

Thesis for the degree of Doctor of Philosophy

March 2011

UNIVERSITY OF SOUTHAMPTON

ABSTRACT

FACULTY OF PHYSICAL AND APPLIED SCIENCES
SCHOOL OF PHYSICS AND ASTRONOMY

Doctor of Philosophy

OPTICAL COOLING USING THE DIPOLE FORCE

by André Xuereb

The term 'laser cooling' is applied to the use of optical means to cool the motional energies of either atoms and molecules, or micromirrors. In the literature, these two strands are kept largely separate; both, however suffer from severe limitations. Laser cooling of atoms and molecules largely relies on the internal level structure of the species being cooled. As a result, only a small number of elements and a tiny number of molecules can be cooled this way. In the case of micromirrors, the problem lies in the engineering of micromirrors that need to satisfy a large number of constraints—these include a high mechanical Q-factor, high reflectivity and very good optical quality, weak coupling to the substrate, etc.—in order to enable efficient cooling.

During the course of this thesis, I will draw these two sides of laser cooling closer together by means of a single, generically applicable scattering theory that can be used to explain the interaction between light and matter at a very general level. I use this 'transfer matrix' formalism to explore the use of the retarded dipole–dipole interaction as a means of both enhancing the efficiency of micromirror cooling systems and rendering the laser cooling of atoms and molecules less species selective. In particular, I identify the 'external cavity cooling' mechanism, whereby the use of an optical memory in the form of a resonant element (such as a cavity), *outside* which the object to be cooled sits, can potentially lead to the construction of fully integrated optomechanical systems and even two-dimensional arrays of translationally cold atoms, molecules or even micromirrors.

The concept of an optical memory is a very general one, and I use it to link together mechanisms that would otherwise appear disparate, including the cavity cooling of atoms and cooling mechanisms based on the non-adiabatic following of atomic populations. A fully vectorial three-dimensional scattering theory including the effects of such a memory is also presented and used to explore several different experimentally-realisable cooling configurations.

Contents

List of Figures

Declaration of Authorship

I, **André Xuereb**, declare that this thesis titled '**Optical Cooling Using the Dipole Force**' and the work presented in it are my own. I confirm that:

- This work was done wholly or mainly while in candidature for a research degree at this University.

- Where any part of this thesis has previously been submitted for a degree or any other qualification at this University or any other institution, this has been clearly stated.

- Where I have consulted the published work of others, this is always clearly attributed.

- Where I have quoted from the work of others, the source is always given. With the exception of such quotations, this thesis is entirely my own work.

- I have acknowledged all main sources of help.

- Where the thesis is based on work done by myself jointly with others, I have made clear exactly what was done by others and what I have contributed myself.

- Parts of this work have been published—please see list in Appendix A.

Signed:
_____

Date:
_____

Acknowledgements

I started my doctoral research not knowing quite a bit. I will forever be indebted to all those who were there to patiently guide me along the way and, perhaps just as patiently, point me in the right direction in the 1,001 occasions where I interrupted their thoughts to ask some basic question.

The Quantum Control group at the University of Southampton has always been a bit of a mystery to me: moments of tremendous insight are generally punctuated by periods where we all seem to be eight years old. I appreciate being thrown into the deep, dark end of experimental atomic physics during the first few weeks of my stay at Southampton when James Bateman and Matthew Himsworth asked me to do some work in their laboratory. My subsequent prediliction for theoretical work should not be interpreted as being due to that experience! James also provided some much needed physical insight at times. Richard Murray, who I am fond of disagreeing with, often provided an extra point of view on whatever it was that we would be discussing at the time. Being an opinionated Mediterranean, I found this rather useful (in retrospect, of course). Hamid Ohadi, the experimentalist *par excellence* and former ion trapper, and his laboratory provided a well-needed distraction whenever I got bored with my sums. I'd also like to thank Nathan Cooper, who is working with Hamid to explore experimentally some of our less crazy ideas and who took over my duty as official tea-maker on Fridays.

I must also mention Peter Domokos, whose insight triggered off a sequence of events that led to the results in this thesis that I am perhaps most proud of. Sandro Grech and the various advisers and tutors I had at the University of Malta, especially David Buhagiar and Charles Sammut, always encouraged me to pursue my fascination with mathematics and physics.

Finally, I must thank my family for their support; every one of them[†] was an inspiration, and I would have been a very different person were it not for them. Sharon, who always stuck by my side, listening to my grumbling, pushing me along, and generally being there for me, I cannot help but thank from the bottom of my heart.

"Oh, and just one more thing..."—words probably cannot express how exasperated my supervisors, Tim Freegarde and Peter Horak, must have felt at times because of my hard-headedness. Without their help this work would have never gotten *to* the starting blocks and, at the risk of repeating myself, I feel I have to tell them a deeply heartfelt "thanks!" Working with both of them proved to be a tremendous learning experience and I have nothing but words of praise for them, both in their role as advisers and in their role as scientists.

[†] And there are quite a few: Zak, Rebekah, Luke, Konrad, Charmaine, Maria, and of course my parents.

" It is an important and popular fact that things are not always what they seem. For instance, on the planet Earth, man had always assumed that he was more intelligent than dolphins because he had achieved so much—the wheel, New York, wars and so on—while all the dolphins had ever done was muck about in the water having a good time. But conversely, the dolphins had always believed that they were far more intelligent than man—for precisely the same reasons. "

Douglas Adams, *The Hitchhiker's Guide to the Galaxy*

For Sharon, for my family, and for a hot cup of tea

(u lil ommi, li għallmitni ngħodd)

Introduction

Motivation

The fundamental quest to know more about the nature of the world around us and the universe of which it is both an incomprehensibly insignificant part, objectively speaking, and a rather important part, subjectively speaking, has driven mankind to the edge of sanity[1] and sometimes beyond. Amidst all of this, cold atoms can be seen as the ideal prototypical system with which to explore nature. In contrast to the sledgehammer approach so typical of high-energy physics experiments, clouds of ultracold matter provide an almost blank canvas that one can use as a microscope to probe the behaviour of matter at the atomic, and even subatomic [2], scale. Optical cooling is perhaps the only direct way of producing these ultracold clouds.

Therein lies the catch, however. Whereas the most sensitive probes of various physical laws are perhaps the more complicated molecules, most optical cooling methods in use today are applicable to only a small (albeit growing) fraction of the periodic table. Experiments are quickly advancing to the point where a select few "normal"[2] molecules will soon be optically cooled on demand [5, 6] and the race is now on to find methods of cooling any given molecule to ultracold temperatures.

In the related field of optomechanics, and I will in due course examine how the relation with cold atoms runs deeper than the widespread use of the word "cold" in the literature, the aim of cooling a macroscopic vibrating object to its ground state has been achieved

---

[1] I am somewhat fond, however unfairly, of mentioning string theory in this context. See Ref. [1] for an overview into the birth of string theory that suggests otherwise.

[2] Ultracold di-alkali molecules are reasonably common (see Refs. [3] and [4] for reviews), but require ultracold atoms as building blocks.

using cryogenic methods [7], but several experimental groups [8–10] are tirelessly working to achieve the same using optical cooling methods.

New cooling paradigms thus have to be devised, perhaps borrowing a healthy dose of inspiration from those currently in use, to bridge the gaps between the cooling of simple atoms, the cooling of arbitrary molecules, and even the cooling of micro- and mesoscopic structures.

Brief overview of past work

Optical cooling of the motion of particles was originally observed in the regime of small dielectric particles, with Ashkin hypothesising [11] that similar ideas might be applicable to the control of atomic and molecular motion. Wonderful progress was made, both in experiment [12, 13] and in theory [14, 15] in extending these ideas to three dimensions and in exploiting the internal structure of simple atoms. Cloud temperatures of tens of μK have long been considered routine in magneto–optical traps [16]. Cooling the motion of dielectric particles proved to be more challenging, especially because the initial explorations [11] were conducted with the particles in suspension whereas a more desirable configuration [17] would be with the particle suspended in vacuum; cooling of a microscopic particle to millikelvin temperatures was indeed reported very recently [18].

Sub-Doppler cooling mechanisms, of the type reported in Ref. [14], shift the energy loss process from the decay of the excited state population to the non-adiabatic decay of the population of different hyperfine levels. In the search for more generally-applicable cooling methods, it was realised that one can similarly shift the energy loss process to the decay of a degree of freedom external to the atom. This led to the proposal for the cooling of atomic motion inside a driven cavity [19]—demonstrated recently in experiments by the Vuletić [20] and Rempe [21] groups—by extension of similar mechanisms for cooling atomic motion using the modified vacuum field present in a cavity [22]. Following a separate line of research, Braginsky and co-workers [23] suggested using cavity fields to cool the motion of micro- or mesoscopic mirrors, initially in the context of gravitational wave detectors. Experimentally, this idea lay dormant until technology improved to the point where such effects could be unambiguously demonstrated [24, 25], for example

by cooling the vibrational motion of a micromechanical oscillator from an occupation number of around 53 000 quanta (2.25 K) to ca. 32 quanta (1.3 mK) [26].

These two streams can be seen as two limiting cases of a general 'matter interacting with a cavity field' configuration, with the matter interacting weakly (atom) or strongly (microscopic mirror) with the cavity field. One of my aims in this thesis will be to combine these two fields through the use of a generic matrix-based theoretical approach. The virtues of this approach are that such models are solvable in the fully general case, and that no restriction is placed on the strength of the light–matter interaction.

On a more general level, these ideas can be united with Sisyphus–type cooling mechanisms that make use of internal atomic variables following external ones non-adiabatically. This link comes about because a cavity field also introduces a non-adiabatic 'delay' element into the dynamics of the situation. This idea of a system with a delay, or memory, as a means to a generic optical cooling mechanism will also be one of the recurring themes throughout this thesis.

Outline of thesis

This thesis will begin with a general, if somewhat brief, overview of atomic physics, which will allow me to discuss several of the "standard" cooling or trapping methods in current use. In Chapter 2 I will look at what can be viewed as a prototypical system for cavity cooling of atoms, which I call 'mirror-mediated cooling', and explore it from the semiclassical perspective.

The discussion in Part II will see me exploring two classical theories of light–matter interactions: one based on the transfer matrix method, in Chapter 3, and one based on a delayed fully vectorial three-dimensional scattering theory, in Chapter 5. The transfer matrix theory is developed in Section 3.1, solved in the general case in Section 3.2, and extended in Section 3.4 to describe multi-level atoms. It is then applied to the mirror-mediated cooling paradigm and, in Chapter 4, to another system, 'external cavity cooling', which promises to be very important in optomechanical experiments. As a final application of the matrix formalism, I will explore another configuration, in a unidirectional ring cavity with a gain medium, which allows one to dispense with certain (somewhat stringent) requirements in mirror-mediated cooling. The scattering theory developed in Chapter 5 is also initially applied to the one-dimensional mirror-mediated

cooling geometry, in order to verify the method, and is then used to describe mirror-mediated cooling in three dimensions and also the "optical binding" of a refractive particle to its own reflection.

In the final part, I will first discuss the experimental work that is currently underway in the laboratories at the University of Southampton to explore both the consequences of the above, and atom–surface interactions in a more general context. Finally, I will analyse several of the cooling configurations discussed throughout this thesis from an experimental point of view and give an estimate for the performance that can be expected from each configuration under realistic experimental conditions.

Logical connections between chapters
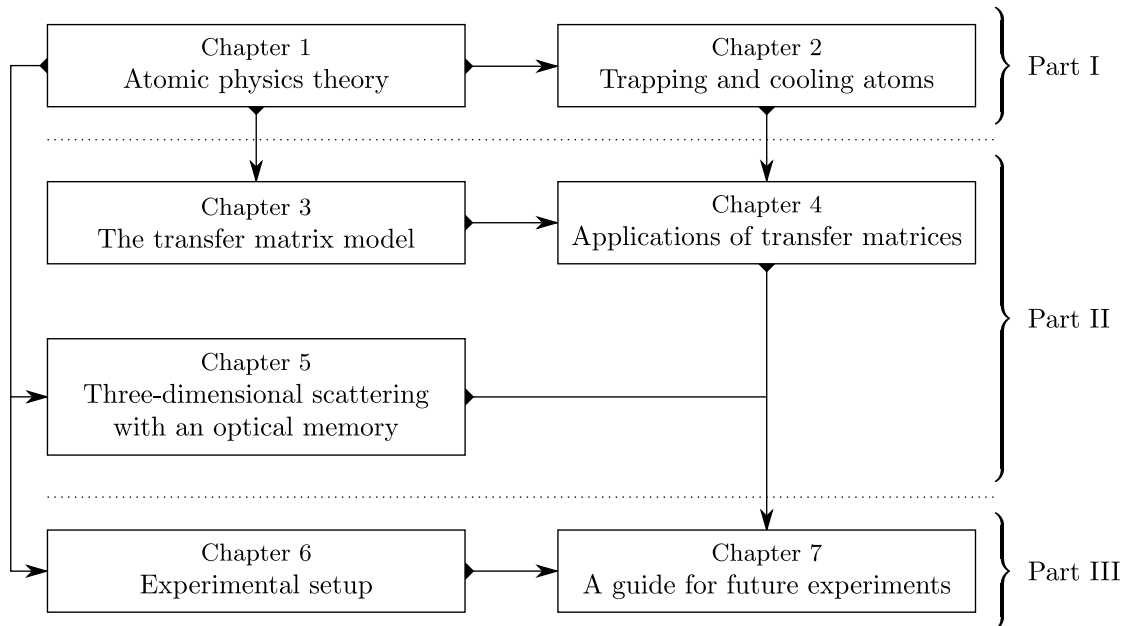
Part I

Atomic Physics Theory

&

Cooling Methods

Chapter 1

Atom–field interactions

> [...] [T]he semiclassical theory, when extended to take into account both the effect of the field on the molecules and the effect of the molecules on the field, reproduces almost quantitatively the same laws of energy exchange and coherence properties as the quantised field theory, even in the limit of one or a few quanta in the field mode.
>
> ———
>
> E. T. Jaynes and F. W. Cummings, Proceedings of the IEEE **51**, 89 (1963)

I begin this chapter with a very brief review of atomic structure, covering the fine and hyperfine structures as well as the magnetic sublevels within the hyperfine manifold; these ideas will be used later to discuss trapping and cooling of atoms. The following sections describe the density matrix approach and build up to a derivation of the Optical Bloch Equations. These equations are the tools necessary to examine the interaction between an atom and the electromagnetic field and, ultimately, to derive an expression for the forces acting on an atom, as parametrised by the polarisability of that atom. The chapter continues with a note on the fluctuation–dissipation theorem and shows how the calculation of the full force acting on the atom allows the prediction of the equilibrium temperature a population of such atoms will tend to, and concludes with a short discussion on multi-level atoms. The reader is referred to Refs. [27–33], and references therein, for a more in-depth and complete treatment of certain parts of this chapter.

1.1   Atomic structure

It has been known for centuries that the spectrum of the light emitted by excited atomic gases is made up of a finite, and usually large, number of distinct spectral lines. These lines are not randomly distributed but can be divided into various closely-spaced groups. Each of these groups can be thought of as being due to the coarse structure of the energy levels of the atom; i.e., each group of lines in the coarse structure originates from a particular transition between two (electron) energy levels. Each energy level has an associated orbital angular momentum, $\boldsymbol{L}$. The total angular momentum $\boldsymbol{J}$ of an electron includes a contribution from both $\boldsymbol{L}$ and the electron's intrinsic spin angular momentum $\boldsymbol{S}$:

$$\boldsymbol{J} = \boldsymbol{L} + \boldsymbol{S} \,, \tag{1.1}$$

whereby the corresponding quantum number J is an integer or half-integer in the range $|L-S| \leq J \leq L+S$. This is called the LS coupling scheme [31]. We adopt the convention that a quantised momentum vector $\boldsymbol{v}$ has magnitude $\sqrt{v(v + 1)}\hbar$. The different possible values of J give rise to the fine structure in the spectrum.

Drilling down further, each line in the fine structure spectrum can be subdivided. This arises from the coupling, or interaction, between the total angular momentum of the electron and the angular momentum $\boldsymbol{I}$ of the nucleus. We can then define an atomic angular momentum $\boldsymbol{F}$ as [31]

$$\boldsymbol{F} = \boldsymbol{J} + \boldsymbol{I} \,, \tag{1.2}$$

where F again takes any integer or half-integer value in the range $|J - I| \leq F \leq J + I$. Finally, we denote the quantisation axis of our system as z, whereby the projection of $\boldsymbol{F}$ along z is denoted $F_z \equiv m_F \hbar$, with $-F \leq m_F \leq F$, m_F again being an integer or half-integer. In general, F can take several values for each of the fine structure levels; this gives rise to the hyperfine structure in the observed spectrum.

We will temporarily constrain ourselves to the transition of perhaps largest experimental interest in cold atoms, the $L = 0 \rightarrow L = 1$ transition in alkali atoms (the so-called D line), where $S = 1/2$. First of all, we note that the ground state ($L = 0$) has only one fine structure level ($J = 1/2$) whereas the excited state ($L = 1$) has two: $J = 1/2$ and $J = 3/2$. The D line is therefore composed of two separate lines: the D_1 line ($^2S_{1/2} \rightarrow {}^2P_{1/2}$) and the D_2 line ($^2S_{1/2} \rightarrow {}^2P_{3/2}$). In the preceding sentence we used spectroscopic

notation, whereby the levels with $L = 0, 1, \ldots$ are denoted by $S, P, \ldots$, and where the superscript is equal to $2S + 1$. The Hamiltonian that describes the hyperfine structure for the D line transitions is, to lowest order [34],

$$\hat{H}_{\text{hfs}} = A_{\text{hfs}} \boldsymbol{I} \cdot \boldsymbol{J} + B_{\text{hfs}} \frac{3(\boldsymbol{I} \cdot \boldsymbol{J})^2 + \frac{3}{2}(\boldsymbol{I} \cdot \boldsymbol{J}) - I(I+1)J(J+1)}{2I(2I-1)J(2J-1)}, \tag{1.3}$$

with A_{hfs} being the magnetic dipole constant and B_{hfs} the electric quadrupole constant. These are experimentally determined and can be found in standard references, such as Ref. [35] for ^{85}Rb. The two terms in the preceding equation are due to the magnetic dipole and electric quadrupole interaction between $\boldsymbol{I}$ and $\boldsymbol{J}$, respectively. Higher-order multipole components were ignored in the above expression. The hyperfine levels subsequently incur an energy shift

$$\Delta E_{\text{hfs}} = \tfrac{1}{2} A_{\text{hfs}} K + B_{\text{hfs}} \frac{\frac{3}{2}K(K+1) - 2I(I+1)J(J+1)}{4I(2I-1)J(2J-1)}, \tag{1.4}$$

where we have defined $K = F(F+1) - I(I+1) - J(J+1)$ for convenience.

In the presence of a static external magnetic field $\boldsymbol{\mathcal{B}}$, it is convenient to define the quantisation axis z as being aligned with the applied field. The different m_F levels (magnetic sublevels) undergo a shift depending on $\mathcal{B} = |\boldsymbol{\mathcal{B}}|$. The effect on the atom of its interaction with $\boldsymbol{\mathcal{B}}$ is qualitatively different for various regimes, depending on the size of the energy shifts compared to the splitting between the levels. We will only be concerned with the simplest of these cases, where the energy shift is small compared to the splitting between the hyperfine levels. In such cases, F is a good quantum number (i.e., its value is well-defined as the system evolves in time) and the interaction Hamiltonian can be written

$$\hat{H}_{\text{B}} = \mu_{\text{B}} g_F \boldsymbol{F} \cdot \boldsymbol{\mathcal{B}}, \tag{1.5}$$

where μ_{B} is the Bohr magneton and g_F the Landé g-factor given approximately by[1]

$$g_F \approx \left[\frac{3J(J+1) + S(S+1) - L(L+1)}{2J(J+1)} \right] \times \left[\frac{F(F+1) - I(I+1) + J(J+1)}{2F(F+1)} \right]. \tag{1.6}$$

The associated energy shift for each magnetic sublevel is then

$$\Delta E_{\text{B}} = \mu_{\text{B}} g_F m_F \mathcal{B}, \tag{1.7}$$

---

[1] See Ref. [31, 35]; we approximate $g_S \approx 2$ in their notation.

which is therefore different for each value of m_F, giving rise to the splitting between the magnetic sublevels known as the Zeeman effect.

A similar effect, called the DC Stark effect, occurs in the presence of DC electric fields. The DC Stark effect is generally less pronounced than the Zeeman effect. To lowest order, the energy shift for each level is [31]

$$\Delta E_{\mathrm{E}} \propto \mathcal{E}_z^2 \,, \tag{1.8}$$

where $\mathcal{E}_z$ is the electric field along the quantisation axis. It is only the higher order terms, omitted in the above expression, that lift the degeneracy for the different levels.

1.2 The density matrix

Any physical Hamiltonian that acts on a system is Hermitian; i.e., $\hat{H}^\dagger = \hat{H}$. As such, it is diagonalisable and therefore affords a basis of *eigenstates*. The system acted on by the Hamiltonian is said to be in a pure state if it can be represented as a weighted sum of the eigenstates of the Hamiltonian; in other words, if the Hamiltonian has eigenstates $|\psi_0\rangle, |\psi_1\rangle, \ldots, |\psi_n\rangle$ $(n = 0, 1, \ldots)$, a pure state can be described by

$$|\Psi\rangle = \sum_i c_i |\psi_i\rangle \,, \tag{1.9}$$

with the c_i being complex numbers normalised according to the condition $\sum_i |c_i|^2 = 1$. Often, the above eigenstates are represented as the basis vectors, with

$$\psi_i = \begin{pmatrix} 0 \\ \vdots \\ 0 \\ 1 \\ 0 \\ \vdots \\ 0 \end{pmatrix} \begin{matrix} \left.\vphantom{\begin{matrix}0\\ \vdots \\ 0\end{matrix}}\right\} i-1 \\ \\ \left.\vphantom{\begin{matrix}0\\ \vdots \\ 0\end{matrix}}\right\} n-i \end{matrix} \tag{1.10}$$

being the ith basis vector in an n-dimensional complex Hilbert space. In general this description does not suffice since the state of the system may be a statistical mixture of

the different states $|\Psi_i\rangle$, each of which is itself a weighted sum of the eigenstates of the Hamiltonian, as in Eq. (1.9):

$$|\Psi_i\rangle = \sum_j c_j^{(i)} |\psi_j\rangle \,. \tag{1.11}$$

We can conveniently express the state of such a system using the density matrix formalism [27], in which we define the density matrix

$$\boldsymbol{\rho} = \sum_i p_i |\Psi_i\rangle\langle\Psi_i| \,, \tag{1.12}$$

where each p_i is interpreted as the probability of the system being in state $|\Psi_i\rangle$; i.e., $\sum_i p_i = 1$ and $0 \le p_i \le 1$. We note that the diagonal elements of $\boldsymbol{\rho}$ are of the form $\boldsymbol{\rho}_{ii} = \sum_j p_j \big|c_j^{(i)}\big|^2$, where i runs from 1 to n. $\boldsymbol{\rho}_{ii}$ can be interpreted as the probability of finding the system in the eigenstate ψ_i. It is therefore called the population of this state. The off-diagonal elements of this matrix are related to interference effects between pairs of different eigenstates, and are called coherences.

The usefulness of the density matrix formalism is readily apparent when calculating expectation values of quantum mechanical operators, for let $\hat{A}$ be such an operator with expectation value $\langle\hat{A}\rangle$. Then,

$$\langle\hat{A}\rangle = \mathrm{Tr}\big(\boldsymbol{\rho A}\big) \,, \tag{1.13}$$

with $\boldsymbol{A}$ being the matrix representation of $\hat{A}$:

$$\boldsymbol{A} \equiv \big[\langle\psi_i|\hat{A}|\psi_j\rangle\big]_{i,j} \,. \tag{1.14}$$

We will adopt this notation throughout: an operator $\hat{A}$ and a matrix $\boldsymbol{A}$ correspond to the same operation in different representations; the (i,j)th matrix element of $\boldsymbol{A}$ will be denoted $\boldsymbol{A}_{ij}$. Let us see how Eq. (1.13) arises. For a system in pure state $|\Psi\rangle$, the expectation value of $\hat{A}$ is given by $\langle\hat{A}\rangle = \langle\Psi|\hat{A}|\Psi\rangle = \sum_{i,j} c_i^* c_j \langle\psi_i|\hat{A}|\psi_j\rangle = \sum_{i,j} \boldsymbol{\rho}_{ji}\boldsymbol{A}_{ij} = \mathrm{Tr}\big(\boldsymbol{\rho A}\big)$, where $\boldsymbol{\rho} = |\Psi\rangle\langle\Psi| = \sum_{i,j} c_i c_j^* |\psi_i\rangle\langle\psi_j|$. This relation similarly holds in the case of a statistical mixture of states.

The time-dependent Schrödinger equation [36] for a Hamiltonian $\hat{H}$ acting on a state $|\psi\rangle$, $\hat{H}|\psi\rangle = i\hbar\frac{\partial}{\partial t}|\psi\rangle$, can be used to show that

$$i\hbar\dot{\boldsymbol{\rho}} = [\boldsymbol{H}, \boldsymbol{\rho}] \equiv \boldsymbol{H}\boldsymbol{\rho} - \boldsymbol{\rho}\boldsymbol{H} \,, \tag{1.15}$$

where we use the notation that a dot above a symbol represents its derivative with respect to time:

$$
\begin{aligned}
\dot{\boldsymbol{\rho}} &= \sum_i p_i \big(\tfrac{\partial}{\partial t} |\Psi_i\rangle \big) \langle \Psi_i| + \sum_i p_i |\Psi_i\rangle \big(\tfrac{\partial}{\partial t} \langle \Psi_i| \big) \\
&= \sum_i p_i \big(\tfrac{1}{\mathrm{i}\hbar} \hat{H} |\Psi_i\rangle \big) \langle \Psi_i| + \sum_i p_i |\Psi_i\rangle \big(-\tfrac{1}{\mathrm{i}\hbar} \langle \Psi_i| \hat{H}^\dagger \big) \\
&= \frac{1}{\mathrm{i}\hbar} \left[\hat{H} \left(\sum_i p_i |\Psi_i\rangle \langle \Psi_i| \right) - \left(\sum_i p_i |\Psi_i\rangle \langle \Psi_i| \right) \hat{H} \right] \\
&= \tfrac{1}{\mathrm{i}\hbar} [\boldsymbol{H}, \boldsymbol{\rho}],
\end{aligned}
\tag{1.16}
$$

since $\hat{H}$ is Hermitian.[2] Eq. (1.15) is valid for systems that have no dissipation. Incoherent processes—such as the decay of the electromagnetic field inside a cavity, spontaneous emission, etc.—are a result of the system coupling to an infinity of modes, for example the vacuum electromagnetic field. In most cases [37, §5.1.1], such processes can be most conveniently described not by directly including them in the Hamiltonian but by adding so-called *Lindblad terms* to the preceding relation [38].[3] These terms are represented by a 'superoperator' $\hat{\mathcal{L}}$ acting on $\boldsymbol{\rho}$, giving the full quantum master equation [37, §5.4.2]:

$$
\dot{\boldsymbol{\rho}} = \tfrac{1}{\mathrm{i}\hbar} [\boldsymbol{H}, \boldsymbol{\rho}] + \hat{\mathcal{L}} \boldsymbol{\rho}.
\tag{1.17}
$$

If the system described by $\boldsymbol{\rho}$ is coupled to a zero-temperature environment with a decay constant κ, then the Lindblad terms take the generic form

$$
\hat{\mathcal{L}} \boldsymbol{\rho} = -\kappa \big(\hat{c}^\dagger \hat{c} \boldsymbol{\rho} + \boldsymbol{\rho} \hat{c}^\dagger \hat{c} - 2 \hat{c} \boldsymbol{\rho} \hat{c}^\dagger \big),
\tag{1.18}
$$

with $\hat{c}$ being an operator that describes the system coupled to $\boldsymbol{\rho}$. For example, the decay of a cavity field to which an atom is coupled is described by setting κ to be the cavity field decay rate and $\hat{c}$ the annihilation operator, more commonly denoted $\hat{a}$, of the cavity field; $\hat{c}^\dagger$, or $\hat{a}^\dagger$, is then the corresponding creation operator. This description is used in Section 2.6, as adapted from the literature (see, in particular, Ref. [39]), in our semiclassical exploration of the mirror-mediated cooling mechanism.

---

[2] It is perhaps interesting to note that Eq. (1.15) differs in sign from the Heisenberg equation of motion of an operator [27, Complement G$_{\mathrm{III}}$]. Mathematically, this is due to the operator ordering, of the form $\hat{U}^\dagger \hat{H} \hat{U}$, used to transform from the Schrödinger picture, where the state vector is time-dependent and observables correspond to time-independent operators, to the Heisenberg picture, where only the observables are time-dependent.

[3] Formally, the Lindblad terms arise upon tracing the master equation Eq. (1.16) over the bath variables.

The result embodied in Eqs. (1.17) and (1.18) is surprisingly independent of the properties of the *bath*, or environment, that gives rise to the incoherent processes. The reader is referred to Ref. [37], especially Ch. 5, for more discussion about this point. Throughout this thesis, we will assume: (i) weak coupling between the system and the bath, (ii) that the dynamics is Markovian [40, Ch. 3], (iii) that the rotating wave approximation (see Section 1.3.2) is a valid approximation, and (iv) that the bath is effectively at zero temperature. These assumptions are crucial in deriving Eq. (1.18).

We now introduce what we shall refer to as the two-level atom (TLA). This is a system that is assumed to have two levels, a ground state $|g\rangle$ labelled 'g' and an excited state $|e\rangle$ labelled 'e'. In terms of the atomic model we introduced in Section 1.1, a TLA can be emulated by a $J = 0 \to J' = 1$ transition pumped by purely positive-handed circularly polarised light, such that only the $m_J = 0$ and $m_{J'} = 1$ sublevels are coupled. In the so-called D transitions of the alkali atoms, atoms can be made to cycle between two hyperfine levels in exactly the same fashion. Whilst the TLA is an idealisation, therefore, it can be approximated quite well in the laboratory.

A justification of Eq. (1.17) is provided in Ref. [37, §1.5; see Eq. (1.5.39)] for the case of a TLA coupled to the radiation field. Such a description encompasses stimulated absorption and emission as well as spontaneous emission processes.

1.3 The Optical Bloch Equations

The Optical Bloch Equations (OBE) are a set of equations that explore the behaviour of the elements of $\boldsymbol{\rho}$ when a TLA interacts with an incident harmonic electric field. To derive the OBE, we start off from the Hamiltonian of a TLA at rest in a radiation field [32]:

$$\hat{H} = \hat{H}_\mathrm{A} + \hat{H}_\mathrm{R} + \hat{H}_\mathrm{I}\,. \tag{1.19}$$

The terms on the right-hand side of the above equation are the Hamiltonian of: the atom, the quantised radiation field, and the interaction between the atom and the field, respectively. Let us now assume that the energy difference between $|g\rangle$ and $|e\rangle$ is equal to $\hbar\omega_0$, including any level shifts due to coupling to the quantised field. We can immediately write down $\hat{H}_\mathrm{A} = \hbar\omega_0|e\rangle\langle e|$, where we have taken the ground state as defining zero energy. The interaction Hamiltonian has two contributions, $\hat{H}_\mathrm{I,i}$ arising from the incident

electric field and $\hat{H}_{\mathrm{I,q}}$ arising from the quantised field, which we will henceforth assume to be initially in the vacuum state, denoted $|0\rangle$. Let us consider these two contributions separately.

1.3.1   Interaction with the quantised field

The density matrix of the TLA interacting with the quantised field evolves according to

$$\dot{\boldsymbol{\rho}} = \tfrac{1}{\mathrm{i}\hbar}[\boldsymbol{H}_{\mathrm{A}} + \boldsymbol{H}_{\mathrm{R}} + \boldsymbol{H}_{\mathrm{I,q}}, \boldsymbol{\rho}],\tag{1.20}$$

Following the standard procedure outlined in the literature (see, for example, Ref. [32, §V.A]), we may derive the following equations for the density matrix elements:

$$\dot{\boldsymbol{\rho}}_{\mathrm{gg}} = 2\Gamma\boldsymbol{\rho}_{\mathrm{ee}},\tag{1.21a}$$

$$\dot{\boldsymbol{\rho}}_{\mathrm{ee}} = -2\Gamma\boldsymbol{\rho}_{\mathrm{ee}},\tag{1.21b}$$

$$\dot{\boldsymbol{\rho}}_{\mathrm{ge}} = \mathrm{i}\omega_0\boldsymbol{\rho}_{\mathrm{ge}} - \Gamma\boldsymbol{\rho}_{\mathrm{ge}}, \text{ and}\tag{1.21c}$$

$$\dot{\boldsymbol{\rho}}_{\mathrm{eg}} = -\mathrm{i}\omega_0\boldsymbol{\rho}_{\mathrm{eg}} - \Gamma\boldsymbol{\rho}_{\mathrm{eg}}.\tag{1.21d}$$

The first pair of these equations describes the decay, with a time constant 2Γ,[4] of atoms in the excited state to the ground state by means of spontaneous emission. The second pair describes the harmonic evolution, at a frequency ω_0, and decay of the coherences of the atom.

Spontaneous emission as an irreversible process is a result of the coupling of the atomic dipole to the infinity of quantised vacuum modes in free space. It can therefore be described as an incoherent process using Lindblad terms. The decay terms in the above equations can be derived by adapting Eq. (1.18) for the coupling between the atom and the vacuum field. In this case, $\kappa \to \Gamma$, and $\hat{c} \to |g\rangle\langle e|$ is the lowering operator. Eqs. (1.21) then follow if we assume that the TLA, effectively, has infinite mass and suffers no momentum recoil from spontaneous emission.

---

[4] This differs from standard notation by a factor of 2; our Γ is frequently denoted γ in the literature. We use this notation for simplicity of presentation and consistency with Refs. [41] and [42].

1.3.2 Interaction with the incident field

Atoms and molecules, whose sizes are usually in the range of 10^{-10}–$10^{-9}\,\mathrm{m}$, are much smaller than the wavelength of visible electromagnetic radiation (ca. 400–$800 \times 10^{-9}\,\mathrm{m}$) and the spatial variation of the electric field over the extent of the electron cloud can therefore be neglected. Several cases violate this criterion, such as the interaction of highly excited Rydberg atoms with visible radiation, but we will only consider cases where we can make this *long-wavelength* assumption. We can thus write the interaction between the atom and the radiation field, by modelling the atom as a point dipole, as $\hat{H}_{\mathrm{I,i}} = -\boldsymbol{d} \cdot \boldsymbol{\mathcal{E}}$ [32], where $\boldsymbol{d}$ is the dipole moment of the atom and $\boldsymbol{\mathcal{E}} = \boldsymbol{\mathcal{E}}_0 \cos(\omega_{\mathrm{L}}t)$ the incident electric field at the position of the atom. In the basis $\{|g\rangle, |e\rangle\}$, $\boldsymbol{d}$ is a Hermitian matrix having only off-diagonal elements.[5] We define the Rabi frequency Ω of the interaction:

$$\Omega = -\tfrac{1}{\hbar}\boldsymbol{d}_{\mathrm{eg}} \cdot \boldsymbol{\mathcal{E}}_0 \,, \tag{1.22}$$

with $\boldsymbol{d}_{\mathrm{eg}} = \langle e|\boldsymbol{d}|g\rangle$ as usual. By a suitable choice of phase we can ensure that Ω is real, in which case $\boldsymbol{d}$ is a symmetric matrix; however, we will keep the rest of this chapter general and do not make this simplification. The evolution of the density matrix under the influence of this interaction is given by

$$\dot{\boldsymbol{\rho}} = \tfrac{1}{\mathrm{i}\hbar}[-\boldsymbol{d} \cdot \boldsymbol{\mathcal{E}}_0 \cos(\omega_{\mathrm{L}}t), \boldsymbol{\rho}] \,, \tag{1.23}$$

which can be expanded to

$$\dot{\boldsymbol{\rho}}_{\mathrm{gg}} = -\mathrm{i}\big(\Omega^*\boldsymbol{\rho}_{\mathrm{eg}} - \Omega\boldsymbol{\rho}_{\mathrm{ge}}\big)\cos(\omega_{\mathrm{L}}t)\,, \tag{1.24a}$$

$$\dot{\boldsymbol{\rho}}_{\mathrm{ee}} = \mathrm{i}\big(\Omega^*\boldsymbol{\rho}_{\mathrm{eg}} - \Omega\boldsymbol{\rho}_{\mathrm{ge}}\big)\cos(\omega_{\mathrm{L}}t)\,, \tag{1.24b}$$

$$\dot{\boldsymbol{\rho}}_{\mathrm{ge}} = -\mathrm{i}\Omega^*\big(\boldsymbol{\rho}_{\mathrm{ee}} - \boldsymbol{\rho}_{\mathrm{gg}}\big)\cos(\omega_{\mathrm{L}}t)\,, \text{ and} \tag{1.24c}$$

$$\dot{\boldsymbol{\rho}}_{\mathrm{eg}} = \mathrm{i}\Omega\big(\boldsymbol{\rho}_{\mathrm{ee}} - \boldsymbol{\rho}_{\mathrm{gg}}\big)\cos(\omega_{\mathrm{L}}t)\,. \tag{1.24d}$$

---

[5] The dipole operator has odd parity and its diagonal elements are therefore zero.

In the same basis as before, we can write the atomic dipole $\boldsymbol{d} = \boldsymbol{d}_{\text{eg}}|e\rangle\langle g| + \boldsymbol{d}_{\text{ge}}|g\rangle\langle e|$. We can also rewrite $\cos(\omega_{\text{L}}t) = \frac{1}{2}\big[\exp(i\omega_{\text{L}}t) + \exp(-i\omega_{\text{L}}t)\big]$. Then, we have

$$
\begin{aligned}
-\boldsymbol{d}\cdot\boldsymbol{\mathcal{E}} = \tfrac{1}{2}\hbar\big[\Omega|e\rangle\langle g|\exp(-i\omega_{\text{L}}t) + \Omega^*|g\rangle\langle e|\exp(i\omega_{\text{L}}t) \\
+ \Omega|e\rangle\langle g|\exp(-i\omega_{\text{L}}t) + \Omega^*|g\rangle\langle e|\exp(i\omega_{\text{L}}t)\big]\,. \quad (1.25)
\end{aligned}
$$

The first two terms inside the brackets in the above expression are resonant when ω_{L} is close to ω_0. They describe the raising of the atomic energy level from $|g\rangle$ to $|e\rangle$ by absorption of a photon or the lowering of the energy level from $|e\rangle$ to $|g\rangle$ accompanied by the emission of a photon. The other two terms describe nonresonant processes and can be ignored when the incident radiation is sufficiently close to the atomic resonance. This is called the *rotating-wave approximation* (RWA), and allows us to rewrite Eqs. (1.24) as

$$\dot{\boldsymbol{\rho}}_{\text{gg}} = -\tfrac{1}{2}i\big(\Omega^*\boldsymbol{\rho}_{\text{eg}}e^{i\omega_{\text{L}}t} - \Omega\boldsymbol{\rho}_{\text{ge}}e^{-i\omega_{\text{L}}t}\big)\,, \tag{1.26a}$$

$$\dot{\boldsymbol{\rho}}_{\text{ee}} = \tfrac{1}{2}i\big(\Omega^*\boldsymbol{\rho}_{\text{eg}}e^{i\omega_{\text{L}}t} - \Omega\boldsymbol{\rho}_{\text{ge}}e^{-i\omega_{\text{L}}t}\big)\,, \tag{1.26b}$$

$$\dot{\boldsymbol{\rho}}_{\text{ge}} = -\tfrac{1}{2}i\Omega^*\big(\boldsymbol{\rho}_{\text{ee}} - \boldsymbol{\rho}_{\text{gg}}\big)e^{i\omega_{\text{L}}t}\,, \text{ and} \tag{1.26c}$$

$$\dot{\boldsymbol{\rho}}_{\text{eg}} = \tfrac{1}{2}i\Omega\big(\boldsymbol{\rho}_{\text{ee}} - \boldsymbol{\rho}_{\text{gg}}\big)e^{-i\omega_{\text{L}}t}\,. \tag{1.26d}$$

We are now in a position to obtain the full time-independent OBE. The right-hand sides of Eqs. (1.26) and (1.21) can be added together, according to the approximation of independent rates,[6] to give the full time derivative of the elements of $\boldsymbol{\rho}$. Our final manipulation is to set $\tilde{\boldsymbol{\rho}}_{\text{gg}} = \boldsymbol{\rho}_{\text{gg}}$, $\tilde{\boldsymbol{\rho}}_{\text{ee}} = \boldsymbol{\rho}_{\text{ee}}$, $\tilde{\boldsymbol{\rho}}_{\text{ge}} = \boldsymbol{\rho}_{\text{ge}}\exp(-i\omega_{\text{L}}t)$, and $\tilde{\boldsymbol{\rho}}_{\text{eg}} = \boldsymbol{\rho}_{\text{eg}}\exp(i\omega_{\text{L}}t)$, whereby

$$\dot{\tilde{\boldsymbol{\rho}}}_{\text{gg}} = -\tfrac{1}{2}i\big(\Omega^*\tilde{\boldsymbol{\rho}}_{\text{eg}} - \Omega\tilde{\boldsymbol{\rho}}_{\text{ge}}\big) + 2\Gamma\tilde{\boldsymbol{\rho}}_{\text{ee}}\,, \tag{1.27a}$$

$$\dot{\tilde{\boldsymbol{\rho}}}_{\text{ee}} = \tfrac{1}{2}i\big(\Omega^*\tilde{\boldsymbol{\rho}}_{\text{eg}} - \Omega\tilde{\boldsymbol{\rho}}_{\text{ge}}\big) - 2\Gamma\tilde{\boldsymbol{\rho}}_{\text{ee}}\,, \tag{1.27b}$$

$$\dot{\tilde{\boldsymbol{\rho}}}_{\text{ge}} = -\tfrac{1}{2}i\Omega^*\big(\tilde{\boldsymbol{\rho}}_{\text{ee}} - \tilde{\boldsymbol{\rho}}_{\text{gg}}\big) - \big(\Gamma + i\Delta_{\text{L}}\big)\tilde{\boldsymbol{\rho}}_{\text{ge}}\,, \text{ and} \tag{1.27c}$$

$$\dot{\tilde{\boldsymbol{\rho}}}_{\text{eg}} = \tfrac{1}{2}i\Omega\big(\tilde{\boldsymbol{\rho}}_{\text{ee}} - \tilde{\boldsymbol{\rho}}_{\text{gg}}\big) - \big(\Gamma - i\Delta_{\text{L}}\big)\tilde{\boldsymbol{\rho}}_{\text{eg}}\,, \tag{1.27d}$$

---

[6]   Since the two systems of equations generally describe time evolution on two vastly different timescales, it is reasonable to assume that the physical processes they describe do not interfere, and that the time derivatives can simply be added.

with $\Delta_{\mathrm{L}} = \omega_{\mathrm{L}} - \omega_0$. These are the Optical Bloch Equations for a TLA at rest [32].

1.4 Polarisability of a two-level atom

Eqs. (1.27) can be expressed in terms of three independent parameters, $u = \frac{1}{2}\big(\tilde{\boldsymbol{\rho}}_{\mathrm{ge}} + \tilde{\boldsymbol{\rho}}_{\mathrm{eg}}\big)$, $v = \frac{1}{2\mathrm{i}}\big(\tilde{\boldsymbol{\rho}}_{\mathrm{ge}} - \tilde{\boldsymbol{\rho}}_{\mathrm{eg}}\big)$ and $w = \frac{1}{2}\big(\tilde{\boldsymbol{\rho}}_{\mathrm{ee}} - \tilde{\boldsymbol{\rho}}_{\mathrm{gg}}\big)$, since the total population of atoms is fixed, i.e., $\tilde{\boldsymbol{\rho}}_{\mathrm{gg}} + \tilde{\boldsymbol{\rho}}_{\mathrm{ee}} = 1$. These three parameters are all real, since $\boldsymbol{\rho}$ is Hermitian, and can be used to describe the coherent evolution of the state of the atom geometrically, with the 'Bloch' vector (u, v, w) describing a path on the so-called Bloch Sphere. We will not be concerned with the Bloch Sphere in this thesis but will use u, v and w as a shortcut to deriving some results in this section.

If an atom is moving at not too fast a speed, say its velocity $\boldsymbol{v}$ is such that $\tau_{\mathrm{i}}|\boldsymbol{v}|, \tau_{\mathrm{L}}|\boldsymbol{v}| \ll \lambda_{\mathrm{L}}$, with $\tau_{\mathrm{L}} = 2\pi/\omega_{\mathrm{L}}$ being the duration of an optical period of the incident radiation, $\lambda_{\mathrm{L}} = 2\pi c/\omega_{\mathrm{L}}$ its wavelength, and $\tau_{\mathrm{i}} = \min\big\{(2\Gamma)^{-1}, \Omega^{-1}\big\}$ the timescale for the internal evolution of the atom, then we can assume that at each point in time the internal variables of the atom—represented by $\tilde{\boldsymbol{\rho}}$ or, equivalently, (u, v, w)—will reach a state of equilibrium [32]. In other words, we need only concern ourselves with the steady-state value of $\tilde{\boldsymbol{\rho}} \equiv \tilde{\boldsymbol{\rho}}^{\mathrm{st}}$ (this process is known as *adiabatic elimination* [43] of the external variables). Let us substitute u, v and w for the matrix elements of $\tilde{\boldsymbol{\rho}}$ in Eqs. (1.27), and let us set all the time derivatives to zero. Then we can write

$$\dot{u} = 0 = -2\Gamma u^{\mathrm{st}} + 2\Delta_{\mathrm{L}} v^{\mathrm{st}} - \big(\Omega^* - \Omega\big)w^{\mathrm{st}}\,, \tag{1.28a}$$

$$\dot{v} = 0 = -2\Delta_{\mathrm{L}} u^{\mathrm{st}} - 2\Gamma v^{\mathrm{st}} - \big(\Omega^* + \Omega\big)w^{\mathrm{st}}\,, \text{ and} \tag{1.28b}$$

$$\dot{w} = 0 = \tfrac{1}{2}\mathrm{i}\big(\Omega^* - \Omega\big)u^{\mathrm{st}} + \tfrac{1}{2}\big(\Omega^* + \Omega\big)v^{\mathrm{st}} - 2\Gamma w^{\mathrm{st}} - \Gamma\,, \tag{1.28c}$$

with the superscript 'st' again denoting steady-state values. In particular, then,

$$\tilde{\boldsymbol{\rho}}_{\mathrm{gg}}^{\mathrm{st}} = 1 - \frac{|\Omega|^2}{4}\frac{1}{\Delta_{\mathrm{L}}^2 + \Gamma^2 + |\Omega|^2/2} = \frac{1}{2}\frac{2+s}{1+s}\,, \tag{1.29a}$$

$$\tilde{\boldsymbol{\rho}}_{\mathrm{ee}}^{\mathrm{st}} = \frac{|\Omega|^2}{4}\frac{1}{\Delta_{\mathrm{L}}^2 + \Gamma^2 + |\Omega|^2/2} = \frac{1}{2}\frac{s}{1+s}\,, \tag{1.29b}$$

$$\tilde{\boldsymbol{\rho}}_{\mathrm{ge}}^{\mathrm{st}} = \frac{\Omega}{2}\frac{\Delta_{\mathrm{L}} + \mathrm{i}\Gamma}{\Delta_{\mathrm{L}}^2 + \Gamma^2 + |\Omega|^2/2} = \frac{\Omega/2}{\Delta_{\mathrm{L}} - \mathrm{i}\Gamma}\frac{1}{1+s}\,, \text{ and} \tag{1.29c}$$

$$\tilde{\boldsymbol{\rho}}_{\mathrm{eg}}^{\mathrm{st}} = \frac{\Omega^*}{2}\frac{\Delta_{\mathrm{L}} - \mathrm{i}\Gamma}{\Delta_{\mathrm{L}}^2 + \Gamma^2 + |\Omega|^2/2} = \frac{\Omega^*/2}{\Delta_{\mathrm{L}} + \mathrm{i}\Gamma}\frac{1}{1+s}\,, \tag{1.29d}$$

where we have defined the saturation parameter $s = \left(|\Omega|^2/2\right)\big/\left(\Delta_{\mathrm{L}}^2 + \Gamma^2\right)$, which is proportional to the intensity of the field interacting with the atom, since $|\Omega| \propto |\boldsymbol{\mathcal{E}}_0|$. Much physical insight can be gained by exploring how $\tilde{\boldsymbol{\rho}}^{\mathrm{st}}$ behaves when s is varied. For very large s, we have $\tilde{\boldsymbol{\rho}}_{\mathrm{gg}}^{\mathrm{st}}, \tilde{\boldsymbol{\rho}}_{\mathrm{ee}}^{\mathrm{st}} \approx \frac{1}{2}$, in which case the population is evenly distributed between the two states, and $\tilde{\boldsymbol{\rho}}_{\mathrm{ge}}^{\mathrm{st}}, \tilde{\boldsymbol{\rho}}_{\mathrm{eg}}^{\mathrm{st}} \approx 0$, so that the coherences between the two states essentially disappear. Conversely, for very small s, we have $\tilde{\boldsymbol{\rho}}_{\mathrm{gg}}^{\mathrm{st}} \approx 1$ and $\tilde{\boldsymbol{\rho}}_{\mathrm{ee}}^{\mathrm{st}} \approx 0$; i.e., practically the entire atomic population is in the ground state, and in the limit of small s we have

$$\tilde{\boldsymbol{\rho}}_{\mathrm{ge}}^{\mathrm{st}} = \frac{\Omega/2}{\Delta_{\mathrm{L}} - \mathrm{i}\Gamma} \ \text{ and } \ \tilde{\boldsymbol{\rho}}_{\mathrm{eg}}^{\mathrm{st}} = \frac{\Omega^*/2}{\Delta_{\mathrm{L}} + \mathrm{i}\Gamma} \, . \tag{1.30}$$

The average value of the (induced) atomic dipole moment in the steady state is given by

$$\begin{aligned} \langle \boldsymbol{d} \rangle &= \mathrm{Tr}\left(\boldsymbol{\rho}^{\mathrm{st}} \boldsymbol{d}\right) = 2\,\mathrm{Re}\left\{\boldsymbol{\rho}_{\mathrm{eg}}^{\mathrm{st}} \boldsymbol{d}_{\mathrm{ge}}\right\} \\ &= 2\,\mathrm{Re}\left\{\frac{\Omega^*/2}{\Delta_{\mathrm{L}} + \mathrm{i}\Gamma} \frac{1}{1+s} \boldsymbol{d}_{\mathrm{ge}} e^{-\mathrm{i}\omega_{\mathrm{L}} t}\right\} . \end{aligned} \tag{1.31}$$

We can assume that the induced atomic dipole moment is aligned, in space, with the incident electric field, at which point we can set $\boldsymbol{d}_{\mathrm{ge}} = |\boldsymbol{d}_{\mathrm{ge}}|e^{i\phi}$, with ϕ being some phase, and $\boldsymbol{d}_{\mathrm{ge}} \cdot \boldsymbol{\mathcal{E}}_0 = |\boldsymbol{d}_{\mathrm{ge}}|\mathcal{E}_0 e^{i\phi}$, such that

$$\langle \boldsymbol{d} \rangle = \mathrm{Re}\left\{-\frac{1}{\hbar} \frac{|\boldsymbol{d}_{\mathrm{ge}}|^2 e^{2i\phi}}{\Delta_{\mathrm{L}} + \mathrm{i}\Gamma} \frac{1}{1+s} \mathcal{E}_0 e^{-\mathrm{i}\omega_{\mathrm{L}} t}\right\} . \tag{1.32}$$

Let χ be the (complex) polarisability of the atom, whereby $\langle \boldsymbol{d} \rangle = \epsilon_0\,\mathrm{Re}\left\{\chi \mathcal{E}_0 e^{-\mathrm{i}\omega_{\mathrm{L}} t}\right\}$ [44], ϵ_0 being the vacuum permittivity. It can be verified by direct calculation that, within the RWA, $\mathrm{Re}\{\boldsymbol{d} \cdot \boldsymbol{\mathcal{E}}\} = \mathrm{Re}\{\boldsymbol{d}\} \cdot \mathrm{Re}\{\boldsymbol{\mathcal{E}}\}$; this justifies the form of the equation in the preceding sentence. Thus,

$$\chi = -\frac{|\langle e|\boldsymbol{d}|g\rangle|^2}{\epsilon_0 \hbar} \frac{1}{\Delta_{\mathrm{L}} + \mathrm{i}\Gamma} \frac{1}{1+s} \, , \tag{1.33}$$

where we have made the simplification $\phi = 0$, corresponding to assuming that the matrix elements of $\boldsymbol{d}$ are real, and have also used the relation $|\boldsymbol{d}_{\mathrm{ge}}| = |\boldsymbol{d}_{\mathrm{eg}}| = |\langle e|\boldsymbol{d}|g\rangle|$. Let us now simplify this expression. First, consider Eq. (1.29b), which describes the population in the excited state, and note that atoms in the excited state decay at a rate 2Γ, as also

implied by Eq. (1.27b). The total scattering rate is therefore given by

$$R = 2\Gamma\boldsymbol{\rho}_{\mathrm{ee}}^{\mathrm{st}} = \Gamma\frac{|\Omega|^2/2}{\Delta_{\mathrm{L}}^2 + \Gamma^2 + |\Omega|^2/2} = \Gamma\frac{I/I_{\mathrm{sat}}}{1 + \left(\Delta_{\mathrm{L}}/\Gamma\right)^2 + I/I_{\mathrm{sat}}}\,, \tag{1.34}$$

which will be justified in Section 1.5, and where the second equality defines the saturation intensity

$$I_{\mathrm{sat}} = \frac{2I\Gamma^2}{|\Omega|^2}\,, \tag{1.35}$$

with $I = \frac{1}{2}c\epsilon_0\mathcal{E}_0^2$ [45]. We can use the definitions of the Rabi frequency Ω, Eq. (1.22), and I_{sat} to obtain

$$|\langle e|\boldsymbol{d}|g\rangle|^2 = \frac{c\epsilon_0\Gamma^2\hbar^2}{I_{\mathrm{sat}}}\,. \tag{1.36}$$

The scattered power is given by $\hbar\omega_{\mathrm{L}}R$. Let us now define $\sigma_{\mathrm{a}} \equiv \hbar\omega_{\mathrm{L}}R/I = \hbar\omega_{\mathrm{L}}\Gamma/I_{\mathrm{sat}}$ on resonance and in the limit of low incident power. Thus, σ_{a} corresponds to the scattering, or radiative, cross-section (the scattered power divided by the incident energy flux) when $\Delta_{\mathrm{L}} = 0$ and $I \ll I_{\mathrm{sat}}$. But then,

$$\frac{|\langle e|\boldsymbol{d}|g\rangle|^2}{\epsilon_0\hbar} = \frac{\sigma_{\mathrm{a}}c}{\omega_{\mathrm{L}}}\Gamma = \frac{\lambda}{\pi}\frac{\sigma_{\mathrm{a}}}{2}\Gamma,\ \text{ or} \tag{1.37}$$

$$\chi = -\frac{\sigma_{\mathrm{a}}c}{\omega_{\mathrm{L}}}\Gamma\frac{1}{\Delta_{\mathrm{L}} + \mathrm{i}\Gamma}\frac{1}{1+s} = -\frac{\lambda}{\pi}\frac{\sigma_{\mathrm{a}}}{2}\frac{\Gamma}{\Delta_{\mathrm{L}} + \mathrm{i}\Gamma}\frac{1}{1+s}\,. \tag{1.38}$$

It can also be shown that $\sigma_{\mathrm{a}} = 3\lambda^2/(2\pi)$ [46, §68.6], which allows us to relate χ to known quantities. We will use the linear polarisability χ to define the dimensionless 'scattering parameter'[7] ζ. Indeed, let us first look at the 1D wave equation, along the z axis, for a monochromatic plane wave incident normally on a polarisable plane at $z = 0$ [44, 47]:

$$\left(\frac{\partial^2}{\partial z^2} + k^2\right)\boldsymbol{\mathcal{E}} = -k^2\eta\chi\delta(z)\boldsymbol{\mathcal{E}}\,, \tag{1.39}$$

with $\delta(z)$ being the Dirac δ-function, $k = 2\pi/\lambda$ the wavenumber of the wave and η the density of the particles making up the plane per unit area. If the wave interacts with one particle, then we can effectively set $\eta = 1/\sigma_{\mathrm{L}}$, σ_{L} being the mode area of the (possibly focussed) wave. In situations where the atom is at the focus of an extremely tightly-focussed wave, however, this approximation breaks down [48] and we effectively have $\eta < 1/\sigma_{\mathrm{L}}$; we will henceforth assume that the atom is not in the centre of such a

---

[7] We will refer to ζ as 'polarisability' throughout—the linear relation between χ and ζ, as well as the context, allows us to do this without giving rise to any ambiguity. χ is perhaps more correctly referred to as a 'susceptibility'.

tightly-focussed beam.

By defining $\zeta = \frac{1}{2}k\eta\chi$, and making use of the boundary conditions [47]

$$\mathcal{E}\big|_{z\to0^-} = \mathcal{E}\big|_{z\to0^+}\,, \text{ and} \tag{1.40a}$$

$$\left(\tfrac{\partial}{\partial z}\mathcal{E}\right)\big|_{z\to0^-} - \left(\tfrac{\partial}{\partial z}\mathcal{E}\right)\big|_{z\to0^+} = 2k\zeta\left(\mathcal{E}\big|_{z=0}\right), \tag{1.40b}$$

obtained by integrating the wave equation over a small interval centred at $z = 0$, we can show that the complex (amplitude) reflection and transmission coefficients are

$$\mathfrak{r} = \frac{i\zeta}{1 - i\zeta} \text{ and } \mathfrak{t} = \frac{1}{1 - i\zeta}\,, \tag{1.41}$$

respectively. The polarisability of a TLA can therefore be written [42]

$$\zeta = -\frac{\sigma_{\mathrm{a}}}{2\sigma_{\mathrm{L}}}\frac{\Gamma}{\Delta_{\mathrm{L}} + i\Gamma}\frac{1}{1 + s}\,, \text{ or } \zeta = -\frac{\sigma_{\mathrm{a}}}{2\sigma_{\mathrm{L}}}\frac{\Gamma}{\Delta_{\mathrm{L}} + i\Gamma}\,, \tag{1.42}$$

where the low-intensity ($s \to 0$) limit is taken at the end; we will be concerned with this limit in the subsequent work. This form of ζ is independent of the system of units (SI or CGS) used and expresses the polarisability of the TLA as a dimensionless number. One of the advantages of this formalism is that ζ can take, at the outset, any complex value. For far-detuned atoms, for example, ζ is approximately real, while on resonance it is purely imaginary. Going a step further, we can use this parameter as an abstract quantity representing a general 1D 'scatterer' with (amplitude) reflectivity $\mathfrak{r}$ and transmissivity $\mathfrak{t}$, noting that for real ζ the scatterer absorbs none of the incident energy ($|\mathfrak{r}|^2 + |\mathfrak{t}|^2 = 1$). In Part II we will apply this concept to form a very physical link between the cooling of atoms in radiation fields and optomechanics, which concerns itself with the manipulation of mesoscopic optical elements using light.

Let us make some final comments about Eq. (1.42). First of all, as can easily be verified, this definition for ζ obeys the Kramers–Kronig relations [49]. However, if we rewrite

$$\zeta(\omega) = -\frac{\sigma_{\mathrm{a}}}{2\sigma_{\mathrm{L}}}\frac{\Gamma}{\omega - \omega_0 + i\Gamma}\,, \tag{1.43}$$

whereby $\zeta = \zeta(\omega_{\mathrm{L}})$ in Eq. (1.42), we can immediately see that $\zeta(-\omega) \neq \left[\zeta(\omega)\right]^*$. This immediately leads to problems. For let us assume that, in the time domain, $\zeta(t)$ is real, which is equivalent to asserting that $\langle\boldsymbol{d}\rangle$ in Eq. (1.31) is real. Then, using the definition

of the Fourier transform,

$$\zeta(\omega) = \int_{-\infty}^{\infty} e^{-\mathrm{i}\omega t} \zeta(t)\,\mathrm{d}t\,, \text{ so that } \zeta(-\omega) = \int_{-\infty}^{\infty} e^{\mathrm{i}\omega t} \zeta(t)\,\mathrm{d}t = \left[\zeta(\omega)\right]^* ; \qquad (1.44)$$

something is not right in our definition of ζ. Indeed, a more rigorous treatment ignoring the RWA gives [50]

$$\zeta(\omega) = -\frac{\sigma_{\mathrm{a}}}{2\sigma_{\mathrm{L}}} \left(\frac{\Gamma}{\omega - \omega_0 + \mathrm{i}\Gamma} - \frac{\Gamma}{\omega + \omega_0 + \mathrm{i}\Gamma} \right), \qquad (1.45)$$

which satisfies the aforementioned equality. In all cases we will be concerned with, however, $|\omega - \omega_0|, \Gamma \lll \omega, \omega_0$—the RWA is valid—in which case the second term in the above expression can be safely neglected and Eq. (1.45) reduces to Eq. (1.43).

1.5 Energy balance: Work done on a two-level atom

Consider a small interval between a time t and a time $t + \mathrm{d}t$, where $\mathrm{d}t$ is infinitesimally small. During this time interval, the electric field incident on the TLA can be taken to be constant, $\boldsymbol{\mathcal{E}}_0 \cos(\omega_{\mathrm{L}} t)$, but the dipole moment of the TLA can change, say, due to the more rapid motion of the atomic electrons. The rate of work done, averaged over an optical cycle, by the field on the dipole is then [44]

$$\begin{aligned} P &= \overline{\boldsymbol{\mathcal{E}}_0 \cos(\omega_{\mathrm{L}} t) \cdot \langle \dot{\boldsymbol{d}} \rangle} \\ &= 2\epsilon_0 \omega_{\mathrm{L}} |\boldsymbol{\mathcal{E}}_0|^2 \, \mathrm{Im}\{\chi\} \,. \end{aligned} \qquad (1.46)$$

By making use of the definition of χ, the OBE, and the assumption that Ω is real, we can show that $P = 2\hbar\omega_{\mathrm{L}}\Gamma\boldsymbol{\rho}_{\mathrm{ee}}^{\mathrm{st}}$. Physically, P is the average power absorbed by the atom. For an atom at rest, this must be equal to the energy lost by the atom per unit time through scattering of photons. Dividing P by the energy per incident photon, $\hbar\omega_{\mathrm{L}}$, gives the number of photons scattered per unit time by the atom, $R = 2\Gamma\boldsymbol{\rho}_{\mathrm{ee}}^{\mathrm{st}}$. This justifies Eq. (1.34).

Two facts emerge from Eq. (1.46) that are important for our discussion. First of all, a TLA with real χ will experience no photon scattering, i.e., scattering is significantly suppressed when $\Delta_{\mathrm{L}} \gg 2\Gamma$. Secondly, and more importantly, suppose that $\boldsymbol{d}$ is delayed with respect to $\boldsymbol{\mathcal{E}}$. Then an extra phase factor, let us say φ, appears in Eq. (1.46) such

that $P = 2\epsilon_0\omega_{\mathrm{L}}|\boldsymbol{\mathcal{E}}_0|^2 \operatorname{Im}\{\chi e^{\mathrm{i}\varphi}\}$. For $\varphi \neq 0$, the *real* component of χ can also lead to exchange of energy between the TLA and the electric field. This is exploited in cooling mechanisms that rely on optical pumping in polarisation gradients (see, for example, Section 3.4 and Ref. [14] as well as the concluding remarks in the next section).

A final remark can be made about the work done on a TLA in an optical potential. Indeed, the work done on a TLA undergoing small displacements in the field is not, in general, equal to the change in the potential energy of the atom in the field [14] because the energy in the electromagnetic field itself changes. The relation "work done = change of potential energy" is only valid for closed systems, and because the system we are considering is patently open (the light leaving the system carries away energy) we can not expect these two quantities to be equal. Care must be taken, then, when deriving forces from gradients of optical potentials.

1.6   Forces on a two-level atom

Under most circumstances, excluding of course Bose–Einstein condensation and related phenomena, we can assume that the spread of the wavefunction of a TLA is much smaller than the optical wavelength. The force on a TLA interacting with an incident field is $\boldsymbol{F} = \boldsymbol{\nabla}\big(\langle\boldsymbol{d}\rangle \cdot \boldsymbol{\mathcal{E}}\big)$, evaluated at the position of the atom $(\boldsymbol{r} = \boldsymbol{0})$; this follows from Ehrenfest's theorem [32]. Let us set $\boldsymbol{\mathcal{E}} = \boldsymbol{\mathcal{E}}_0 \cos\big[\omega_{\mathrm{L}}t + \phi(\boldsymbol{r})\big]$, with $\phi(\boldsymbol{0}) = 0$. Then, we have

$$\boldsymbol{F} = \left[\sum_i \langle\boldsymbol{d}_i\rangle \cdot \boldsymbol{\nabla}\big(\boldsymbol{\mathcal{E}}_0\big)_i\right]\cos\big(\omega_{\mathrm{L}}t\big) - \big[\boldsymbol{\nabla}\phi(\boldsymbol{r})\big]\langle\boldsymbol{d}\rangle \cdot \boldsymbol{\mathcal{E}}_0 \sin\big(\omega_{\mathrm{L}}t\big)\,, \qquad (1.47)$$

where the subscripted i denotes the spatial dimension and the sum runs over $i = x, y, z$. Moreover, Eq. (1.31) reduces to

$$\langle\boldsymbol{d}\rangle = 2\boldsymbol{d}_{\mathrm{eg}}\big[u^{\mathrm{st}}\cos\big(\omega_{\mathrm{L}}t\big) - v^{\mathrm{st}}\sin\big(\omega_{\mathrm{L}}t\big)\big]\,. \qquad (1.48)$$

Putting the last two equations together, we can express the time-averaged force acting on the TLA, assuming real Ω, as

$$\begin{aligned}\boldsymbol{F} &= u^{\mathrm{st}}\boldsymbol{\nabla}\big(\boldsymbol{d}_{\mathrm{eg}} \cdot \boldsymbol{\mathcal{E}}_0\big) + v^{\mathrm{st}}\boldsymbol{d}_{\mathrm{eg}} \cdot \boldsymbol{\mathcal{E}}_0\boldsymbol{\nabla}\phi(\boldsymbol{r}) \\ &= -\hbar u^{\mathrm{st}}\boldsymbol{\nabla}\Omega - \hbar\Omega v^{\mathrm{st}}\boldsymbol{\nabla}\phi(\boldsymbol{r})\,,\end{aligned} \qquad (1.49)$$

since $\boldsymbol{d}_{\mathrm{eg}}$ has no spatial dependence on this scale. We can give this equation more physical meaning by using Eqs. (1.29) to obtain

$$u^{\mathrm{st}} = \frac{\Omega}{2}\frac{\Delta_{\mathrm{L}}}{\Delta_{\mathrm{L}}^2 + \Gamma^2 + \Omega^2/2} \ \ \text{and} \ \ v^{\mathrm{st}} = \frac{\Omega}{2}\frac{\Gamma}{\Delta_{\mathrm{L}}^2 + \Gamma^2 + \Omega^2/2}, \tag{1.50}$$

whereby

$$F = \underbrace{-\frac{1}{2}\frac{\hbar\Omega\Delta_{\mathrm{L}}}{\Delta_{\mathrm{L}}^2 + \Gamma^2 + \Omega^2/2}\boldsymbol{\nabla}\Omega}_{\text{reactive force}} \underbrace{-\frac{1}{2}\frac{\hbar\Omega^2\Gamma}{\Delta_{\mathrm{L}}^2 + \Gamma^2 + \Omega^2/2}\boldsymbol{\nabla}\phi(\boldsymbol{r})}_{\text{dissipative force}} \tag{1.51a}$$

$$= \begin{cases} -\dfrac{1}{2}\dfrac{\hbar\Omega\Delta_{\mathrm{L}}}{\Delta_{\mathrm{L}}^2 + \Gamma^2}\boldsymbol{\nabla}\Omega - \dfrac{1}{2}\dfrac{\hbar\Omega^2\Gamma}{\Delta_{\mathrm{L}}^2 + \Gamma^2}\boldsymbol{\nabla}\phi(\boldsymbol{r}) & \text{for } s \to 0 \\[3mm] -\hbar\Delta_{\mathrm{L}}\dfrac{\boldsymbol{\nabla}\Omega}{\Omega} - \hbar\Gamma\boldsymbol{\nabla}\phi(\boldsymbol{r}) & \text{for } s \to \infty\,. \end{cases} \tag{1.51b}$$

We note that, in the limit of high intensity ($s \to \infty$), the force acting on the TLA tends towards a limit of a dissipative force whose strength is independent of the intensity. In the following sections we will restrict ourselves to the limit of small s. This is useful in considering the interaction of a TLA with a standing wave. For small intensities, the TLA behaves as if it interacts with the two running waves making up the standing wave independently. For very high intensities, the process of absorption of photons from one running wave and stimulated emission into the other running wave can become important and modify the interaction significantly.

Another way of looking at this is to recall that the force is the gradient of the product of the induced dipole and the local electric field. The gradient operation is linear, so we need not concern ourselves with its effects. However, suppose that the electric field at the position of the TLA is a sum of two fields, $\boldsymbol{\mathcal{E}}_1 + \boldsymbol{\mathcal{E}}_2$, with the corresponding induced dipole being equal to $\langle \boldsymbol{d}_1 \rangle + \langle \boldsymbol{d}_2 \rangle$. Then, the force on the TLA is $\boldsymbol{\nabla}\big[(\langle \boldsymbol{d}_1 \rangle + \langle \boldsymbol{d}_2 \rangle) \cdot (\boldsymbol{\mathcal{E}}_1 + \boldsymbol{\mathcal{E}}_2)\big]$, which has two extra terms in addition to the sum of the two independent forces, $\boldsymbol{\nabla}(\langle \boldsymbol{d}_1 \rangle \cdot \boldsymbol{\mathcal{E}}_1) + \boldsymbol{\nabla}(\langle \boldsymbol{d}_2 \rangle \cdot \boldsymbol{\mathcal{E}}_2)$. If the spatial (temporal) average of these extra two terms over a wavelength is zero (this happens, e.g., when there is no coherence between the two electric fields), the two forces can therefore be computed separately and added to give the total spatially (temporally) averaged force.

Let us end this section with a note on the dipole force, which corresponds to the term

in the force proportional to $\boldsymbol{\nabla}\Omega$ (the reactive force). Eq. (1.31) and Eq. (1.46) tell us that only v^{st} can give rise to a global exchange of energy between the TLA and the light field. The reactive component of F above can, in fact, be derived from a potential. In other words, the dipole force is conservative. This is not true in general, however. Employing the same arguments as before, if $\langle \boldsymbol{d} \rangle$ is delayed with respect to the field, a component of v^{st} enters the dipole force and it is therefore no longer constrained to be strictly conservative.

1.7   The Fluctuation–Dissipation Theorem

In the case of the systems that we will investigate, the fluctuation–dissipation theorem is a relation between the systematic (dissipative) and fluctuating components of a force acting on a particle. We shall make extensive use of this theorem in the form of Eq. (1.61) below.

Consider a particle interacting with the radiation field, such that the force acting on the particle, as a function of time, is $F(t) = F_0(t) + F_{\mathrm{L}}(t)$, where the first term describes a continuous force that, for example, acts to dampen the particle's motion and the second term is a Langevin force, which has a zero time average and describes the instantaneous fluctuations of the force about its average. In other words, $\langle F(t) \rangle = \langle F_0(t) \rangle$.[8] Now, consider

$$
\begin{aligned}
\langle F(t)F(t') \rangle &= \langle F_0(t)F_0(t') \rangle + \langle F_0(t)F_{\mathrm{L}}(t') \rangle + \langle F_{\mathrm{L}}(t)F_0(t') \rangle + \langle F_{\mathrm{L}}(t)F_{\mathrm{L}}(t') \rangle \\
&= \langle F_0(t) \rangle\langle F_0(t') \rangle + \langle F_0(t) \rangle\langle F_{\mathrm{L}}(t') \rangle + \langle F_{\mathrm{L}}(t) \rangle\langle F_0(t') \rangle + \langle F_{\mathrm{L}}(t)F_{\mathrm{L}}(t') \rangle \\
&= \langle F(t) \rangle\langle F(t') \rangle + \langle F_{\mathrm{L}}(t)F_{\mathrm{L}}(t') \rangle \,,
\end{aligned}
\tag{1.52}
$$

where the time average is taken on a timescale that is short with respect to the timescale for variations in $F_0(t)$ but long with respect to that for $F_{\mathrm{L}}(t)$, whereby $\langle F_0(t)F_{\mathrm{L}}(t') \rangle = \langle F_0(t) \rangle\langle F_{\mathrm{L}}(t') \rangle = 0$. The correlation function for $F_{\mathrm{L}}(t)$ on this timescale is assumed to have the form

$$
\langle F_{\mathrm{L}}(t)F_{\mathrm{L}}(t') \rangle \approx D\,\delta(t - t') \,,
\tag{1.53}
$$

---

[8] A note about notation is due: in this section we use the angle brackets, $\langle \cdot \rangle$, to represent the average for a classical force or the expectation value for a quantised force, depending on the nature of the force.

where D is some real number; i.e.,

$$D\,\delta(t-t') = \langle F(t)F(t')\rangle - \langle F(t)\rangle\langle F(t')\rangle\,, \tag{1.54}$$

cf. Refs. [51] and [52], or

$$\tfrac{1}{2}D = \int_0^\infty \Big(\langle F(t)F(t')\rangle - \langle F(t)\rangle\langle F(t')\rangle\Big)\mathrm{d}t'\,. \tag{1.55}$$

Let us now specify $F_0 = -\varrho v$, where the *cooling coefficient* ϱ is some (positive) damping constant and v the velocity of the particle (in 1D). The total force acting on the particle, say of mass m, is then

$$\begin{aligned}
F(t) = \frac{\mathrm{d}}{\mathrm{d}t}p(t) &= -\varrho v(t) + F_{\mathrm{L}}(t) \\
&= m\frac{\mathrm{d}}{\mathrm{d}t}v(t)\,.
\end{aligned} \tag{1.56}$$

We now multiply this equation by the integrating factor and integrate it from time $t=0$ to some general time t. Then:

$$\begin{aligned}
\int_0^t \left(\frac{\mathrm{d}}{\mathrm{d}t}v(t)\right)\bigg|_{t=t'} e^{(\varrho/m)t'}\mathrm{d}t' &= -\int_0^t (\varrho/m)v(t')e^{(\varrho/m)t'}\mathrm{d}t' + \frac{1}{m}\int_0^t F_{\mathrm{L}}(t')e^{(\varrho/m)t'}\mathrm{d}t' \\
&= -\int_0^t v(t')\left(\frac{\mathrm{d}}{\mathrm{d}t}e^{(\varrho/m)t}\right)\bigg|_{t=t'}\mathrm{d}t' + \frac{1}{m}\int_0^t F_{\mathrm{L}}(t')e^{(\varrho/m)t'}\mathrm{d}t'\,,
\end{aligned} \tag{1.57}$$

so that

$$\begin{aligned}
v(t)e^{(\varrho/m)t} &= v(0) + \frac{1}{m}\int_0^t F_{\mathrm{L}}(t')e^{(\varrho/m)t'}\mathrm{d}t'\,,\ \text{ or} \\
v(t) &= v(0)e^{-(\varrho/m)t} + \frac{1}{m}\int_0^t F_{\mathrm{L}}(t')e^{-(\varrho/m)(t-t')}\mathrm{d}t'\,.
\end{aligned} \tag{1.58}$$

Let us average this relation over the same timescale as above. Then $\langle v(t)\rangle = v(0)e^{-(\varrho/m)t}$, whereby the width of the velocity distribution, defined as

$$\sigma_v^2(t) = \big\langle\big[v(t) - \langle v(t)\rangle\big]^2\big\rangle\,, \tag{1.59}$$

is given by

$$\sigma_v^2(t) = \frac{1}{m^2} \int_0^t \int_0^t \langle F_L(t'') F_L(t') \rangle e^{-(\varrho/m)(t-t')} e^{-(\varrho/m)(t-t'')} dt' dt''$$

$$= \frac{1}{m^2} \int_0^t \int_0^t D\delta(t' - t'') e^{-(\varrho/m)(t-t')} e^{-(\varrho/m)(t-t'')} dt' dt''$$

$$= \frac{D}{m^2} \int_0^t e^{-2(\varrho/m)(t-t')} dt' = \frac{D}{2m\varrho} \left[1 - e^{-2(\varrho/m)t} \right]. \tag{1.60}$$

For small values of t, $\sigma_v^2(t) \approx Dt/m^2$. The width of the momentum distribution is similarly given by $\sigma_p^2(t) \approx Dt$, whereby D is, by definition, the momentum diffusion coefficient. For very long times we can make two observations. Firstly, $\langle v(t) \rangle = 0$, so that the particle is cooled to zero mean velocity; secondly, $\sigma_v^2(t) = D/(2m\varrho)$. We will not go into any further depth here, but it can be shown [53] that all higher-order correlation functions vanish at long timescales. Moreover, this further implies that the velocity distribution of an ensemble of such particles is Gaussian, of the form $\exp\left[-v^2/(\sigma_v/2)^2\right]$, with the factor of $\frac{1}{2}$ arising due to the symmetry of the distribution. Comparing this with a Maxwell-Boltzmann distribution in thermal equilibrium at temperature T, for which $\sigma_v^2 = k_B T/(2m)$ with k_B being the Boltzmann constant, we can therefore calculate the equilibrium temperature of our particle:

$$k_B T = \frac{D}{\varrho}. \tag{1.61}$$

This is in fact of the same form as that obtained by Einstein [54] in his discussion of the Brownian motion of particles suspended in a liquid. Eq. (1.61) links the fluctuating and dissipating forces experienced by the particle to its equilibrium temperature. Although the justification given here is not completely general, namely in terms of demanding a linear friction force and a constant momentum diffusion constant, Eq. (1.61) is a good approximation under most circumstances of interest. See Ref. [55] for a slightly more general treatment, and Ref. [56] for a treatment based on the theory of quantum noise.[9] The results above can easily be adapted for forces acting in 3D by replacing the forces F, F_0, F_L with their vector counterparts $\boldsymbol{F}$, $\boldsymbol{F_0}$, $\boldsymbol{F_L}$; replacing products of the type $\mathcal{F}(t)\mathcal{F}'(t')$ with $\boldsymbol{\mathcal{F}}(t) \cdot \boldsymbol{\mathcal{F}}'(t')$ ($\mathcal{F}, \mathcal{F}' = F, F_0, F_L$); and also replacing v with $\boldsymbol{v}$.

---

[9] Considerations related to the general quantum case imply the failure of the Onsager hypothesis, which states that "the average regression of fluctuations will obey the same laws as the corresponding macroscopic irreversible process" [57], in cases such as where strong coupling between the system and the noise bath is allowed. Put differently, the quantum regression theorem cannot be called a 'theorem' in the mathematical sense. See the discussions in Refs. [58] and [59] for further details.
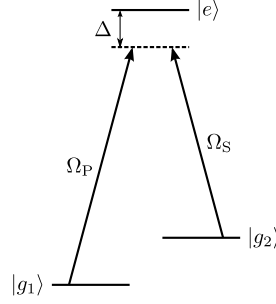
FIGURE 1.1: Prototypical 'Λ'–type system used to describe stimulated Raman transitions. The transition between the ground states is taken to be dipole-forbidden.

1.8   Beyond two-level atoms

The two-level atom is a useful, but rather crude, approximation. As noted by Dalibard, Reynaud and Cohen–Tannoudji [60], amongst many others, several interesting physical mechanisms can only be explained when one includes the manifold of Zeeman sublevels, Section 1.1, that occur in the energy level structure of real atoms into the model. Indeed, this manifold of sublevels can be included into the definition of the ζ, above, by generalising it into the polarisability tensor, defined as the steady-state expectation value of the polarisability operator $\hat{\boldsymbol{\zeta}}$,

$$\boldsymbol{\zeta} = \mathrm{Tr}\big(\tilde{\boldsymbol{\rho}}^{\mathrm{st}} \cdot \hat{\boldsymbol{\zeta}}\big) = \sum_{i,j} \langle j|\tilde{\boldsymbol{\rho}}^{\mathrm{st}}|i\rangle\langle i|\hat{\boldsymbol{\zeta}}|j\rangle \,, \tag{1.62}$$

where $\tilde{\boldsymbol{\rho}}^{\mathrm{st}}$, as defined previously, is the steady-state density matrix describing the system and the summation runs over all the internal sublevels of the atom. The matrix elements of the polarisability operator $\hat{\boldsymbol{\zeta}}$, defined similarly to Eq. (14.9-24) of Ref. [30], read in the general μ, ν basis

$$\langle i|\hat{\boldsymbol{\zeta}}|j\rangle = \zeta_0 \sum_e \begin{bmatrix} \langle i|\hat{\boldsymbol{d}}_\mu|e\rangle\langle e|\hat{\boldsymbol{d}}_\mu|j\rangle & \langle i|\hat{\boldsymbol{d}}_\mu|e\rangle\langle e|\hat{\boldsymbol{d}}_\nu|j\rangle \\ \langle i|\hat{\boldsymbol{d}}_\nu|e\rangle\langle e|\hat{\boldsymbol{d}}_\mu|j\rangle & \langle i|\hat{\boldsymbol{d}}_\nu|e\rangle\langle e|\hat{\boldsymbol{d}}_\nu|j\rangle \end{bmatrix} \,, \tag{1.63}$$

where ζ_0 embodies the dimensional constants and the frequency dependence of the polarisability of the atom (see, for example, Ref. [50]):

$$\zeta_0 = -\frac{k}{2\sigma_{\mathrm{L}}} \frac{1}{\Delta_{\mathrm{L}} + i\Gamma} \,, \tag{1.64}$$

In the above equation, the dipole moment operator $\hat{\boldsymbol{d}}_\mu$ ($\hat{\boldsymbol{d}}_\nu$) is related to the μ (ν) polarised light field and the sum runs over all the internal sublevels, e, of the atom. The

matrix elements of $\hat{\boldsymbol{d}}_\mu$ ($\hat{\boldsymbol{d}}_\nu$) are given by the appropriate Clebsch–Gordan coefficients. We will explore the implications of this generalised polarisability tensor in Part II, where it will be used to give an alternative derivation of Sisyphus cooling [14].

Stimulated Raman transitions [29] also require multilevel atoms by their very definition. The basic model for an atom undergoing a stimulated Raman transition is a three-level 'Λ'–type level system (Fig. 1.1): an atom having two 'ground' states $|g_1\rangle$ and $|g_2\rangle$, and one excited state $|e\rangle$. The transition between $|g_1\rangle$ and $|g_2\rangle$ is always dipole-forbidden,[10] due to parity conservation, and the remaining two transitions are coupled by 'Pump' ($|g_1\rangle \leftrightarrow |e\rangle$) and 'Stokes' ($|g_2\rangle \leftrightarrow |e\rangle$) fields, characterised by strengths Ω_P and Ω_S, respectively. For simplicity, we assume that both coupling fields have a detuning Δ from resonance. Under these conditions, Rabi oscillations occur between the two ground states at an effective frequency [61]

$$\frac{|\Omega_P \Omega_S^*|}{2\Delta}\,. \tag{1.65}$$

It has often been assumed in the literature (see, for example, Ref. [62, §2.1]), that the hyperfine structure of $|e\rangle$ can easily be taken into account by summing over the appropriate multiple routes, giving an effective Rabi frequency

$$\sum_i \frac{|\Omega_{P;i} \Omega_{S;i}^*|}{2\Delta}\,, \tag{1.66}$$

where the label i denotes the coupling to the ith sublevel of $|e\rangle$, and Δ is assumed to be much larger than the energy splittings between the different sublevels. Indeed, it was only in a recent publication by Bateman, Xuereb and Freegarde [61] that this was proven mathematically to be the case in general, by diagonalising the appropriate multilevel Hamiltonian.

For completeness, we will now briefly go through the main arguments in Ref. [61]. This work was originally published as Bateman, J., Xuereb, A., & Freegarde, T., Phys. Rev. A **81**, 043808 (2010).[11] The energy structure of the atom we consider is a straightforward extension of that shown in Fig. 1.1, where we maintain the two ground states $|g_1\rangle$ and

---

[10] In other words, an atom in one of the $|g_i\rangle$ states will remain in that state, justifying their designation as 'ground' states.

[11] JB set up the problem, solved the three-level system case, provided the interpretation and wrote the paper; AX produced the analytical formulation of the eigensystem of the general $(N+2)$-level Hamiltonian.

$|g_2\rangle$, but where a similar hyperfine structure is taken to exist for the excited state—the state $|e\rangle$ splits into $|e_1\rangle, |e_2\rangle, \ldots, |e_N\rangle$, say. The coupling between the two beams and the different excited sublevels may not be identical, and we therefore set $\Omega_{\mathrm{P};i}$ and $\Omega_{\mathrm{S};i}$ to be, respectively, the coupling strengths for the transitions $|g_1\rangle \leftrightarrow |e_i\rangle$ and $|g_2\rangle \leftrightarrow |e_i\rangle$. The Hamiltonian for this system, after making the RWA and transforming to the interaction picture [29],[12] can be written out in state vector notation as

$$\boldsymbol{H}_{\mathrm{A}} = \begin{bmatrix} 0 & 0 & \frac{1}{2}\Omega_{\mathrm{P};1} & \frac{1}{2}\Omega_{\mathrm{P};2} & \ldots \\ 0 & 0 & \frac{1}{2}\Omega_{\mathrm{S};1}e^{\mathrm{i}\delta t} & \frac{1}{2}\Omega_{\mathrm{S};3}e^{\mathrm{i}\delta t} & \ldots \\ \frac{1}{2}\Omega_{\mathrm{P};1}^{*} & \frac{1}{2}\Omega_{\mathrm{S};1}^{*}e^{-\mathrm{i}\delta t} & -\Delta & 0 & \ldots \\ \frac{1}{2}\Omega_{\mathrm{P};2}^{*} & \frac{1}{2}\Omega_{\mathrm{S};2}^{*}e^{-\mathrm{i}\delta t} & 0 & -\Delta & \ldots \\ \vdots & \vdots & \vdots & \vdots & \ddots \end{bmatrix}, \tag{1.67}$$

which acts on the state vector

$$\begin{pmatrix} |g_1\rangle \\ |g_2\rangle \\ |e_1\rangle \\ |e_2\rangle \\ \vdots \end{pmatrix}. \tag{1.68}$$

In Eq. (1.67) we made the approximation that the detuning of the Pump beam is Δ from each of the excited states, and that of the Stokes beam is $\Delta + \delta$. This approximation requires that Δ be much larger than the splittings between the excited state sublevels. We solve the Schrödinger equation with this Hamiltonian by using unitary transformations to find a basis where the time evolution of the states is simple and the transformed Hamiltonian is diagonal. When such a change of basis is done, say by using the transformation matrix $\boldsymbol{O}_{\mathrm{BA}}$, then the Hamiltonian in the new basis, $\boldsymbol{H}_{\mathrm{B}}$, reads [29]

$$\boldsymbol{H}_{\mathrm{B}} = \boldsymbol{O}_{\mathrm{BA}}\left(\boldsymbol{H}_{\mathrm{A}}\boldsymbol{O}_{\mathrm{BA}}^{-1} - \mathrm{i}\frac{\partial}{\partial t}\boldsymbol{O}_{\mathrm{BA}}^{-1}\right). \tag{1.69}$$

Choosing $\boldsymbol{O}_{\mathrm{BA}}$ to be the matrix of eigenvectors of $\boldsymbol{H}_{\mathrm{A}}$, the first term in this equation is simply the matrix of its eigenvalues. Upon diagonalising $\boldsymbol{H}_{\mathrm{A}}$, it turns out that two of the eigenvectors are superpositions of the two ground states and are decoupled from the

---

[12] The interaction picture, essentially, removes the fast time evolution from the state vectors and is accomplished by a transformation of the type in Eq. (1.69) where the transformation matrix is the diagonal matrix of eigenvalues of the time-independent part of the Hamiltonian. It lies in between the Schrödinger and the Heisenberg pictures. See Ref. [27, Complement G_{III}].

rest of the levels in the limit of large detuning. The system can therefore be described as an effective two-level system.

Indeed, we set

$$\|\boldsymbol{H}_{\mathrm{B}} - \lambda\boldsymbol{I}\| = 0\,, \tag{1.70}$$

where $\boldsymbol{I}$ is the $(N + 2) \times (N + 2)$ identity matrix and λ a parameter. This equation simplifies to the fourth-order polynomial equation

$$16\lambda^2(\Delta - \lambda)^2 + 4\lambda(\Delta - \lambda)\big(\|\boldsymbol{\Omega}_{\mathrm{P}}\|^2 + \|\boldsymbol{\Omega}_{\mathrm{S}}\|^2\big) + \|\boldsymbol{\Omega}_{\mathrm{P}}\|^2\|\boldsymbol{\Omega}_{\mathrm{S}}\|^2 - |\boldsymbol{\Omega}_{\mathrm{P}} \cdot \boldsymbol{\Omega}_{\mathrm{S}}^*|^2 = 0\,, \tag{1.71}$$

where we have defined the vectors

$$\boldsymbol{\Omega}_{\mathrm{P}} = \begin{pmatrix} \Omega_{\mathrm{P};1} \\ \Omega_{\mathrm{P};2} \\ \vdots \end{pmatrix} \text{ and } \boldsymbol{\Omega}_{\mathrm{S}} = \begin{pmatrix} \Omega_{\mathrm{S};1} \\ \Omega_{\mathrm{S};2} \\ \vdots \end{pmatrix}. \tag{1.72}$$

The constant term, which is independent of λ, in Eq. (1.71) is also independent of Δ, so that the product of all the solutions, $\prod_i \lambda_i$, is also independent of Δ. Since not all the λ_i are independent of Δ, because the equation is also a second-order polynomial in Δ, then *at least one* eigenvalue must disappear as $|\Delta| \to \infty$. In this limit, we can therefore make the approximation $(\Delta - \lambda) \to \Delta$. The resulting equation has roots

$$\lambda_{\pm} = \frac{-\big(\|\boldsymbol{\Omega}_{\mathrm{P}}\|^2 + \|\boldsymbol{\Omega}_{\mathrm{S}}\|^2\big) \pm \sqrt{\big(\|\boldsymbol{\Omega}_{\mathrm{P}}\|^2 - \|\boldsymbol{\Omega}_{\mathrm{S}}\|^2\big)^2 + 4|\boldsymbol{\Omega}_{\mathrm{P}} \cdot \boldsymbol{\Omega}_{\mathrm{S}}^*|^2}}{8\Delta}\,; \tag{1.73}$$

the respective eigenvectors are superpositions of $|g_1\rangle$ and $|g_2\rangle$. We now return to $\boldsymbol{H}_{\mathrm{B}}$ and constrain ourselves to the Hilbert space of the two ground states, whereupon we can write

$$\boldsymbol{H}_{\mathrm{B}} = \begin{bmatrix} -\delta\sin^2(\theta) & -\delta e^{\mathrm{i}\delta t}\cos(\theta)\sin(\theta) \\ -\delta e^{-\mathrm{i}\delta t}\cos(\theta)\sin(\theta) & \delta\sin^2(\theta) + \tilde{\Omega}_{\mathrm{B}} \end{bmatrix}\,; \tag{1.74}$$

in this restricted Hilbert space, we have

$$\boldsymbol{O}_{\mathrm{BA}} = \begin{bmatrix} \cos(\theta) & e^{\mathrm{i}\delta t}\sin(\theta) \\ -e^{-\mathrm{i}\delta t}\sin(\theta) & \cos(\theta) \end{bmatrix}. \tag{1.75}$$

In the preceding Hamiltonian, we have made use of the definitions, analogous to the two-level Rabi system,

$$\tilde{\Omega}_{\mathrm{B}} = \sqrt{\Omega_{\mathrm{B}}^2 + \Delta_{\mathrm{B}}^2}, \text{ and } \tan(\theta) = \frac{\Delta_{\mathrm{B}} - \tilde{\Omega}_{\mathrm{B}}}{\Omega_{\mathrm{B}}}, \tag{1.76}$$

where

$$\Omega_{\mathrm{B}} = \frac{|\boldsymbol{\Omega}_{\mathrm{P}} \cdot \boldsymbol{\Omega}_{\mathrm{S}}^*|}{2\Delta}, \text{ and } \Delta_{\mathrm{B}} = \frac{\|\boldsymbol{\Omega}_{\mathrm{P}}\|^2 - \|\boldsymbol{\Omega}_{\mathrm{S}}\|^2}{4\Delta}. \tag{1.77}$$

Indeed, we immediately notice that the first relation in Eq. (1.77) implies that the naive summing over states is formally correct in this limit. In the second relation, Δ_{B} can be identified as the light shift, as justified below.

We further transform this system into a simplified basis by first switching to a time-independent Hamiltonian by means of the matrix

$$\boldsymbol{O}_{\mathrm{CB}} = \begin{bmatrix} 1 & 0 \\ 0 & e^{\mathrm{i}\delta t} \end{bmatrix}, \tag{1.78}$$

followed by the rotation through an angle ϕ, through a matrix $\boldsymbol{O}_{\mathrm{DC}}$, defined by

$$\tan(2\phi) = \frac{\delta \sin(2\theta)}{\tilde{\Omega}_{\mathrm{B}} - \delta \cos(2\theta)}. \tag{1.79}$$

The difference between the two diagonal elements of the resulting Hamiltonian gives the oscillation frequency for phase evolution of the two dressed states, $\tilde{\Omega}_{\mathrm{D}} = \sqrt{\Omega_{\mathrm{B}}^2 + \Delta_{\mathrm{D}}^2}$, where $\Delta_{\mathrm{D}} = \Delta_{\mathrm{B}} - \delta$ is the modified detuning, justifying our identification of Δ_{B} with the light shift.

By concatenating the unitary transformations, we can rewrite the bare states in terms of these final dressed states, giving an expression of the form

$$\cos(\theta + \phi)d_1 - \sin(\theta + \phi)d_2 e^{\mathrm{i}\tilde{\Omega}_{\mathrm{D}}t} \tag{1.80}$$

for the amplitude of $|g_1\rangle$, where d_1 and d_2 are the initial amplitudes of the two dressed states. Immediately, we note that the oscillation between $|g_1\rangle$ and $|g_2\rangle$ has a peak-to-peak amplitude that is bounded by

$$\sin[2(\theta + \phi)] = \frac{\Omega_{\mathrm{B}}}{\sqrt{\Omega_{\mathrm{B}}^2 + \Delta_{\mathrm{D}}^2}} \tag{1.81}$$

This envelope function describes a power-broadened Lorentzian, centred on the light-shifted frequency difference between the two ground states. It represents the maximum possible population transfer, and any oscillation will be contained within this envelope.

Chapter 2

Trapping and cooling atoms

> There is room for one further general remark. [...] [I]n general one restricts oneself to a discussion of the *energy* exchange, without taking the *momentum* change into account. One feels easily justified in this, because the smallness of the impulses transmitted by the radiation field implies that these can almost always be neglected in practice [...].
>
> A. Einstein, Physikalische Zeitschrift **18**, 121 (1917)

The general description given previously of the forces acting on two-level atoms allows the exploration of a number of laser trapping and cooling configurations currently used. In particular, I will look at dipole traps in Section 2.1, optical molasses in Section 2.2, and the magneto–optical trap (MOT) in Section 2.3. Following these, I will discuss a more recent attempt at a generally applicable laser cooling method, so-called 'mirror-mediated cooling', Section 2.6, which naturally lends itself to being extended in various ways, as shall be seen in Section 2.7 and Part II.

2.1 Dipole traps

We have already remarked that the 'reactive force' in Eq. (1.51a) is often called the dipole force. The dipole force is proportional to the gradient of the magnitude of the Rabi frequency and is therefore sensitive to spatial nonuniformities in the electric field intensity that the atom is interacting with. In other words, an atom immersed in a tightly focussed light field will experience a force that attracts it to, or repels it from,

the focus. Specifically, if $\Delta_\mathrm{L} < 0$ the force will point towards increasing light intensity; conversely if $\Delta_\mathrm{L} > 0$, the force points away from the focus. In the former case, the atom can be trapped at the focus of the beam, whereas in the latter case configurations can be found having a field minimum at some point in space [63], raising the possibility of trapping the atom in such regions.

The dipole force is a very general mechanism; it applies not only to TLAs, as explained in the preceding paragraph, but to any object that has a nonzero polarisability. Let us consider an object with an induced dipole moment $\boldsymbol{d}$ interacting with an electric field $\boldsymbol{\mathcal{E}}$. Then, the object will experience a (dipole) potential $U = -\boldsymbol{d} \cdot \boldsymbol{\mathcal{E}}$. This potential then gives rise to the dipole force $\boldsymbol{F} = -\boldsymbol{\nabla} U$ in a manner similar to the force experienced by a TLA. We note that this derivation of $\boldsymbol{F}$ implies that the dipole force is conservative; essentially identical arguments to those used when describing the TLA in Section 1.6 hold in the general case too, whereby a delay between $\boldsymbol{d}$ and $\boldsymbol{\mathcal{E}}$ can give rise to a nonconservative term in the dipole force.

This universality inherent in the dipole force makes it a very versatile experimental tool. It has been used to trap atoms in free space [64] and cavities [65], manipulate microspheres [66], viruses and even living cells [67]; it is also essential in achieving fully optical Bose–Einstein condensation [68].

2.2   Optical molasses

Optical molasses historically provided the first proof that purely optical mechanisms can be used to slow down the motion of ensembles of atoms [12]. Let us see how optical molasses work by looking at the behaviour of a TLA inside a standing wave composed of two weak ($s \ll 1$) counterpropagating travelling waves. Eq. (1.51a) is again the key to exploring this interaction. For each travelling wave, having a propagation vector $\pm \boldsymbol{k}$ [i.e., $\phi(\boldsymbol{r}) = \pm \boldsymbol{k} \cdot \boldsymbol{r}$], we can easily see that $\boldsymbol{\nabla}\Omega = 0$—we are thus only concerned with the dissipative force—and $\boldsymbol{\nabla}\phi(\boldsymbol{r}) = \pm \boldsymbol{k}$. Adding the two forces together thus seems to give a zero net force, but this is only because the Doppler shift has not yet been taken into account. Indeed, the frequency for the $\pm \boldsymbol{k}$ wave is seen by the atom to be shifted by $\pm \boldsymbol{k} \cdot \boldsymbol{v}$, i.e., $\Delta_\mathrm{L} \to \Delta_\mathrm{L} \pm \boldsymbol{k} \cdot \boldsymbol{v}$. In effect, then, the total force seen by the atom is

therefore

$$
\begin{aligned}
F_{\mathrm{OM}} &= -\frac{\hbar\Omega^2\Gamma/2}{\left(\Delta_{\mathrm{L}}+\boldsymbol{k}\cdot\boldsymbol{v}\right)^2+\Gamma^2}\boldsymbol{k} + \frac{\hbar\Omega^2\Gamma/2}{\left(\Delta_{\mathrm{L}}-\boldsymbol{k}\cdot\boldsymbol{v}\right)^2+\Gamma^2}\boldsymbol{k} \\
&\approx \frac{2\hbar\Omega^2\Delta_{\mathrm{L}}\Gamma}{\left(\Delta_{\mathrm{L}}^2+\Gamma^2\right)^2}(\boldsymbol{k}\cdot\boldsymbol{v})\boldsymbol{k} \\
&= \frac{2\hbar\Omega^2\Delta_{\mathrm{L}}\Gamma}{\left(\Delta_{\mathrm{L}}^2+\Gamma^2\right)^2}(\boldsymbol{k}\otimes\boldsymbol{k})\boldsymbol{v}\,,
\end{aligned}
\tag{2.1}
$$

with the approximation holding only up to linear order in $\boldsymbol{k}\cdot\boldsymbol{v}\Gamma/\left(\Delta_{\mathrm{L}}^2+\Gamma^2\right)$, and the vector outer product being defined as

$$
\boldsymbol{k}\otimes\boldsymbol{k} = \begin{pmatrix} k_1 \\ k_2 \\ k_3 \end{pmatrix} \otimes \begin{pmatrix} k_1 \\ k_2 \\ k_3 \end{pmatrix} = \begin{bmatrix} k_1^2 & k_1 k_2 & k_1 k_3 \\ k_1 k_2 & k_2^2 & k_2 k_3 \\ k_1 k_3 & k_2 k_3 & k_3^2 \end{bmatrix}.
\tag{2.2}
$$

Let us now constrain ourselves to one dimension, whereby $F, \boldsymbol{v}, \boldsymbol{k} \to F, v, k$. For every photon absorption or emission event that the atom undergoes, it experiences a momentum change $\hbar k$; this process occurs at a rate $2R$, with the factor of 2 arising because of the presence of the two identical beams, and R given by Eq. (1.34). Thus, over small times t, we have $(\delta p)^2/t = 2\hbar^2 k^2 R$. Identifying $\delta p = \sigma_p(t)$, we therefore have the diffusion and cooling coefficients,

$$
D = 2\hbar^2 k^2 R = \frac{\hbar^2 k^2 \Omega^2}{\Delta_{\mathrm{L}}^2+\Gamma^2}\,, \text{ and } \varrho = -\frac{2\hbar k^2 \Omega^2 \Delta_{\mathrm{L}}\Gamma}{\left(\Delta_{\mathrm{L}}^2+\Gamma^2\right)^2}\,,
\tag{2.3}
$$

respectively (cf. Ref. [52]), whereby the equilibrium temperature of the atom is given by

$$
T = \frac{\hbar\Gamma}{2k_{\mathrm{B}}}\left(\frac{|\Delta_{\mathrm{L}}|}{\Gamma}+\frac{\Gamma}{|\Delta_{\mathrm{L}}|}\right),
\tag{2.4}
$$

which only makes sense for $\Delta_{\mathrm{L}} < 0$. T attains its lower bound, known as the Doppler temperature T_{D}, when $\Delta_{\mathrm{L}} = -\Gamma$, at which point

$$
T_{\mathrm{D}} = \frac{\hbar\Gamma}{k_{\mathrm{B}}}\,.
\tag{2.5}
$$

Remarkably, this limiting temperature is independent of the atom's mass m or the intensity of the light beam (recall, however, that we have assumed $s \ll 1$).

A more fundamental limit than the Doppler temperature is due to what is called the

recoil limit; this gives rise to the recoil temperature T_R. Any time an atom absorbs or emits a photon, it undergoes a momentum change of magnitude $\Delta p = \hbar k$. As such, then, the momentum of the atom can be described as a discrete one-dimensional random walk of step size $\pm \hbar k$. After n steps in such a walk, the momentum $p = S_n \hbar k$ of the atom is described by the quantity $S_n = \sum_{i=1}^{n} c_i$, where each $c_i = \pm 1$. The statistics of S_n obeys

$$\langle S_n \rangle = \sum_{i=1}^{n} \langle \pm 1 \rangle = 0 \ \text{and} \ \langle S_n^2 \rangle = \sum_{i=1}^{n} \langle (\pm 1)^2 \rangle = n \,, \qquad (2.6)$$

whereby

$$\sigma_p^2 = \left(\langle S_n^2 \rangle - \langle S_n \rangle^2 \right)(\hbar k)^2 = n(\hbar k)^2 \,, \qquad (2.7)$$

such that the momentum diffusion experienced by the atom is $D = (\hbar k)^2 (n/t)$; the quantity (n/t) has to be interpreted as the rate at which photons interact with the atom. The recoil limit applies to any cooling process involving scattering of photons, and therefore at least one scattering event has to occur on average during such a process. The minimum value for σ_p is therefore achieved when $n = 1$; $\sigma_p = (\hbar k)^2$. Assuming the momentum distribution is Maxwell–Boltzmann,[1] this corresponds to a temperature

$$T_R = \frac{\hbar^2 k^2}{2 k_B m} \,. \qquad (2.8)$$

For a ^{85}Rb atom cycling on the D_2 transition, $T_D = 146 \, \mu K$ and $T_R = 185 \, nK$ (see Ref. [35], but their definition of the recoil temperature is a factor of 2 larger than ours; we use a definition consistent with, e.g., Ref. [71]). Not even the recoil limit is a hard limit, though, with several schemes—such as evaporative cooling [72], and even all-optical schemes like velocity-selective coherent population trapping [71]—being devised to overcome it. Such schemes generally work by ensuring that the target state is subject to much less than one scattering event, on the average.

2.3   Magneto–optical traps

To describe MOTs, we have to give up the TLA model we have pursued throughout most of the preceding sections and appeal to the multilevel structure of realistic atoms.

---

[1] This assumption is not very well-founded; ensembles close to, or below, the recoil limit generally obey different statistics (see, for example, Refs. [69] and [70], and Fig. 2 in Ref. [71]). Nonetheless, in the absence of well-definition, assuming Maxwell–Boltzmann statistics allows us to assign a 'temperature' to such an ensemble.

In particular, let us consider a $J = 1 \to J' = 2$ transition.[2] Our description of the cooling mechanism that dominates in a MOT will be cursory here—to present a unified approach to laser cooling, we will in Section 3.4 treat this type of cooling using an extended form of the transfer matrix method that will be introduced in Part II.

The 'sub-Doppler' cooling mechanism in a MOT relies on the phenomenon of optical pumping between the multiple magnetic sublevels in the ground ($J = 1$) state. Let us assume that the atom is interacting with two counterpropagating travelling waves of identical frequencies but opposite circular polarisations; this is often referred to as the σ^+–σ^- configuration. The resulting standing wave pattern is linearly polarised everywhere, but this linear polarisation rotates in space on the wavelength scale. Consider now a ground-state static atom in such a field. Optical pumping processes between different magnetic sublevels of the $J = 1$ level proceed at rates given by the various Clebsch–Gordan coefficients for the transitions involved. We note that this mechanism relies on pumping between these magnetic sublevels and therefore needs a ground state with $J \geq 1$. The physics behind cooling in this configuration [14] is rather involved but we can summarise it as follows. In its rest frame, an atom moving with (constant) velocity sees a linear polarisation rotating with a constant angular velocity which, by Larmor's theorem, acts like a fictitious magnetic field parallel to the motion of the atom. This magnetic field acts to effectively couple the magnetic sublevels of the ground state. The motion of the atom also induces an imbalance in the populations of these sublevels, causing it to preferentially scattering photons from one of the two running waves. It can be shown that, under the right conditions, this preferential scattering can lead to a significant friction force acting on the atom, enough to cool a population of such atoms to well below the Doppler temperature [13–15].

We can now describe the theory of operation of MOTs. A MOT is formed at the zero of a quadrupole magnetic field; let us use this magnetic field to define our coordinate system: the z-axis points along the axis of symmetry of this magnetic field and the x and y axes define what we will call the 'symmetry plane'. The origin of our coordinate system will be taken at the zero of the magnetic field. Traditionally, a MOT requires three pairs of counterpropagating red-detuned circularly-polarised beams, one pair along each of the coordinate axes. The beams in the symmetry plane all have the same helicity, and opposite to that of the beams along the z-axis. The polarisation of

---

2 We use the standard notation here, with J denoting the ground state and J' the excited state.
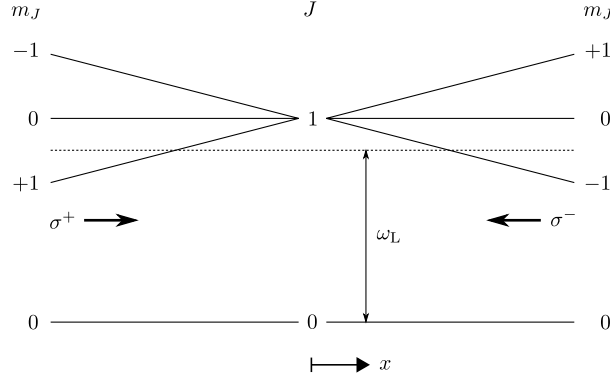
FIGURE 2.1: Close to the centre of a magneto–optical trap, the magnetic field has a constant gradient, taken here to be positive along the positive x direction. An atom to the right of the origin will see the σ^+ beam as further detuned than the σ^- beam, even though both have the same frequency ω_L, and therefore preferentially scatter from the latter, causing it to experience a restoring force towards $x = 0$. A similar principle operates when the atom is to the left of the origin, whereby it will preferentially scatter from the σ^+ beam. We depict a $J = 0 \rightarrow J' = 1$ transition here. The designation $\sigma^\pm$ relates to the effective circular polarisation of the light, and *not* its helicity.

the beams is as yet undetermined; sub-Doppler cooling occurs for either configuration, depending on the sign of the detuning of the cooling light from the atomic transition. This degree of freedom is therefore fixed by choosing whether to operate above or below atomic resonance.

We have thus far discussed only the cooling mechanism in a MOT. Trapping in a MOT operates as follows. Let us suppose that the magnetic field is such that the gradient is positive in the x direction, and consider a static atom with a positive x coordinate. Due to the nonzero magnetic field, the energy levels of the atom will be split. We will now, for simplicity, consider an atom with a $J = 0$ ground state (similar conclusions will hold for $J \neq 0$). The atom is in a region where the magnetic field strength is positive; in other words, the $\Delta m_J = -1$ ($\Delta m_J = +1$) transition is shifted to a lower (higher) energy; this statement follows from Eq. (1.5). If the counterpropagating beam (i.e., the beam from the *positive x direction*) is σ^- polarised, whereby the opposite beam is σ^+ polarised, the atom will preferentially scatter photons from the positive x direction and therefore experience a force towards the origin; see Fig. 2.1. Conversely, if the magnetic field gradient is negative in the x direction, we require the beam from the positive x direction to be σ^+ polarised.

2.4 Memory-based approach to cooling in laser light: the dipole force delayed[3]

We have stated previously that the dipole force, in its 'bare' form, is a conservative force, but if we introduce a delay between the dipole moment of our particle and the field that the particle interacts with, this restriction evaporates and the dipole force gains a non-conservative character [73]. In the atomic domain, this is generally referred to as a 'Sisyphus'–type cooling mechanism, following the nomenclature first applied by Aspect and co-workers [74] with reference to the ancient Greek myth. We will now generalise this idea and see that it leads us to several potentially promising cooling configurations that rely solely upon the dipole force.

In the previous section we considered 'standard' Sisyphus cooling. A similar mechanism can be seen to act for atoms inside optical resonators [75]. Let us consider a simplified model of a resonant optical resonator having almost perfect mirrors. The electric field inside the resonator is, to a very good approximation, a sinusoidal standing wave. If one introduces an atom into the resonator, the effect that the atom has on the resonator will depend greatly on its position in this standing wave. An atom at a node of the field will not affect the field, whereas an atom at an antinode will affect the field rather more strongly.[4] In such a picture, the atom is constantly being pumped into a dressed-state from which it preferentially decays in such a way as to lose kinetic energy. We note that a very similar mechanism is in operation here as in traditional Sisyphus cooling but—crucially—the delay process has been shifted from an internal delay mechanism (optical pumping between the different magnetic sublevels of the atom) to an external one (optical pumping between the atom–cavity dressed states), since the response of the cavity field is necessarily a viscous one.

To illustrate the generality of this idea, let us consider the potential energy $U[x, x_{\mathrm{a}}(t), v]$ at time t on a test particle at position x due to an atom following a path $x_{\mathrm{a}}(t) = x_0 + vt$. We suppose that the dependence of U on the motion of the atom is mediated entirely through the action of a 'memory' in the system, or another time-delayed effect, that can

---

[3] With sincere apologies to J. Dalibard and C. Cohen-Tannoudji.

[4] A similar point, with implications for photonic crystals, is made about atoms in an optical lattice in Ref. [47].

be represented by

$$U[x, x_{\mathrm{a}}(t), v] = \int_0^\infty U[x, x_{\mathrm{a}}(t-T), v=0]\, M(T)\, \mathrm{d}T\,, \tag{2.9}$$

where M is some function that represents the memory of the system. We can Taylor-expand U in the second variable around $x_{\mathrm{a}}(t)$ to first order in v and write

$$\begin{aligned}
U[x, x_{\mathrm{a}}(t), v] = U[x, x_{\mathrm{a}}(t), v=0] \int_0^\infty M(T)\, \mathrm{d}T \\
- v\left[\left.\frac{\partial U(x, y, v=0)}{\partial y}\right|_{y=x_0}\right] \int_0^\infty T\, M(T)\, \mathrm{d}T\,.
\end{aligned} \tag{2.10}$$

Finally, we assume that M is normalised, $\int_0^\infty M(T)\, \mathrm{d}T = 1$, and set

$$\tau = \int_0^\infty T\, M(T)\, \mathrm{d}T\,, \tag{2.11}$$

which has the units of time. Thus, we obtain

$$U[x, x_{\mathrm{a}}(t), v] = U[x, x_{\mathrm{a}}(t), v=0] - \tau v\left[\left.\frac{\partial U(x, y, v=0)}{\partial y}\right|_{y=x_{\mathrm{a}}(t)}\right]\,. \tag{2.12}$$

A similar relation holds for any distributive functional of U.[5] In the prototypical Sisyphus mechanism, the system memory lies in the delayed populations. Indeed, if we concentrate on one sublevel having population $\Pi(x, v) \propto -U[x, x_{\mathrm{a}}(t), v]$, then

$$\Pi[x_{\mathrm{a}}(t), v] = \Pi^{\mathrm{st}}[x_{\mathrm{a}}(t)] - \tau_{\mathrm{p}} v\left[\left.\frac{\partial \Pi^{\mathrm{st}}(y)}{\partial y}\right|_{y=x_{\mathrm{a}}(t)}\right]\,, \tag{2.13}$$

cf. Eq. (4.22) in Ref. [14], with τ_{p} being the *pumping time* associated with our choice of memory function $M(T) = \delta(T - \tau_{\mathrm{p}})$, or equivalently $M(T) = \exp(-t/\tau_{\mathrm{p}})/\tau_{\mathrm{p}}$, and $\Pi^{\mathrm{st}}(y) \propto -U[x_{\mathrm{a}}(t), y, v=0]$ the steady-state population when the atom is static. Consider now a situation where the interaction between the particle and the field is mediated through the dipole force, such that the force acting on the particle is

$$F[x_{\mathrm{a}}(t), v] = -\left.\frac{\partial U[x, x_{\mathrm{a}}(t), v]}{\partial x}\right|_{x=x_{\mathrm{a}}(t)}\,. \tag{2.14}$$

---

[5] That is, any $\mathcal{F}$ such that $\mathcal{F}(\alpha U + \beta V) = \alpha \mathcal{F}(U) + \beta \mathcal{F}(V)$ for real α and β.

By using this relation in Eq. (2.12), we obtain

$$F[x_{\mathrm{a}}(t), v] = F_0[x_{\mathrm{a}}(t)] + \tau v \left[\frac{\partial^2 U(x, y, v = 0)}{\partial x \, \partial y} \bigg|_{x=x_{\mathrm{a}}(t), y=x_{\mathrm{a}}(t)} \right], \qquad (2.15)$$

with F_0 being the force acting on the particle when it is static. Eq. (2.15) may not be trivial to evaluate in practice, and in other circumstances the model itself may not apply; for a given situation τ may be ill-defined, for example. Nevertheless, it allows us to make a general and powerful prediction that applies to a wide range of systems: by simply endowing a system with a memory, the dipole force can be used to cool the motion of the particle interacting with the system. It also provides a physical link between models that use an external memory, such as a cavity field, and those that use an internal memory, such as populations in different hyperfine levels.

2.5 Cavity fields and atomic motion: A brief review of current work

The first few sections of this chapter discussed various ways of capturing atoms or slowing their motion down. In the sections following this, we will explore novel methods that use an optical memory, cf. Section 2.4, to achieve cooling. At this stage, therefore, it would be good to briefly summarise the existing work that uses cavities to slow atoms down or otherwise control their motion. Our later work will borrow heavily from the ideas presented here.

2.5.1 Cavity-mediated cooling

The electromagnetic field inside a cavity differs from that in free space in several respects. On the most basic level, the zeroth-order approximation of a (resonant) cavity field is a region in physical space where the electromagnetic field is, for a given driving power, stronger than in other locations. Such a coarse approximation, however, has limited applicability.[6] A first-order approximation to a cavity field would include memory effects which, as we have seen above, imply that the cavity field can be used to control atomic

---

[6] This point is, of course, arguable: the strong coupling of atoms to the electromagnetic field is an interesting field of research with several applications [76].

motion. Quantum mechanically, however, the field inside a good cavity is modified in a highly nontrivial way, for even the vacuum fluctuations themselves are modified. This phenomenon is the origin of the Purcell effect [77] and was recognised in the early 1990's as a way of inducing cooling forces on atoms [22]. The theory of cavity-mediated cooling of atoms subsequently developed in the direction of driven high-Q cavities [78]. Ref. [19] was the first to point out evidence for a novel cooling process taking place inside such cavities that is reminiscent of Sisyphus–type sub-Doppler cooling mechanisms (cf. Ref. [14], but see also above): the basis of the mechanism here being that the photon number in a cavity is, in the strong coupling regime, intimately connected with the position of the atom inside the cavity. By choosing the right system parameters, this connection can be used to slow down the atomic motion. Cavity-mediated cooling of atoms was observed only in recent experiments [20, 21]. The potential application of this mechanism to the cooling of the motion of dielectric particles has also been noted [79, 80] and progress is rapidly being made towards the experimental realisation of cavity cooling of microscopic dielectric 'particles', both in the form of microspheres [79] and in the form of micromirrors [81, 82], with profound implications for the study of the foundations of quantum mechanics and even relativity [18].

Our work in later sections, in particular Section 4.1, will explore the use of cavities in a different way. By placing a particle outside a cavity, we can still benefit from the presence of the cavity in lengthening the time delay, but without subjecting the particle to the strong field present inside a resonant cavity.

2.5.2   Ring cavity cooling

Investigations of cavity cooling inside Fabry–Pérot cavities have focussed on the 'good-cavity' limit, where the bare cavity has a very high finesse or Q-factor. Ring cavities, by their very topology, tend to be larger and with a lower Q-factor. This has, perhaps, been one reason why cooling of atoms inside ring cavities has not been explored as thoroughly as cavity-mediated cooling. One distinct advantage of ring cavities is that the system is translationally invariant with respect to the position of the atom; any friction forces developed on the atom are subsequently not dependent on the position of the atom (this will be seen to be a serious limitation of cavity-mediated cooling in Section 4.2.2.1). The theory for cooling atoms inside ring cavities [83–88] is similar to that for cavity-mediated

cooling. Experimental work on atoms inside ring cavities is rather sparse and tends to focus on recoil-induced effects [89, 90], which will be discussed next. It has also been proposed (see Refs. [91] and [92]; see also Section 4.3) that the practical limitation of ring cavities as low-Q devices can be lifted by the use of a gain medium inside the ring cavity. This approach holds promise towards improving the performance of such cavity systems to the point that they may be useful in practical realisations of optomechanics experiments.

2.5.3 Self-organisation of atoms inside cavities

The strong feedback between atoms and cavity fields may, under the right conditions, result in self-organisation of an atomic ensemble inside a cavity. We mention here two distinct effects. In Fabry–Pérot cavities, it was proposed [93] and subsequently observed [94] that above a threshold pump power, an ensemble of atoms will organise into a checkerboard pattern. Two possible configurations are possible, with the atoms occupying either set of sites in the checkerboard, and transitions occur between the two due to the presence of noise in the system.

Collective atomic recoil lasing (CARL) [89, 90, 95, 96] is a related phenomenon that occurs inside ring cavities. CARL occurs when a pump beam inside a ring cavity is reflected off an ensemble of atoms into the counterpropagating mode. The motion of the atoms will Doppler-shift this reflection. An exponential build-up of this latter mode can then occur, accompanied by a spontaneous self-organisation of the ensemble into a grating-like structure. In such a setup, the atomic ensemble acts as a gain medium for the counterpropagating wave, and in its reliance on a gain medium CARL is related to the 'amplified optomechanics' idea we discuss in Section 4.3. However, amplified optomechanics uses a gain medium that is spatially separated from the atomic ensemble, in a similar way to the ideas discussed in Ref. [91], whereas in CARL the two are one and the same.

2.6 Mirror-mediated cooling

As explained Section 2.4, the dipole force can be invested with a dissipative character by endowing the system as a whole with a memory. Exploring the cooling of atoms
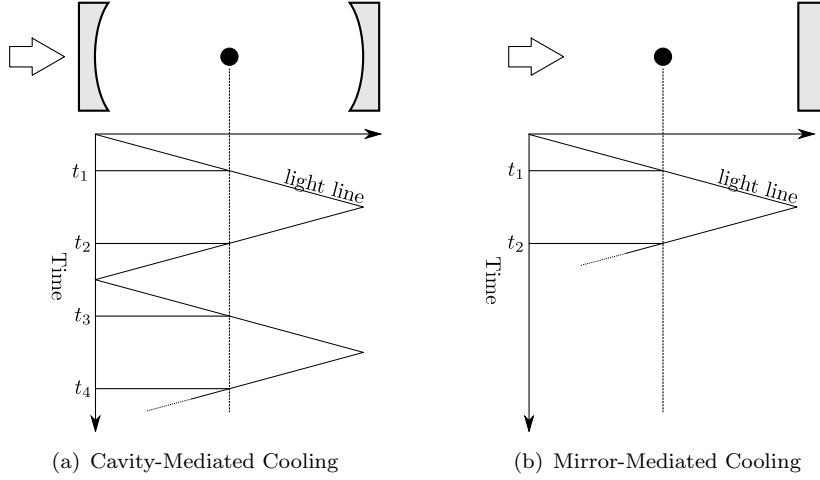
(a) Cavity-Mediated Cooling   (b) Mirror-Mediated Cooling

FIGURE 2.2: Space–time diagrams showing the interaction of an atom with light when the atom is (a) inside an optical resonator, and (b) in front of a mirror. It is clear that in case (a) one gets multiple interactions between the two and a 'memory time' is not well-defined, whereas in case (b) a definite memory time can be assigned. The blank arrow indicates the pump beam.

inside cavities using this terminology is fine in principle, since a cavity may be viewed as the archetypal optical memory element, but is not easy in practice. Indeed, in such a system, a well-defined "delay time" does not exist: a cavity has several memories, each one arising from a separate interaction of *the same light* with the atom. By simplifying the system and removing one of the cavity mirrors, we can once again talk about such a concept as a delay time τ. In this configuration, light interacts with the atom twice, at times $t = 0$ and $t = \tau$, say, and no more.[7] These two pictures are illustrated schematically in Fig. 2.2. Whereas we can readily define the system memory time

$$\tau = t_2 - t_1 \tag{2.16}$$

for Fig. 2.2(b), no such intuitive definition is possible in Fig. 2.2(a) because (i) if the atom is not at the centre of the cavity, then $t_2 - t_1 \neq t_3 - t_2 \neq \ldots$, and (ii) each interaction has a different weighting due to the imperfect reflectivity of the mirrors; it is however possible to assign an effective memory time $\tau = 1/(2\kappa)$, where κ is the HWHM linewidth of the cavity. Indeed, it will be shown in Appendix 3.A.3 that the finesse of a cavity can be written as

$$\mathcal{F} = \pi N \,, \tag{2.17}$$

---

[7] This is a very 'classical' picture, where we describe the light by means of point-like photons. This description is used here to illustrate the physics of the situation. Quantitative calculations can only be made by properly describing the light in terms of the solutions to Maxwell's equations.

where N is the number of round-trips made by the light inside the cavity before the intracavity intensity decays by a factor $1/e^2$. The dipole energy U is proportional to the delayed electric field; so one would expect that the effect of the cavity field on U decays by a factor $1/e$ over N round-trips. It seems reasonable, therefore, to set

$$M(T) = \left(1 - e^{-1/N}\right) \sum_{n \text{ even}} \delta\left(T - nL_1/c\right)e^{-n/N} + \left(1 - e^{-1/N}\right) \sum_{n \text{ odd}} \delta\left(T - nL_2/c\right)e^{-n/N} ,$$

(2.18)

with L_1 and L_2 being the distances from the atom to the two cavity mirrors and $L = L_1 + L_2$ the cavity length. This memory function represents an infinite number of discrete interactions, each one being weaker than the previous, of the cavity field with the atom. Thus, in the good-cavity limit of large N,

$$\tau = \frac{L_1 + L_2}{c} \frac{1}{e^{1/N} - 1} \to \frac{LN}{c} = \frac{\mathcal{F}L}{\pi c} .$$

(2.19)

It will also be shown (see Appendix 3.A.3) that $\kappa = \pi c/(2\mathcal{F}L)$. It thus follows that $\tau = 1/(2\kappa)$ is a good definition for the effective memory time of the system in this model. Throughout the rest of this chapter and in later chapters, we shall see how this memory time τ governs the interaction of the particle with the field.

The remainder of this section will be devoted to the mathematical description of mirror-mediated cooling and follows closely Ref. [41]. It was published as Xuereb, A., Horak, P. & Freegarde, T. Phys. Rev. A **80**, 013836 (2009) and several parts are reproduced *verbatim*. This paper was the first to introduce the 'mirror-mediated cooling' mechanism, but was accompanied by another paper [97] that discusses the more computationally-oriented aspects of the Monte–Carlo simulations performed.

A semiclassical model of the situation is presented in Section 2.6.1. The model is then explored analytically in a perturbative manner (Section 2.6.2), and numerically using Monte–Carlo simulations (Section 2.6.3). Finally, a few brief comments are made about some of the approximations made to describe the system.

2.6.1 Mathematical model

We shall use the TLA model explored in detail in Chapter 1. The atom will be assumed to have a transition frequency ω_0 and upper-state decay rate 2Γ, as before, and be coupled to a continuum of quantised electromagnetic modes with frequencies ω and

standing-wave mode functions

$$f(\omega, x) = \sin(\omega x/c)\,, \tag{2.20}$$

with the mirror being at $x = 0$. The field modes have annihilation and creation operators $\hat{a}(\omega)$ and $\hat{a}^\dagger(\omega)$, respectively, and the atom–field coupling is described by a single, frequency-independent, coupling coefficient g. The mode at frequency $\omega = \omega_{\mathrm{L}}$ is pumped in a coherent field by a laser, and we assume that the detuning, defined as

$$\Delta_{\mathrm{L}} = \omega_{\mathrm{L}} - \omega_0\,, \tag{2.21}$$

obeys the condition $|\Delta_{\mathrm{L}}| \gg \Gamma$; i.e., we assume far off-resonant operation. The numerical examples we give will be for a ^{85}Rb atom cycling in the $5\mathrm{S}_{1/2} \leftrightarrow 5\mathrm{P}_{3/2}$ transition. The starting point for our description is the quantum master equation, Eq. (1.17), where the Hamiltonian now reads

$$\hat{H} = \frac{\hat{p}^2}{2m} - \hbar\Delta\hat{\sigma}^+\hat{\sigma}^- + \int \hbar(\omega - \omega_{\mathrm{L}})\hat{a}^\dagger(\omega)\hat{a}(\omega)\,\mathrm{d}\omega - \mathrm{i}\hbar g \int [\hat{\sigma}^+\hat{a}(\omega)f(\omega,\hat{x}) - \mathrm{H.c}]\,\mathrm{d}\omega\,, \tag{2.22}$$

where $\hat{x}$ and $\hat{p}$ are the position and momentum operators of the atom and 'H.c.' denotes the Hermitian conjugate. We also use the Liouvillian terms

$$\mathcal{L}\hat{\rho} = -\Gamma\left[\hat{\sigma}^+\hat{\sigma}^-\hat{\rho} + \hat{\rho}\hat{\sigma}^+\hat{\sigma}^- - 2\int_{-1}^{1} N(u)\hat{\sigma}^- e^{-\mathrm{i}u\hat{x}}\hat{\rho}\mathrm{e}^{\mathrm{i}u\hat{x}}\hat{\sigma}^+\,\mathrm{d}u\right]\,. \tag{2.23}$$

In this expression, $N(u)$ describes the 1D projection of the spontaneous emission pattern of the atomic dipole. In the low-saturation regime, we can adiabatically eliminate the internal atomic dynamics and formally express the dipole operator as

$$\hat{\sigma}^- = -\frac{\mathrm{i}\Delta + \Gamma}{\Delta^2 + \Gamma^2}\,g\int f(\omega,\hat{x})\hat{a}(\omega)\,\mathrm{d}\omega + \hat{\xi}^-\,, \tag{2.24}$$

where $\hat{\xi}^-$ is a noise term [43].

2.6.2   A perturbative approach to exploring the model

2.6.2.1   Force on a static atom

The aim of this section is to derive an analytical expression for the friction force acting on the atom when the latter is not moving. To achieve this, we treat the atomic position classically, effecting the replacement $\hat{x} \to x_0$ in Eq. (2.22) to obtain

$$
\hat{H} = \int \hbar(\omega - \omega_\mathrm{L})\hat{a}^\dagger(\omega)\hat{a}(\omega)\,\mathrm{d}\omega
$$
$$
+ \hbar\frac{g^2\Delta_\mathrm{L}}{\Delta_\mathrm{L}^2 + \Gamma^2}\iint \sin(\omega_1 x_0/c)\sin(\omega_2 x_0/c)\hat{a}^\dagger(\omega_1)\hat{a}(\omega_2)\,\mathrm{d}\omega_1\,\mathrm{d}\omega_2\,. \quad (2.25)
$$

A consequence of assuming $|\Delta_\mathrm{L}| \gg \Gamma$, and operating in the low-saturation regime, is that the population of the excited state is negligible, and therefore last term in Eq. (2.23) does not contribute to the dynamics. With this simplification, the master equation for the annihilation operators reduces to

$$
\frac{\mathrm{d}}{\mathrm{d}t}\hat{a}(\omega,t) = \frac{\mathrm{i}}{\hbar}\left[\hat{H}, \hat{a}(\omega,t)\right]. \quad (2.26)
$$

By substituting Eq. (2.22) into this equation, we obtain the integro-differential equation

$$
\frac{\mathrm{d}}{\mathrm{d}t}\hat{a}(\omega,t) = -\mathrm{i}(\omega - \omega_\mathrm{L})\hat{a}(\omega,t) - \mathrm{i}\frac{g^2\Delta_\mathrm{L}}{\Delta_\mathrm{L}^2 + \Gamma^2}\sin(\omega x_0/c)\int \sin(\omega_1 x_0/c)\hat{a}(\omega_1,t)\,\mathrm{d}\omega_1\,. \quad (2.27)
$$

We now assume coherent states at all times for the fields and replace the operators with their respective expectation values. Since we are pumping the atom at a single frequency, we take the initial condition $a(\omega,0) = A\,\delta(\omega - \omega_\mathrm{L})$, where A is the amplitude of the pump field, such that $|A|^2$ is the pump power in units of photons per second, and δ is the Dirac δ-function. We now expand the fields $a(\omega,t)$ in the weak-coupling limit in powers of the coupling constant,

$$
a(\omega,t) = \sum_n a_n(\omega,t)\left(\frac{g^2\Delta_\mathrm{L}}{\Delta_\mathrm{L}^2 + \Gamma^2}\right)^n, \quad (2.28)
$$

with $a_n(\omega,t)$ being the nth coefficient of the series expansion. Solving Eq. (2.27) to successive orders in $g^2\Delta_\mathrm{L}/(\Delta_\mathrm{L}^2 + \Gamma^2)$ yields the zeroth order term in this parameter,

$$
a_0(\omega,t) = A\delta(\omega - \omega_\mathrm{L})\,, \quad (2.29)
$$

and the first order term

$$a_1(\omega, t) = A \frac{\exp\left[-\mathrm{i}(\omega - \omega_\mathrm{L})t\right] - 1}{\omega - \omega_\mathrm{L}} \sin(\omega x_0/c) \sin(\omega_\mathrm{L} x_0/c)\,. \tag{2.30}$$

To the same level of approximation, we can now find the force acting on the atom to second order in $g^2 \Delta_\mathrm{L}/(\Delta_\mathrm{L}^2 + \Gamma^2)$.[8] The (classical) force acting on the atom is, then,

$$F(x_0) = -\frac{\partial H}{\partial x}\,, \quad \text{or} \tag{2.31}$$

$$F(x_0) = \frac{\hbar}{c}\,|A|^2\,\frac{g^2 \Delta_\mathrm{L}}{\Delta_\mathrm{L}^2 + \Gamma^2} \omega_\mathrm{L} \Bigg\{ \sin(2\omega_\mathrm{L} x_0/c) \\ - \frac{\pi}{2}\frac{g^2 \Delta_\mathrm{L}}{\Delta_\mathrm{L}^2 + \Gamma^2} \sin^2(\omega_\mathrm{L} x_0/c)\left[4\cos^2(\omega_\mathrm{L} x_0/c) - 1\right] \Bigg\}\,. \tag{2.32}$$

The two terms making up this force have different origins. The first term represents the interaction between the dipole induced in the atom and the (unperturbed) pump field. The second term is the lowest-order correction to the force when the back-action of the atom on the light field is taken into account. The latter term therefore represents the interaction between the dipole induced in the atom by the pump field and the electric field propagated from this same dipole. What we shall see, in the next subsection, is that this propagated electric field can, after being reflected by the mirror, re-interact with the atomic dipole. The motion of the atom between these two interactions gives rise to a velocity-dependent force, i.e., a friction force, on the atom.

2.6.2.2   Force on a moving atom: Friction forces

Let us now assume that the atom is moving at a constant velocity, v. $\hat{x}$ is now a function of time, such that $\hat{x} \to x(t) = x_0 + vt$, assuming that by $t = 0$ the system has already reached steady-state; in other words, the pump beam has been on for a time longer than $\tau = 2x_0/c$, which is the time taken for a disturbance to travel from the position of the atom to the mirror and back again. With this replacement for $\hat{x}$, we proceed to solve Eq. (2.27), keeping terms up to first order in $g^2 \Delta_\mathrm{L}/(\Delta_\mathrm{L}^2 + \Gamma^2)$, as before. The friction

---

[8]   Mathematically, the fact that the force is at a higher order arises from $\hat{H}$ not having any zeroth order terms [see Eq. (2.22)]; physically, the force is an interaction of an electric field with an induced dipole moment, and the electric field in this case is itself caused by the induced dipole at an earlier time. Both the induced dipole and this electric field are then, to lowest order, linear in $g^2 \Delta_\mathrm{L}/(\Delta_\mathrm{L}^2 + \Gamma^2)$. This term in the force is therefore quadratic in the same parameter.

force (in the longitudinal direction, i.e., along x) can finally be obtained:

$$F_{\parallel}(x_0) = 2\pi\hbar k_{\mathrm{L}}\frac{v}{c}|A|^2\left(\frac{g^2\Delta_{\mathrm{L}}}{\Delta_{\mathrm{L}}^2 + \Gamma^2}\right)^2\sin^2(2k_{\mathrm{L}}x_0) - \pi\hbar k_{\mathrm{L}}^2 v\tau|A|^2\left(\frac{g^2\Delta_{\mathrm{L}}}{\Delta_{\mathrm{L}}^2 + \Gamma^2}\right)^2\sin(4k_{\mathrm{L}}x_0),$$

(2.33)

with $k_{\mathrm{L}} = \omega_{\mathrm{L}}/c$ being the wavenumber of the pump field; this force lacks the usual 'optical molasses' friction force that is produced by the interaction between the atomic dipole and the Doppler-shifted, unperturbed, pump beam because the atomic excited state has been adiabatically eliminated. The first term in the friction force expression is the velocity-dependent analogue of the second term in $F(x_0)$ above: it represents the interaction between the induced dipole of the atom and the instantaneous Doppler-shifted field produced by that same dipole. It is the second, 'delayed', term, however, that we will be concerned with in the following. Indeed, this term represents the interaction between the atomic dipole and the reflected field it itself produces; the Doppler shift here can effectively be looked at as changing the phase accrued by the reflected field in arriving back at the atom.

The delayed friction force is larger than the instantaneous friction force by a factor $k_{\mathrm{L}}x_0$, and we are therefore fully justified in setting

$$F_{\parallel}(x_0) = -\pi\hbar k_{\mathrm{L}}^2 v\tau|A|^2\left(\frac{g^2\Delta_{\mathrm{L}}}{\Delta_{\mathrm{L}}^2 + \Gamma^2}\right)^2\sin(4k_{\mathrm{L}}x_0)$$

(2.34)

if we constrain ourselves to the far-field limit, $k_{\mathrm{L}}x_0 \ggg 1$.

Supposing that the species we are cooling is ^{85}Rb, and setting $|A|^2 = 62.5\Gamma/(2\pi)$, $\Delta_{\mathrm{L}} = -10\Gamma$, $\tau = 0.5/\Gamma$, and Gaussian beam waist $w = 1.4\,\mu$m, Eq. (2.34) predicts $1/e$ cooling times of the order of $2\,$ms. The value for τ that we use implies a separation between the atom and the mirror of the order of several metres. We suggest that this problem can be overcome through the coupling of the light into an optical fibre, thereby avoiding the effects of diffraction. A recent experiment making use of a similar technique is described in Ref. [98].

Eq. (2.34) indicates an exponential decay or increase in velocity. We define the *cooling coefficient* as $\varrho = -F/v$, whereby we obtain the relation $\mathrm{d}p^2/\mathrm{d}t = -2\varrho p^2$, which thus depends on position as $\sin(4k_{\mathrm{L}}x_0)$. Moreover, since $p^2 \propto T$ for a thermal ensemble, we also have $\mathrm{d}T/\mathrm{d}t = -2\varrho T$. Fig. 2.3 shows a plot of ϱ against atomic position, where we introduced the coordinate x_0' relative to the nearest node of the standing wave pump. It
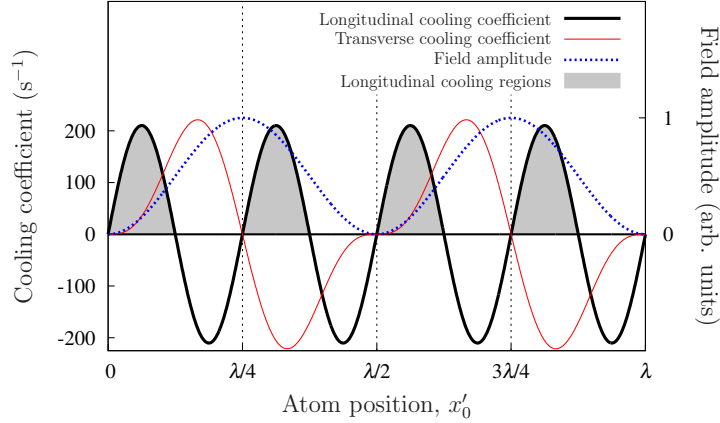
FIGURE 2.3: Spatial dependence of the longitudinal cooling coefficient ϱ (thick solid line). The shaded areas promote cooling in the longitudinal direction. Also drawn is the transverse heating coefficient (thin solid line) and the field amplitude (dotted line). Parameters are for ^{85}Rb atoms and $|A|^2 = 62.5\Gamma/(2\pi)$, $\Delta_{\mathrm{L}} = -10\Gamma$, $\tau = 0.5/\Gamma$, $w = 1.4\,\mu\mathrm{m}$.

is only in certain intervals that we expect the longitudinal force to be a damping force, as indicated in this figure by the shaded regions.

In order to complete the picture, we will now derive the friction force acting in the transverse direction (i.e., in a direction orthogonal to the pump beam). This force arises from the spatial variation of the coupling constant g when the pump field is assumed to be a tightly-focussed Gaussian beam. In this case the coupling constant g becomes a function $g(r)$, where r is the coordinate in the transverse direction. For an atom moving at small constant velocity, we may write $g(r_0 + vt) \approx g(r_0) + vtg'(r_0)$, where $g'(r) = \mathrm{d}g/\mathrm{d}r$ and time $t = 0$, at which $r = r_0$, is defined as before. Substituting this into Eq. (2.27) we can derive an expression for the friction force, $F_\perp(x_0) = -\partial H/\partial r$, in the direction of r:

$$F_\perp(x_0) = -2\pi\hbar v\tau|A|^2 \left(\frac{2gg'\Delta_{\mathrm{L}}}{\Delta_{\mathrm{L}}^2 + \Gamma^2} \right)^2 \sin^3(k_{\mathrm{L}}x_0)\cos(k_{\mathrm{L}}x_0)\,, \qquad (2.35)$$

with g and g' being evaluated at $r = r_0$. This transverse friction force is also shown in Fig. 2.3, for comparison with the longitudinal friction force, assuming a Gaussian mode function of waist $w = 1.4\,\mu\mathrm{m}$. Note that $F_\parallel$ and $F_\perp$ are comparable in magnitude for the parameters chosen here, i.e., where the mode waist is comparable to the optical wavelength. Moreover, we can see that there exist regions where both these forces

promote cooling. In the remainder of this section, however, we will concentrate on a one-dimensional treatment of the problem and therefore only consider the longitudinal friction force.

In terms of more familiar parameters, we can rewrite Eq. (2.34) in the limit $|\Delta_{\mathrm{L}}| \gg \Gamma$ as

$$F_{\|}(x_0) = -vs\Gamma \frac{\sigma_{\mathrm{a}}}{\sigma_{\mathrm{L}}} \hbar k_{\mathrm{L}}^2 \tau \sin(4k_{\mathrm{L}} x_0) \,, \tag{2.36}$$

where $s = g^2 |A|^2/(\Delta_{\mathrm{L}}^2 + \Gamma^2)$ is the maximum saturation parameter of the atom in the standing wave, $\sigma_{\mathrm{a}} = 3\lambda_{\mathrm{L}}^2/(2\pi)$ is the atomic radiative cross-section at a wavelength $\lambda_{\mathrm{L}} = 2\pi/k_{\mathrm{L}}$, as defined in Section 1.4, and where we used the relation $2\pi g^2/\Gamma = 4\sigma_a/(2\sigma_{\mathrm{L}})$, with $\sigma_{\mathrm{L}} = \pi w^2/8$ being the mode area of the pump beam of waist w, and where the factor of 4 arises from the standing wave amplitude.

Aside from allowing us to make predictions of cooling times, Eqs. (2.34) and (2.36) also highlight the dependence of this cooling effect on the variation of important physical parameters. In particular, $F_{\|}$ depends on the square of the detuning, which means that it is possible to obtain cooling with both positive and negative detuning, in stark contrast with the standard Doppler cooling force. The friction force also scales with w^{-4} and $|A|^2$. Hence, for a fixed laser intensity, proportional to $|A|^2/w^2$, i.e., for a fixed atomic saturation, the friction still scales with w^{-2} and thus a tight focus is needed in order to have a sizeable effect. The physical reason for this dependence is that the dipole moment induced in the atom by the pump light is proportional to $|A|^2 g^2 \propto |A|^2/w^2$; this polarisation couples to the electric field and, after being reflected by the mirror, polarises the atom again. The size of the force therefore scales as $|A|^2 g^4$, or $|A|^2/w^4$.

A very promising feature of these two equations is the linear dependence of the cooling rate on τ: by increasing the distance between the atom and the mirror, we can increase the strength of the friction force acting on the atom. In Section 2.6.3 we further analyze the dependence of the cooling rate on the various parameters and support the validity of the analytical solution by comparing it with the results of simulations.

2.6.2.3 Localising the atom: The effects of adding a harmonic trap

Eq. (2.34) shows that, in order to observe any cooling effects, we need to localise the particle within around $\lambda_{\mathrm{L}}/8$. This may be achieved, for example, by an additional

far off-resonant and tightly focussed laser beam propagating parallel to the mirror and forming a dipole trap centred at a point x_0. In this section, we aim to characterise the effects of this dipole trap, or indeed any harmonic trap, on the atom–field interaction. We characterise this trap by means of its spring constant k_t, such that the trapping force is given by $F_t = -k_t(x - x_0)$, or equivalently by the harmonic oscillator frequency $\omega_t = \sqrt{k_t/m}$, where m is the mass of the atom.

With the atom being in a harmonic trap, we can now write down its time-dependent velocity as $v(t) = v_m \cos(\omega_t t)$, with a maximum velocity of the atom v_m. Using this expression, it is possible to derive a modified cooling coefficient by performing a perturbative expansion in the dimensionless parameter v_m/c. Proceeding along the lines of the preceding section, we arrive at a modified expression for the friction force,

$$F_\parallel(x_0) = -\pi \hbar k_L^2 v_m \tau \, \mathrm{sinc}(\omega_t \tau)|A|^2 \left(\frac{g^2 \Delta}{\Delta^2 + \Gamma^2}\right)^2 \sin(4k_L x_0) \,. \tag{2.37}$$

By way of confirmation, it is easy to see that this expression reduces to Eq. (2.34) in the limit of small w_t; i.e., in the free-particle limit for the atomic motion. The sinusoidal dependence on $\omega_t \tau$ can be justified in an intuitive manner: the effect on the particle is unchanged if the particle undergoes an integer number of oscillations in the round-trip time τ.

While Eq. (2.37) was derived for an oscillating atom, it only accounts for the sinusoidal variation of the velocity, and therefore does not include the effect of the finite spatial distribution of the position of the atom. In order to obtain an estimate for the friction force in the presence of this spatial broadening, we calculate the overall energy loss rate experienced by the particle in terms of the time average of Eq. (2.34):

$$\left\langle \frac{\mathrm{d}p^2}{\mathrm{d}t} \right\rangle = -\frac{\hbar k_L^2 p_0^2}{m} \tau |A|^2 \left(\frac{g^2 \Delta}{\Delta^2 + \Gamma^2}\right)^2 \int_0^{2\pi} \sin\big[4k_L x_0 + 4k_L x_m \sin(T)\big] \cos^2(T) \, \mathrm{d}T \,, \tag{2.38}$$

where $p_0 = m v_m$ is the maximum momentum of the particle in the trap, given by $p_0 = x_m \sqrt{m k_t}$. The value of the integral in Eq. (2.38) can be expressed as

$$\frac{2\pi}{4k_L x_m} \big[\sin(4k_L x_0) J_1(4k_L x_m) + \cos(4k_L x_0) H_1(4k_L x_m)\big] \,, \tag{2.39}$$
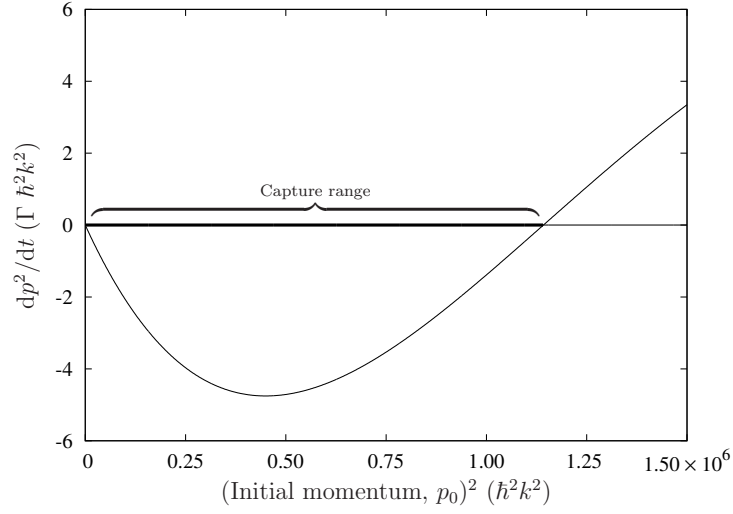
FIGURE 2.4: Dependence of $\mathrm{d}p^2/\mathrm{d}t$ on the square of the initial momentum, p_0^2, for $\omega_\mathrm{t} = 0.45 \times 2\pi\Gamma$ and $x_0' = 3\lambda_\mathrm{L}/16$. Other parameters are as in Fig. 2.3. Cooling is achieved only for a finite range of initial momenta.

where J_1 is the order-1 Bessel function of the first kind and H_1 is the order-1 Struve function [99]. At the point of maximum friction, which occurs at $x_0 = -3\lambda_\mathrm{L}/16 + n\lambda_\mathrm{L}$ for some integer n, the integral in the above equation reduces to $2\pi J_1(4k_\mathrm{L}x_\mathrm{m})/(4k_\mathrm{L}x_\mathrm{m})$; this function can be readily evaluated numerically for a given trap frequency.

For small values of the trap frequency, the effect of the above averaging process is to introduce a factor of $\frac{1}{2}$ into Eq. (2.37). The result can be seen as being physically equivalent to the effect of cooling only one degree of freedom when the atom is in a harmonic trap. Finally, we combine the above two ideas to include both the effects of harmonic oscillation and the spatial extent of the atomic motion into Eq. (2.38). This can be done, effectively, by replacing $\tau \to \sin(\omega_\mathrm{t}\tau)/\omega_\mathrm{t}$. The resulting approximate expression for the friction force, taking into account the periodicity in the time delay as well as spatial averaging effects, becomes

$$\left\langle F_\parallel(x_0) \right\rangle = -\tfrac{1}{2}\hbar k_\mathrm{L}^2 v_\mathrm{m}\tau |A|^2 \left(\frac{g^2\Delta}{\Delta^2 + \Gamma^2} \right)^2 \mathrm{sinc}(\omega_\mathrm{t}\tau)$$
$$\times \int_0^{2\pi} \sin\!\left[4k_\mathrm{L}x_0 + 4k_\mathrm{L}x_\mathrm{m}\sin(T)\right]\cos^2(T)\,\mathrm{d}T\,. \quad (2.40)$$

2.6.2.4   Momentum capture range

As discussed above, the addition of the dipole trap introduces several features into the friction force. Plotting the variation of the friction force in Eq. (2.38) with the initial
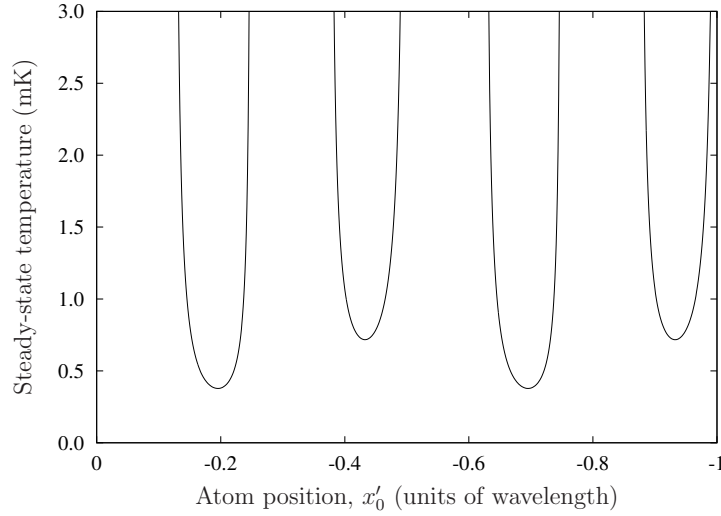
FIGURE 2.5: Calculated steady-state temperature T_M for an atom confined in a harmonic trap as a function of position whilst keeping the detuning and pump field constant. $\omega_t = 0.1 \times 2\pi\Gamma$; other parameters are as in Fig. 2.3.

momentum, p_0, of the atom, as in Fig. 2.4, shows that the amplitude of the force is not monotonic. In fact, it increases from zero, for increasing p_0, achieves a maximum, and then decreases again until it reaches zero at some value for p_0. Physically, this is due to the broader spatial distribution for faster particles in the harmonic trap. For fast enough velocities, the particle oscillates into the heating regions, as can be deduced from Fig. 2.3, even if the trap is centred at the position of maximum cooling. This defines a range of initial momenta, starting from zero, within which a particle is cooled by this mechanism; faster particles are heated and ejected from the trap. Note that this result was derived from the friction to lowest order in velocity v, and higher-order terms are expected to affect the capture range for high values of p_0.

At particular values of x'_0, e.g. at $-3\lambda_L/16$, this capture range can be conveniently estimated by using the location of the first zero of the Bessel function, giving a momentum capture range

$$p_m \approx 0.958\sqrt{mk_t}/k_L = 0.958m\omega_t/k_L \,. \tag{2.41}$$

Thus, $p_m^2 \propto \omega_t^2$, for values of ω_t that are not too large, and the capture range as defined in Fig. 2.4 is expected to scale with the square of the trap frequency. We will compare this later, in Section 2.6.3, with the results of Monte–Carlo numerical simulations.

2.6.2.5 Diffusion and steady-state temperature

The main result of the preceding discussion was a friction force, which of course cools an atom towards zero momentum in the absence of any other effects. Momentum diffusion due to spontaneous scattering, in a manner similar to that discussed in Section 1.7, introduces a constant in the equation for $\mathrm{d}p^2/\mathrm{d}t$ and results in a constant upward shift of the curve in Fig. 2.4. This slightly reduces the capture range for fast particles, but its main effect is to introduce a specific value of the momentum where friction and diffusion exactly compensate each other in the small p_0 range. This point corresponds to the steady-state temperature achievable through the cooling mechanism discussed here.

To lowest order in the coupling frequency g^2, the momentum diffusion is given by the interaction of the atom with the unperturbed, standing-wave pump field. In this limit, diffusion in our system is therefore identical to that encountered in the usual Doppler cooling mechanism [51, 52, 100, 101], where the diffusion coefficient D is given to lowest order in s by

$$D = \hbar^2 k_\mathrm{L}^2 \Gamma s \left[\cos^2(k_\mathrm{L} x_0) + \tfrac{2}{5} \sin^2(k_\mathrm{L} x_0) \right]. \tag{2.42}$$

The steady-state temperature T_M of mirror-mediated cooling is then obtained from Eq. (1.61) using $\varrho = -F_\parallel(x_0)/v_\mathrm{m}$, with $F_\parallel(x_0)$ given by Eq. (2.37). For $|\Delta_\mathrm{L}| \gg \Gamma$ we thus find

$$T_\mathrm{M} = \frac{1}{5\pi} \frac{\hbar}{k_B} \frac{\omega_\mathrm{t}\Gamma}{g^2} \frac{2 + 3\cos^2(k_\mathrm{L} x_0)}{\sin(\omega_\mathrm{t}\tau)\sin(4k_\mathrm{L} x_0)} \,. \tag{2.43}$$

An example of the dependence of T_M on the trap position is shown in Fig. 2.5, predicting a minimum temperature of the order of $400\,\mu\mathrm{K}$. Whilst this may seem large in comparison to the Doppler temperature of $141\,\mu\mathrm{K}$, one has to keep in mind that T_M, given by Eq. (2.43), is insensitive to detuning and, for far off-resonant operation of the order of tens of linewidths, it will be the dominant mechanism. This is further discussed in Section 2.6.4. We also note that Fig. 2.5 further highlights the importance of the requirement for localising the particle.

Using Eq. (2.36) we can approximate the steady-state temperature at the point of maximum friction by

$$T_\mathrm{M} \approx \frac{\hbar}{2k_\mathrm{B}\tau} \frac{\sigma_\mathrm{L}}{\sigma_\mathrm{a}} \,. \tag{2.44}$$

It is interesting to note that this expression is closely related to the expression for the limiting temperature in Doppler cooling, $k_B T = \hbar\Gamma$, but where the upper state lifetime

$1/(2\Gamma)$ is replaced by the atom–mirror delay time, τ, and where a geometrical factor equal to the mode area divided by the atomic radiative cross-section is included.

This last point will turn out to be a general trend in the cooling methods we discuss. The steady-state temperature is in general described by a function of the form

$$T = \frac{\hbar}{2k_{\mathrm{B}}\tilde{\tau}}\phi \,, \tag{2.45}$$

where $\tilde{\tau}$ is the characteristic time—e.g., the memory time—of the system and ϕ depends on the geometry of the situation. In Doppler cooling, the characteristic time is the lifetime of the upper state, $\tilde{\tau} = 1/(2\Gamma)$, whereas in mirror-mediated cooling it is naturally the delay time τ. In cavity-mediated cooling, where the atom is inside a cavity, the energy loss mechanism is due to the decay of the cavity field, and we thereby have $\tilde{\tau} = 1/(2\kappa)$ [19], where κ is the linewidth of the cavity field.

2.6.3 Numerical analysis of mirror-mediated cooling

In this section we now investigate a more accurate numerical model to corroborate the simplified analytical results obtained above.[9] In order to render the problem numerically tractable, the continuum of modes is replaced by a discrete set of modes with frequencies ω_k, with $k = 1, \ldots, N$. The master equation Eq. (1.17) is then converted by use of the Wigner transform [37] into a Fokker–Planck equation for the atomic and field variables. Applying a semiclassical approximation and restricting the equation of motion to second-order derivatives, one arrives at an equivalent set of stochastic differential equations for a single atom with momentum p and position x in a discrete multimode field with mode amplitudes α_k [102],

$$\mathrm{d}x = \frac{p}{m}\mathrm{d}t \,, \tag{2.46a}$$

$$\mathrm{d}p = \mathrm{i}\gamma_0\big[\mathcal{E}(x)\tfrac{\mathrm{d}}{\mathrm{d}x}\mathcal{E}^*(x) - \mathcal{E}^*(x)\tfrac{\mathrm{d}}{\mathrm{d}x}\mathcal{E}(x)\big]\mathrm{d}t - U_0\big[\mathcal{E}(x)\tfrac{\mathrm{d}}{\mathrm{d}x}\mathcal{E}^*(x) + \mathcal{E}^*(x)\tfrac{\mathrm{d}}{\mathrm{d}x}\mathcal{E}(x)\big]\mathrm{d}t$$
$$\qquad - k_{\mathrm{t}}(x - x_{\mathrm{t}})\mathrm{d}t + \mathrm{d}P \,, \text{ and} \tag{2.46b}$$

$$\mathrm{d}\alpha_k = \mathrm{i}\Delta_k\alpha_k\mathrm{d}t - (\mathrm{i}U_0 + \gamma_0)\mathcal{E}(x)f_k^*(x)\mathrm{d}t + \mathrm{d}A_k \,, \tag{2.46c}$$

---

[9] The Fokker–Planck equation was obtained, through the use of a suitably extended Wigner transform, by Peter Horak. The basis for the Monte–Carlo code was also written by PH, and then extended by AX. The simulations and data analysis were performed by AX.

where $f_k(x) = \sin(\omega_k x/c)$ are the individual mode functions, $\mathcal{E}(x) = \sum_k \alpha_k f_k(x)$ is the total electric field, $\Delta_k = \omega_k - \omega_\mathrm{L}$ is the detuning of each mode from the pump, U_0 is the light shift per photon, and γ_0 is the photon scattering rate. The terms $\mathrm{d}P$ and $\mathrm{d}A_k$ are correlated noise terms [102] responsible for momentum and field diffusion.

In the following, we set the trap centre to $x_\mathrm{t} = -3\lambda_\mathrm{L}/16$, modulo λ_L, which is the point where the analytical solution predicts the maximum of the damping force. We use $N = 256$ field modes with a mode spacing of $\Gamma/10$. At the start of every simulation, all field modes are empty with the exception of the pump mode which is initialised at 625 photons, corresponding to a laser power of around $50\,\mathrm{pW}$ for our chosen parameters.

The simulations were performed in runs of several thousand trajectories. Each such run was performed at a well-defined initial temperature, with the starting momenta of the particles chosen from a Gaussian distribution, and the starting position being the centre of the trap.

2.6.3.1 Friction force and capture range

Fig. 2.6 presents the results of a set of simulations performed when setting the noise terms $\mathrm{d}P$ and $\mathrm{d}A_k$ in equations Eq. (2.46) to zero, i.e., neglecting momentum and photon number diffusion. The simulation data are compared with the result of the perturbative calculations Eq. (2.40). For modest values of ω_t, Fig. 2.6(a) justifies the averaging process used to derive Eq. (2.38), which was based on spatial averaging but neglecting higher order terms in v. In contrast, for larger trap frequencies, the numerical simulations diverge significantly from the analytical result, as can be seen in Fig. 2.6(b). We expect that the terms in higher powers of the initial speed, which were dropped in the perturbative solution, are responsible for this discrepancy.

We have already seen, in Eq. (2.41), that the capture range is expected to scale as ω_t^2. For weak traps, as shown in Fig. 2.7, the numerical simulations agree well with these expectations. For stiffer traps, however, the capture range is consistently larger than that predicted; in fact, the simulations predict a capture range of around $450\,\mathrm{mK}$ for a trap frequency of $0.5 \times 2\pi\Gamma$

(a) $\omega_t = 0.3 \times 2\pi\Gamma$

(b) $\omega_t = 0.5 \times 2\pi\Gamma$
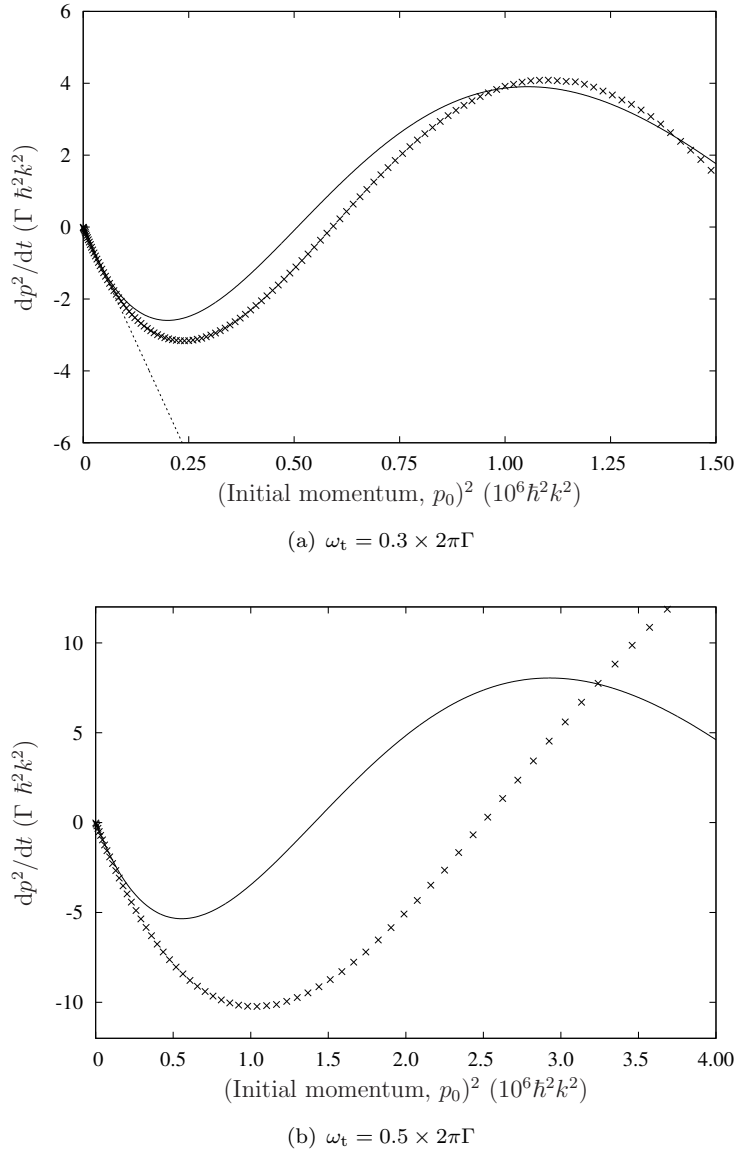
FIGURE 2.6: Comparison of dp^2/dt for the simulations without noise (data points) with the analytical approximation, Eq. (2.40), including the harmonic trap (solid line). (a) Weak harmonic trap, $\omega_t = 0.3 \times 2\pi\Gamma$, showing also the linear dependence in the limit of small momenta, Eq. (2.37) (dotted line). (b) Stiff trap, $\omega_t = 0.5 \times 2\pi\Gamma$. The trap position $x'_0 = -3\lambda/16$ and other parameters are as in Fig. 2.3.

2.6.3.2   Steady-state temperature

The next step in our investigation was to run simulations involving the full dynamics given by Eqs. (2.46) including the diffusion terms. Because of the discrete nature of the field modes with uniform frequency spacing used in the simulations, the numerically modelled behaviour is always periodic in time with a periodicity given by the inverse of the frequency spacing. The simulations therefore cannot follow each trajectory to its steady-state unless an unfeasibly large number of modes is used. Instead, simulations
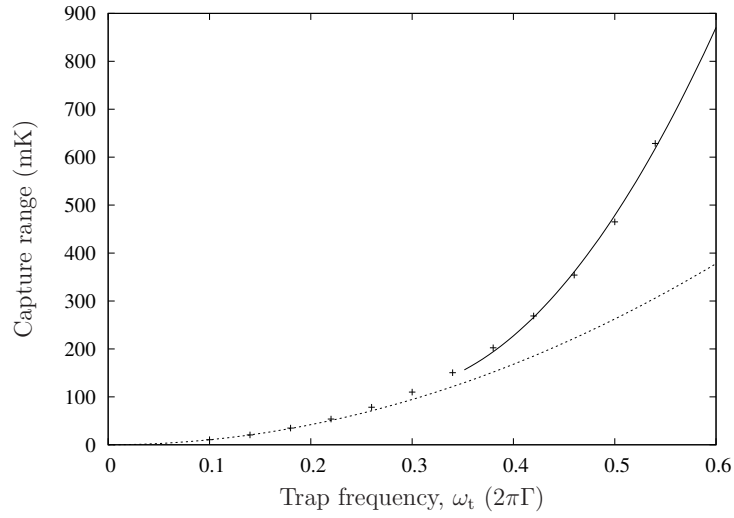
FIGURE 2.7: Capture range extracted from the simulations (data points) as compared to the analytical solution (dotted line) for various values of ω_t. The solid line is a quadratic fit to the data for $\omega_t \geq 0.3 \times 2\pi\Gamma$ and is only intended as a guide to the eye. Other parameters are as in Fig. 2.6.
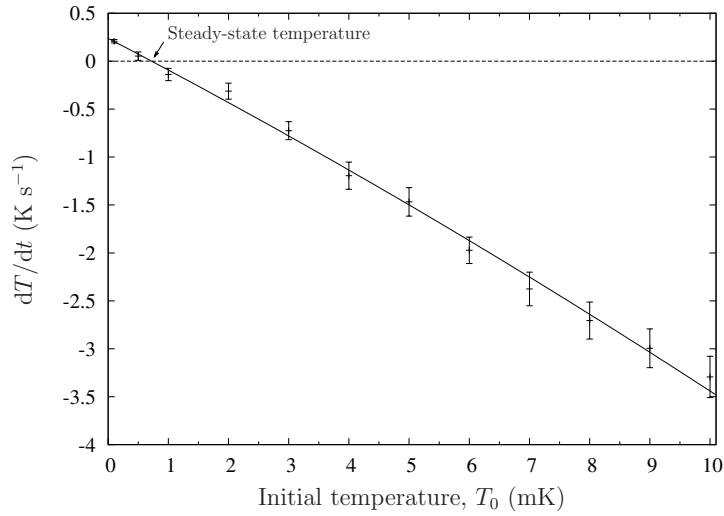
FIGURE 2.8: Cooling rate $(-\mathrm{d}T/\mathrm{d}t)$ extracted from the simulations starting at a number of initial temperatures. The solid line represents a quadratic fit to the data. $\omega_t = 0.5 \times 2\pi\Gamma$; other parameters are as in Fig. 2.6.

were performed in several groups of trajectories, each group forming a thermal ensemble at a well-defined initial temperature. For each such group of trajectories the initial value of $\mathrm{d}T/\mathrm{d}t$ was calculated. The results for $\omega_t = 0.5 \times 2\pi\Gamma$ are shown in Fig. 2.8, where the error bars are due to statistical fluctuations for a finite number of stochastic integrations. The steady-state temperature is that temperature at which $\mathrm{d}T/\mathrm{d}t = 0$ as clearly illustrated in this figure. For the chosen parameters, our data suggest a steady-state temperature of $722 \pm 54\,\mu\mathrm{K}$ with a $1/e$ cooling time of around $3.0\,\mathrm{ms}$. This compares reasonably well with the steady-state temperature of $597\,\mu\mathrm{K}$ predicted by Eq. (2.43).
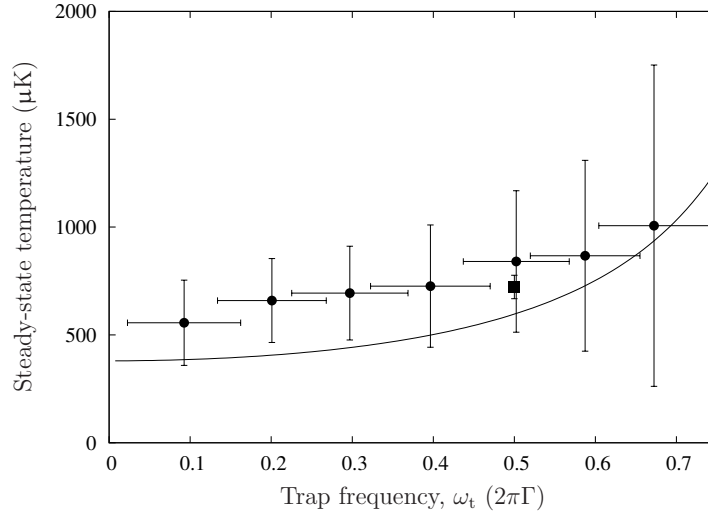
FIGURE 2.9: Steady-state temperature for a number of simulations (circles) compared to the analytical formula Eq. (2.43) (solid line). The solid square represents the equivalent data from Fig. 2.8, resulting from a much larger number of simulations. Parameters are as in Fig. 2.6.

We finally performed a large number of simulations to investigate the dependence of the steady-state temperature on the trap frequency. Eq. (2.43) indicates that as one decreases ω_t the steady state temperature decreases. This is clearly seen in Fig. 2.9, which compares the prediction of Eq. (2.43) with a set of numerical simulations. The trend in the data is reproduced well by the analytical expression. However, the simulated steady-state temperature is consistently a little higher than predicted. We expect that this discrepancy is due mainly to two reasons: (i) Eq. (2.43) was derived from the friction Eq. (2.37), i.e., without the spatial averaging of Eq. (2.40) which would reduce the friction force; and (ii) higher order terms in the velocity v are also expected to reduce friction compared to the lowest order analytical result. For both these reasons, therefore, the analytical expression is expected to overestimate the friction force and thus to predict equilibrium temperatures that are too low.

2.6.4 Beyond adiabatic theory

All the theoretical analysis and simulations discussed so far have been based on adiabatic elimination of the internal atomic degrees of freedom, and therefore neglected Doppler cooling. In Fig. 2.10, we explore the variation of T_M and the Doppler temperature, T_D, as a function of detuning from resonance when the particle is at the point of greatest
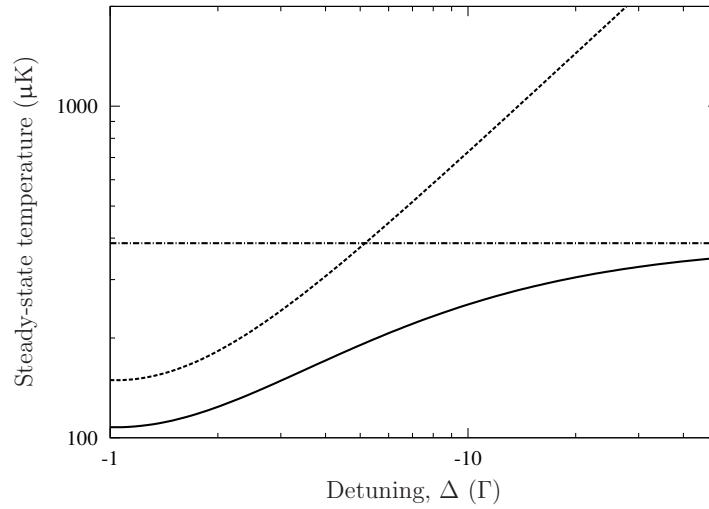
FIGURE 2.10: Comparison between the calculated steady-state temperatures for mirror-mediated cooling T_{M} (dash-dotted line), Doppler cooling T_{D} (dashed), and in the presence of both effects T (solid), drawn as a function of detuning whilst keeping the saturation parameter constant. $\omega_{\mathrm{t}} = 0.1 \times 2\pi\Gamma$; other parameters are as in Fig. 2.6.

friction $(x_0' = -3\lambda/16)$, where T_{D} is given by

$$T_{\mathrm{D}} = \hbar\Gamma \, \frac{\Delta_{\mathrm{L}}^2 + \Gamma^2}{2\left(-\Delta_{\mathrm{L}}\right)} \,, \tag{2.47}$$

for $\Delta_{\mathrm{L}} < 0$. In the presence of both cooling effects, and assuming that the momentum diffusion terms are identical for both mechanisms, the stationary temperature achieved by the system is given by

$$T = \left(\frac{1}{T_{\mathrm{M}}} + \frac{1}{T_{\mathrm{D}}} \right)^{-1} . \tag{2.48}$$

Thus, for the parameters of Fig. 2.9, the calculated steady-state temperature T reduces to $250\,\mu\mathrm{K}$ in the limit of vanishing ω_{t}.

From Fig. 2.10 one can see that the mirror-mediated force, for our tightly focussed pump, is stronger than the Doppler force for detunings larger than around 10Γ in magnitude. In practice this has two implications: for large negative detunings, we expect the steady-state temperature of the system to be significantly lower than that predicted by Doppler cooling; whereas for large *positive* detunings, we still predict equilibrium temperatures of the order of mK.

Both our perturbative expressions and our simulations are calculated to lowest orders in the atomic saturation. However, it is well known that in the limit of very large detunings also higher order terms in the saturation parameter s become significant. Using the full

expression for the diffusion constant [52], we can estimate the detuning for which we expect minimum diffusion and temperature. For the value of the saturation parameter $s \lesssim 0.1$ used throughout this section, it can be shown that T_{M} attains a minimum at detunings of up to several tens of linewidths. Our chosen parameters are therefore within the range of validity of the model.

2.6.5   Concluding remarks

In conclusion, we have presented a mechanism for cooling particles by optical means which is based fundamentally on the dipole interaction of a particle with a light beam and therefore does not rely on spontaneous emission. The particle is assumed to be trapped and is simultaneously driven by an off-resonant laser beam. After the interaction with the particle the beam is reflected back onto the particle by a distant mirror. The time-delay incurred during the light round-trip to the mirror and back is exploited to create a non-conservative cooling force.

The system was analysed using stochastic simulations of the semiclassical equations of motion representing a single two-level atom coupled to a continuum of electromagnetic modes. The results of these computations were found to agree with the expectations of a perturbative analysis. Our models predict sub-mK steady-state temperatures for ^{85}Rb atoms interacting with a tightly focussed laser beam several metres from the mirror, in an arrangement similar to that of Ref. [103]. While most of the theory is presented for a one-dimensional model, results for the friction force in the transverse direction suggest that three-dimensional cooling is possible with this scheme.

The model presented here requires a large separation between the atom and the mirror, of the order of several metres, for an observable cooling effect. This limitation can be overcome in several ways. First, the light could propagate in an optical fibre between the atom and the mirror to avoid the effects of diffraction. Second, the required delayed reflection could be achieved through the use of a cavity instead of a mirror; in contrast to cavity-mediated cooling schemes [19, 104–107], the atom would remain external to the cavity. For a time delay τ of order $1\,\mathrm{ns}$ one would require a cavity quality factor $Q = \omega\tau$ [108] of the order of $10^6 - 10^7$, which is achievable with present-day technology [109]. This mechanism is explored heuristically in Section 2.7.1, and subsequently investigated

in greater depth in Section 4.1, after we have developed the necessary mathematical tools.

2.6.A   Appendix: A note on units

The units used in the preceding work can perhaps best be called 'quantum mechanical'. Here, we provide a number of useful conversions and numerical values, which could be of benefit to readers with a more experimental leaning.

Quantity in this work	Experimental value
A	$2\sqrt{2\pi P/(\hbar k_\mathrm{L})}$
g	$\sqrt{\Gamma\sigma_\mathrm{a}/(\pi\sigma_\mathrm{L})}$
s	$g^2|A|^2/\Delta_\mathrm{L}^2 = 8\Gamma P\sigma_\mathrm{a}/(\hbar k_\mathrm{L}\sigma_\mathrm{L}\Delta_\mathrm{L}^2)$

In the above, P is the incident travelling-wave electromagnetic power, related to the incident electric field $\mathcal{E}$ by

$$P = \tfrac{1}{2}\epsilon_0 c\sigma_\mathrm{L}|\mathcal{E}|^2\,. \tag{2.49}$$

Γ is the HWHM linewidth of the upper state. For the D$_2$ line of some common alkali species we have:

Quantity	^{23}Na [110]	^{85}Rb [35], ^{87}Rb [111]	^{133}Cs [112]
Γ	$2\pi \times 4.897\,\mathrm{MHz}$	$2\pi \times 3.033\,\mathrm{MHz}$	$2\pi \times 2.617\,\mathrm{MHz}$
ω_a	$2\pi \times 508.848\,\mathrm{THz}$	$2\pi \times 384.230\,\mathrm{THz}$	$2\pi \times 351.726\,\mathrm{THz}$
$\lambda_\mathrm{a} = 2\pi c/\omega_\mathrm{a}$	$589.158\,\mathrm{nm}$	$780.241\,\mathrm{nm}$	$852.347\,\mathrm{nm}$
$k_\mathrm{a} = 2\pi/\lambda_\mathrm{a}$	$10.665 \times 10^6\,\mathrm{m}^{-1}$	$8.055 \times 10^6\,\mathrm{m}^{-1}$	$7.372 \times 10^6\,\mathrm{m}^{-1}$
$\sigma_\mathrm{a} = 3\lambda_\mathrm{a}^2/(2\pi)$	$1.657 \times 10^{-13}\,\mathrm{m}^2$	$2.905 \times 10^{-13}\,\mathrm{m}^2$	$3.469 \times 10^{-13}\,\mathrm{m}^2$
T_D	$235.03\,\mathrm{\mu K}$	$145.57\,\mathrm{\mu K}$	$125.61\,\mathrm{\mu K}$

2.7   Exploiting an optical memory in other geometries

Section 2.6 provided us with a sound theoretical basis, in the case of the simplest possible geometry that permits a memory, for the arguments we put forward in Section 2.4. In the present section, we will explore other geometries with which we can investigate the

retarded dipole–dipole interaction. The ideas developed here will be fleshed out in later chapters, after we develop the necessary formalisms, but it is fairly instructive at this early stage to intuitively explore how the different mechanisms arise from very similar physical arguments.

Let us first start by addressing the two major issues with the mirror-mediated cooling mechanism as described in the previous section. To recapitulate, the cooling force in this mechanism arises from the retarded dipole–dipole interaction of a particle with its own reflection in a mirror but (i) requires a distance of 'several metres' between the particle and the mirror for a sizeable effect, and (ii) the friction force oscillates between cooling and heating on a sub-wavelength scale and has a zero spatial average. Following the discussion of these two points, we will turn our attention to three-dimensional geometries to see how we can exploit the focussing properties of optics to achieve cooling.

2.7.1   Lengthening the time delay: External cavity cooling

From the general arguments in Section 2.4, as well as the expressions in Section 2.6, we can see that the time delay is what governs the overall strength of the friction force in the retarded dipole–dipole interaction. This can be exploited in what we term 'external cavity cooling' (Section 4.1), where the particle to be cooled interacts with a cavity field despite being outside the cavity. The nature of the interaction here is practically identical to mirror-mediated cooling; in particular, it suffers from the same drawback of having the friction force oscillate between a cooling and a heating force several times over the space of a single wavelength. Nevertheless, this is not a problem if what is to be cooled is not the motional energy of an atom but that of a micromirror since (i) a micromirror can be positioned, using piezoelectric actuators, with sub-nanometre-scale resolution [113], and (ii) the oscillation amplitude for the Brownian motion of a micromirror is also in the picometre to nanometre range. To illustrate the latter point, let us use the effective spring constant of a commercially-available micromirror as calculated in Ref. [114], $k_{\mathrm{M}} = 28\,\mathrm{N\,m^{-1}}$. Then, the RMS displacement for the micromirror at a temperature $T = 300\,\mathrm{K}$, calculated as

$$\sqrt{\langle x^2 \rangle} = \sqrt{\frac{k_{\mathrm{B}}T}{k_{\mathrm{M}}}} \,, \tag{2.50}$$

is of the order of 10^{-11} m.
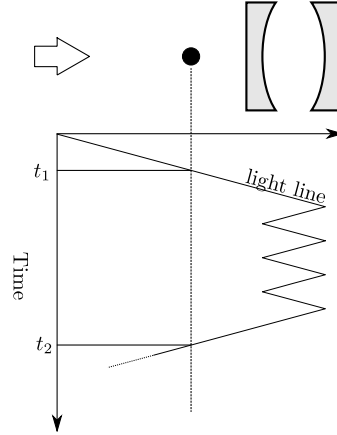
FIGURE 2.11: Space–time diagram showing the distance folding argument used to explain the action of external cavity cooling. This figure should be compared to Fig. 2.2. The blank arrow indicates the pump beam.

Having established the rationale, then, we can introduce 'external cavity cooling' by means of the distance folding argument (see Fig. 2.11). For suppose we place a particle (atom or micromirror) in front of a cavity. The light that interacts with the particle is then allowed to couple into the cavity. This light then undergoes several round trips inside the cavity, and with each round-trip some light leaks out and re-interacts with the particle. An effective delay time can be defined that is related to the finesse (or, equivalently, the linewidth) of the cavity, and it is this concept that we show in Fig. 2.11. One notes that this delay time is, for a good cavity, orders of magnitude larger than that due to either mirror separately. Using a good cavity, with a finesse of the order of 10^5, thereby allows us to squeeze the 'several metres' into a sub-millimetre-scale device. This opens the door to several important advances, of which we mention a few here. First of all, one is not constrained to use Fabry–Pérot-type cavities, whereby the system can be constructed monolithically on a chip-scale device. Secondly, the cavity does not need to have good optical or mechanical access, which allows one to make significantly better and more stable cavities. Finally, having the micromirror or atom outside the cavity means that there is less chance of burning or saturation effects, since the local field surrounding the particle is not amplified by the cavity.

2.7.2 Lifting the sub-wavelength dependence: Ring cavity cooling

A cursory physical analysis of the mirror-mediated cooling mechanism will reveal that the origin of the $\sin(4k_{\mathrm{L}}x_0)$ dependence lies in the fact that the atom is in a standing

(a) Mirror-Mediated Cooling

(b) Ring Cavity Cooling, position 1

(c) Ring Cavity Cooling, position 2
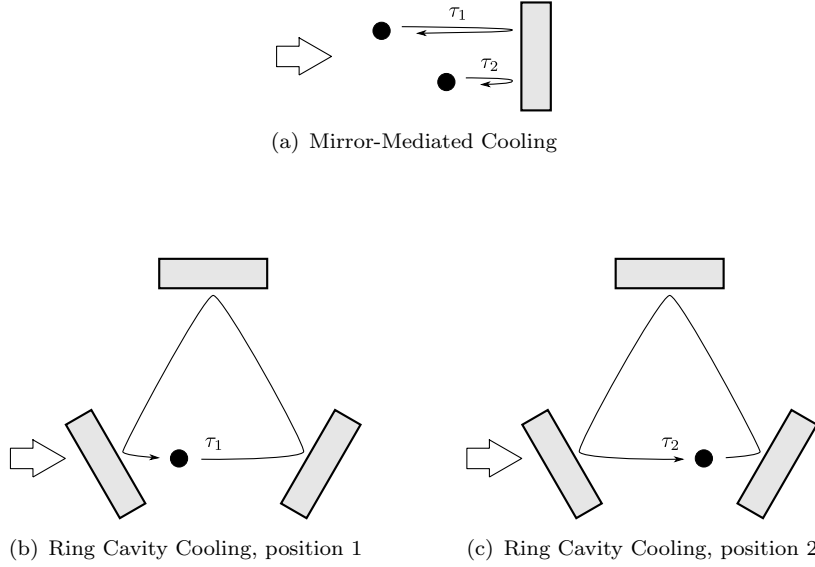
FIGURE 2.12: In (a) mirror-mediated cooling, the time delay depends on the atomic position ($\tau_1 \neq \tau_2$), whereas in (b, c) ring cavity cooling, it is independent of the atomic position ($\tau_1 = \tau_2$). The blank arrow indicates the pump beam.

wave inside a system that is *not* translationally invariant. To see this latter point, one simply needs to observe that, with the atom at two different places the time delay is of course different. One way of restoring translational invariance into the system is by using a ring cavity, rather than a plane mirror, to introduce a delay; see Fig. 2.12. The expectation of the physical mechanism being preserved, albeit without the position dependence in the friction force, is borne out when the system is examined in detail, as we shall see in Section 4.3 after we have developed the necessary mathematical model.

2.7.3 Exploiting three-dimensional electromagnetism

Perhaps the two biggest conceptual differences between electromagnetism in one dimension and that in three dimensions are orthogonal polarisations (which can nevertheless be mathematically mimicked in a quasi-one-dimensional geometry) and the spreading out of waves. Indeed, a travelling wave in one dimension can be represented as

$$\cos[\omega(t - x/c)], \tag{2.51}$$

whereby the amplitude of the wave is 1, for any value of x. In three dimensions, however [44] [see, for example, Eq. (9.19) in this reference], the amplitude of the electric field is dependent on the distance r from the source, and scales as $1/r$ for $r \gg \lambda$. Thus,

(a) Optical binding

(b) Self–tweezing, static

(c) Self–tweezing, moving
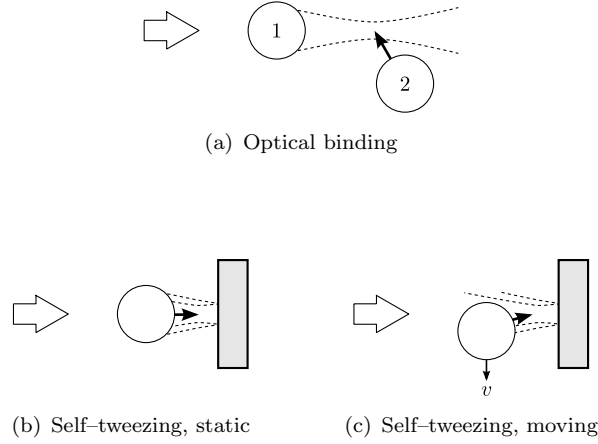
FIGURE 2.13: In (a) optical binding, particle 2 is in a potential well caused by particle 1. Self–tweezing, (b), occurs when a particle is in a potential well caused by itself; if the particle is moving, (c), it will experience a force opposing its motion. The blank arrow indicates the pump beam and the thick black arrows the force.

suppose a particle has a dipole induced by a local electric field E. This dipole will subsequently emit a spherical wave, and let us suppose that we reflect this wave back onto the dipole. The potential energy mediated by the interaction between the instantaneous dipole polarisation and the reflected field (which has travelled through a distance r) is, up to some phase and constants,

$$U \sim -\frac{E^2}{r}\,. \tag{2.52}$$

We can now apply the result in Eq. (2.15): the dipole will experience a friction force proportional to $\tau c/r^3 = 1/r^2$.

The spreading out of waves in three dimensions is but one instance of the more general concept of (de)focussing of an electric field. Let us examine a simple way in which we can exploit this idea, *self-tweezing*. Optical binding [115], Fig. 2.13(a), is an interesting phenomenon whereby light incident on a dielectric sphere is focussed by the sphere itself. This focus, in turn, produces a potential well for a second particle, which is thereby optically bound to the first. Suppose, then that we only have one particle, and that we put a plane mirror 'downstream' of that particle, Fig. 2.13(b). The mirror will, if the geometry is chosen properly, cause the focus to appear close enough to the particle that it will feel the potential well caused by this electric field. This situation, then is similar to the case with two particles, but the single particle is now optically bound to *itself*. Any motion of the particle around this position will cause its image to lag behind it and a restoring, viscous, force to act on it, Fig. 2.13(c).

Part II

SCATTERING MODELS

&

THEIR APPLICATIONS

Chapter 3

The transfer matrix model

> The reader might wonder why it is of interest, physically, to consider n-manifolds
> for which n is larger than 4, since ordinary spacetime has just four dimensions.
> In fact many modern theories [...] operate within a 'spacetime' whose dimension is
> much larger than 4.
>
> R. Penrose, *The Road to Reality* (2004)

Chapter 1, and in particular Section 1.4, developed the necessary tools to describe the
interaction of an atom with the electromagnetic field, as parametrised by the atom's
characteristic polarisability. In one dimension, one can succinctly describe the fields in-
teracting with a linear scatterer through what is called the transfer matrix approach [47].
Restricting ourselves to one spatial dimension is not an overly restrictive approximation,
despite the quote at the beginning of this chapter; the formalism that is discussed in
this chapter allows us to describe a wealth of physical situations. The purpose of this
chapter is to extend this model significantly, enabling it to account for moving as well as
static scatterers; this is done in Section 3.1 and the model that results is solved gener-
ally in Section 3.2. The extended model discussed here takes into account the first-order
Doppler shift but not relativistic effects, and it is therefore correct only to first order
in the velocity of the scatterer.

The transfer matrix method is more general than an analysis based on modal decompo-
sition, and is therefore used to describe the optomechanics of scatterers inside cavities
in Section 3.3. This method is extended even further in Section 3.4, where it is shown
that the concept of polarisability can also be applied to atoms having a Zeeman man-
ifold and interacting with circularly polarised light. The results of these sections are

confirmed by showing that the standard results for optical molasses, mirror-mediated cooling and cooling of cavity mirrors, as well as sub-Doppler cooling mechanisms [14], can be reproduced by simple applications of the transfer matrix method. In Chapter 4, the theory developed over the present chapter will then be applied to describe two novel cooling schemes, outside cavities (Section 4.1) and inside ring cavities (Section 4.3).

3.1   An extended scattering theory

In this first section we develop and present a scattering theory for optomechanically coupled systems, allowing for the efficient description of the motion of arbitrary combinations of atoms and mirrors interacting through the radiation field. We will restrict the model to one-dimensional motion and small velocities. The main building block is the beamsplitter transfer matrix [47, 116], i.e., the *local relation* between light field amplitudes at the two sides of a scatterer. We will calculate the radiation force acting on a moving scatterer up to linear order in the velocity. The model is completed by including the quantum fluctuations of the radiation force which stem from the quantised nature of the field. We will determine the momentum diffusion coefficient corresponding to the minimum quantum noise level.

One system we will consider in some detail is composed of two mirrors; one of them is fixed in space, whilst the other one is mobile. This is the generic scheme for radiation pressure cooling of moving mirrors [117–119]. At the same time, in the limit of low reflection the moving mirror can equally well represent the a single atomic dipole interacting with its mirror image in front of a highly reflecting surface (Section 2.6; see also Refs. [41, 103, 120]).

The work in this chapter is published as Xuereb, A., Domokos, P., Asbóth, J., Horak, P., & Freegarde, T. Phys. Rev. A **79**, 053810 (2009) and Xuereb, A., Freegarde, T., Horak, P., & Domokos, P., Phys. Rev. Lett. **105**, 013602 (2010) and is in part reproduced *verbatim*. After our initial exploration of the transfer matrix description of moving scatterers, we subsequently apply this description to several systems, and also extend it in several ways. The resulting model is very general and can be solved to give analytical formulations of the friction forces and momentum diffusion processes acting in a generic optomechanical system.
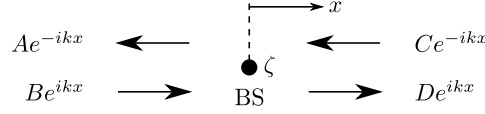
FIGURE 3.1: The four different modes that interact through a point-like beamsplitter
in one dimension.

3.1.1 Basic building blocks of the model

Consider a point-like scatterer (or beamsplitter), BS, moving along the 'x' axis on the
trajectory $x_{\text{BS}}(t)$. Outside the scatterer, the electric field $\mathcal{E}$ can be expressed in terms
of a discrete sum[1] of left- and right-propagating plane wave modes with different wave
numbers, k, and hence different frequencies, $\omega = kc$:

$$\mathcal{E} = \begin{cases} \sum_k \left[A(k)e^{-\mathrm{i}kx-\mathrm{i}\omega t} + B(k)e^{\mathrm{i}kx-\mathrm{i}\omega t} \right] + \text{c.c.} & x < x_{\text{BS}} \\ \sum_k \left[C(k)e^{-\mathrm{i}kx-\mathrm{i}\omega t} + D(k)e^{\mathrm{i}kx-\mathrm{i}\omega t} \right] + \text{c.c.} & x > x_{\text{BS}}, \end{cases} \tag{3.1}$$

where $A(k)$ and $B(k)$ are the mode amplitudes on the left side, $x < x_{\text{BS}}(t)$, while $C(k)$
and $D(k)$ are the amplitudes on the right side, $x > x_{\text{BS}}(t)$, of BS, and where c.c. denotes
the complex conjugate. In accordance, the magnetic field is [44]

$$c\mathcal{B} = \begin{cases} \sum_k \left[-A(k)e^{-\mathrm{i}kx-\mathrm{i}\omega t} + B(k)e^{\mathrm{i}kx-\mathrm{i}\omega t} \right] + \text{c.c.} & x < x_{\text{BS}} \\ \sum_k \left[-C(k)e^{-\mathrm{i}kx-\mathrm{i}\omega t} + D(k)e^{\mathrm{i}kx-\mathrm{i}\omega t} \right] + \text{c.c.} & x > x_{\text{BS}}. \end{cases} \tag{3.2}$$

As depicted schematically in Fig. 3.1, the scatterer mixes these waves. Our first goal
is the derivation of the transfer matrix M connecting the field amplitudes on the right
to those on the left side of a beamsplitter moving at a fixed velocity v. This rela-
tion is well-known [47] for an immobile scatterer. Therefore, let us first transform the
electromagnetic field into a frame moving with the instantaneous velocity v of the BS.

3.1.1.1 Transfer matrix for an immobile beamsplitter

In the frame co-moving with the BS, the interaction of the field with the scatterer at
$x' = 0$ can be characterised by the single parameter ζ by means of the one-dimensional

---

[1] This is a simplifying assumption and all our results also hold for a continuum of field modes.

wave equation [44, 47],

$$\left(\partial_{x'}^2 - \frac{1}{c^2}\partial_{t'}^2\right)\mathcal{E}'(x',t') = \frac{2}{kc^2}\zeta\,\delta(x')\,\partial_{t'}^2\mathcal{E}'(x',t')\,. \tag{3.3}$$

The electric field can be considered in a modal decomposition similar to Eq. (3.1). Since a fixed beamsplitter couples only the plane waves with identical frequency and wave number, the stationary scattering can be fully described within the closed set of modes

$$\mathcal{E}'(x',t') = \begin{cases} \left(A'e^{-\mathrm{i}kx'-\mathrm{i}\omega t'} + B'e^{\mathrm{i}kx'-\mathrm{i}\omega t'}\right) + \text{c.c.} & x' < 0 \\ \left(C'e^{-\mathrm{i}kx'-\mathrm{i}\omega t'} + D'e^{\mathrm{i}kx'-\mathrm{i}\omega t'}\right) + \text{c.c.} & x' > 0\,, \end{cases} \tag{3.4}$$

where the index k has been dropped. A linear relation between the field amplitudes on the right of the scatterer and those on the left can be derived from the wave equation [47],

$$\begin{pmatrix} C' \\ D' \end{pmatrix} = M \begin{pmatrix} A' \\ B' \end{pmatrix}\,,\text{ with} \tag{3.5}$$

$$M = \begin{bmatrix} 1 - \mathrm{i}\zeta & -\mathrm{i}\zeta \\ \mathrm{i}\zeta & 1 + \mathrm{i}\zeta \end{bmatrix} = \frac{1}{\mathfrak{t}}\begin{bmatrix} 1 & -\mathfrak{r} \\ \mathfrak{r} & \mathfrak{t}^2 - \mathfrak{r}^2 \end{bmatrix}\,. \tag{3.6}$$

In the second form of the transfer matrix M, we expressed it in terms of the reflectivity $\mathfrak{r}$ and transmissivity $\mathfrak{t}$ of the beamsplitter. This latter form is more convenient to describe moving mirrors, while for atoms the scattering strength parameter ζ can be readily expressed in terms of its polarisability α [see Section 1.4, and especially Eq. (1.42)]. In this case the transfer matrix depends on the wave number k, which might lead to significant effects, e.g., Doppler cooling, close to resonance with the atom (see Section 3.1.1.5).

3.1.1.2   Transfer matrix for a moving beamsplitter

The transformation back into the laboratory-fixed frame involves the change of the coordinates, $x' = x - vt$ and $t' = t$, and the Lorentz-boost of the electric field up to linear order in v/c [44, §11.10]:

$$\mathcal{E} = \mathcal{E}' + v\mathcal{B}'\,, \tag{3.7}$$

where we assumed that $\mathcal{E}$ and $\mathcal{E}'$ are polarised in the 'y' direction, $\mathcal{B}$ and $\mathcal{B}'$ are polarised in the 'z' direction, and the velocity is along the x axis. The electric field in the

laboratory frame becomes

$$
\begin{aligned}
\mathcal{E}(x,t) = \sum_{k'} \Bigg\{ & A'(k')e^{-ik'(x-vt)-i\omega't} + B'(k')e^{ik'(x-vt)-i\omega't} \\
& - \frac{v}{c}\Big[A'(k')e^{-ik'(x-vt)-i\omega't} - B'(k')e^{ik'(x-vt)-i\omega't} \Big] \Bigg\} + \text{c.c.} \\
= \sum_{k} \Big[& \big(1 - \tfrac{v}{c}\big) A'\big(k + kv/c\big)\, e^{-ik(1+v/c)x-i\omega t} \\
& + \big(1 + \tfrac{v}{c}\big) B'\big(k - kv/c\big)\, e^{ik(1-v/c)x-i\omega t} \Big] + \text{c.c.} \,,
\end{aligned}
\tag{3.8}
$$

which can be expressed as a linear transformation $\hat{L}(v)$ of the amplitudes,

$$
\begin{pmatrix} A(k) \\ B(k) \end{pmatrix} = \hat{L}(-v) \begin{pmatrix} A'(k) \\ B'(k) \end{pmatrix} , \text{ with}
\tag{3.9}
$$

$$
\hat{L}(v) = \begin{bmatrix} \big(1 + \tfrac{v}{c}\big)\hat{P}_{-v} & 0 \\ 0 & \big(1 - \tfrac{v}{c}\big)\hat{P}_{v} \end{bmatrix} .
\tag{3.10}
$$

This construction is explored further in Appendix 3.1.A. Here we defined the operator $\hat{P}_v : f(k) \mapsto f\big(k + k\tfrac{v}{c}\big)$, which represents the Doppler shift of the plane waves in a moving frame. Obviously, $\hat{L}^{-1}(v) = \hat{L}(-v)$ to first order in v/c. The total action of the moving BS,

$$
\begin{pmatrix} C(k) \\ D(k) \end{pmatrix} = \hat{M} \begin{pmatrix} A(k) \\ B(k) \end{pmatrix} ,
\tag{3.11}
$$

can then be obtained from

$$
\begin{aligned}
\hat{M} &= \hat{L}(-v)M\hat{L}(v) \\
&= \frac{1}{\mathfrak{t}} \begin{bmatrix} 1 & -(1 - 2\tfrac{v}{c})\mathfrak{r}\hat{P}_{2v} \\ (1 + 2\tfrac{v}{c})\mathfrak{r}\hat{P}_{-2v} & \mathfrak{t}^2 - \mathfrak{r}^2 \end{bmatrix} ,
\end{aligned}
\tag{3.12}
$$

where we have assumed that $\mathfrak{r}$ and $\mathfrak{t}$ do not depend on the wave number. Compared to M in Eq. (3.6), the difference lies in the off-diagonal terms including the Doppler shift imposed by the reflection on a moving mirror. In other words, the coupled counter-propagating plane wave modes differ in wave number, i.e., $k\big(1 + \tfrac{v}{c}\big)$ right-propagating waves couple to $-k\big(1 - \tfrac{v}{c}\big)$ left-propagating waves. Furthermore, if the polarisability itself depends on the wave number k, e.g., as in Eq. (1.42), the Doppler shift operator

acts also on it. To see this effect explicitly, to linear order in v/c, $\hat{M}$ can be written as

$$
\begin{bmatrix}
1 - \mathrm{i}\zeta - \mathrm{i}\frac{v}{c}\omega\frac{\partial\zeta}{\partial k} & -\mathrm{i}\zeta\left[1 - \frac{v}{c}\left(2 - \frac{k}{\zeta}\frac{\partial\zeta}{\partial k}\right)\right]\hat{P}_{2v} \\
\mathrm{i}\zeta\left[1 + \frac{v}{c}\left(2 - \frac{k}{\zeta}\frac{\partial\zeta}{\partial k}\right)\right]\hat{P}_{-2v} & 1 + \mathrm{i}\zeta - \mathrm{i}\frac{v}{c}k\frac{\partial\zeta}{\partial k}
\end{bmatrix} . \tag{3.13}
$$

The transfer matrix in the laboratory frame can thus be conceived as a 2-by-2 supermatrix acting also in the k-space. The amplitude C at a given wave number k, i.e., $C(k)$, is combined with the amplitudes $A(k)$ and $B\left(k - 2k\frac{v}{c}\right)$. A similar statement holds for $D(k)$.

Starting from the knowledge of the incoming field amplitudes, this transfer matrix allows for calculating the total electromagnetic field around a beamsplitter moving with a fixed velocity. In the next step, we derive the force on the moving scatterer through the Maxwell stress tensor.

3.1.1.3   Force on a medium in an electromagnetic field

The Maxwell stress tensor (see [44, §6.7]) is defined, for a homogeneous medium in one dimension, x, as

$$
\boldsymbol{T}_{xx} = -\frac{\epsilon_0}{2}\left(|\mathcal{E}|^2 + c^2|\mathcal{B}|^2\right) , \tag{3.14}
$$

where the electric field $\mathcal{E}$ and the magnetic field $\mathcal{B}$, Eq. (3.1) and Eq. (3.2), respectively, have no components along x. It is trivial, then, to see that after applying the rotating wave approximation, we obtain

$$
\boldsymbol{T}_{xx} = -2\epsilon_0\left[\left|\sum_k A(k)e^{-\mathrm{i}kx - \mathrm{i}\omega t}\right|^2 + \left|\sum_k B(k)e^{\mathrm{i}kx - \mathrm{i}\omega t}\right|^2\right] , \tag{3.15}
$$

since the cross terms in $|\mathcal{E}|^2$ and $|\mathcal{B}|^2$ have opposite signs. Note that $\boldsymbol{T}_{xx}$ varies on time scales of the order of the optical period. Let us now introduce a characteristic time, $\tau \gg 2\pi/\omega_0$, over which the variations in $\boldsymbol{T}_{xx}$ will be averaged, ω_0 being the central

frequency of the pump beam. At $x = 0$,

$$\frac{1}{\tau}\int_0^\tau \Big|\sum_k A(k)e^{-\mathrm{i}\omega t}\Big|^2 \mathrm{d}t = \sum_k |A(k)|^2 + \sum_{i\neq j}\frac{1}{\tau}\int_0^\tau A(k_i)\big[A(k_j)\big]^* e^{-\mathrm{i}(\omega_i-\omega_j)t}\mathrm{d}t$$

$$\approx \sum_k |A(k)|^2 + \sum_{i\neq j} A(k_i)\big[A(k_j)\big]^*$$

$$= \Big|\sum_k A(k)\Big|^2 . \tag{3.16}$$

In the approximation we assumed that the frequency bandwidth of the excited modes, $\Delta = \max\{\omega_i - \omega_j\}$, around ω_0 is so narrow that $\tau \ll 2\pi/\Delta$. Since the broadening is due to the Doppler shift, $\Delta \sim 2\omega_0\frac{v}{c}$, where v is the speed of the beamsplitter. For example, taking v to be the typical speed of atoms in a magneto-optical trap, we require $\tau \ll \pi/\big(\omega_0\frac{v}{c}\big) \sim 10^{-4}$ s. The time needed to reach the stationary regime of scattering is typically much shorter and thus this condition imposed on the averaging time τ can be safely fulfilled.

The force on the medium is given by the surface integral of $\boldsymbol{T}_{xx}$ on the surface, $\mathcal{S}$, of a fictitious volume $V = \sigma_\mathrm{L}\,\delta l$ enclosing the medium, where σ_L is the mode area and δl the infinitesimal length of the volume along the 'x' axis. Then, this force is given by

$$F = \oint_{\mathcal{S}} \boldsymbol{T}_{xx} n_x \mathrm{d}\mathcal{S}$$

$$= \sigma_\mathrm{L}\big[\boldsymbol{T}_{xx}(x\to 0^+) - \boldsymbol{T}_{xx}(x\to 0^-)\big], \tag{3.17}$$

where $n_x = \mathrm{sgn}(x)$ is the normal to $\mathcal{S}$. Substituting the relevant expressions for $\boldsymbol{T}_{xx}$ into the preceding formula gives

$$F = \frac{\hbar\omega_0}{c}\Big(|A|^2 + |B|^2 - |C|^2 - |D|^2\Big), \tag{3.18}$$

where $A = [\hbar\omega_0/(2\sigma_\mathrm{L}\epsilon_0 c)]^{-1/2}\sum_k A(k)$ is the photo-current amplitude, and similarly for B, C and D, their modulus square giving the number of photons per unit time. Although we considered first the electric field composed of independent modes, in the force expression only the sums of the mode amplitudes occur. An identical result holds when we replace the discrete sum over k by an integral, defining $A = [\hbar\omega_0/(2\sigma_\mathrm{L}\epsilon_0 c)]^{-1/2}\int A(k)\mathrm{d}k$, etc.

3.1.1.4   Quantum fluctuations of the force

In the previous section the force was derived based on the assumption that the field amplitudes are c-numbers. In order to describe the inherent quantum fluctuations of the force, we need to resort to the quantum theory of fields and represent the mode amplitudes by operators: $A(k) \rightarrow \hat{A}(k)$. To leading order the fluctuations of the force acting on a beamsplitter amount to a momentum diffusion process [14, 121]. The diffusion coefficient will be evaluated in the case of coherent-state fields [122].

The diffusion coefficient can be deduced from the second-order correlation function of the force operator, Eq. (1.54). The evaluation of this quantum correlation is system-specific. Quantum correlations, i.e., the operator algebra of the mode amplitudes $\hat{A}(k)$, $\hat{B}(k)$, $\hat{C}(k)$, and $\hat{D}(k)$, are influenced by multiple scattering and thus depend on the total transfer matrix of the entire system. The simplest case is a single beamsplitter at rest where the "input" modes $\hat{B}(k)$ and $\hat{C}(k)$ have independent fluctuations. The calculation, delegated to Appendix 3.1.B, includes all the steps needed for the treatment of a general system. The diffusion coefficient for a single beamsplitter is obtained as

$$D = (\hbar k)^2 \Big(|A|^2 + |B|^2 + |C|^2 + |D|^2 + 2\,\mathrm{Re}\{\mathfrak{r}A^*B - \mathfrak{t}A^*C\} + 2\,\mathrm{Re}\{\mathfrak{r}D^*C - \mathfrak{t}D^*B\} \Big),$$

(3.19)

where $A = \langle \hat{A} \rangle, B = \langle \hat{B} \rangle, C = \langle \hat{C} \rangle, D = \langle \hat{D} \rangle$ are the photo-current amplitudes (their modulus square is of the units of 1/sec), obeying Eq. (3.11) for $v = 0$.

As an example, let us consider the diffusion coefficient for a two-level atom illuminated by counter-propagating monochromatic light waves. Using the polarisability ζ, the transmission and reflection coefficients can be expressed as $\mathfrak{t} = 1/(1 - \mathrm{i}\zeta)$ and $\mathfrak{r} = \mathrm{i}\zeta/(1 - \mathrm{i}\zeta)$, respectively [see Eq. (3.6)]. Eq. (3.19) can then be rewritten in the form

$$D = (\hbar k)^2 \left[\frac{2\,\mathrm{Im}\{\zeta\}}{|1 - \mathrm{i}\zeta|^2} |B - C|^2 + \frac{4|\zeta|^2}{|1 - \mathrm{i}\zeta|^2} \Big(|B|^2 + |C|^2 \Big) \right],$$

(3.20)

where the first term, apart from the factor $|1 - \mathrm{i}\zeta|^2$, corresponds to the result well-known from laser cooling theory. Second- and higher-order terms in $|\zeta|$ correspond to the back-action of the atom on the field and are usually absent in treatments of laser cooling due to the fact that $|\zeta| \ll 1$ is generally implicit in such treatments. Note that the diffusion process due to the recoil accompanying the spontaneous emission of a photon

(see Ref. [52]) is missing from this result. The detailed modelling of absorption, i.e., scattering photons into the three-dimensional space, is not included in our approach.

3.1.1.5 Example: Force on a moving beamsplitter

We will now use Eq. (3.18) to derive a general expression for the force on a moving beamsplitter illuminated by two counterpropagating, monochromatic, plane waves with amplitudes B_0 and C_0. On using Eq. (3.11) to express the outgoing field modes in terms of the incoming ones, we note that the outgoing amplitudes comprise two monochromatic terms each:

$$A = \frac{\mathrm{i}\zeta \left[1 - \frac{v}{c}\left(2 + \frac{k}{\zeta}\frac{\partial\zeta}{\partial k} \right) \right]}{1 - \mathrm{i}\zeta\left(1 - \frac{v}{c}\frac{k}{\zeta}\frac{\partial\zeta}{\partial k} \right)} B_0 + \frac{1}{1 - \mathrm{i}\zeta\left(1 + \frac{v}{c}\frac{k}{\zeta}\frac{\partial\zeta}{\partial k} \right)} C_0 \,. \tag{3.21}$$

and

$$D = \frac{1}{1 - \mathrm{i}\zeta\left(1 - \frac{v}{c}\frac{k}{\zeta}\frac{\partial\zeta}{\partial k} \right)} B_0 + \frac{\mathrm{i}\zeta \left[1 + \frac{v}{c}\left(2 + \frac{k}{\zeta}\frac{\partial\zeta}{\partial k} \right) \right]}{1 - \mathrm{i}\zeta\left(1 + \frac{v}{c}\frac{k}{\zeta}\frac{\partial\zeta}{\partial k} \right)} C_0 \,. \tag{3.22}$$

These relations are substituted into Eq. (3.18), giving

$$
\begin{aligned}
F = \frac{2\hbar\omega}{\left| 1 - \mathrm{i}\zeta \right|^2} \Bigg\{ & \left(\mathrm{Im}\{\zeta\} + |\zeta|^2 \right)\left(|B_0|^2 - |C_0|^2 \right) - 2\,\mathrm{Re}\{\zeta\}\,\mathrm{Im}\{B_0 C_0^*\} \\
& - \frac{v}{c}\Bigg[\left(\omega\,\mathrm{Im}\left\{ \frac{1 + \mathrm{i}\zeta^*}{1 - \mathrm{i}\zeta}\frac{\partial\zeta}{\partial\omega} \right\} + 2|\zeta|^2 \right)\left(|B_0|^2 + |C_0|^2 \right) \\
& \qquad\qquad + 2\,\mathrm{Im}\left\{ \omega\frac{1 + \mathrm{i}\zeta^*}{1 - \mathrm{i}\zeta}\frac{\partial\zeta}{\partial\omega} + 2\zeta \right\}\mathrm{Re}\{B_0 C_0^*\} \Bigg] \Bigg\},
\end{aligned} \tag{3.23}
$$

accurate to first order in v/c. For $v = 0$ this result reduces to the one in Ref. [116]. Most of the v-dependent terms arise from the frequency dependence of the polarisability. These are the dominant terms in the case of a quasi-resonant excitation of a resonant scatterer, such as a two-level atom, since the prefactor $\frac{k}{\zeta}\frac{\partial\zeta}{\partial k} \sim \frac{\omega}{\Gamma}$ expresses resonant enhancement. The v-dependent terms linear in the polarisability ζ are in perfect agreement with the friction forces known from standard laser cooling theory, both for propagating and for standing waves. For example, assuming identical laser powers from the two sides, giving a standing wave with wavenumber k_0, and averaging spatially gives

$$F = -4\hbar k_0^2 |B_0|^2\,\mathrm{Im}\left\{ \frac{\partial\zeta}{\partial\omega} \right\} v \,, \tag{3.24}$$
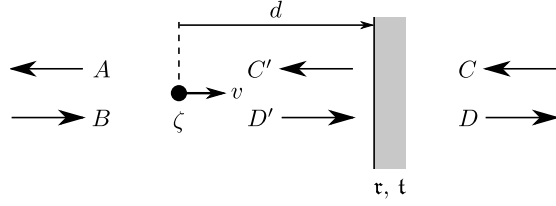
FIGURE 3.2: Physical parameters of our model. A, B, etc. represent the field mode amplitudes.

for small $|\zeta|$ and to first order in v/c, which can be immediately recognised as the friction force in ordinary Doppler cooling, Eq. (2.1), when one uses the definition of ζ in Eq. (1.42). Finally, by making similar substitutions into Eq. (3.20), we obtain

$$D = 8(\hbar k_0)^2 \, \mathrm{Im}\{\zeta\} \left|B_0\right|^2 \sin^2(k_0 x) \,, \tag{3.25}$$

which, excluding the diffusion effects due to spontaneous emission, matches the standard result in Eq. (2.3). Note, however, that the scattering theory leads to a more general result which is represented by the terms of higher order in ζ. These terms describe the back-action of the scatterer on the field, which we re-iterate is generally neglected in free-space laser cooling theory. The general result in Eq. (3.23) reveals that this velocity-dependent force also acts on a scatterer whose polarisability is independent of the frequency. This is a very general class and we will only focus on such scatterers in the following.

3.1.2   General system of a fixed and a mobile scatterer

Consider the model in Fig. 3.2 where the scatterer, or 'atom', has a polarisability ζ constant over the frequency range of interest. Letting M_a, M_p and M_m be the transfer matrices for the atom, propagation and mirror, respectively, we obtain the relation:

$$\begin{pmatrix} A(k) \\ B(k) \end{pmatrix} = M_\mathrm{a} M_\mathrm{p} M_\mathrm{m} \begin{pmatrix} C(k) \\ D(k) \end{pmatrix} \,, \tag{3.26}$$

where

$$M_{\mathrm{a}} = \begin{bmatrix} 1 + \mathrm{i}\zeta & \mathrm{i}\zeta \left(1 - 2\frac{v}{c}\right) \hat{P}_{2v} \\ -\mathrm{i}\zeta \left(1 + 2\frac{v}{c}\right) \hat{P}_{-2v} & 1 - \mathrm{i}\zeta \end{bmatrix}$$

$$= \begin{bmatrix} M_{11} & M_{12}\hat{P}_{2v} \\ M_{21}\hat{P}_{-2v} & M_{22} \end{bmatrix},$$

$$(3.27)$$

$$M_{\mathrm{p}} = \begin{bmatrix} e^{\mathrm{i}kd} & 0 \\ 0 & e^{-\mathrm{i}kd} \end{bmatrix}, \text{ and } M_{\mathrm{m}} = \frac{1}{\mathfrak{t}} \begin{bmatrix} \mathfrak{t}^2 - \mathfrak{r}^2 & \mathfrak{r} \\ -\mathfrak{r} & 1 \end{bmatrix}. \qquad (3.28)$$

The distance between the atom and the mirror is denoted by d. Note that the free-propagation transfer matrix M_{p} is non-uniform in the k-space, and therefore the Doppler shift has an influence on the phase shift accumulated between two scattering events.

The boundary condition is set as follows. We assume that there is no incoming field from the right; therefore $C(k) = 0$ for all k. The incoming field from the left is assumed to be monochromatic, $B(k) = \mathcal{B}\,\delta(k - k_0)$, with k_0 being the pump wavenumber. The resulting field comprises modes with wavenumbers in a narrow region around k_0. In the laboratory frame the field mode $A(k)$ interacts with $B(k - 2k\frac{v}{c})$ and $C'(k)$ through the Doppler shift, and similarly for $D'(k)$. From $C(k) = 0$ it directly follows that

$$A(k) = \left(\mathfrak{r}M_{11}e^{\mathrm{i}kd} + M_{12}\hat{P}_{2v}e^{-\mathrm{i}kd}\right)\left(\mathfrak{r}M_{21}\hat{P}_{-2v}e^{\mathrm{i}kd} + M_{22}e^{-\mathrm{i}kd}\right)^{-1}B(k)$$

$$= \frac{1}{M_{22}}\left(\mathfrak{r}M_{11}e^{\mathrm{i}kd} + M_{12}\hat{P}_{2v}e^{-\mathrm{i}kd}\right)e^{\mathrm{i}kd}\sum_{n=0}^{\infty}\left(-\mathfrak{r}\frac{M_{21}}{M_{22}}\right)^n e^{2\mathrm{i}nkd\left[1-(n+1)\frac{v}{c}\right]}B\left(k - 2nk\frac{v}{c}\right).$$

$$(3.29)$$

We will need the sum of amplitudes, $\mathcal{A} = \int A(k)\mathrm{d}k/\mathcal{B}$, defined relative to the incoming amplitude $\mathcal{B} = \int B(k)dk$. Note that $\int \hat{P}_v f(k)\mathrm{d}k = \int f(k)\mathrm{d}k$. Thus, to first order in $\frac{v}{c}$,

$$\mathcal{A} = \frac{M_{12}}{M_{22}} + \left(\frac{M_{12}}{M_{22}} - \frac{M_{11}}{M_{21}}\right)\sum_{n=1}^{\infty}\left(-\mathfrak{r}\frac{M_{21}}{M_{22}}\right)^n \left[1 + 2in(n-1)k_0 d\frac{v}{c}\right]e^{2ink_0 d}. \qquad (3.30)$$

It is worth introducing the reference point at a distance $L = 2N\pi/k_0$ from the fixed mirror, where the integer N is such that the moving atom's position x is within a wavelength of this reference point. Then the atom–mirror distance can be replaced by $d = L - x$, and $k_0 L$ drops from all the trigonometric functions. The solution, Eq. (3.30), has a clear physical meaning, in that the reflected field, $\mathcal{A}$, can be decomposed into an

interfering sum of fields: the first term is the reflection directly from the atom, whereas the summation is over the electric field undergoing successive atom–mirror round-trips. We can also write the preceding expression in closed form:

$$
\mathcal{A} = \frac{1}{1 - \mathrm{i}\zeta} \left\{ \mathrm{i}\zeta + \mathfrak{r}\frac{e^{-2\mathrm{i}k_0 x}}{1 - \mathrm{i}\zeta - \mathfrak{r}\mathrm{i}\zeta e^{-2\mathrm{i}k_0 x}} \right.
$$
$$
\left. - 2\mathrm{i}\frac{v}{c}\zeta \left[1 - \frac{\mathfrak{r}^2 e^{-4\mathrm{i}k_0 x}}{\left(1 - \mathrm{i}\zeta - \mathfrak{r}\mathrm{i}\zeta e^{-2\mathrm{i}k_0 x}\right)^2} - 2\mathrm{i}k_0(L - x)\frac{\mathfrak{r}^2(1 - \mathrm{i}\zeta)e^{-4\mathrm{i}k_0 x}}{\left(1 - \mathrm{i}\zeta - \mathfrak{r}\mathrm{i}\zeta e^{-2\mathrm{i}k_0 x}\right)^3} \right] \right\}.
$$
$$
(3.31)
$$

This result is valid for arbitrary ζ. The main virtue of our approach is clearly seen, in that we can smoothly move from $\zeta = 0$, which indicates the absence of the mobile scatterer, to $|\zeta| \to \infty$, which corresponds to a perfectly reflecting mirror, i.e., a moving boundary condition for the electromagnetic field.

Let us outline some of the generic features of the above calculation that would be encountered in a general configuration of scatterers. By using the formal Doppler shift operators, we benefit from the transfer matrix method in keeping the description of the system as a whole within 2×2 matrices. The input-output relation for the total system is always obtained in a form similar to that of Eq. (3.29). As long as the Doppler broadening is well below the transient time broadening of the system, the calculation of forces and diffusion requires solely the sum of the mode amplitudes. An important point is that the integrated action of the Doppler shift operator $\hat{P}_v$ on monochromatic fields is a shift in k-space. Therefore, by interchanging the order of terms and putting the $\hat{P}_v$ terms just to the left of the input field amplitudes, they can be eliminated, such as in Eq. (3.30). Finally, up to first order in v/c, the resulting power series, a trace of multiple reflections, can be evaluated in a closed form, as shown in Eq. (3.31). In conclusion, the illustrated method lends itself for the description of more complex schemes, for example, the cooling of a moving, partially reflective mirror in a high-finesse Fabry-Perot resonator [123]. This scheme, however, rapidly increases in complexity with the summations becoming potentially unmanageable. An alternative is possible, in that the matrix $\hat{M}$ is invertible to first order in v/c so that F and D can be evaluated in closed form for a mobile scatterer in a generic optical system. We will investigate this solution in Section 3.2 after some illustrative examples.

3.1.2.1 Force acting on the mobile scatterer

To obtain the force on the moving scatterer, we also need to evaluate $C'(k)$ and $D'(k)$:

$$\begin{pmatrix} C'(k) \\ D'(k) \end{pmatrix} = \begin{bmatrix} 1 - \mathrm{i}\zeta & -\mathrm{i}\zeta \left(1 - 2\frac{v}{c}\right)\hat{P}_{2v} \\ \mathrm{i}\zeta \left(1 + 2\frac{v}{c}\right)\hat{P}_{2v}^{-1} & 1 + \mathrm{i}\zeta \end{bmatrix} \begin{pmatrix} A(k) \\ B(k) \end{pmatrix}, \tag{3.32}$$

where we applied the inverse of the transfer matrix M_{a}. Next, we make the following definitions:

$$\mathbb{A} = |\mathcal{A}|^2, \quad \mathbb{B} = |\mathcal{B}|^2, \mathbb{C} = \frac{1}{\mathbb{B}}\left|\int C'(k)\mathrm{d}k\right|^2, \text{ and } \mathbb{D} = \frac{1}{\mathbb{B}}\left|\int D'(k)\mathrm{d}k\right|^2, \tag{3.33}$$

and a simple calculation leads to

$$\mathbb{C} = |1 - \mathrm{i}\zeta|^2\,\mathbb{A} + \left|\mathrm{i}\zeta\left(1 - 2\frac{v}{c}\right)\right|^2 + 2\,\mathrm{Re}\left\{\mathrm{i}\zeta^*(1 - \mathrm{i}\zeta)\left(1 - 2\frac{v}{c}\right)\mathcal{A}\right\}, \tag{3.34}$$

$$\mathbb{D} = \left|\mathrm{i}\zeta\left(1 + 2\frac{v}{c}\right)\right|^2\mathbb{A} + |1 + \mathrm{i}\zeta|^2 + 2\,\mathrm{Re}\left\{\mathrm{i}\zeta(1 + \mathrm{i}\zeta^*)\left(1 + 2\frac{v}{c}\right)\mathcal{A}\right\}. \tag{3.35}$$

Thereby the force acting on the scatterer is obtained as

$$\begin{aligned} F &= (\hbar\omega/c)\mathbb{B}\left(\mathbb{A} + 1 - \mathbb{C} - \mathbb{D}\right) \\ &= -2\hbar k_0\mathbb{B}\left\{\left[|\zeta|^2\left(1 + 2\frac{v}{c}\right) + \mathrm{Im}\{\zeta\}\right]\mathbb{A} + |\zeta|^2\left(1 - 2\frac{v}{c}\right) - \mathrm{Im}\{\zeta\}\right. \\ &\qquad\left. + 2\,\mathrm{Re}\left\{\left(\mathrm{i}\,\mathrm{Re}\{\zeta\} + |\zeta|^2 + 2\frac{v}{c}\,\mathrm{Im}\{\zeta\}\right)\mathcal{A}\right\}\right\}, \end{aligned} \tag{3.36}$$

where $\mathcal{A}$ has to be substituted from Eq. (3.31). The cooling coefficient ϱ, defined through the relation $F = -\varrho v$, is plotted in Fig. 3.3 as a function of the position x in a half-wavelength range for various values of ζ. When varying the coupling strength from $\zeta = 0.01$ up to $\zeta = 1$, the cooling coefficient transforms between two characteristic regimes. For small coupling the linear velocity dependence tends to a simple sinusoidal function while, for large coupling, the friction exhibits a pronounced resonance in a narrow range. This resonance arises from the increased number of reflections between the mobile scatterer and the fixed mirror. It can be observed that the resonance shifts towards $k_0 x = \pi$ on increasing ζ. In the opposite limit of small ζ, the maximum friction is obtained periodically at $\left(n - \frac{1}{4}\right)\pi/2$ according to the sinusoidal function. The position of the maximum friction is plotted in Fig. 3.4(a), showing the transition from $7\pi/8$ to π. The maximum friction force is plotted in Fig. 3.4(b), showing the two limiting cases
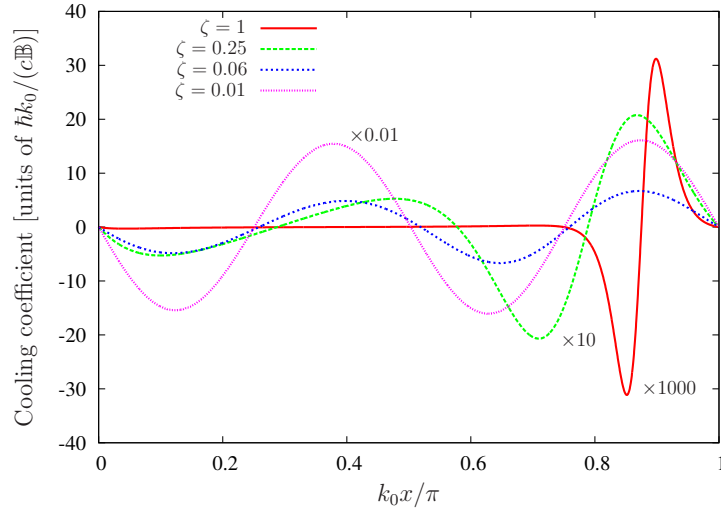
FIGURE 3.3: The position dependence of the cooling coefficient ϱ in the relation $F = -\varrho v$ for the velocity-dependent force acting on the mobile scatterer in Fig. 3.2, for various scattering parameters ζ, evaluated by using Eq. (3.31) and Eq. (3.36) with $k_0 L = 2\pi \times 100$. The fixed mirror is assumed to be a perfect mirror. In order to fit all the curves into the same range, they are divided by the factors indicated in the figure. Note that x is defined differently from Fig. 2.3; the mobile scatterer here is closer to the fixed mirror for *increasing* x.

of ζ^2 behaviour, in the limit of small ζ, and ζ^6 behaviour, in the limit of large ζ. These two cases are described in Section 3.1.3 and Section 3.1.4, respectively.

3.1.2.2   Diffusion coefficient

The calculation of the diffusion coefficient proceeds along the same lines as that corresponding to a single beamsplitter, shown in Appendix 3.1.B. The difference is that the modes $B(k)$ and $C'(k)$ around the mobile scatterer are not independent, for the reflection at the fixed mirror mixes them. Therefore, all the modes A, B, C', and D' have to be expressed in terms of the leftmost and rightmost incoming modes, $B(k)$ and $C(k)$, respectively. Instead of the derivation of such a general result for the diffusion, here we will restrict ourselves to the special case of $\mathfrak{r} = -1$ ($\Leftrightarrow$ perfect mirror) and real ζ ($\Leftrightarrow$ no absorption in the moving mirror). In this special case the diffusion calculation simplifies a lot, because (i) the perfect mirror prevents the modes C from penetrating into the interaction region, and (ii) quantum noise accompanying absorption does not intrude in the motion of the scatterer.

Only the modes $\hat{B}(k)$ impart independent quantum fluctuations. When all the amplitudes around the scatterer are expressed in terms of $\hat{B}(k)$, and are inserted into the

(a)

(b)

FIGURE 3.4: (a) The position of the maximum friction force, $k_0 x_m$, as a function of the dimensionless scattering parameter ζ (on a semilog scale) acting on the scatterer in Fig. 3.2, with the fixed mirror being a perfect mirror. This position shifts from $7\pi/8$ to π on increasing ζ. (b) A similar plot, showing the maximum friction force as a function of ζ (on a log-log scale) with $k_0 L = 2\pi \times 100$. In the limit of small ζ, the force scales as ζ^2 [cf. Eq. (3.41); dashed line] whereas in the limit of large zeta it scales as ζ^6 [cf. Eq. (3.48); dotted line].

force correlation function given in Eq. (1.54), the commutator $[\hat{b}(t), \hat{b}^\dagger(t')]$ appears in all the terms (see Appendix 3.1.B). Straightforward algebra leads to

$$D = \hbar^2 k_0^2 \mathbb{B}(\mathbb{A} + 1 - \mathbb{C} - \mathbb{D})^2 \,. \tag{3.37}$$

We emphasise that the above result is not general: the diffusion is not necessarily proportional to the square of the force. This simple relation here follows from the assumptions,
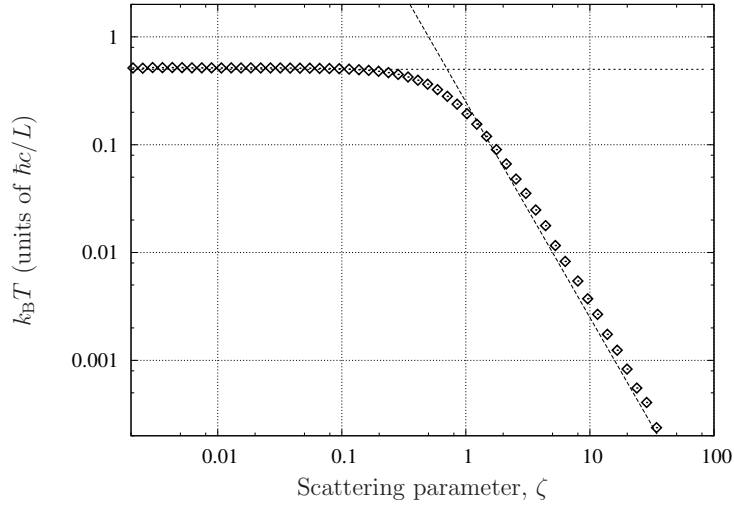
FIGURE 3.5: Characteristic temperature for the two-scatterer system of Fig. 3.2, given by the ratio of the diffusion and cooling coefficients in the points where the friction is maximum, as a function of the dimensionless scattering parameter ζ on a log-log scale. Constant and $1/\zeta^2$ dependence can be read off in the limits of small and large ζ, respectively. The fixed mirror is a perfect mirror.

$\mathfrak{r} = -1$ and $\mathrm{Im}\{\zeta\} = 0$, declared above.

To be consistent with the calculation of the friction force linear in velocity, the diffusion should be evaluated only for $v = 0$. From the ratio of these two coefficients, the steady-state temperature can be deduced. The velocity-independent components of the modes obey the following relations: $\mathbb{A} = 1$ and $\mathbb{C}' = \mathbb{D}'$ (all incoming power is reflected). Therefore the diffusion coefficient further simplifies,

$$D = 4\hbar^2 k_0^2 \mathbb{B} \left(1 - \frac{1}{\left| 1 - \mathrm{i}\zeta + \mathrm{i}\zeta e^{-2\mathrm{i}k_0 x} \right|^2} \right)^2 . \tag{3.38}$$

In Fig. 3.5, the temperature $k_B T = D/\varrho$, is plotted as a function of the scattering parameter ζ. The friction and the diffusion coefficients are taken at the position where the friction is maximum, as shown in Fig. 3.4(a). The two limits of small and large scattering parameter ζ will be analysed in Section 3.1.3 and Section 3.1.4, respectively.

3.1.3 Atom in front of a perfect mirror

An atom pumped with a far off-resonance beam can be modelled as a moving mirror with small and real ζ. In this section we accordingly truncate our expressions to second

order in ζ. We also assume that the fixed mirror is perfect; i.e., $\mathfrak{r} = -1$ and $\mathfrak{t} = 0$. Thus,

$$F = 2\hbar k_0 \mathbb{B} \left[2\zeta \operatorname{Im}\{\mathcal{A}\} - 2\zeta^2 \operatorname{Re}\{\mathcal{A}\} - \zeta^2 \left(1 + \tfrac{v}{c} \right) \mathbb{A} - \zeta^2 \left(1 - \tfrac{v}{c} \right) \right]. \tag{3.39}$$

To obtain F to second order in ζ, we need $\mathcal{A}$ to first order. Using Eq. (3.30) and Eq. (3.39), we obtain:

$$\mathcal{A} = -e^{-2\mathrm{i}k_0 x} + \zeta(\mathrm{i} - 2\mathrm{i}e^{-2\mathrm{i}k_0 x} + \mathrm{i}e^{-4\mathrm{i}k_0 x}) + \zeta\tfrac{v}{c} \left[-2\mathrm{i} + 2\mathrm{i}e^{-4\mathrm{i}k_0 x} - 4k_0(L-x)e^{-4\mathrm{i}k_0 x} \right], \tag{3.40}$$

and

$$\begin{aligned}
F = 4\hbar k_0 \mathbb{B} \big(& \zeta \sin(2k_0 x) - \zeta^2 \big\{ 2\sin^2(k_0 x) \big[4\cos^2(k_0 x) - 1 \big] \big\} \\
& - \zeta^2 \tfrac{v}{c} \big[4\sin^2(2k_0 x) - 4k_0(L-x)\sin(4k_0 x) \big] \big),
\end{aligned} \tag{3.41}$$

in agreement with Eq. (2.34). In the far field ($x \gg \lambda$), the dominant friction term in the preceding expression is the last term, which renders the $\sin(4k_0 x)$ position dependence shown in Fig. 4.2 for $\zeta = 0.01$.

We are now in a position to derive the diffusion coefficient for this system. By substituting Eq. (3.40) into Eq. (3.37) and setting $v = 0$, we obtain

$$D = 8(\hbar k_0)^2 \zeta^2 \mathbb{B}. \tag{3.42}$$

This allows us to estimate the equilibrium temperature for such a system at a position of maximum friction:

$$T \approx \frac{\hbar}{k_{\mathrm{B}}\tau}, \text{ where } \tau = 2(L-x)/c, \tag{3.43}$$

which we note is identical in form to the Doppler temperature for a two-level atom undergoing free-space laser cooling [124], but where we have replaced the upper state lifetime, $1/\Gamma$, by the round-trip time delay between the atom and the mirror.[2] Note that this temperature corresponds to the constant value presented in Fig. 3.5 for $\zeta < 0.1$.

---

[2] This expression lacks the geometrical factor in Eq. (2.44); the reason for this is that the semiclassical treatment of a TLA is, strictly speaking, inconsistent with the assumption $\operatorname{Im}\{\zeta\} = 0$; the dominant term of the diffusion is then the first term in Eq. (3.20).

3.1.4   Optical resonator with mobile mirror

After the small polarisability case of the previous section, we will now consider the $|\zeta| \to \infty$ limit. We again assume that the fixed mirror of the resonator is perfect, with $\mathfrak{r} = -1$, and that $C = 0$. For simplicity, we assume that the moving mirror has a real polarisability; i.e., it is lossless. We expand the field mode amplitudes as power series in v/c, such that $\mathcal{A} = \mathcal{A}_0 + \frac{v}{c}\mathcal{A}_1 + \ldots$, and similarly for $\mathcal{C}'$.

Let us first calculate the field in the resonator for $v = 0$. It follows from Eq. (3.32) that

$$\mathcal{C}'_0 = (1 - \mathrm{i}\zeta)\mathcal{A}_0 - \mathrm{i}\zeta = -\frac{e^{-2\mathrm{i}\varphi}}{1 - \mathrm{i}\zeta + \mathrm{i}\zeta e^{-2\mathrm{i}\varphi}} \,, \tag{3.44}$$

with $\varphi = k_0 d$, which has a maximum at φ_0 obeying

$$\tan(2\varphi_0) = -\frac{1}{\zeta} \,. \tag{3.45}$$

In the limit of $\zeta \to \infty$, the resonance is Lorentzian:

$$\mathcal{C}'_0 = -\frac{e^{-2\mathrm{i}\varphi}}{2\mathrm{i}(1 - \mathrm{i}\zeta)\left[(\varphi - \varphi_0) - \mathrm{i}\frac{1}{4\zeta^2}\right]} \,, \tag{3.46}$$

with a width of $1/(4\zeta^2)$.

The perfect mirror reflects the total power incoming from the left, $\mathbb{B}$. Moreover, for real ζ, there is no absorption in the moving mirror, so the outgoing intensity has to be equal to the incoming one: $\mathbb{A} = 1$. This is true if $v = 0$; for $v \neq 0$, the field can do work on the mirror. The expansion of the back-reflected intensity to linear order in velocity reads $\mathbb{A} = 1 + 2\frac{v}{c}\,\mathrm{Re}\{\mathcal{A}_0^*\mathcal{A}_1\}$. Extracting the velocity-dependent terms for the general form of the force in Eq. (3.36), it reduces to

$$F_1 = \frac{v}{c}4\hbar k_0 \mathbb{B}\zeta\,\mathrm{Im}\big\{\mathcal{A}_1 \big/ \big(1 + \mathrm{i}\zeta - \mathrm{i}\zeta e^{2\mathrm{i}\varphi}\big)\big\} \,, \tag{3.47}$$

which, after some algebra, leads to

$$F_1 = -\frac{1}{2}\frac{v}{c}\hbar k_0^2 L \frac{(\varphi - \varphi_0)}{\zeta^4 \left[\left(\frac{1}{4\zeta^2}\right)^2 + (\varphi - \varphi_0)^2\right]^3}\mathbb{B} \,. \tag{3.48}$$

On substituting $\kappa = c/\left(4L\zeta^2\right)$, $\Delta_C = -c(\varphi - \varphi_0)/L$, $\eta^2/(2\kappa) = \mathbb{B}$, and $G = c^2 k_0^2/L^2$, the friction force renders that derived from the usual radiation pressure Hamiltonian in Appendix 3.1.C.

Expressing the field modes interacting with the mobile mirror in terms of the input field mode and performing a calculation similar to that leading to Eq. (3.19) readily gives

$$D \approx 4(\hbar k_0)^2 |\mathcal{C}_0'|^4 \mathbb{B} \approx \frac{(\hbar k_0)^2 \mathbb{B}}{4\zeta^4 \left[\left(\frac{1}{4\zeta^2}\right)^2 + (\varphi - \varphi_0)^2\right]^2} \,. \tag{3.49}$$

The resulting temperature thereby attains a minimum at $4\zeta^2(\varphi - \varphi_0) = 1$, i.e., $\Delta_C = -\kappa$, in analogy with free-space Doppler cooling, at which point we have

$$k_{\mathrm{B}}T \approx \frac{\hbar c}{4\zeta^2 L} = \hbar\kappa \,. \tag{3.50}$$

Again, this asymptotic behaviour is reflected in Fig. 3.5 for large ζ. We note the similarity of the preceding expression with the temperature of an atom cooled in a cavity, in the good-cavity limit [102]. We conjecture that this is due to the fact that both systems can be considered to involve the coupling of a laser with a system having a decay rate κ. This result also holds for the case of an atom undergoing mirror-mediated cooling, as can be seen in Eq. (3.43).

It is also important to note that the above discussion only treats the effects of the light fields on the scatterer. As such, the temperature limit, Eq. (3.50), is intrinsic to the light forces, and the mechanical damping and heating processes present in a real, macroscopic mirror-cooling setup are not taken into account. In practice, these heating processes may dominate over the heating induced by the quantum noise in the light field [24, 125]. In such cases, radiation pressure cooling is a possible means to lower the equilibrium temperature owing to the additional, optical, damping process.

3.1.A   Appendix: The Doppler shift operator

Consider the situation in Fig. 3.6, in the laboratory frame, where S is a scatterer, and suppose that B and C are known. $A(k)$ has contributions arising from both $B\left(k + 2k\frac{v}{c}\right)$
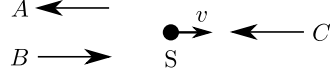
FIGURE 3.6: Reflection and transmission of a moving scatterer. B and C are the input field modes, and A is the output field mode. A further output field mode ('D') is not drawn because it is not relevant to our discussion here.

and $C(k)$, where k is any arbitrary wave number, written separately as:

$$A_B(k) = a_1 B(k + 2k\tfrac{v}{c})\,, \text{ and} \tag{3.51}$$

$$A_C(k) = a_2 C(k)\,. \tag{3.52}$$

We can therefore express $A(k)$ as

$$A(k) = a_1 B(k + 2k\tfrac{v}{c}) + a_2 C(k)\,. \tag{3.53}$$

Defining $\hat{P}_v$ by $\hat{P}_v : f(k) \mapsto f(k + k\tfrac{v}{c})$, we have

$$A(k) = \hat{P}_{2v} a_1 B(k) + a_2 C(k)\,. \tag{3.54}$$

A similar expression, involving $\hat{P}_v^{-1} = \hat{P}_{-v}$, holds for $D(k)$. These two operators can then be introduced into Eq. (3.5) as part of the Lorentz transformation, and thus into the transfer matrix for the moving scatterer, giving rise to the form shown in Eq. (3.12). The resulting transformation, for the transfer matrix M, of a scatterer moving with velocity v can be written as:

$$\begin{bmatrix} (1 - \tfrac{v}{c})\hat{P}_v & 0 \\ 0 & (1 + \tfrac{v}{c})\hat{P}_v^{-1} \end{bmatrix} M \begin{bmatrix} (1 + \tfrac{v}{c})\hat{P}_v^{-1} & 0 \\ 0 & (1 - \tfrac{v}{c})\hat{P}_v \end{bmatrix}, \tag{3.55}$$

to first order in $\tfrac{v}{c}$, where the ordering of the elements of M is as described in the text. Note that this relation is general, in the sense that the elements of M can depend on k (see Section 3.1.1.5).

For any finite v, $\hat{P}_v$ is trivially a bounded operator, having unit norm. This property follows from the important relation $\int \hat{P}_v^m f(k)\mathrm{d}k = \int f(k)\mathrm{d}k$, for any function $f(k)$ and any integer m.

This operation can be generalised to $n = 2, 3$ pairs of modes in n orthogonal dimensions. In two dimensions, this could correspond to a beamsplitter oriented at $45°$ to the x-axis;

in three dimensions, the beamsplitter would be oriented at $45°$ to all three coordinate axes. We define a new operator by $\hat{S}_i(\boldsymbol{v}) : f(\boldsymbol{k}) \mapsto f(\boldsymbol{k} + k_i \frac{v_i}{c}\mathbf{e}_i)$, where $\mathbf{e}_i$ is the unit vector along the ith coordinate axis, $\boldsymbol{v}$ is the velocity vector of the scatterer, and $\mathbf{x} = (x_1, x_2, \dots)$ for any vector $\mathbf{x}$. In particular, we have $\hat{P}_v = \hat{S}_1(v\mathbf{e}_1)$. Now, let $\hat{\boldsymbol{L}}(\boldsymbol{v})$ be the $2n \times 2n$ matrix operator:

$$
\begin{bmatrix}
(1 + \frac{v_1}{c})\hat{S}_1^{-1}(\boldsymbol{v}) & 0 & 0 & \cdots \\
0 & (1 - \frac{v_1}{c})\hat{S}_1(\boldsymbol{v}) & 0 & \cdots \\
0 & 0 & (1 + \frac{v_2}{c})\hat{S}_2^{-1}(\boldsymbol{v}) & \cdots \\
\vdots & \vdots & \vdots & \ddots
\end{bmatrix} .
\tag{3.56}
$$

Then, the transfer matrix for the scatterer moving with velocity $\boldsymbol{v}$ is given by

$$
\hat{\boldsymbol{L}}(-\mathbf{v})\, M\, \hat{\boldsymbol{L}}(\boldsymbol{v}) ,
\tag{3.57}
$$

where M is the original transfer matrix for the scatterer, obtained in a manner such as that used to obtain Eq. (3.6), for example. The ordering of the elements of M is such that it acts on the vector $\big(A_1(\boldsymbol{k}), B_1(\boldsymbol{k}), A_2(\boldsymbol{k}), \dots\big)$:

$$
\begin{pmatrix}
C_1(\boldsymbol{k}) \\
D_1(\boldsymbol{k}) \\
C_2(\boldsymbol{k}) \\
\vdots
\end{pmatrix}
= \hat{\boldsymbol{L}}(-\mathbf{v})\, M\, \hat{\boldsymbol{L}}(\boldsymbol{v})
\begin{pmatrix}
A_1(\boldsymbol{k}) \\
B_1(\boldsymbol{k}) \\
A_2(\boldsymbol{k}) \\
\vdots
\end{pmatrix} ,
\tag{3.58}
$$

with $A_i(\boldsymbol{k})$ being the outgoing mode and $B_i(\boldsymbol{k})$ the incoming mode along the ith axis in the negative half-space (assuming that the scatterer is at the origin); and $C_i(\boldsymbol{k})$ the incoming mode and $D_i(\boldsymbol{k})$ the outgoing mode in the positive half-space.

3.1.B   Appendix: Quantum correlation function of the force operator

In quantum theory, we need to replace the mode amplitudes $A(k)$ by operators $\hat{A}(k)$, and similarly for the B, C, and D modes. The cross-correlation of these operators is not trivial because of the boundary condition connecting the mode amplitudes $A(k)$, $B(k)$, $C(k)$ and $D(k)$. The input modes $\hat{C}(k)$ and $\hat{B}(k)$ can be considered independent, and the commutator is non-vanishing for the creation and annihilation operators of the same

mode, e.g.,

$$\left[\hat{B}(k), \hat{B}^\dagger(k')\right] = \left[\hat{C}(k), \hat{C}^\dagger(k')\right] = \frac{\hbar\omega}{2\epsilon_0 V}\delta_{k,k'}, \qquad (3.59)$$

$$\left[\hat{B}(k), \hat{C}^\dagger(k')\right] = 0, \qquad (3.60)$$

assuming a discrete mode index of k, and a quantisation volume $V = \sigma_\mathrm{L} l$ with σ_L being the mode area and l a fictitious total length of the space in one dimension.

In using Eq. (1.61), expressions for F correct to order n in v/c are compared to D to order $(n-1)$ in this same parameter. Since our force expressions are accurate up to first order in v/c, therefore, we need only consider terms that contribute to the diffusion in the $v=0$ case. In the quantum description, the linear relation for the output modes is

$$A(k) = \mathfrak{t}C(k) + \mathfrak{r}B(k) + \sqrt{\epsilon}E \qquad (3.61)$$

$$D(k) = \mathfrak{r}C(k) + \mathfrak{t}B(k) + \sqrt{\epsilon}E, \qquad (3.62)$$

where the transmission $\mathfrak{t} = 1/M_{22} = 1/(1-\mathrm{i}\zeta)$, and reflection $\mathfrak{r} = M_{12}/M_{22} = \mathrm{i}\zeta/(1-\mathrm{i}\zeta)$, as above. The amplitude E represents the quantum noise fed into the system by the absorption. For $\epsilon = 1 - \left(|\mathfrak{r}|^2 + |\mathfrak{t}|^2\right)$, this noise ensures that the output modes obey the same commutation relations as the input ones, namely

$$\left[\hat{A}(k), \hat{A}^\dagger(k')\right] = \left[\hat{D}(k), \hat{D}^\dagger(k')\right] = \frac{\hbar\omega}{2\epsilon_0 V}\delta_{k,k'}, \qquad (3.63)$$

$$\left[\hat{A}(k), \hat{D}^\dagger(k')\right] = 0. \qquad (3.64)$$

However, the linear dependence implies that commutators between input and output mode operators are

$$\left[\hat{A}(k), \hat{B}^\dagger(k')\right] = \mathfrak{r}\left[\hat{B}(k), \hat{B}^\dagger(k')\right], \qquad (3.65)$$

$$\left[\hat{A}(k), \hat{C}^\dagger(k')\right] = \mathfrak{t}\left[\hat{C}(k), \hat{C}^\dagger(k')\right], \qquad (3.66)$$

and similar relations hold for the cross-commutators with $D(k)$.

The proper treatment of quantum fluctuations and the derivation of correlation functions

require that the explicit time dependence be considered. Let us introduce the time-varying operators

$$\hat{a}(t) = \sum_k \hat{A}(k) e^{-i\omega t}, \tag{3.67}$$

and similarly for $\hat{b}(t)$, $\hat{c}(t)$ and $\hat{d}(t)$. It follows that

$$\left[\hat{a}(t), \hat{a}^\dagger(t')\right] = \frac{\hbar\omega}{2\epsilon_0 V} \sum_k e^{-i\omega(t-t')} \approx \frac{\hbar\omega}{2c\epsilon_0\sigma_L} \delta(t - t'). \tag{3.68}$$

Here we made use of the fact that the non-excited vacuum modes, having a bandwidth that is much broader than that of the pump, also contribute to the summation, allowing us to approximate the summation as an integral over all frequencies. The Fourier-type integral then yields δ-function on the much slower timescale of interest. A similar commutation relation applies to the operators $\hat{b}(t)$, $\hat{c}(t)$, and $\hat{d}(t)$. The cross-commutators can be derived directly from those concerning the modes, e.g.,

$$\left[\hat{a}(t), \hat{b}^\dagger(t')\right] = \mathfrak{r}\frac{\hbar\omega}{2c\epsilon_0\sigma_L} \delta(t - t'). \tag{3.69}$$

The force operator is

$$\hat{F} = \sigma_L \left[\hat{\boldsymbol{T}}_{xx}(x \to 0^+) - \hat{\boldsymbol{T}}_{xx}(x \to 0^-)\right], \tag{3.70}$$

as before, where

$$\hat{\boldsymbol{T}}_{xx}(x \to 0) = \begin{cases} -2\epsilon_0 \left[\hat{a}^\dagger(t)\hat{a}(t) + \hat{b}^\dagger(t)\hat{b}(t)\right] & \text{for } x \to 0^- \\ -2\epsilon_0 \left[\hat{c}^\dagger(t)\hat{c}(t) + \hat{d}^\dagger(t)\hat{d}(t)\right] & \text{for } x \to 0^+ \end{cases} \tag{3.71}$$

is the quantised stress tensor. Assuming that the field is in a coherent state, in all normally ordered products, the mode amplitude operators can be replaced by the corresponding coherent state amplitudes, which are c-numbers: e.g., $\hat{A}(k) \to A(k)$ and $\hat{A}^\dagger(k) \to A^*(k)$. The force operator in Eq. (3.70) is normally ordered in this way; therefore coherent-state fields render, as a mean value of the quantum expressions, the force Eq. (3.18) derived from the classical theory based on the definition Eq. (3.17). Non-trivial quantum effects arise from non-normally ordered products, such as the fourth-order product terms of the second order correlation function of the force Eq. (1.54).

These terms can be evaluated straightforwardly by invoking the above-derived commutators to rearrange the product into normal order. As an example, consider

$$\langle \hat{a}^\dagger(t)\hat{a}(t)\hat{a}^\dagger(t')\hat{a}(t')\rangle = \langle \hat{a}^\dagger(t)\hat{a}^\dagger(t')\hat{a}(t)\hat{a}(t')\rangle - \langle \hat{a}^\dagger(t)\hat{a}(t')\rangle \frac{\hbar\omega}{2c\epsilon_0\sigma_L}\delta(t-t')\,. \qquad (3.72)$$

For radiation fields in coherent state, the first term is cancelled from the correlation function by the $\langle \hat{a}^\dagger(t)\hat{a}(t')\rangle^2$ term. The coefficient of $\delta(t-t')$ in the second term is in normal order and can be replaced by c-numbers and then calculated identically as the force in Section 3.1.1.5,

$$\langle \hat{a}^\dagger(t)\hat{a}(t)\rangle \approx \Big| \sum A(k) \Big|^2 = \frac{\hbar\omega}{2c\epsilon_0\sigma_L}|A|^2\,, \qquad (3.73)$$

in terms of the photo-current intensity $|A|^2$.

Assembling all similar contributions, originating from the non-vanishing commutators $[b,b^\dagger]$, $[c,c^\dagger]$, $[d,d^\dagger]$, $[a,b^\dagger]$, etc., one obtains Eq. (3.19) presented in Section 3.1.1.4.

3.1.C   Appendix: Mirror cooling via the radiation pressure coupling Hamiltonian

We describe a generic optomechanical system composed of a single, damped-driven field mode coupled to the motion of a massive particle, whose Hamiltonian is given by [126, 127]

$$\hat{\mathcal{H}} = \hbar\omega_c\hat{a}^\dagger\hat{a} + \mathrm{i}\hbar\eta(\hat{a}^\dagger e^{-\mathrm{i}\omega t} - \hat{a}e^{\mathrm{i}\omega t}) + \frac{\hat{p}^2}{2m} + V(\hat{x}) + \hbar G\hat{a}^\dagger\hat{a}\hat{x}\,. \qquad (3.74)$$

where $\hat{a}$ and $\hat{a}^\dagger$ are the annihilation and creation operators, respectively, of the mode; $\hat{x}$ and $\hat{p}$ are the position and momentum operators associated with the motion; and where we drop the carets to signify expectation values. The mode is driven by a coherent field with an effective amplitude η and frequency ω. This Hamiltonian describes, for example, the radiation pressure coupling of a moving mirror to the field in a Fabry-Perot resonator. In this case the coupling constant is $G = \omega_c/L$, rendering the cavity mode frequency detuning $\omega_c x/L$ provided the mirror is shifted by an amount x. Since the cavity mode is lossy with a photon escape rate of 2κ, the total system is dissipative. Thereby, with a proper setting of the parameters, in particular the cavity detuning $\Delta_C = \omega - \omega_C$, the

mirror motion can be cooled. We will determine the corresponding friction force linear in velocity.

In a frame rotating at frequency ω, the Heisenberg equation of motion for the field mode amplitude reads

$$\dot{\hat{a}} = [\mathrm{i}(\Delta_C - G\hat{x}) - \kappa]\,\hat{a} + \eta\,. \tag{3.75}$$

where the noise term is omitted. We assume that the mirror moves along the trajectory $x(t) \approx x + vt$ with fixed velocity v during the short time that is needed for the field mode to relax to its steady-state. The variation of $\hat{a}$ arises from the explicit time dependence and from the motion of the mirror. A steady-state solution is sought in the form of $\hat{a} \approx \hat{a}^{(0)}(x) + v\hat{a}^{(1)}(x)$. On replacing this expansion into the above equation, and using the hydrodynamic derivative $\frac{\mathrm{d}}{\mathrm{d}t} \to \frac{\partial}{\partial t} + v\frac{\partial}{\partial x}$, one obtains a hierarchy of equations of different orders of the velocity v. To zeroth order the adiabatic field is obtained as

$$a^{(0)} = \frac{\eta}{-\mathrm{i}(\Delta_C - Gx) + \kappa}\,. \tag{3.76}$$

The linear response of a to the mirror motion is then

$$a^{(1)} = \frac{1}{\mathrm{i}(\Delta_C - Gx) - \kappa}\frac{\partial}{\partial x}a^{(0)} = \frac{\mathrm{i}\eta G}{\big[-\mathrm{i}(\Delta_C - Gx) + \kappa\big]^3}\,. \tag{3.77}$$

The force acting on the mirror derives from the defining equation $\dot{\hat{p}} = \frac{\mathrm{i}}{\hbar}[\hat{\mathcal{H}}, \hat{p}] = -\hbar G\hat{a}^\dagger\hat{a}$ and, up to linear order in velocity, is

$$F_1 = -2v\hbar G\,\mathrm{Re}\Big\{a^{(0)*}a^{(1)}\Big\} = 4v\frac{\hbar\eta^2 G^2\kappa\Delta_C}{\big(\Delta_C^2 + \kappa^2\big)^3}\,, \tag{3.78}$$

where we used $x = 0$ without loss of generality. It can be seen that mirror cooling requires that $\Delta_C < 0$, i.e., the cavity resonance frequency is above the pump frequency. In this case, for efficient excitation of the field in the resonator, the frequency of the pump photons is up-shifted at the expense of the mirror's kinetic energy. This cooling force has been derived in Section 3.1.4, as a limiting case of the more general scattering theory. To check the perfect agreement between the two results, the quantity corresponding to η can be deduced from the total field energy in the resonator for an immobile mirror, which is $\hbar\omega_C\hat{a}^{(0)\dagger}\hat{a}^{(0)}$ here.

3.2   General solution to the transfer matrix approach

The approach used to find F in the previous section illustrates the nature of this quantity, arising from the multiple round-trips of the light between the static and moving mirrors, very well. However, the series summation does not lend itself to easy direct evaluation in a mechanical fashion. By rewriting the Doppler shift operator, however, this limitation can be lifted and F and D evaluated for a fully general optical system. The basis of this current section was published as Xuereb, A., Freegarde, T., Horak, P., & Domokos, P. Phys. Rev. Lett. **105**, 013602 (2010), and will be elaborated on in a manuscript that is currently being prepared. In this section, we will first summarise the general transfer matrix approach and show how solutions in closed form can be found to the friction force, in Section 3.2.1, and momentum diffusion, in Section 3.2.2, acting on the scatterer. Section 3.3 subsequently explores the linear and nonlinear optomechanical coupling that can be achieved between the field of a cavity and the position of a micromirror placed inside it.

Given a static scatterer represented by the transfer matrix $\hat{M}$, the effect of the motion of the scatterer on the fields it is interacting with is included by applying the transformation [cf. Eq. (3.12)]

$$\hat{M} \to \hat{L}(-v)\hat{M}\hat{L}(v)\,, \tag{3.79}$$

where the 'Doppler shift' operator matrix $\hat{L}(v)$ for a scatterer moving with velocity v can be written, from Eq. (3.10), as

$$\hat{L}(v) = \begin{bmatrix} 1 + \frac{v}{c}\big(1 - k_0\partial_k\big) & 0 \\ 0 & 1 - \frac{v}{c}\big(1 - k_0\partial_k\big) \end{bmatrix}, \tag{3.80}$$

to linear order in v/c and under the assumption that the pump beam has a very narrow spread of wavenumbers about a central k_0. We also use the shorthand notation $\partial_k \equiv \frac{\partial}{\partial k}$ throughout and will drop the label k wherever this is not necessary.

3.2.1   Force acting on moving scatterer

Let us now apply this description to the general model represented by the system in Fig. 3.7. Our aim is to obtain the force acting on scatterer S; to do this we need to
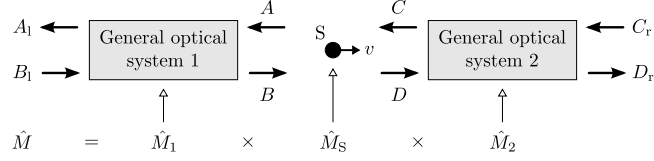
FIGURE 3.7: The model we consider in this section, drawn schematically. A scatterer S interacts with two 'general optical systems' in one dimension, composed of immobile linear optical elements, one to either side. S and these two systems are each represented by a 2×2 matrix.

express the fields it interacts with, A, B, C, and D, in terms of the input fields B_l and C_r. As in Ref. [128], we define

$$\hat{M} = M_1 \times \hat{M}_S \times M_2 \equiv \begin{bmatrix} \hat{\gamma} & \hat{\alpha} \\ \hat{\delta} & \hat{\beta} \end{bmatrix} \text{ and } \left(M_1\right)^{-1} \equiv \left[\theta_{ij}\right]. \tag{3.81}$$

We also define the convenient velocity-independent quantities α_0, $\alpha_1^{(0)}$, $\alpha_1^{(1)}$, etc., by

$$\hat{\alpha} \equiv \alpha_0 + \frac{v}{c}\left(\alpha_1^{(0)} + \alpha_1^{(1)}\partial_k\right), \tag{3.82}$$

$$\hat{\beta} \equiv \beta_0 + \frac{v}{c}\left(\beta_1^{(0)} + \beta_1^{(1)}\partial_k\right), \tag{3.83}$$

$$\hat{\gamma} \equiv \gamma_0 + \frac{v}{c}\left(\gamma_1^{(0)} + \gamma_1^{(1)}\partial_k\right), \text{ and} \tag{3.84}$$

$$\hat{\delta} \equiv \delta_0 + \frac{v}{c}\left(\delta_1^{(0)} + \delta_1^{(1)}\partial_k\right). \tag{3.85}$$

A final assumption is needed to be able to express the fields in closed form—we assume that the two input fields are at the same frequency and have only a very small spread in wavenumber:

$$B_l = B_0\,\delta(k - k_0) \text{ and } C_r = C_0\,\delta(k - k_0). \tag{3.86}$$

Then, the field amplitudes $\mathcal{A} = \int A(k)\,\mathrm{d}k$ and $\mathcal{B} = \int B(k)\,\mathrm{d}k$ are given, to first order in v/c, by:

$$\mathcal{A} = \left(\theta_{11}\frac{\alpha_0}{\beta_0} + \theta_{12} + \frac{v}{c}\left\{\frac{\theta_{11}}{\beta_0^2}\left(\alpha_1^{(0)}\beta_0 - \alpha_0\beta_1^{(0)}\right) - \frac{1}{\beta_0}\left[\partial_k\frac{\theta_{11}}{\beta_0}\left(\alpha_1^{(1)}\beta_0 - \alpha_0\beta_1^{(1)}\right)\right]\right\}\right)B_0$$
$$+ \left(\theta_{11}\frac{\gamma_0\beta_0 - \alpha_0\delta_0}{\beta_0} + \frac{v}{c}\left\{\frac{\theta_{11}}{\beta_0^2}\left[\beta_0^2\gamma_1^{(0)} - \alpha_0\beta_0\delta_1^{(0)} - \left(\alpha_1^{(0)}\beta_0 - \alpha_0\beta_1^{(0)}\right)\delta_0\right]\right.$$
$$\left.- \left[\partial_k\frac{\theta_{11}}{\beta_0}\left(\beta_0\gamma_1^{(1)} - \alpha_0\delta_1^{(1)}\right)\right] + \frac{\delta_0}{\beta_0}\left[\partial_k\frac{\theta_{11}}{\beta_0}\left(\alpha_1^{(1)}\beta_0 - \alpha_0\beta_1^{(1)}\right)\right]\right\}\right)C_0, \quad (3.87)$$

and

$$\mathcal{B} = \left(\theta_{21}\frac{\alpha_0}{\beta_0} + \theta_{22} + \frac{v}{c}\left\{\frac{\theta_{21}}{\beta_0^2}\left(\alpha_1^{(0)}\beta_0 - \alpha_0\beta_1^{(0)}\right) - \frac{1}{\beta_0}\left[\partial_k\frac{\theta_{21}}{\beta_0}\left(\alpha_1^{(1)}\beta_0 - \alpha_0\beta_1^{(1)}\right)\right]\right\}\right)B_0$$
$$+ \left(\theta_{21}\frac{\gamma_0\beta_0 - \alpha_0\delta_0}{\beta_0} + \frac{v}{c}\left\{\frac{\theta_{21}}{\beta_0^2}\left[\beta_0^2\gamma_1^{(0)} - \alpha_0\beta_0\delta_1^{(0)} - \left(\alpha_1^{(0)}\beta_0 - \alpha_0\beta_1^{(0)}\right)\delta_0\right]\right.\right.$$
$$\left.\left. - \left[\partial_k\frac{\theta_{21}}{\beta_0}\left(\beta_0\gamma_1^{(1)} - \alpha_0\delta_1^{(1)}\right)\right] + \frac{\delta_0}{\beta_0}\left[\partial_k\frac{\theta_{21}}{\beta_0}\left(\alpha_1^{(1)}\beta_0 - \alpha_0\beta_1^{(1)}\right)\right]\right\}\right)C_0, \quad (3.88)$$

where the derivatives are all evaluated at $k = k_0$. We shall find it useful to express these results in the form $\mathcal{A} = \mathcal{A}_0 + \frac{v}{c}\mathcal{A}_1$ and $\mathcal{B} = \mathcal{B}_0 + \frac{v}{c}\mathcal{B}_1$, with $\mathcal{A}_{0,1}$ and $\mathcal{B}_{0,1}$ being independent of v. For conciseness, let us now assume that ζ does not depend on k. Then, using the elements of $\hat{M}_{\mathrm{S}}$, we obtain

$$\mathcal{C} = (1 - \mathrm{i}\zeta)\mathcal{A} - \left(1 - 2\frac{v}{c}\right)\mathrm{i}\zeta\mathcal{B}$$
$$= \left[(1 - \mathrm{i}\zeta)\mathcal{A}_0 - \mathrm{i}\zeta\mathcal{B}_0\right] + \frac{v}{c}\left[(1 - \mathrm{i}\zeta)\mathcal{A}_1 + 2\mathrm{i}\zeta\mathcal{B}_0 - \mathrm{i}\zeta\mathcal{B}_1\right], \quad (3.89)$$

and

$$\mathcal{D} = \left(1 + 2\frac{v}{c}\right)\mathrm{i}\zeta\mathcal{A} + (1 + \mathrm{i}\zeta)\mathcal{B}$$
$$= \left[\mathrm{i}\zeta\mathcal{A}_0 + (1 + \mathrm{i}\zeta)\mathcal{B}_0\right] + \frac{v}{c}\left[2\mathrm{i}\zeta\mathcal{A}_0 - \mathrm{i}\zeta\mathcal{A}_1 - (1 + \mathrm{i}\zeta)\mathcal{B}_1\right]. \quad (3.90)$$

We denote the velocity-independent parts of $\mathcal{C}$ and $\mathcal{D}$ by $\mathcal{C}_0$ and $\mathcal{D}_0$, respectively. The *friction* force acting on the scatterer can be finally written down as

$$F = -4\hbar k_0\frac{v}{c}\left[|\zeta|^2\left(|\mathcal{A}_0|^2 - |\mathcal{B}_0|^2\right) + \left(|\zeta|^2 + \mathrm{Im}\{\zeta\}\right)\mathrm{Re}\{\mathcal{A}_0\mathcal{A}_1^*\} - 2\,\mathrm{Im}\{\zeta\}\,\mathrm{Re}\{\mathcal{A}_0\mathcal{B}_0^*\}\right.$$
$$+ \left(|\zeta|^2 - \mathrm{Im}\{\zeta\}\right)\mathrm{Re}\{\mathcal{B}_0\mathcal{B}_1^*\} + \mathrm{Im}\{\zeta\}\,\mathrm{Re}\{\mathcal{A}_0\mathcal{B}_1^*\}$$
$$\left. + \mathrm{Re}\left\{\left(|\zeta|^2 + \mathrm{i}\,\mathrm{Re}\{\zeta\}\right)\mathcal{A}_1\mathcal{B}_0^*\right\}\right]. \quad (3.91)$$

3.2.2   Momentum diffusion experienced by scatterer

Photon number fluctuations in the input fields B_{l} and C_{r} give rise to a stochastic force, added to F, that averages out to zero; this stochastic force is, however, responsible for preventing the momentum of the scatter from reaching zero under the action of a friction force [124]. A complete theory based on the input-output operator formalism can be built along the lines of the previous section. The results we have obtained so far correspond

to assuming that the input fields are in a coherent state, see Section 3.1.1.4, whereby the fields A, B, etc., are the expectation values of analogous bosonic annihilation operators: $\langle \hat{A} \rangle = A$, $\langle \hat{A}^\dagger \rangle = A^*$, and so on. The two input modes are the only independent modes in our system, and their corresponding operators obey the usual bosonic commutation relations:

$$\left[\hat{B}_\text{l}, \hat{B}_\text{l}^\dagger \right] = \left[\hat{C}_\text{r}, \hat{C}_\text{r}^\dagger \right] = \frac{\hbar k_0}{2\epsilon_0 \sigma_\text{L}} \delta(t - t'), \text{ and } \left[\hat{B}_\text{l}, \hat{C}_\text{r}^\dagger \right] = 0, \tag{3.92}$$

with $\omega = kc$ being the (angular) frequency. Since we are working to first order in v/c, we need to evaluate everything in this section to zeroth order in v/c.

Besides photon number fluctuations, lossy beamsplitters also induce noise into the system; this is equivalent to having a noise mode $\hat{E}$ that modifies the output fields interacting with that component. The noise input in the system by any of its components is independent of the noise input by any other component; in other words, if $\hat{E}_1$ and $\hat{E}_2$ are two noise modes that interact with the system,

$$\left[\hat{E}_1, \hat{E}_1^\dagger \right] = \left[\hat{E}_2, \hat{E}_2^\dagger \right] = \frac{\hbar k_0}{2\epsilon_0 \sigma_\text{L}} \delta(t - t'), \left[\hat{E}_1, \hat{E}_2^\dagger \right] = 0, \tag{3.93}$$

and

$$\langle \hat{E}_1 \rangle = \langle \hat{E}_2 \rangle = 0, \tag{3.94}$$

with the last pair of equalities being true by construction. We can therefore treat each of the noise modes independently. Moreover, the noise modes are independent of the input modes; for any such noise mode $\hat{E}$:

$$\left[\hat{E}, \hat{B}_\text{l}^\dagger \right] = \left[\hat{E}, \hat{C}_\text{r}^\dagger \right] = 0. \tag{3.95}$$

In this section, we will generalise the treatment in Section 3.1 to the situation where the loss-inducing beamsplitter is part of a generic optical system. Let us now assume, for concreteness, that the moving scatterer S from Section 3.2.1 introduces the only noise mode, $\hat{E}$, in the system. In the case of an isolated scatterer, $\hat{B}$ and $\hat{C}$ represent independent input modes and the above equations guarantee that the two-time self-commutators of $\hat{A}$ and $\hat{D}$ behave as expected; see Appendix 3.1.B. Let us now solve the general problem. One can rewrite Eqs. (3.61) using a matrix similar to the transfer

matrix, obtaining:

$$
\begin{aligned}
\begin{pmatrix} \hat{A} \\ \hat{B} \end{pmatrix}
&= \frac{1}{\mathfrak{t}} \begin{bmatrix} (\mathfrak{t}^2 - \mathfrak{r}^2) & \mathfrak{r} \\ -\mathfrak{r} & 1 \end{bmatrix} \begin{pmatrix} \hat{C} \\ \hat{D} \end{pmatrix} + \frac{\sqrt{\epsilon}}{\mathfrak{t}} \begin{pmatrix} \hat{E} \\ \hat{E} \end{pmatrix} \\[2mm]
&= \frac{1}{\mathfrak{t}} \left[\begin{array}{cc|c} (\mathfrak{t}^2 - \mathfrak{r}^2) & \mathfrak{r} & \sqrt{\epsilon} \\ -\mathfrak{r} & 1 & -\sqrt{\epsilon} \end{array} \right] \begin{pmatrix} \hat{C} \\ \hat{D} \\ \hat{E} \end{pmatrix} \\[2mm]
&= \left[\begin{array}{c|c} \hat{M}_{\mathrm{S}} & \sqrt{\epsilon}/\mathfrak{t} \\ & -\sqrt{\epsilon}/\mathfrak{t} \end{array} \right] \begin{pmatrix} \hat{C} \\ \hat{D} \\ \hat{E} \end{pmatrix},
\end{aligned}
\tag{3.96}
$$

where $\hat{M}_{\mathrm{S}}$ is included as a 2×2 submatrix in the new 2×3 matrix, which can in turn be embedded in a 3×3 square matrix:[3]

$$
\begin{pmatrix} \hat{A} \\ \hat{B} \\ \hat{E} \end{pmatrix} = \left[\begin{array}{cc|c} & & \sqrt{\epsilon}/\mathfrak{t} \\ & \hat{M}_{\mathrm{S}} & -\sqrt{\epsilon}/\mathfrak{t} \\ \hline 0 & 0 & 1 \end{array} \right] \begin{pmatrix} \hat{C} \\ \hat{D} \\ \hat{E} \end{pmatrix}.
\tag{3.97}
$$

This assumes that the noise mode is essentially unaffected by the presence of the scatterer. In summary, then, each transfer matrix in the optical system is replaced by one of two matrices:

$$
\hat{M} \rightarrow \left[\begin{array}{cc|c} & & 0 \\ & \hat{M} & 0 \\ \hline 0 & 0 & 1 \end{array} \right],
\tag{3.98}
$$

if the scatterer introduces no noise into the system, or

$$
\hat{M} \rightarrow \left[\begin{array}{cc|c} & & \sqrt{\epsilon}/\mathfrak{t} \\ & \hat{M} & -\sqrt{\epsilon}/\mathfrak{t} \\ \hline 0 & 0 & 1 \end{array} \right],
\tag{3.99}
$$

if the scatterer introduces the noise mode; as before, the properties of the scatterer are fully specified by $\mathfrak{r}$ and $\mathfrak{t}$. The third row and column of *every* such matrix refer to the same, singular, noise mode being treated. Applying the above transformation to the matrices representing the generic system in Fig. 3.7, one obtains the field operators to

---

[3] Note that Eq. (3.97) does *not* imply violation of the principle of conservation of energy; indeed, the matrix is not a transfer matrix and the $\hat{E}$ mode is the same mode on either side of the equality.

zeroth order in v/c:

$$\hat{A} = \left(\theta_{11}\frac{\alpha_0}{\beta_0} + \theta_{12}\right)\hat{B}_{\mathrm{l}} + \theta_{11}\frac{\gamma_0\beta_0 - \alpha_0\delta_0}{\beta_0}\hat{C}_{\mathrm{r}} + \theta_{11}\frac{\sqrt{\epsilon}}{\mathfrak{t}}\left[\left(m_{11} - m_{12}\right) + \left(m_{22} - m_{21}\right)\frac{\alpha_0}{\beta_0}\right]\hat{E}\,,$$
(3.100)

and

$$\hat{B} = \left(\theta_{21}\frac{\alpha_0}{\beta_0} + \theta_{22}\right)\hat{B}_{\mathrm{l}} + \theta_{21}\frac{\gamma_0\beta_0 - \alpha_0\delta_0}{\beta_0}\hat{C}_{\mathrm{r}} + \theta_{21}\frac{\sqrt{\epsilon}}{\mathfrak{t}}\left[\left(m_{11} - m_{12}\right) + \left(m_{22} - m_{21}\right)\frac{\alpha_0}{\beta_0}\right]\hat{E}\,,$$
(3.101)

where we have used the shorthand notation $\left[m_{ij}\right] \equiv M_1$. Here, $\hat{E}$ is the noise mode introduced by the scatterer itself. Other noise modes would give rise to contributions that are computed analogously. Now, denote $\hat{A} = b_{\mathrm{a}}\hat{B}_{\mathrm{l}} + c_{\mathrm{a}}\hat{C}_{\mathrm{r}} + e_{\mathrm{a}}\hat{E}$ and $\hat{B} = b_{\mathrm{b}}\hat{B}_{\mathrm{l}} + c_{\mathrm{b}}\hat{C}_{\mathrm{r}} + e_{\mathrm{b}}\hat{E}$ to this order in v/c; $b_{\mathrm{a,b}}$, $c_{\mathrm{a,b}}$, and $e_{\mathrm{a,b}}$ can be read off Eqs. (3.100) and (3.101). Then

$$\left[\hat{A}, \hat{A}^{\dagger}\right] = \frac{\hbar k_0}{2\epsilon_0\sigma_{\mathrm{L}}}\delta(t - t')\left(|b_{\mathrm{a}}|^2 + |c_{\mathrm{a}}|^2 + |e_{\mathrm{a}}|^2\right),$$
(3.102)

$$\left[\hat{B}, \hat{B}^{\dagger}\right] = \frac{\hbar k_0}{2\epsilon_0\sigma_{\mathrm{L}}}\delta(t - t')\left(|b_{\mathrm{b}}|^2 + |c_{\mathrm{b}}|^2 + |e_{\mathrm{b}}|^2\right), \text{ and}$$
(3.103)

$$\left[\hat{A}, \hat{B}^{\dagger}\right] = \frac{\hbar k_0}{2\epsilon_0\sigma_{\mathrm{L}}}\delta(t - t')\left(b_{\mathrm{a}}b_{\mathrm{b}}^* + c_{\mathrm{a}}c_{\mathrm{b}}^* + e_{\mathrm{a}}e_{\mathrm{b}}^*\right).$$
(3.104)

We can also express $\hat{C} = b_{\mathrm{c}}\hat{B}_{\mathrm{l}} + c_{\mathrm{c}}\hat{C}_{\mathrm{r}} + e_{\mathrm{c}}\hat{E}$ and $\hat{D} = b_{\mathrm{d}}\hat{B}_{\mathrm{l}} + c_{\mathrm{d}}\hat{C}_{\mathrm{r}} + e_{\mathrm{d}}\hat{E}$, where

$$b_{\mathrm{c}} = b_{\mathrm{a}}/\mathfrak{t} - b_{\mathrm{b}}\mathfrak{r}/\mathfrak{t}, \; c_{\mathrm{c}} = c_{\mathrm{a}}/\mathfrak{t} - c_{\mathrm{b}}\mathfrak{r}/\mathfrak{t}, \text{ and } e_{\mathrm{c}} = e_{\mathrm{a}}/\mathfrak{t} - e_{\mathrm{b}}\mathfrak{r}/\mathfrak{t} - \sqrt{\epsilon}/\mathfrak{t};$$
(3.105)

$$b_{\mathrm{d}} = b_{\mathrm{a}}\mathfrak{r}/\mathfrak{t} + b_{\mathrm{b}}\left(\mathfrak{t}^2 - \mathfrak{r}^2\right)/\mathfrak{t}, \; c_{\mathrm{d}} = c_{\mathrm{a}}\mathfrak{r}/\mathfrak{t} + c_{\mathrm{b}}\left(\mathfrak{t}^2 - \mathfrak{r}^2\right)/\mathfrak{t}, \text{ and}$$

$$e_{\mathrm{d}} = e_{\mathrm{a}}\mathfrak{r}/\mathfrak{t} + e_{\mathrm{b}}\left(\mathfrak{t}^2 - \mathfrak{r}^2\right)\mathfrak{r}/\mathfrak{t} + \sqrt{\epsilon}/\mathfrak{t}.$$
(3.106)

Therefore, e.g.,

$$\left[\hat{C}, \hat{C}^{\dagger}\right] = \frac{\hbar k_0}{2\epsilon_0\sigma_{\mathrm{L}}}\delta(t - t')\left(|b_{\mathrm{c}}|^2 + |c_{\mathrm{c}}|^2 + |e_{\mathrm{c}}|^2\right), \text{ and}$$
(3.107)

$$\left[\hat{D}, \hat{D}^{\dagger}\right] = \frac{\hbar k_0}{2\epsilon_0\sigma_{\mathrm{L}}}\delta(t - t')\left(|b_{\mathrm{d}}|^2 + |c_{\mathrm{d}}|^2 + |e_{\mathrm{d}}|^2\right).$$
(3.108)

Several other nontrivial commutators need to be computed, due to the presence of $\hat{E}$; for example,

$$\left[\hat{A}, \hat{D}^{\dagger}\right] = \frac{\hbar k_0}{2\epsilon_0\sigma_{\mathrm{L}}}\delta(t - t')\left(b_{\mathrm{a}}b_{\mathrm{d}}^* + c_{\mathrm{a}}c_{\mathrm{d}}^* + e_{\mathrm{a}}e_{\mathrm{d}}^*\right).$$
(3.109)

For an isolated scatterer in free space, $b_{\mathrm{b}} = c_{\mathrm{c}} = 1$, $b_{\mathrm{c}} = c_{\mathrm{b}} = 0$, $e_{\mathrm{b}} = e_{\mathrm{c}} = 0$, etc., and one can show that the various commutators behave as expected. Finally, the momentum

diffusion constant is given by

$$D\,\delta(t-t') = 2\epsilon_0\sigma_{\mathrm{L}}\,\hbar k_0\Big(|\mathcal{A}_0|^2\Big[\hat{A},\hat{A}^\dagger\Big] + |\mathcal{B}_0|^2\Big[\hat{B},\hat{B}^\dagger\Big] + |\mathcal{C}_0|^2\Big[\hat{C},\hat{C}^\dagger\Big] + |\mathcal{D}_0|^2\Big[\hat{D},\hat{D}^\dagger\Big]$$
$$+\,2\,\mathrm{Re}\,\Big\{\mathcal{A}_0^*\mathcal{B}_0\Big[\hat{A},\hat{B}^\dagger\Big] - \mathcal{A}_0^*\mathcal{C}_0\Big[\hat{A},\hat{C}^\dagger\Big]$$
$$-\mathcal{A}_0^*\mathcal{D}_0\Big[\hat{A},\hat{D}^\dagger\Big] - \mathcal{B}_0^*\mathcal{C}_0\Big[\hat{B},\hat{C}^\dagger\Big]$$
$$-\mathcal{B}_0^*\mathcal{D}_0\Big[\hat{B},\hat{D}^\dagger\Big] + \mathcal{C}_0^*\mathcal{D}_0\Big[\hat{C},\hat{D}^\dagger\Big]\Big\}\Big), \qquad (3.110)$$

where, for example, $\mathcal{A}_0^*\mathcal{D}_0 = \int\langle\hat{A}^\dagger\rangle\mathrm{d}k\int\langle\hat{D}\rangle\mathrm{d}k = b_{\mathrm{a}}^*b_{\mathrm{d}}|B_0|^2 + c_{\mathrm{a}}^*c_{\mathrm{d}}|C_0|^2 + b_{\mathrm{a}}^*c_{\mathrm{d}}B_0^*C_0 + c_{\mathrm{a}}^*b_{\mathrm{d}}C_0^*B_0$, recalling that $\langle\hat{E}\rangle = 0$, and analogously for the rest of the terms. This result again reduces to the expected one for an isolated scatterer in free space; it can alternatively be extended to include further noise modes.

3.3   Optomechanics of a micromirror inside a cavity

Placing a micromirror inside a cavity is actively being explored, both theoretically [123, 130] and experimentally [114, 129, 131], as a means of realising strong optomechanical coupling between a movable scatterer and the cavity field. In a recent experiment, Sankey and co-workers [131] looked at both linear and nonlinear coupling between the mechanical degree of freedom of the micromirror and the cavity field. The physical mechanism by which optomechanical coupling, and subsequently cooling, is enhanced by the presence of the cavity can be looked at either using the standard theory of cavity-mediated cooling [19, 75], in the case of weakly reflective micromirrors, or by considering the micromirror to form the boundary between two coupled cavities [123, 130], in the case of more strongly reflective micromirrors. The transfer matrix approach detailed in the previous sections provides a natural way to explore this interaction no matter what the optical properties of the micromirror are.

We begin by modelling the system in Ref. [114]: a two–mirror Fabry-Pérot cavity with a micromirror near its centre, operating at a wavelength $\lambda = 1064\,\mathrm{nm}$ and having a length $L_{\mathrm{C}} = 6.7\,\mathrm{cm}$. The micromirror is modelled by its polarisability ζ which, in light of the small losses observed in practice, is taken to be real and negative. Whereas the real experimental system corresponds to $\zeta \gtrsim -1$, we allow ζ to vary freely in our model. The two quantities of interest in this section are the intensity of the field close to the
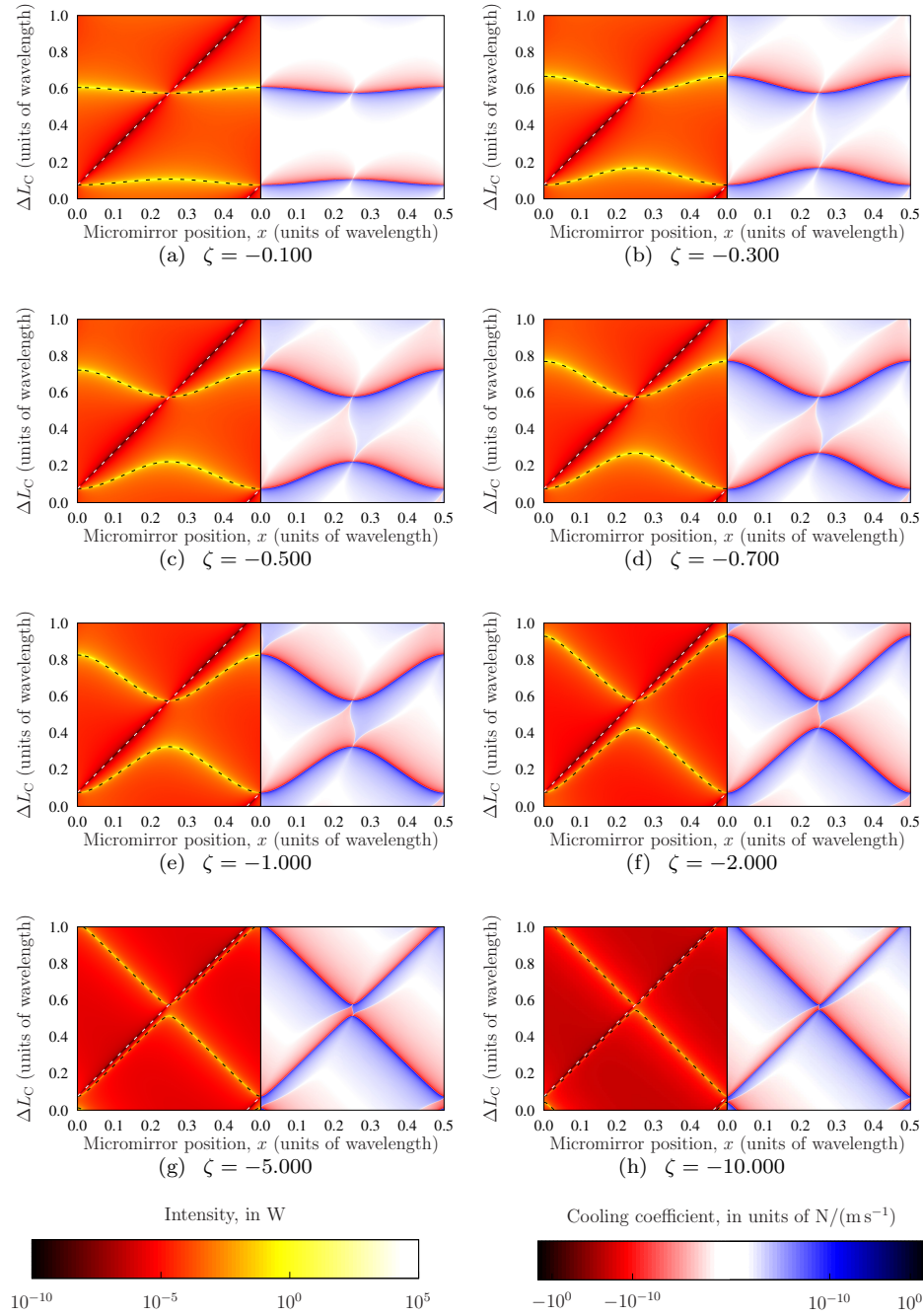
FIGURE 3.8: Field intensity (left panels) at and cooling coefficient (right panels) acting on the micromirror as the micromirror position (x) and cavity length ($L_C + \Delta L_C$) are scanned. The subfigures differ only in the polarisability of the mirror, as indicated. The cavity parameters are modelled from Ref. [114]. In the series of left panels, we note the progression from an almost bare cavity situation (a) to a very strong perturbation by the micromirror, leading to avoided crossings (h). The white dashed line traces a cavity node, whereas the black dashed lines [Eq. (3.111)] trace the cavity resonances. In the series of right panels, note that the cooling coefficient is—as expected—a cooling force (blue) for red cavity detuning and a heating force (red) for blue detuning. The colourbars are on a logarithmic scale and are for 1 W of input power; the large dynamic range is needed to bring out the detail in the panels, due to the very narrow features present.
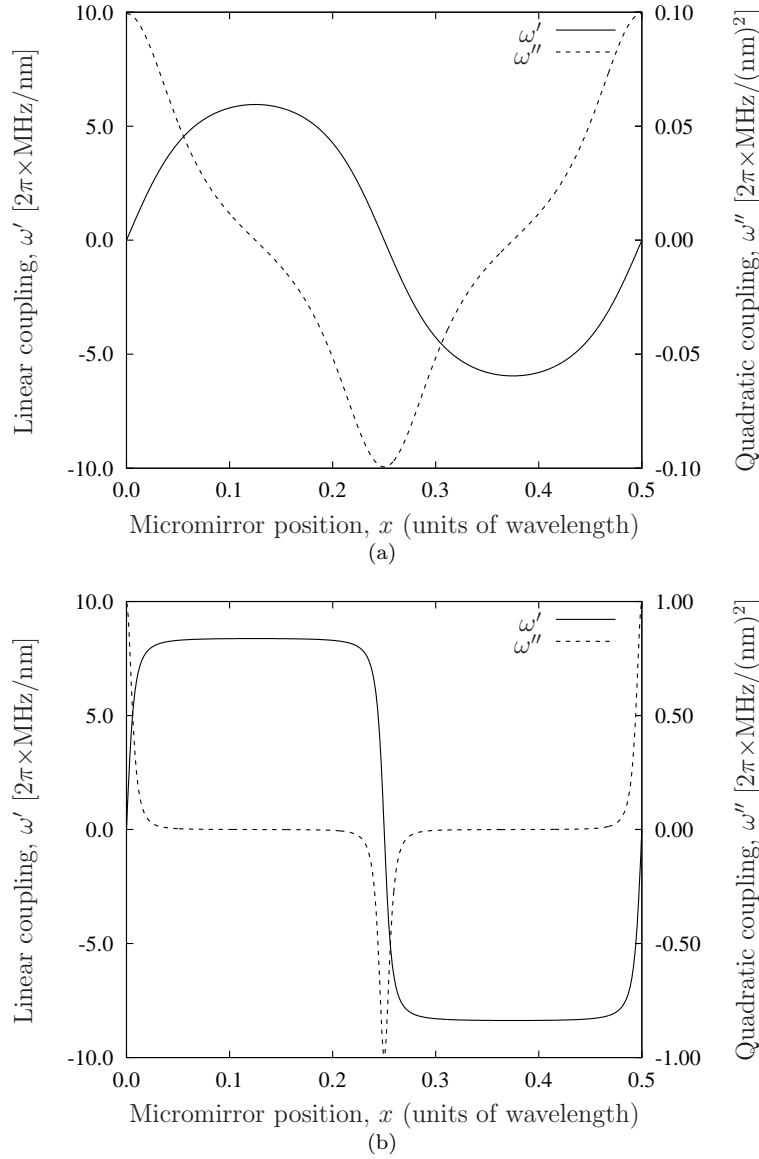
Figure 3.9: Linear and quadratic optomechanical couplings as a function of mirror position for a very good cavity and for (a) $\zeta = -1$, and (b) $\zeta = -10$. In each figure we show the linear (solid curve) and quadratic (dashed curve) couplings, from Eqs. (3.114) and (3.115). Note that the peak value of ω'' is roughly proportional to ζ whereas ω' is bounded.

micromirror, and the cooling coefficient acting on the micromirror. The former gives us knowledge of the resonant frequencies of the cavity and, therefore, of the optomechanical coupling, to all orders, between the cavity field and the micromirror. The latter is useful in optomechanical cooling experiments; the interest here lies in the fact that cooling the motion of a micromirror is one way towards achieving higher sensitivity in sensing applications, most notably in gravitational-wave detectors [132].

These quantities are summarised in Fig. 3.8, with the left panels showing the intensity at the mirror and the right panels the cooling coefficient acting on the mirror. Each
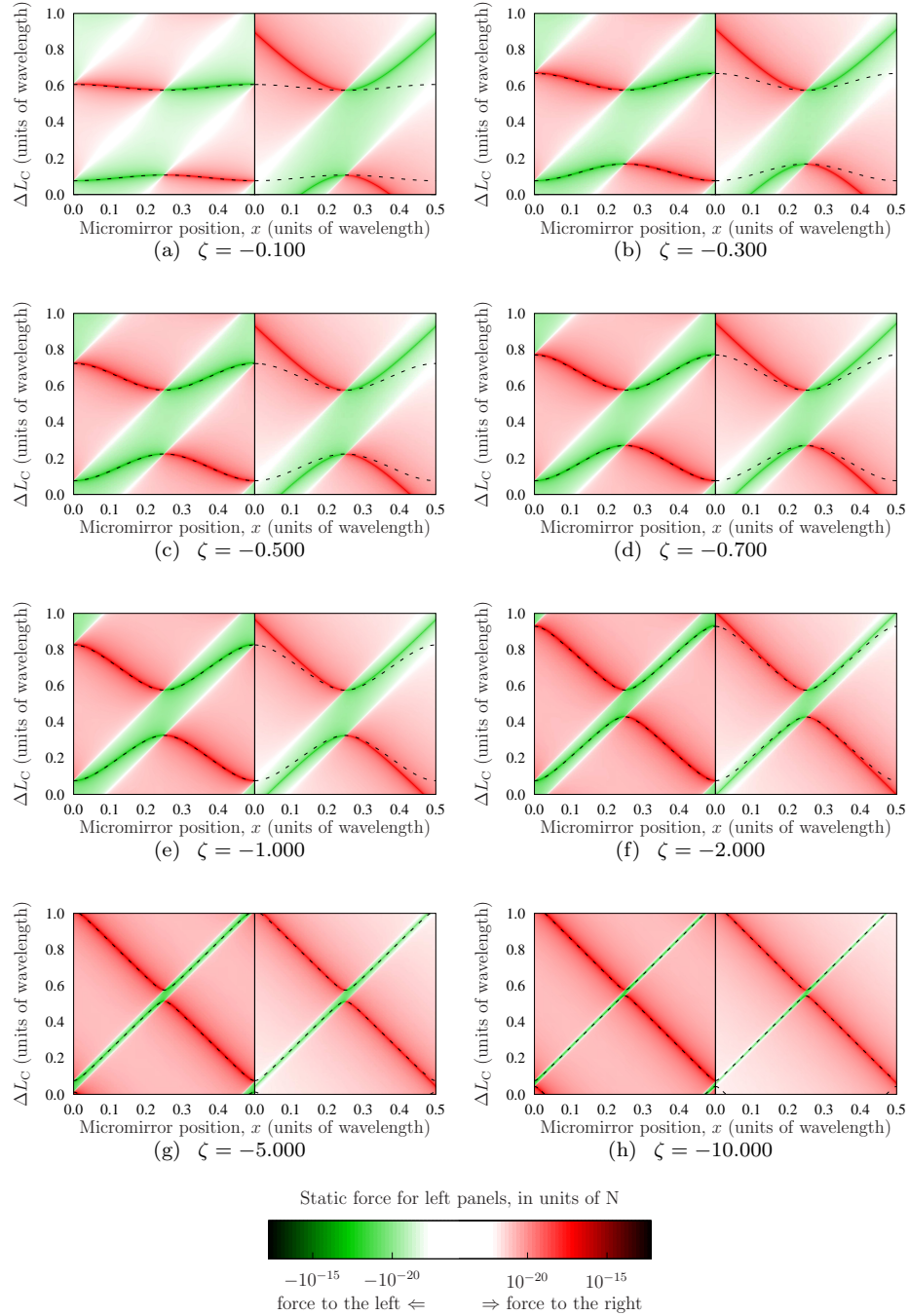
FIGURE 3.10: Static friction force (i.e., the force acting on the mirror when $v = 0$) computed from the scattering model presented here (left panels) and a model based on a modal decomposition [129] (right panels), showing only one pair of modes. Red and green regions represent forces pointing in opposite directions, as indicated on the colourbar. We note qualitative agreement between the two models for $x \approx 0.25\lambda$ and for ΔL_C close to the resonances, especially for large $|\zeta|$. The discrepancies between the two sets of data, that are more pronounced for small polarisability, have significant consequences for any theory based on a coupled-cavity modal decomposition model. The black dashed lines [Eq. (3.111)] trace the cavity resonances in the scattering model. The absolute values on the colourbar relate to the left panels.

subfigure (a)–(h) explores a different value for ζ. For $\zeta \approx 0$, the cavity field is similar to the bare-cavity field; in particular, the cavity resonances are only slightly perturbed by the presence and position of the micromirror. The opposite is true of the $\zeta \ll -1$ case, where there is strong coupling between pairs of cavity modes, typified by the avoided crossings in the spectra. The resonance frequencies can be obtained analytically, in the limit of a good bare cavity, as frequency shifts from the bare resonances:

$$\Delta\omega = \frac{c}{L_{\mathrm{C}}} \tan^{-1}\left\{ \frac{\zeta \cos(2k_0 x) \mp \zeta\left[1 + \zeta^2 \sin^2(2k_0 x)\right]}{\zeta^2 \cos(2k_0 x) \pm \left[1 + \zeta^2 \sin^2(2k_0 x)\right]} \right\}, \qquad (3.111)$$

with L_{C} being the length of the cavity, x the position of the micromirror, and $k_0 = 2\pi/\lambda$ the wavenumber of the light inside the cavity. The two sets of solutions to Eq. (3.111) are, in the $\zeta \to 0$ limit or at $x = \lambda/8$, separated by a free spectral range. These cavity resonances, plotted as detuned cavity lengths $\Delta L_{\mathrm{C}} = (L_{\mathrm{C}}/\omega)\Delta\omega$, are traced by means of the dashed black curves in the left panels of Fig. 3.8.

In the standard optomechanical coupling Hamiltonian, the mirror–field coupling is represented by a term of the form

$$\hat{H}_{\mathrm{OM}}^{(1)} \sim \hbar\omega'\hat{x}\hat{a}^\dagger\hat{a}\,, \qquad (3.112)$$

where $\hat{x}$ is the position operator of the mirror, and $\omega' \equiv \partial(\Delta\omega)/\partial x$. $\hat{a}$ is the annihilation operator of the field mode that has the dominant interaction with the micromirror; in the $|\zeta| \to 0$ limit, these field modes are the bare cavity modes of the whole cavity. However, as $|\zeta|$ increases, the micromirror effectively splits the main cavity into two coupled cavities, giving rise to symmetric and antisymmetric modes, seen as the higher (bright) and lower (dark) branches in Fig. 3.8(h) for $0 < x < \lambda/4$; in such cases a is the annihilation operator belonging to one of these eigenmodes. We note that similar behaviour was observed in Ref. [129].

Certain effects, such as mechanical squeezing of the mirror position [133] and quantum non-demolition measurements on the mirror [134], require not *linear coupling* to $\hat{x}$ but *quadratic coupling* to $\hat{x}^2$:

$$\hat{H}_{\mathrm{OM}}^{(2)} \sim \hbar\omega''\hat{x}^2\hat{a}^\dagger\hat{a}\,, \qquad (3.113)$$

with $\omega'' \equiv \partial^2(\Delta\omega)/\partial x^2$. In our notation, we have

$$\omega' = \mp \frac{2k_0 c}{L_{\rm C}} \frac{\zeta \sin(2k_0 x)}{\left[1 + \zeta^2 \sin^2(2k_0 x)\right]^{1/2}} \,, \tag{3.114}$$

and

$$\omega'' = \mp \frac{4k_0^2 c}{L_{\rm C}} \frac{\zeta \cos(2k_0 x)}{\left[1 + \zeta^2 \sin^2(2k_0 x)\right]^{3/2}} \,. \tag{3.115}$$

One thing we note immediately is that there is no value for x such that $\omega' = \omega'' = 0$; in other words, the optomechanical coupling is restricted to be linear or quadratic, to lowest order. Higher-order nonlinearities may be achieved by coupling different transverse modes of the cavity (see, e.g., the experimental results in Ref. [131]) but are overwhelmed by the linear or quadratic couplings in a single-mode cavity. Moreover, the linear coupling ω' is bounded in the $\zeta \to \infty$ limit:

$$|\omega'| \le \frac{2k_0 c}{L_{\rm C}} \approx 2\pi \times 8.42\,{\rm MHz/nm} \,, \tag{3.116}$$

with the numeric value corresponding to our parameters. In the same limit, ω'' exhibits resonant behaviour (see Fig. 3.9), indicative of avoided crossings in the spectrum, peaking at a value of:

$$|\omega''| \to \frac{4k_0^2 c}{L_{\rm C}}|\zeta| \approx 2\pi \times 0.10\,|\zeta|\,{\rm MHz/(nm)}^2 \,. \tag{3.117}$$

We plot the lower ($\mp \to -$) branches of Eqs. (3.114) and (3.115) in Fig. 3.9 for two values for ζ: $\zeta = -1$, representative of realistic micromirrors, and $\zeta = -10$, representative of highly reflective micromirrors. These correspond to cases (e) and (h) in Fig. 3.8, respectively. Coupling between the pairs of modes is not very strong for the $\zeta = -1$ case; this is manifested by means of the smooth variation with x of ω' and ω'' in Fig. 3.9(a). The second case shows strong signs of the avoided crossing behaviour seen in Fig. 3.8(h), with ω' no longer behaving smoothly and ω'' acquiring a resonance-like character. Note that, independently of the magnitude of ζ, the strongest quadratic coupling always occurs at the points where $\omega' = 0$.

The linear frequency shifts, Eq. (3.114) and the solid curves in Fig. 3.9, describe the same quantity as do the curves in Fig. 5 of Ref. [123]. In other words, our results match those in Ref. [123] in the relevant limit of a high-reflectivity micromirror, but the self-consistent scattering solution presented here is also applicable to the general situation

where ζ can take any complex value. Thus, our 'micromirror' could represent an actual micromirror, a poorly reflective membrane, or even an atom, whereas in the latter two cases the decomposition of the system into two coupled cavities is not valid. Fig. 3.10 presents a comparison of the static force acting on the micromirror, for various values of ζ, as calculated both from the model presented in this work (left panels) and from a modal decomposition model (Ref. [129], right panels). We note that the two sets of data agree in the large $|\zeta|$ limit, where the 'two coupled cavities' model is formally valid, but there are significant qualitative differences when $|\zeta| \ll 1$, where the model used most often is that of a single cavity mode interacting with a scatterer [75].

The behaviour of the cooling coefficient acting on the micromirror, as shown on the right panels of Fig. 3.8, also has a number of interesting properties. Its overall trend follows the structure of the field intensity closely, as can be seen from an inspection of this figure. As is expected from earlier investigations [75, 129] optomechanical cooling inside cavities proceeds when the light pumped into the cavity is tuned below resonance. This is shown quite clearly in Fig. 3.8, in that the friction force generally acts to cool the micromirror when ΔL_{C} is smaller than the resonant length, and it acts to heat when ΔL_{C} is larger. One notes that for weak mirror–field coupling [Fig. 3.8(a)] the behaviour of the cooling coefficient at a given ΔL_{C} close to resonance is approximately well-defined: the motion of the mirror is either cooled or heated, almost irrespectively of the value of x. The situation is qualitatively different for very strong mirror–field coupling [Fig. 3.8(h)], where the cooling coefficient changes sign very rapidly as x is scanned over the resonance at a fixed ΔL_{C}. This has profound implications for experimental explorations, since the localisation of the micromirror within the cavity becomes of critical importance to the qualitative behaviour of the system.

3.4   Optical pumping and multilevel atoms

The work in this section is published as Xuereb, A., Domokos, P., Horak, P., & Freegarde, T. Phys. Scr. **T140**, 014010 (2010) and is reproduced essentially *verbatim* [135]. The transfer matrix method described previously is extended here to handle multilevel atoms and arbitrarily polarised incident fields.
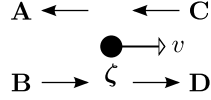
FIGURE 3.11: Moving scatterer interacting with four field modes represented by the Jones vectors **A**, **B**, **C**, and **D**. The scatterer has velocity v and is described by means of its polarisability tensor $\boldsymbol{\zeta}$. The field mode amplitudes are, in general, functions of the wavenumber k.

The extended model we describe in the present section allows us to treat multi-level atoms as classical scatterers in light fields modified by, in principle, arbitrarily complex optical components such as mirrors, resonators, dispersive or dichroic elements, or filters. After we introduce the general extension in the next section, we verify our formalism for two prototypical sub-Doppler cooling mechanisms—the $J = \frac{1}{2} \to J' = \frac{3}{2}$ transition, leading to the Sisyphus cooling mechanism, and the $J = 1 \to J' = 2$ transition—in Section 3.4.2 and Section 3.4.3, respectively, and show that it agrees with the standard literature.

3.4.1 A transfer matrix relating Jones vectors

We investigate the interaction of atoms with light of different polarisations. To this end, we denote the two polarisation basis vectors by μ and ν, whereby the standard circular polarisation basis is equivalent to setting $\mu = \sigma^+$ and $\nu = \sigma^-$. Starting from the transfer matrix model explored in Section 3.1 and using the definitions in Fig. 3.11, we replace each of the field modes by a corresponding Jones vector, similar to the model used in Ref. [136]. Thus, for example,

$$A(k) \to \mathbf{A}(k) = \begin{pmatrix} A_\mu(k) \\ A_\nu(k) \end{pmatrix} , \tag{3.118}$$

and similarly for B, C and D, which are the mode amplitudes in the positive frequency part of the electric field. The transfer matrix M, describing the effect of the scatterer on the four field modes by means of the relation

$$\begin{pmatrix} A(k) \\ B(k) \end{pmatrix} = M \begin{pmatrix} C(k) \\ D(k) \end{pmatrix} , \tag{3.119}$$

is now transformed into an order 4 tensor of the form

$$M = \begin{bmatrix} m_{11} & m_{12} \\ m_{21} & m_{22} \end{bmatrix}, \qquad (3.120)$$

where each of $m_{\alpha\beta}$ $(\alpha, \beta = 1, 2)$ is a 2×2 matrix relating the respective Jones vector components. A general recipe for transforming the formulae for the field mode amplitudes, as given in Section 3.1.1, can be summarised by means of the two replacements

$$1 \to \mathbb{1} = \begin{bmatrix} 1 & 0 \\ 0 & 1 \end{bmatrix} \text{ and } \zeta \to \boldsymbol{\zeta}, \qquad (3.121)$$

wherever necessary. In particular, then,

$$M = \begin{bmatrix} 1 - \mathrm{i}\zeta & -\mathrm{i}\zeta \\ \mathrm{i}\zeta & 1 + \mathrm{i}\zeta \end{bmatrix} \to M = \begin{bmatrix} \mathbb{1} - \mathrm{i}\boldsymbol{\zeta} & -\mathrm{i}\boldsymbol{\zeta} \\ \mathrm{i}\boldsymbol{\zeta} & \mathbb{1} + \mathrm{i}\boldsymbol{\zeta} \end{bmatrix}. \qquad (3.122)$$

The polarisability tensor $\boldsymbol{\zeta}$ is defined in Eq. (1.62). We note that this new transfer matrix still allows us to model the interaction of the multilevel atom with an arbitrary system of immobile optical elements such as mirrors, cavities, waveplates, etc. As was done in Section 3.1, this interaction is accounted for by the multiplication of the various transfer matrices of the elements making up the system; this model is, in principle, applicable to systems of arbitrary complexity.

Finally, we recall that the diagonal elements, $\langle i|\boldsymbol{\rho}^{\mathrm{st}}|i\rangle$, of the steady-state density matrix $\boldsymbol{\rho}^{\mathrm{st}}$ are the populations in each of the sublevels, whereas its off-diagonal elements, $\langle i|\boldsymbol{\rho}^{\mathrm{st}}|j\rangle$, are the respective coherences. The matrix elements of $\boldsymbol{\rho}^{\mathrm{st}}$ are obtained from the appropriate optical Bloch equations (see, for example, the procedure outlined in Ref. [137]). We note here that, through its dependence on $\boldsymbol{\rho}^{\mathrm{st}}$, M depends on the fields that it helps to determine, and thus Eq. (3.119) will in general become a set of nonlinear equations. In cases like the ones considered in the following sections, where only one multilevel atom is interacting with a linear optical system, this problem may be solved using a procedure similar to the one outlined below: the fields surrounding the atom are obtained from the input fields through linear operations and then used with the optical Bloch equations to obtain the populations and coherences of the atom's various levels. Knowledge of these quantities then determines the fields, and hence the forces acting on the atom, completely.
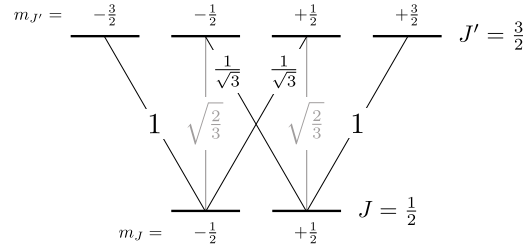
FIGURE 3.12: Clebsch-Gordan coefficients for a $J = \frac{1}{2} \to J' = \frac{3}{2}$ transition.

In the following sections we will restrict our discussion to the case where the input field is not modified by other transfer matrices. We will apply this mechanism to investigate the behaviour of atoms in two cases where the polarisation of the light varies in space on scales of the order of the wavelength to verify the validity of the model given by Eq. (3.122), Eq. (1.62), and Eq. (1.63). In the first instance, we illuminate our atom with two counterpropagating linearly polarised beams. We choose the planes of polarisation of the two beams to be orthogonal to each other. The second configuration we will investigate involves illuminating the atom with two circularly polarised beams, choosing opposite handedness for the two beams. These two cases mirror those in Ref. [14].

3.4.2 Atoms in a gradient of polarisation

In this and the following sections, we will adopt the low-intensity hypothesis. This allows us to simplify the optical Bloch equations and resulting system considerably by neglecting the populations and coherences of the excited state sublevels. We can thus replace $\boldsymbol{\rho}^{\mathrm{st}}$ by the ground state steady-state density matrix, $\boldsymbol{\rho}^{\mathrm{st}}_{\mathrm{g}}$. We denote the diagonal element (i, i) of $\boldsymbol{\rho}^{\mathrm{st}}_{\mathrm{g}}$, the population in sublevel i, by Π_i, and the off-diagonal element (i, j), the coherence between sublevels i and j, by $C_{i,j}$.

Here we will discuss what is perhaps the simplest transition between two levels with multiple magnetic sublevels: the $J = \frac{1}{2} \to J' = \frac{3}{2}$ transition. In this case, we have two ground sublevels so that $\boldsymbol{\rho}^{\mathrm{st}}_{g}$ is a 2×2 matrix. Fig. 3.12 tabulates the Clebsch-Gordan coefficients required to evaluate $\boldsymbol{\zeta}$. We thus have:

$$\boldsymbol{\rho}^{\mathrm{st}}_{g} = \begin{bmatrix} \Pi_{-\frac{1}{2}} & C_{-\frac{1}{2},+\frac{1}{2}} \\ C_{+\frac{1}{2},-\frac{1}{2}} & \Pi_{+\frac{1}{2}} \end{bmatrix} \tag{3.123}$$

and

$$\hat{\boldsymbol{\zeta}} = \zeta_0 \begin{pmatrix} \begin{bmatrix} \frac{1}{3} & 0 \\ 0 & 1 \end{bmatrix} & \mathbf{0} \\ \\ \mathbf{0} & \begin{bmatrix} 1 & 0 \\ 0 & \frac{1}{3} \end{bmatrix} \end{pmatrix}, \tag{3.124}$$

whereby

$$\boldsymbol{\zeta} = \zeta_0 \left(\begin{bmatrix} \frac{1}{3} & 0 \\ 0 & 1 \end{bmatrix} \Pi_{-\frac{1}{2}} + \begin{bmatrix} 1 & 0 \\ 0 & \frac{1}{3} \end{bmatrix} \Pi_{+\frac{1}{2}} \right). \tag{3.125}$$

Suppose, now, that we illuminate the atom with two counterpropagating beams having orthogonal linear polarisation and equal intensity. This can be represented by setting

$$\mathbf{B}(k) = \frac{B}{\sqrt{2}} \begin{pmatrix} 1 \\ 1 \end{pmatrix} \exp(\mathrm{i}kx - \mathrm{i}\pi/4) \tag{3.126}$$

and

$$\mathbf{C}(k) = \frac{\mathrm{i}B}{\sqrt{2}} \begin{pmatrix} 1 \\ -1 \end{pmatrix} \exp(-\mathrm{i}kx + \mathrm{i}\pi/4), \tag{3.127}$$

where the shift in the x coordinate is introduced to simplify our expressions. Using the optical Bloch equations, we can show that the steady state populations in the ground sublevels at zero atomic velocity are given by

$$\Pi_{-\frac{1}{2}} = \cos^2(kx) \text{ and } \Pi_{+\frac{1}{2}} = \sin^2(kx), \tag{3.128}$$

noting that the populations do not depend on the field amplitudes in the low intensity regime.

We work to lowest order in ζ_0 and make use of the above relations to find the net force acting on the atom [116]; cf. Eq. (3.18):

$$\begin{aligned} F &= \hbar k \left(|\mathbf{A}|^2 + |\mathbf{B}|^2 - |\mathbf{C}|^2 - |\mathbf{D}|^2 \right) \\ &= 2\hbar k \,\mathrm{Im}\big\{ \big[\boldsymbol{\zeta}(\mathbf{B} + \mathbf{C}) \big] \cdot (\mathbf{B} - \mathbf{C})^* \big\} + 4\tfrac{v}{c}\hbar k \,\mathrm{Im}\big\{ (\boldsymbol{\zeta}\mathbf{B}) \cdot \mathbf{C}^* + (\boldsymbol{\zeta}\mathbf{C}) \cdot \mathbf{B}^* \big\} \\ &\quad - 2\tfrac{v}{c}\hbar k^2 \,\mathrm{Im}\bigg\{ \bigg[\frac{\partial \boldsymbol{\zeta}}{\partial k}(\mathbf{B} + \mathbf{C}) \bigg] \cdot (\mathbf{B} + \mathbf{C})^* \bigg\} \\ &\approx 2\hbar k \,\mathrm{Im}\big\{ \big[\boldsymbol{\zeta}(\mathbf{B} + \mathbf{C}) \big] \cdot (\mathbf{B} - \mathbf{C})^* \big\} + 2\tfrac{v}{c}\hbar k^2 \,\mathrm{Im}\bigg\{ \bigg[\frac{\partial \boldsymbol{\zeta}}{\partial k}(\mathbf{B} + \mathbf{C}) \bigg] \cdot (\mathbf{B} + \mathbf{C})^* \bigg\}, \end{aligned}$$
$$\tag{3.129}$$
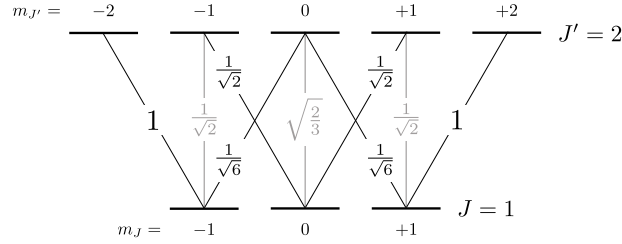
FIGURE 3.13: Clebsch-Gordan coefficients for a $J = 1 \to J' = 2$ transition.

where we have assumed that $\|k \, \partial \boldsymbol{\zeta}/\partial k\| \gg \|\boldsymbol{\zeta}\|$. The velocity-dependent force terms in the above expression arise through the Doppler shifting of photons both between field modes in the same polarisation and between field modes in different polarisations; these mechanisms are accounted for by the diagonal and off-diagonal terms in $\boldsymbol{\zeta}$,[4] respectively. These terms emerge through the velocity-dependent terms in the generalised transfer matrix.

In the present case, Eq. (3.129) simplifies approximately to

$$F = \tfrac{4}{3}\hbar k \zeta_0 |B|^2 \sin(2kx)\left(\Pi_{+\frac{1}{2}} - \Pi_{-\frac{1}{2}}\right) = -\tfrac{2}{3}\hbar k |B|^2 \zeta_0 \sin(4kx), \tag{3.130}$$

assuming that ζ_0 is real for simplicity.

Apart from the velocity-dependent terms in Eq. (3.129), a second type of friction force emerges from the dynamics of the populations in the ground-state sublevels. Upon solving the optical Bloch equations [14], expressions for $\Pi_{\pm\frac{1}{2}}$ are obtained that have a velocity-dependent term due to the time τ_{p} it takes for an atom in one sublevel to be pumped to the other. This adds a further velocity-dependent term to Eq. (3.130), giving an overall force

$$F = -\tfrac{2}{3}\hbar k |B|^2 \zeta_0 \sin(4kx) - \tfrac{8}{3}\hbar k^2 |B|^2 \zeta_0 v \tau_{\mathrm{p}} \sin^2(2kx), \tag{3.131}$$

which agrees precisely with the standard literature [cf. Eqs. (4.20) and (4.23) in Ref. [14]].

3.4.3 Atoms in a gradient of ellipticity

If we illuminate an atom with two counterpropagating beams of light in a $\sigma^+\!-\!\sigma^-$ configuration, rich dynamics are obtained not in the simplest $(J = \tfrac{1}{2} \to J' = \tfrac{3}{2})$ case, but

---

[4] We note that, whilst Eq. (3.129) is a general expression, the form of $\boldsymbol{\zeta}$ in this section has no nonzero off-diagonal terms, and only the first type of term contributes.

in the next simplest, where the ground state has three magnetic sublevels ($J = 1$) and the excited state five ($J' = 2$). In this case, then, we can express $\boldsymbol{\rho}_g^{\text{st}}$ and $\hat{\boldsymbol{\zeta}}$ as

$$\boldsymbol{\rho}_g^{\text{st}} = \begin{bmatrix} \Pi_{-1} & C_{-1,0} & C_{-1,+1} \\ C_{0,-1} & \Pi_0 & C_{0,+1} \\ C_{+1,-1} & C_{+1,0} & \Pi_{+1} \end{bmatrix} \tag{3.132}$$

and

$$\hat{\boldsymbol{\zeta}} = \zeta_0 \begin{pmatrix} \begin{bmatrix} \frac{1}{6} & 0 \\ 0 & 1 \end{bmatrix} & \mathbf{0} & \begin{bmatrix} 0 & \frac{1}{6} \\ 0 & 0 \end{bmatrix} \\ \\ \mathbf{0} & \begin{bmatrix} \frac{1}{2} & 0 \\ 0 & \frac{1}{2} \end{bmatrix} & \mathbf{0} \\ \\ \begin{bmatrix} 0 & 0 \\ \frac{1}{6} & 0 \end{bmatrix} & \mathbf{0} & \begin{bmatrix} 1 & 0 \\ 0 & \frac{1}{6} \end{bmatrix} \end{pmatrix}, \tag{3.133}$$

using the Clebsch-Gordan coefficients in Fig. 3.13. Together, these give

$$\boldsymbol{\zeta} = \zeta_0 \left(\begin{bmatrix} \frac{1}{6} & 0 \\ 0 & 1 \end{bmatrix} \Pi_{-1} + \begin{bmatrix} \frac{1}{2} & 0 \\ 0 & \frac{1}{2} \end{bmatrix} \Pi_0 + \begin{bmatrix} 1 & 0 \\ 0 & \frac{1}{6} \end{bmatrix} \Pi_{+1} + \begin{bmatrix} 0 & \frac{1}{6} \\ 0 & 0 \end{bmatrix} C + \begin{bmatrix} 0 & 0 \\ \frac{1}{6} & 0 \end{bmatrix} C^* \right), \tag{3.134}$$

with $C = C_{+1,-1} = C_{-1,+1}^* = \langle +1 | \rho_{\text{g}}^{\text{st}} | -1 \rangle$ representing the nonzero coherence between the $m_J = +1$ and the $m_J = -1$ sublevels. Note that we again apply the low intensity hypothesis, thereby replacing $\boldsymbol{\rho}^{\text{st}}$ with $\boldsymbol{\rho}_{\text{g}}^{\text{st}}$.

We now illuminate the atom with two counterpropagating beams of equal intensity, $\mathbf{B}$ and $\mathbf{C}$, possessing σ^+ and σ^- polarisation, respectively:

$$\mathbf{B}(k) = B \begin{pmatrix} 1 \\ 0 \end{pmatrix} \exp(\mathrm{i}kx) \text{ and } \mathbf{C}(k) = B \begin{pmatrix} 0 \\ 1 \end{pmatrix} \exp(-\mathrm{i}kx). \tag{3.135}$$

We again use Eq. (3.129) to derive the force acting on the atom, which is given by

$$\begin{aligned} \mathcal{F} = {}& 2\hbar k |B|^2 \, \mathrm{Im} \, \tfrac{5}{6}\zeta_0 \left(\Pi_{+1} - \Pi_{-1} \right) + \tfrac{1}{6}\mathrm{i}\zeta_0 \, \mathrm{Im}\{ C \exp(-2\mathrm{i}kx) \} \\ & - 2\tfrac{v}{c}\hbar k^2 |B|^2 \, \mathrm{Im}\{\partial \zeta_0 / \partial k\} \left(\tfrac{7}{6}\left(\Pi_{+1} + \Pi_{-1} \right) + \Pi_0 + \tfrac{1}{3}\, \mathrm{Re}\{ C \exp(-2\mathrm{i}kx) \} \right), \end{aligned} \tag{3.136}$$

where the populations and coherences are again obtained from the optical Bloch equations, and can be found in Ref. [14]. By observing the natural correspondence between ζ_0 and $s_\pm$ in this reference, we can see that our expression for the force acting on the atom

again agrees with the standard literature to first order in $\frac{v}{c}$ [cf. Eq. (5.9) in Ref. [14]]. The resulting friction force is thus due to both the Doppler shift, as evident in the terms shown explicitly in Eq. (3.136), as well as to the non-adiabatic following of the atomic sublevel populations.

3.A Appendix: Cavity properties from the transfer matrix model

In this section we will derive a consistent set of relations used to describe cavities, based on the transfer matrix formalism. Specifically, we will relate the cavity HWHM linewidth κ, its finesse $\mathcal{F}$, and its Q-factor to one another and to the reflectivity of the cavity mirrors.

3.A.1 Cavity finesse

The finesse of a cavity is defined as

$$\mathcal{F} = \frac{\Delta\lambda}{\delta\lambda}\,, \tag{3.137}$$

where $\delta\lambda$ is the FWHM linewidth of the cavity transmission peak and $\Delta\lambda$ is the free spectral range (FSR) of the cavity. We model the cavity as a Fabry–Pérot resonator having mirrors of reflectivity r_1 and r_2 and a length L. On resonance, we can find some integer n such that

$$L = \tfrac{1}{2}n\lambda\,. \tag{3.138}$$

The FSR is defined [138] as the wavelength interval such that

$$L = \tfrac{1}{2}(n+1)(\lambda - \Delta\lambda)\,. \tag{3.139}$$

We approximate $\Delta\lambda \ll \lambda$, whereby

$$\Delta\lambda = \frac{\lambda^2}{2L}\,. \tag{3.140}$$

The cavity is described by the transfer matrix equation:

$$\begin{pmatrix} A \\ B \end{pmatrix} = \frac{1}{t_1 t_2} \begin{bmatrix} t_1^2 - r_1^2 & r_1 \\ -r_1 & 1 \end{bmatrix} \begin{bmatrix} e^{-ikL} & 0 \\ 0 & e^{ikL} \end{bmatrix} \begin{bmatrix} t_2^2 - r_2^2 & r_2 \\ -r_2 & 1 \end{bmatrix} \begin{pmatrix} C \\ D \end{pmatrix}. \tag{3.141}$$

We set $C = 0$ and write the transmitted field D in terms of the only input field, B:

$$|D|^2 = \frac{|t_1 t_2|^2}{|1 - |r_1 r_2| \exp(2ikL)|^2} |B|^2, \tag{3.142}$$

where the phase shifts induced by r_1 and r_2 have been absorbed in L. For a reasonably good cavity ($|t_{1,2}| \ll 1$, $\delta\lambda \ll \lambda$), the transmission is therefore Lorentzian, with a FWHM linewidth

$$\delta\lambda = \frac{\lambda}{kL} \frac{1 - |r_1 r_2|}{\sqrt{|r_1 r_2|}}. \tag{3.143}$$

Finally, we substitute Eq. (3.140) and Eq. (3.143) into Eq. (3.137) to obtain

$$\mathcal{F} = \frac{\pi \sqrt{|r_1 r_2|}}{1 - |r_1 r_2|}. \tag{3.144}$$

If the approximations $|t_{1,2}| \ll 1$ and $\delta\lambda \ll \lambda$ no longer hold, it can be similarly shown that Eq. (3.142) implies

$$\mathcal{F} = \frac{\pi/2}{\sin^{-1}\left(\frac{1 - |r_1 r_2|}{2\sqrt{|r_1 r_2|}}\right)}. \tag{3.145}$$

3.A.2 Physical meaning of the cavity finesse

The factor $\rho = |r_1 r_2|$ present in the above relations is related to the power lost by the cavity after one round-trip, $1 - \rho^2$. Let us set $N = \sqrt{\rho}/(1 - \rho)$. The power remaining in the cavity after N round-trips is then

$$\rho^{2N} = \rho^{\frac{2\sqrt{\rho}}{1-\rho}} \to \frac{1}{e^2}, \tag{3.146}$$

where we have taken the good-cavity ($\rho \to 1$) limit. In other words, we can write

$$\mathcal{F} = \pi N, \tag{3.147}$$

where N is the number of round-trips the light makes inside the cavity before the intensity decays by a factor of $1/e^2$.

3.A.3 Cavity linewidth and quality factor

The HWHM cavity linewidth in frequency space can be defined in terms of the FWHM linewidth in wavelength space by means of the relation

$$2\kappa = \frac{\omega}{\lambda}\,\delta\lambda\,, \tag{3.148}$$

whereupon

$$\delta\lambda = \frac{\kappa\lambda^2}{\pi c}\,, \tag{3.149}$$

and substituting this expression for the linewidth into Eq. (3.137) gives

$$\mathcal{F} = \frac{\pi c}{2\kappa L}\,, \text{ or } \kappa = \frac{\pi c}{2\mathcal{F}L}\,. \tag{3.150}$$

The quality factor, or Q-factor, is defined as the ratio of the cavity frequency to its FWHM linewidth in frequency space: $Q = \omega/(2\kappa)$, or

$$Q = \frac{2\mathcal{F}L}{\lambda}\,. \tag{3.151}$$

Chapter 4

Applications of transfer matrices

> [...] [T]he sciences do not try to explain, they hardly even try to interpret, they mainly make models. By a model is meant a mathematical construct which, with the addition of certain verbal interpretations, describes observed phenomena. The justification of such a mathematical construct is solely and precisely that it is expected to work [...].
>
> J. von Neumann, *Method in the Physical Sciences* (1955)

In this chapter, I will apply the transfer matrix method developed in Chapter 3 to novel cooling geometries outside cavities (Section 4.1 and Section 4.2), as well as inside active ring cavities (Section 4.3).

4.1   External cavity cooling

The basis for this current section was published as Xuereb, A., Freegarde, T., Horak, P., & Domokos, P. Phys. Rev. Lett. **105**, 013602 (2010). We will apply the general solution detailed above to the external cavity cooling configuration, Section 2.7.1, in the case of a micro-mechanical mirror. As a reference system for the analysis of the cooling force in this setup, we also consider the mirror-mediated cooling configuration, which is the optomechanical cooling scheme used in many experiments [25, 139–141]. Note that in the external cavity cooling scheme with a near mirror of complex transmissivity t, the limits of small and large $|t|$ render the situation where the cavity is replaced respectively by the near mirror only or the far mirror only. For intermediate t compared
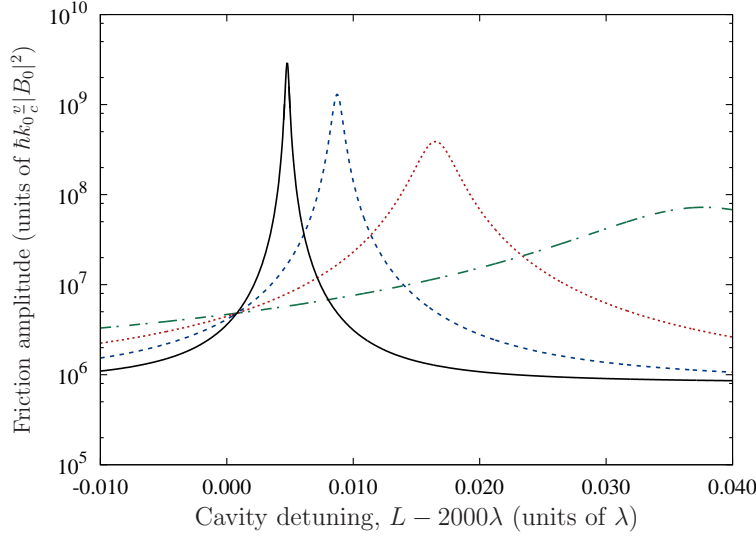
FIGURE 4.1: The amplitude of the friction force acting on the scatterer, for various near-mirror transmissivities, is shown as a function of the mirror separation in the cavity. The different curves represent different near-mirror transmissivities: $|t| = 0.45$ (dashed–dotted curve), $|t| = 0.20$ (dotted), $|t| = 0.10$ (dashed), $|t| = 0.05$ (solid). (Scatterer polarisability $\zeta = -1$, scatterer–cavity separation $x \approx 400\lambda_0$, $|T| = 0.01$, $\lambda_0 = 780$ nm.)

with the transmissivity of the far mirror, T, the moving scatterer interacts with a field reflected back from the cavity and is subject to the interference created by the multiple reflections between the two mirrors. Throughout most of this section, although not initially, we consider in particular an object having low reflectivity, around 50%, which corresponds to a polarisability $\zeta = -1$ and is representative of typical experimental conditions [139]. This ensures that a high-finesse resonator cannot be formed between the object and the near mirror, thereby guaranteeing a parameter range where the cavity formed between the immobile mirrors dominates the interaction. For the sake of simplicity, we restrict ourselves to the special case of scatterers that can be characterised by a real polarisability; this is equivalent to assuming that no absorption takes place in the scatterer. Similar results hold when ζ is not real.

A numerical fit to Eq. (3.91) for $|t| \sim |T|$ and $|\zeta| \ll 1$ renders a friction force of the approximate form

$$F \approx -8\hbar k_0^2 \zeta^2 \frac{v}{c}(2x + 0.17\mathcal{F}L)\sin(4k_0 x + \phi)|B_0|^2 \,, \qquad (4.1)$$

where $\mathcal{F}$ is the cavity finesse, L the cavity length (optimised as discussed below), x the separation between the scatterer and the near mirror, and ϕ a phase factor. The gross spatial variation of the friction force is linear in both L and x; this is simply because of the

linear increase of the retardation time of the reflected field with the distance between the scatterer and the mirrors. This dependence is modulated by a wavelength-scale oscillation of the friction force, which thereby follows the same oscillatory dependence as mirror-mediated cooling [cf. Eq. (3.41)] and constrains cooling to regions of the size of $\lambda_0/8$, where $\lambda_0 = 2\pi/k_0$. In the case of a micro-mechanical mirror, where the vibrational amplitude is naturally much less than the wavelength, this presents no problem. The form of Eq. (4.1) is dependent on the properties of the scatterer and of the mirrors; for realistic mirrors and $\zeta = -1$, the enhancement factor $0.17\mathcal{F}$ drops to $0.04\mathcal{F}$. With typical experimental parameters this results in an enhancement of 10^3–10^4 over the standard setup.

As shown in Fig. 4.1, the fine tuning of the cavity length by varying L on the wavelength scale shows a Lorentzian-like resonant enhancement of the friction amplitude (i.e., the amplitude of the cooling coefficient), following that of the intracavity field intensity. If we denote the complex reflectivities of the near and far mirror by r and R, respectively, we can show that the peaks of Fig. 4.1 lie around the cavity resonances, at approximately $L = \frac{1}{2}m\lambda_0 - \frac{1}{2k_0}\arg\left(rR\right)$, with m being an integer, and have approximately the same full-width at half-maximum, $\left(1 - |rR|\right)/\left(k_0\sqrt{|rR|}\right) = \lambda_0/(2\mathcal{F})$. The enhancement of the friction force by the cavity is due to the multiplication of the retardation time by the number of round trips in the cavity, which thereby acts as a 'distance folding' mechanism. For the chosen parameters, the optical path length is effectively $2x+0.04\mathcal{F}L$; i.e., determined predominantly by the cavity length L.

The friction force depends not only upon the retardation but also upon the cavity reflectivity, which drops near resonance in the well-known behaviour of a Fabry–Pérot resonator. Fig. 4.2 shows the friction amplitude as a function of the near mirror transmissivity $|t|$ for a fixed far mirror transmissivity, $T = 1/(1 + 100\mathrm{i})$. We note that this nonideal reflectivity of the far mirror could equivalently arise from absorption, of ca. 0.01% with the given parameters, of the incident power by the mirror. For each value of $|t|$, the cavity length L has been adjusted to maximise the friction force, according to curves such as those in Fig. 4.1. The calculated result follows the intracavity field (shown dashed) except where the cavity reflectivity drops near resonance [region (b)], and in the extremes of regions (a) and (c), where the geometry is dominated by the near ($|t| \to 0$) or far ($|t| \to 1$) mirrors, respectively. Fig. 4.3 shows the effect of the drop in reflectivity as the cavity is scanned through resonance for similar mirror reflectivities.
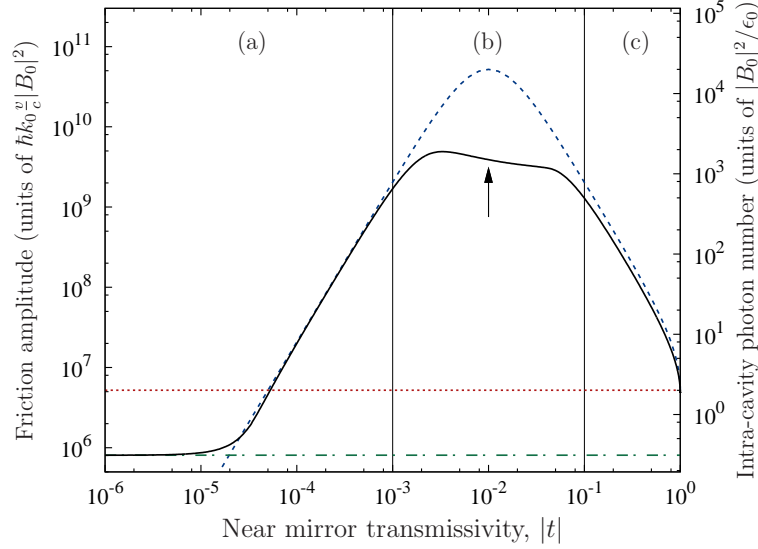
FIGURE 4.2: Amplitude of the friction acting on a scatterer of polarisability $\zeta = -1$ interacting with a cavity tuned to achieve maximum friction, for varying transmissivity of the near mirror. The friction amplitude (solid curve) approaches that for mirror-mediated cooling using the far (dotted line, $t \to 1$) or the near (dashed–dotted line, $t \to 0$) mirror only in the appropriate limits. The arrow indicates the point at which the two cavity mirrors have the same reflectivity. Also shown is the intracavity field (dashed). ($x \approx 400\lambda_0$, $L \approx 2000\lambda_0$, $|T| = 0.01$, $\lambda_0 = 780$ nm, finesse at peak friction 5.0×10^4.)
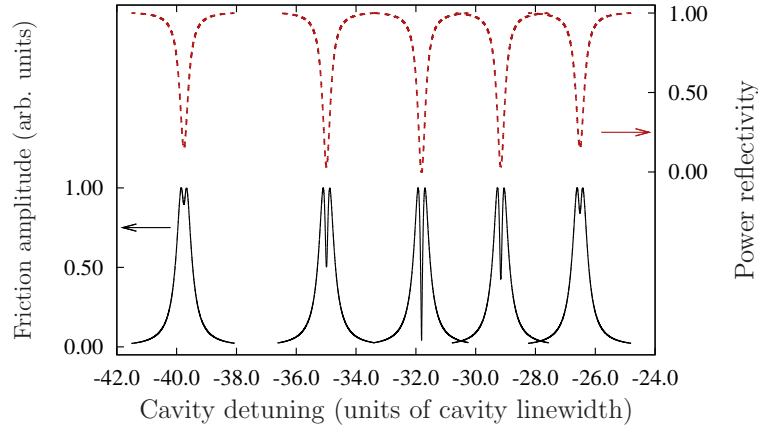
FIGURE 4.3: In region (b) of Fig. 4.2, the cooling coefficient amplitude (solid curves) is attenuated due to the attenuation in the field reflected from the cavity (dashed). $|T| = 0.01$ in every plot; $|t|$ is, from left to right, 6.7×10^{-3}, 8.3×10^{-3}, 1.0×10^{-2}, 1.2×10^{-2}, and 1.5×10^{-2}. (Parameters as in Fig. 4.2.)

When this causes a dip in the friction amplitude peak, the optimum values plotted in Fig. 4.2 occur to either side of the resonance, and the friction force in this region is effectively limited by this interference effect. We note that the friction amplitude is not maximised at the point of maximum intracavity field ($t = T$) because more light is lost through the cavity for larger $|t|$.

The external cavity cooling mechanism may prove particularly valuable when the scatterer is a small mirror or other micro-mechanical optical component. In such cases, the advantage gained by using the external cavity over the standard optomechanical cooling scheme depends heavily upon the polarisability or reflectivity of the moving scatterer, which in the above calculations have so far been taken to be modest ($\zeta = -1$; $|r| = 0.7$) in comparison with those of the cavity mirrors. For $|\zeta| \ll 1$, the friction force is enhanced by a factor approximately equal to $\mathcal{F}$ because of the distance folding argument explained above. For larger $|\zeta|$, the system turns into a three–mirror resonator and the advantage of external cavity cooling is not as big, but is still significant. For $|\zeta| \approx 1$ we find enhancement by a factor $0.04\mathcal{F}$, as discussed above. For even larger ζ, when the reflectivity of the moving mirror becomes comparable to that of the fixed mirrors, the scheme behaves similarly to the mirror-mediated cooling configuration. The main heating process that counteracts the cooling effect in the case of micromirrors is thermal coupling to the environment, which depends on the geometry. In the case of isolated scatterers that undergo no absorption, the heating is due to quantum fluctuations in the fields (see Appendix 3.1.B); the limit temperature here is $\approx \hbar c/\left(0.34 k_{\mathrm{B}} \mathcal{F} L\right) = 1.87 \hbar \kappa / k_{\mathrm{B}}$ when $|\zeta| \ll 1$, which evaluates to $\approx 0.1\,\mathrm{mK}$ for the parameters in Fig. 4.2. This expression for the temperature conforms to the form expected from Eq. (2.45).

The usual cavity-mediated cooling mechanism [114, 142], where the moving scatterer is inside a two-mirror cavity, can also be described by our general framework in terms of Eqs. (3.87) and (3.91). Compared with this scheme, external cavity cooling has the advantage of always having a sinusoidal spatial dependence; the narrow resonances in the friction force for particles inside a cavity, as seen in the next section, impose more stringent positioning requirements.

4.2 Cavity cooling of atoms: within and without a cavity

In Section 4.1 we explored the cooling of a micromirror outside a high-finesse cavity as a means of enhancing the optomechanical interaction of the mirror with the field. Our formalism is general and, indeed, so are our results: the mechanism works similarly for atoms. Inside a resonator, the enhancement of the interaction is accompanied by an enhancement in the field itself, which precludes using high optical powers in order not to saturate the atom. Outside a cavity, the enhancement in the friction force is lower,

but the field itself is not amplified by the presence of a cavity, and therefore one can use much higher powers. The important question, then, is whether these two effects compensate for one another in such a way as to render the cooling forces experienced by an atom outside a cavity similar to those it experiences inside.

To answer this question we will first describe the two models, in Section 4.2.1.1 and Section 4.2.1.2, respectively, using realistic parameters for state-of-the-art optical devices. Taking into account saturation effects, it is seen that the two different models result in similar cooling forces and equilibrium temperatures. An examination of scaling properties of the force acting on the atom in the two schemes then follows in Section 4.2.2. The work in this section has been accepted for publication in the Eur. Phys. J. D topical issue on *Cold Quantum Matter – Achievements and Prospects.*

4.2.1 Comparison of cavity cooling schemes

4.2.1.1 Cavity-mediated cooling: Atom inside the cavity

Placing a scatterer—atom [19–21], micromirror [114, 130], or 'point polarisable particle' [143]—inside a cavity has long been pointed out to be a generic means of cooling the translational motion of that scatterer. Cooling of atoms inside resonators has been observed: first [20] as a means of counteracting the heating of a trapped ion inside a cavity, leading to a steady-state occupation number for the motion of the atom of around 20 quanta; and later [21] as an increase in the storage time for a neutral atom inside a cavity from 35 ms to 1100 ms. The generic layout of such an experiment is shown in Fig. 4.4(a). For our purposes, we place the scatterer inside a symmetric Fabry–Pérot cavity of length L_c, which we pump from one side; the dominant field inside the cavity is a standing wave field if the reflectivity of the mirrors, $\mathfrak{r}$, is high enough. For a numeric example, we use the same cavity properties as Ref. [65]: finesse $\mathcal{F} = 56\,000$ modelled by using mirrors with $\mathfrak{t} = \mathfrak{r} + 1 = 1/(1 + 133.5\mathrm{i})$, cavity length 495 μm, and mode waist 30 μm; we use a wavelength $\lambda = 780$ nm. In contrast with Ref. [65], however, let us reiterate that our cavity is pumped along its axis.

We also take the scatterer to be a two-level atom, with the cavity field detuned 10Γ to the red of the atom transition frequency. Thus, the polarisability of the atom is $\zeta = 4.1 \times 10^{-5} + 4.1 \times 10^{-6}\mathrm{i}$. The maximum cooling coefficient is found at a detuning of $-2.6\,\kappa$ from the cavity resonance. As expected [143], the optimal cooling coefficient
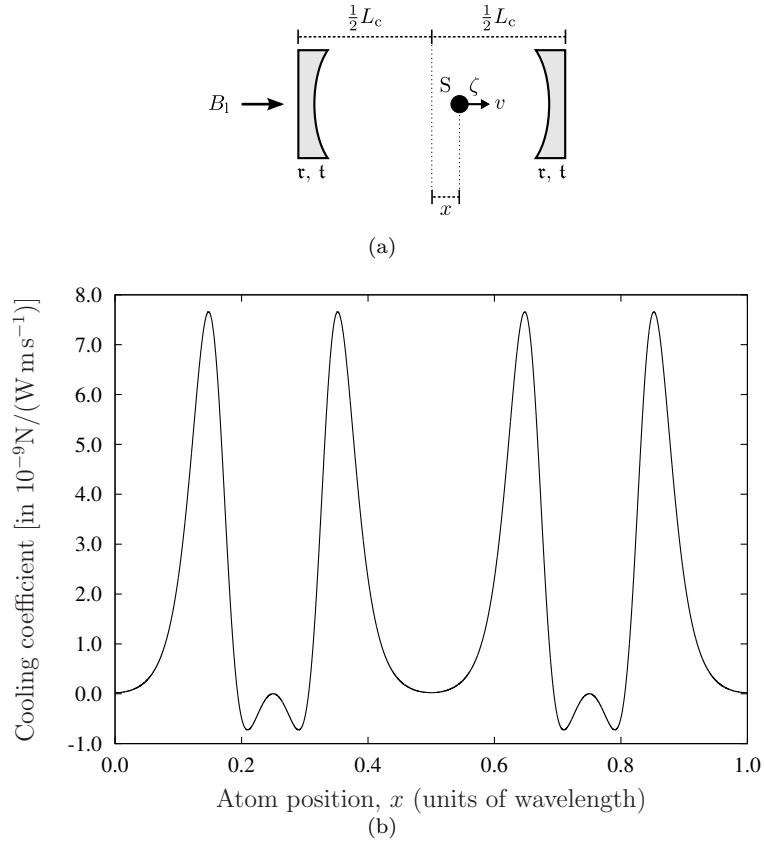
FIGURE 4.4: (a) Model of a scatterer, S, inside a symmetric Fabry–Pérot cavity of length L_c. The cavity mirrors have reflection and transmission coefficients, $\mathfrak{r}$ and $\mathfrak{t}$, and ζ is the polarisability of S. (b) Cooling coefficient ϱ per unit input power, experienced by the scatterer at different positions in the cavity for realistic parameters (see text for details).

occurs for a negative detuning of the pump from the *bare* cavity resonance, but for a positive detuning from the dressed atom–cavity resonance.

The dependence of the friction force, Eq. (3.91), on the position of the scatterer, scanned over a wavelength, is shown in Fig. 4.4(b). The presence of the cavity manifests itself primarily through a strong enhancement of both the cooling coefficient $-F/v$ and the intracavity field intensity. The scattering model explored above is only valid in the limit of small saturation. For the ^{85}Rb D$_2$ transition, assuming that the beam is circularly polarised, the saturation intensity is $1.67\,\text{mW}\,\text{cm}^{-2}$ [35]. In order to avoid saturation effects, we restrict the power input into the cavity to $2\,\text{pW}$; this equates to an intracavity intensity of $23\,\text{mW}\,\text{cm}^{-2}$ and hence a saturation parameter $s = 0.14$; this is because s is inversely proportional to the square of the detuning, -10Γ in this case, of the pump beam from resonance. In turn, this input power also yields a maximum cooling coefficient of
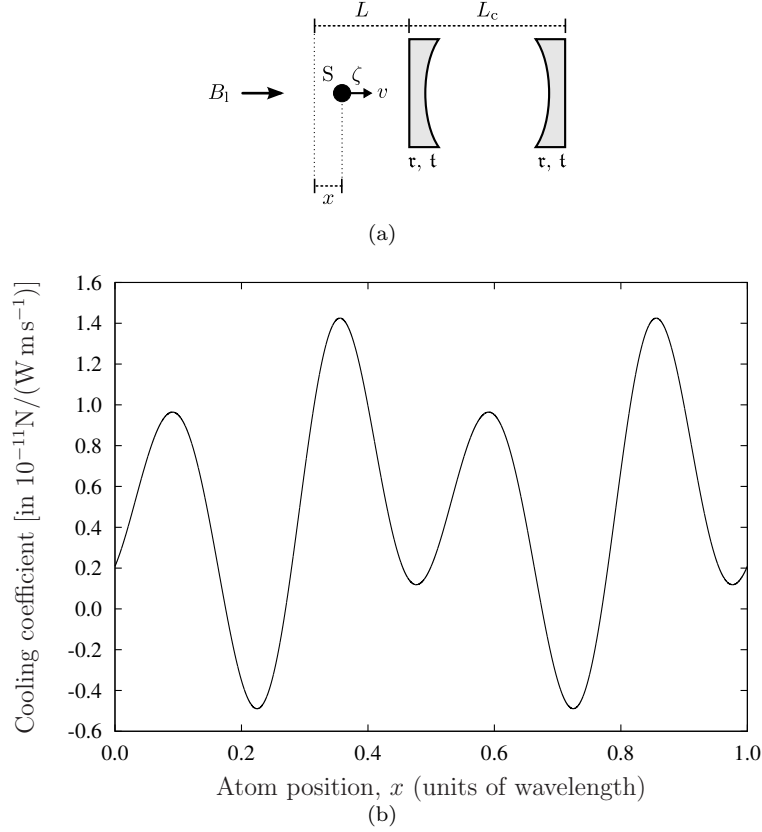
FIGURE 4.5: External cavity cooling. (a) Model, similar to Fig. 4.4, but with the atom at a distance $L - x$ outside the cavity. (b) Cooling coefficient ϱ per unit input power experienced by the scatterer as x is varied for realistic parameters (see text for details). Note the change of scale, on the vertical axis, from Fig. 4.4(b).

$1.5 \times 10^{-20}\,\mathrm{N}/(\mathrm{m\,s^{-1}})$, which corresponds to a $1/e$ velocity cooling time of $9\,\mathrm{\mu s}$ for the same atom; averaging the friction force over a wavelength gives a cooling time of $37\,\mathrm{\mu s}$.

The friction force and the momentum diffusion both scale linearly with the input power, in the low-saturation regime. Therefore, the equilibrium temperature is independent of the pump power in this regime. For the parameters used above, the equilibrium temperature predicted for a scatterer at the point of maximum friction is $56\,\mathrm{\mu K}$; averaging the cooling coefficient, as well as the diffusion coefficient, over a wavelength, gives a higher equilibrium temperature of $220\,\mathrm{\mu K}$.

4.2.1.2 External cavity cooling: Atom outside the cavity

In Section 4.1 above, we also proposed [128] that even with the scatterer *outside* the cavity, the cavity's resonance can be exploited to greatly enhance the optomechanical friction experienced by the scatterer *vis-à-vis* standard optomechanical cooling setups [8,

23, 139], which place the scatterer in front of a single mirror. It is the aim of this subsection to explore this cooling mechanism, using experimental parameters similar to those in the previous subsection, and compare it to the cavity-mediated cooling mechanism discussed there.

Our mathematical model, Fig. 4.5, represents the cavity as a standard, symmetric Fabry–Pérot cavity. However, we emphasise that in principle what is required is simply an optical resonance: the cavity in the model can indeed be replaced by whispering gallery mode resonators [144] or even solid-state resonators. As a basis for numerical calculations, and to enable direct comparison, we model the same resonator as in the previous subsection. It is important to emphasise that the achievable quality factors of the resonators used for external cavity cooling can intrinsically be made larger than the ones in the previous subsection (see, e.g., Ref. [108]) because there does not need to be any form of optical or mechanical access inside the resonator itself.

The pump beam frequency is again taken to be detuned by 10Γ to the red of the atomic transition. By placing the atom outside the cavity, one is free to use high-numerical-aperture optics to produce a tighter focus than might be possible in a cavity with good optical and mechanical access. Having a tight focus strengthens the atom–field coupling because of the $1/w^2$ dependence of ζ on the beam waist w; whereas the friction force scales linearly with the input power, it also scales as $\zeta^2 \sim 1/w^4$ [cf. Eq. (3.41)]. Focussing the beam therefore increases the atom–field coupling more than the local intensity. Thus, it is now assumed that the beam is focussed down to $1\,\mu$m, which gives $\zeta = 3.7 \times 10^{-2} + 3.7 \times 10^{-3}$i.

In order to make a fair comparison between the two cases, we choose to set the saturation parameter $s = 0.14$, as in the previous subsection. The maximum achievable cooling coefficient is then $2.9 \times 10^{-21}\,\mathrm{N}/(\mathrm{m\,s}^{-1})$ for $200\,\mathrm{pW}$ of input power, which is an order of magnitude smaller than the previous result and leads to a $1/e$ velocity cooling time of $50\,\mu$s and an equilibrium temperature of $280\,\mu$K. The magnitude of the force in this case results from the much smaller pumping beam mode waist and the use of much higher powers, subsequently leading to a stronger atom–field interaction. With this beam waist and finesse we would be restricted to input powers several orders of magnitude smaller if the atom were inside such a cavity.

In summary, whereas the friction force inside a cavity is much stronger *per unit input*
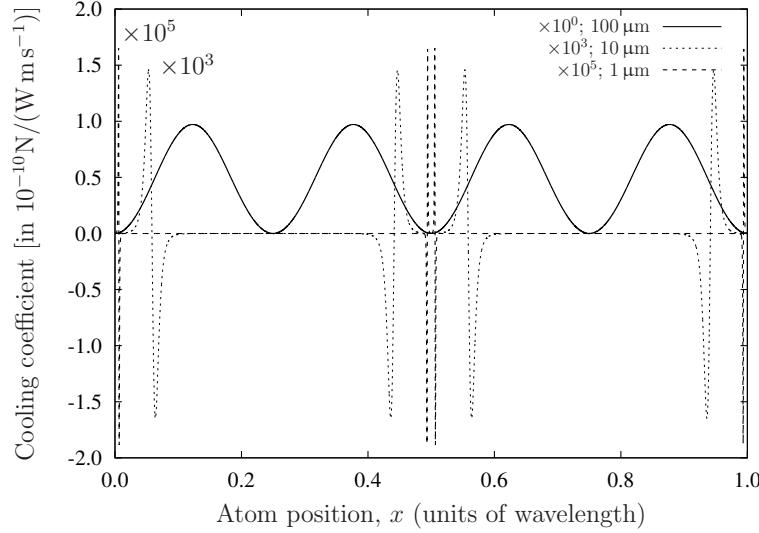
FIGURE 4.6: Spatial dependence of the friction force acting on an atom *inside* a cavity with different mode waists (i.e., different polarisabilities) but equal detuning from resonance, 10Γ to the red. The smaller the mode waist the stronger the friction force, by several orders of magnitude, but the more significant localisation issues become. (Parameters as in Section 4.2.1.1 but with $\partial\zeta/\partial k = 0$.)

power and for the same beam waist, the restrictions imposed on the magnitude of these quantities when the atom is inside the cavity reduce the maximally achievable friction force to a figure comparable to when it lies outside the cavity.

4.2.2   Scaling properties of cavity cooling forces

4.2.2.1   Localisation issues

The broad nature of the spatial variations in the force shown in Fig. 4.4(b) is a consequence of the small polarisability of the atom in such a cavity. This is in sharp contrast to the case of large polarisability, achieved by an atom at a tight beam focus, as shown in Fig. 4.6, or by a micromirror. A scatterer of larger polarisability would experience extremely narrow ($\ll \lambda$) peaks in the friction force inside a cavity but not outside it. Within the scattering model used in this section, the atom–cavity coupling can be tuned by varying either the beam waist or the laser detuning from atomic resonance. Experimentally, however, atom–cavity coupling is rarely investigated close to resonance, in order to minimise the effects of atomic decorehence through spontaneous emission. In such cases, this coupling can be increased by operating a cavity with a small mode waist; this may in turn be detrimental to the performance of the system due to the strong sub-wavelength nature of the interaction, as explored in Fig. 4.6. The net effect of having a
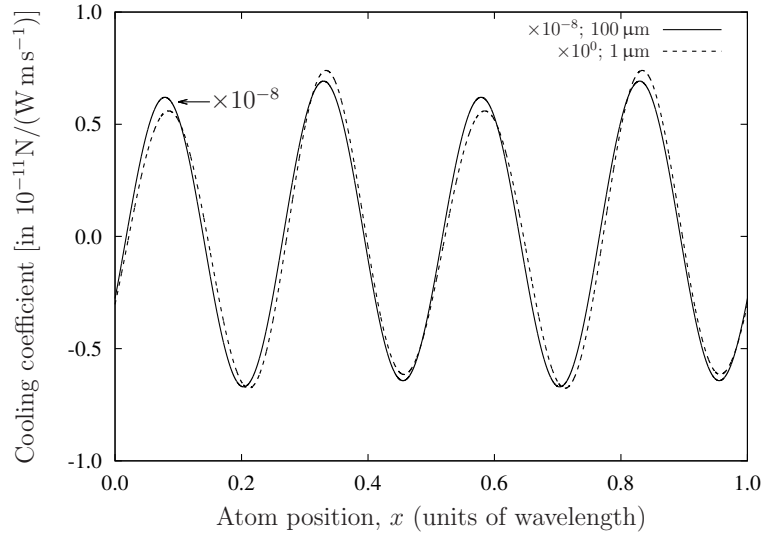
FIGURE 4.7: Spatial dependence of the friction force acting on an atom *outside* a cavity, with different pumping field waists but equal detuning from resonance, 10Γ to the red. The friction force scales roughly as the inverse fourth power of the waist [cf. Eq. (3.41)], but the length scale of the cooling and heating regions is unaffected. (Parameters as in Section 4.2.1.2 but with $\partial\zeta/\partial k = 0$.)

smaller mode waist is that this not only demands extremely good localisation but also tends to decrease the effective cooling coefficient drastically—by up to several orders of magnitude—because of spatial averaging effects.

In Section 4.2.1.2, no mention was made of the average friction force acting on the scatterer; indeed this average computes to approximately zero for any case involving far-detuned atoms, or other particles with an approximately constant polarisability, outside cavities. This, then, also demands strong localisation of the atom; whilst experimentally challenging this disadvantage is somewhat mitigated by the easy mechanical and optical access afforded by external cavity cooling schemes. In Fig. 4.7 it is shown that the polarisability of the atom can be varied over a very wide range without affecting the length scale of the cooling and heating regions. The friction force can be seen to vary as $1/w^4$ for a beam waist w; in turn, this originates from the ζ^2 scaling of the friction force [cf. Eq. (3.41)].

In contrast with the atomic situation, if the scatterer is a micromirror mounted on a cantilever, localisation does not present a problem, since such micromirrors naturally undergo small oscillations and can be positioned with sub-nm accuracy.
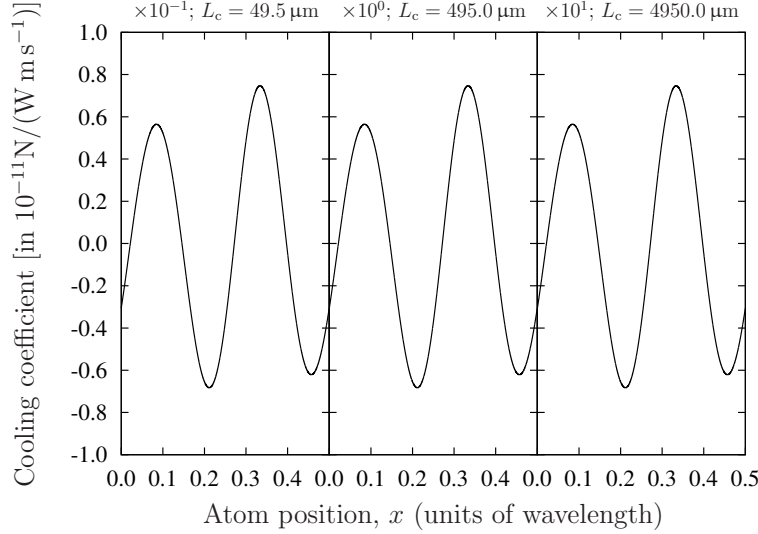
FIGURE 4.8: Spatial dependence of the friction force acting on an atom *outside* a cavity, with detuning 10Γ to the red of resonance. Three different cavity lengths are shown; the friction force scales almost linearly with the cavity length. Note the different scaling factors and cavity lengths, given above each curve. (Parameters as in Section 4.2.1.2 but with $\partial \zeta / \partial k = 0$.)

4.2.2.2   Scaling with cavity finesse and linewidth

Cavity-mediated cooling mechanisms are heavily dependent on the physical properties of the cavity, namely its linewidth κ and finesse $\mathcal{F}$. These parameters can be tuned independently by changing the length of the cavity and the reflectivity of its mirrors. This subsection briefly explores how the two mechanisms we are considering scale with κ and $\mathcal{F}$.

Expressions for the force acting on an atom inside a good cavity are not simple to write down. Nevertheless, in the good-cavity limit one may obtain an analytical formulation for the limiting temperature [19]:

$$T = \frac{\hbar \kappa}{k_{\mathrm{B}}} \, , \tag{4.2}$$

i.e., making a cavity longer decreases the equilibrium temperature proportionately. This result can be justified by observing that whereas the diffusion constant depends only on the intensity inside the cavity ($\propto \mathcal{F}$), the friction force scales linearly with both the intensity and, if the intensity is kept constant, with the lifetime of the cavity field ($\propto 1/\kappa$). The friction force is therefore proportional to $\mathcal{F}/\kappa$, and the equilibrium temperature proportional to κ.

As is known from Section 4.1, the friction force (F) acting on an atom outside a cavity scales approximately linearly with both the length and the finesse of the cavity. This is interpreted in terms of a 'distance folding' mechanism: the lifetime of the light inside a cavity scales inversely with its linewidth $\kappa \propto 1/(\mathcal{F} L_{\mathrm{C}})$ if all other parameters are kept fixed. Within the range of parameters where the light coupled into the cavity dominates the optomechanical effects, this implies that $F \propto 1/\kappa$. One can see this behaviour reproduced in Fig. 4.8, where the cooling coefficient acting on an atom outside each of three cavities having different lengths is shown. This mechanism loses its importance if the atomic polarisability is too large, whereby the system behaves more like two coupled cavities, or if the cavity is too long. The momentum diffusion affecting the atom outside a cavity is essentially independent of the length of the properties of a good cavity, since it depends on the local intensity surrounding the scatterer. Putting these two results together, then, gives (Section 4.1)

$$T \approx 1.9 \frac{\hbar \kappa}{k_{\mathrm{B}}} \, , \tag{4.3}$$

in the limiting case of small polarisability and at the point of maximum friction; i.e., the temperature scales in the same way as for an atom inside the cavity. The numeric factor in the preceding equation depends on ζ and is larger for $|\zeta| \sim 1$.

4.3   Amplified optomechanics in a ring cavity

In the limit of strong scatterers, friction forces in standing-wave cavities become increasingly position-dependent (cf. Section 4.2), which limits the overall, averaged cooling efficiency. This can be overcome by using ring cavities [83–90] where the translational symmetry guarantees position-independent forces. On the other hand, ring cavities are usually much larger and of lower Q-factor than their standing-wave counterparts. Using a gain medium inside a ring cavity has been proposed [91, 92] to offset these losses, allowing one to effectively 'convert' a low-Q cavity into a high-Q one, and thus to increase the effective optomechanical interaction by orders of magnitude. This same concept has also been discussed in theoretical proposals investigating the use of optical parametric amplifiers in standard optomechanical systems [145], or nonlinear media inside

cavities [146] as a tool to control the dynamics of a micromechanical oscillator. A further application of ring cavities is in the investigation of collective atomic recoil lasing (CARL) [95], which exploits the spontaneous self-organisation of an atomic ensemble within a ring cavity, induced by a strong pump beam, to amplify a probe beam through Doppler-shifted reflection of the pump. The gain medium is in this case the atomic ensemble itself.

Let us now consider a different system that shares several features with the above mechanisms. In particular, we consider a scatterer inside a ring cavity that includes a gain medium, spatially separated from the scatterer. An isolator is also included in the ring cavity, in such a way as to prevent the pump beam from circulating in the cavity and being amplified; this ensures that the intensity of the field surrounding the scatterer is always low and thereby circumvents any problems caused by atomic saturation or mirror burning. The Doppler-shifted reflection of the pump from the scatterer is, on the other hand, allowed to circulate, and its amplification in turn enhances the velocity-dependent forces acting on the scatterer.

In such a situation, one is able to take advantage of properties inherent to the ring cavity system, such as the fact that the forces acting on the particle do not exhibit any sub-wavelength spatial modulation; this is due to the translational symmetry present in the system [83]. Moreover, modest amplification allows one to use optical fibres to form the ring cavity, opening the door towards increasing the optical length of such cavities. It is necessary to have amplification in such cases to compensate for the losses introduced when coupling to a fibre; such losses would otherwise limit the quality factor of the cavity. The optomechanical force is, as we will see and in the parameter domain of interest, linearly dependent on the cavity length; lengthening the cavity thus provides further enhancement of the interaction.

This section is structured as follows. We shall first introduce the physical model, which we proceed to solve using the transfer matrix method to obtain the friction force and momentum diffusion acting on the particle. In the good-cavity limit, Section 4.3.1.1, simple expressions for these quantities can be obtained, yielding further insight into the system and allowing us to draw some parallels with traditional cavity cooling. In this limit, our model becomes equivalent to one based on a standard master equation approach [83] as outlined in Section 4.3.1.2. Realistic numerical values for the various parameters are then used in Section 4.3.2 to explore the efficiency and limits of the
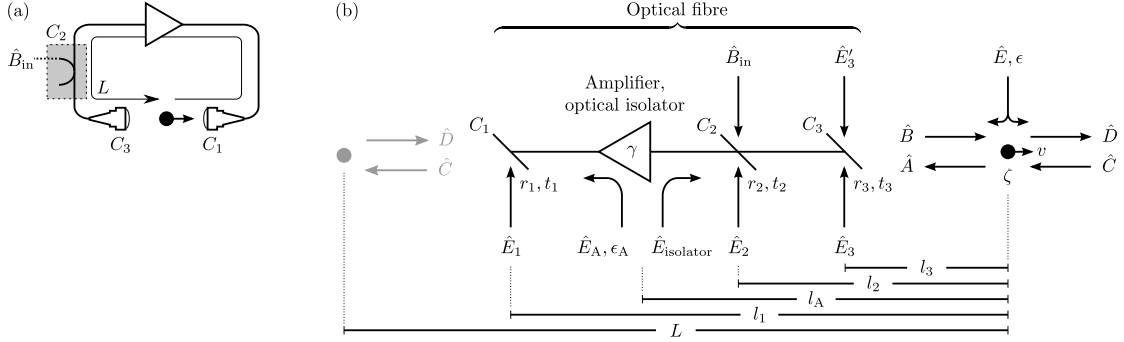
FIGURE 4.9: (a) Physical schematic of a polarisable particle in a unidirectional ring cavity, showing the input field $\hat{B}_\text{in}$. (b) Equivalent 'transfer matrix'–style (unfolded) model; the particle is drawn on both sides of this schematic to illustrate the recursive nature of the cavity. The various components are defined in Section 4.3.1.

cooling mechanism. Finally, we will conclude by mentioning some possible extensions to the scheme. The work in this section will be published in the J. Mod. Opt. topical issue on *New cooling mechanisms for atoms and molecules.*

4.3.1   General expressions and equilibrium behaviour

The mathematical model of the ring cavity system, schematically drawn in Fig. 4.9(a), is shown in Fig. 4.9(b). A particle, characterised by its polarisability ζ, is in a ring cavity of round-trip length L. $C_{1,3}$ are the couplers, between which lies the particle, that terminate the fibre-based cavity, and C_2 is the input coupler that injects the pump beam into the cavity. The amplifier, having a gain $\gamma \geq 1$, is assumed to also function as an optical isolator. r_i and $t_i = r_i + 1$ are the (amplitude) transmission and reflection coefficients of coupler C_i ($i = 1, 2, 3$). All the "$\hat{E}$" modes are noise modes introduced by specific elements. ϵ_A, the amplitude of $\hat{E}_\text{A}$ introduced into the system, depends on γ; similarly, ϵ depends on ζ. The values of $l_1 > l_\text{A} > l_2 > l_3 > 0$ are not important. One of the travelling wave modes of the cavity is pumped by light with wavenumber k_0, but is prevented from circulating inside the cavity. This avoids resonant enhancement of the pumped mode in the cavity and thus avoids saturating the particle. The backscattered counterpropagating mode, on the other hand, is amplified on every round trip by a factor γ by means of the optical amplifier. The TMM is used to self-consistently solve for the four field amplitudes at every point in the cavity in the presence of the pump field and the noise modes introduced by the coupler losses and by the amplifier. Note that in the limit where the amplifier is compensating for the ring cavity losses, the amplifier noise

is also comparable to the loss-induced noise and must therefore be taken into account in our model.

Using the notation in Fig. 4.9(a) we can relate the expectation values of the amplitudes of the two input and two scattered field modes interacting with the particle in a one-dimensional scheme, $A(k) = \langle \hat{A}(k) \rangle$, $B(k) = \langle \hat{B}(k) \rangle$, $C(k) = \langle \hat{C}(k) \rangle$, and $D(k) = \langle \hat{D}(k) \rangle$, to $B_{\mathrm{in}}(k) = \langle \hat{B}_{\mathrm{in}}(k) \rangle$ by means of the relations

$$B = r_2 t_3 e^{ik_0 l_2} B_{\mathrm{in}}\,,\ \ C = \alpha A\,,\ \text{and}\ \begin{pmatrix} A \\ B \end{pmatrix} = \hat{M} \begin{pmatrix} C \\ D \end{pmatrix}\,, \qquad (4.4)$$

where $\alpha(k) = t_1 t_2 t_3 \gamma \exp(ikL)$ is the factor multiplied to the field amplitude every round trip. In the preceding equations, as well as in the following, we do not write the index k for simplicity of presentation. The operators $\hat{A}(k)$, etc., denote the annihilation operators of the various field modes. The three equations Eqs. (4.4) have a readily apparent physical significance—respectively, they correspond to: the propagation of $\hat{B}_{\mathrm{in}}$ to reach the particle; the feeding back of $\hat{A}$ to $\hat{C}$ through the ring cavity; and the usual transfer matrix relation for a particle interacting with the four fields surrounding it. The first two of these relations are substituted into the third, which subsequently simplifies to

$$\begin{pmatrix} A \\ B_{\mathrm{in}} \end{pmatrix} = \left(\begin{bmatrix} 1 & 0 \\ 0 & r_2 t_3 e^{ik_0 l_2} \end{bmatrix} - \hat{M} \begin{bmatrix} \alpha & 0 \\ 0 & 0 \end{bmatrix} \right)^{-1} \hat{M} \begin{pmatrix} 0 \\ D \end{pmatrix} \qquad (4.5)$$

If we assume far off-resonant operation, i.e., $\partial\zeta/\partial k = 0$, the velocity-dependent transfer matrix $\hat{M}$ can be written as, cf. Eq. (3.80),

$$\begin{bmatrix} 1 + i\zeta & i\zeta - 2i\zeta\frac{v}{c} + 2ik_0\zeta\frac{v}{c}\partial_k \\ -i\zeta - 2i\zeta\frac{v}{c} + 2ik_0\zeta\frac{v}{c}\partial_k & 1 - i\zeta \end{bmatrix}\,. \qquad (4.6)$$

Note that the partial derivative ∂_k acts not only on $\alpha(k)$ but also on the field mode amplitudes it precedes. Eq. (4.5) can be inverted in closed form to first order in v/c, similarly to Section 3.2, and can thus be used to find $\mathcal{A} = \sqrt{2\epsilon_0\sigma_{\mathrm{L}}/(\hbar k_0)} \int A(k)\mathrm{d}k$, $\mathcal{B} = \sqrt{2\epsilon_0\sigma_{\mathrm{L}}/(\hbar k_0)} \int B(k)\mathrm{d}k$, $\mathcal{C} = \sqrt{2\epsilon_0\sigma_{\mathrm{L}}/(\hbar k_0)} \int C(k)\mathrm{d}k$, and $\mathcal{D} = \sqrt{2\epsilon_0\sigma_{\mathrm{L}}/(\hbar k_0)} \int D(k)\mathrm{d}k$, where the normalisation is with respect to the pump beam mode area σ_{L} and where a monochromatic pump is assumed: $B_{\mathrm{in}}(k) = B_0 \delta(k - k_0)$. Here, $|\mathcal{A}|^2$, $|\mathcal{B}|^2$, etc., are the photon currents in units of photons per second. The expectation value of the force

acting on the scatterer is then given by Eq. (3.18):

$$\hbar k_0 \left(|\mathcal{A}|^2 + |\mathcal{B}|^2 - |\mathcal{C}|^2 - |\mathcal{D}|^2 \right). \tag{4.7}$$

The values of $\mathcal{A}$, $\mathcal{B}$, etc., from the solution of Eq. (4.5) are then substituted in Eq. (4.7), which we evaluate to first order in v/c, in terms of B_0. After some algebra, we obtain the first main result of this section—the friction force acting on the particle:

$$F = -8\hbar k_0^2 \frac{v}{c} \operatorname{Re}\left\{ \frac{(1 - \alpha^*)\zeta \operatorname{Re}\{\zeta\} + i\alpha^* \zeta |\zeta|^2}{1 - \alpha - i\zeta} \frac{\partial \alpha}{\partial k} \right\} \frac{|r_2 t_3 B_0|^2}{|1 - \alpha - i\zeta|^2}. \tag{4.8}$$

By extending the TMM appropriately, one can keep track of the various noise modes interacting with the system. Eqs. (4.4) then become

$$\hat{A} = \frac{i\zeta}{1 - i\zeta}\hat{B} + \frac{1}{1 - i\zeta}\hat{C} + \epsilon\hat{E}, \tag{4.9a}$$

$$\hat{B} = r_2 t_3 e^{ik_0 l_2} \hat{B}_{\text{in}} + t_2 t_3 e^{ik_0 l_A} \hat{E}_{\text{isolator}} + r_3 e^{ik_0 l_3} \hat{E}_3', \tag{4.9b}$$

$$\hat{C} = \alpha\hat{A} + r_1 e^{ik_0(L-l_1)}\hat{E}_1 + t_1 r_2 \gamma e^{ik_0(L-l_2)}\hat{E}_2 + t_1 t_2 r_3 \gamma e^{ik_0(L-l_3)}\hat{E}_3 + t_1 \epsilon_A e^{ik_0(L-l_A)}\hat{E}_A, \text{ and} \tag{4.9c}$$

$$\hat{D} = \frac{1}{1 - i\zeta}\hat{B} + \frac{i\zeta}{1 - i\zeta}\hat{C} + \epsilon\hat{E}, \tag{4.9d}$$

with $\epsilon = \sqrt{1 - (1 + |\zeta|)/|1 - i\zeta|^2}$ (see Appendix 3.1.B) and $\epsilon_A = \sqrt{1 - 1/|\gamma|^2}$ [37]. These equations can be solved simultaneously for $\hat{A}$, $\hat{B}$, $\hat{C}$, and $\hat{D}$, and the solution used to evaluate the momentum diffusion constant, D, defined as the two-time auto-correlation function of the force operator (cf. Section 3.1.1.4), keeping in mind that most of the noise modes, as well as $\hat{B}_{\text{in}}$, obey the commutation relation $\left[\hat{E}(t), \hat{E}^\dagger(t')\right] = \hbar k_0/(2\epsilon_0 \sigma_{\text{L}}) \delta(t - t')$. The sole exception is the noise introduced by the amplifier, $\hat{E}_A$, for which $\left[\hat{E}_A(t), \hat{E}_A^\dagger(t')\right] = -\hbar k_0/(2\epsilon_0 \sigma_{\text{L}}) \delta(t - t')$; this is due to the model of the amplifier as a negative temperature heat-bath, whereby the creation and annihilation operators effectively switch rôles. Further discussion of this model can be found in Ref. [37, §7.2]. All the noise modes are independent from one another and from $\hat{B}_{\text{in}}$, which simplifies the expressions considerably.

4.3.1.1   The good-cavity limit as a simplified case

Before discussing the result of Section 4.3.1, we shall make several approximations to obtain a transparent set of equations to briefly explore the equilibrium behaviour of the scatterer and to compare with a standard master equation approach. In particular, ζ is assumed to be real, which is tantamount to assuming that the scatterer suffers no optical absorption or, if it is an atom, that it is pumped far off-resonance. Moreover, the cavity is assumed to be very good ($|t_{1,2,3}| \to 1$) and thus no gain medium is introduced in the cavity ($\gamma = 1$). With these simplifications, Eq. (4.8) reduces to

$$F \approx -8\hbar k_0^2 \frac{v}{c} \frac{\zeta^2}{|1-\alpha|^4} \operatorname{Re}\left\{ \left(1-\alpha^*\right)^2 \frac{\partial \alpha}{\partial k} \right\} \left|r_2 B_0\right|^2$$
$$\approx 16\hbar k_0^2 \zeta^2 v \frac{\kappa \Delta_{\mathrm{C}}}{\left(\Delta_{\mathrm{C}}^2 + \kappa^2\right)^2} \frac{1}{\tau} \left|r_2 B_0\right|^2 . \tag{4.10}$$

In the preceding equations, Δ_{C} is the detuning of the pump from cavity resonance, κ is the HWHM cavity linewidth,

$$\kappa = \frac{1}{\tau} \frac{1 - |t_1 t_2 t_3|\gamma}{\sqrt{|t_1 t_2 t_3|\gamma}} , \tag{4.11}$$

for $|\zeta| \ll 1$, and $\tau = L/c$ is the round-trip time. Using the same approximations as for Eq. (4.10), we also obtain the diffusion constant

$$D \approx 8\hbar^2 k_0^2 \zeta^2 \frac{\kappa}{\Delta_{\mathrm{C}}^2 + \kappa^2} \frac{1}{\tau} \left|r_2 B_0\right|^2 . \tag{4.12}$$

Note that $\gamma = 1$ here and therefore $\hat{E}_{\mathrm{A}}$ does not contribute to the diffusion constant. Eqs. (4.10) and (4.12) hold for the case where $\Delta_{\mathrm{C}}/\kappa$ is not too large. The cavity can be fully described by means of κ and the finesse $\mathcal{F} = \pi c/(2L\kappa)$. Let us now set $\Delta_{\mathrm{C}} = -\kappa$ in Eqs. (4.10) and (4.12), whereby

$$F = -\tfrac{8}{\pi}\hbar k_0^2 \zeta^2 v \frac{\mathcal{F}}{\kappa} \left|r_2 B_0\right|^2 , \text{ and } D = \tfrac{8}{\pi}\hbar^2 k_0^2 \zeta^2 \mathcal{F} \left|r_2 B_0\right|^2 . \tag{4.13}$$

These two expressions have a readily-apparent physical significance; at a constant finesse, decreasing the cavity linewidth is equivalent to making the cavity longer, whereupon the retardation effects that underlie this cooling mechanism lead to a stronger friction force. At the same time, this has no effect on the intracavity field strength and therefore does not affect the diffusion. On the other hand, improving the cavity finesse by reducing

losses at the couplers increases the intracavity intensity, thereby increasing both the friction force and the momentum diffusion.

Using the above results, we obtain, for $\Delta_{\mathrm{C}} < 0$,

$$T_{\mathrm{A}} \approx \frac{\hbar}{k_{\mathrm{B}}} \left(\frac{|\Delta_{\mathrm{C}}|}{\kappa} + \frac{\kappa}{|\Delta_{\mathrm{C}}|} \right) \frac{\kappa}{2} \geq \frac{\hbar}{k_{\mathrm{B}}} \kappa \,, \tag{4.14}$$

with the minimum temperature occurring at $\Delta_{\mathrm{C}} = -\kappa$. One notes that this expression is identical to the corresponding one for standard cavity-mediated cooling [19]. Like the corresponding results in Section 3.1.3 and Section 3.1.4, it can be interpreted in a similar light as the Doppler temperature, albeit with the energy dissipation process shifted from the decay of the atomic excited state to the decay of the cavity field.

A particular feature to note in all the preceding expressions is that they are not spatial averages over the position of the particle, but they do not depend on this position either. As a result of this, the force, momentum diffusion and equilibrium temperature do not in any way depend on the position of the particle along the cavity field in a 1D model. The issue of sub-wavelength modulation of the friction force is a major limitation of cooling methods based on intracavity standing fields, in particular mirror-mediated cooling (Section 3.1.2) and cavity-mediated cooling (Section 4.2).

4.3.1.2 Comparison with a semiclassical model

In the good-cavity limit and without gain our TMM model is equivalent to a standard master equation approach with the Hamiltonian

$$
\begin{aligned}
\hat{H} = & -\hbar\Delta_{\mathrm{a}}\hat{\sigma}^{+}\hat{\sigma}^{-} - \hbar\Delta_{\mathrm{C}}\hat{a}_{\mathrm{C}}^{\dagger}\hat{a}_{\mathrm{C}} \\
& + \hbar g\big(\hat{a}_{\mathrm{C}}^{\dagger}\hat{\sigma}^{-} e^{\mathrm{i}k_0 x} + \hat{\sigma}^{+}\hat{a}_{\mathrm{C}} e^{-\mathrm{i}k_0 x}\big) + \hbar g\big(a_{\mathrm{P}}^{*}\hat{\sigma}^{-} e^{-\mathrm{i}k_0 x} + \hat{\sigma}^{+} a_{\mathrm{P}} e^{\mathrm{i}k_0 x}\big) \,,
\end{aligned}
\tag{4.15}
$$

and the Liouvillian terms

$$\mathcal{L}\hat{\rho} = -\Gamma\big(\hat{\sigma}^{+}\hat{\sigma}^{-}\hat{\rho} - 2\hat{\sigma}^{-}\hat{\rho}\hat{\sigma}^{+} + \hat{\rho}\hat{\sigma}^{+}\hat{\sigma}^{-}\big) - \kappa\big(\hat{a}_{\mathrm{C}}^{\dagger}\hat{a}_{\mathrm{C}}\hat{\rho} - 2\hat{a}_{\mathrm{C}}\hat{\rho}\hat{a}_{\mathrm{C}}^{\dagger} + \hat{\rho}\hat{a}_{\mathrm{C}}^{\dagger}\hat{a}_{\mathrm{C}}\big) \,, \tag{4.16}$$

as adapted from Ref. [83] and modified for a unidirectional cavity where only the unpumped mode is allowed to circulate. Here, $\hat{\rho}$ is the density matrix of the system, g the atom–field coupling strength, $\hat{a}_{\mathrm{C}}$ the annihilation operator of the cavity field, $\hat{\sigma}^{+}$ the
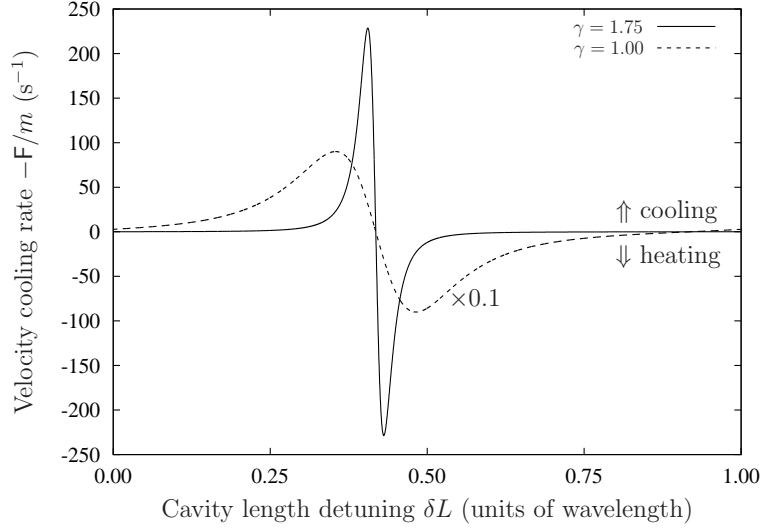
FIGURE 4.10: Cooling rate $-(\mathrm{d}v/\mathrm{d}t)/v$ for ^{85}Rb pumped -10Γ from D_2 resonance inside a ring cavity with a round-trip length $L = 300\,\mathrm{m}$, for two different values of the amplifier gain γ. Note that the curve for $\gamma = 1$, as drawn, is scaled *up* by a factor of 10. The cavity waist is taken to be $10\,\mu\mathrm{m}$. ($|t_1|^2 = |t_3|^2 = 0.5$, $|t_2|^2 = 0.99$, B_0 is chosen such as to give an atomic saturation $s = 0.1$.)

atomic dipole raising operator, Δ_a the detuning from atomic resonance, Γ the atomic upper state HWHM linewidth, and x the coordinate of the atom inside the cavity. The pump field is assumed to be unperturbed by its interaction with the atom, and in the above is replaced by a c-number, a_P. Calculating the friction force from this model leads again to Eq. (4.10), thus confirming our TMM results by a more standard technique. The advantage of the TMM approach lies in the simplicity and generality of expressions such as Eq. (4.7), and the ease with which more optical elements can be introduced into the system. As shown above, the momentum diffusion coefficient is easily calculated from the TMM.

4.3.2   Numerical results and discussion

We can use the conversion factor $|B_0|^2 = P/(\hbar k_0 c)$, where P is the power of the input beam, to evaluate the above equations numerically in a physically meaningful way. Specifically, the particle is now assumed to be a (two–level) ^{85}Rb atom, pumped -10Γ from D_2 resonance, where $\Gamma = 2\pi \times 3.03\,\mathrm{MHz}$ is the HWHM linewidth of this same transition at a wavelength of ca. $780\,\mathrm{nm}$; because the detuning is much larger than the linewidth, we simplify the calculations by setting $\partial\zeta/\partial\omega = 0$. The beam waist where the particle interacts with the field is taken to be $10\,\mu\mathrm{m}$. With the parameters in Fig. 4.10,
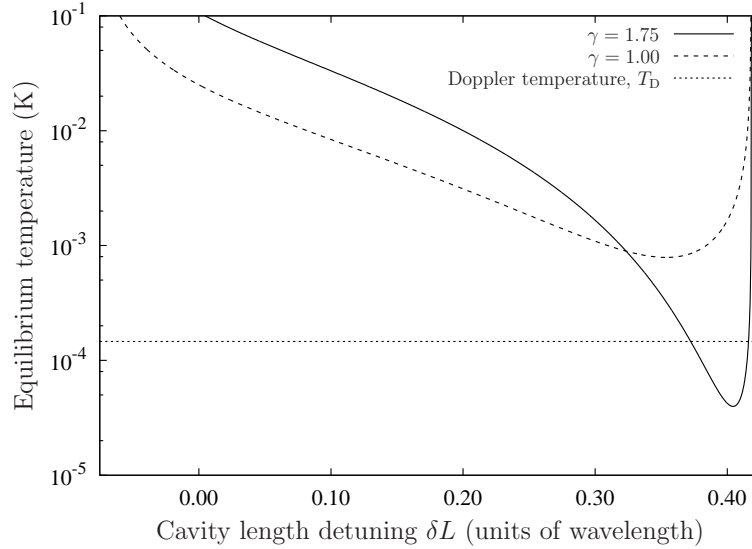
FIGURE 4.11: Equilibrium temperature predicted by the transfer matrix model for two values of the amplifier gain γ. The Doppler temperature for ^{85}Rb is also indicated. The horizontal axis differs from that in Fig. 4.10 mainly because the temperature is only well-defined for regions where the friction force promotes cooling. (Parameters are as in Fig. 4.10.)

the power is reduced by a factor of $1/|t_1 t_2 t_3|^2 = 4.04$ with each round-trip, in the presence of no gain in the amplifier. We shall compare this case to the low-gain case; the gain of the amplifier we consider is constrained to be small enough that $|\alpha|^2 = |t_1 t_2 t_3 \gamma|^2 < 1$. Under these conditions, there is no exponential build-up of intensity inside the cavity and the system is stable. A cavity with a large enough gain that $|\alpha|^2 > 1$ would effectively be a laser cavity. Such a system would have no stable state in our model, since we assume that the gain medium is not depleted, and will therefore not be considered further in the following.

Fig. 4.10 shows the friction force acting on the particle, and Fig. 4.11 the equilibrium temperature, as the length of the cavity is tuned on the scale of one wavelength. In each of these two figures two cases are shown, one representing no gain in the amplifier ($\gamma = 1$) and one representing a low-gain amplifier ($\gamma = 1.75$); note that in both cases the condition $|\alpha|^2 < 1$ is satisfied.

In order to provide a fair comparison between these two cases, we choose the pump amplitude B_{in} such that the saturation of the particle is the same in the two cases. This ensures that any difference in cooling performance is not due to a simple increase in intensity. Since the TMM as presented here is based on a *linear* model of the particle, our results presented above are only valid in the limit of saturation parameter much smaller

than 1. Thus, as a basis for the numerical comparisons between the two different cases, we choose to set the saturation parameter to 0.1. Fig. 4.10 shows that under these conditions the amplified system leads to a significant, approximately 25-fold, enhancement of the maximum friction force. This can therefore be attributed unambiguously to the effective enhancement of the cavity Q-factor by the amplifier.

However, for the parameters considered here, in particular for small particle polarisability ζ and for $|\alpha|^2 < 1$, the counterpropagating mode intensity is much smaller than that of the pumped mode, even if the former is amplified. Thus, the intracavity field is always dominated by the pump beam, whereas the friction force is mostly dependent on the Doppler-shifted reflection of the pump from the particle. Specifically, for the parameters used above we find that the total field intensity changes by less than 1% when the gain is increased from 1 to 1.75. Hence, similar results to those of Fig. 4.10 are obtained even *without* pump normalisation.

The steady-state temperature, obtained by the ratio of diffusion and friction, is shown in Fig. 4.11 for the same parameters as above. We observe that the broader resonance in the friction as a function of cavity detuning (i.e., of cavity length), shown in Fig. 4.10, also leads to a wider range of lower temperatures compared to the amplified case. However, as expected, within the narrower resonance of the amplified system where the friction is significantly enhanced, the stationary temperature is also significantly reduced. We see that while the maximum friction force is increased by a factor of 25.4, the lowest achievable temperature is decreased by a factor of 19.9 when switching from $\gamma = 1$ to $\gamma = 1.75$. While the overall cavity intensity is dominated by the pump field, and is therefore hardly affected by the amplifier, the diffusion is actually dominated by the interaction of the weak counterpropagating field with the pump field. This can be seen most clearly by the strong detuning dependence of the analytical expression for D in the good-cavity limit, Eq. (4.12). As a consequence, the lowest achievable temperature is improved by a slightly smaller factor than the maximum cooling coefficient. This is consistent with the idea that the amplifier not only increases the cavity lifetime, but also adds a small amount of additional noise into the system. Nevertheless, a strong enhancement of the cooling efficiency is observed in the presence of the amplifier.

Chapter 5

Three-dimensional scattering with an optical memory

Homogeneal Rays which flow from several Points of any Object, and fall almost Perpendicularly on any reflecting or refracting Plane or Spherical Surface, shall afterwards diverge from so many other Points, or be Parallel to so many other Lines, or converge to so many other Points, either accurately or without any sensible Error. And the same thing will happen, if the Rays be reflected or refracted successively by two or three or more Plane or spherical Surfaces.
[...]
Wherever the Rays which come from all the Points of any Object meet again in so many Points after they have been made to converge by Reflexion or Refraction, there they will make a Picture of the Object upon any white Body on which they fall.

I. Newton, *Opticks* (1704)

The scattering theory presented in the previous chapters can be used to describe a wide variety of one-dimensional, or quasi-one-dimensional, situations involving mobile scatterers and immobile optics. The three-dimensional nature of the electromagnetic field can, however, be exploited to give rise to a different type of retarded dipole-dipole interaction, one mediated not only by the relative phase difference between the successive reflections but also the spreading nature of spherical waves in three dimensions.

I start this chapter with an extension of a self-consistent scattering theory that was used to describe optical binding phenomena [147]. Our treatment essentially identifies the two particles described in Ref. [147] such that the 'binding' that takes place really is
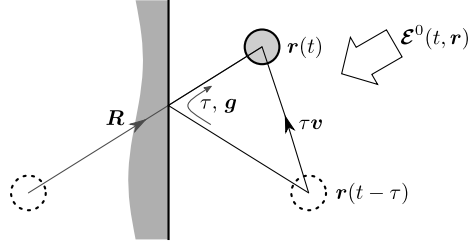
FIGURE 5.1: Polarised by incident radiation $\boldsymbol{\mathcal{E}}^0(t, \boldsymbol{r})$, a particle moving with velocity $\boldsymbol{v}$ is bound to its retarded reflection in a surface, characterised by round-trip time τ and field propagator $\boldsymbol{g}$.

between a particle and itself, as mediated by a mirror or other delay element. After describing this extension to the theory in Section 5.1, I shall apply it to the mirror-mediated cooling described earlier in this work, both in one dimension (cf. Section 5.2) and in three (Section 5.3). I will use these results in Chapter 7 to discuss experimentally-accessible configurations for exploring the various mechanisms described in this thesis.

5.1   Optical self-binding of Rayleigh particles

The work in this section is being prepared for publication by James Bateman, AX, and Tim Freegarde. Its basis originated from TF and was subsequently elaborated upon by all three authors. The *Mathematica* code used to solve the equations and verify the solutions was written largely by JB.

We first analyse the retarded classical electrostatic interaction between the induced dipoles of a particle, moving along a path $\boldsymbol{r}(t)$, and its reflection, as shown in Fig. 5.1, following the ideas set forth in Ref. [147]. The unperturbed illuminating field is denoted $\boldsymbol{\mathcal{E}}^0(t, \boldsymbol{r})$. A tensor propagator, $\boldsymbol{g}$, is used to describe the propagation of the scattered field from the particle and back to itself through reflection in the mirror. In one dimension,

$$\boldsymbol{g}(t, \boldsymbol{r}) = -\mathrm{i}e^{\mathrm{i}\omega\tau(t,\boldsymbol{r})}\mathbb{1}\,, \tag{5.1}$$

where the pre-factor $-\mathrm{i}$ accounts for the phase shift upon reflection as well as the Gouy phase shift: in our 1D model we take the particle to be a point-like dipole at the focus

of a tightly-focussed beam of mode area $\sigma_{\rm L}$. In three dimensions,

$$\boldsymbol{g}(t, \mathbf{r}) = \frac{\sigma_{\rm L}}{R(t)\lambda} e^{{\rm i}\omega\tau(t,\boldsymbol{r})} \left\{ \frac{1 - {\rm i}kR(t) - \left[kR(t)\right]^2}{\left[kR(t)\right]^2} \mathbb{1} \right.$$
$$\left. - \frac{3 - 3{\rm i}kR(t) - \left[kR(t)\right]^2}{\left[kR(t)\right]^2} \boldsymbol{n}(t) \otimes \boldsymbol{n}(t) \right\}. \qquad (5.2)$$

In the preceding equations, $R(t) = \|\boldsymbol{R}(t)\|$, $\boldsymbol{n}(t) = \boldsymbol{R}(t)/R(t)$, $\boldsymbol{R}(t)$ is the position vector of a test particle at time t relative to its image at time $t - \tau[t, \boldsymbol{r}(t)]$ (see Fig. 5.1), and $\otimes$ represents the vector outer product. $\boldsymbol{g}$ in Eq. (5.2) is the tensor Green's function for free-space propagation [148, 149] of an electromagnetic wave, normalised to render it dimensionless.

The interaction of the particle with the electric field is assumed to be through the dipole interaction, whereby the particle is described by means of its polarisability χ; this polarisability allows us to define a dimensionless polarisability

$$\zeta = \chi k/(2\sigma_{\rm L}), \qquad (5.3)$$

as before. The form for ζ we choose is identical for both one- and three-dimensional cases, despite arising from different considerations; in one dimension ζ is defined in Section 1.6, whereas in three dimensions we define ζ through a particular grouping of constants to yield dimensionless ζ and $\boldsymbol{g}$. In this chapter we will, for simplicity, assume a real, scalar value for χ. The resulting equations can be subsequently generalised for complex, vector or tensor polarisabilities. Multiple scattering between the particle and the mirror is taken into account self-consistently by solving for the total electric field $\boldsymbol{\mathcal{E}}[t, \boldsymbol{r}(t)]$, experienced by the particle at position $\boldsymbol{r}(t)$ and time t:

$$\boldsymbol{\mathcal{E}} = \boldsymbol{\mathcal{E}}^0 + \zeta \boldsymbol{g} \cdot \boldsymbol{\mathcal{E}}, \qquad (5.4)$$

where all the terms are evaluated at $[t, \boldsymbol{r}(t)]$. The solution of this equation can be given analytically to lowest order in $\boldsymbol{v}$ and τ, and for the case when $(\mathbb{1} - \zeta\boldsymbol{g})$ is invertible (i.e.,

when $\|\zeta\boldsymbol{g}\| \ll 1$) [147],

$$\boldsymbol{\mathcal{E}} = \begin{pmatrix} \mathcal{E}_x \\ \mathcal{E}_y \\ \mathcal{E}_z \end{pmatrix} = \left[\mathbb{1} - (\mathbb{1} - \zeta\boldsymbol{g})^{-1} \cdot \tau\zeta\boldsymbol{g} \cdot \mathrm{D}_t \right] (\mathbb{1} - \zeta\boldsymbol{g})^{-1} \cdot \boldsymbol{\mathcal{E}}^0 \,, \qquad (5.5)$$

where $\mathrm{D}_t = \partial_t + \boldsymbol{v} \cdot \nabla$ is the total time derivative. All the terms in the preceding two equations are evaluated in a frame rotating with the angular frequency ω, in order to remove the fast time variation, at $[t, \boldsymbol{r}(t)]$. The non-retarded result of Ref. [147], applied to the particle and its reflection, is thus modified by the appearance of an additional, time- and velocity-dependent, term. The dipole force experienced by the particle may be obtained as in Ref. [147]:

$$F = \begin{pmatrix} F_x \\ F_y \\ F_z \end{pmatrix} ; \text{ where } F_i = \tfrac{1}{2}\epsilon_0 \, \mathrm{Re}\left\{ \chi \sum_j \mathcal{E}_j \partial_i \mathcal{E}_j^* \right\} \,, \qquad (5.6)$$

with i, j separately representing the three spatial dimensions x, y, z. A series expansion in powers of $\|\zeta\mathbf{g}\|$ reveals the leading terms for a stationary particle to be the dipole force from the unperturbed field, and then the dipole force upon the polarised particle due to the field propagated from the induced polarisation.

5.2   Mirror-mediated cooling in one dimension

For a one-dimensional geometry with the particle a distance x from a perfect mirror, the incident illumination combines with its reflection to give an electric field $\boldsymbol{\mathcal{E}}^0(x) = \mathcal{E}_0 \hat{\boldsymbol{y}} \sin(kx)$, and $\tau = 2x/c$; $\hat{\boldsymbol{y}}$ is a unit vector in the y direction. The force in the x direction upon the moving particle is therefore

$$\begin{aligned} F_x = \frac{1}{4}\epsilon_0 \chi k \mathcal{E}_0^2 \Bigg\{ &\sin(2kx) + \frac{\chi k}{\sigma_{\mathrm{L}}}\left(1 - \frac{v}{c}\right)\sin^2(kx)\left[4\cos^2(kx) - 1\right] \\ &- \frac{\chi k^2 \tau v}{\sigma_{\mathrm{L}}}\sin(4kx) \Bigg\} \,. \end{aligned} \qquad (5.7)$$

The force thus comprises three terms. The first two are the dipole force exerted by the unperturbed field, and a Doppler-shifted optical binding force between the particle and

(a) Laboratory frame (b) Particle frame
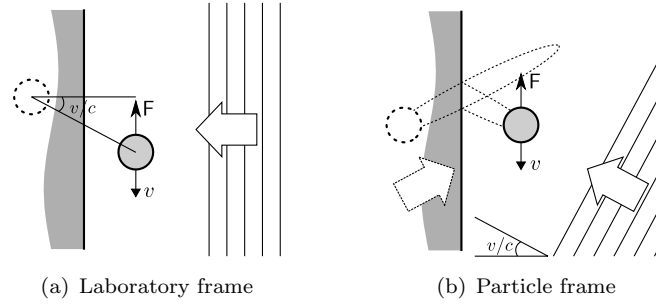
FIGURE 5.2: Retarded binding of a normally-illuminated particle, moving with velocity v, to its own reflection, depicted (a) in the laboratory frame, in which the image lags behind; (b) in the rest frame of particle, whereby the 'wake' trails behind.

its reflection: the Doppler shift here changes the wavelengths of the Fourier field components and hence the gradient of the field formed by their superposition. The third term, which depends upon the particle velocity, the electric field propagator and the round-trip retardation time, is the velocity-dependent force, and dominates the velocity-dependent part of the second term when the distance from the mirror is many wavelengths. When the sign of this component is such as to oppose the particle velocity, cooling ensues. This third term is qualitatively and quantitatively identical to the equivalent terms derived from a semiclassical approach (Section 2.6.2.2) and using a one-dimensional scattering theory (Section 3.1.3).

5.3 Self-binding: mirror-mediated cooling in three dimensions

When a particle or ensemble is strongly coupled to its reflection, we must consider higher-order terms in the expansion of Eq. (5.5), such as the interaction between the propagated particle polarisation and the further polarisation which that induces. This corresponds to the optical binding [150, 151] of the particle to its reflection, due to the tweezing of the particle by light that it has focussed, as shown in Fig. 5.2(a). The finite time taken for light from the particle to return via the mirror causes the reflected image to trail behind the moving particle, providing a component of the binding force in the direction of the particle velocity and therefore a transverse force even when the geometry shows translational symmetry. Fig. 5.2(b) shows the same geometry in the frame of the particle: it is now the inclination of the transformed incident illumination that causes the focussed 'wake' again to lie behind the particle. The sign of the frictional component

again alternates with distance from the mirror, but it does so asymmetrically because the apparent field strength described by Eq. (5.5) is also modulated. The result is a non-zero force, when averaging over the x coordinate,

$$\left\langle \begin{pmatrix} F_x \\ F_y \\ F_z \end{pmatrix} \right\rangle = (-v)\frac{\epsilon_0 \mathcal{E}_0^2 k^2 \chi^2}{128\pi c x^2} \begin{pmatrix} 1 \\ 3 \\ 3 \end{pmatrix} , \tag{5.8}$$

under circularly-polarised illumination and taking into account the near-field effects in $\boldsymbol{g}$. This force becomes comparable with the amplitude of the position-dependent force when $x \lesssim \lambda$, and could therefore be particularly significant for refractive nanoparticles in, for example, colloidal photonic crystals.

Part III

EXPERIMENTAL WORK

Chapter 6

Experimental setup

> Each piece, or part, of the whole nature is always an approximation to the complete truth, or the complete truth so far as we know it. In fact, everything we know is only some kind of approximation, because we know that we do not know all the laws as yet. Therefore, things must be learned only to be unlearned again or, more likely, to be corrected. [...] The test of all knowledge is experiment. Experiment is the sole judge of scientific "truth".
>
> R. Feynman, *The Feynman Lectures on Physics* (1964)

The mechanisms described in the previous chapters, especially mirror-mediated cooling and external cavity cooling, present several exciting avenues not only for theoretical, but also for experimental, research. This chapter presents an overview of the vacuum and laser systems employed by our group in our ongoing investigations into these mechanisms and into MOT miniaturisation and atomic trap arrays. In the first section I describe the physical makeup of the vacuum and laser systems; the second section describes the novel trap geometry and imaging process employed in our system.

6.1   Vacuum and laser system

The aim of the current experiment is to investigate atom–surface interactions. A 'clean' cloud of ultracold ^{85}Rb atoms in a magneto-optical trap was chosen as the starting point for these investigations. In designing the experiment, the apparatus had to satisfy a number of criteria, chiefly:

- the cold atom cloud needs to be formed close to a surface and the vacuum chamber windows;

- the surface, or 'sample', may be simply plane or structured on the micro- or nano-scale;

- rapid (on the order of one or two weeks) turnaround time for changing the sample; and

- very good optical access.

Let us look at each of these criteria in turn to explore the design choices they impose on the system.

6.1.1   Atom cloud close to surface

The mirror magneto-optical trap [152] (mirror MOT) was devised as a way to obtain cold atom samples close to a surface. In the present context, however, the standard mirror MOT has a number of disadvantages: the plane of the mirror lies obliquely to the coils that generate the magnetic field necessary to form the MOT, and the beam that forms the MOT illuminates a large cross-section of the mirror directly below the atom cloud—the former will be discussed below in the context of optical access, whereas the latter can be solved by using what we term the 'ΛMOT' beam geometry, as will be discussed in Section 6.2.

6.1.2   Structured surface

The interaction between atoms and plane surfaces has been investigated both in the context of near field [153] and far field effects [103]. The use of structured surfaces allows the coupling of fluorescence from the atom to surface plasmons. A number of advances by Bartlett and co-workers [154, 155] over the past decade have permitted the rapid production of two-dimensional arrays of hemispherical dimples, with radii of 0.1–$100\,\mu$m, on gold surfaces and with extremely small surface roughness. This process is illustrated schematically in Fig. 6.1; the result is an array of dimples in a small area of an otherwise plane mirror.

The initial characterisation of the system in the Southampton Laboratory was conducted
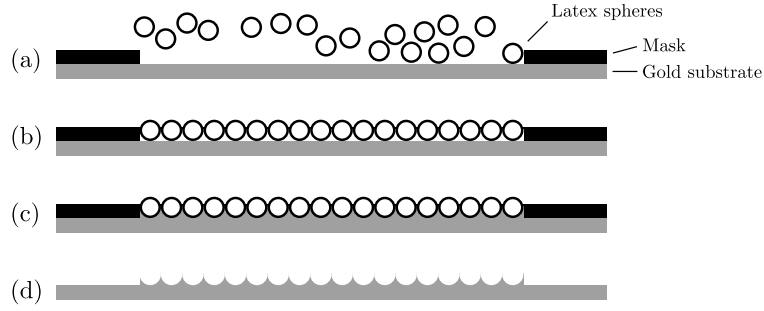
FIGURE 6.1: Templating process used to make the structured surfaces. (a) A colloidal suspension of latex spheres in water is allowed to evaporate on a gold substrate within a masked region. (b) An ordered, close-packed monolayer of spheres is formed on the substrate. (c) Gold is electrodeposited and grows from the substrate upwards, around the latex spheres. (d) The spheres and mask are removed by using conventional solvents.
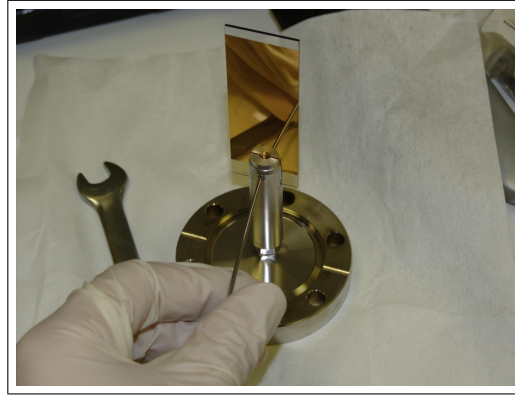
FIGURE 6.2: First sample used in the vacuum chamber, pictured being secured into the holder. This sample consisted of a microscope slide onto which a layer of gold was evaporated.

using a plane mirror sample, Fig. 6.2. This sample was then replaced by one templated with $100\,\mu$m hemispherical dimples, Fig. 6.3.

6.1.3 Rapid changing of surface

The physical mechanisms behind the dominant interaction between the atom and the surface depend on the length scale of the structure present on the surface. In the case of a plane sample, the dominant interaction is the Casimir–Polder force in the extreme near field [156, 157] and the retarded dipole force in the extreme far field (see Section 2.6; see also Ref. [158]). For a surface with hemispherical dimples having radii of the order of the wavelength, plasmonic effects [159] are expected to dominate. For larger dimples, say those with radii of $10\,\mu$m or greater, the system is approximated better by geometrical optics and one expects the formation of a dipole trap at the focus of each hemisphere. In this regime, one can also envisage depositing magnetically polarised films on the surface

FIGURE 6.3: Second sample used, mounted on the vacuum-compatible translation stage. This sample was templated with hemispherical concave mirrors; the bright dot in the mirror is the reflection of light off the hemispheres.

that would allow the formation of a microscopic MOT at the focus of each dimple. For these reasons, it is important to be able to switch samples, in order to vary the length scale of the structure, rapidly. This imposes restrictions on the size of the vacuum chamber used: it must be as small as possible without hindering optical access.

6.1.4   Good optical access

A good compromise for a vacuum chamber that satisfies the above restrictions was found in the Kimball Physics Spherical Octagon (part number MCF600-SO200800) chamber, shown in Fig. 6.4. The two large ports and large aspect ratio enable the use of high numerical aperture fluorescence collection optics. The sample close to which the MOT is formed is placed in the centre of the chamber with its plane parallel to the large ports. This in turn allows the use of a purpose-built high-magnification microscope objective (spatial resolution: ca. 2 μm) to be used with its focal plane coincident with the sample. Two of the smaller ports on the chamber are used for the mount holding the sample and for connecting the chamber to the ion pump and ^{85}Rb dispensers. The other six are therefore left free, allowing almost unrestricted optical access to the cold atom cloud.
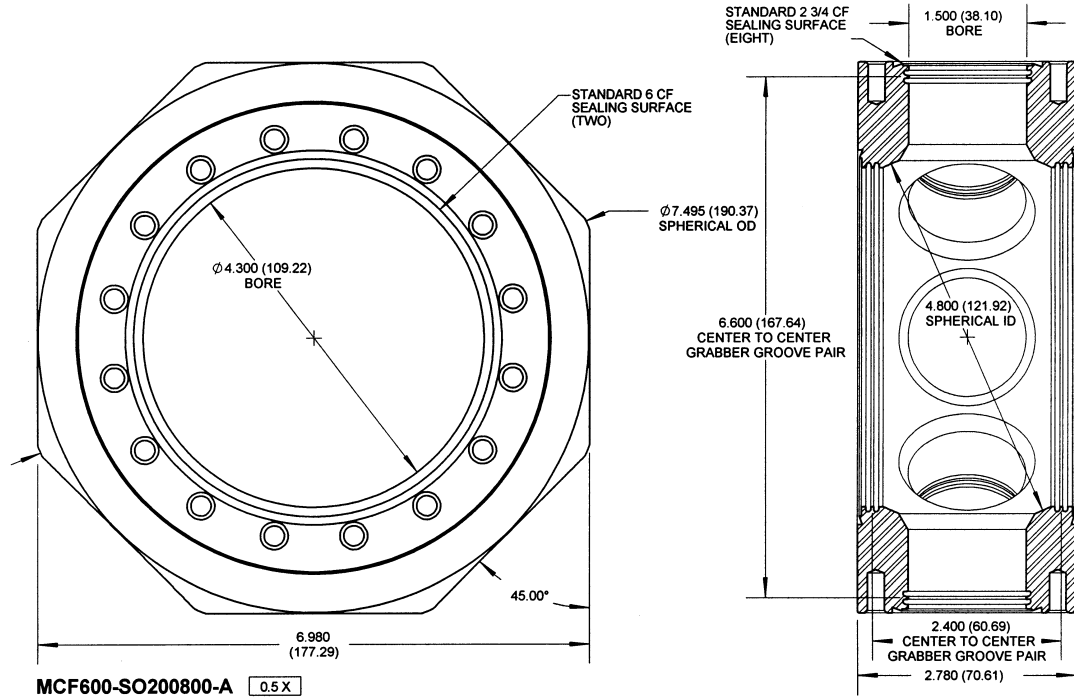
FIGURE 6.4: Technical drawing for the Kimball Physics MCF600-SO200800 spherical octagon. All dimensions are in inches (and millimetres in parentheses). Image reproduced from Ref. [160].

The sample, Fig. 6.3, is mounted on a vacuum-compatible translation stage, allowing the templated surface to be positioned correctly with respect to the MOT beams.

6.1.5 Laser system

The MOT cooling and repump beams are generated by external cavity diode lasers similar to the design in Ref. [161]. More details of the frequency locking system used are given in the next section.

6.2 The ΛMOT and multiphoton imaging

The work in this section is published as Ohadi, H., Himsworth, M., Xuereb, A., & Freegarde, T. Opt. Express **17**, 23003 (2010) and is reproduced *verbatim* [162].[1] Here, we describe and characterise the combined magneto–optical trap and imaging system

---

[1] All authors contributed equally to this paper. Hamid Ohadi and Matthew Himsworth performed the measurements; AX and HO processed the data and wrote the paper. Tim Freegarde supervised the project at all stages.

that we developed in our laboratory to be able to explore atom–surface interactions in great detail and with considerable experimental flexibility.

We demonstrate a combined magneto–optical trap and imaging system that is suitable for the investigation of cold atoms near surfaces. In particular, we are able to trap atoms close to optically scattering surfaces and to image them with an excellent signal-to-noise ratio. We also demonstrate a simple magneto–optical atom cloud launching method. We anticipate that this system will be useful for a range of experimental studies of novel atom-surface interactions and atom trap miniaturisation.

6.2.1   Introduction and motivation

Over the past two decades, several configurations for magneto–optical traps have been demonstrated [163–167]. The starting point for most geometries has been the original, '6-beam', configuration [163], where the atom trap is created in the intersection of three counterpropagating laser beams. Despite it having the advantage that the atoms can be trapped far from any surface, thereby reducing spurious scatter in the imaging of such a trap, one cannot easily use this configuration for investigations into atom–surface interactions, for precisely the same reason. Another, more recent, configuration is the so-called 'mirror MOT' [167], where the trap is formed a short distance away from a mirror, which also serves to reduce the number of necessary incident laser beam paths to two. The major drawback of such a configuration is its reduced optical access, due to the oblique angle of the field coils with respect to the mirror. The presence of a reflecting surface close to the trap also presents a problem of an entirely different nature. If the object of one's investigation is to observe the interaction between atoms and surfaces structured at the micrometre scale, for example hemispherical mirrors of the type investigated in [159], the signal from the atoms will almost certainly be lost due to unwanted scattering of light into the optical system. MOTs on the meso- and microscopic scale, in particular, have received some recent interest [168], but the small atom numbers in such traps have so far hindered their imaging and characterisation [169]. In this section we detail a modified configuration that we call the 'ΛMOT' and implement an imaging system based on a two-stage excitation process [170], which help us overcome each of these limitations and aid our exploration of different atom–surface interactions.
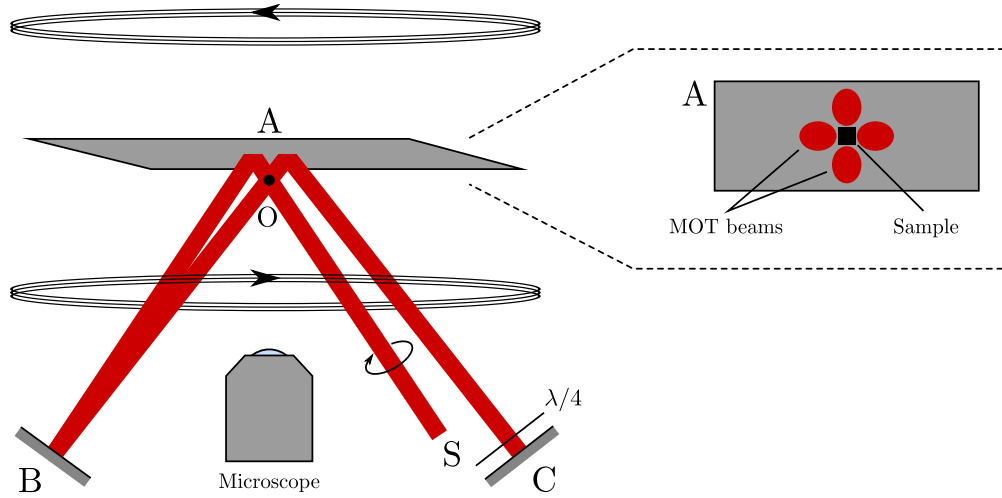
FIGURE 6.5: Schematic of one of the two beam paths involved in our MOT geometry. S is the incoming beam; A, B, and C are mirrors. The component marked '$\lambda/4$' is a quarter-wave plate. The cold atom cloud forms in the intersection region, O. In this diagram we do not show a second, identical, beam, which provides trapping and cooling forces in the plane normal to the paper. The area of mirror A immediately adjacent to the trapped atoms is not illuminated, and can therefore be patterned or structured to explore atom–surface interactions. *Inset:* The lower surface of mirror A, showing the MOT beams and the sample area, which is not illuminated by any of the beams.

This section is structured as follows. The next subsection is devoted to the description and characterisation of our trap geometry. We then discuss the mechanism behind our multilevel imaging system and show how it does indeed allow for practically background-free imaging of the atom trap. The subsequent subsection discusses surface loading by magneto-optic launching, which allows us to load atoms onto a surface with a three-dimensional range of motion.

6.2.2 The ΛMOT

6.2.2.1 Description

A single beam of circularly polarised light of the right helicity is split using a non-polarising beamsplitter, to generate the two beams that produce the trap, and a half-wave plate is inserted in one of the two resulting beams to achieve the correct polarisations. Each of these beams, denoted S, is then used to construct the geometry shown in Fig. 6.5. Mirror C is set up so as to retroreflect the beam. Mirrors B and C, together with the quarter-wave plate, allow us to change the polarisation in the retroreflected branch independently of the incoming polarisation. In a normal mirror MOT, the polarisations cannot be modified independently of each other and the quadrupole axis has
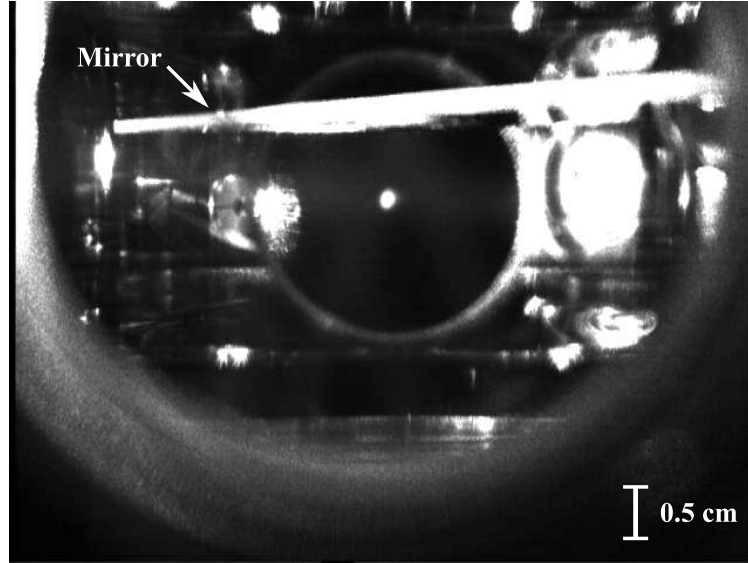
FIGURE 6.6: Image of our MOT in operation, corresponding to Fig. 6.5; mirror A is indicated in the picture.

to be at an oblique angle to the mirror. The four beams travelling towards O thus have the correct polarisations to produce the trapping and cooling forces necessary to form a MOT in this plane. Combined with the second set of beams, this means that the MOT is formed in the intersection region of four pairs of counterpropagating beams. We note that alignment of mirror B such that the beam is retroreflected perfectly will recover the traditional mirror MOT beam geometry, albeit with the incorrect polarisations for a MOT cloud to form.

Several advantages are apparent in the use of this geometry. The trapping volume is the entire overlap of the trapping beams, unlike that in a mirror MOT where half the trapping volume is rendered inaccessible by the presence of the mirror. Optical access is also much improved, both because the coils are oriented in such a way as to be less obstructive, and because we have removed the necessity of having a beam travelling in a plane parallel to mirror A. This allows us to use as much of the 360° viewing angle in that plane as is necessary for imaging or manipulation beams. If this is not a requirement, a simpler set-up can alternatively be used, where only one set of beams is used in the double-'Λ' geometry, the trapping and cooling forces in the plane normal to the paper in Fig. 6.5 being produced by means of a separate pair of counterpropagating beams. An important advantage of this geometry is that the double-'Λ' shape of the MOT beams affords better imaging of the trap, allowing microscope objectives to be mounted very close to it. With a custom-made objective, we can achieve high-NA imaging (NA >

0.5) and a diffraction-limited resolution of $< 2\,\mu$m. While a similar degree of optical access may be possible in the traditional 6-beam configuration, we note that this latter configuration is unsuitable for atom–surface interaction studies. In contrast, mirror A in our geometry can be replaced by any other suitable reflecting surface. One candidate for such a reflecting surface would be one of the surfaces of a Dove prism, which could then be used to form a two-dimensional bichromatic evanescent-field trap [171] close to the mirror surface. This trap would be loaded from the MOT cloud using such techniques as magneto-optic launching, which is explained in Section 6.2.4.

Aside from this marked increase in optical access, our system is simple to set up and operate. In particular, it requires fewer beam paths than a traditional MOT (two rather than three) and alignment of the beams is also easy: a CCD camera looking up at the mirror can be used to align the beams coarsely; once this is done, optimisation of the cold atom signal provides the fine-tuning of the alignment.

6.2.2.2 Characterisation

A typical trap, shown in Fig. 6.6, is ellipsoidal in shape with a $1/e$ diameter of the order of $400\,\mu$m along its minor axes and contains around 4×10^4 ^{85}Rb atoms. Combined with a measured trap lifetime $\tau_0 \approx 6\,$s, this allows us to infer the trap loading rate, $N_0/\tau_0 \approx 6.7 \times 10^3\,$s^{-1}. We measured a cloud temperature of $110 \pm 40\,\mu$K, the large uncertainty being due to the imprecision in measuring the cloud size.

Typical parameters for the operation of our trap are: a detuning of $-14.9\,$MHz, or $-5.0\,\Gamma$ ($\Gamma \approx 3.0\,$MHz [172]), for the cooling laser and a power of $6\,$mW divided between the two trapping beams (beam diameter: $6\,$mm). The minimum power necessary to produce the MOT was found to be $\approx 1.3\,$mW in each of the two beams. The trap was loaded from background gas of a natural isotopic mixture of rubidium at a pressure of $10^{-9}\,$mbar. The cooling and repump lasers were locked using the DAVLL technique [173] for long-term stability and flexibility of operation.

6.2.3 Multilevel imaging system

The most common method of imaging a cold atom cloud in a MOT is fluorescence imaging. When the cloud is close to a reflecting surface both the cloud and its reflections
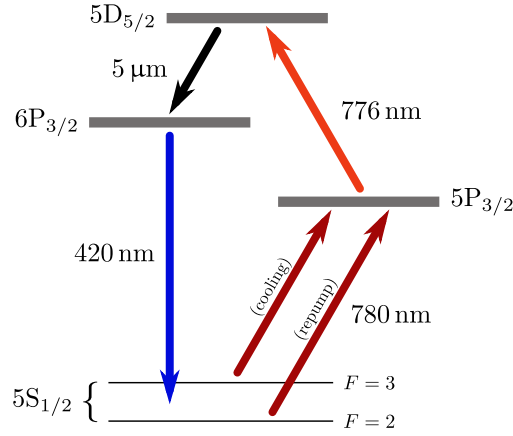
FIGURE 6.7: The four-level system in ^{85}Rb that we use to image our atoms. The MOT lasers (780 nm) and a laser at 776 nm are used to induce a ladder transition. The population decays back to the ground state, via an intermediate state, and emits a 420 nm photon in the process. The hyperfine splitting of the excited states is not drawn for clarity.

will be seen by the imaging system (see Ref. [152], for example). This situation is exacerbated by the presence of surfaces that reflect unwanted light into the imaging optics and thereby decreasing the signal-to-noise ratio of the imaging system. Fig. 6.6, shows an example of the mirror in our system scattering the MOT beams into the imaging system.

This problem may be overcome using two-stage excitation imaging. We make use of a four-level system in ^{85}Rb (see Fig. 6.7 for details), similarly to Refs. [174] and [175]; atoms in the $5S_{1/2}$ ground state are pumped to the $5D_{5/2}$ state via 780 nm and 776 nm radiation, the former being provided by one of the MOT beams, and then decay back to the ground state via an intermediate $6P_{3/2}$ state, emitting 420 nm radiation, which we detect. We note that a very similar system was recently used to produce a multiphoton MOT [176]. In our system, this process gives a significantly smaller signal than can be obtained through 780 nm fluorescence imaging. However, it has the benefit of being entirely background-free: in a well-shielded system, the entire 420 nm signal reaching the detector has its origin in the cold atom cloud. Off-the-shelf filters can then be used to remove the 780 nm radiation reaching the detector.

Generation of the 776 nm beam

The 776 nm beam is produced using a Sanyo DL7140-201S diode and the same external cavity diode laser design used to produce the MOT cooling and trapping beams. Since
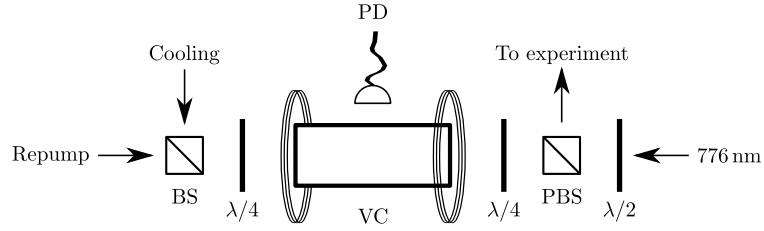
FIGURE 6.8: 776 nm spectroscopy and locking system. (P)BS: (polarising) beam splitter cube; $\lambda/4$: quarter-wave plate; $\lambda/2$: half-wave plate; VC: heated vapour cell; PD: filtered photodiode.
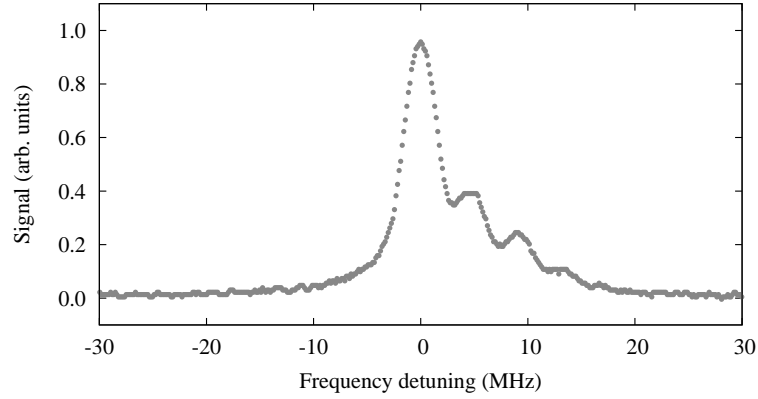
FIGURE 6.9: 420 nm fluorescence from the vapour cell, observed on PD (see Fig. 6.8) as a function of the detuning of the 776 nm beam, with the cooling and repump beams locked and shifted by 80 MHz with respect to the frequencies required to make a MOT. The various peaks are due the hyperfine structure in ^{85}Rb. To obtain these data, we removed the quarter-wave plates on either end of the vapour cell, thus having linearly polarised light entering the cell from both ends.

^{85}Rb has no spectral features in this wavelength range that are suitable for locking the laser frequency, a multilevel locking system is used (see Fig. 6.8). 5 mW from each of the MOT cooling and repump beams (≈ 780 nm) and 1.5 mW from the 776 nm beam, all rendered circularly polarised by the quarter-wave plates, enter the heated vapour cell (VC) from opposite ends. A large-area UV-enhanced filtered silicon photodiode (PD), operating in photovoltaic mode, picks up the resulting Doppler-free fluorescence and is amplified by means of a LMP7721 amplifier chip. Magnetic coils surrounding the heated vapour cell control the Zeeman shift of the magnetic sublevels of the atoms inside the cell, shifting this signal, and therefore the lock point, as required. Around 4 mW of the 776 nm beam is then mixed in with the MOT cooling and repump beams and sent through an optical fibre to the MOT.

We show a sample 420 nm signal, as detected at the photodiode, in Fig. 6.9, where the hyperfine splitting of the $5D_{5/2}$ level in ^{85}Rb is evident in the shoulders on the right-hand side of the peak in the figure. The 776 nm laser diode is locked to the side of one the
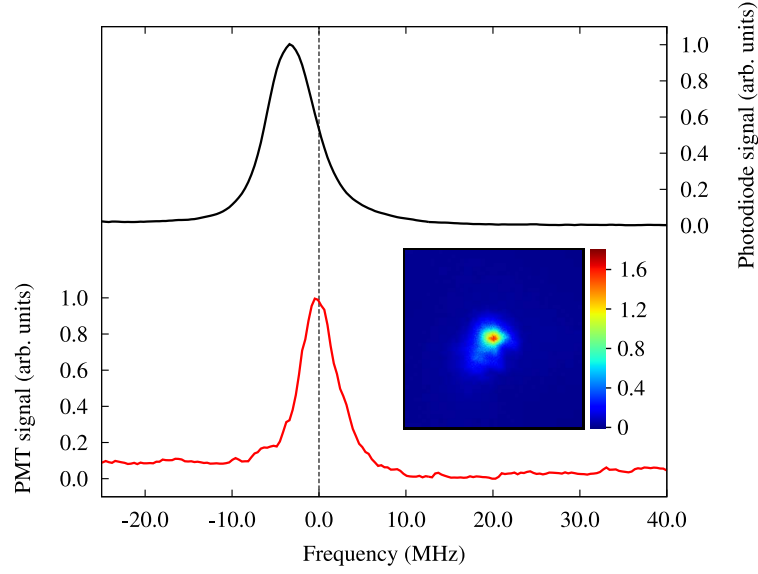
FIGURE 6.10: 420 nm fluorescence observed on PD (solid black line, see Fig. 6.8) and on a PMT imaging the MOT cloud (solid red line) as a function of the detuning of the 776 nm beam. The zero on the frequency axis corresponds to the point at which the signal from the MOT cloud is highest; we lock to this point. The magnitude and sign of the shift between the two curves can be set arbitrarily by varying the magnetic field generated by the coils around the vapour cell. *Inset:* MOT cloud imaged at 420 nm (scale in 10^3 counts per second). This image is naturally background-free and has a spatial resolution, limited by the optics used, of ca. 2 μm.
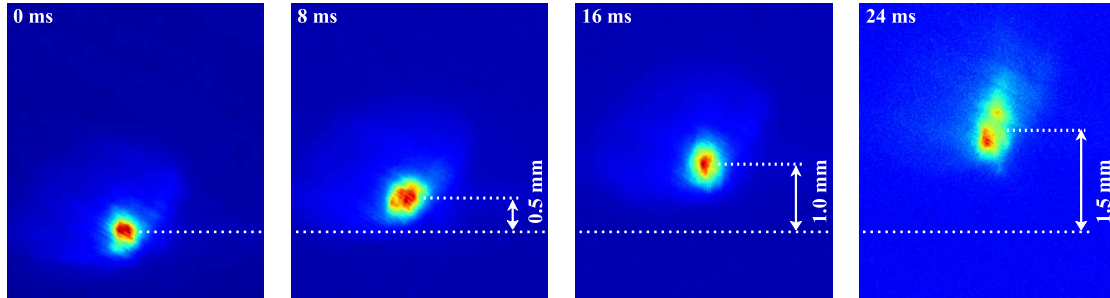
FIGURE 6.11: A sequence of four false colour fluorescence images, taken at 8 ms intervals, of the cloud before and after it has been given a magnetic impulse. The first shot (leftmost picture) shows the cloud just before the magnetic field is pulsed. The second, and subsequent, shots show the cloud at later times. The transfer efficiency after 24 ms is over 40%.

main peak, at the point indicated by the dashed line in Fig. 6.10, using a conventional PID circuit. The lock point is found by manually and slowly adjusting the frequency offset of the 776 nm laser to maximise the fluorescence from the MOT cloud. Depending on the parameters chosen, the spectra corresponding to the latter figure may exhibit two well-resolved peaks due to the Autler–Townes splitting [177]; in the spectrum shown in Fig. 6.10, however, the presence of the second peak manifests itself as a slight shoulder on the photodiode signal. Locking at a detuning of around 6.5 MHz from the peak of

absorption in the vapour cell gives the strongest signal in the MOT cloud, as recorded by the photomultiplier tube trace shown in the same figure.

6.2.4 Surface loading by magneto-optic launching

Transporting cold atoms from the region where the trap naturally forms to the sample is an essential part of many experiments investigating atom–surface effects. Several methods have been devised for moving cold atom clouds, including the use of push beams [178] and moving magnetic coils [179]. Push beams are easy to set up, requiring either the addition of one extra beam or the switching off of one of the counterpropagating beams, but cannot be used to push atom clouds towards highly reflective surfaces. Using moving magnetic coils requires a rather involved mechanical setup.

We make use of a third method, which we call magneto-optic launching, for transport of the atom cloud by rapidly moving the trap centre and then releasing the cloud, thereby imparting momentum to it. An auxiliary coil is added to the system in Fig. 6.5, above the upper MOT coil. After the MOT cloud forms, a long current pulse is applied to this auxiliary coil, which launches the cloud upward with a speed determined by the size and duration of the current pulse, and then the cloud is released from the trap by switching off the MOT beams after 20 ms. Fig. 6.11 shows a series of photographs of the cloud after being launched by a magnetic pulse. It can be seen that the pulse results in an approximately uniform vertical cloud speed of $0.063\,\mathrm{m\,s^{-1}}$. The physical orientation of our system, with the mirror and sample being *above* the trapping region, allows us to launch the cloud upwards with a much greater degree of control than would be possible if the cloud were merely dropped downwards.

Finally, we note that the equilibrium distance of the MOT cloud from the mirror surface depends on the beam diameter and the size of the 'sample area', i.e., the section of the mirror that acts as a sample and is not usable as a plane mirror. With a sample area diameter of 2 mm and beam diameter of 4 mm, the cloud can be made to form less than 4 mm away from the surface, allowing us to use the magneto-optic launching method to move the atoms closer to the surface for interaction studies.

Chapter 7

A guide for future experiments

> [...] [I]t is more important to have beauty in one's equations than to have them fit experiment.

<div align="right">P. A. M. Dirac, Scientific American **208**, 5 (1963)</div>

This chapter aims to provide a guide for experimentalists seeking to observe the effects we predicted in earlier chapters. Section 7.1 presents an overview of the different geometries explored in the previous chapters. For each of these geometries, Section 7.2 calculates and compares the relevant friction forces acting on the particle. Section 7.3 discusses a number of experimentally-accessible configurations and calculates cooling times and equilibrium temperatures that can be expected in each situation. The first appendix to this chapter is a technical note discussing electric fields inside dielectrics and the origin of the Clausius–Mossotti equation that describes the response of a bulk dielectric to an applied electric field. Finally, two appendices then follow that discuss, respectively, some problems encountered when calculating electric fields inside microscopic hemispherical mirrors, and general expressions for the force acting on an atom inside an arbitrary monochromatic field, ignoring delay effects.

7.1   Overview of several different possibilities

It has been outlined in the preceding chapters that several different geometries exist that allow a memory. Moreover, within each such geometry, one can choose to investigate cooling mechanisms on different classes of particle. The aim of this section is to briefly

summarise these different possibilities, noting the advantages and disadvantages of each: Section 7.1.1 to Section 7.1.4 look at species that can be cooled, and Section 7.1.5 to Section 7.1.9 at the geometries themselves.

7.1.1 Trapped ions

Ions can be trapped in radio-frequency traps, and laser cooled down to the ground vibrational state of such traps,[1] with remarkable ease. The lifetime of trapped ions can be of the order of hours [180], which is orders of magnitude longer than the comparable figure for neutral atoms. For these reasons, ions would make ideal test subjects for exploring forces that vary significantly over length scales of the order of a wavelength [103, 181]. Interest in using trapped ions also arises from their potential applications in quantum information storage and processing [182].

7.1.2 Neutral atoms

The ease of manipulation of trapped ions using electric fields is a double-edged sword, in the sense that this very feature also makes trapped ions highly sensitive to the environment they are immersed in. One can avoid these issues through the use of neutral atoms rather than ions. Neutral atoms, however, cannot easily be confined to subwavelength regions without complex experimental systems such as the one used in a recent proof-of-concept experiment presented in Ref. [183].

7.1.3 Optomechanics—Cantilevers and micromirrors

Recent years have seen a surge in the popularity of optomechanics experiments, mostly with the aim of reaching the ground vibrational state of a vibrating reflective cantilever [8], or of a reflective micro-membrane [114]. The use of such optical elements introduces a number of interesting possibilities:

---

[1] It must be pointed out that such ions would have a translational temperature lower than that which can be achieved through mirror-mediated cooling setups using typical experimental parameters. The aims of such experiments would be (i) a proof-of-principle demonstration, and (ii) an exploration of the wavelength-scale variations of the forces.

- Engineered internal resonances—Ref. [184] looks at using resonances inside a photonic crystal as a means of controlling its motion, in much the same way as one uses atomic resonances in Doppler cooling. In contrast with the case of an atom or ion, however, one can engineer the system to have a wide range of different properties.

- Strong mirror–field coupling—Single atoms or ions do not have a large polarisability unless the driving field is close to resonance; this is problematic because strong heating effects become important under such conditions. Mirrors, even microscopic ones, consist of vast numbers of atoms, each of which is essentially an individual dipole, and therefore experience correspondingly stronger effects.

- Positioning—micromirrors enjoy the advantages of both ease of positioning, shared with ions, and the immunity to electrostatic forces, shared with neutral atoms. Moreover, the technology exists to make silicon nitride (SiN) membranes much thinner than an optical wavelength [129], so such mirrors can indeed be used to explore sub-wavelength structure in the forces.

7.1.4 Dielectric particles

Spherical dielectric particles, of sizes on the nanometre [17, 79] or micrometre [185] scales, have been proposed as replacements for individual atoms in cooling experiments. On the small end of the scale, the particles can be suspended using purely optical forces and are therefore not coupled to any physical heat bath. Nevertheless, even such small particles exhibit polarisabilities much larger than that of an individual atom, and therefore correspondingly stronger interactions with the light field. The larger particles would need to be physically supported, perhaps by being mounted on the end of a tapered fibre. This could, in turn, be achieved by ablating the tapered end of the fibre to form a microsphere. The mechanical properties of such a fibre would ensure poor coupling of phonons between the microsphere and the bulk fibre.

The response to the electric field of a dielectric particle on the nanometre scale is related to its complex permeability ϵ through the Clausius–Mossotti relation:

$$\chi = 3V \frac{\epsilon - 1}{\epsilon + 2} \, . \tag{7.1}$$
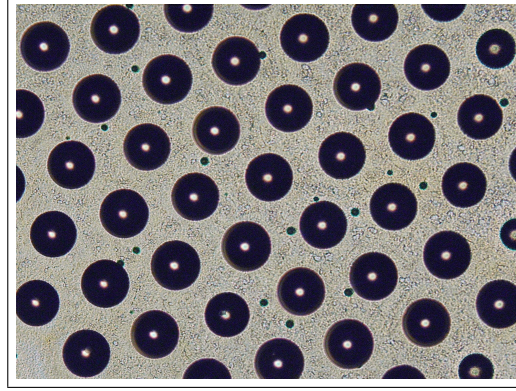
FIGURE 7.1: Optical micrograph of a section of a templated gold surface. The bright spot in each of the dimples is the focus. The centre–to–centre distance is 100 μm and the depth of the electrodeposited gold is 15 μm. (Courtesy Nathan Cooper.)

The derivation of the Clausius–Mossotti equation itself has some interesting subtleties that are discussed in Appendix 7.A. ϵ is furthermore related to the real, η, and imaginary, κ, parts of the refractive index $n = \sqrt{\epsilon}$ by

$$\text{Re}\{\epsilon\} = \eta^2 - \kappa^2 \,, \text{ and} \tag{7.2}$$

$$\text{Im}\{\epsilon\} = 2\eta\kappa \,. \tag{7.3}$$

Finally, κ is related to the $1/e$ power absorption length of a substance, $1/\alpha$, by $\alpha = 2k\kappa$ at wavenumber k. For the common dielectric PMMA [poly(methyl methacrylate)] $\eta = 1.5$ and, conservatively, $\alpha = 50\,\text{m}^{-1}$ at a wavelength $\lambda = 1\,\mu\text{m}$ in vacuum [186]; i.e., $\epsilon = 2.2 + \left(1.2 \times 10^{-5}\right)\text{i}$. The imaginary part of ϵ is much smaller than the real part and can generally be neglected when calculating optical forces. It is, however, responsible for absorption of part of the incident light and its effects cannot be neglected when calculating the power absorbed by an illuminated dielectric.

7.1.5 Dipole trap arrays

Two-dimensional arrays of dipole traps have been built using microfabricated lens arrays [64] and used to site-selectively address trapped atoms [187]. However, the use of refractive elements such as lens arrays brings with it a number of disadvantages, of which we mention two:

- Fabrication costs—each array has to be custom-made and it is difficult to mass-produce such optical elements.
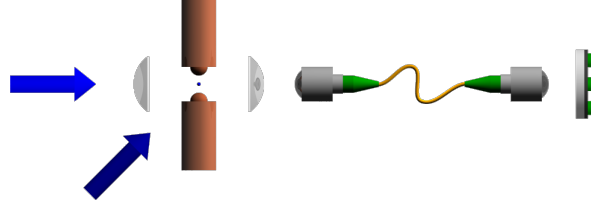
FIGURE 7.2: Schematic of an experiment to explore the mirror-mediated cooling mechanism. Light is focussed onto an ion trapped in an endcap trap, then coupled into a fibre. This light is retroreflected back into the fibre by means of a mirror whose position can be adjusted through piezoelectric elements.

- Integration—lens arrays require optical access from both sides, leading to a larger apparatus and making it difficult to integrate them into so-called atom chips [168].

One way to overcome both these issues is to use arrays of reflective concave mirrors, which can be manufactured easily (this was explored in Fig. 6.1). The end product, as shown in Fig. 7.1, is indeed close to ideal in terms of periodicity and surface quality. These concave mirrors can be used to construct individual dipole traps for either neutral atoms or ions.

The interest in using such arrays of mirrors lies not only in their ease of manufacture but also in the surface plasmon resonances that are exhibited by the individual hemispherical mirrors [159]. Such resonances couple to the incident light and give rise the possibility of mechanisms of the "external cavity cooling" type, Section 4.1, using not Fabry–Pérot cavities but material resonances. The advantages of using such a system are immediately obvious; we mention only that such a setup introduces the possibility of two-dimensional arrays of individual optical resonant elements that require essentially no alignment. Coupled with the fact that external cavity cooling, as with any mechanism based on the dipole force, is not species-selective, this leads to the possibility of producing two-dimensional arrays of cold ions, atoms, or even micromirrors. Such arrays would potentially revolutionise quantum information processing by implementing a scalable two-dimensional register for quantum information.

7.1.6 Plane mirror cooling

The mirror-mediated cooling setup would be the most basic proof-of-concept experiment of optical cooling using a memory, seeing as it involves merely one mirror. As has been discussed previously, the friction force in such a setup oscillates on a sub-wavelength

scale and, moreover, is only sizeable for atom–mirror distances of the order of metres. A realistic approach to implementing this delay is to couple the light, after interacting with the atom, into a single-mode fibre. The light inside the fibre is then retroreflected and imaged back onto the atom itself. This setup, shown schematically in Fig. 7.2, is conceptually similar to the one used in Ref. [103]. In Fig. 7.2, the species to be cooled is shown to be a trapped ion rather than a neutral atom. The reason for this is again the small length scale over which the friction force changes from a cooling to a heating force, necessitating very good localisation of the particle to be cooled. One also notes that the delay line length must be stabilised interferometrically.

7.1.7   External cavity cooling

The use of an optical resonance to enhance the cooling effect of the retarded dipole–dipole interaction presents a novel way of enhancing the performance of current optomechanical experiments. Indeed, such setups would be less sensitive to misalignment of the mirror to be cooled than traditional optomechanical setups [82], which require micromirrors with extremely good optical and mechanical properties. The sub-wavelength modulation of the friction force is an issue with this mechanism too, which necessitates the use of particles—such as thin micromirrors, membranes, or trapped ions—that can be localised to within a small fraction of a wavelength.

7.1.8   Ring cavity cooling

One may wish to do away with the sub-wavelength localisation problem inherent in mirror-mediated cooling altogether. Ring cavity cooling, discussed under the guise of "amplified optomechanics" in Section 4.3, provides one way of achieving this aim. This mechanism works best with particles that are rather poorly reflective, otherwise the advantages of the amplifier gain are lost, and is therefore more suited towards the cooling of atoms rather than micromirrors. In this instance, both neutral atoms and trapped ions are good candidates; it must also be mentioned that in the case of ions, cooling down to a very low vibrational state is *not* needed in this case. The constraint on the delay line length is not lifted, however: this must still be stabilised interferometrically.
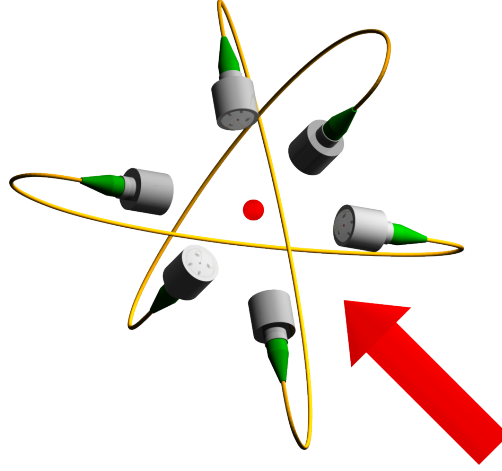
FIGURE 7.3: Highly schematic illustration of a three-dimensional ring cavity cooling setup. The pump light does not couple directly into any cavity, allowing one to use gain media in the fibres similarly to the amplified optomechanics scheme (see Section 4.3).

An extension of this scheme can be envisaged where the pump light is not injected into the cavity but is directed off-axis at the particle. This geometry would not require an isolator, since the pump light never enters the cavity, and can easily be extended to three dimensions; see Fig. 7.3.

7.1.9 Concave mirror cooling

A final possibility is that of using the reflection from a concave hemispherical mirror itself, and not any material resonances supported by the mirror, to cool the motion of a particle at the centre of curvature of the mirror. One would expect that for the effect to be sizeable, the mirror radius would need to be much larger than a wavelength, perhaps of the order of millimetres or centimetres. A brief justification for why a cooling effect is expected to exist in such a geometry is possible using the ideas developed in Section 2.4 in the case where the particle experiences a repulsive interaction with its image. Such a case could correspond to an atom illuminated by light tuned to the blue of its resonance.

When the particle is near the centre of the mirror, a real image is formed that in steady-state is at the same distance from, but on the opposite side of, the centre. Given the symmetry of the situation, it is enough to decompose the motion of the particle into two orthogonal motions, radially and tangentially in a polar coordinate system centred on the centre of curvature of the mirror. In the case of radial motion, we will appeal to Eq. (2.15). The repulsive potential U seen by a motionless particle at a small distance
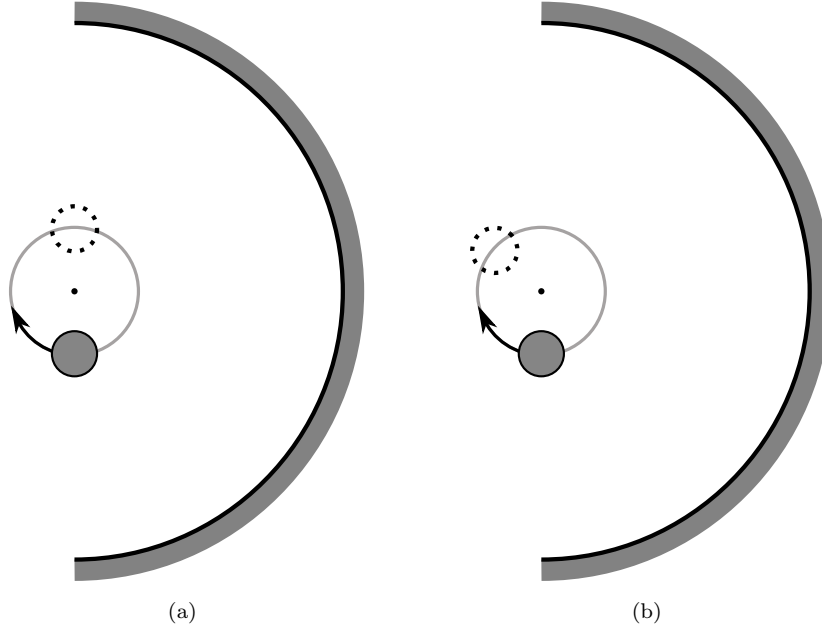
FIGURE 7.4: Origin of the friction force for tangential "racetrack" motion of a particle around the centre of curvature of a hemispherical mirror. (a) In the absence of delay, the particle and its image are at diametrically opposite points in the circular locus of the motion of the particle. (b) Due to delay, the image trails behind its equilibrium position slowing the particle down due to the repulsive interaction between the two. Note that the length scales are greatly exaggerated; in reality, the particle, and the path it moves along, would be much smaller than depicted.

r from the centre can be described by a Gaussian[2], having a peak at $r = 0$ and tailing off to zero as r increases. For concreteness, let us take

$$U(\tilde{r}, r, v = 0) = U_0 \exp\left[-(r + \tilde{r})^2/w^2\right],$$
(7.4)

using the notation of Section 2.4, where w is the width of the potential, taken to be the same in every direction, and U_0 is non-negative. Thus, using Eq. (2.15), we obtain the delayed friction force

$$F = 2U_0 \tau v \frac{8r^2 - w^2}{w^4} \exp\left(-4r^2/w^2\right),$$
(7.5)

which is a cooling force for small r, and where $\tau = 2R/c$ is the delay time for a mirror of radius of curvature R.

The origin of the cooling force for motion in the tangential direction is best explained pictorially. Fig. 7.4 shows the particle moving in a circle of constant radius around the centre of the mirror. In the absence of delay, Fig. 7.4(a), the particle and its image

---

[2] To a good approximation, a small particle close to the centre of a spherical mirror produces a spherical Gaussian image upon focussing by the mirror [138].

would be in diametrically opposite positions along this circle. Due to the delay, however, the image lags behind its equilibrium position, as shown in Fig. 7.4(b). The repulsive interaction between the particle and its image thereby produces a force opposing the motion of the particle. This force can easily be seen to increase with both v and τ, since the distance between the particle and its image decreases with both these quantities, and therefore acts to cool the tangential motion of the particle. Putting these two arguments together implies that a particle undergoing any motion around the centre of curvature of a spherical mirror experiences a friction force mediated by the delayed dipole–dipole interaction.

7.2 Cooling forces experienced in different geometries

In this section we shall use the three-dimensional scattering theory developed in Chapter 5 to obtain the cooling forces experienced by a point-like dipole in a number of different configurations, both (quasi-)one-dimensional and three-dimensional.

7.2.1 Longitudinal mirror-mediated cooling

In one dimension, the mirror-mediated cooling force is given, in agreement with Eq. (5.7), as

$$F = -\frac{1}{2c}\epsilon_0 \frac{\mathcal{E}_0^2}{\sigma_{\mathrm{L}}}\chi^2 k^3 x \sin(4kx)v + \mathcal{O}\left(\chi^4\right), \tag{7.6}$$

where x is the position of the particle with respect to the mirror, and χ is the polarisability of the particle. Note that this force is oscillatory in the position of the particle and therefore has a zero spatial average on the wavelength scale.

A close analogue to the one-dimensional case in three dimensions is that of longitudinal pumping, where the pump field forms a standing wave with the mirror; this is the case considered earlier. When the electric field is assumed to be circularly polarised in the

y–z plane, there arises a dominant (oscillatory) component of the friction force,

$$
\begin{pmatrix} F_x \\ F_y \\ F_z \end{pmatrix} = \frac{1}{32\pi c}\epsilon_0 \mathcal{E}_0^2 \chi^2 k^4 \frac{1}{kx}
$$

$$
\times \begin{bmatrix} 4kx\cos(4kx) + \sin(2kx) + 3\sin(4kx) & 0 & 0 \\ 0 & \cos(kx)\sin^3(kx) & 0 \\ 0 & 0 & \cos(kx)\sin^3(kx) \end{bmatrix}
$$

$$
\cdot \begin{pmatrix} v_x \\ v_y \\ v_z \end{pmatrix} + \mathcal{O}\left[\chi^2/(kx)^2\right] + \mathcal{O}\left(\chi^3\right), \quad (7.7)
$$

which averages over a wavelength[3] to give the non-oscillatory terms,

$$
\begin{pmatrix} F_x \\ F_y \\ F_z \end{pmatrix} = -\frac{1}{128\pi c}\epsilon_0 \mathcal{E}_0^2 \chi^2 k^4 \frac{1}{(kx)^2} \begin{bmatrix} 1 & 0 & 0 \\ 0 & 3 & 0 \\ 0 & 0 & 3 \end{bmatrix} \cdot \begin{pmatrix} v_x \\ v_y \\ v_z \end{pmatrix}
$$

$$
- \frac{1}{1024\pi c}\epsilon_0 \mathcal{E}_0^2 \chi^3 k^7 \frac{1}{(kx)^3} \begin{bmatrix} 4 & 0 & 0 \\ 0 & 3 & 0 \\ 0 & 0 & 3 \end{bmatrix} \begin{pmatrix} v_x \\ v_y \\ v_z \end{pmatrix} + \mathcal{O}\left(\chi^4\right). \quad (7.8)
$$

It must be noted that these expressions are valid for kx large enough that the point-dipole approximation holds ($kx \gg 1$). In order to explore the physical origin of the above forces, it is helpful to introduce some auxiliary notation. We denote the pump field $\mathcal{E}_0$, as before, and the polarisation it induces in the particle $\mathcal{P}_0$. $\mathcal{P}_0$ is responsible for producing an electric field $\mathcal{E}_1$. Upon reflection by the mirror, $\mathcal{E}_1$ is in turn responsible for inducing a polarisation $\mathcal{P}_1$ in the particle. For each index i, $\mathcal{E}_i$ is of the order χ^i and $\mathcal{P}_i$ of the order χ^{i+1}. The force acting on the particle due to a term of the form $\mathcal{P}_i^* \cdot \mathcal{E}_j$ is thereby of order χ^{i+j+1}. Implicit in each of the above friction force expressions is a factor of order x due to the retardation effects. This has to be understood as being physically separate from the factors of x introduced by the spreading of wavefronts in three dimensions; indeed, in one dimension $F \propto x$ despite the fact that wavefronts do not spread. We will factor this term out in the following.

---

[3] The averaging is done by assuming $kx \gg 1$, which allows us to hold the $1/(kx)^n$ terms constant and average only over the periodic functions.

Let us first decompose the friction force in Eq. (7.7): there are two sets of terms, of order $\chi^2/(kx)$ and $\chi^2/(kx)^2$, both of which arise from interactions of the form $\boldsymbol{\mathcal{P}}_0^* \cdot \boldsymbol{\mathcal{E}}_1$ and $\boldsymbol{\mathcal{P}}_1^* \cdot \boldsymbol{\mathcal{E}}_0$. Respectively, these interactions represent the interaction of the polarisation induced by the incident field with the retarded re-radiated field, and that of the polarisation induced by this retarded field with the incident electric field. The first term in the non-zero spatially averaged force, Eq. (7.8), is in this case entirely due to the geometrical spreading out of the wavefronts in the same terms. The second term, which arises from a term that is not written explicitly in Eq. (7.7), has a different origin: it arises from the phase-locked interaction between $\boldsymbol{\mathcal{P}}_1$ and $\boldsymbol{\mathcal{E}}_1$, which has no sub-wavelength spatial dependence, since $\boldsymbol{\mathcal{E}}_1$ is a travelling wave and therefore any sub-wavelength dependences are factored out of the product $\boldsymbol{\mathcal{P}}_1^* \cdot \boldsymbol{\mathcal{E}}_1$. It is this friction force that therefore arises from a delayed 'self-binding' interaction.

7.2.2 Transverse mirror-mediated cooling

In three dimensions one is of course free to choose the direction of illumination. Let us again consider the usual mirror-mediated cooling geometry, but where the pump light is a circularly polarised wave in the x–y plane travelling in the z-direction, i.e., propagating parallel to the mirror. The resulting friction forces can again be written down as

$$
\begin{pmatrix} F_x \\ F_y \\ F_z \end{pmatrix} = \frac{1}{32\pi c} \epsilon_0 \mathcal{E}_0^2 \chi^2 k^4 \frac{1}{kx}
$$

$$
\times \begin{bmatrix} -2kx\cos(2kx) & 0 & -2kx\cos(2kx) - \sin(2kx) \\ 0 & \sin(2kx) & 0 \\ 2kx\cos(2kx) & 0 & 2kx\cos(2kx) + \sin(2kx) \end{bmatrix}
$$

$$
\cdot \begin{pmatrix} v_x \\ v_y \\ v_z \end{pmatrix} + \mathcal{O}\left[\chi^2/(kx)^2\right] + \mathcal{O}\left(\chi^3\right), \quad (7.9)
$$

and averaged over a wavelength to give

$$
\begin{pmatrix} F_x \\ F_y \\ F_z \end{pmatrix} = -\frac{1}{512\pi c}\epsilon_0 \mathcal{E}_0^2 \chi^3 k^7 \frac{1}{(kx)^3} \begin{bmatrix} 2 & 0 & 0 \\ 0 & 1 & 0 \\ 0 & 0 & 0 \end{bmatrix} \cdot \begin{pmatrix} v_x \\ v_y \\ v_z \end{pmatrix} + \mathcal{O}(\chi^4). \tag{7.10}
$$

The oscillatory forces have the same origin as those in the longitudinal case. Note, however, that because of the geometry of this situation the only non-oscillatory forces that survive to this order are due to the self-binding terms of the form $\mathcal{P}_1^* \cdot \mathcal{E}_1$. In a transverse-pumping geometry, it is this self-binding force that is the dominant effect.

7.2.3 Ring cavity cooling

The mechanism involved in ring cavity cooling is essentially the same as that involved in (one-dimensional) mirror-mediated cooling. Indeed, we can compare Eq. (4.10) to Eq. (3.41) and deduce that the dominant friction force acting on a particle inside a ring cavity will be of the form

$$
F = -\frac{1}{4c}\epsilon_0 \frac{\mathcal{E}_0^2}{\sigma_{\mathrm{L}}} \chi^2 k^3 \Lambda L v, \tag{7.11}
$$

where Λ is a factor due to the properties of the cavity, and L the length of the cavity.

7.2.4 Summary: Orders of magnitude

The table below is a convenient reference for the forms of the dominant friction forces acting on a particle in the geometries discussed in this section. Symbols of the form F_{xx}, for example, denote the force in the x direction proportional to the x-component of the velocity.

		Oscillatory terms	Spatial average
Mirror-mediated cooling (MMC; 1D)		$\chi^2(kx)$	0
MMC (3D)	Longitudinal	$\chi^2/(kx)$ [F_{xx}: χ^2]	$\chi^2/(kx)^2$
	Transverse	χ^2 [F_{yy}: $\chi^2/(kx)$]	$\chi^3/(kx)^3$ [F_{zz}: $\chi^2/(kx)^5$]
Ring cavity cooling (1D)		—	$\chi^2(kx)$

We reiterate that the χ^2 and χ^3 terms forming the spatial average of the friction forces have different origins, with the former being due to the spreading of wavefronts and the latter the phase-locked interaction between $\mathcal{P}_1$ and $\mathcal{E}_1$.

7.3   Cooling times and base temperatures

In the previous sections we identified a number of configurations that may be used to show cooling effects mediated by the dipole–dipole force. The aim of this section is to evaluate the cooling forces and base temperatures for a few specific situations.

7.3.1   One-dimensional mirror-mediated cooling: Trapped ion

The 'fine structure' in the friction force produced in the mirror-mediated cooling geometry in one dimension is perhaps best explored using trapped ions, as shown schematically in Fig. 7.2. We assume that the species being cooled is a Ba^+ ion, and that the pump beam is at a wavelength of $\lambda = 493\,\text{nm}$, detuned by $\Delta = \pm 10\Gamma$ from resonance and focussed down to a $10\,\mu\text{m}$ spot at the position of the ion. The length of the fibre-based delay line is taken to be $L = 2\,\text{m}$. In order to ensure operation in the low-saturation regime, we set the pump power to be $P = 1\,\text{nW}$. The mass of the ion is $m = 2.3 \times 10^{-25}\,\text{kg}$. These numbers result in:

$$1/e \text{ velocity cooling time: } 12\,\text{ms, and}$$
$$\text{steady-state temperature: } 570\,\mu\text{K}.$$

Both of these numbers decrease linearly with increasing L and include a factor of $\frac{1}{2}$ originating from the presence of the harmonic trap confining the motion of the ion, as explained in Section 2.6.2.3. Doppler cooling of the ion, after which the position spread of the particle would be smaller than a wavelength (specifically, ca. 35 nm in the setup of Ref. [103]), would be necessary to resolve the sub-wavelength features in the friction force.

7.3.2 External cavity cooling: Transmissive membrane

We have already remarked that external cavity cooling would act to enhance optomechanical cooling mechanisms, such as those used to cool the vibrational motion of reflective mirrors. Let us suppose we use a membrane with power transmissivity of 50% and couple the transmitted light into a Fabry-Pérot cavity, whose mirrors have power transmissivities of 1%. A typical commercially-available SiN membrane would have an effective mass $m = 5 \times 10^{-14}$ kg [114] for the centre-of-mass mode and negligible absorption. Coupling in 1 mW of light at a wavelength $\lambda = 780$ nm thereby gives

$$1/e \text{ velocity cooling time: 1 ms, and}$$
$$\text{steady-state temperature: } 35\,\mu\text{K,}$$

with the steady-state temperature being a lower limit in the absence of any absorbed power or coupling to a substrate.

7.3.3 Amplified optomechanics: Neutral atom

The friction force in amplified optomechanics, or ring cavity cooling in general, is not dependent on the position of the particle to be cooled. To explore this mechanism, we therefore suggest using neutral atoms. Our atom of choice is ^{85}Rb (mass $m = 1.4 \times 10^{-25}$ kg), which can be Doppler-cooled and confined to a small cloud beforehand. We assume that the pump beam, of wavelength $\lambda = 780$ nm and detuning $\Delta = -10\Gamma$, is focussed down to a 10 μm spot at the position of the atom, and that the power at the input coupler is 13 nW to guarantee operation in the low-saturation regime. The fibre-based cavity is taken to be 300 m long, the power loss at each of the two couplers terminating the cavity is assumed to be 50%, and the input coupler to transmit only 1% of the incident power. A gain medium, with gain 1.75, is assumed to form part of the cavity. We therefore obtain

$$1/e \text{ velocity cooling time: 4 ms, and}$$
$$\text{steady-state temperature: } 40\,\mu\text{K.}$$

7.A   Appendix: Electric fields inside dielectrics

Within a simple model of the dielectric of volume V as a collection of closely spaced dipoles at random positions, its response to an electric field can be embodied entirely in the relative permittivity ϵ, defined by the relation

$$\boldsymbol{\mathcal{P}} = V(\epsilon - 1)\epsilon_0 \boldsymbol{\mathcal{E}} \,, \tag{7.12}$$

The Clausius–Mossotti relation, as quoted in Eq. (7.1), connects the susceptibility χ of the dielectric to the bulk refractive index of the dielectric. Many derivations of this relation (see, for example, Ref. [44, §4.5]) divide the dielectric into two regions: a spherical section of the dielectric, large enough to contain several dipoles but small enough that the polarisation is practically constant within; and the rest of the dielectric. One objection to this argument is that it depends critically on the first region chosen as being spherical, an assertion that has no real physical justification and no immediate connection to the main assumption, mentioned below, present in the Clausius–Mossotti relation. Hannay [188] presented an alternative derivation of this same expression that does not make use of this model. Let us briefly recapitulate Hannay's argument.
The electric field $\boldsymbol{\mathcal{E}}$ produced by an ideal point-like dipole $\boldsymbol{p}$ is, as a function of the displacement $\boldsymbol{r}$ from the dipole,

$$\boldsymbol{\mathcal{E}} = \frac{1}{4\pi\epsilon_0}\left[\frac{3(\boldsymbol{p}\cdot\boldsymbol{r})\boldsymbol{r}}{|\boldsymbol{r}|^5} - \frac{\boldsymbol{p}}{|\boldsymbol{r}|^3}\right] - \frac{\boldsymbol{p}}{3\epsilon_0}\delta(\boldsymbol{r})\,. \tag{7.13}$$

The central assumption that leads to the Clausius–Mossotti equation is that a "test" dipole inserted at a random position in the dielectric experiences an electric field that is free from the influence of the δ-spikes that occur at each of the dipoles making up the dielectric. These δ-spikes, of which there are N, contribute a spatially-averaged field

$$-\frac{N\boldsymbol{p}}{3V\epsilon_0} = -\frac{\boldsymbol{\mathcal{P}}}{3V\epsilon_0}\,, \tag{7.14}$$

defining the macroscopic polarisation of the medium by $\boldsymbol{\mathcal{P}} \equiv N\boldsymbol{p}$. Thus, the field experienced by the test dipole—and, therefore, the field inside the medium—is equal to the "normalised" field

$$\boldsymbol{\mathcal{E}}_{\mathrm{norm}} = \boldsymbol{\mathcal{E}} + \frac{\boldsymbol{\mathcal{P}}}{3V\epsilon_0}\,, \tag{7.15}$$

where $\mathcal{E}$ is the local microscopic spatial average of the electric field that the dielectric is immersed in. Finally, $\mathcal{E}_{\mathrm{norm}}$ is related to $\mathcal{P}$ through the definition of χ [44, §4.5],

$$\mathcal{P} = \epsilon_0 \chi \mathcal{E}_{\mathrm{norm}} = \epsilon_0 \chi \left(\mathcal{E} + \frac{\mathcal{P}}{3V\epsilon_0} \right). \tag{7.16}$$

Thus,

$$\mathcal{P} = V(\epsilon - 1)\epsilon_0 \mathcal{E} = \frac{\epsilon_0 \chi \mathcal{E}}{1 - \chi/(3V)}, \tag{7.17}$$

which can be rearranged to give the Clausius–Mossotti equation:

$$\chi = 3V \frac{\epsilon - 1}{\epsilon + 2}. \tag{7.18}$$

For a particle of volume V made from a typical dielectric with a refractive index $n = 1.5$, $\chi = 0.9V \approx V$. An intuitive understanding of χ is therefore possible as the volume of dielectric that is polarised by an incoming field. It is perhaps interesting to note that this means that each single molecular dipole in the dielectric has an effective susceptibility

$$\chi_{\mathrm{eff}} \approx \frac{4}{3}\pi a^3, \tag{7.19}$$

where $2a$ is the mean distance between the molecules making up the dielectric; $a \sim 10^{-10}$ m is typically several orders of magnitude larger than the molecular radius itself. However, χ_{eff} is of the same order as the susceptibility of a free molecule [189]. In other words, the polarisation of an individual dipole due to an off-resonant electric field is of about the same order whether that dipole is isolated or in a bulk solid.

This χ can be used to calculate the power dissipated by a small dielectric sphere, modelled as a single point dipole, due to blackbody radiation. At a temperature T there are $n_k = 1/\{\exp[\hbar ck/(k_{\mathrm{B}}T)] - 1\}$ photons with a wavevector $\boldsymbol{k}$ and wavenumber k. These photons produce an equivalent electric field of optical power $P_k = \hbar k c^2 n_k \sigma_{\mathrm{L}}/V_{\mathrm{q}}$, V_{q} being the quantisation volume, and therefore lead to an absorbed power due to that mode

$$P_{\mathrm{abs},k} \approx \frac{\hbar k^2 c^2 n_k}{V_{\mathrm{q}}} \operatorname{Im}\{\chi\}, \tag{7.20}$$

for small $|\chi|$. We must now sum over every mode to obtain the total absorbed power $P_{\mathrm{abs}} = \sum_{\boldsymbol{k}} P_{\mathrm{abs},k}$, which quickly becomes cumbersome since the number of modes becomes infinite as the quantisation volume grows indefinitely. By assuming that the
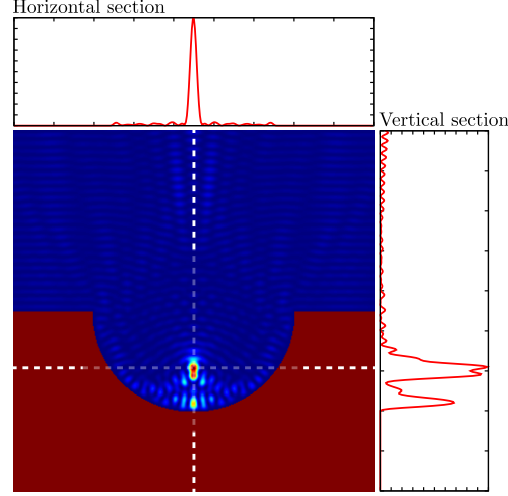
FIGURE 7.5: Finite-difference time-domain analysis of the electric field intensity on a 2D slice of a $10\,\mu\text{m}$ diameter hemispherical void in an ideal metal substrate. The incident field is a linearly polarised plane wave, with a wavelength of $780\,\text{nm}$, propagating downwards. Two sections, both intersecting the focus, are also shown: the vertical (horizontal) section runs along the vertical (horizontal) dashed line.

modes are evenly distributed in $\boldsymbol{k}$-space, with a density $(2\pi)^3/V_{\text{q}}$, we can transform this sum into a three-dimensional integral

$$
\begin{aligned}
P_{\text{abs}} &= \frac{2V_{\text{q}}}{(2\pi)^3} \iiint \frac{\hbar k^2 c^2 n_k}{V_{\text{q}}} \operatorname{Im}\{\chi\} \, \mathrm{d}^3\boldsymbol{k} \\
&= \frac{\hbar c^2}{4\pi^3} \operatorname{Im}\{\chi\} \int_0^{2\pi} \int_0^{\pi} \int_0^{\infty} \frac{k^4}{\exp\left[\hbar c k/(k_{\text{B}}T)\right]-1} \sin(\theta) \, \mathrm{d}k \, \mathrm{d}\theta \, \mathrm{d}\phi \\
&= \frac{24\zeta(5)}{\pi^2 c^3 \hbar^4} \operatorname{Im}\{\chi\} \left(k_{\text{B}}T\right)^5,
\end{aligned}
\tag{7.21}
$$

where the extra factor of 2 accounts for the two polarisations, where χ was assumed to be independent of k, and where $\zeta(5)$ is the Riemann zeta function. The k-integral is performed by appealing to the definition of the $\zeta(z) \equiv \zeta(z,1)$ [99, §9.51]. Our final step is to note that in thermal equilibrium, P_{abs} is equal to the power dissipated by the sphere, P_{diss}.

7.B   Appendix: Calculating the electric field inside hemispherical mirrors

Hemispherical voids templated on gold surfaces are a good system to work with experimentally: once made, they require no further alignment; and regular, close-packed arrays
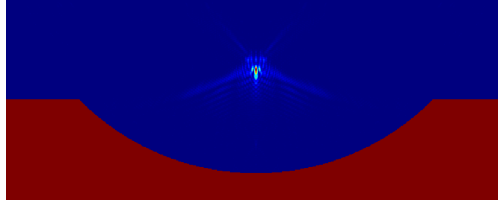
FIGURE 7.6: Electric field intensity inside a 100 μm diameter hemispherical void in an
ideal metal substrate. The size of the hemispherical template and the depth of the void
(15 μm vertically from the bottom to the lip) match the surface in Fig. 7.1.

can be made with several tens (for large diameters) up to several hundreds (for diameters
of the order of 1 μm [190]) of dimples. However, the analysis of the electromagnetic fields
inside the dimples presents a challenge. The most direct route to exploring these fields
is through the numerical solution of Maxwell's equations. A large number of software
packages are available, with several operating either on finite element method (FEM) or
finite-difference time-domain (FDTD) principles or employing Mie theory (see Ref. [191]
for a recent review of such techniques). Analyses of scattering of electromagnetic radi-
ation off spherical particles are usually performed using Mie theory [44], which exploits
the fact that the vector spherical harmonics form a complete orthogonal set of modes on
the sphere. In the case of a hemisphere, however, no such set of modes exists—and the
situation is even worse for truncated hemispheres—and FEM or FDTD techniques are
more desirable. It is interesting to note that this problem can be formally circumvented
in certain situations. For example, the authors of Ref. [181] implicitly assume knowledge
of the field outside the spherical region defined by a perfect truncated hemispherical mir-
ror to explore the behaviour of the vacuum field inside this same spherical region. In
the absence of a compact analytical solution, we use an open-source software package
called MEEP [192] for our analysis.

We show an example of such a simulated field in Fig. 7.5. Close to the geometrical focus
of the dimple, a strong focus is found; the size and peak intensity of this focus can be
used to explore the possibility of producing single- or few-atom dipole traps inside such
cavities. 2D arrays of dipole traps were demonstrated [64] a number of years ago, and
recently used to perform site-selective manipulation of atoms [187]—both these exper-
iments relied on a purpose-built refractive micro-lens array. Using templated surfaces
offers a number of advantages over the micro-lens array, not least ease of manufacture
and the possibility of integration into so-called atom chips [168]; in this regard, the use
of reflective rather than refractive optical elements is of paramount importance.

The dimples in the first surface produced for the experimental investigations in Southampton were not grown to full hemispheres. Rather, latex spheres with a diameter of 100 μm were used and gold was only templated up to a depth of 15 μm. Part of the resulting surface is shown in Fig. 7.1, with the field inside one such dimple simulated in Fig. 7.6. Note that aliasing artifacts are more apparent in this figure than in Fig. 7.5, the reason being that the 0.05 μm resolution possible in the case of the latter was not possible in simulating the larger sample, due to computer memory constraints. In the case of Fig. 7.6, a resolution of 0.17 μm was used. In both cases, the incoming field was a plane wave with a wavelength of $\lambda = 780\,\text{nm}$.

7.C Appendix: Force acting on an atom inside an arbitrary monochromatic field

In a remarkable piece of work dating to 1980, Gordon and Ashkin [52] give several useful expressions for the force and diffusion experienced by an atom inside what they called a 'radiation trap'—essentially an arbitrary (monochromatic) electric field. Implicit in their work is the assumption that the system has no 'memory'; we cannot directly apply their equations to mirror-mediated or external cavity cooling systems, for example. Nonetheless, such a model is perhaps the easiest way of exploring the behaviour of atoms inside fields as complex as those in hemispherical voids on a metal surface. Unfortunately, the authors of Ref. [52] do not give explicit general formulae for the velocity-dependent force acting on an atom; we will now generalise their expressions [specifically, Eqs. (14) and (15)] to the case when the atom is not motionless. Let us first briefly introduce the notation we will use in this section:[4] F is the force acting on the atom; D is the difference in the populations of the upper and lower states; σ is the atomic lowering operator; $\Delta = \omega - \omega_{\text{a}}$, with ω the frequency of the driving field and ω_{a} the atomic resonance frequency; $\gamma = \Gamma - \text{i}\Delta$; $\boldsymbol{\mu}_{21}$ the atomic dipole operator; $\boldsymbol{v}$ the atomic velocity; and $\mathcal{E}e^{-\text{i}\omega t}$ the classical incident electric field. We also define

$$g = \tfrac{\text{i}}{\hbar}\boldsymbol{\mu}_{21} \cdot \mathcal{E}\,, \tag{7.22}$$

---

[4] Our notation will be identical to Ref. [52] wherever possible.

and the saturation parameter $s = 2|g|^2/|\gamma|^2$. It is also convenient to define the vectors $\boldsymbol{\alpha}$ and $\boldsymbol{\beta}$ by $\operatorname{grad} g = (\boldsymbol{\alpha} + \mathrm{i}\boldsymbol{\beta})g$. In practice, numerical simulation gives us knowledge of $\mathcal{E}$, assuming that the perturbation of the atom on the field is quite small. By specifying the magnetic field, we can determine ω_a, and therefore Δ. Given the atomic species, we also know Γ and $\boldsymbol{\mu}_{21}$; knowledge of γ, g, s, $\boldsymbol{\alpha}$, $\boldsymbol{\beta}$ and $\langle\sigma\rangle$ then follows, as we will see. Finally, this determines $\langle F\rangle$, the classical force acting on the atom.

To first order in $\boldsymbol{v}$, we have

$$\langle F\rangle = -\mathrm{i}\hbar\big[\langle\sigma\rangle^*\operatorname{grad} g - \langle\sigma\rangle\operatorname{grad} g^*\big]\,, \tag{7.23}$$

$$\langle\dot\sigma\rangle + \gamma\langle\sigma\rangle = \langle D\rangle g\,, \tag{7.24}$$

$$\langle\dot D\rangle + 2\Gamma\langle D\rangle = 2\Gamma - 2(g^*\langle\sigma\rangle + g\langle\sigma\rangle^*)\,, \tag{7.25}$$

$$\langle\dot D\rangle = -\tfrac{2s}{1+s}(\boldsymbol{v}\cdot\boldsymbol{\alpha})\langle D\rangle\,, \tag{7.26}$$

$$\langle\dot\sigma\rangle = \big[(\boldsymbol{v}\cdot\boldsymbol{\alpha})\tfrac{1-s}{1+s} + \mathrm{i}(\boldsymbol{v}\cdot\boldsymbol{\beta})\big]\langle\sigma\rangle\,, \text{ and} \tag{7.27}$$

$$\dot g = \boldsymbol{v}\cdot(\boldsymbol{\alpha} + \mathrm{i}\boldsymbol{\beta})g\,, \tag{7.28}$$

directly from Ref. [52]. Thus, to the same order,

$$\langle D\rangle = \big[1 - \tfrac{1}{\Gamma}(g^*\langle\sigma\rangle + g\langle\sigma\rangle^*)\big] + \tfrac{1}{\Gamma}\tfrac{s}{1+s}(\boldsymbol{v}\cdot\boldsymbol{\alpha})\big[1 - \tfrac{1}{\Gamma}(g^*\langle\sigma\rangle + g\langle\sigma\rangle^*)\big]\,, \tag{7.29}$$

whereby

$$\langle\sigma\rangle\big[\gamma + (\boldsymbol{v}\cdot\boldsymbol{\alpha})\tfrac{1-s}{1+s} + \mathrm{i}(\boldsymbol{v}\cdot\boldsymbol{\beta})\big] = \big[1 - \tfrac{1}{\Gamma}(g^*\langle\sigma\rangle + g\langle\sigma\rangle^*)\big]g$$
$$+ \tfrac{1}{\Gamma}\tfrac{s}{1+s}(\boldsymbol{v}\cdot\boldsymbol{\alpha})\big[1 - \tfrac{1}{\Gamma}(g^*\langle\sigma\rangle + g\langle\sigma\rangle^*)\big]\,. \tag{7.30}$$

We can solve this for $\langle\sigma\rangle$ to obtain

$$\langle\sigma\rangle = \frac{g}{\gamma(1+s)} + \frac{g}{|\gamma|^2(1+s)}\big(\tfrac{1}{2\Gamma}\gamma^* + \tfrac{1-s}{1+s}\big)(\boldsymbol{v}\cdot\boldsymbol{\alpha})$$
$$- 2\big[\Gamma(1-s) + \tfrac{1}{\Gamma}|g|^2\big]\frac{g}{\gamma|\gamma|^2(1+s)^3}(\boldsymbol{v}\cdot\boldsymbol{\alpha})$$
$$+ \frac{[2\Delta - \mathrm{i}\gamma(1+s)]g}{\gamma|\gamma|^2(1+s)^2}(\boldsymbol{v}\cdot\boldsymbol{\beta})\,, \tag{7.31}$$

which we can plug into Eq. (7.23), together with g, to obtain the (velocity-dependent) force acting on the atom.

Conclusions and outlook

Cold atom experiments have progressed significantly over the 25 years since the first cold atoms were observed in optical molasses. Increasingly, research is focussing more and more towards the use of cold atoms in applications such as sensing, metrology and information processing. This trend has made it ever more important to find means of cooling more general species of atoms and molecules; current methods are simply too species-selective. Throughout the course of this thesis I have shown how the retarded dipole–dipole interaction can be used to achieve this aim; by investing the dipole force with a non-conservative nature, one can transfer energy from a moving polarisable particle to or from the light field—the nature of the particle itself is largely irrelevant. Several key theoretical results were reported in this thesis; these are summarised below:

- By introducing a time delay, in a very general sense, into an optical system, one can endow the dipole interaction with a non-conservative nature.

- This delayed dipole–dipole interaction is a very general mechanism and applies to anything that is acted upon by the dipole force.

- In order to explore these interactions, we devised an extended formalism based on the transfer matrix method and applied it successfully to various cooling schemes.

- The prototypical mirror-mediated cooling mechanism was explored in great detail and its shortcomings addressed through external cavity cooling and amplified optomechanics.

- Apart from rendering the exploration of the above cooling mechanisms possible, the formalisms we extended also naturally lead to the unification of cooling mechanisms for atomic motion, and optomechanical cooling mechanisms for micromirror vibrations.

The basis for an experimental investigation of these cooling mechanisms was also laid in the latter parts of this thesis, the main results of which are

- an experimental apparatus that simplifies the investigation of the interactions between atoms and surfaces structured on the nano- or micro-scale;

- a multi-level imaging system for exploring cold atom clouds near highly reflective and highly scattering surfaces; and

- the exploration of a number of physical configurations that promise experimentally-observable effects under realisable conditions.

Work is currently underway to better understand the nature of the retarded dipole–dipole interaction in three dimensions and in a more general geometric setting; it is hoped that this understanding will greatly facilitate the production of systems, perhaps of an integrated nature, that can be tailored to generate cold samples of any arbitrary species. Such systems would revolutionise sensing and metrology applications and also provide an unprecedented means of interfacing with the quantum nature of matter at the micro- and mesoscopic scales.

Several questions are raised by the work in this thesis that are as yet unanswered, but which can form the basis of theoretical work in the future, are:

- Can the vectorial electromagnetic field inside a possibly truncated, micro- or mesoscopic, hemispherical mirror be expressed succinctly? Small hemispherical mirrors violate the approximations usually assumed in optics, namely the paraxial and ray approximations. The resulting behaviour of the electric field inside such deeply curved surfaces is very intricate. Some work has been done using scattering theories (see, for example, Refs. [193] and [194]), but these theories lead to numerically-intensive computations and do not give the insight required to explore the system from the point of view of the retarded dipole–dipole interaction.

- A natural generalisation of the transfer matrix method for static scatterers in three dimensions is the scattering matrix theory; can this latter theoretical framework be extended to account for the motion of scatterers? The transfer matrix method explored in this thesis provides a very general formalism for exploring light–matter

interactions. It is, however, limited to systems that are inherently in one dimension, systems that can be reduced to one dimension (such as ring cavities), or systems interacting with an electric field that can be described in terms of plane waves along orthogonal dimensions. Systems such as colloidal crystals in two or three dimensions cannot be explored using the matrix theory described in this thesis, and yet potentially present highly interesting dynamics mediated by light.

- The transfer matrix approach presented is based on the assumption of a quasi-static system. Within such a framework, the motion of any scatterer must be slow enough for the system to reach optical steady-state at every point. Thus, any motion must be slow on the timescale defined by the decay lifetime of any cavity interacting with the scatterer. This condition specifically rules out operation in the so-called 'resolved sideband' regime which, in the case of both micromirrors [82] and ions [195], has been shown to lead to the most efficient cooling processes. In particular, it is not yet known whether the external cavity cooling mechanism would be as effective in this regime.

Part IV

Appendices:

PUBLICATIONS

&

TALKS

Appendix A

Publications

Wherever published work was used in this thesis, this was clearly indicated. The following is a complete list of my work published in peer–reviewed journals or on preprint archives, in chronological order. Preprints of the peer-reviewed publications, marked with a '⋆' in the following list, that are most relevant to this thesis are then reproduced in the same order over the following several pages.

A.1   Peer-reviewed journal articles

⋆ 2009 **André Xuereb**, Peter Domokos, Janos Asbóth, Peter Horak, and Tim Freegarde; *Scattering theory of heating and cooling in optomechanical systems*; Phys. Rev. A **79**, 053810 (2009); `arXiv:0903.3132`. Given a synopsis in the APS journal *Physics* and mentioned in the Research Highlights section of Nature Photonics **3**, 7 (2009)

⋆ 2009 **André Xuereb**, Peter Horak, and Tim Freegarde; *Atom cooling using the dipole force of a single retroreflected laser beam*; Phys. Rev. A **80**, 013836 (2009); `arXiv:0903.2945`

⋆ 2009 Hamid Ohadi, Matthew Himsworth, **André Xuereb**, and Tim Freegarde; *Magneto-optical trapping and background-free imaging for atoms near nanostructured surfaces*; Opt. Express **17**, 25, 23003 (2009); `arXiv:0910.5003`

2010 **André Xuereb**, Mathias Groth, Karl Krieger, Otto Asunta, Taina Kurki-Suonio, Jari Likonen, David P Coster, ASDEX Upgrade Team; *DIVIMP-B2-EIRENE modelling of ^{13}C migration and deposition in ASDEX Upgrade L-mode plasmas*; J. Nucl. Mater. **396**, 2–3, 228 (2010). Based on work done whilst on an IAESTE traineeship at the

Helsinki University of Technology (TKK), July–August 2006

⋆ ₂₀₁₀ James Bateman, **André Xuereb**, and Tim Freegarde; *Stimulated Raman transitions via multiple atomic levels*; Phys. Rev. A **81**, 043808 (2010); `arXiv:0908.2389`

⋆ ₂₀₁₀ **André Xuereb**, Tim Freegarde, Peter Horak and Peter Domokos; *Optomechanical cooling with generalized interferometers*; Phys. Rev. Lett. **105**, 013602 (2010); `arXiv:1002.0463`

₂₀₁₀ James Bateman, Richard Murray, Matthew Himsworth, Hamid Ohadi, **André Xuereb**, and Tim Freegarde; *Hänsch–Couillaud locking of Mach–Zehnder interferometer for carrier removal from a phase-modulated optical spectrum*; J. Opt. Soc. Am. B **27**, 1530 (2010); `arXiv:0911.1695`

⋆ ₂₀₁₀ Peter Horak, **André Xuereb**, and Tim Freegarde; *Optical cooling of atoms in microtraps by time–delayed reflection*; J. Comput. Theor. Nanosci. **7**, 1747 (2010); `arXiv:0911.4805`

⋆ ₂₀₁₀ **André Xuereb**, Peter Domokos, Peter Horak, and Tim Freegarde; *Scattering theory of multilevel atoms interacting with arbitrary radiation fields*; Phys. Scr. **T140**, 014010 (2010); `arXiv:0910.0802`

⋆ ɪɴ ᴘʀᴇss **André Xuereb**, Peter Horak, and Tim Freegarde; *Amplified optomechanics in a unidirectional ring cavity*; to appear in J. Mod. Opt.; `arXiv:1101.0130`

⋆ ɪɴ ᴘʀᴇss **André Xuereb**, Peter Domokos, Peter Horak, and Tim Freegarde; *Cavity cooling of atoms: Within and without a cavity*; to appear in Eur. Phys. J. D; `arXiv:1101.2739`

A.2 Conference proceedings

₂₀₁₁ Peter Domokos, **André Xuereb**, Peter Horak, and Tim Freegarde; *Efficient optomechanical cooling in one-dimensional interferometers*; presented at SPIE Photonics West 2011 (invited contribution)

Scattering theory of cooling and heating in opto-mechanical systems

André Xuereb,[1, *] Peter Domokos,[2] János Asbóth,[2, 3] Peter Horak,[4] and Tim Freegarde[1]

[1]*School of Physics and Astronomy, University of Southampton, Southampton SO17 1BJ, United Kingdom*
[2]*Research Institute of Solid State Physics and Optics,*
Hungarian Academy of Sciences, H-1525 Budapest P.O. Box 49, Hungary
[3]*Leiden Institute of Physics, NL 2300 RA Leiden, P.O. Box 9504, The Netherlands*
[4]*Optoelectronics Research Centre, University of Southampton, Southampton SO17 1BJ, United Kingdom*
(Dated: April 9, 2009)

We present a one-dimensional scattering theory which enables us to describe a wealth of effects arising from the coupling of the motional degree of freedom of scatterers to the electromagnetic field. Multiple scattering to all orders is taken into account. The theory is applied to describe the scheme of a Fabry-Perot resonator with one of its mirrors moving. The friction force, as well as the diffusion, acting on the moving mirror is derived. In the limit of a small reflection coefficient, the same model provides for the description of the mechanical effect of light on an atom moving in front of a mirror.

I. INTRODUCTION

The use of light forces to manipulate mechanical motion has been extended by now from the translational motion of single atoms [1, 2] to the motional modes of massive systems, such as the oscillations of a micromechanical mirror [3, 4, 5]. The theoretical approach to describe the mechanical effect of light on the center-of-mass motion of atoms is completely distinct from the models dealing with vibrating optical resonators. In the first case, theories are based on the assumption that atoms are very weak scatterers in free space, negligibly perturbing the impinging bright laser beams [6]. In the other case, the influence of the moving massive component on the radiation field is so strong that it is considered a (moving) boundary condition defining a single or a few modes of the field participating in the opto-mechanical coupling [7, 8]. This is clearly the case for a Fabry-Perot type resonator with one of its mirrors moving [9, 10, 11]. We argue that these two cases can be dealt with as two extremes of a general system that can be described in a unified theoretical framework.

In this paper we develop and present a scattering theory for opto-mechanically coupled systems, allowing for the efficient description of the motion of arbitrary combinations of atoms and mirrors interacting through the radiation field. We will restrict the model to one-dimensional motion and small velocities. The main building block is the beamsplitter transfer matrix [12, 13], *i.e.*, the *local relation* between light field amplitudes at the two sides of a scatterer. We will calculate the radiation force acting on a moving scatterer up to linear order in the velocity. The model is completed by including the quantum fluctuations of the radiation force which stem

from the quantized nature of the field. We will determine the momentum diffusion coefficient corresponding to the minimum quantum noise level.

The system we will consider in some detail is composed of two mirrors; one of them is fixed in space, whilst the other one is mobile. This is the generic scheme for radiation-pressure cooling of moving mirrors [14, 15, 16]. At the same time, in the limit of low reflection the moving mirror can equally well represent a single atomic dipole interacting with its mirror image in front of a highly reflecting surface [17, 18, 19]. The scattering model description of this example gives a clear recipe for generalizing the method to more complex systems.

II. MODEL
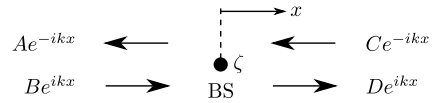
FIG. 1: The four different modes that interact through a point-like beamsplitter in 1D.

Consider a point-like scatterer (or beamsplitter), BS, moving along the 'x' axis on the trajectory $x_{\text{BS}}(t)$. Outside the scatterer, the electric field $\boldsymbol{E}$ can be expressed in terms of a discrete sum of left- and right-propagating plane wave modes with different wave numbers, k, and hence different frequencies, $\omega = kc$:

$$\boldsymbol{E} = \begin{cases} \sum_k \left[A(k)e^{-ikx-i\omega t} + B(k)e^{ikx-i\omega t} \right] + \text{c.c.} \\ \sum_k \left[C(k)e^{-ikx-i\omega t} + D(k)e^{ikx-i\omega t} \right] + \text{c.c.}, \end{cases}$$

$$(1)$$

where $A(k)$ and $B(k)$ are the mode amplitudes on the left side, $x < x_{\text{BS}}(t)$, while $C(k)$ and $D(k)$ are the amplitudes on the right side, $x > x_{\text{BS}}(t)$, of BS. This is a simplifying

assumption and all our results also hold for a continuum of field modes. In accordance, the magnetic field is [20]

$$c\boldsymbol{B} = \begin{cases} \sum_k \left[-A(k)e^{-ikx-i\omega t} + B(k)e^{ikx-i\omega t} \right] + \text{c.c.} \\ \sum_k \left[-C(k)e^{-ikx-i\omega t} + D(k)e^{ikx-i\omega t} \right] + \text{c.c.} \, . \end{cases} \tag{2}$$

As depicted schematically in Fig. 1, the scatterer mixes these waves. Our first goal is the derivation of the transverse matrix M connecting the field amplitudes on the right to those on the left side of a beamsplitter moving at a fixed velocity v. This relation is well-known [12] for an immobile scatterer. Therefore, let us first transform the electromagnetic field into a frame moving with the instantaneous velocity v of the BS.

A. Transfer matrix for an immobile beamsplitter

In the frame co-moving with BS, the interaction of the field with the scatterer at $x' = 0$ can be characterized by the single parameter ζ by means of the one dimensional wave equation [12, 20],

$$\left(\partial_{x'}^2 - \frac{1}{c^2} \partial_{t'}^2 \right) \boldsymbol{E}'(x', t') = \frac{2}{kc^2} \zeta \, \delta(x') \, \partial_{t'}^2 \boldsymbol{E}'(x', t') \, .$$

The electric field can be considered in a modal decomposition similar to Eq. (1). Since a fixed beamsplitter couples only the plane waves with identical frequency and wave number, the stationary scattering can be fully described within the closed set of modes

$$\boldsymbol{E}'(x', t') = \begin{cases} A'e^{-ikx'-i\omega t'} + B'e^{ikx'-i\omega t'} + \text{c.c.} & x' < 0 \\ C'e^{-ikx'-i\omega t'} + D'e^{ikx'-i\omega t'} + \text{c.c.} & x' > 0 \, , \end{cases}$$

where the index k has been dropped. A linear relation between the field amplitudes on the right of the scatterer and those on the left can be derived from the wave equation,

$$\begin{pmatrix} C' \\ D' \end{pmatrix} = M_0 \begin{pmatrix} A' \\ B' \end{pmatrix} \, , \text{ with} \tag{3}$$

$$M_0 = \begin{bmatrix} 1 - i\zeta & -i\zeta \\ i\zeta & 1 + i\zeta \end{bmatrix} = \frac{1}{\mathfrak{t}} \begin{bmatrix} 1 & -\mathfrak{r} \\ \mathfrak{r} & \mathfrak{t}^2 - \mathfrak{r}^2 \end{bmatrix} \, . \tag{4}$$

In the second form of the transfer matrix M_0, we expressed it in terms of the reflectivity $\mathfrak{r}$ and transmissivity $\mathfrak{t}$ of the beamsplitter. This latter form is more convenient to describe moving mirrors, while for atoms the scattering strength parameter ζ can be readily expressed in terms of the polarizability [12],

$$\zeta = \frac{\pi\alpha}{\epsilon_0 \lambda S} \, ,$$

where α is the linear polarizability and S is the effective beam cross section. For a two-level, unsaturated atom

with transition frequency ω_A and linewidth Γ (HWHM), for example,

$$\zeta = \frac{\sigma_A}{2S} \frac{\Gamma}{\omega_A - \omega - i\Gamma} \, , \tag{5}$$

where $\sigma_A = \frac{3\lambda^2}{2\pi}$ is the resonant radiative cross section of an atom. In this case the transfer matrix depends on the wave number k, which might lead to essential effects, e.g., Doppler cooling, close to resonance with the atom (see Section II E).

B. Transfer matrix for a moving beamsplitter

The transformation back into the laboratory-fixed frame involves the change of the coordinates, $x' = x - vt$ and $t' = t$, and the Lorentz-boost of the electric field up to linear order in v/c [20, §11.10]:

$$\boldsymbol{E} = \boldsymbol{E}' + v\boldsymbol{B}' \, ,$$

where we assumed that $\boldsymbol{E}$ and $\boldsymbol{E}'$ are polarized in the 'y' direction, $\boldsymbol{B}$ and $\boldsymbol{B}'$ are polarized in the 'z' direction, and the velocity is along the x axis. The electric field in the laboratory frame becomes

$$\boldsymbol{E}(x, t) = \sum_{k'} \Bigg\{ A'(k')e^{-ik'(x-vt)-i\omega' t} + B'(k')e^{ik'(x-vt)-i\omega' t}$$

$$- \frac{v}{c} \Big[A'(k')e^{-ik'(x-vt)-i\omega' t} - B'(k')e^{ik'(x-vt)-i\omega' t} \Big] \Bigg\} + \text{c.c.}$$

$$= \sum_k \left(1 - \frac{v}{c} \right) A' \left(k + kv/c \right) e^{-ik(1+v/c)x - i\omega t}$$

$$+ \left(1 + \frac{v}{c} \right) B' \left(k - kv/c \right) e^{ik(1-v/c)x - i\omega t} \, ,$$

which can be expressed as a linear transformation $\hat{L}(v)$ of the amplitudes,

$$\begin{pmatrix} A(k) \\ B(k) \end{pmatrix} = \hat{L}(-v) \begin{pmatrix} A'(k) \\ B'(k) \end{pmatrix} \, , \text{ with}$$

$$\hat{L}(v) = \begin{bmatrix} \left(1 + \frac{v}{c} \right) \hat{P}_{-v} & 0 \\ 0 & \left(1 - \frac{v}{c} \right) \hat{P}_v \end{bmatrix} \, .$$

This construction is explored further in Appendix A. Here we defined the operator $\hat{P}_v : f(k) \mapsto f \left(k + k\frac{v}{c} \right)$, which represents the Doppler-shift of the plane waves in a moving frame. Obviously, $\hat{L}^{-1}(v) = \hat{L}(-v)$ to first order in $\frac{v}{c}$. The total action of the moving BS,

$$\begin{pmatrix} C(k) \\ D(k) \end{pmatrix} = \hat{M} \begin{pmatrix} A(k) \\ B(k) \end{pmatrix} \, , \tag{6}$$

can then be obtained from

$$\hat{M} = \hat{L}(-v) M_0 \hat{L}(v) \tag{7}$$

$$= \frac{1}{\mathfrak{t}} \begin{bmatrix} 1 & -(1 - 2\frac{v}{c})\mathfrak{r}\hat{P}_{2v} \\ (1 + 2\frac{v}{c})\mathfrak{r}\hat{P}_{-2v} & \mathfrak{t}^2 - \mathfrak{r}^2 \end{bmatrix} \, ,$$

where we have assumed that $\mathfrak{r}$ and $\mathfrak{t}$ do not depend on the wave number.

Compared to M_0 in Eq. (4), the difference lies in the off-diagonal terms including the Doppler-shift imposed by the reflection on a moving mirror. In other words, the coupled counter-propagating plane wave modes differ in wave numbers, i.e., $k\left(1 + \frac{v}{c}\right)$ right-propagating waves couple to $-k\left(1 - \frac{v}{c}\right)$ left-propagating waves. Furthermore, if the polarizability itself depends on the wave number k, e.g., as in Eq. (5), the Doppler-shift operator acts also on it. To make this effect explicit, to linear order in $\frac{v}{c}$, $\hat{M}$ can be written as

$$\begin{bmatrix} 1 - i\zeta - i\frac{v}{c}\omega\frac{\partial\zeta}{\partial\omega} & -i\zeta\left[1 - \frac{v}{c}\left(2 - \frac{\omega}{\zeta}\frac{\partial\zeta}{\partial\omega}\right)\right]\hat{P}_{2v} \\ i\zeta\left[1 + \frac{v}{c}\left(2 - \frac{\omega}{\zeta}\frac{\partial\zeta}{\partial\omega}\right)\right]\hat{P}_{-2v} & 1 + i\zeta - i\frac{v}{c}\omega\frac{\partial\zeta}{\partial\omega} \end{bmatrix}.$$

The transfer matrix in the laboratory frame can thus be conceived as a 2-by-2 supermatrix acting also in the k-space. The amplitude C at a given wave number k, i.e., $C(k)$, is combined with the amplitudes $A(k)$ and $B\left(k - 2k\frac{v}{c}\right)$. A similar statement holds for $D(k)$.

Starting from the knowledge of the incoming field amplitudes, this transfer matrix allows for calculating the total electromagnetic field around a beamsplitter moving with a fixed velocity. In the next step, we derive the force on the moving scatterer through the Maxwell stress tensor.

C. Force on a medium in an electromagnetic field

The Maxwell stress tensor (see [20, §6.7]) is defined, for a homogeneous medium in one dimension, x, as

$$\boldsymbol{T} = -\frac{\epsilon_0}{2}\left(|\boldsymbol{E}|^2 + c^2|\boldsymbol{B}|^2\right),$$

where the electric field $\boldsymbol{E}$ and the magnetic field $\boldsymbol{B}$, Eq. (1) and Eq. (2), respectively, have no components along x. It is trivial, then, to see that after applying the rotating wave approximation, we obtain

$$\boldsymbol{T}_{xx} = -2\epsilon_0\left[\left|\sum_k A(k)e^{-ikx-i\omega t}\right|^2 + \left|\sum_k B(k)e^{ikx-i\omega t}\right|^2\right],$$

since the cross terms in $|\boldsymbol{E}|^2$ and $|\boldsymbol{B}|^2$ have opposite signs. Note that $\boldsymbol{T}$ varies on time scales of the order of the optical period. Let us now introduce a characteristic time, τ, over which the variations in $\boldsymbol{T}$ will be averaged. At $x = 0$,

$$\frac{1}{\tau}\int_0^\tau \left|\sum_k A(k)e^{-i\omega t}\right|^2 \mathrm{d}t$$
$$= \sum_k |A(k)|^2 + \sum_{i\neq j}\frac{1}{\tau}\int_0^\tau A(k_i)\left[A(k_j)\right]^\star e^{-i(\omega_i-\omega_j)t}\,\mathrm{d}t$$
$$\approx \sum_k |A(k)|^2 + \sum_{i\neq j} A(k_i)\left[A(k_j)\right]^\star = \left|\sum_k A(k)\right|^2.$$

In the approximation we assumed that the frequency bandwidth of the excited modes, $\Delta = \max\{\omega_i - \omega_j\}$, around the central frequency, ω_0, is so narrow that $\Delta\tau \ll 2\pi$. Since the broadening is due to the Doppler-shift, $\Delta \sim 2\omega_0\frac{v}{c}$, where v is the speed of the beamsplitter. For example, taking v to be the typical speed of atoms in a magneto-optical trap, we require $\tau \ll \pi/\left(\omega_0\frac{v}{c}\right) \sim 10^{-4}$ s. The time needed to reach the stationary regime of scattering is typically much shorter and thus this condition imposed on the averaging time τ can be safely fulfilled.

The force on the medium is given by the surface integral of $\boldsymbol{T}$ on the surface, $\mathcal{S}$, of a fictitious volume $V = S\,\delta l$ enclosing the medium, where S is the mode area and δl the infinitesimal length of the volume along the 'x' axis. Then, this force is given by

$$\boldsymbol{F} = \oint_\mathcal{S} \boldsymbol{T}_{xx} n_x\,\mathrm{d}\mathcal{S}$$
$$= S\left[\boldsymbol{T}_{xx}(x \to 0^+) - \boldsymbol{T}_{xx}(x \to 0^-)\right], \qquad (8)$$

where $n_x = \mathrm{sgn}(x)$ is the normal to $\mathcal{S}$. Substituting the relevant expressions for $\boldsymbol{T}$ into the preceding formula gives

$$\boldsymbol{F} = \frac{\hbar\omega}{c}\left(|A|^2 + |B|^2 - |C|^2 - |D|^2\right), \qquad (9)$$

where $A = [\hbar\omega/(2S\epsilon_0 c)]^{-1/2}\sum_k A(k)$ is the photo-current amplitude, and similarly for B, C and D, their modulus square giving the number of photons crossing a unit surface per unit time. Although we considered first the electric field composed of independent modes, in the force expression only the sums of the mode amplitudes occur.

D. Quantum fluctuations of the force

In the previous subsection the force was derived based on the assumption that the field amplitudes are c-numbers. In order to describe the inherent quantum fluctuations of the force, we need to resort to the quantum theory of fields and represent the mode amplitudes by operators: $A(k) \to \hat{A}(k)$. To leading order the fluctuations of the force acting on a beamsplitter amount to a momentum diffusion process [21, 22]. The diffusion coefficient will be evaluated in the following in the minimum, quantum noise limit, which occurs in the case of coherent-state fields [23].

The diffusion coefficient can be deduced from the second-order correlation function of the force operator [24, 25]

$$\left\langle \hat{\boldsymbol{F}}(t)\hat{\boldsymbol{F}}(t')\right\rangle - \left\langle \hat{\boldsymbol{F}}(t)\right\rangle^2 = \boldsymbol{D}(t)\delta(t - t'). \qquad (10)$$

The evaluation of this quantum correlation is system specific. Quantum correlations, i.e., the operator algebra of the mode amplitudes $\hat{A}(k)$, $\hat{B}(k)$, $\hat{C}(k)$, and $\hat{D}(k)$, are influenced by multiple scattering and thus depend on the

total transfer matrix of the entire system. The simplest case is a single beam splitter where the "input" modes $\hat{B}(k)$ and $\hat{C}(k)$ have independent fluctuations. The calculation, delegated to Appendix B, includes all the steps needed for the treatment of a general system. The diffusion coefficient for a single beamsplitter is obtained as

$$
\begin{aligned}
\boldsymbol{D} = (\hbar k)^2 \Big(&|A|^2 + |B|^2 + |C|^2 + |D|^2 \\
&+ 2\,\mathrm{Re}\{\mathfrak{r}A^*B - \mathfrak{t}A^*C\} \\
&+ 2\,\mathrm{Re}\{\mathfrak{r}D^*C - \mathfrak{t}D^*B\}\Big), \quad (11)
\end{aligned}
$$

where A, B, C, D are the photo-current amplitudes (their modulus square is of the units of 1/sec), obeying Eq. (6) for $v = 0$.

As an example, let us consider the diffusion coefficient for a two-level atom illuminated by counter-propagating monochromatic light waves. Using the polarizability ζ, the transmission and reflection coefficients can be expressed as $\mathfrak{t} = 1/(1 - i\zeta)$ and $\mathfrak{r} = i\zeta/(1 - i\zeta)$, respectively (see Eq. (4)). Eq. (11) can then be rewritten in the form

$$
\boldsymbol{D} = (\hbar k)^2 \left[\frac{2\,\mathrm{Im}\{\zeta\}}{|1 - i\zeta|^2} |B - C|^2 + \frac{4|\zeta|^2}{|1 - i\zeta|^2} \left(|B|^2 + |C|^2 \right) \right], \tag{12}
$$

where the first term, apart from the factor $|1 - i\zeta|^2$, corresponds to the result well-known from laser cooling theory, as shown in the next section. Note that the diffusion process due to the recoil accompanying the spontaneous emission of a photon (see [25]) is missing from this result—the detailed modeling of absorption, *i.e.*, scattering photons into the three dimensional space, is not included in our approach.

E. Example: Force on a moving beamsplitter

We will now use Eq. (9) to derive a general expression for the force on a moving beamsplitter illuminated by two counterpropagating, monochromatic, plane waves with amplitudes B_0 and C_0. On using Eq. (6) to express the outgoing field modes in terms of the incoming ones, we note that the outgoing amplitudes comprise two monochromatic terms each:

$$
A = \frac{i\zeta \left[1 - \frac{v}{c}\left(2 - \frac{\omega}{\zeta}\frac{\partial\zeta}{\partial\omega} \right) \right] B_0 + C_0}{1 - i\zeta \left(1 + \frac{v}{c}\frac{\omega}{\zeta}\frac{\partial\zeta}{\partial\omega} \right)},
$$

and

$$
D = \frac{\left(1 - 2i\frac{v}{c}\omega\frac{\partial\zeta}{\partial\omega} \right) B_0 + i\zeta \left[1 + \frac{v}{c}\left(2 - \frac{\omega}{\zeta}\frac{\partial\zeta}{\partial\omega} \right) \right] C_0}{1 - i\zeta \left(1 + \frac{v}{c}\frac{\omega}{\zeta}\frac{\partial\zeta}{\partial\omega} \right)}.
$$

These relations are substituted into Eq. (9), giving

$$
\begin{aligned}
\boldsymbol{F} = &\left\{ 2\frac{\hbar\omega}{c} \Big/ \left| 1 - i\zeta\left(1 + \frac{v}{c}\frac{\omega}{\zeta}\frac{\partial\zeta}{\partial\omega}\right) \right|^2 \right\} \\
&\times \Bigg\{ \left(\mathrm{Im}\{\zeta\} + |\zeta|^2 + \tfrac{1}{2}\frac{v}{c}\omega\frac{\partial|\zeta|^2}{\partial\omega} \right) \left(|B_0|^2 - |C_0|^2 \right) \\
&\quad - \frac{v}{c}\left(\omega\frac{\partial\,\mathrm{Im}\{\zeta\}}{\partial\omega} - \tfrac{1}{2}\omega\frac{\partial|\zeta|^2}{\partial\omega} + 2|\zeta|^2 \right) \left(|B_0|^2 + |C_0|^2 \right) \\
&\quad + 2\left(\frac{v}{c}\omega\,\mathrm{Im}\left\{ \zeta^\star\frac{\partial\zeta}{\partial\omega} \right\} - \mathrm{Re}\{\zeta\} \right) \mathrm{Im}\{B_0 C_0^\star\} \\
&\quad + 2\frac{v}{c}\left(2\,\mathrm{Im}\{\zeta\} - \omega\frac{\partial\,\mathrm{Im}\{\zeta\}}{\partial\omega} + \tfrac{1}{2}\omega\frac{\partial|\zeta|^2}{\partial\omega} \right) \mathrm{Re}\{B_0 C_0^\star\} \Bigg\}.
\end{aligned}
\tag{13}
$$

For $v = 0$ this result reduces to the one in [13]. Most of the v-dependent terms arise from the frequency-dependence of the polarisability. These are the dominant terms in the case of a quasi-resonant excitation of a resonant scatterer, such as a two-level atom, since the prefactor $\frac{\omega}{\zeta}\frac{\partial\zeta}{\partial\omega} \sim \frac{\omega}{\Gamma}$ expresses resonant enhancement. The v-dependent terms linear in the polarizability ζ are in perfect agreement with the friction forces known from standard laser cooling theory, both for propagating and for standing waves. For example, assuming identical laser powers from the two sides, giving a standing wave with wavenumber k_0, and averaging spatially gives

$$
\boldsymbol{F} = -4\hbar k_0^2 |B_0|^2 \,\mathrm{Im}\left\{ \frac{\partial\zeta}{\partial\omega} \right\} v, \tag{14}
$$

for small $|\zeta|$ and to first order in $\frac{v}{c}$, which can be immediately recognized as the friction force in ordinary Doppler cooling [6] when one uses the definition of ζ in Eq. (5). Finally, by making similar substitutions into Eq. (12), we obtain

$$
\boldsymbol{D} = 8(\hbar k_0)^2 \,\mathrm{Im}\{\zeta\} |B_0|^2 \sin^2(k_0 x), \tag{15}
$$

which, excluding the diffusion effects due to spontaneous emission, matches the standard result in [25]. Note, however, that the scattering theory leads to a more general result which is represented by the terms of higher order in ζ. These terms describe the back-action of the scatterer on the field, an effect neglected in free-space laser cooling theory.

The general result in Eq. (13) reveals that this velocity-dependent force also acts on a scatterer whose polarisability is independent of the frequency. This is a very general class and we will only focus on such scatterers in the following.

III. GENERAL SYSTEM OF A FIXED AND A MOBILE SCATTERER

Consider the model in Fig. 2 where the scatterer, or 'atom', has a polarizability ζ uniform over the frequency range of interest. Letting M_a, M_p and M_m be the transfer
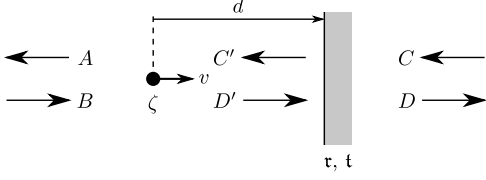
FIG. 2: Physical parameters of our model. A, B, etc. represent the field mode amplitudes.

matrices for the atom, propagation and mirror, respectively, we obtain the relation:

$$\begin{pmatrix} A(k) \\ B(k) \end{pmatrix} = M_{\mathrm{a}} M_{\mathrm{p}} M_{\mathrm{m}} \begin{pmatrix} C(k) \\ D(k) \end{pmatrix} , \text{ where}$$

$$M_{\mathrm{a}} = \begin{bmatrix} 1 + i\zeta & i\zeta\left(1 - 2\frac{v}{c}\right)\hat{P}_{2v} \\ -i\zeta\left(1 + 2\frac{v}{c}\right)\hat{P}_{-2v} & 1 - i\zeta \end{bmatrix}$$
$$= \begin{bmatrix} M_{11} & M_{12}\hat{P}_{2v} \\ M_{21}\hat{P}_{-2v} & M_{22} \end{bmatrix} ,$$

$$M_{\mathrm{p}} = \begin{bmatrix} e^{ikd} & 0 \\ 0 & e^{-ikd} \end{bmatrix}, \text{ and } M_{\mathrm{m}} = \frac{1}{\mathfrak{t}}\begin{bmatrix} \mathfrak{t}^2 - \mathfrak{r}^2 & \mathfrak{r} \\ -\mathfrak{r} & 1 \end{bmatrix} .$$

The distance between the atom and the mirror is denoted by d. Note that the free propagation transfer matrix M_p is non-uniform in the k-space, and therefore the Doppler-shift has an influence on the phase shift accumulated between two scattering events.

The boundary condition is set as follows. Since there is no incoming field from the right, $C(k) = 0$ for all k. The incoming field from the left is assumed to be monochromatic, $B(k) = \mathcal{B}\delta(k - k_0)$, with k_0 being the pump wavenumber. The resulting field comprises modes with wavenumbers in a narrow region around k_0. In the laboratory frame the field mode $A(k)$ interacts with $B(k - 2k\frac{v}{c})$ and $C'(k)$ through the Doppler-shift, and similarly for $D'(k)$. From $C(k) = 0$ it directly follows that

$$A(k) = \left[\mathfrak{r}M_{11}e^{ikd} + M_{12}\hat{P}_{2v}e^{-ikd}\right]$$
$$\times \left[\mathfrak{r}M_{21}\hat{P}_{-2v}e^{ikd} + M_{22}e^{-ikd}\right]^{-1}B(k)$$
$$= \frac{1}{M_{22}}\left[\mathfrak{r}M_{11}e^{ikd} + M_{12}\hat{P}_{2v}e^{-ikd}\right]e^{ikd}$$
$$\times \sum_{n=0}^{\infty}\left(-\mathfrak{r}\frac{M_{21}}{M_{22}}\right)^n e^{2inkd[1-(n+1)\frac{v}{c}]}$$
$$\times B\left(k - 2nk\frac{v}{c}\right) . \quad (16)$$

We will need the sum of amplitudes, $\mathcal{A} = \int A(k)\,\mathrm{d}k/\mathcal{B}$, defined relative to the incoming amplitude $\mathcal{B} = \int B(k)dk$. Note that $\int \hat{P}_v f(k)\,\mathrm{d}k = \int f(k)\,\mathrm{d}k$. Thus,

to first order in $\frac{v}{c}$,

$$\mathcal{A} = \frac{M_{12}}{M_{22}} + \left(\frac{M_{12}}{M_{22}} - \frac{M_{11}}{M_{21}}\right)$$
$$\times \sum_{n=1}^{\infty}\left(-\mathfrak{r}\frac{M_{21}}{M_{22}}\right)^n \left[1 + 2in(n-1)k_0 d\frac{v}{c}\right] e^{2ink_0 d} . \quad (17)$$

It is worth introducing the reference point at a distance $L = 2N\pi/k_0$ from the fixed mirror, where the integer N is such that the moving atom's position x is within a wavelength of this reference point. Then the atom–mirror distance can be replaced by $d = L - x$, and $k_0 L$ drops from all the trigonometric functions. The solution, Eq. (17), has a clear physical meaning, in that the reflected field, $\mathcal{A}$, can be decomposed into an interfering sum of fields: the first term is the reflection directly from the atom, whereas the summation is over the electric field undergoing successive atom–mirror round-trips. We can also write the preceding expression in closed form:

$$\mathcal{A} = \frac{1}{1 - i\zeta}\left\{i\zeta + \mathfrak{r}\frac{e^{-2ik_0 x}}{1 - i\zeta - \mathfrak{r}i\zeta e^{-2ik_0 x}}\right.$$
$$- 2i\frac{v}{c}\zeta\left[1 - \frac{\mathfrak{r}^2 e^{-4ik_0 x}}{\left(1 - i\zeta - \mathfrak{r}i\zeta e^{-2ik_0 x}\right)^2}\right.$$
$$\left.\left. - 2ik_0(L-x)\frac{\mathfrak{r}^2(1 - i\zeta)e^{-4ik_0 x}}{\left(1 - i\zeta - \mathfrak{r}i\zeta e^{-2ik_0 x}\right)^3}\right]\right\} . \quad (18)$$

This result is valid for arbitrary ζ. The main virtue of our approach is clearly seen, in that we can smoothly move from $\zeta = 0$, which indicates the absence of the mobile scatterer, to $|\zeta| \to \infty$, which corresponds to a perfectly reflecting mirror, i.e., a moving boundary condition.

Let us outline some of the generic features of the above calculation that would be encountered in a general configuration of scatterers. By using the formal Doppler-shift operators, we benefit from the transfer matrix method in keeping the description of the system as a whole within two-by-two matrices. The input-output relation for the total system is always obtained in a form similar to that of Eq. (16). As long as the Doppler broadening is well below the transient time broadening of the system, the calculation of forces and diffusion requires solely the sum of the mode amplitudes. An important point is that the integrated action of the Doppler-shift operator $\hat{P}_v$ on monochromatic fields is a shift in k-space. Therefore, by interchanging the order of terms and putting the $\hat{P}_v$ terms just to the left of the input field amplitudes, they can be eliminated, such as in Eq. (17). Finally, up to first order in v/c, the resulting power series, a trace of multiple reflections, can be evaluated in a closed form, as shown in Eq. (18). In conclusion, the illustrated method lends itself for the description of more complex schemes, for example, the cooling of a moving, partially reflective mirror in a high-finesse Fabry-Perot resonator [26].

A. Force acting on the mobile scatterer

To obtain the force on the moving scatterer, we also need to evaluate $C'(k)$ and $D'(k)$:

$$\begin{pmatrix} C'(k) \\ D'(k) \end{pmatrix} = \begin{bmatrix} 1 - i\zeta & -i\zeta\left(1 - 2\frac{v}{c}\right)\hat{P}_{2v} \\ i\zeta\left(1 + 2\frac{v}{c}\right)\hat{P}_{2v}^{-1} & 1 + i\zeta \end{bmatrix} \begin{pmatrix} A(k) \\ B(k) \end{pmatrix}, \tag{19}$$

where we applied the inverse of the transfer matrix M_a. Next, we make the following definitions:

$$\mathbb{A} = |\mathcal{A}|^2, \quad \mathbb{B} = |\mathcal{B}|^2,$$
$$\mathbb{C} = \frac{1}{\mathbb{B}}\left|\int C'(k)\,dk\right|^2, \quad \mathbb{D} = \frac{1}{\mathbb{B}}\left|\int D'(k)\,dk\right|^2,$$

and a simple calculation leads to

$$\mathbb{C} = |1 - i\zeta|^2\,\mathbb{A} + \left|i\zeta\left(1 - 2\frac{v}{c}\right)\right|^2$$
$$+ 2\,\mathrm{Re}\left\{i\zeta^\star(1 - i\zeta)\left(1 - 2\frac{v}{c}\right)\mathcal{A}\right\},$$
$$\mathbb{D} = \left|i\zeta\left(1 + 2\frac{v}{c}\right)\right|^2\,\mathbb{A} + |1 + i\zeta|^2$$
$$+ 2\,\mathrm{Re}\left\{i\zeta(1 + i\zeta^\star)\left(1 + 2\frac{v}{c}\right)\mathcal{A}\right\}.$$

Thereby the force acting on the scatterer is obtained as

$$\boldsymbol{F} = (\hbar\omega/c)\mathbb{B}\left(\mathbb{A} + 1 - \mathbb{C} - \mathbb{D}\right)$$
$$= -2\hbar k_0\mathbb{B}\Big(\left[|\zeta|^2\left(1 + 2\frac{v}{c}\right) + \mathrm{Im}\{\zeta\}\right]\mathbb{A}$$
$$+ |\zeta|^2\left(1 - 2\frac{v}{c}\right) - \mathrm{Im}\{\zeta\}$$
$$+ 2\,\mathrm{Re}\{i\zeta(1 - i\zeta)\mathcal{A}\}\Big), \tag{20}$$

where $\mathcal{A}$ has to be substituted from Eq. (18). The coefficient of the term linear in velocity, the 'friction coefficient' β, is plotted in Fig. 3 as a function of the position x in a half-wavelength range for various values of ζ. When varying the coupling strength from $\zeta = 0.01$ up to $\zeta = 1$, the friction coefficient transforms between two characteristic regimes. For small coupling the linear velocity dependence tends to a simple sinusoidal function while, for large coupling, the friction exhibits a pronounced resonance in a narrow range. This resonance arises from the increased number of reflections between the mobile scatterer and the fixed mirror. It can be observed that the resonance shifts towards $k_0 x = \pi$ on increasing ζ. In the opposite limit of small ζ, the maximum friction is obtained periodically at $\left(n - \frac{1}{4}\right)\pi/2$ according to the sinusoidal function. The position of the maximum friction is plotted in Fig. 4(a), showing the transition from $7\pi/8$ to π. The maximum friction force is plotted in Fig. 4(b), showing the two limiting cases of ζ^2 behavior, in the limit of small ζ, and ζ^6 behavior, in the limit of large ζ. These two cases are described in section IV and section V, respectively.
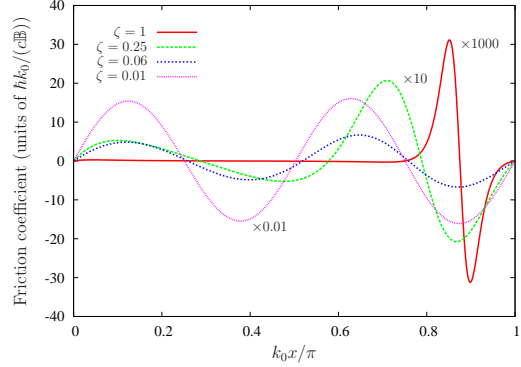
FIG. 3: (Color online.) The position dependence of the linear coefficient of the velocity-dependent force acting on the mobile scatterer in Fig. 2, for various scattering parameters ζ, evaluated by using Eq. (18) and Eq. (20) with $k_0 L = 100$. The fixed mirror is assumed to be a perfect mirror. In order to fit all the curves into the same range, they are divided by the factors indicated in the figure.

B. Diffusion coefficient

The calculation of the diffusion coefficient proceeds along the same lines as that corresponding to a single beamsplitter, shown in Appendix B. The difference is that the modes $B(k)$ and $C'(k)$ around the mobile scatterer are not independent, for the reflection at the fixed mirror mixes them. Therefore, all the modes A, B, C', and D' have to be expressed in terms of the leftmost and rightmost incoming modes, $B(k)$ and $C(k)$, respectively. Instead of the derivation of such a general result for the diffusion, here we will restrict ourselves to the special case of $\mathfrak{r} = -1$ ($\Leftrightarrow$ perfect mirror) and real ζ ($\Leftrightarrow$ no absorption in the moving mirror). In this special case the diffusion calculation simplifies a lot, because (i) the perfect mirror prevents the modes C from penetrating into the interaction region, and (ii) quantum noise accompanying absorption does not intrude in the motion of the scatterer.

Only the modes $\hat{B}(k)$ impart independent quantum fluctuations. When all the amplitudes around the scatterer are expressed in terms of $\hat{B}(k)$, and are inserted into the force correlation function given in Eq. (10), the commutator $[\hat{b}(t), \hat{b}^\dagger(t')]$ appears in all the terms (see Appendix B). Straightforward algebra leads to

$$\boldsymbol{D} = \hbar^2 k_0^2 \mathbb{B}(\mathbb{A} + 1 - \mathbb{C} - \mathbb{D})^2. \tag{21}$$

We emphasize that the above result is not general: the diffusion is not necessarily proportional to the square of the force. This simple relation here follows from the assumptions, $\mathfrak{r} = -1$ and $\mathrm{Im}\{\zeta\} = 0$, declared above.

To be consistent with the calculation of the friction force linear in velocity, the diffusion should be evaluated only for $v = 0$. From the ratio of these two coefficients,

(a)

(b)
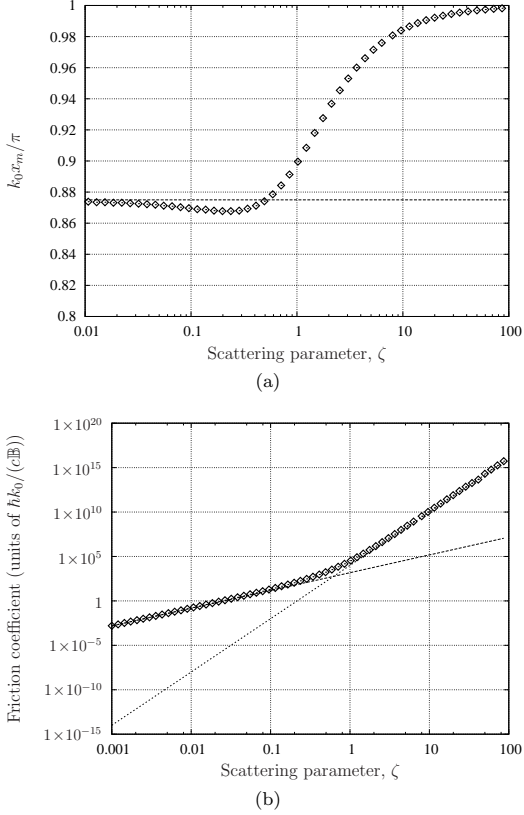
FIG. 4: (a) The position of the maximum friction force, $k_0 x_m$, as a function of the dimensionless scattering parameter ζ (on a semilog scale) acting on the scatterer in Fig. 2, with the fixed mirror being a perfect mirror. This position shifts from $7\pi/8$ to π on increasing ζ. (b) A similar plot, showing the maximum friction force as a function of ζ (on a log-log scale) with $k_0 L = 100$. In the limit of small ζ, the force scales as ζ^2 (cf. Eq. (25); dashed line) whereas in the limit of large zeta it scales as ζ^6 (cf. Eq. (27); dotted line).

the steady-state temperature can be deduced. The velocity independent components of the modes obey the following relations: $\mathbb{A} = 1$ and $\mathbb{C}' = \mathbb{D}'$ (all incoming power is reflected). Therefore the diffusion coefficient further simplifies,

$$\boldsymbol{D} = 4\hbar^2 k_0^2 \mathbb{B} \left(1 - \frac{1}{\left| 1 - i\zeta + i\zeta e^{-2ik_0 x} \right|^2} \right)^2 . \quad (22)$$

In Fig. 5, the temperature $k_B T = \boldsymbol{D}/(2\beta)$, where β is the friction coefficient, is plotted as a function of the scattering parameter ζ. The friction and the diffusion coefficients are taken at the position where the friction is maximum, as shown in Fig. 4(a). The two limits of small and large scattering parameter ζ will be analysed in section IV and section V, respectively.
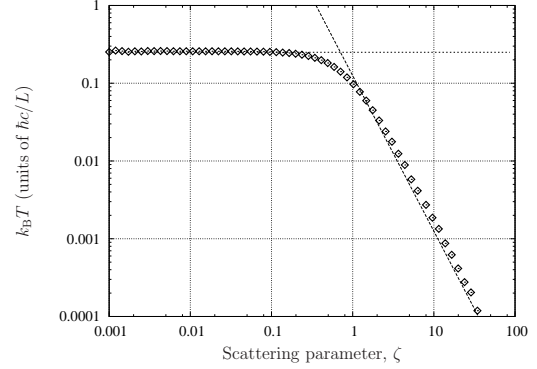
FIG. 5: Characteristic temperature for the two-scatterer system of Fig. 2, given by the ratio of the diffusion and friction coefficients in the points where the friction is maximum, as a function of the dimensionless scattering parameter ζ on a log-log scale. Constant and $1/\zeta^2$ dependence can be read off in the limits of small and large ζ, respectively. The fixed mirror is a perfect mirror.

IV. ATOM IN FRONT OF A PERFECT MIRROR

An atom pumped with a far off-resonance beam can be modelled as a moving mirror with small and real ζ. In this section we accordingly truncate our expressions to second order in ζ. We also assume that the fixed mirror is perfect; *i.e.*, $\mathfrak{r} = -1$ and $\mathfrak{t} = 0$. Thus,

$$\boldsymbol{F} = 2\hbar k_0 \mathbb{B} \{ 2\zeta \operatorname{Im}\{\mathcal{A}\} - 2\zeta^2 \operatorname{Re}\{\mathcal{A}\} \\ - \zeta^2 \left(1 + \tfrac{v}{c} \right) \mathbb{A} - \zeta^2 \left(1 - \tfrac{v}{c} \right) \} . \quad (23)$$

To obtain $\boldsymbol{F}$ to second order in ζ, we need $\mathcal{A}$ to first order. Using Eq. (17) and Eq. (23), we obtain:

$$\mathcal{A} = - e^{-2ik_0 x} + \zeta (i - 2ie^{-2ik_0 x} + ie^{-4ik_0 x}) \\ + \zeta \tfrac{v}{c} \left[-2i + 2ie^{-4ik_0 x} - 4k_0(L - x)e^{-4ik_0 x} \right] , \quad (24)$$

and

$$\boldsymbol{F} = 4\hbar k_0 \mathbb{B} \big(\zeta \sin(2k_0 x) \\ - \zeta^2 \{ 2\sin^2(k_0 x) \left[4\cos^2(k_0 x) - 1 \right] \} \\ - \zeta^2 \tfrac{v}{c} \left[4\sin^2(2k_0 x) \right. \\ \left. - 4k_0(L - x)\sin(4k_0 x) \right] \big) , \quad (25)$$

in agreement with [19]. In the far field $(x \gg \lambda)$, the dominant friction term in the preceding expression is the last term, which renders the $\sin(4k_0 x)$ position dependence shown in Fig. 3 for $\zeta = 0.01$.

We are now in a position to derive the diffusion coefficient for this system. By substituting Eq. (24) into Eq. (21) and setting $v = 0$, we obtain

$$\boldsymbol{D} = 8(\hbar k_0)^2 \zeta^2 \mathbb{B} .$$

This allows us to estimate the equilibrium temperature for such a system at a position of maximum friction:

$$k_\mathrm{B} T \approx \frac{\hbar}{2\tau}, \text{ where } \tau = 2(L - x)/c, \qquad (26)$$

which we note is identical in form to the Doppler temperature for a two-level atom undergoing free-space laser cooling [6], but where we have replaced the upper state lifetime, $1/(2\Gamma)$, by the round-trip time delay between the atom and the mirror. Note that this temperature corresponds to the constant value presented in Fig. 5 for $\zeta < 0.1$.

V.   OPTICAL RESONATOR WITH MOBILE MIRROR

After the small polarizability case of the previous section, we will now consider the $|\zeta| \to \infty$ limit. We again assume that the fixed mirror of the resonator is perfect, with $\mathfrak{r} = -1$, and that $C = 0$. For simplicity, we assume that the moving mirror has a real polarizability. We expand the field mode amplitudes as power series in v/c, such that $\mathcal{A} = \mathcal{A}_0 + \frac{v}{c}\mathcal{A}_1 + \ldots$, and similarly for $\mathcal{C}'$.

Let us first calculate the field in the resonator for $v = 0$. It follows from Eq. (19) that

$$\mathcal{C}'_0 = (1 - i\zeta)\mathcal{A}_0 - i\zeta = -\frac{e^{-2i\varphi}}{1 - i\zeta + i\zeta e^{-2i\varphi}},$$

with $\varphi = k_0 d$, which has a maximum at φ_0 obeying

$$\tan(2\varphi_0) = -\frac{1}{\zeta}.$$

In the limit of $\zeta \to \infty$, the resonance is Lorentzian:

$$\mathcal{C}'_0 = -\frac{e^{-2i\varphi}}{2i(1 - i\zeta)\left[(\varphi - \varphi_0) - i\frac{1}{4\zeta^2}\right]},$$

with a width of $1/(4\zeta^2)$.

The perfect mirror reflects the total power incoming from the left, $\mathbb{B}$. Moreover, for real ζ, there is no absorption in the moving mirror, so the outgoing intensity has to be equal to the incoming one: $\mathbb{A} = 1$. This is true if $v = 0$; for $v \neq 0$, the field can do work on the mirror. The expansion of the back reflected intensity to linear order in velocity reads $\mathbb{A} = 1 + 2\frac{v}{c}\,\mathrm{Re}\{\mathcal{A}_0^*\mathcal{A}_1\}$. Extracting the velocity-dependent terms for the general form of the force in Eq. (20), it reduces to

$$\boldsymbol{F}_1 = \frac{v}{c} 4\hbar k_0 \mathbb{B}\zeta\, \mathrm{Im}\{\mathcal{A}_1 / \left(1 + i\zeta - i\zeta e^{2i\varphi}\right)\},$$

which, after some algebra, leads to

$$\boldsymbol{F}_1 = -\frac{1}{2}\frac{v}{c}\hbar k_0^2 L \frac{(\varphi - \varphi_0)}{\zeta^4\left[\left(\frac{1}{4\zeta^2}\right)^2 + (\varphi - \varphi_0)^2\right]^3}\mathbb{B}. \qquad (27)$$

On substituting $\kappa = c/\left(4L\zeta^2\right)$, $\Delta_C = -c(\varphi - \varphi_0)/L$, $\eta^2/(2\kappa) = \mathbb{B}$, and $G = c^2 k_0^2/L^2$, the friction force renders that derived from the usual radiation pressure Hamiltonian in Appendix C.

Expressing the field modes interacting with the mobile mirror in terms of the input field mode and performing a calculation similar to that leading to Eq. (11) readily gives

$$\boldsymbol{D} \approx 4(\hbar k_0)^2|\mathcal{C}'_0|^4\mathbb{B} \approx \frac{(\hbar k_0)^2\mathbb{B}}{4\zeta^4\left[\left(\frac{1}{4\zeta^2}\right)^2 + (\varphi - \varphi_0)^2\right]^2}.$$

The resulting temperature thereby attains a minimum at $4\zeta^2(\varphi - \varphi_0) = 1$, i.e., $\Delta_C = -\kappa$, in analogy with free-space Doppler cooling, at which point we have

$$k_\mathrm{B} T \approx \frac{\hbar c}{8\zeta^2 L} = \tfrac{1}{2}\hbar\kappa. \qquad (28)$$

Again, this asymptotic behavior is reflected in Fig. 5 for large ζ. We note the similarity of the preceding expression with the temperature of an atom cooled in a cavity, in the good cavity limit [27]. We conjecture that this is due to the fact that both systems can be considered to involve the coupling of a laser with a system having a decay rate κ. This result also holds for the case of an atom undergoing mirror-mediated cooling, as can be seen in Eq. (26).

It is also important to note that the above discussion only treats the effects of the light fields on the scatterer. As such, the temperature limit, Eq. (28), is intrinsic to the light forces, and the mechanical damping and heating processes present in a real, macroscopic mirror-cooling setup are not taken into account. In practice, these heating processes may dominate over the heating induced by the quantum noise in the light field [28, 29]. In such cases, radiation pressure cooling is a possible means to lower the equilibrium temperature owing to the additional, optical damping process.

VI.   CONCLUSIONS

We have presented a powerful extension of an existing theoretical framework to analyse the interaction between light and matter. The theory we presented is based on the transfer matrix method for dealing with the interaction between scatterers and a light field, and is therefore able to handle complex optical systems, made from several elements, with relative ease. Through the use of the Maxwell stress tensor one can calculate the force acting on any of the elements in the system. We have generalized the transfer matrix for slowly moving scatterers, thereby the corrections first-order in v/c can be calculated for the electromagnetic field as well as for the radiation force acting on the scatterer. Furthermore, one can express this force in terms of the operators representing the quantized field modes interacting with the

scatterer and consequently derive the momentum diffusion of the scatterer due to the quantum noise present in the fields. Our scattering theory can also transparently cover the whole range of interaction strengths, from the perturbative interaction between a weak standing wave and a single atom to the very strong (quasi boundary-condition) interaction between a pump light field and a Fabry-Perot cavity with a moving mirror.

We also applied this framework to three different laser cooling configurations: optical molasses, mirror-mediated cooling and cooling of micromirrors. We derived the forces on an atom arising from its interaction with the light field, as well as an estimate for the equilibrium temperature an ensemble of atoms is expected to reach through this interaction. In the case of optical molasses, which corresponds to the well-known Doppler temperature limit, the theory provides for additional force and diffusion terms related to the effect of the back-action of the atom on the radiation field. Although for single atoms in free space this back-action is feeble, it is responsible for the modification of equilibrium properties [30, 31] and for collective effects in large optical lattices [32]. In the latter cases of a moving scatterer in front of a fixed mirror, our results are valid for arbitrary scattering strength, *i.e.*, spanning the parameter range from a single atom to high-reflectivity mirror.

Acknowledgments

APPENDIX A: THE DOPPLER-SHIFT OPERATOR
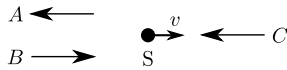
FIG. 6: Reflection and transmission of a moving scatterer. B and C are the input field modes, and A is the output field mode. A further output field mode ('D') is not drawn because it is not relevant to our discussion in this section.

Consider the situation in Fig. 6, in the laboratory frame, where S is a scatterer and suppose that B and C are known. $A(k)$ has contributions arising from both $B\left(k + 2k\frac{v}{c}\right)$ and $C(k)$, where k is any arbitrary wave number, written separately as:

$$A_B(k) = a_1 B(k + 2k\tfrac{v}{c}),\text{ and}$$
$$A_C(k) = a_2 C(k).$$

We can therefore express $A(k)$ as

$$A(k) = a_1 B(k + 2k\tfrac{v}{c}) + a_2 C(k).$$

Defining $\hat{P}_v$ by $\hat{P}_v : f(k) \mapsto f(k + k\frac{v}{c})$, we have

$$A(k) = \hat{P}_{2v} a_1 B(k) + a_2 C(k).$$

A similar expression, involving $\hat{P}_v^{-1} = \hat{P}_{-v}$, holds for $D(k)$. These two operators can then be introduced into Eq. (3) as part of the Lorentz transformation, and thus into the transfer matrix for the moving scatterer, giving rise to the form shown in Eq. (7). The resulting transformation, for the transfer matrix M, of a scatterer moving with velocity v can be written as:

$$\begin{bmatrix} (1 - \frac{v}{c})\hat{P}_v & 0 \\ 0 & (1 + \frac{v}{c})\hat{P}_v^{-1} \end{bmatrix} M \begin{bmatrix} (1 + \frac{v}{c})\hat{P}_v^{-1} & 0 \\ 0 & (1 - \frac{v}{c})\hat{P}_v \end{bmatrix},$$

to first order in $\frac{v}{c}$, where the ordering of the elements of M is as described in the text. Note that this relation is general, in the sense that the elements of M can depend on k (see section II E).

For any finite v, $\hat{P}_v$ is trivially a bounded operator, having unit norm. This property follows from the important relation $\int \hat{P}_v^m f(k)\, \mathrm{d}k = \int f(k)\, \mathrm{d}k$, for any function $f(k)$ and any integer m.

This operation can be generalized to $n = 2, 3$ dimensions. We define a new operator by $\hat{S}_i(\mathbf{v}) : f(\mathbf{k}) \mapsto f(\mathbf{k} + k_i \frac{v_i}{c}\mathbf{e}_i)$, where $\mathbf{e}_i$ is the unit vector along the ith coordinate axis, $\mathbf{v}$ is the velocity vector of the scatterer, and $\mathbf{x} = (x_1, x_2, \dots)$ for any vector $\mathbf{x}$. In particular, we have $\hat{P}_v = \hat{S}_1(v\mathbf{e}_1)$. Now, let $\hat{\mathbf{L}}(\mathbf{v})$ be the $2n \times 2n$ matrix operator:

$$\begin{bmatrix} (1 + \frac{v_1}{c})\hat{S}_1^{-1}(\mathbf{v}) & 0 & 0 & \cdots \\ 0 & (1 - \frac{v_1}{c})\hat{S}_1(\mathbf{v}) & 0 & \cdots \\ 0 & 0 & (1 + \frac{v_2}{c})\hat{S}_2^{-1}(\mathbf{v}) & \cdots \\ \vdots & \vdots & \vdots & \ddots \end{bmatrix}.$$

Then, the transfer matrix for the scatterer moving with velocity $\mathbf{v}$ is given by

$$\hat{\mathbf{L}}(-\mathbf{v})\, M\, \hat{\mathbf{L}}(\mathbf{v}),$$

where M is the original transfer matrix for the scatterer, obtained in a manner such as that used to obtain Eq. (4), for example. The ordering of the elements of M is such that it acts on the vector $(A_1(\mathbf{k}), B_1(\mathbf{k}), A_2(\mathbf{k}), \dots)$:

$$\begin{pmatrix} C_1(\mathbf{k}) \\ D_1(\mathbf{k}) \\ C_2(\mathbf{k}) \\ \vdots \end{pmatrix} = \hat{\mathbf{L}}(-\mathbf{v})\, M\, \hat{\mathbf{L}}(\mathbf{v}) \begin{pmatrix} A_1(\mathbf{k}) \\ B_1(\mathbf{k}) \\ A_2(\mathbf{k}) \\ \vdots \end{pmatrix},$$

with $A_i(\mathbf{k})$ being the outgoing mode and $B_i(\mathbf{k})$ the incoming mode along the ith axis in the negative half-space (assuming that the scatterer is at the origin); and $C_i(\mathbf{k})$ the incoming mode and $D_i(\mathbf{k})$ the outgoing mode in the positive half-space.

APPENDIX B: QUANTUM CORRELATION FUNCTION OF THE FORCE OPERATOR

In quantum theory, we need to replace the mode amplitudes $A(k)$ by operators $\hat{A}(k)$, and similarly for the B, C, and D modes. The cross correlation of these operators is not trivial because of the boundary condition connecting the mode amplitudes $A(k)$, $B(k)$, $C(k)$ and $D(k)$. The input modes $\hat{C}(k)$ and $\hat{B}(k)$ can be considered independent, and the commutator is non-vanishing for the creation and annihilation operators of the same mode, e.g.,

$$\left[\hat{B}(k),\hat{B}^\dagger(k')\right] = \left[\hat{C}(k),\hat{C}^\dagger(k')\right] = \frac{\hbar\omega}{2\epsilon_0 V}\delta_{k,k'},$$
$$\left[\hat{B}(k),\hat{C}^\dagger(k')\right] = 0\,,$$

assuming a discrete mode index of k, and a quantisation volume $V = Sl$ with S being the mode area and l a fictitious total length of the space in one dimension.

We consider only the $v = 0$ case, since our expressions are accurate up to first order in v/c. In the quantum description, the linear relation for the output modes is

$$A(k) = \mathfrak{t}C(k) + \mathfrak{r}B(k) + \sqrt{\gamma}E$$
$$D(k) = \mathfrak{r}C(k) + \mathfrak{t}B(k) + \sqrt{\gamma}E\,,$$

where the transmission $\mathfrak{t} = 1/M_{22} = 1/(1 - i\zeta)$, and reflection $\mathfrak{r} = M_{12}/M_{22} = i\zeta/(1 - i\zeta)$, as above. The fictitious amplitude E represents the quantum noise fed into the system by the absorption. For $\gamma = 1 - (|\mathfrak{r}|^2 + |\mathfrak{t}|^2)$, this noise ensures that the output modes obey the same commutation relations as the input ones, namely

$$\left[\hat{A}(k),\hat{A}^\dagger(k')\right] = \left[\hat{D}(k),\hat{D}^\dagger(k')\right] = \frac{\hbar\omega}{2\epsilon_0 V}\delta_{k,k'}\,,$$
$$\left[\hat{A}(k),\hat{D}^\dagger(k')\right] = 0\,.$$

However, the linear dependence implies that commutators between input and output mode operators are

$$\left[\hat{A}(k),\hat{B}^\dagger(k')\right] = \mathfrak{r}\left[\hat{B}(k),\hat{B}^\dagger(k')\right]\,,$$
$$\left[\hat{A}(k),\hat{C}^\dagger(k')\right] = \mathfrak{t}\left[\hat{C}(k),\hat{C}^\dagger(k')\right]\,,$$

and similar relations hold for the cross-commutators with $D(k)$.

The proper treatment of quantum fluctuations and the derivation of correlation functions require that the explicit time dependence be considered. Let us introduce the time-varying operators

$$\hat{a}(t) = \sum_k \hat{A}(k)e^{-i\omega t}\,,$$

and similarly for $\hat{b}(t)$, $\hat{c}(t)$ and $\hat{d}(t)$. It follows that

$$\left[\hat{a}(t),\hat{a}^\dagger(t')\right] = \frac{\hbar\omega}{2\epsilon_0 V}\sum_k e^{-i\omega(t-t')} \approx \frac{\hbar\omega}{2\epsilon_0 cS}\delta(t - t')\,.$$

Here we used that the non-excited, vacuum modes also contribute to force fluctuations. Therefore the Fourier-type summation extends to a broad frequency range and yields a $\delta(t-t')$ on the much slower timescale of interest. A similar commutation relation applies to the operators $\hat{b}(t)$, $\hat{c}(t)$, and $\hat{d}(t)$. The cross-commutators can be derived directly from those concerning the modes, e.g.,

$$\left[\hat{a}(t),\hat{b}^\dagger(t')\right] = \mathfrak{r}\frac{\hbar\omega}{2\epsilon_0 cS}\delta(t - t')\,.$$

The force operator is

$$\hat{\boldsymbol{F}} = S\left[\hat{\boldsymbol{T}}_{xx}(x \to 0^+) - \hat{\boldsymbol{T}}_{xx}(x \to 0^-)\right]\,, \qquad \text{(B1)}$$

as before, where

$$\hat{\boldsymbol{T}}_{xx}(x \to 0) = \begin{cases} -2\epsilon_0\left[\hat{a}^\dagger(t)\hat{a}(t) + \hat{b}^\dagger(t)\hat{b}(t)\right] & x \to 0^- \\ -2\epsilon_0\left[\hat{c}^\dagger(t)\hat{c}(t) + \hat{d}^\dagger(t)\hat{d}(t)\right] & x \to 0^+ \end{cases}$$

is the quantized stress tensor. Assuming that the field is in a coherent state, in all normally ordered products, the mode amplitude operators can be replaced by the corresponding coherent state amplitudes, which are c-numbers: e.g., $\hat{A}(k) \to A(k)$ and $\hat{A}^\dagger(k) \to A^\star(k)$. The force operator in Eq. (B1) is normally ordered in this way; therefore coherent-state fields render, as a mean value of the quantum expressions, the force Eq. (9) derived from the classical theory based on the definition Eq. (8). Non-trivial quantum effects arise from non-normally ordered products, such as the 4th-order product terms of the second order correlation function of the force Eq. (10). These terms can be evaluated straightforwardly by invoking the above-derived commutators to rearrange the product into normal order. As an example, consider

$$\langle\hat{a}^\dagger(t)\hat{a}(t)\hat{a}^\dagger(t')\hat{a}(t')\rangle = \langle\hat{a}^\dagger(t)\hat{a}^\dagger(t')\hat{a}(t)\hat{a}(t')\rangle$$
$$- \langle\hat{a}^\dagger(t)\hat{a}(t')\rangle\frac{\hbar\omega}{2\epsilon_0 cS}\delta(t - t')\,.$$

For radiation fields in coherent state, the first term is canceled from the correlation function by the $\langle\hat{a}^\dagger(t)\hat{a}(t')\rangle^2$ term. The coefficient of $\delta(t - t')$ in the second term is in normal order and can be replaced by c-numbers and then calculated identically as the force in section II E,

$$\langle\hat{a}^\dagger(t)\hat{a}(t)\rangle \approx \left|\sum A(k)\right|^2 = \frac{\hbar\omega}{2\epsilon_0 cS}|A|^2\,,$$

in terms of the photo-current intensity $|A|^2$.

Assembling all similar contributions, originating from the non-vanishing commutators $[b, b^\dagger]$, $[c, c^\dagger]$, $[d, d^\dagger]$, $[a, b^\dagger]$, etc., one obtains Eq. (11) presented in section II D.

APPENDIX C: MIRROR COOLING VIA THE RADIATION PRESSURE COUPLING HAMILTONIAN

We describe a generic opto-mechanical system composed of a single, damped-driven field mode coupled to the motion of a massive particle, whose Hamiltonian is given by [33, 34]

$$\hat{\mathcal{H}} = \hbar\omega_c\hat{a}^\dagger\hat{a} + i\hbar\eta(\hat{a}^\dagger e^{-i\omega t} - \hat{a}e^{i\omega t})$$
$$+ \frac{\hat{p}^2}{2m} + V(\hat{x}) + \hbar G\hat{a}^\dagger\hat{a}\hat{x}\,.$$

where $\hat{a}$ and $\hat{a}^\dagger$ are the annihilation and creation operators of the mode, $\hat{x}$ and $\hat{p}$ are the position and momentum operators associated with the motion and we drop the carets to signify expectation values. The mode is driven by a coherent field with an effective amplitude η and frequency ω. This Hamiltonian describes, for example, the radiation pressure coupling of a moving mirror to the field in a Fabry-Perot resonator. In this case the coupling constant is $G = \omega_c/L$, rendering the cavity mode frequency detuning $\omega_c x/L$ provided the mirror is shifted by an amount x. Since the cavity mode is lossy with a photon escape rate of 2κ, the total system is dissipative. Thereby, with a proper setting of the parameters, in particular the cavity detuning $\Delta_C = \omega - \omega_C$, the mirror motion can be cooled. We will determine the corresponding friction force linear in velocity.

In a frame rotating at frequency ω, the Heisenberg equation of motion for the field mode amplitude reads

$$\dot{a} = [i(\Delta_C - G\hat{x}) - \kappa]\,a + \eta\,.$$

where the noise term is omitted. We assume that the mirror moves along the trajectory $x(t) \approx x + vt$ with fixed velocity v during the short time that is needed for the field mode to relax to its steady-state. The variation of $\hat{a}$ arises from the explicit time dependence and from the motion of the mirror. A steady-state solution is sought in the form of $\hat{a} \approx \hat{a}^{(0)}(x) + v\hat{a}^{(1)}(x)$. On replacing this expansion into the above equation, and using the hydrodynamic derivative $\frac{d}{dt} \to \frac{\partial}{\partial t} + v\frac{\partial}{\partial x}$, one obtains a hierarchy of equations of different orders of the velocity v. To zeroth order the adiabatic field is obtained as

$$a^{(0)} = \frac{\eta}{-i(\Delta_C - Gx) + \kappa}\,.$$

The linear response of a to the mirror motion is then

$$a^{(1)} = \frac{1}{i(\Delta_C - Gx) - \kappa}\frac{\partial}{\partial x}a^{(0)}$$
$$= \frac{i\eta G}{\left[-i(\Delta_C - Gx) + \kappa\right]^3}\,.$$

The force acting on the mirror derives from the defining equation $\dot{p} = \frac{i}{\hbar}[\hat{\mathcal{H}}, \hat{p}] = -\hbar G\hat{a}^\dagger\hat{a}$. The force linear in velocity is

$$\boldsymbol{F}_1 = -2v\hbar G\,\mathrm{Re}\left\{a^{(0)\star}a^{(1)}\right\} = 4v\frac{\hbar\eta^2 G^2\kappa\Delta_C}{\left[\Delta_C^2 + \kappa^2\right]^3}\,,$$

where we used $x = 0$ without loss of generality. It can be seen that mirror cooling requires that $\Delta_C < 0$, i.e., the cavity resonance frequency is above the pump frequency. In this case, for efficient excitation of the field in the resonator, the frequency of the pump photons is up-shifted at the expense of the mirror's kinetic energy. This cooling force has been derived in section V, as a limiting case of the more general scattering theory. To check the perfect agreement between the two results, the quantity corresponding to η can be deduced from the total field energy in the resonator for an immobile mirror, which is $\hbar\omega_C\hat{a}^{(0)\dagger}\hat{a}^{(0)}$ here.

[1] T. W. Hänsch and A. L. Schawlow, Opt. Commun. **13**, 68 (1975).
[2] D. J. Wineland and W. M. Itano, Phys. Rev. A **20**, 1521 (1979).
[3] C. H. Metzger and K. Karrai, Nature **432**, 1002 (2004).
[4] T. Corbitt, C. Wipf, T. Bodiya, D. Ottaway, D. Sigg, N. Smith, S. Whitcomb, and N. Mavalvala, Phys. Rev. Lett. **99**, 160801 (2007).
[5] A. Schliesser, R. Riviere, G. Anetsberger, O. Arcizet, and T. J. Kippenberg, Nat Phys **4**, 415 (2008).
[6] H. J. Metcalf and P. van der Straten, J. Opt. Soc. Am. B **20**, 887 (2003).
[7] V. Braginsky, Phys. Lett. A **293**, 228 (2002).
[8] C. K. Law, Phys. Rev. A **51**, 2537 (1995).
[9] S. Gigan, H. R. Bohm, M. Paternostro, F. Blaser, G. Langer, J. B. Hertzberg, K. C. Schwab, D. Bauerle, M. Aspelmeyer, and A. Zeilinger, Nature **444**, 67 (2006).
[10] O. Arcizet, P. F. Cohadon, T. Briant, M. Pinard, and A. Heidmann, Nature **444**, 71 (2006).
[11] D. Kleckner and D. Bouwmeester, Nature **444**, 75 (2006).
[12] I. H. Deutsch, R. J. C. Spreeuw, S. L. Rolston, and W. D. Phillips, Phys. Rev. A **52**, 1394 (1995).
[13] J. K. Asbóth, H. Ritsch, and P. Domokos, Phys. Rev. A **77**, 063424 (2008).
[14] C. Genes, D. Vitali, P. Tombesi, S. Gigan, and M. Aspelmeyer, Phys. Rev. A **77**, 033804 (2008).
[15] I. Wilson-Rae, N. Nooshi, W. Zwerger, and T. J. Kippenberg, Phys. Rev. Lett. **99**, 093901 (2007).
[16] F. Marquardt, J. P. Chen, A. A. Clerk, and S. M. Girvin, Phys. Rev. Lett. **99**, 093902 (2007).
[17] J. Eschner, C. Raab, F. Schmidt-Kaler, and R. Blatt, Nature **413**, 495 (2001).
[18] P. Bushev, A. Wilson, J. Eschner, C. Raab, F. Schmidt-Kaler, C. Becher, and R. Blatt, Phys. Rev. Lett. **92**, 223602 (2004).
[19] A. Xuereb, P. Horak, and T. Freegarde, arXiv e-prints (2009), arXiv:0903.2945 [quant-ph].
[20] J. D. Jackson, *Classical Electrodynamics* (Wiley, 1998),

3rd ed., ISBN 047130932X.

[21] J. Dalibard and C. Cohen-Tannoudji, J. Opt. Soc. Am. B **6**, 2023 (1989).

[22] Y. Castin and K. Molmer, J. Phys. B: At. Mol. Opt. Phys. **23**, 4101 (1990).

[23] R. J. Glauber, Physical Review **131**, 2766 (1963).

[24] C. Cohen-Tannoudji, in *Fundamental Systems in Quantum Opt., Proceedings of the Les Houches Summer School, Session LIII*, edited by J. Dalibard, J. Zinn-Justin, and J. M. Raimond (North Holland, 1992), pp. 1–164.

[25] J. P. Gordon and A. Ashkin, Phys. Rev. A **21**, 1606 (1980).

[26] M. Bhattacharya, H. Uys, and P. Meystre, Phys. Rev. A **77**, 033819 (2008).

[27] P. Horak and H. Ritsch, Phys. Rev. A **64**, 033422 (2001).

[28] P. R. Saulson, Phys. Rev. D **42**, 2437 (1990).

[29] P. F. Cohadon, A. Heidmann, and M. Pinard, Phys. Rev. Lett. **83**, 3174 (1999).

[30] M. Weidemüller, A. Görlitz, T. W. Hänsch, and A. Hemmerich, Phys. Rev. A **58**, 4647 (1998).

[31] J. K. Asbóth and P. Domokos, Phys. Rev. A **76**, 057801 (2007).

[32] J. K. Asbóth, H. Ritsch, and P. Domokos, Phys. Rev. Lett. **98**, 203008 (2007).

[33] J. M. Courty, A. Heidmann, and M. Pinard, The European Physical Journal D - Atomic, Molecular, Optical and Plasma Phys. **17**, 399 (2001).

[34] D. Vitali, S. Mancini, L. Ribichini, and P. Tombesi, J. Opt. Soc. Am. B **20**, 1054 (2003).

Atom cooling using the dipole force of a single retroflected laser beam

André Xuereb,[1, *] Peter Horak,[2] and Tim Freegarde[1]

[1]*School of Physics and Astronomy, University of Southampton, Southampton SO17 1BJ, United Kingdom*
[2]*Optoelectronics Research Centre, University of Southampton, Southampton SO17 1BJ, United Kingdom*
(Dated: August 5, 2009)

We present a mechanism for cooling atoms by a laser beam reflected from a single mirror. The cooling relies on the dipole force and thus in principle applies to arbitrary refractive particles including atoms, molecules, or dielectric spheres. Friction and equilibrium temperatures are derived by an analytic perturbative approach. Finally, semiclassical Monte-Carlo simulations are performed to validate the analytic results.

I. INTRODUCTION

Optical cooling of atoms has come a long way since it was first proposed; magneto–optical traps are even found in undergraduate laboratories [1, 2, 3]. The field of ultracold molecules, in contrast, is still in its infancy. Ultracold diatomic alkali molecules (< 100 μK for Rb_2 [4]) are routinely produced from Bose-Einstein condensates through Feshbach resonances. Some groups (see, for example, [5] and [6]) have demonstrated the possibility of cooling the internal degrees of such molecules, cooling ultracold di-alkali molecules to their lowest rovibronic levels by means of laser-stimulated state transfer processes.

Present methods of producing ultracold samples suffer from one of two major drawbacks: either they are specific to particular species, or they produce very low densities. The bulk of optical cooling methods are applicable only to a handful of species because they rely on a closed optical transition within which the population can cycle [7]. Most atoms and molecules do not have such a transition available, but instead exhibit a large number of loss channels through which the population is gradually lost, halting the cooling. Samples of cold molecules are therefore generally produced by capturing the low-velocity tail of the Maxwell-Boltzmann distribution of a hotter initial sample [8]. However, such filtering methods do not lead to an increase of the phase-space density and thus only capture a small fraction of the initial population, leading to very dilute samples.

One possibility to solve this problem is through the use of non-resonant processes [9] or cavities [10, 11, 12, 13, 14]. The latter require extremely high precision alignment of the cavity mirrors as well as complicated loading of the molecules into the optical cavity mode. The requirements for integrated systems near the surface of a substrate in the form of atom chips [15] are even more stringent.

Here, we investigate a mechanism for the cooling of a particle using only a single plane mirror in place of a cavity. In principle, this scheme only relies on the dipole force of a refractive particle in a laser beam and thus applies to a wide range of atomic and molecular species as well as, for example, dielectric micro- or nanospheres. However, in the present work we focus on the basic principles of the cooling scheme and thus restrict the analysis to the simplest case of a two-level atom.

Conceptually, one can view the interaction between the atom and the mirror as being closely related to that between a micromechanical oscillator, acting as a mobile mirror, and a second mirror. Such schemes have been investigated both theoretically [16, 17] and experimentally [18, 19] in various configurations. Although we have recently shown that one can treat these two situations as two opposite limits of the same model [20], the situation we explore here behaves differently, and this can be attributed to two facts. Firstly, the coupling strength between the static and moving scatterer (atom or mirror) is very different in the two cases: an atom merely perturbs the field it interacts with, whereas a mirror acts as a moving boundary condition and changes the field significantly. Secondly, the effect we investigate here is only dominant at large atom–mirror separations. Thus, our proposed cooling scheme operates in a parameter regime that is as yet mostly unexplored.

This paper is structured as follows. In the next section we introduce the key features of our system and propose a simple classical explanation of the cooling scheme. In section III the relevant quantum equations of motion are introduced. Section IV solves these equations of motion analytically through the use of perturbative methods, whereas section V gives the results of numerical simulations used to explore the implications of the theory in further detail. Section VI compares our results with those of traditional Doppler cooling, and finally section VII summarizes and concludes our discussion.

II. MOTIVATION

We start with a classical explanation of the situation, which provides the motivation for the mathematical

---

*To whom all correspondence should be addressed. Electronic address: andre.xuereb@soton.ac.uk
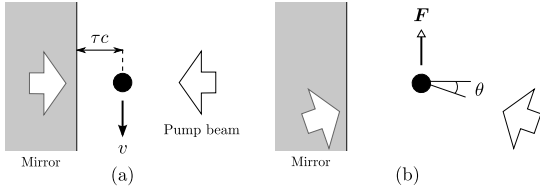
FIG. 1: Schematic of the cooling scheme. (a) In the laboratory frame, an atom moving with velocity v parallel to a mirror, a distance τc away, interacts with a pump beam and its time-delayed reflection. (b) In the frame of the atom, the (relativistically transformed) pump beam and its reflection are tilted by an angle $\theta = \arcsin(v/c)$ and produce a net retarding force, $\boldsymbol{F}$.

FIG. 2: Schematic representation of the key components of the system under consideration. The atom is separated from the mirror by a distance τc and lies in a standing wave maintained by the pump beam.

model presented in the next section. The phenomenon of optical binding has been known for some time (see, for example, [21, 22, 23]) and is now a common occurrence. At a basic level, optical binding takes place between two dielectric spheres when one sphere focuses the light onto a second sphere, which is subsequently trapped. If we now consider just one such sphere in front of a mirror, the modified electric field will be reflected back towards the sphere itself. In essence, then, the sphere will be attracted to its own image. However, this interaction is delayed by the time 2τ it takes the disturbance in the electric field to travel from the sphere to the mirror and back, where τ is the time that light from the atom takes to reach the mirror. Suppose, now, that the sphere is moving parallel to the plane of the mirror with velocity v, as shown in Fig. 1(a). In this case, the sphere moves a distance $2v\tau$ during the light roundtrip time. Thus, the disturbed light field lags behind the particle and creates an attractive force in the direction opposite to the motion of the particle. This attractive force can be shown to be a viscous force, i.e., it is proportional to v. This scenario also applies to the case of a single atom interacting with an off-resonant beam, where the atom can effectively be modeled as a refractive particle. Note that the interaction between a single atom and its image in a distant mirror has already been demonstrated [24, 25].

Alternatively, we may consider the same situation in the reference frame of the moving particle, as shown in Fig. 1(b). In this case both the incident laser beam and its reflection are tilted by an angle $\theta = \arcsin(v/c)$ with respect to normal incidence on the mirror. The sum potential is therefore offset from the particle position by an amount proportional to its velocity, leading again to a velocity-dependent force opposing the motion.

Similar arguments apply for a particle moving along the direction of the pump beam, i.e., orthogonal to the mirror. In this case, the phase of the reflected beam is determined by the interaction of the particle with the pump at the earlier time 2τ. In effect, the atom exerts a delayed phase change on the light field, dragging the potential along with itself while moving and thus creating a non-conservative force. This effect is similar to the
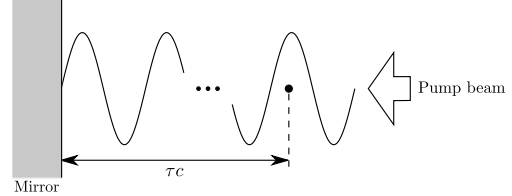
"position dependent phase locking" described in [26].

III. MATHEMATICAL MODEL

In order to analyze the principles of the proposed cooling scheme most clearly, we simplify the situation described above to a one-dimensional (1D) scheme and assume a single two-level atom as the particle to be cooled. A schematic of the system is shown in Fig. 2.

The atom has a transition frequency ω_a and a decay rate 2Γ and is described by the operators $\hat{p}$ and $\hat{x}$ associated with the atomic momentum and position, respectively, and by the atomic dipole raising ($\hat{\sigma}^+$) and lowering ($\hat{\sigma}^-$) operators. The atom is coupled to a continuum of quantized electro-magnetic modes with frequencies ω and standing-wave mode functions $f(\omega, x) = \sin(\omega x/c)$, described by the field annihilation $\hat{a}(\omega)$ and creation operators $\hat{a}^\dagger(\omega)$. The mirror is at position $x = 0$. For simplicity, we neglect the frequency-dependence of the atom-field coupling and assume a single coupling coefficient g. Finally, mode ω_0 is pumped by a laser, which enters our analysis as an initial condition, and far off resonant pumping is assumed, $|\Delta| = |\omega_a - \omega_0| \gg \Gamma$, where the atom mainly acts as a refractive particle and spontaneous scattering is reduced. For the numerical examples given in this paper, we consider ^{85}Rb atoms and a realistic pump beam that is detuned from the $5S_{1/2} \to 5P_{3/2}$ transition of ^{85}Rb by several linewidths.

The starting point for describing the coupling between the atom and the field modes is the quantum master equation:

$$\dot{\hat{\rho}} = -\frac{i}{\hbar}\left[\hat{H}, \hat{\rho}\right] + \mathcal{L}\hat{\rho}, \qquad (1)$$

where $\hat{\rho}$ is the density operator of the full system comprising all modes and the atom. Applying the dipole and rotating wave approximations and in a frame rotating with the driving frequency ω_0, the Hamiltonian $\hat{H}$ reads

$$\hat{H} = \frac{\hat{p}^2}{2m} + \hbar\Delta\hat{\sigma}^+\hat{\sigma}^- \int \hbar(\omega - \omega_0)\hat{a}^\dagger(\omega)\hat{a}(\omega)\,\mathrm{d}\omega$$
$$- i\hbar g \int [\hat{\sigma}^+\hat{a}(\omega)f(\omega, \hat{x}) - \text{h.c.}]\,\mathrm{d}\omega, \qquad (2)$$

and the damping term associated with atomic decay into modes other than the 1D system modes reads

$$\mathcal{L}\hat{\rho} = -\Gamma\left[\hat{\sigma}^+\hat{\sigma}^-\hat{\rho} + \hat{\rho}\hat{\sigma}^+\hat{\sigma}^- \right.$$
$$\left. - 2\int_{-1}^1 N(u)\hat{\sigma}^- e^{-iu\hat{x}}\hat{\rho}e^{iu\hat{x}}\hat{\sigma}^+ \, du\right]. \quad (3)$$

Here $N(u)$ describes the 1D projection of the spontaneous emission pattern of the atomic dipole. In the low saturation regime we can adiabatically eliminate the internal atomic dynamics and formally express the dipole operator as

$$\hat{\sigma}^- = -\frac{i\Delta + \Gamma}{\Delta^2 + \Gamma^2}\, g \int f(\omega, \hat{x})\hat{a}(\omega)\, d\omega + \hat{\xi}^-, \quad (4)$$

where $\hat{\xi}^-$ is a noise term [27].

In the following, we present two different ways of proceeding from this point. In the first instance we approximate further and use perturbation theory to derive the force experienced by the atom analytically, in section IV, and in the second instance we derive semiclassical equations of motion. The latter approach is then applied to numerical simulations of the situation in section V.

IV. ANALYZING THE MODEL: A PERTURBATIVE APPROACH

A. Friction force

We first derive an analytical approximation for the friction on the atom. To this end, we treat atomic motion semiclassically and thus replace the operator $\hat{x}$ by an atomic position x. After inserting Eq. (4) into Eq. (2) and Eq. (3), we obtain the Hamiltonian

$$\hat{H} = \int \hbar(\omega - \omega_0)\hat{a}^\dagger(\omega)\hat{a}(\omega)\, d\omega + \hbar g^2 D(\Delta)$$
$$\times \iint \sin(\omega_1 x/c)\sin(\omega_2 x/c)\hat{a}^\dagger(\omega_1)\hat{a}(\omega_2)\, d\omega_1 \, d\omega_2,$$

where we have defined $D(\Delta) = \Delta/(\Delta^2 + \Gamma^2)$. As a consequence of the assumed large pump detuning Δ, we in the following neglect that part of the decay term $\mathcal{L}\hat{\rho}$ which leads to spontaneous scattering of photons between the quantized modes by the atom.

Let us first consider a stationary atom at a fixed position $x = x_0$. Starting with the Heisenberg equation of motion for the annihilation operators

$$\frac{d}{dt}\hat{a}(\omega, t) = \frac{i}{\hbar}\left[\hat{H}, \hat{a}(\omega, t)\right],$$

we arrive at the integro-differential equation

$$\frac{d}{dt}\hat{a}(\omega, t) = -i(\omega - \omega_0)\hat{a}(\omega, t)$$
$$- ig^2 D(\Delta)\sin(\omega x/c)\int \sin(\omega_1 x/c)\hat{a}(\omega_1, t)\, d\omega_1. \quad (5)$$

We now assume coherent states at all times for the fields and replace the operators with their respective expectation values. Since we are pumping the atom at a single frequency, we take the initial condition $a(\omega, 0) = A\delta(\omega - \omega_0)$, where A is the amplitude of the pump field, such that $|A|^2$ is the pump power in units of photons per second, and δ is the Dirac δ-function. We now expand the fields $a(\omega, t)$ in the weak-coupling limit in powers of the coupling constant,

$$a(\omega, t) = \sum_n a_n(\omega, t)[g^2 D(\Delta)]^n, \quad (6)$$

with $a_n(\omega, t)$ being the nth coefficient of the series expansion. Solving Eq. (5) by perturbation theory then yields the zeroth order term in $g^2 D(\Delta)$

$$a_0(\omega, t) = A\delta(\omega - \omega_0), \quad (7)$$

and the first order term

$$a_1(\omega, t) = A\frac{\exp\left[-i(\omega - \omega_0)t\right] - 1}{\omega - \omega_0}\sin(\omega x/c)\sin(\omega_0 x/c).$$

We now proceed to find, to second order in $g^2 D(\Delta)$, the static force, $\boldsymbol{F}(x_0, t) = -\partial\hat{H}/\partial x$, acting on the atom:

$$\boldsymbol{F}(x_0, t) = \frac{\hbar}{c}|A|^2 g^2 D(\Delta)\omega_0\left\{\sin(2\omega_0 x_0/c)\right.$$
$$\left. - \frac{\pi}{2}g^2 D(\Delta)\sin^2(\omega_0 x_0/c)\left[4\cos^2(\omega_0 x_0/c) - 1\right]\right\}.$$

The first term in the above equation describes the interaction of the atom with the unperturbed pump field, whereas the second term is the lowest order correction of the force due to the back-action of the atom on the light fields. Note that this force is independent of time.

Similarly, we can now calculate the force on an atom moving at a constant velocity v. For this we assume that the atom follows a trajectory given by $x(t) = x_0 + v(t - t_0)$, where t_0 is a long enough time for the system to reach a stationary state, *i.e.*, t_0 is larger than twice the propagation time $\tau = x_0/c$ of the light from the atom to the mirror. We can then solve Eq. (5) up to first order in both v and $g^2 D(\Delta)$. The friction force in the longitudinal direction is finally obtained as

$$\boldsymbol{F}_\parallel(x_0, t) = \frac{2\pi\hbar\omega_0}{c^2}v|A|^2\left[g^2 D(\Delta)\right]^2 \sin^2(2k_0 x_0)$$
$$- \frac{2\pi\hbar\omega_0^2}{c^2}v\tau|A|^2\left[g^2 D(\Delta)\right]^2 \sin(4k_0 x_0). \quad (8)$$

The second term in Eq. (8) is larger than the first by a factor of the order $k_0 x_0 = \omega_0 x_0/c$ and is therefore dominant if the distance of the atom from the mirror is much larger than an optical wavelength. We may then approximate the longitudinal friction force by

$$\boldsymbol{F}_\parallel(x_0, t) = -2\pi\hbar k_0^2 v\tau|A|^2\left(\frac{g^2\Delta}{\Delta^2 + \Gamma^2}\right)^2 \sin(4k_0 x_0). \quad (9)$$
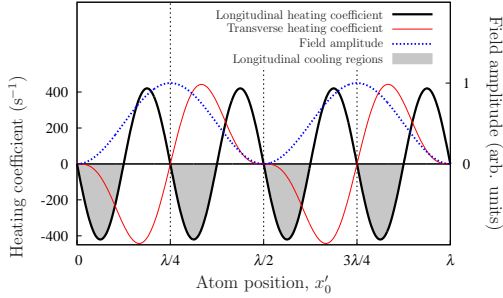
FIG. 3: (Color online) Spatial dependence of the longitudinal heating coefficient Υ (thick solid line). The shaded areas promote cooling in the longitudinal direction. Also drawn is the transverse heating coefficient (thin solid line) and the field amplitude (dotted line). Parameters are for Rb atoms and $|A|^2 = 62.5\Gamma/(2\pi)$, $\Delta = -10\Gamma$, $\tau = 0.25/\Gamma$, $w = 0.7$ μm.

Supposing that the species we are cooling is ^{85}Rb, and setting $|A|^2 = 62.5\Gamma/(2\pi)$, $\Delta = -10\Gamma$, $\tau = 0.25/\Gamma$, and Gaussian beam waist $w = 0.7$ μm, Eq. (9) predicts $1/e$ cooling times of the order of 2 ms. The value for τ that we use implies a separation between the atom and the mirror of the order of several metres. We suggest that this problem can be overcome through the coupling of the light into an optical fibre, thereby avoiding the effects of diffraction. A recent experiment making use of a similar technique is described in [28].

Equation (9) indicates an exponential decay or increase in velocity. We define the *heating coefficient* Υ of an ensemble of atoms as the proportionality constant in the relation $dp^2/dt = \Upsilon p^2$, which thus depends on position as $\sin(4k_0x_0)$. Moreover, since $p^2 \propto T$ for a thermal ensemble, we also have $dT/dt = \Upsilon T$. Figure 3 shows a plot of Υ against atomic position, where we introduced the coordinate x_0' relative to the nearest node of the standing wave pump. It is only in certain intervals that we expect the longitudinal force to be a damping force, as indicated in this figure by the shaded regions.

We now derive the friction force in the transverse direction, *i.e.*, orthogonal to the pump beam. In this case the coupling constant g becomes a function $g(r)$, where r is the coordinate in the transverse direction. For an atom moving at small constant velocity, we may write $g[r_0 + v(t - t_0)] \approx g(r_0) + v(t - t_0)g'(r_0)$ where $g'(r) = dg/dr$. Substituting this in Eq. (5) we can derive an expression for the friction force, $\boldsymbol{F}_\perp(x_0, t) = -\partial \hat{H}/\partial r$, in the direction of r:

$$\boldsymbol{F}_\perp(x_0, t_0) = -4\pi\hbar v\tau|A|^2 \left(\frac{2gg'\Delta}{\Delta^2 + \Gamma^2}\right)^2$$
$$\times \ \sin^3(k_0x_0)\cos(k_0x_0).$$

This transverse friction force is also shown in Fig. 3 as-

suming a Gaussian mode function of waist $w = 0.7$μm. Note that $\boldsymbol{F}_\parallel$ and $\boldsymbol{F}_\perp$ are comparable in magnitude for the parameters chosen here where the mode waist is comparable to the optical wavelength, and that there exist regions where both these forces promote cooling.

In the remainder of this paper, however, we will concentrate on a one-dimensional treatment of the problem and therefore only consider the longitudinal friction force. This could correspond, for example, to the imaging arrangement of Eschner at al. [24].

In terms of more familiar parameters, we can rewrite Eq. (9) in the limit $|\Delta| \gg \Gamma$ as

$$\boldsymbol{F}_\parallel(x_0, t) = -4vs\Gamma\frac{\sigma_\mathrm{a}}{\pi w^2}\hbar k_0^2\tau \sin(4k_0x_0), \qquad (10)$$

where $s = g^2|A|^2/(\Delta^2 + \Gamma^2)$ is the maximum saturation parameter of the atom in the standing wave, $\sigma_\mathrm{a} = 3\lambda^2/(2\pi)$ is the atomic radiative cross-section, and where we used the relation $2\pi g^2/\Gamma = 4\sigma_a/(\pi w^2)$.

Aside from allowing us to make predictions of cooling times, Eq. (9) and Eq. (10) also highlight the dependence of this cooling effect on the variation of certain physical parameters. In particular, $\boldsymbol{F}_\parallel$ depends on the square of the detuning, which means that it is possible to obtain cooling with both positive and negative detuning. The friction force also scales with w^{-4} and $|A|^2$. Hence, for a fixed laser intensity, proportional to $|A|^2/w^2$, *i.e.*, fixed atomic saturation, friction still scales with w^{-2} and thus a tight focus is needed in order to have a sizeable effect. A very promising feature of these two equations is the linear dependence of the cooling rate on τ. In section V we further analyze the dependence of the cooling rate on the various parameters and support the validity of the analytic solution by comparing it with the results of simulations.

B. Localizing the particle

Equation (9) shows that, in order to observe any cooling effects, we need to localize the particle within around $\lambda/8$. This can be achieved, for example, by an additional far-off resonant and tightly focused laser beam propagating parallel to the mirror forming a dipole trap centered at a point x_0. We characterize this trap by means of its spring constant k_t, such that the trapping force is given by $F_t = -k_t(x - x_0)$, or equivalently by the harmonic oscillator frequency $\omega_\mathrm{t} = \sqrt{(k_t/m)}$, where m is the mass of the atom.

If we now assume that the atom oscillates as $x(t) = x_0 + x_\mathrm{m}\sin[\omega_\mathrm{t}(t - t_0)]$ in the trap with a maximum distance x_m of the particle from the trap center and a corresponding maximum velocity v_m, it is possible to derive a new friction coefficient by perturbation theory in x_m.

Proceeding along the lines of section IV A, we arrive at

$$\boldsymbol{F}_\parallel(x_0, t) = -2\pi\hbar k_0^2 v_m \tau \, \mathrm{sinc}(2\omega_\mathrm{t}\tau)$$
$$\times \; |A|^2 \left(\frac{g^2\Delta}{\Delta^2+\Gamma^2}\right)^2 \sin(4k_0 x_0) \; . \quad (11)$$

Note that this formula reduces to Eq. (9) in the limit of small w_t. The sinusoidal dependence on $\omega_\mathrm{t}\tau$ can be explained in an intuitive manner: the effect on the particle is unchanged if the particle undergoes an integer number of oscillations in the round-trip time 2τ.

While Eq. (11) was derived for an oscillating particle, it is still only correct to lowest order in x_m and therefore does not include the effect of a finite spatial distribution. In order to obtain an estimate for the friction force in the presence of spatial broadening, we calculate the overall energy loss rate experienced by the particle in terms of the time average of Eq. (9):

$$\left\langle \frac{\mathrm{d}p^2}{\mathrm{d}t} \right\rangle = -\frac{2\hbar k_0^2 p_0^2}{m}\tau|A|^2\left(\frac{g^2\Delta}{\Delta^2+\Gamma^2}\right)^2$$
$$\times \int_0^{2\pi} \sin[4k_0 x_0 + 4k_0 x_\mathrm{m}\sin(T)]\cos^2(T)\,\mathrm{d}T, \quad (12)$$

where $p_0 = mv_m$ is the maximum momentum of the particle in the trap given by $p_0 = x_\mathrm{m}\sqrt{mk_\mathrm{t}}$. The value of the integral in (12) can be expressed as

$$\frac{2\pi}{4k_0 x_\mathrm{m}}[\sin(4k_0 x_0)J_1(4k_0 x_\mathrm{m}) + \cos(4k_0 x_0)H_1(4k_0 x_\mathrm{m})],$$

where J_1 is the order-1 Bessel function of the first kind and H_1 is the order-1 Struve function [29]. At the point of maximum friction, $x_0' = -3\lambda/16$, the integral in the above equation reduces to $2\pi J_1(4k_0 x_\mathrm{m})/(4k_0 x_\mathrm{m})$ which can be readily evaluated.

For small values of x_m, the effect of this averaging process is to introduce a factor of one half into Eq. (11), which can be seen as being equivalent to the effect of cooling merely one degree of freedom when the atom is in a harmonic trap. Finally, Eq. (12) is modified similarly to Eq. (11) to include the effects of the harmonic oscillation by replacing $\tau \to \sin(2\omega_\mathrm{t}\tau)/(2\omega_\mathrm{t})$. This results in an approximate expression for the friction, taking into account the periodicity in the time delay as well as spatial averaging effects,

$$\langle \boldsymbol{F}_\parallel(x_0, t) \rangle = -\hbar k_0^2 v_m \tau |A|^2 \left(\frac{g^2\Delta}{\Delta^2+\Gamma^2}\right)^2 \mathrm{sinc}(2\omega_\mathrm{t}\tau)$$
$$\times \int_0^{2\pi} \sin[4k_0 x_0 + 4k_0 x_\mathrm{m}\sin(T)]\cos^2(T)\,\mathrm{d}T. \quad (13)$$

C. Capture range

As discussed above, the addition of the dipole trap introduces several features into the friction force. Plotting the variation of the friction force in Eq. (12) with
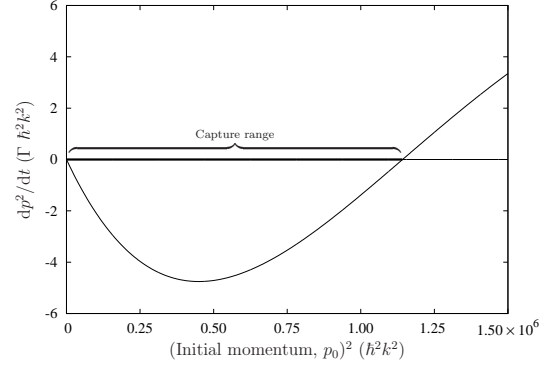
FIG. 4: Dependence of the heating rate $(\mathrm{d}p^2/\mathrm{d}t)$ on the square of the initial momentum, p_0^2, for $\omega_\mathrm{t} = 0.45 \times 2\pi\Gamma$ and $x_0' = 3\lambda/16$. Other parameters are as in Fig. 3. Cooling is achieved only for a finite range of initial momenta.

the particle's initial momentum, as in Fig. 4, shows that the force changes sign for high enough initial momentum. This is due to the broader spatial distribution for faster particles in the harmonic trap. For fast enough velocities, the particle oscillates into the heating regions, as shown in Fig. 3, even if the trap is centered at the position of maximum cooling. This defines a range of initial momenta, starting from zero, within which a particle is cooled by this mechanism; faster particles are heated and ejected from the trap. Note that this result was derived from the friction to lowest order in velocity v, and higher order terms are expected to affect the capture range further.

At particular values of x_0', e.g. at $-3\lambda/16$, this capture range can be conveniently estimated by using the location of the first zero of the Bessel function,

$$p_0 \approx 0.958\sqrt{(mk_t)}/k_0 = 0.958m\omega_\mathrm{t}/k_0. \quad (14)$$

Thus, $p_0^2 \propto \omega_\mathrm{t}^2$, and the capture range as defined in Fig. 4 is expected to scale with the square of the trap frequency. We compare this later in section V with the results of numerical simulations.

D. Diffusion and steady-state temperature

In the preceding discussion we found a friction force which cools an atom towards zero momentum. In practice, the cooling process is counteracted by momentum diffusion due to spontaneous scattering by the atom of photons from the pump beam into other electromagnetic modes and between the two counterpropagating components of the standing wave pump itself. In a simplified Brownian motion model, this diffusion introduces a constant in the equation for $\mathrm{d}p^2/\mathrm{d}t$, resulting in a constant upward shift of the curve in Fig. 4. This slightly reduces the capture range for fast particles, but its main
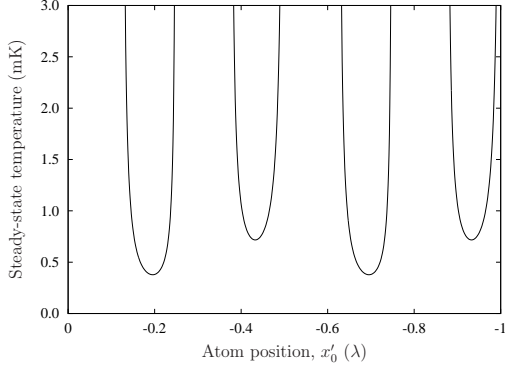
FIG. 5: Calculated steady-state temperature T_M for an atom confined in a harmonic trap as a function of position whilst keeping the detuning and pump field constant. $\omega_t = 0.1 \times 2\pi\Gamma$; other parameters are as in Fig. 3.

effect is to introduce a specific value of the momentum where friction and diffusion exactly compensate each other. This point corresponds to the steady-state temperature achievable through the cooling mechanism discussed here.

To lowest order in the coupling coefficient g^2, the diffusion is given by the interaction of the atom with the unperturbed, standing-wave pump field. In this limit, diffusion in our system is therefore identical to that of Doppler cooling [30, 31, 32, 33], where the diffusion coefficient $\boldsymbol{D}$ is given to lowest order in s by

$$\boldsymbol{D} = \hbar^2 k_0^2 \Gamma s \Big[\cos^2(k_0 x_0) + \tfrac{2}{5} \sin^2(k_0 x_0) \Big]. \quad (15)$$

The steady-state temperature T_M of mirror-mediated cooling is then obtained from $k_B T_M = \boldsymbol{D} v_m / \boldsymbol{F}_\parallel (x_0, t)$ where $\boldsymbol{F}_\parallel (x_0, t)$ is the friction force given by Eq. (11). For $|\Delta| >> \Gamma$ we find

$$T_M = \frac{1}{5\pi} \frac{\hbar}{k_B} \frac{\omega_t \Gamma}{g^2} \frac{2 + 3\cos^2(k_0 x_0)}{\sin(2\omega_t \tau)\sin(4k_0 x_0)}. \quad (16)$$

An example of the dependence of T_M on the trap position is shown in Fig. 5, predicting a minimum temperature of the order of 400 µK. Whilst this may seem large in comparison to the Doppler temperature of 141 µK, one has to keep in mind that T_M, given by Eq. (16), is insensitive to detuning and, for far off-resonant operation of the order of tens of linewidths, it will be the dominant mechanism. This is further discussed in section VI. We also note that Fig. 5 further highlights the importance of the requirement for localizing the particle. Using Eq. (10) we can approximate the steady-state temperature at the point of maximum friction by

$$k_B T_M \approx \frac{\hbar}{\tau} \frac{\pi w^2}{8\sigma_a}.$$

It is interesting to note that this expression is closely related to the expression for the limiting temperature in Doppler cooling, $k_B T = \hbar \Gamma$, but where Γ is replaced by the inverse of the atom–mirror delay time, $1/\tau$, and where a geometrical factor related to the mode area divided by the atomic cross section is included.

V. NUMERICAL SIMULATIONS

In this section we now investigate a more accurate numerical model to corroborate the simplified analytical results obtained above. In order to render the problem numerically tractable, the continuum of modes is replaced by a discrete set of modes with frequencies ω_k, $k = 1, \ldots, N$. The master equation (1) is then converted by use of the Wigner transform into a Fokker-Planck equation for the atomic and field variables. Applying a semiclassical approximation and restricting the equation of motion to second-order derivatives, one arrives at an equivalent set of stochastic differential equations for a single atom with momentum p and position x in a discrete multimode field with mode amplitudes α_k [34],

$$dx = \frac{p}{m} dt, \quad (17a)$$

$$\begin{aligned} dp = &\, i\gamma \big[\mathcal{E}(x)\tfrac{d}{dx}\mathcal{E}^\star(x) - \mathcal{E}^\star(x)\tfrac{d}{dx}\mathcal{E}(x) \big] dt \\ &- U_0 \big[\mathcal{E}(x)\tfrac{d}{dx}\mathcal{E}^\star(x) + \mathcal{E}^\star(x)\tfrac{d}{dx}\mathcal{E}(x) \big] dt \\ &- k_t(x - x_t)dt + dP, \quad (17b) \end{aligned}$$

$$d\alpha_k = i\Delta_k \alpha_k dt - (iU_0 + \gamma)\mathcal{E}(x) f_k^\star(x)dt + dA_k, \quad (17c)$$

where $f_k(x) = \sin(\omega_k x/c)$ are the mode functions, $\mathcal{E}(x) = \sum_k \alpha_k f_k(x)$ is the total electric field, $\Delta_k = \omega_0 - \omega_k$ is the detuning of each mode from the pump, U_0 is the light shift per photon, and γ is the photon scattering rate. The terms dP and dA_k are correlated noise terms [34] responsible for momentum and field diffusion.

In the following, we set the trap center to $x_0' = -3\lambda/16$, which is the point where the analytic solution predicts the maximum of the damping force. We use $N = 256$ field modes with a mode spacing of $\Gamma/10$. At the start of every simulation, all field modes are empty with the exception of the pump mode which is initialized at 625 photons, corresponding to a laser power of around 50 pW for our chosen parameters.

The simulations were performed in runs of several thousand trajectories. Each such run was performed at a well-defined initial temperature, with the starting momenta of the particles chosen from a Gaussian distribution, and the starting position being the center of the trap.

A. Friction force and capture range

Fig. 6 presents the results of a set of simulations performed when setting the noise terms dP and dA_k in equations (17a) to zero, i.e., neglecting momentum and photon number diffusion. The simulation data are compared

(a)

(b)
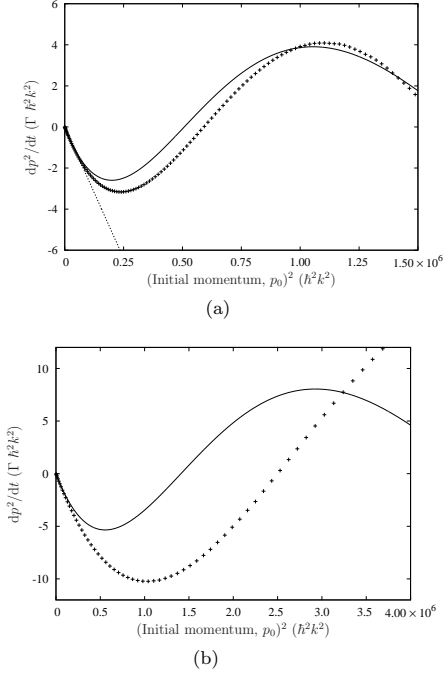
FIG. 6: Comparison of heating rate (dp^2/dt) for the simulations without noise (data points) with the analytic approximation, Eq. (13), including the harmonic trap (solid line). (a) Weak harmonic trap, $\omega_t = 0.3 \times 2\pi\Gamma$, showing also the linear dependence in the limit of small momenta, Eq. (11) (dotted line). (b) Stiff trap, $\omega_t = 0.5 \times 2\pi\Gamma$. The trap position $x_0' = -3\lambda/16$ and other parameters are as in Fig. 3.

with the result of the perturbative calculations Eq. (13). For modest values of ω_t, Fig. 6(a) justifies the averaging process used to derive (12) which was based on spatial averaging but neglecting higher order terms in v. In contrast, for larger trap frequencies, the numerical simulations diverge significantly from the analytic result, as can be seen in Fig. 6(b). We expect that the terms in higher powers of the initial speed, which were dropped in the perturbative solution, are responsible for this discrepancy.

We have already seen, in Eq. (14), that the capture range is expected to scale as ω_t^2. For weak traps, as shown in Fig. 7, the numerical simulations agree well with these expectations. For stiffer traps, however, the capture range is consistently larger than that predicted; in fact, the simulations predict a capture range of around 450 mK for a trap frequency of $0.5 \times 2\pi\Gamma$

B. Steady-state temperature

The next step in our investigation was to run simulations involving the full dynamics given by Eqs. (17a)
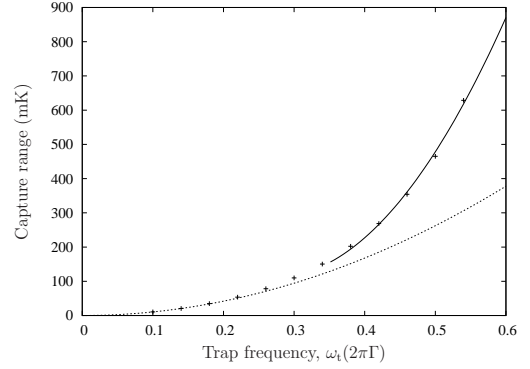
FIG. 7: Capture range extracted from the simulations (data points) as compared to the analytic solution (dotted line) for various values of ω_t. The solid line is a quadratic fit to the data for $\omega_t \geq 0.3 \times 2\pi\Gamma$ and is only intended as a guide to the eye. Other parameters are as in Fig. 6.
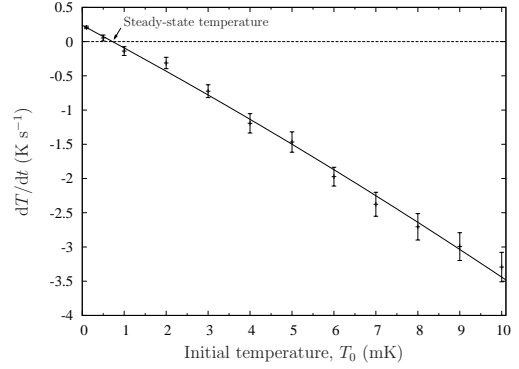
FIG. 8: Heating rate (dT/dt) extracted from the simulations starting at a number of initial temperatures. The solid line represents a quadratic fit to the data. $\omega_t = 0.5 \times 2\pi\Gamma$; other parameters are as in Fig. 6.

including the diffusion terms. Because of the discrete nature of the field modes with uniform frequency spacing used in the simulations, the numerically modeled behavior is always periodic in time with a periodicity given by the inverse of the frequency spacing. The simulations therefore cannot follow each trajectory to its steady-state. Instead, simulations were performed in several groups of trajectories, each group forming a thermal ensemble at a well-defined initial temperature. For each such group of trajectories the initial value of dT/dt was calculated. The results for $\omega_t = 0.5 \times 2\pi\Gamma$ are shown in Fig. 8, where the error bars are due to statistical fluctuations for a finite number of stochastic integrations. The steady-state temperature is that temperature at which $dT/dt = 0$ as clearly illustrated in this figure. For the chosen parameters, our data suggest a steady-state temperature of 722 ± 54 μK with a $1/e$ cooling time of around
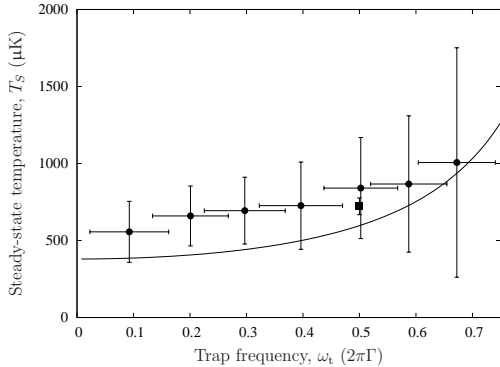
FIG. 9: Steady-state temperature for a number of simulations (circles) compared to the analytic formula (16) (solid line). The solid square represents the equivalent data from Fig. 8, resulting from a much larger number of simulations. Parameters are as in Fig. 6.

FIG. 10: Comparison between the calculated steady-state temperatures for mirror-mediated cooling T_{M} (dash-dotted line), Doppler cooling T_{D} (dashed), and in the presence of both effects T (solid), drawn as a function of detuning whilst keeping the saturation parameter constant. $\omega_{\mathrm{t}} = 0.1 \times 2\pi\Gamma$; other parameters are as in Fig. 6.

3.0 ms. This compares reasonably well with the steady-state temperature of 597 μK predicted by Eq. (16).

We finally performed a large number of simulations to investigate the dependence of the steady-state temperature on the trap frequency. Equation (16) indicates that as one decreases ω_{t} the steady state temperature decreases. This is clearly seen in Fig. 9, which compares the prediction of Eq. (16) with a set of numerical simulations. The trend in the data is reproduced well by the analytic expression. However, the simulated steady-state temperature is consistently a little higher than predicted. We expect that this discrepancy is due to one of two reasons. (i) Equation (16) was derived from the friction Eq. (11), i.e., without the spatial averaging of (13) which would reduce friction. (ii) Higher order terms in the velocity v are also expected to reduce friction compared to the lowest order analytical result. In both cases, therefore, the analytic expression is expected to overestimate the friction force and thus to predict too low temperatures.

VI. BEYOND ADIABATIC THEORY

All the theoretical analysis and simulations discussed so far have been based on adiabatic elimination of the internal atomic degrees of freedom, and therefore neglected Doppler cooling. In Fig. 10, we explore the variation of T_{M} and the Doppler temperature, T_{D}, as a function of detuning from resonance when the particle is at the point of greatest friction ($x'_0 = 3\lambda/16$), where T_D is given by $T_D = -\hbar\Gamma(\Delta^2 + \Gamma^2)/(2\Delta)$ for negative values of Δ. In the presence of both cooling effects, the stationary temperature achieved by the system is given by

$$T = \left(\frac{1}{T_{\mathrm{M}}} + \frac{1}{T_{\mathrm{D}}} \right)^{-1}. \qquad (18)$$
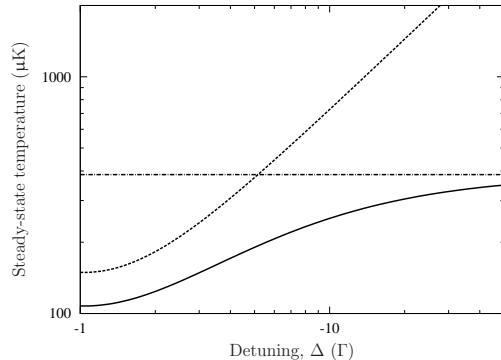
Thus, for the parameters of Fig. 9, the calculated steady-state temperature T reduces to 250 μK in the limit of vanishing ω_{t}.

From Fig. 10 one can see that the mirror-mediated force, for our tightly focused pump, is stronger than the Doppler force for detunings larger than around 10Γ in magnitude. In practice this has two implications: for large negative detunings, we expect the steady-state temperature of the system to be significantly lower than that predicted by Doppler cooling; whereas for large *positive* detunings, we still predict equilibrium temperatures of the order of mK.

Both our perturbative expressions and our simulations are calculated to lowest orders in the atomic saturation. However, it is well known that in the limit of very large detunings also higher order terms in the saturation parameter s become significant. Using the full expression for the diffusion constant [30], we can estimate the detuning for which we expect minimum diffusion and temperature. For the value of the saturation parameter $s \lesssim 0.1$ used throughout this paper, it can be shown that T_{M} attains a minimum at detunings of up to several tens of linewidths. Our chosen parameters are therefore within the range of validity of the model.

VII. CONCLUSION

We have presented a mechanism for cooling particles by optical means which is based fundamentally on the dipole interaction of a particle with a light beam and therefore does not rely on spontaneous emission. The particle is assumed to be trapped and is simultaneously driven by an off-resonant laser beam. After the interaction with the particle the beam is reflected back onto the particle by a distant mirror. The time-delay incurred

during the light round-trip to the mirror and back is exploited to create a non-conservative cooling force.

The system was analyzed using stochastic simulations of the semiclassical equations of motion representing a single two-level atom coupled to a continuum of electromagnetic modes. The results of these computations were found to agree with the expectations of a perturbative analysis. Our models predict sub-mK steady-state temperatures for ^{85}Rb atoms interacting with a tightly focused laser beam several meters from the mirror, in an arrangement similar to that of Ref. [24]. While most of the theory is presented for a one-dimensional model, results for the friction force in the transverse direction suggest that three-dimensional cooling is possible with this scheme.

The model presented here requires a large separation between the atom and the mirror, of the order of several meters, for an observable cooling effect. This limitation can be overcome in several ways. First, the light could propagate in an optical fiber between the atom and the mirror to avoid the effects of diffraction. Second, the required delayed reflection could be achieved through the use of a cavity instead of a mirror; in contrast to cavity-mediated cooling schemes [10, 11, 12, 13, 14], the atom would remain external to the cavity. For a time delay τ of order 1 ns one would require a cavity quality factor $Q = \omega\tau$ [35] of the order of $10^6 - 10^7$, which is achievable with present-day technology [36].

[1] T. W. Hänsch and A. L. Schawlow, Opt. Commun. **13**, 68 (1975).
[2] D. J. Wineland and W. M. Itano, Phys. Rev. A **20**, 1521 (1979).
[3] A. S. Mellish and A. C. Wilson, Am. J. Phys. **70**, 965 (2002).
[4] C. Gabbanini, A. Fioretti, A. Lucchesini, S. Gozzini, and M. Mazzoni, Phys. Rev. Lett. **84**, 2814 (2000).
[5] J. M. Sage, S. Sainis, T. Bergeman, and D. DeMille, Phys. Rev. Lett. **94**, 203001 (2005).
[6] K. Winkler, F. Lang, G. Thalhammer, P. v. d. Straten, R. Grimm, and J. H. Denschlag, Phys. Rev. Lett. **98**, 043201 (2007).
[7] H. J. Metcalf and P. van der Straten, J. Opt. Soc. Am. B **20**, 887 (2003).
[8] P. W. H. Pinkse, P. T. Junglen, T. Rieger, S. A. Rangwala, and G. Rempe, in *European Quantum Electronics Conference (EQEC 2003), Munich, Germany* (IEEE, 2003), p. 271.
[9] A. J. Kerman, V. Vuletic, C. Chin, and S. Chu, Phys. Rev. Lett. **84**, 439 (2000).
[10] P. Horak, G. Hechenblaikner, K. M. Gheri, H. Stecher, and H. Ritsch, Phys. Rev. Lett. **79**, 4974 (1997).
[11] V. Vuletic and S. Chu, Phys. Rev. Lett. **84**, 3787 (2000).
[12] P. Maunz, T. Puppe, I. Schuster, N. Syassen, P. W. H. Pinkse, and G. Rempe, Nature **428**, 50 (2004).
[13] M. Y. Vilensky, Y. Prior, and I. S. Averbukh, Phys. Rev. Lett. **99**, 103002 (2007).
[14] B. L. Lev, A. Vukics, E. R. Hudson, B. C. Sawyer, P. Domokos, H. Ritsch, and J. Ye, Phys. Rev. A **77**, 023402 (2008).
[15] R. Folman, P. Krueger, J. Schmiedmayer, J. Denschlag, and C. Henkel, Adv. At. Mol. Opt. Phy. **48**, 263 (2002).
[16] V. Braginsky, Phys. Lett. A **293**, 228 (2002).
[17] M. Bhattacharya, H. Uys, and P. Meystre, Phys. Rev. A **77**, 033819 (2008).
[18] T. Corbitt, C. Wipf, T. Bodiya, D. Ottaway, D. Sigg, N. Smith, S. Whitcomb, and N. Mavalvala, Phys. Rev. Lett. **99**, 160801 (2007).
[19] A. Schliesser, R. Riviere, G. Anetsberger, O. Arcizet, and T. J. Kippenberg, Nat Phys **4**, 415 (2008).
[20] A. Xuereb, P. Domokos, J. Asbóth, P. Horak, and T. Freegarde, Phys. Rev. A **79**, 053810 (2009).
[21] M. M. Burns, J. M. Fournier, and J. A. Golovchenko, Science **249**, 749 (1990).
[22] M. P. Macdonald, L. Paterson, V. K. Sepulveda, J. J. Arlt, W. Sibbett, and K. Dholakia, Science **296**, 1101 (2002).
[23] N. K. Metzger, E. M. Wright, W. Sibbett, and K. Dholakia, Opt. Express **14**, 3677 (2006).
[24] J. Eschner, C. Raab, F. Schmidt-Kaler, and R. Blatt, Nature **413**, 495 (2001).
[25] P. Bushev, A. Wilson, J. Eschner, C. Raab, F. Schmidt-Kaler, C. Becher, and R. Blatt, Phys. Rev. Lett. **92**, 223602 (2004).
[26] M. Gangl and H. Ritsch, Phys. Rev. A **61**, 043405 (2000).
[27] C. W. Gardiner, Phys. Rev. A **29**, 2814 (1984).
[28] S. A. Aljunid, M. K. Tey, B. Chng, Z. Chen, J. Lee, T. Liew, G. Maslennikov, V. Scarani, and C. Kurtsiefer, in *2009 Conference on Lasers and Electro-Optics and the XIth European Quantum Electronics Conference (CLEO®/Europe-EQEC 2009), Munich, Germany* (IEEE, 2009), p. 89.
[29] I. S. Gradshteyn and I. M. Ryzhik, *Table of integrals, series and products* (Academic Press, 1994), 5th ed.
[30] J. P. Gordon and A. Ashkin, Phys. Rev. A **21**, 1606 (1980).
[31] R. J. Cook, Phys. Rev. A **22**, 1078 (1980).
[32] C. Cohen-Tannoudji, in *Fundamental Systems in Quantum Opt., Proceedings of the Les Houches Summer School, Session LIII*, edited by J. Dalibard, J. Zinn-Justin, and J. M. Raimond (North Holland, 1992), pp. 1–164.
[33] K. Berg-Sørensen, Y. Castin, E. Bonderup, and K. Mølmer, J. Phys. B: At. Mol. Opt. Phys. **25**, 4195 (1992).

[34] P. Horak and H. Ritsch, Phys. Rev. A **64**, 033422 (2001).

[35] G. Rempe, R. J. Thompson, H. J. Kimble, and R. Lalezari, Opt. Lett. **17**, 363 (1992).

[36] H. Mabuchi and H. J. Kimble, Opt. Lett. **19**, 749 (1994).

Magneto-optical trapping and background-free imaging for atoms near nanostructured surfaces

Hamid Ohadi, Matthew Himsworth, André Xuereb, and Tim Freegarde

School of Physics and Astronomy, University of Southampton,
Southampton SO17 1BJ, United Kingdom

hamid.ohadi@soton.ac.uk

Abstract: We demonstrate a combined magneto-optical trap and imaging system that is suitable for the investigation of cold atoms near surfaces. In particular, we are able to trap atoms close to optically scattering surfaces and to image them with an excellent signal-to-noise ratio. We also demonstrate a simple magneto-optical atom cloud launching method. We anticipate that this system will be useful for a range of experimental studies of novel atom-surface interactions and atom trap miniaturization.

OCIS codes: 020.3320, 020.4180, 120.1880

References and links

1. E. L. Raab, M. Prentiss, A. Cable, S. Chu, and D. E. Pritchard, "Trapping of neutral sodium atoms with radiation pressure," Phys. Rev. Lett. **59** (1987).
2. F. Shimizu, K. Shimizu, and H. Takuma, "Four-beam laser trap of neutral atoms," Opt. Lett. **16**, 339–341 (1991).
3. O. Emile, F. Bardou, C. Salomon, P. Laurent, A. Nadir, and A. Clairon, "Observation of a new magneto-optical trap," EPL (Europhys. Lett.) **20**, 687–691 (1992).
4. K. I. Lee, J. A. Kim, H. R. Noh, and W. Jhe, "Single-beam atom trap in a pyramidal and conical hollow mirror," Opt. Lett. **21** (1996).
5. J. Reichel, W. Hänsel, and T. W. Hänsch, "Atomic micromanipulation with magnetic surface traps," Phys. Rev. Lett. **83**, 3398 (1999).
6. S. Coyle, M. C. Netti, J. J. Baumberg, M. A. Ghanem, P. R. Birkin, P. N. Bartlett, and D. M. Whittaker, "Confined plasmons in metallic nanocavities," Phys. Rev. Lett. **87**, 176801 (2001).
7. R. Folman, P. Krüger, D. Cassettari, B. Hessmo, T. Maier, and J. Schmiedmayer, "Controlling cold atoms using nanofabricated surfaces: Atom chips," Phys. Rev. Lett. **84**, 4749–4752 (2000).
8. S. Pollock, J. P. Cotter, A. Laliotis, and E. A. Hinds, "Integrated magneto-optical traps on a chip using silicon pyramid structures," Opt. Express **17**, 14109–14114 (2009).
9. F. Nez, "Optical frequency determination of the hyperfine components of the 5s1/2-5d3/2 two-photon transitions in rubidium," Opt. Commun. **102**, 432–438 (1993).
10. Y. B. Ovchinnikov, S. V. Shul'ga, and V. I. Balykin, "An atomic trap based on evanescent light waves," J. Phys. B: At. Mol. Opt. Phys. **24**, 3173–3178 (1991).
11. B. E. Schultz, H. Ming, G. A. Noble, and W. A. van Wijngaarden, "Measurement of the rb d2 transition linewidth at ultralow temperature," Eur. Phys. J. D **48**, 171–176 (2008).
12. K. L. Corwin, Z. T. Lu, C. F. Hand, R. J. Epstein, and C. E. Wieman, "Frequency-stabilized diode laser with the Zeeman shift in an atomic vapor," Appl. Opt. **37**, 3295–3298 (1998).
13. M. A. Clifford, G. P. T. Lancaster, R. H. Mitchell, F. Akerboom, and K. Dholakia, "Realization of a mirror magneto-optical trap," J. Mod. Opt. **48**, 1123–1128 (2001).
14. D. V. Sheludko, S. C. Bell, R. Anderson, C. S. Hofmann, E. J. D. Vredenbregt, and R. E. Scholten, "State-selective imaging of cold atoms," Phys. Rev. A **77**, 033401 (2008).
15. A. Vernier, S. F. Arnold, E. Riis, and A. S. Arnold, "Enhanced frequency up-conversion in Rb vapor," ArXiv e-prints (2009).
16. S. Wu, T. Plisson, R. C. Brown, W. D. Phillips, and J. V. Porto, "Multiphoton magnetooptical trap," Phys. Rev. Lett. **103**, 173003 (2009).

17. S. H. Autler and C. H. Townes, "Stark effect in rapidly varying fields," Phys. Rev. **100**, 703–722 (1955).
18. W. Wohlleben, F. Chevy, K. Madison, and J. Dalibard, "An atom faucet," Eur. Phys. J. D **15**, 237–244 (2001).
19. H. J. Lewandowski, D. M. Harber, D. L. Whitaker, and E. A. Cornell, "Simplified system for creating a Bose-Einstein condensate," J. Low Temp. Phys. **132**, 309–367 (2003).

1. Introduction and motivation

Over the past two decades, several configurations for magneto-optical traps have been demonstrated [1, 2, 3, 4, 5]. The starting point for most geometries has been the original, '6-beam', configuration [1], where the atom trap is created in the intersection of three counterpropagating laser beams. Despite it having the advantage that the atoms can be trapped far from any surface, thereby reducing spurious scatter in the imaging of such a trap, one cannot easily use this configuration for investigations into atom–surface interactions, for precisely the same reason. Another, more recent, configuration is the so-called 'mirror MOT' [5], where the trap is formed a short distance away from a mirror, which also serves to reduce the number of necessary incident laser beam paths to two. The major drawback of such a configuration is its reduced optical access, due to the oblique angle of the field coils with respect to the mirror. The presence of a reflecting surface close to the trap also presents a problem of an entirely different nature. If the object of one's investigation is to observe the interaction between atoms and surfaces structured at the μm scale, for example hemispherical mirrors of the type investigated in [6], the signal from the atoms will almost certainly be lost due to unwanted scattering of light into the optical system. MOTs on the meso- and microscopic scale, in particular, have received some recent interest [7], but the small atom numbers in such traps have so far hindered their imaging and characterisation [8]. In this article we propose a modified configuration that we call the 'ΛMOT' and implement an imaging system based on a two-stage excitation process [9], which help us overcome each of these limitations and aid our exploration of different atom–surface interactions.

This paper is structured as follows. The next section is devoted to the description and characterization of our trap geometry. We then discuss the mechanism behind our multilevel imaging system and show how it does indeed allow for practically background-free imaging of the atom trap. The subsequent section discusses surface loading by magneto-optic launching, which allows us to load atoms onto a surface with a three-dimensional range of motion. Finally, we conclude and summarize the main features of our system.

2. The ΛMOT

2.1. Description

A single beam of circularly polarized light of the right helicity is split using a non-polarizing beamsplitter, to generate the two beams that produce the trap, and a half-wave plate is inserted in one of the two resulting beams to achieve the correct polarizations. Each of these beams, denoted S, is then used to construct the geometry shown in Fig. 1. Mirror C is set up so as to retroreflect the beam. Mirrors B and C, together with the quarter-wave plate, allow us to change the polarization in the retroreflected branch independently of the incoming polarization. In a normal mirror MOT, the polarizations cannot be modified independently of each other and the quadrupole axis has to be at an oblique angle to the mirror. The four beams traveling towards O thus have the correct polarizations to produce the trapping and cooling forces necessary to form a MOT in this plane. Combined with the second set of beams, this means that the MOT is formed in the intersection region of four pairs of counterpropagating beams. We note that alignment of mirror B such that the beam is retroreflected perfectly will recover the traditional mirror MOT beam geometry, albeit with the incorrect polarizations for a MOT cloud to form.
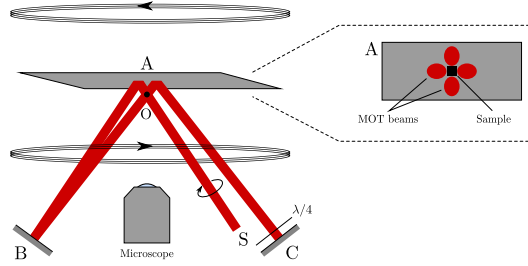
Fig. 1. (Color online.) Schematic of one of the two beam paths involved in our MOT geometry. S is the incoming beam; A, B, and C are mirrors. The component marked '$\lambda/4$' is a quarter-wave plate. The cold atom cloud forms in the intersection region, O. In this diagram we do not show a second, identical, beam, which provides trapping and cooling forces in the plane normal to the paper. The area of mirror A immediately adjacent to the trapped atoms is not illuminated, and can therefore be patterned or structured to explore atom–surface interactions. *Inset:* The lower surface of mirror A, showing the MOT beams and the sample area, which is not illuminated by any of the beams.
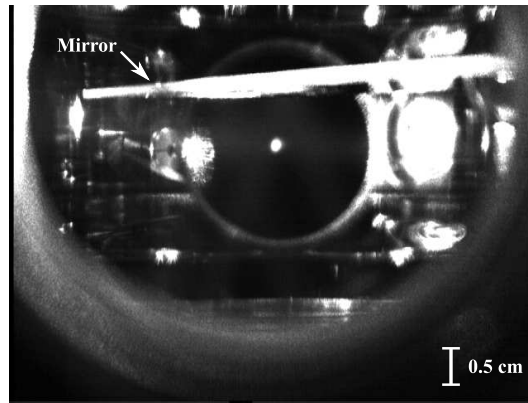
Fig. 2. Image of our MOT in operation, corresponding to Fig. 1; mirror A is indicated in the picture.

Several advantages are apparent in the use of this geometry. The trapping volume is the entire overlap of the trapping beams, unlike that in a mirror MOT where half the trapping volume is rendered inaccessible by the presence of the mirror. Optical access is also much improved, both because the coils are oriented in such a way as to be less obstructive, and because we have removed the necessity of having a beam traveling in a plane parallel to mirror A. This allows us to use as much of the 360° viewing angle in that plane as is necessary for imaging or manipulation beams. If this is not a requirement, a simpler set-up can alternatively be used, where only one set of beams is used in the double-'Λ' geometry, the trapping and cooling forces in the plane normal to the paper in Fig. 1 being produced by means of a separate pair of counterpropagating beams.

An important advantage of this geometry is that the the double-'Λ' shape of the MOT beams affords better imaging of the trap, allowing microscope objectives to be mounted very close to it. With a custom-made objective, we can achieve high-NA imaging (NA $>$ 0.5) and a diffraction-
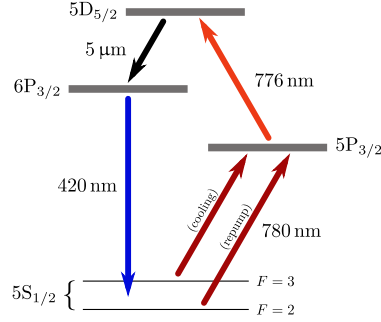
Fig. 3. (Color online.) The four-level system in ^{85}Rb that we use to image our atoms. The MOT lasers (780 nm) and a laser at 776 nm are used to induce a ladder transition. The population decays back to the ground state, via an intermediate state, and emits a 420 nm photon in the process. The hyperfine splitting of the excited states is not drawn for clarity.

limited resolution of $< 2\,\mu$m. While a similar degree of optical access may be possible in the traditional 6-beam configuration, we note that this latter configuration is unsuitable for atom–surface interaction studies. In contrast, mirror A in our geometry can be replaced by any other suitable reflecting surface. One candidate for such a reflecting surface would be one of the surfaces of a Dove prism, which could then be used to form a two-dimensional bichromatic evanescent-field trap [10] close to the mirror surface. This trap would be loaded from the MOT cloud using such techniques as magneto-optic launching, which is explained in Section 4.

Aside from this marked increase in optical access, our system is simple to set up and operate. In particular, it requires fewer beam paths than a traditional MOT (two rather than three) and alignment of the beams is also easy: a CCD camera looking up at the mirror can be used to align the beams coarsely; once this is done, optimization of the cold atom signal provides the fine-tuning of the alignment.

2.2. Characterization

A typical trap, as shown in Fig. 2, contains around 4×10^4 ^{85}Rb atoms and has a $1/e$ diameter of the order of 400 μm along the minor axes. Combined with a measured trap lifetime $\tau_0 \approx 6$ s, this allows us to infer the trap loading rate, $N_0/\tau_0 \approx 6.7 \times 10^3\,\mathrm{s}^{-1}$. We measured a cloud temperature of $110 \pm 40\,\mu$K, the large uncertainty being due to the imprecision in measuring the cloud size.

Typical parameters for the operation of our trap are: a detuning of -14.9 MHz, or $-2.5\,\Gamma$ ($\Gamma \approx 6.1$ MHz [11]), for the cooling laser and a power of 6 mW divided between the two trapping beams (beam diameter: 6 mm). The minimum power necessary to produce the MOT was found to be ≈ 1.3 mW in each of the two beams. The trap was loaded from background gas of a natural isotopic mixture of rubidium at a pressure of 10^{-9} mbar. The cooling and repump lasers were locked using the DAVLL technique [12] for long-term stability and flexibility of operation.

3. Multilevel imaging system

The most common method of imaging a cold atom cloud in a MOT is fluorescence imaging. When the cloud is close to a reflecting surface both the cloud and its reflections will be seen by the imaging system (see Ref. [13], for example). This situation is exacerbated by the presence of surfaces that reflect unwanted light into the imaging optics and thereby decreasing the
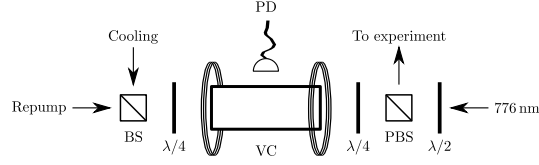
Fig. 4. 776 nm spectroscopy and locking system. (P)BS: (polarizing) beam splitter cube; $\lambda/4$: quarter-wave plate; $\lambda/2$: half-wave plate; VC: heated vapor cell; PD: filtered photo-diode.

signal-to-noise ratio of the imaging system. Fig. 2, shows an example of the mirror in our system scattering the MOT beams into the imaging system.

This problem may be overcome using two-stage excitation imaging. We make use of a four-level system in ^{85}Rb (see Fig. 3 for details), similarly to Refs. [14] and [15]; atoms in the $5S_{1/2}$ ground state are pumped to the $5D_{5/2}$ state via 780 nm and 776 nm radiation, the former being provided by one of the MOT beams, and then decay back to the ground state via an intermediate $6P_{3/2}$ state, emitting 420 nm radiation, which we detect. We note that a very similar system was recently used to produce a multiphoton MOT [16]. In our system, this process gives a significantly smaller signal than can be obtained through 780 nm fluorescence imaging. However, it has the benefit of being entirely background-free: in a well-shielded system, the entire 420 nm signal reaching the detector has its origin in the cold atom cloud. Off-the-shelf filters can then be used to remove the 780 nm radiation reaching the detector.

Generation of the 776 nm beam

The 776 nm beam is produced using a Sanyo DL7140-201S diode and the same external cavity diode laser design used to produce the MOT cooling and trapping beams. Since ^{85}Rb has no spectral features in this wavelength range that are suitable for locking the laser frequency, a multilevel locking system is used (see Fig. 4). 5 mW from each of the MOT cooling and re-pump beams (≈ 780 nm) and 1.5 mW from the 776 nm beam, all rendered circularly polarized by the quarter-wave plates, enter the heated vapor cell (VC) from opposite ends. A large-area UV-enhanced filtered silicon photodiode (PD), operating in photovoltaic mode, picks up the resulting Doppler-free fluorescence and is amplified by means of a LMP7721 amplifier chip. Magnetic coils surrounding the heated vapor cell control the Zeeman shift of the magnetic sub-levels of the atoms inside the cell, shifting this signal, and therefore the lock point, as required. Around 4 mW of the 776 nm beam is then mixed in with the MOT cooling and repump beams and sent through a fiber to the MOT.

We show a sample 420 nm signal, as detected at the photodiode, in Fig. 5, where the hyperfine splitting of the $5D_{5/2}$ level in ^{85}Rb is evident in the shoulders on the right-hand side of the peak in the figure. The 776 nm laser diode is locked to the side of one the main peak, at the point indicated by the dashed line in Fig. 6, using a conventional PID circuit. The lock point is found by manually and slowly adjusting the frequency offset of the 776 nm laser to maximize the fluorescence from the MOT cloud. Evident in this latter figure are two well-resolved peaks, caused by the Autler–Townes splitting [17]. Locking at a detuning of around 6.5 MHz from the peak of absorption in the vapor cell gives the strongest signal in the MOT cloud, as recorded by the photomultiplier tube trace shown in the same figure.
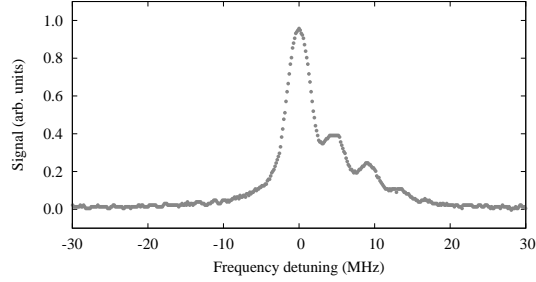
Fig. 5. 420 nm fluorescence from the vapor cell, observed on PD (see Fig. 4) as a function of the detuning of the 776 nm beam, with the cooling and repump beams locked and shifted by 80 MHz with respect to the frequencies required to make a MOT. The various peaks are due the hyperfine structure in ^{85}Rb. To obtain these data, we removed the quarter-wave plates on either end of the vapor cell, thus having linearly polarized light entering the cell from both ends.
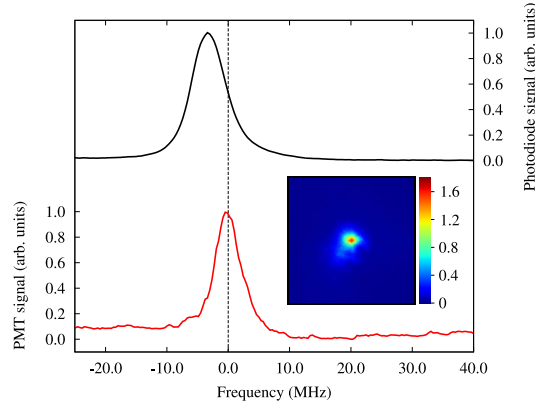
Fig. 6. (Color online.) 420 nm fluorescence observed on PD (solid black line, see Fig. 4) and on a PMT imaging the MOT cloud (solid red line) as a function of the detuning of the 776 nm beam. The zero on the frequency axis corresponds to the point at which the signal from the MOT cloud is highest; we lock to this point. The magnitude and sign of the shift between the two curves can be set arbitrarily by varying the magnetic field generated by the coils around the vapor cell. *Inset:* MOT cloud imaged at 420 nm (scale in 10^3 counts per second). This image is naturally background-free.

4. Surface loading by magneto-optic launching

Transporting cold atoms from the region where the trap naturally forms to the sample is an essential part of many experiments investigating atom–surface effects. Several methods have been devised for moving cold atom clouds, including the use of push beams [18] and moving magnetic coils [19]. Push beams are easy to set up, requiring either the addition of one extra beam or the switching off of one of the counterpropagating beams, but cannot be used to push atom clouds towards highly reflective surfaces. Using moving magnetic coils requires a rather involved mechanical setup.

We make use of a third method, which we call magneto-optic launching, for transport of the
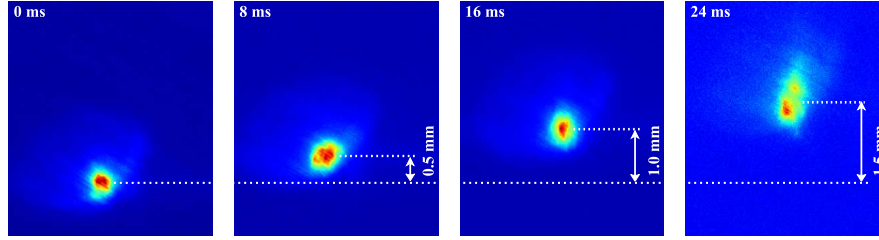
Fig. 7. (Color online.) A sequence of four false color fluorescence images, taken at 8 ms intervals, of the cloud before and after it has been given a magnetic impulse. The first shot (leftmost picture) shows the cloud just before the magnetic field is pulsed. The second, and subsequent, shots show the cloud at later times. The transfer efficiency after 24 ms is over 40%.

atom cloud by rapidly moving the trap center and then releasing the cloud, thereby imparting momentum to it. An auxiliary coil is added to the system in Fig. 1, above the upper MOT coil. After the MOT cloud forms, a long current pulse is applied to this auxiliary coil, which launches the cloud upward with a speed determined by the size and duration of the current pulse, and then the cloud is released from the trap by switching off the MOT beams after 20 ms. Fig. 7 shows a series of photographs of the cloud after being launched by a magnetic pulse. It can be seen that the pulse results in an approximately uniform vertical cloud speed of $0.063\,\mathrm{m\,s^{-1}}$. The physical orientation of our system, with the mirror and sample being *above* the trapping region, allow us to launch the cloud upwards with a much greater degree of control than would be possible if the cloud were merely dropped downwards.

Finally, we note that the equilibrium distance of the MOT cloud from the mirror surface depends on the beam diameter and the size of the 'sample area', *i.e.*, the section of the mirror that acts as a sample and is not usable as a plane mirror. With a sample area diameter of 2 mm and beam diameter of 4 mm, the cloud can be made to form less than 4 mm away from the surface, allowing us to use the magneto-optic launching method to move the atoms closer to the surface for interaction studies.

5. Conclusion

We have introduced and characterized a modified magneto-optical trap geometry that allows the behavior of atoms close to surfaces to be explored with greater flexibility and better optical access than the standard configurations. A multilevel imaging system, which proves to be important in eliminating background signals and unwanted scatter when atoms are close to highly reflecting templated surfaces, was also characterized and explored. The combined system is therefore ideal for exploring the miniaturization of atom traps and is easily applied to a wide range of experiments.

Acknowledgments

Stimulated Raman transitions via multiple atomic levels

James Bateman,* André Xuereb, and Tim Freegarde

School of Physics and Astronomy, University of Southampton, Southampton, SO17 1BJ, United Kingdom

(Dated: April 13, 2010)

We consider the stimulated Raman transition between two long-lived states via multiple intermediate states, such as between hyperfine ground states in the alkali-metal atoms. We present a concise treatment of the general, multilevel, off-resonant case, and we show how the lightshift emerges naturally in this approach. We illustrate our results by application to alkali-metal atoms and we make specific reference to cesium. We comment on some artifacts, due solely to the geometrical overlap of states, which are relevant to existing experiments.

PACS numbers: 42.65.Dr; 32.70.-n; 82.53.Kp; 42.50.Gy

I. INTRODUCTION

The stimulated Raman transition is an extremely powerful tool for laser manipulation of cold atoms and ions. By coupling long-lived states via, but never populating, radiative states, experimenters can emulate near-ideal two-level quantum systems with no significant decay [1–3]. This technique has been used to measure sublinewidth features [4, 5] and to construct atomic interferometers which, by exploiting photon recoil, create spatially separated atomic wave packets which are sensitive to gravity [6, 7] or fundamental constants [8, 9]. The effective two-level system, which emerges from the Raman problem, can exhibit behavior such as Rabi flopping [10, 11], can be used for experiments such as Ramsey interferometry [12, 13], and can provide the qubits for quantum information processing [14–16]. Sequences of Raman pulses can be used to craft arbitrary superpositions in systems with numerous metastable states [17] and to prepare such systems in particular states prior to coherent manipulation [18]. Raman processes have also been used to cool atomic samples to far below the photon recoil limit [19–22].

Throughout the literature, when the Raman transition is discussed, the level structure of the atom is often approximated to three levels—two metastable states and one intermediate (radiative) state. The Raman problem is solved for this prototypical case and then extended, without proof, to include the multilevel structure of the atom by summing over the various possible routes (see, e.g., Ref. [7, §2.1]). Here, by including multiple routes from the outset, we confirm that this simple approach is correct, show how an expression for the lightshift emerges naturally from this treatment, and show that the system behaves as a two-level system with an effective coupling strength and an effective detuning.

There is much existing work related to this problem. The three-level (single intermediate state) off-resonant case has been treated [23], there have been extensions to four levels [24], and the general multilevel problem has

been recast into "serial" and "parallel" cases [25]. It has never been shown rigorously, however, that the three-level case can be extended in the way so often assumed. In the following, we use the semiclassical approach but alternatively one might consider the Jaynes–Cummings model [26, 27].

This article is structured as follows. We first describe, in Sec. II, the Raman transition in a three-level system and we show how this can be generalized to include multiple intermediate states; details of the lengthly calculation are confined to the appendix. We then derive, in Sec. III, expressions for the behavior of the quantum-mechanical amplitudes in the general, off-resonance case. In Sec. IV we show how these results can be applied to alkali-metal atoms, and we conclude in Sec. V.

II. THREE-LEVEL SYSTEMS

The simplest system in which a Raman transition may be driven is the three-level "Λ" system, illustrated in Fig. 1, in which two long-lived ground states are coupled via a radiative upper state which, because the single-photon detuning is sufficiently large, is never significantly populated. We label the states of the system by $|n\rangle$, with states $|0\rangle$ and $|2\rangle$ coupled by the "pump" field of strength Ω_P and frequency ω_P, and states $|1\rangle$ and $|2\rangle$ coupled by the "Stokes" field of strength Ω_S and frequency ω_S. Using the usual correspondence between bra–ket and column vector notation (see, e.g., Ref. [28, §II-C]), the Hamiltonian for this system may be represented by the following matrix (see, e.g., Ref. [11, §3.2]):

$$\begin{pmatrix} \omega_0 & 0 & \Omega_P \cos\omega_P t \\ 0 & \omega_1 & \Omega_S \cos\omega_S t \\ \Omega_P \cos\omega_P t & \Omega_S \cos\omega_S t & \omega_2 \end{pmatrix} . \qquad (1)$$

Here, as in standard treatments, we assume there is no coupling between states $|0\rangle$ and $|2\rangle$ by the Stokes field, or between states $|1\rangle$ and $|2\rangle$ by the pump field.

This Hamiltonian can be simplified by making the rotating wave approximation and transforming to the inter-

---

*Electronic address: jbateman@soton.ac.uk
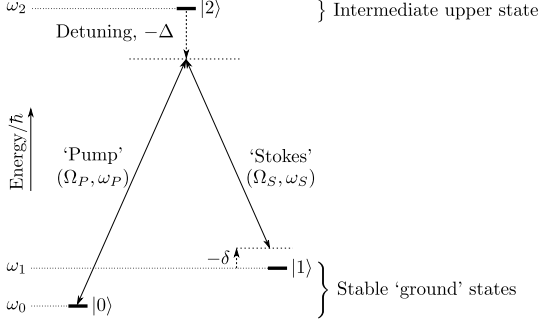
FIG. 1: A simple three-level "Λ" system, in which a Raman transition between states $|0\rangle$ and $|1\rangle$ is driven by "pump" and "Stokes" fields via intermediate state $|2\rangle$. For each field, the coupling strength and frequency are shown in parentheses, and frequencies are chosen to be near two-photon resonance: $\omega_P = (\omega_2 - \omega_0) + \Delta$; $\omega_S = (\omega_1 - \omega_0) + (\Delta + \delta)$. The single-photon detuning Δ is large compared with the couplings, $|\Delta| \gg \Omega_{P,S}$, and, in this illustration, is negative: $\Delta < 0$. The two-photon detuning δ is small compared with the separation between the ground states and, in this illustration, is also negative.

action picture. This yields a slowly varying Hamiltonian,

$$\hat{H} = \begin{pmatrix} 0 & 0 & \frac{1}{2}\Omega_P \\ 0 & 0 & \frac{1}{2}\Omega_S e^{+i\delta t} \\ \frac{1}{2}\Omega_P & \frac{1}{2}\Omega_S e^{-i\delta t} & -\Delta \end{pmatrix}, \qquad (2)$$

where the pump frequency $\omega_P = (\omega_2 - \omega_0) + \Delta$ is detuned from single-photon resonance by Δ, and the difference between the pump frequency and the Stokes frequency $\omega_S = (\omega_1 - \omega_0) + (\Delta + \delta)$ is offset by δ from the two-photon resonance $(\omega_1 - \omega_0)$. We now extend this interaction picture to include multiple levels and define the Hamiltonian $\hat{H}_A$ to be

$$\begin{pmatrix} 0 & 0 & \frac{1}{2}\Omega_{P;2} & \frac{1}{2}\Omega_{P;3} & \cdots \\ 0 & 0 & \frac{1}{2}\Omega_{S;2}e^{+i\delta t} & \frac{1}{2}\Omega_{S;3}e^{+i\delta t} & \cdots \\ \frac{1}{2}\Omega_{P;2}^* & \frac{1}{2}\Omega_{S;2}^* e^{-i\delta t} & -\Delta_2 & 0 & \cdots \\ \frac{1}{2}\Omega_{P;3}^* & \frac{1}{2}\Omega_{S;3}^* e^{-i\delta t} & 0 & -\Delta_3 & \cdots \\ \vdots & \vdots & \vdots & \vdots & \ddots \end{pmatrix}. \tag{3}$$

The second part of the subscript, $2, 3, \ldots, N$, denotes the level to which the pump or Stokes field couples. Note that the oscillation frequency is the same for each Stokes term because this depends on the difference in the frequency of the fields and not on the Bohr energy of the intermediate level. However, the single-photon detunings do depend on the intermediate level Bohr frequencies, but we now make the approximation that the detuning is large compared with the separation of these intermediate levels, and hence $\Delta := \Delta_2 \approx \Delta_3 \approx \ldots \approx \Delta_N$.

In this limit, the above Hamiltonian describes a Raman system and we expect to see oscillations of population between the ground states. We solve the Schrödinger equa-

tion with this Hamiltonian by using unitary transformations to find a basis where the time evolution of the states is simple and the transformed Hamiltonian is diagonal. When one makes such a conversion between bases, is it possible to find an equivalent Schrödinger equation with a transformed Hamiltonian [11]: if $|\psi_B\rangle = \hat{O}_{BA} |\psi_A\rangle$, then $i(\partial/\partial t) |\psi_B\rangle = \hat{H}_B |\psi_B\rangle$ where

$$\hat{H}_B = \hat{O}_{BA} \left(\hat{H}_A \hat{O}_{BA}^{-1} - i\frac{\partial}{\partial t}\hat{O}_{BA}^{-1} \right). \tag{4}$$

For the multistate Hamiltonian $\hat{H}_A$ in Eq. (3), we choose the operator $\hat{O}_{BA}$ to be the matrix of eigenvectors; the first term $\hat{O}\hat{H}\hat{O}^{-1}$ is thus the diagonal matrix of the eigenvalues. In the appendix, we detail a procedure to find the eigensystem of this Hamiltonian; we find two eigenvectors which are superpositions of these ground states, and $N - 2$ more which are superpositions of the remaining intermediate levels. These $N - 2$ upper states are decoupled from the ground states and so we ignore them in the following treatment.

The difference between the eigenvalues for the two ground state eigenvectors is

$$\widetilde{\Omega}_B = \frac{1}{2\Delta} \sqrt{|\boldsymbol{\Omega}_P \cdot \boldsymbol{\Omega}_S^*|^2 + \frac{1}{4}\left(\|\boldsymbol{\Omega}_S\|^2 - \|\boldsymbol{\Omega}_P\|^2\right)^2}, \tag{5}$$

where, for conciseness, we have represented the couplings as vectors $\boldsymbol{\Omega}_P$ and $\boldsymbol{\Omega}_S$ with components $\Omega_{P;i}$ and $\Omega_{S;i}$ respectively, and have used vector notation for dot products and norms. This oscillation frequency is composed of a coupling strength Ω_B and a detuning Δ_B, via $\widetilde{\Omega}_B = \sqrt{\Omega_B^2 + \Delta_B^2}$, analogously to a two-level system:

$$\Omega_B = \frac{|\boldsymbol{\Omega}_P \cdot \boldsymbol{\Omega}_S^*|}{2\Delta}, \tag{6}$$

$$\Delta_B = \frac{\|\boldsymbol{\Omega}_S\|^2 - \|\boldsymbol{\Omega}_P\|^2}{4\Delta}. \tag{7}$$

The detuning Δ_B is readily identified as the lightshift and we justify this in the next section.

The operator which describes the transformation from the bare ground states to these dressed ground states can, because of normalization, be written as a rotation:

$$\hat{O}_{BA} = \begin{pmatrix} \cos\theta & e^{+i\delta t}\sin\theta \\ -e^{-i\delta t}\sin\theta & \cos\theta \end{pmatrix}, \tag{8}$$

and the angle θ is defined by $\tan\theta = \left(\Delta_B - \widetilde{\Omega}_B\right)/\Omega_B$.

This treatment is sufficient for the on two-photon resonance case, where $\delta = 0$, but in general the effective Hamiltonian $\hat{H}_B$ also contains a time-derivative second term, originating from the time-dependence of the operator $\hat{O}_{BA}$. Away from the two-photon resonance, where $\delta \neq 0$, we find the following slowly varying, but nevertheless time-dependent, effective Hamiltonian:

$$\hat{H}_B = \begin{pmatrix} -\delta\sin^2\theta & -\delta e^{+i\delta t}\cos\theta\sin\theta \\ -\delta e^{-i\delta t}\cos\theta\sin\theta & \delta\sin^2\theta + \widetilde{\Omega}_B \end{pmatrix}. \tag{9}$$

III. DETUNING FROM RESONANCE

The Hamiltonian $\hat{H}_B$ in Eq. (9) has the same form as that for the simple two-level problem in the interaction picture and with the rotating-wave approximation. We can, therefore, use familiar tools to solve this problem. First, we transform to find a time-independent Hamiltonian using the operator $\hat{O}_{CB}$ in Eq. (4):

$$\hat{O}_{CB} = \begin{pmatrix} 1 & 0 \\ 0 & e^{i\delta t} \end{pmatrix}$$

$$\implies \hat{H}_C = \begin{pmatrix} -\delta \sin^2\theta & -\delta \cos\theta \sin\theta \\ -\delta \cos\theta \sin\theta & \delta \cos^2\theta + \widetilde{\Omega}_B \end{pmatrix} . \quad (10)$$

Next, analogously to the dressed-states approach, we rotate by an angle θ_2 (thus defining $\hat{O}_{DC}$) where

$$\tan(2\theta_2) = \frac{\delta \sin(2\theta)}{\widetilde{\Omega}_B - \delta \cos(2\theta)} , \quad (11)$$

to find a diagonal Hamiltonian $\hat{H}_D$. The difference between the diagonal elements of $\hat{H}_D$ corresponds to the phase evolution frequency $\widetilde{\Omega}_D$ of the states in this basis. As in the previous section, we see that this oscillation frequency is composed of a coupling strength Ω_B and a modified effective detuning Δ_D: $\widetilde{\Omega}_D = \sqrt{\Omega_B^2 + \Delta_D^2}$, where $\Delta_D = \Delta_B - \delta$ is the detuning relative to Δ_B, which was previously identified as the lightshift.

We now relate the pure phase evolution in this doubly dressed basis to the evolution of the bare states by concatenating the transformations that led us to this final Hamiltonian:

$$\hat{O}_{DA} = \hat{O}_{DC} \cdot \hat{O}_{CB} \cdot \hat{O}_{BA} \quad (12)$$

and $|\psi_D\rangle = \hat{O}_{DA} |\psi_A\rangle$, or

$$\begin{pmatrix} D_0 \\ D_1 \end{pmatrix} = \begin{pmatrix} \cos(\theta+\theta_2) & e^{i\delta t}\sin(\theta+\theta_2) \\ -\sin(\theta+\theta_2) & e^{i\delta t}\cos(\theta+\theta_2) \end{pmatrix} \begin{pmatrix} A_0 \\ A_1 \end{pmatrix} , \quad (13)$$

where $D_{0,1}$ and $A_{0,1}$ are the ground- and excited-state components of the doubly dressed wave function $|\psi_D\rangle$ and the bare (interaction picture) wave function $|\psi_A\rangle$, respectively. Finally, the time evolution of the doubly dressed states is simply

$$\begin{pmatrix} D_0(t) \\ D_1(t) \end{pmatrix} = \begin{pmatrix} D_0(t=0) \\ D_1(t=0)e^{i\widetilde{\Omega}_D t} \end{pmatrix} . \quad (14)$$

Using Eq. (13) we can find the dressed state initial conditions $D_{0,1}(t=0)$ in terms of the bare state initial conditions $A_{0,1}(t=0)$. Using these values, we can then use Eq. (14) to find the dressed state coefficients at some later time. Finally, we can invert the transformation in Eq. (13) to find the time evolution of the bare state amplitudes.

A. Explicit forms of the amplitudes

The time dependence of the bare state coefficients $A_{0,1}(t)$ is readily calculable from the procedure described above and is stated here for completeness:

$$A_0(t) = \left(A_0(0) \left[\cos\left(\tfrac{1}{2}\widetilde{\Omega}_D t\right) - i\frac{\Delta_D}{\widetilde{\Omega}_D} \sin\left(\tfrac{1}{2}\widetilde{\Omega}_D t\right) \right] \right.$$

$$\left. + A_1(0) \, i\frac{\Omega_D}{\widetilde{\Omega}_D} \sin\left(\tfrac{1}{2}\widetilde{\Omega}_D t\right) \right) ; \quad (15a)$$

$$A_1(t) = \left(A_1(0) \left[\cos\left(\tfrac{1}{2}\widetilde{\Omega}_D t\right) + i\frac{\Delta_D}{\widetilde{\Omega}_D} \sin\left(\tfrac{1}{2}\widetilde{\Omega}_D t\right) \right] \right.$$

$$\left. + A_0(0) \, i\frac{\Omega_D}{\widetilde{\Omega}_D} \sin\left(\tfrac{1}{2}\widetilde{\Omega}_D t\right) \right) e^{-i\delta t} . \quad (15b)$$

Hence the system behaves as a two-level system with the coupling strength $\Omega_D = \Omega_B$ and detuning $\Delta_D = \Delta_B - \delta$, relative to the effective detuning Δ_B. This justifies our previous identification of Δ_B with the lightshift.

B. Oscillation amplitude

The complete, but cumbersome, formulas in Eq. (15) describe the behavior of the bare-state amplitudes in terms of the bare state initial conditions. If, instead, we express this evolution in terms of the initial values in the doubly dressed basis, we see clearly that the evolution is composed of a time-independent offset and an oscillation:

$$A_0(t) = \cos(\theta+\theta_2)D_0(0) - \sin(\theta+\theta_2)D_1(0)e^{i\widetilde{\Omega}_D t} . \quad (16)$$

The population $p_0(t) = |A_0(t)|^2$ in state $|0\rangle$ therefore oscillates with peak-to-peak amplitude no greater than $m = \sin[2(\theta+\theta_2)]$ which, expressed in terms of the effective coupling strength and detuning, is

$$m = \frac{\Omega_B}{\sqrt{\Omega_B^2 + \Delta_D^2}} . \quad (17)$$

This envelope function describes a power-broadened Lorentzian, centered on the light shifted frequency difference between the ground states. This expression represents the maximum possible population transfer, and any oscillation will be contained within this envelope.

C. Comments

A few specific cases are provided here for illustration. First, for $\mathbf{\Omega}_P = (0,0,\Omega_P)$ and $\mathbf{\Omega}_S = (0,0,\Omega_S)$ we recover the well-known results for the three level problem. Next we note two interesting cases: for $\|\mathbf{\Omega}_P\| = \|\mathbf{\Omega}_S\|$, the lightshift Δ_B is zero. On the other hand, for $|\mathbf{\Omega}_P \cdot \mathbf{\Omega}_S^*| = 0$, the Rabi frequency Ω_B is zero.

If, as in this last case, the coupling vectors $\boldsymbol{\Omega}_P$ and $\boldsymbol{\Omega}_S^*$ are orthogonal, then the transition is not driven. Examples include the trivial case where there is no intermediate state to which both ground states are coupled and the case where there are states to which both are coupled, but where these individual coupling strengths sum to zero. However, unless the vectors are orthogonal, it is possible to adjust the pump and Stokes field strengths to ensure the norms of the vectors are equal, and hence that the lightshift is zero.

Our approach relies on the slow time-dependence of the interaction-picture Hamiltonian: we require that the system is near two-photon resonance, as previously stated, and that there is no coupling of state $|0\rangle$ by the Stokes field or of state $|1\rangle$ by the pump field. If present, these cross-coupling terms would cause the off-diagonal terms in $\hat{H}_A$ to oscillate in amplitude as well as phase, and the treatment in the appendix would no longer be valid.

For our treatment to be valid, it must therefore be possible to identify clearly which field is resonant with which transition (see Refs [1, §13.1] and [11, §3.9] for further discussion). First, the detuning must be such that no field is close to a single-photon resonance: $|\Delta| \gg \|\boldsymbol{\Omega}_{P,S}\|$ and $|\Delta \pm \omega_{10}| \gg \|\boldsymbol{\Omega}_{P,S}\|$. Additionally, the coupling strength must be sufficiently small that each ground state can be resolved: $\omega_{10} \gg \|\boldsymbol{\Omega}_{P,S}\|$. If this last condition is violated, the system may still appear Ramanlike and exhibit coherent behavior, but it is not described adequately by the treatment in this article.

IV. ALKALI-METAL ATOMS

We are able to calculate the Rabi frequency and lightshift for two states $|0\rangle$ and $|1\rangle$ coupled via a number of upper states. A common embodiment of this situation is the coupling of two ground hyperfine states via a manifold of upper hyperfine states in an alkali-metal atom. Indeed, there typically exists many such pairs of states, but, as ensured by conservation of angular momentum, one state is Raman coupled to at most one other state; hence, the total system may be treated as a collection of independent pairwise couplings.

As a typical example, consider the Raman transition between the ground hyperfine states, via the radiative upper states, in atomic cesium. The pump and Stokes fields, both tuned near to the D_2 transition at 852 nm, couple states $\left|6^2S_{1/2}, F=3\right\rangle$ and $\left|6^2S_{1/2}, F=4\right\rangle$, respectively, to the $6^2P_{3/2}$ manifold, and have a frequency difference near to the hyperfine splitting of 9.2 GHz [29]. The two ground states and the intermediate states are

$$
\begin{aligned}
|0\rangle &= \left|6^2S_{1/2}; F=3; m_F\right\rangle , \\
|1\rangle &= \left|6^2S_{1/2}; F=4; m_F + q_P - q_S\right\rangle , \text{ and} \\
|n\rangle &= \left|6^2P_{3/2}; F=2,3,4,5; m_F + q_P\right\rangle ,
\end{aligned} \tag{18}
$$

where $q_{P,S} = 0, -1, +1$ are the polarizations of the copropagating pump and Stokes fields and correspond to

linear and left and right circular polarizations, respectively; m_F labels the Zeeman sublevel, corresponding to the projection of the total angular momentum F along the quantization axis provided by an external magnetic field [30]. Linear polarization, in this context, refers specifically to the case of the light electric field parallel to the quantization axis; if these axes are orthogonal, the light field interacts with the atom as though it were a superposition of left and right circular polarizations.

The coupling strengths $\Omega_{P,S}$ depend not only on the light intensities but also on the dipole matrix element for the transition. Using the Wigner-Eckart theorem [30–32] we can split the overlap integral needed to find this dipole matrix element and extract from it a purely geometrical term G, leaving a term which embodies the other physical details of the transition:

$$
\begin{aligned}
\left\langle 6^2P_{3/2}, F', m_F' \left|\hat{\mu}\right| 6^2S_{1/2}, F, m_F \right\rangle &= \langle J\|\hat{\mu}\|J'\rangle \\
&\times G\left(I, J, F, m_F, J', F', m_F', q\right) .
\end{aligned} \tag{19}
$$

The "reduced" matrix element, denoted by double bars $\|$, depends on many details of the atom, including nuclear mass, and is not easily calculated; it can, however, be found experimentally from measurements of the upper-state lifetime, as described by Loudon [33, Eq. (2.57)] and Demtröder [34]:

$$
\Gamma = \frac{16\pi^3}{3\epsilon_0 h\lambda^3} \frac{2J+1}{2J'+1} \left|\langle J\|\hat{\mu}\|J'\rangle\right|^2 . \tag{20}
$$

The second part is the product of geometrical terms:

$$
\begin{aligned}
G = (-1)^{2F'+J+I+m_F} &\sqrt{(2F'+1)(2F+1)(2J+1)} \\
&\times \begin{pmatrix} F' & 1 & F \\ m_F' & q & -m_F \end{pmatrix} \begin{Bmatrix} J & J' & 1 \\ F' & F & I \end{Bmatrix}
\end{aligned} \tag{21}
$$

where the arraylike symbol in parentheses $(\ldots)$ is the Wigner 3-j symbol and the similar term in braces $\{\ldots\}$ is the Wigner 6-j symbol [35, §3.3]; both are closely related to the Clebsch-Gordan coefficients. This relation is described in detail by Edmonds [36]. The two states coupled by the Raman interaction are both in $6^2S_{1/2}$ so, in the calculations that follow, it is only this geometrical term which is relevant.

We imagine the atom in a region of uniform magnetic field and consider an experiment where it is possible to adjust the frequency difference in order to sweep across transitions between various Zeeman sublevels. The properties which affect the dipole moment are the various quantum numbers: the nuclear spin $I = 7/2$; the electron angular momentum $J = 1/2$ or $J' = 3/2$; the total angular momentum $F = 3$ to $F = 4$ via $F' = 2, 3, 4, 5$; and the aforementioned projection m_F of F along the quantization axis.

The coupling strength for a dipole transition between states $|n\rangle$ and $|m\rangle$ is proportional to the electric field [1]:

$$
\Omega_{P,S} = E_{P,S} \langle n|\hat{\mu}|m\rangle / \hbar \tag{22}
$$

where $\hat{\mu}$ is the dipole operator. As above, we can extract a geometrical term and, using the vector notation,

$$\boldsymbol{\Omega}_{\mathrm{P,S}} = E_{\mathrm{P,S}}\langle J\|\hat{\mu}\|J'\rangle\boldsymbol{G}_{\mathrm{P,S}}/\hbar. \tag{23}$$

Hence, the relative properties of each of the Zeeman sublevels are determined by the geometrical terms $\boldsymbol{G}_{\mathrm{P,S}}$. If we revisit the equations for the coupling strength (Eq. (6)) and the lightshift (Eq. (7)), we see that these terms appear as $|\boldsymbol{G}_{\mathrm{P}} \cdot \boldsymbol{G}_{\mathrm{S}}|$ and $\|\boldsymbol{G}_{\mathrm{P,S}}\|^2$, respectively. Thus:

$$\Omega_{\mathrm{B}} = \frac{\langle J\|\hat{\mu}\|J'\rangle^2}{2\Delta\,\hbar^2}|E_{\mathrm{P}}E_{\mathrm{S}}^*|\,|\boldsymbol{G}_{\mathrm{P}} \cdot \boldsymbol{G}_{\mathrm{S}}|\text{ and} \tag{24}$$

$$\Delta_{\mathrm{B}} = \frac{\langle J\|\hat{\mu}\|J'\rangle^2}{4\Delta\,\hbar^2}\Big(|E_{\mathrm{S}}|^2\|\boldsymbol{G}_{\mathrm{S}}\|^2 - |E_{\mathrm{P}}|^2\|\boldsymbol{G}_{\mathrm{P}}\|^2\Big). \tag{25}$$

It is simple to calculate these factors for a given initial state and pair of polarizations to examine how the lightshift and the coupling strength depend on the strength of the applied fields. We find that $\|\boldsymbol{G}\|^2$, for transitions from $|J = 1/2, F = I \pm 1/2, m_F\rangle$ to $|J', F', m_F + q\rangle$, driven by light with polarization q, are, for an alkali-metal atom with nuclear spin I, given by

$$\|\boldsymbol{G}\|^2 = \frac{1}{3}\left(1 \pm A(J')\frac{q\,m_F}{2I+1}\right) \tag{26}$$

where $A(1/2) = -2$ for the D_1 transition and $A(3/2) = 1$ for the D_2 transition. The pump vector $\boldsymbol{G}_{\mathrm{P}}$ couples from the lower hyperfine state and corresponds to the negative branch ($F = I - 1/2$); the stokes vector $\boldsymbol{G}_{\mathrm{S}}$ couples from the upper hyperfine state and corresponds to the positive branch ($F = I + 1/2$). Using these expressions and Eq. (25), one may easily calculate the lightshift for a given Raman transition in any alkali-metal atom.

We now turn to the coupling strength Ω_{B} which, for equal polarizations $(q_{\mathrm{P}}, q_{\mathrm{S}}) = (1, 1)$, is symmetrical about $m_F = 0$. We find

$$|\boldsymbol{G}_{\mathrm{P}} \cdot \boldsymbol{G}_{\mathrm{S}}| = \frac{|A(J')|}{3(2I+1)}\sqrt{(I+1/2)^2 - m_F^2}, \tag{27}$$

for the D_1 and D_2 transitions, where A is given above. If we now break this symmetry by choosing, for example, $(q_{\mathrm{P}}, q_{\mathrm{S}}) = (0, 1)$, we find

$$|\boldsymbol{G}_{\mathrm{P}} \cdot \boldsymbol{G}_{\mathrm{S}}| = \frac{|A(J')|}{3(2I+1)}\sqrt{T(I+1/2-m_F)}, \tag{28}$$

where $T(n)$ is the nth triangular number $(1, 3, 6, 10\ldots)$. The dependence of coupling strength on m_F level is illustrated in Fig. 2.

The values for a common arrangement are shown in Table I. While of course linear in any overall scaling of the intensity, the lightshift has a different dependence on the individual field strengths for each of the Zeeman sublevels. It is offset from zero (for unequal intensities) and is linear in m_F; the lightshift between the hyperfine ground states hence has the same dependence on m_F as
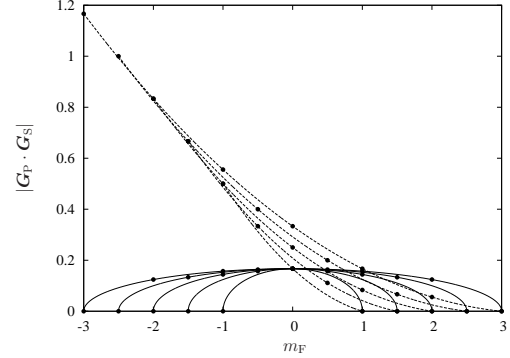
FIG. 2: Illustration of the dependence of coupling strength described by Eqs (27) (solid) and (28) (dashed). The values have physical meaning at integer and half-integer m_F only (dots); continuous lines are shown to guide the eye. A line is shown for each of several nuclear spins, beginning at $I = 1/2$ and increasing in steps of one half out from the center (solid) and from bottom to top (dashed). The strongest coupling is between extremal m_F states by linear and circular polarisations.

m_F	$\|\boldsymbol{G}_{\mathrm{P}} \cdot \boldsymbol{G}_{\mathrm{S}}\|$	$\|\boldsymbol{G}_{\mathrm{S}}\|^2$	$\|\boldsymbol{G}_{\mathrm{P}}\|^2$
-3	$\sqrt{7}/24$	$5/24$	$11/24$
-2	$\sqrt{12}/24$	$6/24$	$10/24$
-1	$\sqrt{15}/24$	$7/24$	$9/24$
0	$\sqrt{16}/24$	$8/24$	$8/24$
$+1$	$\sqrt{15}/24$	$9/24$	$7/24$
$+2$	$\sqrt{12}/24$	$10/24$	$6/24$
$+3$	$\sqrt{7}/24$	$11/24$	$5/24$

TABLE I: Scaling of the coupling strength and the lightshift for the transition $|F = 3, m_F\rangle$ to $|F = 4, m_F + q_{\mathrm{P}} - q_{\mathrm{S}}\rangle$ for $(q_{\mathrm{P}}, q_{\mathrm{S}}) = (1, 1)$, in cesium, in terms of the geometrical parts of the dipole matrix elements, as described by Eqs (26) and (27).

the Zeeman shift, and, in, e.g., Ref. [37], is sufficient to account for the majority of the observed spacing between the spectral peaks.

The coupling strengths are not necessarily symmetrical about $m_F = 0$ and, for an experiment in which damping is important, this may be manifest as a change in the amplitude of the peaks. However, the common arrangement of equal polarizations does not show this asymmetry, and, as noted in Ref. [37], asymmetry in the preparation of the initial states is also important.

V. CONCLUSIONS

We have described the stimulated Raman transition and, by including multiple intermediate states from the outset, have obtained results which give the coupling strength for the multistate system and from which the lightshift naturally emerges. We have applied this

method to the cesium atom, given more general expressions for the alkali-metal atoms, and noted how the linear dependence of the lightshift on the m_F level mimics a Zeeman shift. We comment on the possibility of the dependence of the coupling strength on m_F level manifesting as a variation in peak height in experimental spectra.

Our results were derived in the limit of far detuning and our calculations were simplified greatly by this enforced absence of decoherence. However, for specific coupling strengths and detunings, the problem of finding eigenvalues and vectors can be treated numerically, and many efficient algorithms exist for this task. Hence, a similar approach might be used for situations including coherent population trapping [38, 39] and electromagnetically induced transparency [40, 41].

Acknowledgments

Appendix: Finding the eigensystem of the multilevel Raman Hamiltonian

In this appendix, we find the eigenvalues and eigenvectors for the matrix $\boldsymbol{H}$ representing the Hamiltonian $\hat{H}_A$ of our multilevel system, as described in Sec. II. For brevity in the derivation, we make the replacements $x_n = \frac{1}{2}\Omega_{P,n}/\Omega_0$, $y_n = \frac{1}{2}\Omega_{S,n}e^{i\delta t}/\Omega_0$, and $\delta = \Delta/\Omega_0$. The frequency Ω_0 is, conceptually, the natural frequency scale for the problem.

1. Determinant

We calculate the determinant of the $N \times N$ matrix $\boldsymbol{A} = \boldsymbol{H} - \lambda \boldsymbol{I}$,

$$|\boldsymbol{A}| = \begin{vmatrix} -\lambda & 0 & x_2 & x_3 & \cdots \\ 0 & -\lambda & y_2 & y_3 & \cdots \\ x_2^* & y_2^* & \delta-\lambda & 0 & \cdots \\ x_3^* & y_3^* & 0 & \delta-\lambda & \cdots \\ \vdots & \vdots & \vdots & \vdots & \ddots \end{vmatrix}, \quad (A.1)$$

to find the characteristic equation and hence the eigenvalues λ of $\boldsymbol{H}$. If we define $\boldsymbol{A}^{ij}$ to be the matrix $\boldsymbol{A}$ with row i and column j removed, and A_{ij} to be the element (i,j) of matrix $\boldsymbol{A}$, then using expansion by minors,

$$\begin{aligned} |\boldsymbol{A}| &= \sum (-1)^n A_{n0} |\boldsymbol{A}^{n0}| \\ &= -\lambda |\boldsymbol{A}^{00}| + \sum_{n\geq 2} (-1)^n x_n^* |\boldsymbol{A}^{n0}| . \end{aligned} \quad (A.2)$$

We first evaluate the term $|\boldsymbol{A}^{00}|$:

$$\begin{aligned} |\boldsymbol{A}^{00}| &= \begin{vmatrix} -\lambda & y_2 & y_3 & \cdots \\ y_2^* & \delta-\lambda & 0 & \cdots \\ y_3^* & 0 & \delta-\lambda & \cdots \\ \vdots & \vdots & \vdots & \ddots \end{vmatrix} \\ &= -\lambda \left|\left(\boldsymbol{A}^{00}\right)^{00}\right| + \sum_{n\geq 2}(-1)^n y_n^* \left|\left(\boldsymbol{A}^{00}\right)^{n-1,0}\right| . \quad (A.3) \end{aligned}$$

As before, we decompose the determinant in terms of the elements in the first column. The first minor matrix is diagonal $(\boldsymbol{A}^{00})^{00} = (\delta-\lambda)\boldsymbol{I}$, and hence the first term is $-\lambda(\delta-\lambda)^{N-2}$. For subsequent terms $|(\boldsymbol{A}^{00})^{n-1,0}|$; $n \geq 2$, we find $-y_n^* y_n (\delta - \lambda)^{N-3}$, where the problem of calculating the determinant of each minor matrix is greatly simplified by swapping columns to ensure each is upper diagonal with diagonal elements $(y_n, \delta - \lambda, \delta - \lambda, \ldots)$. Overall, these terms sum to $-\|\boldsymbol{y}\|^2(\delta-\lambda)^{N-3}$. Hence,

$$|\boldsymbol{A}^{00}| = -\lambda(\delta-\lambda)^{N-2} - \|\boldsymbol{y}\|^2(\delta-\lambda)^{N-3} . \quad (A.4)$$

We now consider the terms $|\boldsymbol{A}^{n0}|$ for $n \geq 2$:

$$\boldsymbol{A}^{20} = \begin{vmatrix} 0 & x_2 & x_3 & x_4 & \cdots \\ -\lambda & y_2 & y_3 & y_4 & \cdots \\ y_3^* & 0 & \delta-\lambda & 0 & \cdots \\ y_4^* & 0 & 0 & \delta-\lambda & \cdots \\ \vdots & \vdots & \vdots & \vdots & \ddots \end{vmatrix} . \quad (A.5)$$

Before deconstructing $\boldsymbol{A}^{20}$, we note that the next term, $\boldsymbol{A}^{30}$, is of the same form if we interchange the columns headed x_2 and x_3:

$$\begin{aligned} \boldsymbol{A}^{30} &= \begin{vmatrix} 0 & x_2 & x_3 & x_4 & \cdots \\ -\lambda & y_2 & y_3 & y_4 & \cdots \\ y_2^* & \delta-\lambda & 0 & 0 & \cdots \\ y_4^* & 0 & 0 & \delta-\lambda & \cdots \\ \vdots & \vdots & \vdots & \vdots & \ddots \end{vmatrix} \\ &= -\begin{vmatrix} 0 & x_3 & x_2 & x_4 & \cdots \\ -\lambda & y_3 & y_2 & y_4 & \cdots \\ y_2^* & 0 & \delta-\lambda & 0 & \cdots \\ y_4^* & 0 & 0 & \delta-\lambda & \cdots \\ \vdots & \vdots & \vdots & \vdots & \ddots \end{vmatrix}, \quad (A.6) \end{aligned}$$

with a sign change. The first term of this determinant has prefactor zero and so can be ignored. For the second term, the minor matrix $(\boldsymbol{A}^{20})^{10}$ is upper diagonal and hence has determinant $|(\boldsymbol{A}^{20})^{10}| = x_2(\delta-\lambda)^{N-3}$ and, similarly, $|(\boldsymbol{A}^{n0})^{10}| = (-1)^n x_n(\delta-\lambda)^{N-3}$ for $n \geq 2$.

We now investigate the determinants $|(\boldsymbol{A}^{20})^{m0}|$ for $m \geq 2$. In the expansion of $|(\boldsymbol{A}^{20})^{20}|$, the only terms which have nonzero coefficient are $|((\boldsymbol{A}^{20})^{20})^{00}| = y_3(\delta - \lambda)^{N-4}$ and $|((\boldsymbol{A}^{20})^{20})^{10}| = x_3(\delta-\lambda)^{N-4}$. We can extend

this treatment for $n \geq 2$ and $m \geq 2$. Finally, we find

$$|\boldsymbol{A}| = \lambda^2(\delta - \lambda)^{N-2} + \lambda(\|\boldsymbol{x}\|^2 + \|\boldsymbol{y}\|^2)(\delta - \lambda)^{N-3}$$
$$+ \frac{1}{2}\sum_{i,j}|x_i y_j - x_j y_i|^2 (\delta - \lambda)^{N-4} . \quad \text{(A.7)}$$

2. Eigenvalues

The equation $|\boldsymbol{A}| = 0$ clearly has solution $\lambda = \delta$ with multiplicity $N - 4$. With this factor removed, and using $\|\boldsymbol{x}\|^2\|\boldsymbol{y}\|^2 - |\boldsymbol{x} \cdot \boldsymbol{y}^*|^2 = \frac{1}{2}\sum_{i,j}|x_i y_j - x_j y_i|^2$ to phrase this equation in terms of vectors, we obtain

$$\lambda^2(\delta - \lambda)^2 + \lambda(\|\boldsymbol{x}\|^2 + \|\boldsymbol{y}\|^2)(\delta - \lambda)$$
$$+ \|\boldsymbol{x}\|^2\|\boldsymbol{y}\|^2 - |\boldsymbol{x} \cdot \boldsymbol{y}^*|^2 = 0 , \quad \text{(A.8)}$$

which is a fourth-order polynomial in λ (with leading coefficient 1) and hence the product of the remaining roots λ_i equals the constant term. This term is finite, and so *at least* one λ_i becomes negligible as $\delta \to \pm\infty$, and hence we can make the approximation $(\delta - \lambda) \to \delta$ in this limit. The resulting equation is a quadratic in λ with solutions

$$\lambda_\pm = \frac{-\left(\|\boldsymbol{x}\|^2 + \|\boldsymbol{y}\|^2\right) \pm \sqrt{\left(\|\boldsymbol{x}\|^2 - \|\boldsymbol{y}\|^2\right)^2 + 4|\boldsymbol{x} \cdot \boldsymbol{y}^*|^2}}{2\delta} .$$
$$\text{(A.9)}$$

We now seek the eigenvectors associated with these two finite eigenvalues.

3. Eigenvectors

The eigenvalue equation $\boldsymbol{H}\boldsymbol{a} = \lambda\boldsymbol{a}$ yields the following:

$$\sum_{i \geq 2} x_i a_i = \lambda a_0; \quad \text{(A.10)}$$

$$\sum_{i \geq 2} y_i a_i = \lambda a_1; \quad \text{(A.11)}$$

$$x_i^* a_0 + y_i^* a_1 = (\lambda - \delta)a_i \text{ for } i \geq 2 . \quad \text{(A.12)}$$

If we multiply Eq. (A.12) by a_i^* and sum over $i \geq 2$, and then enforce the normalization condition $\sum a_i^* a_i = 1$, we arrive at

$$(\lambda - \delta)\left[1 - \left(|a_0|^2 + |a_1|^2\right)\right] = \lambda\left(|a_0|^2 + |a_1|^2\right) , \quad \text{(A.13)}$$

and hence

$$|a_0|^2 + |a_1|^2 = 1 - \lambda/\delta , \quad \text{(A.14)}$$

which, in the limit of large δ, tends to unity. By way of confirmation, we see from Eq. (A.12) that

$$a_i = \frac{x_i^* a_0 + y_i^* a_1}{\lambda - \delta} \text{ for } i \geq 2 , \quad \text{(A.15)}$$

which tend to zero in this limit. The two eigenstates associated with the two finite eigenvalues are hence orthogonal superpositions of the two ground eigenstates;

we represent this transformation as a rotation and proceed to find its angle. Using Eqs (A.10) and (A.12), we have

$$a_0 = \frac{1}{\lambda}\sum_{i \geq 2} x_i a_i$$
$$= \frac{1}{\lambda(\lambda - \delta)}\sum_{i \geq 2} x_i \left[x_i^* a_0 + y_i^* a_1\right]$$
$$= \frac{1}{\lambda(\lambda - \delta)}\left[a_0 \boldsymbol{x} \cdot \boldsymbol{x}^* + a_1 \boldsymbol{x} \cdot \boldsymbol{y}^*\right] , \quad \text{(A.16)}$$

and similarly for a_1. Hence we obtain

$$\frac{a_1}{a_0} = \frac{a_0 \boldsymbol{y} \cdot \boldsymbol{x}^* + a_1 \boldsymbol{y} \cdot \boldsymbol{y}^*}{a_0 \boldsymbol{x} \cdot \boldsymbol{x}^* + a_1 \boldsymbol{x} \cdot \boldsymbol{y}^*} , \quad \text{(A.17)}$$

which, because $|a_0|^2 + |a_1|^2 = 1$, we can express as the tangent of an angle:

$$e^{i\phi}\tan\theta = a_1/a_0 = \frac{-\left(\|\boldsymbol{x}\|^2 - \|\boldsymbol{y}\|^2\right) \pm \chi}{2\boldsymbol{x} \cdot \boldsymbol{y}^*} , \quad \text{(A.18)}$$

where $\chi = \sqrt{4|\boldsymbol{x} \cdot \boldsymbol{y}^*|^2 + \left(\|\boldsymbol{y}\|^2 - \|\boldsymbol{x}\|^2\right)^2}$ and $\phi = -\arg(\boldsymbol{x} \cdot \boldsymbol{y}^*)$.

The transformation from the bare-state basis to this dressed-state basis can hence be described by the rotation

$$\begin{pmatrix} |+\rangle \\ |-\rangle \end{pmatrix} = \begin{pmatrix} \cos\theta & e^{+i\phi}\sin\theta \\ -e^{-i\phi}\sin\theta & \cos\theta \end{pmatrix} \begin{pmatrix} |0\rangle \\ |1\rangle \end{pmatrix} , \quad \text{(A.19)}$$

and oscillations are thus driven with amplitude $m = 2\cos\theta\sin\theta$ at the rate

$$\widetilde{\Omega}_\text{B} = \Omega_0 (\lambda_+ - \lambda_-) = \frac{\Omega_0^2}{\Delta}\chi . \quad \text{(A.20)}$$

We identify the effective coupling strength Ω_B and detuning Δ_B in terms of the angle θ defined above:

$$\Omega_\text{B} = \sin 2\theta\, \widetilde{\Omega}_\text{B} \text{ and} \quad \text{(A.21)}$$
$$\Delta_\text{B} = \cos 2\theta\, \widetilde{\Omega}_\text{B} . \quad \text{(A.22)}$$

Using the trigonometric identity $\tan\theta = \frac{1 - \cos 2\theta}{\sin 2\theta}$ we obtain

$$\sin 2\theta = 2|\boldsymbol{x} \cdot \boldsymbol{y}^*|/\chi \text{ and} \quad \text{(A.23)}$$
$$\cos 2\theta = \left(\|\boldsymbol{y}\|^2 - \|\boldsymbol{x}\|^2\right)/\chi , \quad \text{(A.24)}$$

and, finally,

$$\Omega_\text{B} = \frac{\Omega_0^2}{\Delta} 2|\boldsymbol{x} \cdot \boldsymbol{y}^*| \text{ and} \quad \text{(A.25)}$$

$$\Delta_\text{B} = \frac{\Omega_0^2}{\Delta}\left(\|\boldsymbol{y}\|^2 - \|\boldsymbol{x}\|^2\right) . \quad \text{(A.26)}$$

[1] B. W. Shore, *Multilevel Atoms and Incoherence*, The Theory of Coherent Atomic Excitation Vol. 2 (John Wiley & Sons, New York, 1990).

[2] C. J. Foot, *Atomic Physics*, Oxford Master Series in Atomic, Optical and Laser Physics (Oxford University Press, Oxford, 2005).

[3] A. F. Linskens, I. Holleman, N. Dam, and J. Reuss, Phys. Rev. A **54**, 4854 (1996).

[4] J. E. Thomas, P. R. Hemmer, S. Ezekiel, C. C. Leiby, R. H. Picard, and C. R. Willis, Phys. Rev. Lett. **48**, 867 (1982).

[5] J. Ringot, P. Szriftgiser, and J. C. Garreau, Phys. Rev. A **65**, 013403 (2001).

[6] M. Kasevich and S. Chu, Phys. Rev. Lett. **67**, 181 (1991).

[7] M. Kasevich and S. Chu, App. Phys. B **54**, 321 (1992).

[8] D. S. Weiss, B. C. Young, and S. Chu, Phys. Rev. Lett. **70**, 2706 (1993).

[9] D. S. Weiss, B. C. Young, and S. Chu, Appl. Phys. B **59**, 217 (1994).

[10] L. Allen and J. H. Eberly, *Optical Resonance and Two-level Atoms* (Courier Dover Publications, Inc., New York, 1987), ISBN 0-486-65533-4.

[11] B. W. Shore, *Simple Atoms and Fields*, The Theory of Coherent Atomic Excitation, Vol. 1 (John Wiley & Sons, New York, 1989).

[12] N. F. Ramsey, Phys. Rev. **78**, 695 (1950).

[13] T. Zanon, S. Guérandel, E. de Clercq, D. Holleville, N. Dimarcq, and A. Clairon, Phys. Rev. Lett. **94**, 193002 (2005).

[14] C. Monroe, D. M. Meekhof, B. E. King, W. M. Itano, and D. J. Wineland, Phys. Rev. Lett. **75**, 4714 (1995).

[15] F. Schmidt-Kaler, H. Häffner, M. Riebe, S. Gulde, G. P. T. Lancaster, T. Deuschle, C. Becher, C. F. Roos, J. Eschner, and R. Blatt, Nature (London) **422**, 408 (2003).

[16] R. Blatt and D. J. Wineland, Nature (London) **453**, 1008 (2008).

[17] C. Law and J. H. Eberly, Opt. Express **2**, 368 (1998).

[18] A. D. Boozer, R. Miller, T. E. Northup, A. Boca, and H. J. Kimble, Phys. Rev. A **76**, 063401 (2007).

[19] M. Kasevich and S. Chu, Phys. Rev. Lett. **69**, 1741 (1992).

[20] N. Davidson, H. J. Lee, M. Kasevich, and S. Chu, Phys. Rev. Lett. **72**, 3158 (1994).

[21] J. Reichel, O. Morice, G. M. Tino, and C. Salomon, Europhys. Lett.) **28**, 477 (1994).

[22] V. Boyer, L. J. Lising, S. L. Rolston, and W. D. Phillips, Phys. Rev. A **70**, 043405 (2004).

[23] Y. Wu, Phys. Rev. A **54**, 1586 (1996).

[24] Z. Deng, Opt. Comm. **48**, 284 (1983).

[25] E. Kyrölä and M. Lindberg, Phys. Rev. A **35**, 4207 (1987).

[26] A. S. Shumovsky, E. I. Aliskenderov, F. LeKien, and N. D. Vinh, J. Phys. A **19**, 3607 (1986).

[27] B. W. Shore and P. L. Knight, J. Mod. Opt. **40**, 1195 (1993).

[28] C. N. Cohen-Tannoudji, B. Diu, and F. Laloë, *Quantum Mechanics*, (John Wiley & Sons, 1977), Vol. 1.

[29] E. Arimondo, M. Inguscio, and P. Violino, Rev. Mod. Phys. **49**, 31 (1977).

[30] G. K. Woodgate, *Elementary Atomic Structure* (Oxford Scientific Publications, 2000), 2nd ed., ISBN 0-19-851156-6.

[31] D. M. Brink and G. R. Satchler, *Angular Momentum*, 3rd ed. (Clarendon Press, Oxford, 1994).

[32] J. L. Meunier, Euro. J. Phys. **8**, 114 (1987).

[33] R. Loudon, *The Quantum Theory of Light*, 2nd ed. (Clarendon Press, Oxford, 1983).

[34] W. Demtröder, *Laser Spectroscopy: Basic Concepts and Instrumentation*, 3rd ed. (Springer-Verlag, Berlin, 2003.

[35] D. A. Steck, *Cesium D Line Data*, available online at http://steck.us/alkalidata (revision 2.1.2) (2009).

[36] A. R. Edmonds, *Angular Momentum in Quantum Mechanics*, 4th ed. (Princeton University Press, Princeton, NJ, 1996).

[37] I. Dotsenko, W. Alt, S. Kuhr, D. Schrader, M. Muller, Y. Miroshnychenko, V. Gomer, A. Rauschenbeutel, and D. Meschede, App. Phys. B **78**, 711 (2004).

[38] H. Gray, R. Whitley, and C. Stroud Jr., Opt. Lett. **3**, 218 (1978).

[39] G. Alzetta, L. Moi, and G. Orriols, Nuovo Cimento B. **52**, 209 (1979).

[40] M. Fleischhauer, A. Imamoğlu, and J. Marangos, Rev. Mod. Phys. **77**, 633 (2005).

[41] K. J. Boller, A. Imamoğlu, and S. E. Harris, Phys. Rev. Lett. **66**, 2593 (1991).

Optomechanical cooling with generalized interferometers

André Xuereb,[1, *] Tim Freegarde,[1] Peter Horak,[2] and Peter Domokos[3]

[1]*School of Physics and Astronomy, University of Southampton, Southampton SO17 1BJ, United Kingdom*
[2]*Optoelectronics Research Centre, University of Southampton, Southampton SO17 1BJ, United Kingdom*
[3]*Research Institute of Solid State Physics and Optics, H-1525 Budapest P.O. Box 49, Hungary*
(Dated: July 2, 2010)

The fields in multiple-pass interferometers, such as the Fabry–Pérot cavity, exhibit great sensitivity not only to the presence but also to the *motion* of any scattering object within the optical path. We consider the general case of an interferometer comprising an arbitrary configuration of generic 'beam splitters' and calculate the velocity-dependent radiation field and the light force exerted on a moving scatterer. We find that a simple configuration, in which the scatterer interacts with an optical resonator from which it is spatially separated, can enhance the optomechanical friction by several orders of magnitude.

PACS numbers: 42.50.Wk, 42.79.Gn, 07.10.Cm, 07.60.Ly

Optomechanics [1] is a rapidly growing field addressing the manipulation of macroscopic scatterers by making use of the mechanical effects of light. The ponderomotive force exhibits a velocity-dependent character which stems from any retardation of the electromagnetic field present in such systems. With an appropriate choice of parameters, velocity-dependent terms in the force may lead to viscous damping of motion [2].

Pure Doppler frequency shifting results in a velocity dependent force with a relative magnitude of order v/c, which is generally small at room temperature or below. The laser cooling of atoms, for example, produces a significant cooling effect because it is resonantly enhanced by the atom with the Q-factor ω/γ characteristic of an atomic transition (ω is the frequency of the radiation, γ is the linewidth of the transition). This situation can be mimicked in the case of a moving micro-mirror, as was proposed in Ref. [3], whereby a photonic crystal having a steep frequency-dependent reflection coefficient is mounted upon it. In the more general case of a non-resonant scatterer, the sensitivity of the radiation force to the velocity can be enhanced by coupling the moving object to a resonant optical element. This is the case, for example, in several recent optomechanical cooling experiments [4–7]: the thermal vibration of one of the micro-mirrors making up a Fabry–Pérot-type resonator can be quenched through the radiation pressure of the light field enclosed in the resonator. Several factors limit the efficiency of this mechanism in practice, including the quality of the micromirrors that can be fabricated and the precision with which the cavities can be aligned.

In this Letter we generalize the conventional optomechanical cooling scheme [4–7] and calculate the linear response of the electromagnetic field to the motion of an arbitrary scatterer within a general 1D configuration of immobile optical elements on either side of it (see Fig. 1(a)). We find that the field interference can be significantly sensitive to motion even if the scatterer lacks a specific frequency-dependent reflectivity.
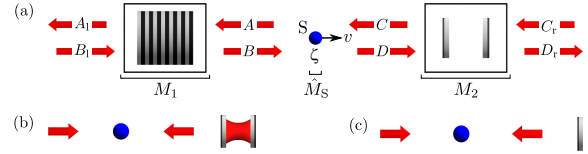
FIG. 1: (a) The general system consisting of a mobile scatterer, S, between two sets of generic immobile optical elements (we show a Bragg reflector, on the left, and a Fabry–Pérot-type cavity, on the right, as an example). The mobile scatterer can, *a priori*, represent anything, e.g., an atom or a mirror. We discuss two specific configurations in this Letter: an atom in front of (b) a two-mirror cavity, and (c) a plane mirror [8].

In the second part of this Letter, the role of interference in enhancing the viscous cooling force is analyzed for a simple geometry, in which the scatterer lies in front of, *but not within*, a standard two-mirror resonator, as in Fig. 1(b). With this scheme, which we label 'external cavity cooling', one can benefit from the high finesse of the cavity even if the moving object has a low reflectivity. We thus propose a very general, efficient optomechanical cooling mechanism applicable to a wide class of micro- or mesoscopic objects.

We begin by presenting the formal solution of the scattering model which we constructed in a recent paper for dealing with a general configuration of one-dimensional optomechanical systems [9]. Each element of the system is described by a transfer matrix which relates linearly the field amplitudes on its left-hand side to those on the right-hand side. Transfer matrices for moving scatterers up to linear order in v/c have been constructed. The transfer matrix of an arbitrary configuration of optical elements is then obtained by matrix multiplication. A difficulty in analyzing complex networks originates from the Doppler shift operator $\hat{P}_v$ [9], which appears in the transfer matrix of the moving scatterer and acts in the space of the wave vectors rather than in the space of amplitudes: $\hat{P}_v f(k) = f(k + k_0 v/c)$, for any function f of

the wavenumber k, where k_0 is the carrier wavenumber in the system. For the mathematical description of the problem, we start with the transfer matrices $\hat{M}_S(k)$ and $M_{1,2}(k)$ for the scatterer and for the general optical systems preceding and following the scatterer, respectively. Explicit forms for such matrices are given in Ref. [9]. We then calculate the transfer matrix $\hat{M}(k)$ of the entire system given by the product $\hat{M}(k) = M_1(k)\,\hat{M}_S(k)\,M_2(k)$, and the matrix inverse $M_1^{-1}(k)$, such that

$$\begin{pmatrix} A_l \\ B_l \end{pmatrix} = \hat{M} \begin{pmatrix} C_r \\ D_r \end{pmatrix} \text{ and } \begin{pmatrix} A \\ B \end{pmatrix} = M_1^{-1} \begin{pmatrix} A_l \\ B_l \end{pmatrix},$$

where we have omitted the k-dependence. We use the hat to indicate that the corresponding matrix contains the Doppler shift operator $\hat{P}_v$. The elements of these matrices, which we denote, for convenience, by

$$M_1^{-1} \equiv \begin{bmatrix} \theta_{ij} \end{bmatrix}, \text{ and } \hat{M} \equiv \begin{bmatrix} \hat{\gamma} & \hat{\alpha} \\ \hat{\delta} & \hat{\beta} \end{bmatrix}, \quad (1)$$

can all be obtained in a straightforward manner using only 2-by-2 matrix multiplication for an arbitrary number of scatterers, and hence can in principle be calculated analytically, or can be derived by using formal computer languages.

In order to make the mathematics more concise, we explicitly consider the case where we pump the system from only one direction. Setting $C_r(k) = 0$ in Eq. (1), we obtain $A_l(k) = \hat{\alpha}\hat{\beta}^{-1} B_l(k)$. Because of the presence of $\hat{\beta}^{-1}$, this relation between the back-reflected and the incoming fields contains the powers of the shift operator $\hat{P}_v$ to all orders. In the simple example of one mirror moving in front of a fixed one, the corresponding summation could be carried out analytically [9]. However, this is not the case generally. The crucial step to overcome this problem is to express the Doppler shift operator in the transfer matrix $\hat{M}_S$ to first order in v/c: $\hat{P}_v = 1 + \frac{v}{c}k_0 \frac{\partial}{\partial k}$. Here we have assumed that we pump at a single wavenumber; i.e., we take $B_l(k) = B_0\,\delta(k - k_0)$, with $\delta(k)$ being the Dirac δ function and k_0 being the wavenumber corresponding to the central pumping frequency. We can thus expand both $\hat{\alpha}$ and $\hat{\beta}$ in v/c and conveniently denote them by

$$\hat{\alpha} = \alpha_0 + \frac{v}{c}\left(\alpha_1^{(0)} + \alpha_1^{(1)}\frac{\partial}{\partial k}\right) \text{ and } \hat{\beta} = \beta_0 + \frac{v}{c}\left(\beta_1^{(0)} + \beta_1^{(1)}\frac{\partial}{\partial k}\right).$$

The auxiliary functions $\alpha_0, \alpha_1^{(0)}, \ldots$, are simply related to the matrix elements defined in Eq. (1) and to the scattering strength parameter [9], or 'polarizability', ζ. We recall that the amplitude reflectivity and transmissivity of the scatterer are related to ζ by $r = i\zeta/(1 - i\zeta)$ and $t = 1 + r$, respectively; the reflectivity and transmissivity of a mirror or scatterer are, in general, complex and account automatically for phase shifts in the reflected and transmitted fields [10]. Thus $\hat{\beta}$ can be inverted in closed form up to linear order in v/c to yield the amplitude $A(k)$. We then calculate the total field amplitudes

$\mathcal{A} = \int A(k)\,\mathrm{d}k$ and $\mathcal{B} = \int B(k)\,\mathrm{d}k$ and obtain

$$\mathcal{A} = \left[\left(\theta_{11}\frac{\alpha_0}{\beta_0} + \theta_{12} \right) + \frac{v}{c}\left(\theta_{11}\frac{\alpha_1^{(0)}\beta_0 - \alpha_0\beta_1^{(0)}}{\beta_0^2} - \frac{1}{\beta_0}\frac{\partial}{\partial k}\theta_{11}\frac{\alpha_1^{(1)}\beta_0 - \alpha_0\beta_1^{(1)}}{\beta_0} \right) \right] B_0 = \mathcal{A}_0 + \frac{v}{c}\mathcal{A}_1,$$

$$(2)$$

and similarly for $\mathcal{B}$. This general solution for the field amplitudes at the scatterer is one of the main results of this Letter, and can be evaluated for an arbitrary system. The amplitudes on the right side of the moving scatterer can be expressed, using the elements of $\hat{M}_S$, as

$$\begin{aligned} \mathcal{C} &= (1 - i\zeta)\mathcal{A} - i\zeta\left(1 - 2\frac{v}{c}\right)\mathcal{B} \text{ and} \\ \mathcal{D} &= i\zeta\left(1 + 2\frac{v}{c}\right)\mathcal{A} + (1 + i\zeta)\mathcal{B}, \end{aligned} \quad (3)$$

where we have used the explicit form of $\hat{M}_S$, and where we have defined $\mathcal{C} = \int C(k)\,\mathrm{d}k$ and $\mathcal{D} = \int D(k)\,\mathrm{d}k$. In Eqs. (3) we have also assumed that ζ is independent of k. Upon using these relations, we obtain an expression for the force acting on the scatterer, from which we can extract the friction force (see Ref. [9] for the details of this derivation):

$$\begin{aligned} \boldsymbol{F} = -4\hbar k_0 \frac{v}{c}\Big[&|\zeta|^2\big(|\mathcal{A}_0|^2 - |\mathcal{B}_0|^2\big) \\ &+ \big(|\zeta|^2 + \mathrm{Im}\{\zeta\}\big)\,\mathrm{Re}\{\mathcal{A}_0\mathcal{A}_1^\star\} - 2\,\mathrm{Im}\{\zeta\}\,\mathrm{Re}\{\mathcal{A}_0\mathcal{B}_0^\star\} \\ &+ \big(|\zeta|^2 - \mathrm{Im}\{\zeta\}\big)\,\mathrm{Re}\{\mathcal{B}_0\mathcal{B}_1^\star\} + \mathrm{Im}\{\zeta\}\,\mathrm{Re}\{\mathcal{A}_0\mathcal{B}_1^\star\} \\ &+ \mathrm{Re}\Big\{\Big(|\zeta|^2 + i\,\mathrm{Re}\{\zeta\}\Big)\mathcal{A}_1\mathcal{B}_0^\star\Big\}\Big]. \end{aligned} \quad (4)$$

All our assumptions—i.e., pumping at a single wavenumber, frequency independent polarizability ($\partial\zeta/\partial k = 0$), and $C_r(k) = 0$—are simplifying assumptions and can be relaxed. However, this would result in forms for the friction force that are less transparent and amenable to analysis. We now apply this to the 'external cavity cooling' configuration, Fig. 1(b). As a reference system for the analysis of the cooling force in this setup, we also consider the 'mirror mediated cooling' configuration (see Fig. 1(c)), which has been previously discussed [8, 9], and which is the optomechanical cooling scheme used in many experiments [4–7]. Note that in the 'external cavity cooling' scheme with a near mirror of complex transmissivity t, the limits of small and large $|t|$ render the situation where the cavity is replaced respectively by the near mirror only or the far mirror only. For intermediate t compared with the transmissivity of the far mirror, T, the moving scatterer interacts with a field reflected back from the cavity and is subject to the interference created by the multiple reflections between the two mirrors. In this text, we consider in particular an object having low reflectivity, around 50%, which corresponds to a polarizability $\zeta = 1$ and is representative of typical experimental
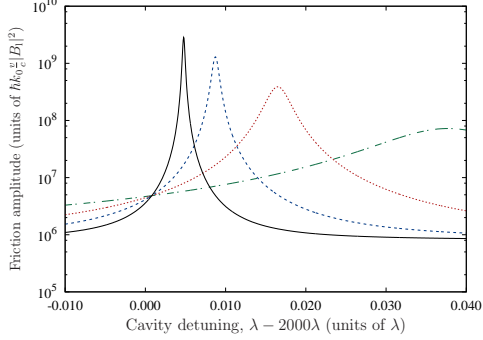
FIG. 2: The amplitude of the friction force acting on the scatterer, for various near-mirror transmissivities, is shown as a function of the mirror separation in the cavity. The different curves represent different near-mirror transmissivities: $|t| = 0.45$ (dashed–dotted curve), $|t| = 0.20$ (dotted), $|t| = 0.10$ (dashed), $|t| = 0.05$ (solid). (Scatterer polarizability $\zeta = 1$, scatterer–cavity separation $x \approx 400\lambda_0$, $|T| = 0.01$, $\lambda_0 = 780$ nm.)

FIG. 3: Amplitude of the friction acting on a scatterer of polarizability $\zeta = 1$ interacting with a cavity tuned to achieve maximum friction, for varying transmissivity of the near mirror. The friction amplitude (solid curve) approaches that for mirror mediated cooling using the far (dotted line, $t \to 1$) or the near (dashed–dotted line, $t \to 0$) mirror only in the appropriate limits. The arrow indicates the point at which the two cavity mirrors have the same reflectivity. Also shown is the intra-cavity field (dashed). ($x \approx 400\lambda_0$, $L \approx 2000\lambda_0$, $|T| = 0.01$, $\lambda_0 = 780$ nm, finesse at peak friction 5.0×10^4.)

conditions [4]. This ensures that a high-finesse resonator cannot be formed between the object and the near mirror, thereby guaranteeing a parameter range where the cavity formed between the immobile mirrors dominates the interaction. For the sake of simplicity, we restrict ourselves to the special case of scatterers that can be characterized by a real polarizability; this is equivalent to assuming that no absorption takes place in the scatterer. Similar results hold when ζ is not real.

A numerical fit to Eq. (4) for $|t| \sim |T|$ and $\zeta \ll 1$ renders a friction force of the approximate form

$$\boldsymbol{F} \approx -8\hbar k_0^2 \zeta^2 \frac{v}{c}(2x + 0.17\mathcal{F}L)\sin(4k_0 x + \phi)|B_0|^2, \quad (5)$$

where $\mathcal{F}$ is the cavity finesse, L the cavity length (optimized as discussed below), x the separation between the scatterer and the near mirror, and ϕ a phase factor. The gross spatial variation of the friction force is linear in both L and x; this is simply because of the linear increase of the retardation time of the reflected field with the distance between the scatterer and the mirrors. This dependence is modulated by a wavelength-scale oscillation of the friction force, which thereby follows the same oscillatory dependence as mirror mediated cooling [8, 9] and constrains cooling to regions of the size of $\lambda_0/8$, where $\lambda_0 = 2\pi/k_0$. In the case of a micro-mechanical mirror, where the vibrational amplitude is naturally much less than the wavelength, this presents no problem. The form of Eq. (5) is dependent on the properties of the scatterer and of the mirrors; for realistic mirrors and $\zeta = 1$, the enhancement factor $0.17\mathcal{F}$ drops to $0.04\mathcal{F}$. With typical experimental parameters this results in an enhancement of 10^3–10^4 over the standard setup; e.g., in Ref. [4] the use of two fixed mirrors could increase the optically induced damping rate, $(\Gamma_{\text{eff}} - \Gamma)$ in their notation, by over 3

orders of magnitude and lower the limiting temperature from $< 20\,\text{K}$ to $< 6\,\text{mK}$.

As shown in Fig. 2, the fine tuning of the cavity length by varying L on the wavelength scale shows a Lorentzian-like resonant enhancement of the friction amplitude, following that of the intra-cavity field intensity. If we denote the complex reflectivities of the near and far mirror by r and R, respectively, we can show that the peaks of Fig. 2 lie around the cavity resonances, at approximately $L = \frac{1}{2}m\lambda_0 - \frac{1}{2k_0}\arg(rR)$, with m being an integer, and have approximately the same full-width at half-maximum, $(1 - |rR|)/(k_0\sqrt{|rR|})$. The enhancement of the friction force by the cavity is due to the multiplication of the retardation time by the number of round trips in the cavity, which thereby acts as a 'distance folding' mechanism. For the chosen parameters, the optical path length is effectively $2x + 0.04\mathcal{F}L$; i.e., determined predominantly by the cavity length L.

The friction force depends not only upon the retardation but also upon the cavity reflectivity, which drops near resonance in the well-known behaviour of a Fabry–Pérot resonator. Fig. 3 shows the friction amplitude as a function of the near mirror transmissivity $|t|$ for a fixed far mirror transmissivity, $T = 1/(1 - 100i)$. We note that this nonideal reflectivity of the far mirror could equivalently arise from absorption, of ca. 0.01% with the given parameters, of the incident power by the mirror. For each value of $|t|$, the cavity length L has been adjusted to maximize the friction force, according to curves such as those in Fig. 2. The calculated result follows the intra-cavity field (shown dashed) except where the cavity reflectivity drops near resonance (region (b)), and in the extremes of
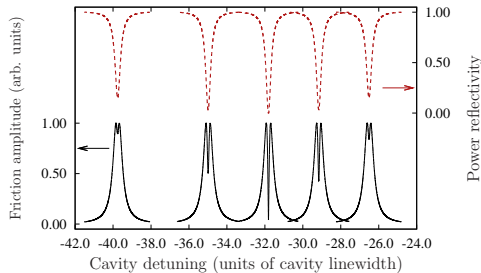
FIG. 4: In region (b) of Fig. 3, the friction coefficient amplitude (solid curves) is attenuated due to the attenuation in the field reflected from the cavity (dashed). $|T| = 0.01$ in every plot; $|t|$ is, from left to right, 6.7×10^{-3}, 8.3×10^{-3}, 1.0×10^{-2}, 1.2×10^{-2}, and 1.5×10^{-2}. (Parameters as in Fig. 3.)

regions (a) and (c), where the geometry is dominated by the near ($|t| \to 0$) or far ($|t| \to 1$) mirrors, respectively. Fig. 4 shows the effect of the drop in reflectivity as the cavity is scanned through resonance for similar mirror reflectivities. When this causes a dip in the friction amplitude peak, the optimum values plotted in Fig. 3 occur to either side of the resonance, and the friction force in this region is effectively limited by this interference effect. We note that the friction amplitude is not maximized at the point of maximum intra-cavity field ($t = T$) because more light is lost through the cavity for larger $|t|$.

The external cavity cooling mechanism of Fig. 1(b) may prove particularly valuable when the scatterer is a small mirror or other micro-mechanical optical component. In such cases, the advantage gained by using the external cavity over the standard optomechanical cooling scheme, Fig. 1(c), depends heavily upon the polarizability or reflectivity of the moving scatterer, which in the above calculations have so far been taken to be modest ($\zeta = 1$; $|r| = 0.7$) in comparison with those of the cavity mirrors. For $\zeta \ll 1$, the friction force is enhanced by a factor approximately equal to $\mathcal{F}$ because of the distance folding argument explained above. For larger ζ, the system turns into a three–mirror resonator and the advantage of external cavity cooling is not as big, but is still significant. For $\zeta \approx 1$ we find enhancement by a factor $0.04\mathcal{F}$, as discussed above. For even larger ζ, when the reflectivity of the moving mirror becomes comparable to that of the fixed mirrors, the scheme behaves similarly to the mirror mediated cooling configuration. The main heating process that counteracts the cooling effect in the case of micromirrors is thermal coupling to the environment, which depends on the geometry. In the case of isolated scatterers that undergo no absorption, the heating is due to quantum fluctuations in the fields [9]; the limit temperature here is $\approx \hbar c / (0.34 k_B \mathcal{F} L)$ when $\zeta \ll 1$, which evaluates to $\approx 0.1 \, \text{mK}$ for the parameters in Fig. 3. The usual cavity mediated cooling mechanism [11, 12], where the moving scatterer is inside a two-mirror cavity,

can also be described by our general framework in terms of Eqs. (2) and (4). Compared with this scheme, external cavity cooling has the advantage of always having a sinusoidal spatial dependence; the narrow resonances in the friction force for well-localized particles in a far-off resonance trap inside a cavity [13], for example, impose more stringent positioning requirements. On the other hand, whereas scatterers travelling distances of many wavelengths within a cavity can experience a net cooling force [14], the friction force outside a cavity averages to zero; we find, however, that a net cooling effect arises in a similar geometry in three dimensions which may be particularly significant for micro-mechanical systems [15]. Finally, we note that when the scatterer is outside, rather than within, the cavity the local field is not amplified by the resonator and the incident field can therefore be made much stronger without causing saturation (when the moving scatterer is an atom) or damage (when it is a mirror).

* Corresponding author. Electronic address: andre.xuereb@soton.ac.uk

[1] F. Marquardt and S. M. Girvin, Physics **2**, 40 (2009).
[2] T. J. Kippenberg and K. J. Vahala, Opt. Express **15**, 17172 (2007).
[3] K. Karrai, I. Favero, and C. Metzger, Phys. Rev. Lett. **100**, 240801 (2008).
[4] C. H. Metzger and K. Karrai, Nature **432**, 1002 (2004).
[5] O. Arcizet, P. F. Cohadon, T. Briant, M. Pinard, and A. Heidmann, Nature **444**, 71 (2006).
[6] S. Gigan, H. R. Bohm, M. Paternostro, F. Blaser, G. Langer, J. B. Hertzberg, K. C. Schwab, D. Bauerle, M. Aspelmeyer, and A. Zeilinger, Nature **444**, 67 (2006).
[7] A. Schliesser, R. Rivière, G. Anetsberger, O. Arcizet, and T. J. Kippenberg, Nat. Phys. **4**, 415 (2008).
[8] A. Xuereb, P. Horak, and T. Freegarde, Phys. Rev. A **80**, 013836 (2009).
[9] A. Xuereb, P. Domokos, J. Asbóth, P. Horak, and T. Freegarde, Phys. Rev. A **79**, 053810 (2009).
[10] I. H. Deutsch, R. J. C. Spreeuw, S. L. Rolston, and W. D. Phillips, Phys. Rev. A **52**, 1394 (1995).
[11] J. D. Thompson, B. M. Zwickl, A. M. Jayich, F. Marquardt, S. M. Girvin, and J. G. E. Harris, Nature **452**, 72 (2008).
[12] I. Favero and K. Karrai, New J. Phys. **10**, 095006 (2008).
[13] S. J. van Enk, J. McKeever, H. J. Kimble, and J. Ye, Phys. Rev. A **64**, 013407 (2001).
[14] G. Hechenblaikner, M. Gangl, P. Horak, and H. Ritsch, Phys. Rev. A **58**, 3030 (1998).
[15] P. Horak, A. Xuereb, and T. Freegarde, arXiv e-prints (2010), arXiv:0904.3059.

Optical cooling of atoms in microtraps by time-delayed reflection

Peter Horak,[1] André Xuereb,[2] and Tim Freegarde[2]

[1]*Optoelectronics Research Centre, University of Southampton, Southampton SO17 1BJ, United Kingdom*
[2]*School of Physics and Astronomy, University of Southampton, Southampton SO17 1BJ, United Kingdom*
(Dated: November 25, 2009)

We present a theoretical analysis of a novel scheme for optical cooling of particles that does not in principle require a closed optical transition. A tightly confined laser beam interacting with a trapped particle experiences a phase shift, which upon reflection from a mirror or resonant microstructure produces a time-delayed optical potential for the particle. This leads to a nonconservative force and friction. A quantum model of the system is presented and analyzed in the semiclassical limit.

Key words: Particle cooling; optical trapping; micro-resonators

I. INTRODUCTION

Standard techniques for optical cooling of atoms mostly rely on spontaneous emission from the atom to carry away the excess momentum. This basic process has been demonstrated to be highly efficient for cooling of two-level or multi-level atoms and for various laser configurations in one, two, or three dimensions, applying various polarization states and frequencies[1]. However, a common requirement is for the atom to exhibit a single, albeit possibly degenerate, ground state such that no atomic population is lost from the cooling cycle by population transfer into internal states decoupled from the laser light. These cooling mechanisms are thus not well suited for most atomic species and hardly for any molecules at all.

Cavity-mediated cooling mechanisms[2,3,4,5] have been suggested to address these shortcomings of laser cooling methods. In this case, only a dipole interaction between the particles and a near resonant cavity mode is required. While this can be fulfilled for a much larger variety of particles, resonator alignment and loading of the particles into the small mode volume of an appropriate cavity is difficult.

We have recently proposed an alternative method for cooling particles that exhibit an electric dipole moment but no closed transitions[6]. In this 'mirror-mediated cooling' scheme, a laser-driven particle interacts with its own image in a mirror and the time-delay incurred during the reflection is exploited to introduce a non-conservative element into the dipole force, thereby leading to friction and cooling. This time delay may be induced by a delay line, e.g., an optical fiber, but more conveniently could arise from an integrated optical micro-resonator[7,8,9,10,11], possibly combined with a plasmonic microstructure for local field enhancement[12,13].

Here we investigate the challenges involved in modeling this novel cooling mechanism. We discuss how the required processes differ from free-space or cavity-mediated laser-cooling methods and propose a theory to overcome these new difficulties. We finally discuss the main results obtained from our method.

II. CONCEPTUAL DIFFERENCES BETWEEN OPTICAL COOLING METHODS
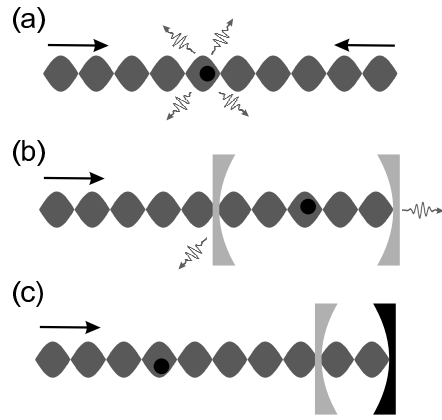
FIG. 1: Schematics of optical cooling methods: (a) Free-space laser cooling, (b) cavity-mediated cooling of a particle between two partially reflective mirrors, (c) mirror-mediated cooling of a particle using one perfectly reflecting and one partially reflective mirror.

We start our discussion with a brief review of the fundamental concepts behind three different laser cooling schemes: (i) free-space laser cooling, (ii) cavity-mediated cooling, and (iii) mirror-mediated cooling.

Free-space laser cooling methods, such as Doppler cooling[14], polarization gradient cooling[15], or velocity-selected coherent population trapping[16], utilize a number of laser beams focused from various directions on a small sample of atoms, as illustrated in Fig. 1(a). In each case, the laser and atomic configuration is set up in such a way that the atom-light coupling is velocity-dependent. For example, the photon scattering rate or the spatial positions where scattering predominantly happens can depend on the atomic velocity, leading to an average net cooling effect. The excess momentum of hot atoms is thereby transferred to spontaneously emitted photons. A mathematical description of the cooling mechanism thus

contains a number of classical, stationary laser beams, and a quantum description of the atomic degrees of freedom. To remove the excess momentum, the excited states of the atoms are coupled to a heat bath, which is assumed to be memory-less (Markovian)[17].

In cavity-mediated cooling schemes[2,3,4,5], Fig. 1(b), the atoms sit inside an optical resonator and are coupled to one or a few resonator modes, while laser beams are used to pump the resonator through its mirrors. Dipole coupling transfers excess momentum coherently from the atoms to the cavity modes, which subsequently decay through the partially-transmitting mirrors. Mathematically, the classical stationary laser beams are now coupled to a quantum system comprising the atom degrees of freedom and the quantum state of the discrete cavity modes. The modes in turn are coupled to a Markovian heat bath.

In mirror-mediated cooling, finally, the particles sit outside a coherent delay device, Fig. 1(c), which could be as simple as a single mirror, a piece of optical fiber with an inscribed Bragg grating, or formed by an integrated optical resonator on a chip[7,8,9,10,11]. Via the dipole coupling, the particle imprints a phase on the pump beam which returns to the position of the particle after reflection with a time delay. Hence, the total dipole potential experienced by the particle depends on the interference of the incoming beam with the time-delayed reflected beam. If the particle has moved during the light round trip, this leads to a non-conservative force that can be exploited for extracting energy from the particle motion. A mathematical description of this situation therefore requires two key ingredients, different from free-space cooling and cavity-mediated cooling: (i) the pump beam itself must be described as dynamic, and (ii) cooling relies on the system state at an earlier time, thus it is non-Markovian. On the other hand, no heat bath is required.

Instead of introducing a system memory in time, we may also decompose the field into a continuum of modes. The model presented here will follow this latter approach. For the sake of simplicity, we model the polarizable particle as a single two-level atom and assume that the time delay arises from a significant distance (several meters) between the atom and the mirror. However, it is envisaged that in a practical realization the time delay will arise from reflection by an integrated micro-optical resonator or a similar structure. Moreover, we restrict the analysis to a single spatial dimension. The electromagnetic modes at angular frequency ω thus are standing waves with mode functions $f(\omega, x) = \sin(\omega x/c)$ if the mirror is assumed at $x = 0$. Upon adiabatic elimination of the internal degrees of freedom of the atom, and treating atomic motion semiclassically, we obtain a continuum quantum model governed by the Hamiltonian

$$\hat{H} = \int \hbar(\omega - \omega_0)\hat{a}^\dagger(\omega)\hat{a}(\omega)\mathrm{d}\omega$$
$$+ \hbar\frac{g^2}{\Delta}\iint \sin\frac{\omega_1 x}{c}\sin\frac{\omega_2 x}{c}\hat{a}^\dagger(\omega_1)\hat{a}(\omega_2)\mathrm{d}\omega_1\mathrm{d}\omega_2 \quad (1)$$

where $\hat{a}(\omega)$ and $\hat{a}^\dagger(\omega)$ are the mode annihilation and creation operators, Δ is the detuning of the atom from the driving laser, and g is the atom-field coupling constant. For a two-level atom with transition wavelength λ and excited state decay rate 2Γ, this coupling constant is related to the mode beam waist w by[18]

$$2\pi g^2 = \Gamma\frac{4\sigma_a}{\pi w^2} \quad (2)$$

where $\sigma_a = 3\lambda^2/(2\pi)$ is the atomic radiative cross section. The force operator describing the action of the field on an atom at position x is derived from the Hamiltonian as

$$\hat{F}(x) = -\frac{\mathrm{d}\hat{H}}{\mathrm{d}x}. \quad (3)$$

We note that the general form of the inter-modal coupling given by the Hamiltonian (1) is valid for any point-like dipole scatterer, and thus will also hold for general multi-level atoms and molecules. Moreover, in order to calculate the force (3) we are interested only in the time evolution of the field in the vicinity of the particle. Hence, it is mainly the relative phase between the mode functions at this position which is important. We thus conclude that, instead of free-space propagation, any dispersive optical device could be used as a delay element, which in particular includes resonant micro- or nanostructures.

III. PERTURBATIVE SOLUTION OF THE MODEL

In the following we apply perturbation theory to the model introduced above to derive the basic properties of the proposed cooling method. We work in the Heisenberg picture where the mode operators become time dependent with the dynamics governed by

$$\begin{aligned}\frac{\mathrm{d}}{\mathrm{d}t}\hat{a}(\omega, t) &= \frac{i}{\hbar}\left[\hat{H}, \hat{a}(\omega, t)\right] \\ &= -i(\omega - \omega_0)\hat{a}(\omega, t) \\ &\quad - i\frac{g^2}{\Delta}\sin\frac{\omega x}{c}\int \sin\frac{\omega_1 x}{c}\hat{a}(\omega_1, t)\mathrm{d}\omega_1. \quad (4)\end{aligned}$$

Next, we apply a semiclassical approximation for the field modes assuming that the state of every mode is given by a coherent state at all times. This is tantamount to replacing the operator $\hat{a}(\omega, t)$ by its expectation value $a(\omega, t)$. We assume that the atom follows a linear trajectory $x(t) = x + v(t - t_0)$ such that at a time $t_0 \gg 2\tau$ the atom is at position x. Here, $2\tau = 2x/c$ is the round-trip time of the delayed reflection. We then expand the mode amplitudes into powers of both the coupling g^2/Δ and the atom velocity v,

$$a(\omega, t) = a_0(\omega, t) + \frac{g^2}{\Delta}\left[a_1(\omega, t) + vb_1(\omega, t)\right] + \cdots. \quad (5)$$

The zeroth order term in g^2/Δ corresponds to the field without back action of the atom. It is thus independent of v and represents the unperturbed driving laser field, which is assumed to be monochromatic,

$$a_0(\omega, t) = A\delta(\omega - \omega_0). \qquad (6)$$

Here, $|A|^2$ gives the pump power in units of photons per second. Inserting (5) with (6) into (4), one can derive the first order terms in g^2/Δ analytically by perturbation theory yielding

$$a_1(\omega, t_0) = A\frac{\exp\left[-i(\omega - \omega_0)t_0\right] - 1}{\omega - \omega_0} \sin\frac{\omega x}{c} \sin\frac{\omega_0 x}{c}, \qquad (7)$$

$$b_1(\omega, t_0) = \frac{A}{c}\left[\omega_0 \sin\frac{\omega x}{c}\cos\frac{\omega_0 x}{c} + \omega\cos\frac{\omega x}{c}\sin\frac{\omega_0 x}{c}\right]$$
$$\times \frac{-1 + [1 + i(\omega - \omega_0)t_0]\exp[-i(\omega - \omega_0)t_0]}{(\omega - \omega_0)^2}. \qquad (8)$$

Expressions (5)-(8) can then be inserted into (3) to calculate the leading terms of the force experienced by the atom at position x at time t_0. Most interesting is the first-order term of the force in velocity v, since this gives the linear friction force and thus describes heating or cooling of the atom in the proposed setup. We find

$$F_v(x, t_0) = 2\pi\hbar k_0^2 v\tau|A|^2 \frac{g^4}{\Delta^2}\sin(4k_0 x) \qquad (9)$$

in leading order of x/λ. Here, $k_0 = \omega_0/c$ is the pump wavenumber. Note that F_v is independent of time. We now define the spatially dependent friction coefficient $\rho(x)$ by the relation $F_v(x) = -\rho(x)mv$ and introduce the atomic saturation parameter $s = |A|^2 g^2/\Delta^2$ at the maximum of the standing-wave pump. Together with (2) this yields

$$\rho(x) = -4s\Gamma\frac{\sigma_a}{\pi w^2}\frac{\hbar k_0^2}{m}\tau\sin(4k_0 x) \qquad (10)$$

which has units of s^{-1} and therefore relates to the inverse of the cooling or heating time.

Fig. 2 shows the dependence of the $1/e$ cooling time for rubidium atoms at a point of maximum friction, $\sin(4k_0 x) = -1$, on the beam waist and for different delay times ranging from 1 ns to 1 μs. Note that this plot assumes constant saturation s and thus the pump laser power is assumed to increase linearly with the mode area. The figure predicts that cooling times of the order of ms can be achieved if the pump is tightly focussed at the atom and the delay time is of the order of tens of ns. Longer delays lead to faster cooling. These conditions are comparable with those explored experimentally in, for example, Ref. 19.

An important feature of the friction coefficient (10) is its spatial dependence with $\sin(4k_0 x)$. This implies that the net friction for an extended spatial distribution is
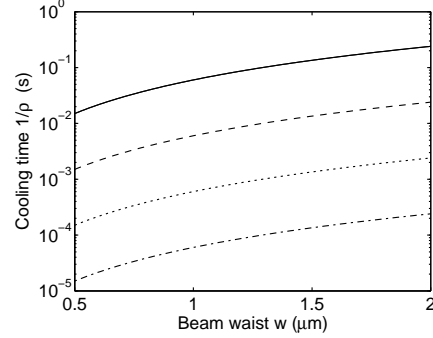
FIG. 2: Cooling time of rubidium atoms at position of maximum friction versus beam waist w for $s = 0.1$ and $\tau = 1$ ns (solid line), 10 ns (dashed), 100 ns (dotted), and 1 μs (dash-dotted).
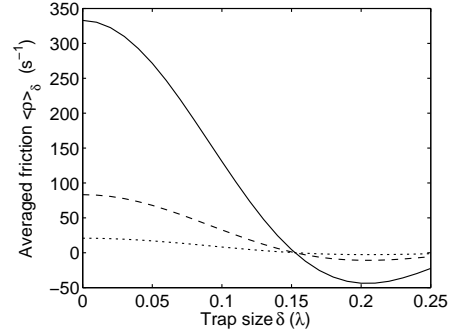
FIG. 3: Averaged friction coefficient $\langle\rho(x)\rangle_\delta$ for a trap centered at a point of maximum friction versus trap size δ for $s = 0.1$, $\tau = 10$ ns, and $w = 0.5$ μm (solid line), $w = 1$ μm (dashes), $w = 2$ μm (dotted).

zero. Significant cooling via this method thus requires localizing the atom in an additional trap. In practice this could be achieved by an additional far-off resonant beam either propagating parallel to the mirror or forming another standing wave superimposed on the driving beam for the cooling. Alternatively, on-chip microtraps can be utilized in conjunction with integrated time-delay reflectors. In the following, we will assume a harmonic trapping potential. We can then calculate an averaged friction coefficient, defined via the loss of kinetic energy over one oscillation, as

$$\langle\rho(x)\rangle_\delta = -4s\Gamma\frac{\sigma_a}{\pi w^2}\frac{\hbar k_0^2}{m}\tau\frac{1}{2\pi}$$
$$\times \int_0^{2\pi} \sin[4k_0 x + 4\delta\sin(T)]\cos^2(T)dT \qquad (11)$$

where δ is the maximum displacement of the atom from the trap center during an oscillation. Fig. 3 shows the averaged friction coefficient versus trap size, assuming
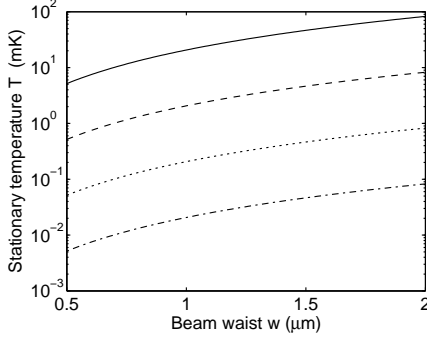
FIG. 4: Stationary temperature T at position of maximum friction versus beam waist w for $s = 0.1$ and $\tau = 1$ ns (solid line), 10 ns (dashed), 100 ns (dotted), and 1 μs (dash-dotted).

that the trap center is at a point of maximum friction. As expected, for increasing δ the cooling force decreases since the atom moves away from the point of optimum cooling. For trap sizes $\delta \gtrsim 0.15\lambda$ cooling finally turns into heating as the atom spends more time in regions of the standing-wave pump where the mirror-mediated force accelerates the atom.

So far, we have neglected momentum diffusion due to spontaneous scattering of photons by the atom, which together with the friction coefficient determines the stationary temperature achievable with this system. To zeroth order in the atom-field coupling, momentum diffusion is due to the interaction with the unperturbed pump field. We may thus expect diffusion to be identical to that observed in free-space Doppler cooling, where the diffusion constant is given by[14]

$$D = \hbar^2 k_0^2 \Gamma s. \tag{12}$$

From this the stationary temperature is obtained as

$$k_B T = \frac{D}{m\rho(x)} = \frac{\hbar}{\tau} \frac{\pi w^2}{4\sigma_a} \frac{-1}{\sin(4k_0 x)} \tag{13}$$

where for simplicity we have used the non-averaged value of the friction (10). This is a remarkably simple expression which, apart from the spatial dependence, only depends on the delay time and the beam cross section. Fig. 4 shows the stationary temperatures corresponding to the friction curves of Fig. 2. For realistic parameters these simple analytic results predict stationary temperatures of the order of mK or even slightly below and thus less than an order of magnitude above the Doppler limit of 141 μK for Rb atoms. However, we emphasize again that the cooling in our scheme is based on the dipole force, in contrast to free-space Doppler cooling which relies on the radiation pressure force. As such, mirror-mediated cooling uniquely also works in the far-off resonant regime.

IV. SEMICLASSICAL MONTE-CARLO SIMULATIONS

In addition to the perturbative solution of the system dynamics, we also performed numerical Monte-Carlo simulations. These semiclassical simulations have a number of advantages: (i) they allow us to include the harmonic dipole trap consistently, (ii) they provide solutions to any order in the coupling g^2/Δ and in the velocity v, and (iii) they include momentum and photon number diffusion. On the other hand, the numerical treatment requires us to restrict the analysis to a discrete set of equally spaced modes of angular frequencies ω_k.

The corresponding set of equations is derived following the approach of Refs. 20 which we only very briefly outline here. Starting from the full quantum master equation including quantized atomic motion and a Liouville-type term for spontaneous atomic decay, a Wigner transform is applied to obtain a Fokker-Planck equation for the joint Wigner function of the complex mode field amplitudes α_k and the atomic momentum p and position x. In the semiclassical approximation, this Fokker-Planck equation is equivalent to the following set of stochastic differential equations:

$$dx = \frac{p}{m}dt, \tag{14}$$

$$dp = i\gamma\left[\mathcal{E}(x)\frac{d}{dx}\mathcal{E}^*(x) - \mathcal{E}^*(x)\frac{d}{dx}\mathcal{E}(x)\right]dt$$
$$-U_0\left[\mathcal{E}(x)\frac{d}{dx}\mathcal{E}^*(x) + \mathcal{E}^*(x)\frac{d}{dx}\mathcal{E}(x)\right]dt$$
$$+k_t(x - x_0)dt + dP, \tag{15}$$

$$d\alpha_k = i\Delta_k\alpha_k dt - (iU_0 + \gamma)\mathcal{E}(x)f_k^*(x)dt + dA_k, \tag{16}$$

where $\mathcal{E}(x) = \sum_k \alpha_k \sin(\omega_k x/c)$ is the total field amplitude at x, x_t and k_t are the position of the trap center and the trap spring constant, respectively, and γ and U_0 are the atomic scattering rate and the optical potential per photon, respectively. The terms dP and dA_k are correlated stochastic white-noise terms describing the spontaneous redistribution of photons between modes by the scattering atom and the subsequent fluctuations in atom momentum and modal photon numbers. They are given by[20]

$$dP = k_0\sqrt{4\gamma/5}|\mathcal{E}(x)|dW_0 + \sqrt{2\gamma}|\frac{d}{dx}\mathcal{E}(x)|dW_+, \tag{17}$$

$$dA_k = \sqrt{\gamma/2}\sin\left(\frac{\omega_k x}{c}\right)\frac{\frac{d}{dx}\mathcal{E}(x)}{|\frac{d}{dx}\mathcal{E}(x)|}(idW_+ - dW_-), \tag{18}$$

where dW_i $(i = 0, +, -)$ are independent stochastic Ito increments with zero mean, $\langle dW_i \rangle = 0$, and unit variance, $\langle dW_i^2 \rangle = dt$[21].

Unfortunately, discretization of the mode frequencies also implies that the light field is periodic in time with a periodicity given by the inverse spectral mode spacing $2\pi/\Delta\omega$. It is thus not possible to follow a single simulation of the stochastic equations (14)-(16) to a quasi-stationary state. Instead, we perform averages over short
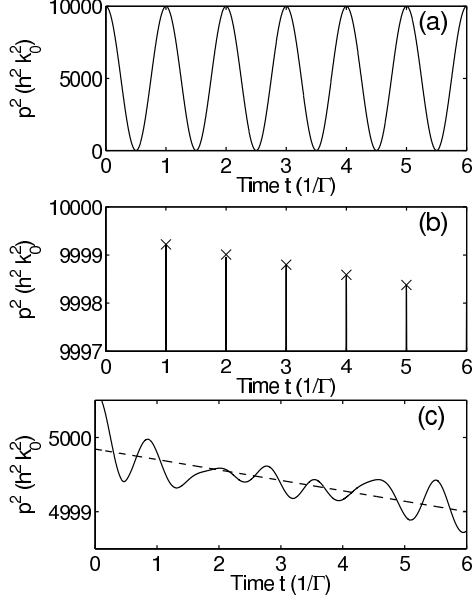
FIG. 5: Momentum of a single-particle trajectory in the absence of diffusion. (a) Square of momentum versus time. (b) Detail of (a) with fitted turning points (crosses) using method 1. (c) Fitting method 2: squared momentum after subtraction of a least-square fit with a sine function (solid line) and linear fit to the result (dashed). Parameters are for Rb atoms, $\Delta = -10\Gamma$, $\tau = 0.25/\Gamma$, $w = 0.7$ μm, $\Delta\omega = 0.1\Gamma$, $\omega_t = 0.5 \times 2\pi\Gamma$, $s = 0.076$. The trap is centered at a point of maximum friction.

FIG. 6: Cooling rate $\mathrm{d}T/\mathrm{d}t$ versus initial temperature. The data points (crosses) and error bars are obtained from Monte-Carlo simulations using 10^4 trajectories per initial temperature. The solid line is a linear fit to the numerical data. The parameters are as in Fig. 5.

propagation times for ensembles of different initial temperatures and derive linear approximations for the rate of temperature change $\mathrm{d}T/\mathrm{d}t$. Numerically, we found that this approach works well, however great care is required in the data analysis and fitting routines as outlined in the following.

Figure 5 shows the principles of our data analysis routines for the example of a single particle trajectory, where momentum diffusion was neglected for the sake of clarity. An atom with an initial momentum of $100\ \hbar k_0$ oscillates in a trap with trap frequency ω_t, Fig. 5(a). A closer look at the maxima of the momentum oscillations, Fig. 5(b), reveals the cooling effect due to friction. Note that this effect is small, only of the order of 10^{-4} for the period of time shown here. It is therefore necessary to remove the fundamental oscillation with very high accuracy from the simulated data, as it can otherwise easily mask the effects of friction.

One possibility (method 1) is to fit each single oscillation with a harmonic motion. From these fits the positions and momentum amplitudes of the individual oscillations are obtained, as indicated by the crosses in the figure. Finally, a linear fit to these data points provides an accurate measure of the averaged friction coefficient which can be compared to the analytic result (11). An

alternative method (method 2) to extract the friction coefficient from a trajectory, or from an ensemble average over many trajectories in the presence of noise, is shown in Fig. 5(c). In this case, a *single* sine function is fitted to the trajectory and subtracted from it. The result is a curve where the large amplitude oscillations have been removed. A linear fit to this curve reveals the average slope and thus the friction coefficient. Both methods, 1 and 2, work well within certain parameter limits, with method 1 in general being more accurate but method 2 being quicker to evaluate.

The results of one set of simulations of the full system of stochastic differential equations (14)-(16) are shown in Fig. 6. Simulations were performed in ensembles of 10^4 independent trajectories, where the initial conditions of each ensemble were chosen to represent an atomic cloud at a given temperature. Every trajectory was propagated for a time 60 Γ^{-1}, and ensemble averages of the squared momentum were taken as a measure of the ensemble temperature as a function of time. Finally, method 2 as outlined above was employed to extract a linear approximation to the cooling rate $\mathrm{d}T/\mathrm{d}t$. The numerical errors related to the finite number of simulations per ensemble were estimated by applying the same analysis to sub-ensembles of 10^3 trajectories.

Figure 6 shows that the numerically obtained values of $\mathrm{d}T/\mathrm{d}t$ are well approximated by a linear function of initial temperature. This linear behavior is expected for Brownian motion with linear friction. For very small initial temperatures, momentum diffusion dominates and the ensemble temperature increases with time. For large initial temperatures, on the other hand, friction dominates and the ensemble is cooled. The stationary temperature where the two effects cancel is obtained as $T = 0.69 \pm 0.17$ mK from the linear fit to the data with Gaussian error propagation. By comparison, the simple analytic estimate (13) predicts a temperature of 0.76 mK, which is in surprisingly good agreement given the

number of approximations made in the derivation of the perturbative result.

V. OUTLOOK: APPLICATION TO MICRO- AND NANODEVICES

In the analysis presented above, the delay time was provided by a meter-scale distance between the particle and the mirror. However, we envisage various routes for integration of this cooling scheme into microchip devices, as outlined in the following.

Microresonators. The necessary delay time can be conveniently achieved using an integrated optical resonator[7,8,9,10,11] instead of a delay line. For example, a 10 ns delay requires a resonator quality factor of $Q \approx 10^7$, which is well within the limits of state-of-the-art microsphere or microdisk resonators. The friction coefficient ρ will then correspond to the average of Eq. (10) over the delay time τ for light exiting the resonator after 1, 2, 3, etc. roundtrips.

Plasmonic field enhancement. In free space, the minimum beam diameter is limited by diffraction to about one optical wavelength. However, it has been shown that microantennas can vastly enhance local field intensities by plasmon effects, and enhancement factors of 300 have already been demonstrated[13]. If the particle could be placed inside such a microantenna, the geometric factor $\sigma_a/(\pi w^2)$ would effectively be increased by this factor, leading to significantly faster, more efficient cooling.

Optomechanics. The scheme discussed in this paper is concerned with cooling of microscopic particles. However, conceptually the proposed cooling method could also be applied to larger objects, e.g., micromechanical mirrors or oscillators[22,23,24] by appropriate device design and scaling of parameters.

With such generalizations we expect that this cooling scheme may be exploited in integrated atom chips[25], quantum information processors[26], atomic clocks[27], or interferometric sensors[28].

VI. CONCLUSIONS

We have analyzed theoretically an optical cooling scheme for neutral particles which, in principle, is not restricted to atoms but can be extended to any polarizable species. The scheme exploits the finite delay-time of light propagating from the particle to a mirror and back to the particle, and is thus non-Markovian in nature, in contrast to free-space laser cooling or cavity-mediated cooling methods. Finally, we proposed extensions of the cooling scheme to chip-based devices, which will open the road towards practical applications.

Acknowledgments

[1] S. Chu, *Rev. Mod. Phys.* 70, 685 (1998); C. N. Cohen-Tannoudji, *Rev. Mod. Phys.* 70, 707 (1998); W. D. Phillips, *Rev. Mod. Phys.* 70, 721 (1998).

[2] P. Horak, G. Hechenblaikner, K. M. Gheri, H. Stecher, and H. Ritsch, *Phys. Rev. Lett.* 79, 4974 (1997).

[3] V. Vuletic and S. Chu, *Phys. Rev. Lett.* 84, 3787 (2000).

[4] P. Domokos and H. Ritsch, *J. Opt. Soc. Am. B* 20, 1098 (2003).

[5] P. Maunz, T. Puppe, I. Schuster, N. Syassen, P. W. H. Pinkse, and G. Rempe, *Nature* 428, 50 (2004).

[6] A. Xuereb, P. Horak, and T. Freegarde, *Phys. Rev. A* in press.

[7] K. J. Vahala, *Nature* 424, 839 (2003).

[8] X. Liu, K.-H. Brenner, M. Wilzbach, M. Schwarz, T. Fernholz, and J. Schmiedmayer, *Appl. Opt.* 44, 6857 (2005).

[9] T. Steinmetz, Y. Colombe, D. Hunger, T. W. Hänsch, A. Balocchi, R. J. Warburton, and J. Reichel, *Appl. Phys. Lett.* 89, 111110 (2006).

[10] P. E. Barclay, K. Srinivasan, O. Painter, B. Lev, and H. Mabuchi, *Appl. Phys. Lett.* 89, 131108 (2006).

[11] M. Trupke, F. Ramirez-Martinez, E. A. Curtis, J. P. Ashmore, S. Eriksson, E. A. Hinds, Z. Moktadir, C. Gollasch, M. Kraft, G. V. Prakashb, and J. J. Baumberg, *Appl. Phys. Lett.* 88, 071116 (2006).

[12] A. Alù and N. Engheta, *Nature Photon.* 2, 307 (2008).

[13] H. Fischer and O. J. F. Martin, *Opt. Express* 16, 9144 (2008).

[14] J. P. Gordon and A. Ashkin, *Phys. Rev. A* 21, 1606 (1980).

[15] P. Lett, R. Watts, C. Westbrook, W. D. Phillips, P. Gould, and H. Metcalf, *Phys. Rev. Lett.* 61, 169 (1988).

[16] A. Aspect, E. Arimondo, R. Kaiser, N. Vansteenkiste, and C. Cohen-Tannoudji, *Phys. Rev. Lett.* 61, 826 (1988).

[17] C. W. Gardiner and P. Zoller, *Quantum Noise*, 3rd ed., Springer, Berlin (2004).

[18] P. Domokos, P. Horak, and H. Ritsch, *Phys. Rev. A* 65, 033832 (2002).

[19] P. Bushev, A. Wilson, J. Eschner, C. Raab, F. Schmidt-Kaler, C. Becher, and R. Blatt, *Phys. Rev. Lett.* 92, 223602 (2004).

[20] P. Domokos, P. Horak, and H. Ritsch, *J. Phys. B: At. Mol. Opt. Phys.* 34, 187 (2001); P. Horak and H. Ritsch, *Phys. Rev. A* 64, 033422 (2001).

[21] C. W. Gardiner, *Handbook of Stochastic Methods*, 3rd ed., Springer, Berlin (2004).

[22] T. Corbitt, C. Wipf, T. Bodiya, D. Ottaway, D. Sigg, N. Smith, S. Whitcomb, and N. Mavalvala, *Phys. Rev. Lett.* 99, 160801 (2007).

[23] A. Schliesser, R. Rivière, G. Anetsberger, O. Arcizet, and

T. J. Kippenberg, *Nature Phys.* **4**, 415 (2008).

[24] A. Xuereb, P. Domokos, J. Asbóth, P. Horak, and T. Freegarde, *Phys. Rev. A* **79**, 053810 (2009).

[25] R. Folman, P. Krüger, J. Schmiedmayer, J. Denschlag, and C. Henkel, *Adv. At. Mol. Opt. Phys.* **48**, 263 (2002).

[26] M. A. Nielsen and I. L. Chuang, *Quantum Computation and Quantum Information*, Cambridge University Press,

Cambridge (2000).

[27] G. Santarelli, P. Laurent, P. Lemonde, A. Clairon, A. G. Mann, S. Chang, A. N. Luiten, and C. Salomon, *Phys. Rev. Lett.* **82**, 4619 (1999).

[28] W. Hänsel, J. Reichel, P. Hommelhoff, and T. W. Hänsch, *Phys. Rev. A* **64**, 063607 (2001).

Scattering theory of multilevel atoms interacting with arbitrary radiation fields

André Xuereb,[1] Peter Domokos,[2] Peter Horak,[3] and Tim Freegarde[1]

[1]*School of Physics and Astronomy, University of Southampton, Southampton SO17 1BJ, United Kingdom*[*]
[2]*Research Institute of Solid State Physics and Optics,*
Hungarian Academy of Sciences, H-1525 Budapest P.O. Box 49, Hungary
[3]*Optoelectronic Research Centre, University of Southampton, Southampton SO17 1BJ, United Kingdom*
(Dated: October 5, 2009)

We present a generic transfer matrix approach for the description of the interaction of atoms possessing multiple ground state and excited state sublevels with light fields. This model allows us to treat multi-level atoms as classical scatterers in light fields modified by, in principle, arbitrarily complex optical components such as mirrors, resonators, dispersive or dichroic elements, or filters. We verify our formalism for two prototypical sub-Doppler cooling mechanisms and show that it agrees with the standard literature.

PACS numbers: 42.50.Wk; 37.10.De; 37.10.Vz; 42.70.Qs

I. INTRODUCTION

The two-level model of atoms interacting with light fields [1] has often been used to explore optical cooling mechanisms [2, 3, 4]. Its inherent simplicity—the atom has one ground state and one excited state—makes the resulting models amenable to analysis, but also suppresses mechanisms [5] that, in the appropriate parameter regimes, dominate the interaction.

A notable example of such an initially overlooked mechanism in atomic physics is three-dimensional optical molasses [6]. By means of the two-level model, one can predict the equilibrium temperature, the so-called "Doppler" temperature T_D, of atoms in molasses to be $\hbar\Gamma$, where Γ is the (half-width at half-maximum) linewidth of the transition from the excited to the ground level [4]. Data from early three-dimensional molasses experiments contradicted this [7], showing that the achievable equilibrium temperature was in fact much lower. This discrepancy was resolved independently by two groups [5, 8], both explanations relying on the inclusion of the manifold of magnetic sublevels in each of the ground and excited states. In particular, the motion of the atoms in the optical field leads to a non-adiabatic following of the magnetic sublevel populations, which gives rise to a strong viscous force and efficient cooling to temperatures significantly lower than the Doppler temperature.

We recently [9] explored a new scattering theory that deals with the interaction of light and matter in a unified form applicable from microscopic to macroscopic systems. In that work we only considered the two-level atom model and showed, in particular, how our model can explain such mechanisms as standard optical molasses and mirror-mediated cooling [10]. In this paper we extend this model to deal with magnetic sublevels, in much the
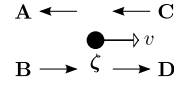
FIG. 1: Moving scatterer interacting with four field modes represented by the Jones vectors **A**, **B**, **C**, and **D**. The scatterwe has velocity v and is described by means of its polarizability tensor ζ. The field mode amplitudes are, in general, functions of the wavenumber k.

same spirit as ref. [5]. In due course, this extension will enable us to deal with multilevel atoms interacting with an arbitrarily complex system composed of immobile mirrors, cavities, MEMS devices, etc., without resorting to a quantized model for such a system.

After we introduce the general extension in the next section, we then proceed to explore two prototypical systems—the $J = \frac{1}{2} \to J' = \frac{3}{2}$ transition, leading to the "Sisyphus" cooling mechanism, and the $J = 1 \to J' = 2$ transition—in Section III and Section IV, respectively.

II. A TRANSFER MATRIX RELATING JONES VECTORS

We investigate the interaction of atoms with light of different polarizations. To this end, we denote the two polarization basis vectors by μ and ν, whereby the standard circular polarization basis is equivalent to setting $\mu = \sigma^+$ and $\nu = \sigma^-$. Starting from the transfer matrix model explored in ref. [9] and using the definitions in Fig. 1, we replace each of the field modes by a corresponding Jones vector, similar to the model used in ref. [11]. Thus, for example,

$$A(k) \to \mathbf{A}(k) = \begin{pmatrix} A_\mu(k) \\ A_\nu(k) \end{pmatrix}, \qquad (1)$$

and similarly for B, C and D. The transfer matrix M, describing the effect of the scatterer on the four field

modes by means of the relation

$$\begin{pmatrix} A(k) \\ B(k) \end{pmatrix} = M \begin{pmatrix} C(k) \\ D(k) \end{pmatrix}, \qquad (2)$$

is now transformed into an order 4 tensor of the form

$$\boldsymbol{M} = \begin{bmatrix} \boldsymbol{m_{11}} & \boldsymbol{m_{12}} \\ \boldsymbol{m_{21}} & \boldsymbol{m_{22}} \end{bmatrix}, \qquad (3)$$

where each of $\boldsymbol{m_{\alpha\beta}}$ $(\alpha, \beta = 1, 2)$ is a 2×2 matrix relating the respective Jones vector components. A general recipe for transforming the formulae for the field mode amplitudes, as given in ref. [9], can be summarized by means of the two replacements

$$1 \to \mathbf{1} = \begin{bmatrix} 1 & 0 \\ 0 & 1 \end{bmatrix} \text{ and } \zeta \to \boldsymbol{\zeta}, \qquad (4)$$

wherever necessary. In particular, then,

$$M = \begin{bmatrix} 1 - i\zeta & -i\zeta \\ i\zeta & 1 + i\zeta \end{bmatrix} \to \boldsymbol{M} = \begin{bmatrix} \mathbf{1} - i\boldsymbol{\zeta} & -i\boldsymbol{\zeta} \\ i\boldsymbol{\zeta} & \mathbf{1} + i\boldsymbol{\zeta} \end{bmatrix}. \qquad (5)$$

We follow ref. [12], Complement E_{III} §3-b, in defining the polarizability tensor $\boldsymbol{\zeta}$ as the steady-state expectation value of the polarizability operator $\hat{\boldsymbol{\chi}}$; $\boldsymbol{\zeta}$ is therefore given by the trace

$$\boldsymbol{\zeta} = \text{Tr}\big(\rho^{\text{st}} \cdot \hat{\boldsymbol{\chi}}\big) = \sum_{i,j} \langle j|\rho^{\text{st}}|i\rangle \langle i|\hat{\boldsymbol{\chi}}|j\rangle, \qquad (6)$$

where ρ^{st} is the steady-state density matrix describing the system and the summation runs over all the internal sublevels of the atom, and where we construct the order 4 polarizability operator tensor $\hat{\boldsymbol{\chi}}$ similarly to ref. [13], Eq. (14.9-24). In the general μ, ν basis:

$$\langle i|\hat{\boldsymbol{\chi}}|j\rangle = \zeta_0 \sum_e \begin{pmatrix} \langle i|\hat{d}_\mu|e\rangle \\ \langle i|\hat{d}_\nu|e\rangle \end{pmatrix} \otimes \begin{pmatrix} \langle j|\hat{d}_\mu|e\rangle \\ \langle j|\hat{d}_\nu|e\rangle \end{pmatrix}$$

$$= \zeta_0 \sum_e \begin{bmatrix} \langle i|\hat{d}_\mu|e\rangle\langle e|\hat{d}_\mu|j\rangle & \langle i|\hat{d}_\mu|e\rangle\langle e|\hat{d}_\nu|j\rangle \\ \langle i|\hat{d}_\nu|e\rangle\langle e|\hat{d}_\mu|j\rangle & \langle i|\hat{d}_\nu|e\rangle\langle e|\hat{d}_\nu|j\rangle \end{bmatrix}, \qquad (7)$$

with ζ_0 being the characteristic polarizability of the atom. In Eq. (7), the dipole moment operator $\hat{d}_\mu$ $(\hat{d}_\nu)$ is related to the μ (ν) polarized light field and the sum runs over all the internal sublevels, e, of the atom. The matrix elements of $\hat{d}_\mu$ $(\hat{d}_\nu)$ are given by the appropriate Clebsch-Gordan coefficients.

Importantly, this new transfer matrix still retains all its properties, allowing us to model the interaction of the multilevel atom with an arbitrary system of immobile optical elements such as mirrors, cavities, waveplates, etc. As in our previous work [9], this interaction is accounted for by the multiplication of the various transfer matrices of the elements making up the system; this model is, in principle, applicable to systems of arbitrary complexity.

Finally, we recall that the diagonal elements, $\langle i|\rho^{\text{st}}|i\rangle$, of ρ^{st} are the populations in each of the sublevels,
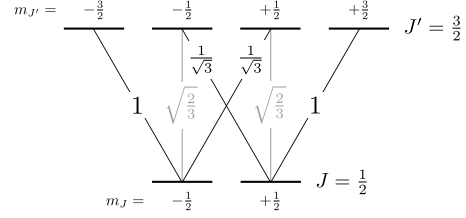
FIG. 2: Clebsch-Gordan coefficients for a $J = \frac{1}{2} \to J' = \frac{3}{2}$ transition.

whereas its off-diagonal elements, $\langle i|\rho^{\text{st}}|j\rangle$, are the respective coherences. The matrix elements of ρ^{st} are obtained from the appropriate optical Bloch equations (see, for example, the procedure outlined in ref. [14]). We note here that, through its dependence on ρ^{st}, $\boldsymbol{M}$ depends on the fields that it helps to determine, and thus Eq. (2) will in general become a set of nonlinear equations. In cases, like the ones considered in the following sections, where only one multilevel atom is interacting with a linear optical system, this problem may be solved using a procedure similar to the one outlined below: the fields surrounding the atom are obtained from the input fields through linear operations and then used with the optical Bloch equations to obtain the populations and coherences of the atom's various levels. Knowledge of these quantities then determines the fields, and hence the forces acting on the atom, completely.

In the following sections we will restrict our discussion to the case where the input field is not modified by other transfer matrices. We will apply this mechanism to investigate the behaviour of atoms in two cases where the polarization of the light varies in space on scales of the order of the wavelength to verify the validity of the model given by Eq. (5) to Eq. (7). In the first instance, we illuminate our atom with two counterpropagating linearly polarized beams. We choose the planes of polarization of the two beams to be orthogonal to each other. The second configuration we will investigate involves illuminating the atom with two circularly polarized beams, choosing opposite handedness for the two beams. These two cases mirror those in ref. [5].

III. ATOMS IN A GRADIENT OF POLARIZATION

In this and the following sections, we will adopt the low-intensity hypothesis. This allows us to simplify the optical Bloch equations and resulting system considerably by neglecting the populations and coherences of the excited state sublevels. We can thus replace ρ^{st} by the ground state steady-state density matrix, $\rho_{\text{g}}^{\text{st}}$. We denote the diagonal element (i, i) of $\rho_{\text{g}}^{\text{st}}$, the population in sublevel i, by Π_i, and the off-diagonal element (i, j), the

coherence between sublevels i and j, by $C_{i,j}$.

Here we will discuss what is perhaps the simplest transition between two levels with multiple magnetic sublevels: the $J = \frac{1}{2} \to J' = \frac{3}{2}$ transition. In this case, we have two ground sublevels so that ρ_g^{st} is a 2×2 matrix. Fig. 2 tabulates the Clebsch-Gordan coefficients required to evaluate $\boldsymbol{\zeta}$. We thus have:

$$\rho_g^{\text{st}} = \begin{bmatrix} \Pi_{-\frac{1}{2}} & C_{-\frac{1}{2},+\frac{1}{2}} \\ C_{+\frac{1}{2},-\frac{1}{2}} & \Pi_{+\frac{1}{2}} \end{bmatrix} \tag{8}$$

and

$$\hat{\boldsymbol{\chi}} = \zeta_0 \begin{pmatrix} \begin{bmatrix} \frac{1}{3} & 0 \\ 0 & 1 \end{bmatrix} & \mathbf{0} \\ \mathbf{0} & \begin{bmatrix} 1 & 0 \\ 0 & \frac{1}{3} \end{bmatrix} \end{pmatrix}, \tag{9}$$

whereby

$$\boldsymbol{\zeta} = \zeta_0 \left(\begin{bmatrix} \frac{1}{3} & 0 \\ 0 & 1 \end{bmatrix} \Pi_{-\frac{1}{2}} + \begin{bmatrix} 1 & 0 \\ 0 & \frac{1}{3} \end{bmatrix} \Pi_{+\frac{1}{2}} \right). \tag{10}$$

Suppose, now, that we illuminate the atom with two counterpropagating beams having orthogonal linear polarization and equal intensity. This can be represented by setting

$$\mathbf{B}(k) = \frac{B}{\sqrt{2}} \begin{pmatrix} 1 \\ 1 \end{pmatrix} \exp(ikx - i\pi/4) \tag{11}$$

and

$$\mathbf{C}(k) = \frac{iB}{\sqrt{2}} \begin{pmatrix} 1 \\ -1 \end{pmatrix} \exp(-ikx + i\pi/4), \tag{12}$$

where the shift in the x coordinate is introduced to simplify our expressions. Using the optical Bloch equations, we can show that the steady state populations in the ground sublevels at zero atomic velocity are given by

$$\Pi_{-\frac{1}{2}} = \cos^2(kx) \quad \text{and} \quad \Pi_{+\frac{1}{2}} = \sin^2(kx), \tag{13}$$

noting that the populations do not depend on the field amplitudes in the low intensity regime.

We work to lowest order in ζ_0 and make use of the above relations to find the net force acting on the atom:

$$\begin{aligned} F &= \hbar k \left(|\mathbf{A}|^2 + |\mathbf{B}|^2 - |\mathbf{C}|^2 - |\mathbf{D}|^2 \right) \\ &= 2\hbar k \, \text{Im}\left\{ \left[\boldsymbol{\zeta}(\mathbf{B} + \mathbf{C}) \right] \cdot (\mathbf{B} - \mathbf{C})^\star \right\} \\ &\quad + 4\frac{v}{c}\hbar k \, \text{Im}\left\{ (\boldsymbol{\zeta}\mathbf{B}) \cdot \mathbf{C}^\star + (\boldsymbol{\zeta}\mathbf{C}) \cdot \mathbf{B}^\star \right\} \\ &\quad - 2\frac{v}{c}\hbar k^2 \, \text{Im}\left\{ \left[\frac{\partial \boldsymbol{\zeta}}{\partial k}(\mathbf{B} + \mathbf{C}) \right] \cdot (\mathbf{B} + \mathbf{C})^\star \right\} \\ &\approx 2\hbar k|B|^2 \, \text{Im}\left\{ \left[\boldsymbol{\zeta}(\mathbf{B} + \mathbf{C}) \right] \cdot (\mathbf{B} - \mathbf{C})^\star \right\} \\ &\quad + 2\frac{v}{c}\hbar k^2 \, \text{Im}\left\{ \left[\frac{\partial \boldsymbol{\zeta}}{\partial k}(\mathbf{B} + \mathbf{C}) \right] \cdot (\mathbf{B} + \mathbf{C})^\star \right\}, \quad (14) \end{aligned}$$
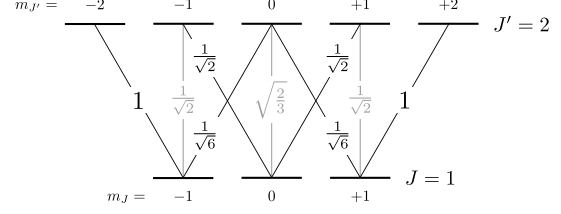
FIG. 3: Clebsch-Gordan coefficients for a $J = 1 \to J' = 2$ transition.

where we have assumed that $\|k\,\partial\boldsymbol{\zeta}/\partial k\| \gg \|\boldsymbol{\zeta}\|$. The velocity-dependent force terms in the above expression arise through the Doppler shifting of photons both between field modes in the same polarization and between field modes in different polarizations; these mechanisms are accounted for by the diagonal and off-diagonal terms in $\boldsymbol{\zeta}$, respectively. These terms emerge through the velocity-dependent terms in the generalised transfer matrix.

In the present case, Eq. (14) simplifies approximately to

$$F = \tfrac{4}{3}\hbar k\zeta_0|B|^2 \sin(2kx)\left(\Pi_{+\frac{1}{2}} - \Pi_{-\frac{1}{2}} \right),$$

assuming that ζ_0 is real for simplicity.

We now let τ_p be a characteristic residence time of the two ground state sublevels; this will introduce a non-adiabatic following term, proportional to v, in the populations of each of the sublevels and emerges from the optical Bloch equations. Thus, we obtain the expression

$$F = -\tfrac{2}{3}\hbar k|B|^2\zeta_0 \sin(4kx) - \tfrac{8}{3}\hbar k^2|B|^2\zeta_0 v\tau_{\text{p}} \sin^2(2kx), \tag{15}$$

which agrees precisely with the standard literature (cf. Eqs. (4.20) and (4.23) in ref. [5]).

IV. ATOMS IN A GRADIENT OF ELLIPTICITY

If we illuminate an atom with two counterpropagating beams of light in a σ^+–σ^- configuration, rich dynamics are obtained not in the simplest ($J = \frac{1}{2} \to J' = \frac{3}{2}$) case, but in the next simplest, where the ground state has three magnetic sublevels ($J = 1$) and the excited state five ($J' = 2$). In this case, then, we can express ρ_g^{st} and $\hat{\boldsymbol{\chi}}$ as

$$\rho_g^{\text{st}} = \begin{bmatrix} \Pi_{-1} & C_{-1,0} & C_{-1,+1} \\ C_{0,-1} & \Pi_0 & C_{0,+1} \\ C_{+1,-1} & C_{+1,0} & \Pi_{+1} \end{bmatrix} \tag{16}$$

and

$$\hat{\boldsymbol{\chi}} = \zeta_0 \begin{pmatrix} \begin{bmatrix} \frac{1}{6} & 0 \\ 0 & 1 \end{bmatrix} & \mathbf{0} & \begin{bmatrix} 0 & \frac{1}{6} \\ 0 & 0 \end{bmatrix} \\ \mathbf{0} & \begin{bmatrix} \frac{1}{2} & 0 \\ 0 & \frac{1}{2} \end{bmatrix} & \mathbf{0} \\ \begin{bmatrix} 0 & 0 \\ \frac{1}{6} & 0 \end{bmatrix} & \mathbf{0} & \begin{bmatrix} 1 & 0 \\ 0 & \frac{1}{6} \end{bmatrix} \end{pmatrix}, \tag{17}$$

using the Clebsch-Gordan coefficients in Fig. 3. Together, these give

$$\boldsymbol{\zeta} = \zeta_0 \left(\begin{bmatrix} \frac{1}{6} & 0 \\ 0 & 1 \end{bmatrix} \Pi_{-1} + \begin{bmatrix} \frac{1}{2} & 0 \\ 0 & \frac{1}{2} \end{bmatrix} \Pi_0 + \begin{bmatrix} 1 & 0 \\ 0 & \frac{1}{6} \end{bmatrix} \Pi_{+1} \right.$$
$$\left. + \begin{bmatrix} 0 & \frac{1}{6} \\ 0 & 0 \end{bmatrix} C + \begin{bmatrix} 0 & 0 \\ \frac{1}{6} & 0 \end{bmatrix} C^\star \right), \tag{18}$$

with $C = C_{+1,-1} = C^\star_{-1,+1} = \langle +1|\rho_{\mathrm{g}}^{\mathrm{st}}|-1\rangle$ representing the nonzero coherence between the $m_J = +1$ and the $m_J = -1$ sublevels. Note that we again apply the low intensity hypothesis, thereby replacing ρ^{st} with $\rho_{\mathrm{g}}^{\mathrm{st}}$.

We now illuminate the atom with two counterpropagating beams of equal intensity, **B** and **C**, possessing σ^+ and σ^- polarization, respectively:

$$\mathbf{B}(k) = B \begin{pmatrix} 1 \\ 0 \end{pmatrix} \exp(ikx) \tag{19}$$

and

$$\mathbf{C}(k) = B \begin{pmatrix} 0 \\ 1 \end{pmatrix} \exp(-ikx). \tag{20}$$

We again use Eq. (14) to derive the force acting on the atom, which is given by

$$F = 2\hbar k |B|^2 \operatorname{Im}\left\{ \tfrac{5}{6}\zeta_0 \big(\Pi_{+1} - \Pi_{-1}\big) \right.$$
$$\left. + \tfrac{1}{6} i \zeta_0 \operatorname{Im}\{C \exp(-2ikx)\} \right\}$$
$$- 2\tfrac{v}{c}\hbar k^2 |B|^2 \operatorname{Im}\{\partial \zeta_0/\partial k\} \left(\tfrac{7}{6}\big(\Pi_{+1} + \Pi_{-1}\big) + \Pi_0 \right.$$
$$\left. + \tfrac{1}{3}\operatorname{Re}\{C\exp(-2ikx)\} \right), \tag{21}$$

where the populations and coherences are again obtained from the optical Bloch equations, and can be found in

ref. [5]. By observing the natural correspondence between ζ_0 and $s_\pm$ in this latter reference, we can see that our expression for the force acting on the atom again agrees with the standard literature to first order in $\frac{v}{c}$ (cf. Eq. (5.9) in ref. [5]). The resulting friction force is thus due to both the Doppler shift, as evident in the terms shown explicitly in Eq. (21), as well as through the non-adiabatic following of the atomic sublevel populations.

V. CONCLUSIONS

By revisiting the transfer matrix formalism and expressing the polarizability of a scatterer as the expectation value of a quantum operator, we have endowed it with a strong quantum character that allows us to handle atoms with multiple ground and excited state sublevels. In principle, our extended formalism is only limited by its reliance on the optical Bloch equations to give expressions for the ground state populations and coherences; we have retained the character of our earlier formalism that allowed us to work to arbitrary order in the polarizability. We have applied this theory to two standard sub-Doppler cooling configurations, the so-called "lin–⊥–lin" and "σ^+–σ^-" configurations, and thereby reproduced the known expressions for the force acting on the atom.

[1] B. W. Shore, *The Theory of Coherent Atomic Excitation: Simple Atoms and Fields, Volume 1* (Wiley VCH, 1990).
[2] J. P. Gordon and A. Ashkin, Phys. Rev. A **21**, 1606 (1980).
[3] J. Dalibard and C. Cohen-Tannoudji, Journal of Physics B (Atomic, Molecular and Optical Physics) **18**, 1661 (1985).
[4] H. J. Metcalf and P. van der Straten, J. Opt. Soc. Am. B **20**, 887 (2003).
[5] J. Dalibard and C. Cohen-Tannoudji, J. Opt. Soc. Am. B **6**, 2023 (1989).
[6] S. Chu, L. Hollberg, J. E. Bjorkholm, A. Cable, and A. Ashkin, Phys. Rev. Lett. **55**, 48 (1985).
[7] P. D. Lett, R. N. Watts, C. I. Westbrook, W. D. Phillips, P. L. Gould, and H. J. Metcalf, Phys. Rev. Lett. **61**, 169 (1988).
[8] P. J. Ungar, D. S. Weiss, E. Riis, and S. Chu, J. Opt.
Soc. Am. B **6**, 2058 (1989).
[9] A. Xuereb, P. Domokos, J. Asbóth, P. Horak, and T. Freegarde, Phys. Rev. A **79**, 053810 (2009).
[10] A. Xuereb, P. Horak, and T. Freegarde, Phys. Rev. A **80**, 013836 (2009).
[11] R. J. C. Spreeuw, M. W. Beijersbergen, and J. P. Woerdman, Phys. Rev. A **45**, 1213 (1992).
[12] C. Cohen-Tannoudji, B. Diu, and F. Laloe, *Quantum Mechanics, Volume 1* (Wiley-Interscience, 1978), ISBN 047116433X.
[13] B. W. Shore, *The Theory of Coherent Atomic Excitation: Simple Atoms and Fields, Volume 2* (Wiley VCH, 1990).
[14] C. Cohen-Tannoudji, in *Frontiers in laser spectroscopy, Proceedings of the Les Houches Summer School, Session XXVII*, edited by R. Balian, S. Haroche, and S. Liberman (North Holland, 1977), pp. 1–104.

arXiv:1101.0130v1 [physics.optics] 30 Dec 2010

Amplified optomechanics in a unidirectional ring cavity

André Xuereb,[a,∗] Peter Horak,[b] and Tim Freegarde[a]

[a]School of Physics and Astronomy, University of Southampton, Southampton SO17 1BJ, United Kingdom; [b]Optoelectronics Research Centre, University of Southampton, Southampton SO17 1BJ, United Kingdom

We investigate optomechanical forces on a nearly lossless scatterer, such as an atom pumped far off-resonance or a micromirror, inside an optical ring cavity. Our model introduces two additional features to the cavity: an isolator is used to prevent circulation and resonant enhancement of the pump laser field and thus to avoid saturation of or damage to the scatterer, and an optical amplifier is used to enhance the effective Q-factor of the counterpropagating mode and thus to increase the velocity-dependent forces by amplifying the back-scattered light. We calculate friction forces, momentum diffusion, and steady-state temperatures to demonstrate the advantages of the proposed setup.

Keywords: optomechanics; cavity cooling; ring cavities; optical forces; gain media

1. Introduction and Motivation

Free-space laser cooling [1] has proven to be remarkably successful in cooling simple atomic systems, especially alkali atoms [2]. Relying on the availability of a (quasi-)closed two-level [3] or multi-level [4, 5] system, however, only occasional successes were had with more complicated systems, such as molecules [6, 7]. An alternative to such schemes is cavity–mediated cooling [8–11], where the interaction of a polarisable particle with a cavity field leads to a Sisyphus–type mechanism [12] that can cool the motion of the particle; no specific energy level scheme is required for this mechanism to operate. Much of this work has been focused on standing-wave (Fabry–Pérot) cavities, where high Q-factors can be achieved experimentally to significantly enhance optomechanical forces. However, in the limit of strong scatterers, friction forces in standing-wave cavities become increasingly position-dependent [13], which limits the overall, averaged cooling efficiency. This can be overcome by using ring cavities [14–21] where the translational symmetry guarantees position-independent forces. On the other hand, ring cavities are usually much larger and of lower Q-factor than their standing-wave counterparts. Using a gain medium inside a ring cavity has been proposed [22, 23] to offset these losses, allowing one to effectively 'convert' a low-Q cavity into a high-Q one, and thus to increase the effective optomechanical interaction by orders of magnitude. This same concept has also been raised in connection with using optical parametric amplifiers in standard optomechanical systems [24]. Research is also being conducted into using nonlinear media inside cavities [25] as a tool to control the dynamics of a micromechanical oscillator. Another application of ring cavities is in the investigation of collective atomic recoil lasing (CARL) [26], which exploits the spontaneous self-organisation of an atomic ensemble within a ring cavity, induced by a strong pump beam, to amplify a probe beam through Doppler-shifted reflection of the pump. The gain medium is in this case the atomic ensemble itself.

∗Corresponding author. Electronic address: andre.xuereb@soton.ac.uk

2
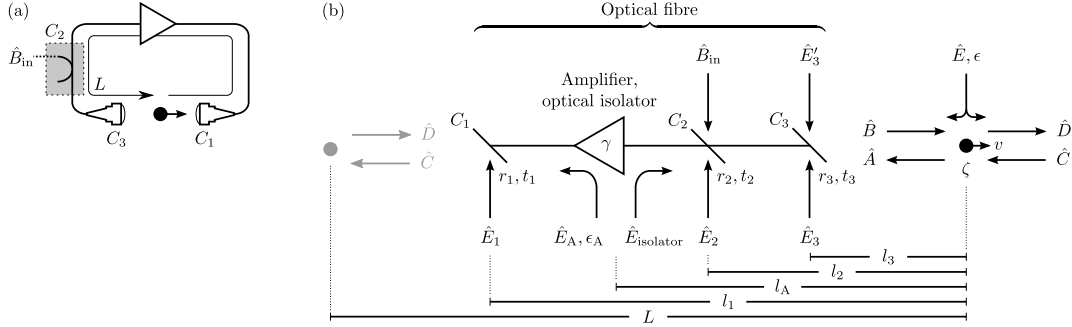
Figure 1. (a) Physical schematic of a polarisable particle in a unidirectional ring cavity, showing the input field $\hat{B}_{\text{in}}$. (b) Equivalent 'transfer matrix'–style (unfolded) model; the particle is drawn on both sides of this schematic to illustrate the recursive nature of the cavity. The various components are defined in Section 2.

Here, we investigate a different system that shares several features with the above mechanisms. In particular, we consider a particle inside a ring cavity that includes a gain medium, spatially separated from the particle. An isolator is also included in the ring cavity, in such a way as to prevent the pump beam from circulating in the cavity and being amplified; this ensures that the intensity of the field surrounding the particle is always low and thereby circumvents any problems caused by atomic saturation or mirror burning. The Doppler-shifted reflection of the pump from the particle is, on the other hand, allowed to circulate, and its amplification in turn enhances the velocity-dependent forces acting on the particle.

In such a situation, one is able to take advantage of properties inherent to the ring cavity system, such as the fact that the forces acting on the particle do not exhibit any sub-wavelength spatial modulation; this is due to the translational symmetry present in the system [14]. Moreover, modest amplification allows one to use optical fibres to form the ring cavity, opening the door towards increasing the optical length of such cavities. The optomechanical force is, as we will see and in the parameter domain of interest, linearly dependent on the cavity length; lengthening the cavity thus provides further enhancement of the interaction.

This paper is structured as follows. We shall first introduce the physical model, which we proceed to solve using the transfer matrix method (TMM) [27] to obtain the friction force and momentum diffusion acting on the particle. In the good-cavity limit, Section 2.1, simple expressions for these quantities can be obtained, yielding further insight into the system and allowing us to draw some parallels with traditional cavity cooling. In this limit, our model becomes equivalent to one based on a standard master equation approach [14] as outlined in Section 2.2. Realistic numerical values for the various parameters are then used in Section 3 to explore the efficiency and limits of the cooling mechanism. Finally, we will conclude by mentioning some possible extensions to the scheme.

2.   General expressions and equilibrium behaviour

The mathematical model of the ring cavity system, schematically drawn in Fig. 1(a), is shown in Fig. 1(b). A particle, characterised by its polarisability ζ, is in a ring cavity of round-trip length L. $C_{1,3}$ are the couplers, between which the particle lies, that terminate the fibre-based cavity, and C_2 is the input coupler that injects a pump beam with wavenumber k_0 into one of the travelling modes of the cavity. The couplers C_i ($i = 1, 2, 3$) have (amplitude) reflection and transmission coefficients r_i and $t_i = r_i + 1$, respectively, and are associated with corresponding noise modes $\hat{E}_i$. Similarly, the particle itself couples a noise mode $\hat{E}$ into the system with an amplitude ϵ depending on ζ. The length scales $l_1 > l_{\text{A}} > l_2 > l_3 > 0$ are introduced for clarity, but their values are not important for the results of this paper. The cavity contains an optical

isolator which prevents the pumped mode from circulating inside the cavity. This avoids resonant enhancement of the pumped mode in the cavity and thus avoids saturating the particle. The backscattered counterpropagating mode, on the other hand, is amplified on every round trip by means of an optical amplifier with gain $\gamma \geq 1$. The amplifier also introduces a noise mode $\hat{E}_A$ with an amplitude ϵ_A which depends on γ. The TMM [27] is used to self-consistently solve for the two counterpropagating field amplitudes at every point in the cavity in the presence of the pump field and the noise modes. Note that in the limit where the amplifier is compensating for the ring cavity losses, the amplifier noise is also comparable to the loss-induced noise and must therefore be taken into account in our model.

Using the notation in Fig. 1(a) we can relate the expectation values of the amplitudes of the two input and two scattered field modes interacting with the particle in a one-dimensional scheme, $A(k) = \langle \hat{A}(k) \rangle$, $B(k) = \langle \hat{B}(k) \rangle$, $C(k) = \langle \hat{C}(k) \rangle$, and $D(k) = \langle \hat{D}(k) \rangle$, to $B_{\text{in}}(k) = \langle \hat{B}_{\text{in}}(k) \rangle$ by means of the relations

$$B = r_2 t_3 e^{ik_0 l_2} B_{\text{in}}, \ \ C = \alpha A, \ \ \text{and} \ \ \begin{pmatrix} A \\ B \end{pmatrix} = \hat{M} \begin{pmatrix} C \\ D \end{pmatrix}, \tag{1}$$

where $\alpha(k) = t_1 t_2 t_3 \gamma \exp(ikL)$ is the factor multiplied to the field amplitude every round trip. In the preceding equations, as well as in the following, we do not write the index k for simplicity of presentation. The operators $\hat{A}(k)$, etc., denote the annihilation operators of the various field modes. The three equations Eqs. (1) have a readily apparent physical significance—respectively, they correspond to: the propagation of $\hat{B}_{\text{in}}$ to reach the particle; the feeding back of $\hat{A}$ to $\hat{C}$ through the ring cavity; and the usual transfer matrix relation for a particle interacting with the four fields surrounding it. The first two of these relations are substituted into the third, which subsequently simplifies to

$$\begin{pmatrix} A \\ B_{\text{in}} \end{pmatrix} = \left(\begin{bmatrix} 1 & 0 \\ 0 & r_2 t_3 e^{ik_0 l_2} \end{bmatrix} - \hat{M} \begin{bmatrix} \alpha & 0 \\ 0 & 0 \end{bmatrix} \right)^{-1} \hat{M} \begin{pmatrix} 0 \\ D \end{pmatrix} \tag{2}$$

If we assume far off-resonant operation, i.e., $\partial \zeta / \partial k = 0$, the velocity-dependent transfer matrix $\hat{M}$ can be written as [27, 28]

$$\begin{bmatrix} 1 + i\zeta & i\zeta - 2i\zeta \frac{v}{c} + 2ik_0 \zeta \frac{v}{c} \partial_k \\ -i\zeta - 2i\zeta \frac{v}{c} + 2ik_0 \zeta \frac{v}{c} \partial_k & 1 - i\zeta \end{bmatrix}. \tag{3}$$

The notation $\partial_k \equiv \frac{\partial}{\partial k}$ is used throughout; note that this partial derivative acts not only on $\alpha(k)$ but also on the field mode amplitudes it precedes. Eq. (2) can be inverted in closed form to first order in v/c, similarly to Ref. [28], and can thus be used to find $\mathcal{A} = \sqrt{2\epsilon_0 S/(\hbar k_0)} \int A(k) \, dk$, $\mathcal{B} = \sqrt{2\epsilon_0 S/(\hbar k_0)} \int B(k) \, dk$, $\mathcal{C} = \sqrt{2\epsilon_0 S/(\hbar k_0)} \int C(k) \, dk$, and $\mathcal{D} = \sqrt{2\epsilon_0 S/(\hbar k_0)} \int D(k) \, dk$, where the normalisation is with respect to the pump beam mode area S and where a monochromatic pump is assumed: $B_{\text{in}}(k) = B_0 \delta(k - k_0)$. Here, $|\mathcal{A}|^2$, $|\mathcal{B}|^2$, etc., are the photon currents in units of photons per second. The expectation value of the force acting on the particle is then given by [27]:

$$\boldsymbol{F}_{\text{full}} = \hbar k_0 \left(|\mathcal{A}|^2 + |\mathcal{B}|^2 - |\mathcal{C}|^2 - |\mathcal{D}|^2 \right). \tag{4}$$

The values of $\mathcal{A}$, $\mathcal{B}$, etc., from the solution of Eq. (2) are then substituted into Eq. (4), which we evaluate to first order in v/c, in terms of B_0. After some algebra, we obtain the first main

4

result of this paper—the friction force acting on the particle:

$$\boldsymbol{F} = -8\hbar k_0^2 \frac{v}{c} \operatorname{Re}\left\{\frac{(1-\alpha^*)\zeta \operatorname{Re}\{\zeta\} + i\alpha^*\zeta|\zeta|^2}{1-\alpha-i\zeta}\frac{\partial\alpha}{\partial k}\right\} \frac{\left|r_2 t_3 B_0\right|^2}{\left|1-\alpha-i\zeta\right|^2}\,. \tag{5}$$

By extending the TMM appropriately, one can keep track of the various noise modes interacting with the system. Eqs. (1) then become

$$\hat{A} = \frac{i\zeta}{1-i\zeta}\hat{B} + \frac{1}{1-i\zeta}\hat{C} + \epsilon\hat{E}\,, \tag{6a}$$

$$\hat{B} = r_2 t_3 e^{ik_0 l_2}\hat{B}_{\text{in}} + t_2 t_3 e^{ik_0 l_{\text{A}}}\hat{E}_{\text{isolator}} + r_3 e^{ik_0 l_3}\hat{E}_3'\,, \tag{6b}$$

$$\hat{C} = \alpha\hat{A} + r_1 e^{ik_0(L-l_1)}\hat{E}_1 + t_1 r_2\gamma e^{ik_0(L-l_2)}\hat{E}_2 + t_1 t_2 r_3\gamma e^{ik_0(L-l_3)}\hat{E}_3 + t_1\epsilon_{\text{A}}e^{ik_0(L-l_{\text{A}})}\hat{E}_{\text{A}}\,,\text{ and } \tag{6c}$$

$$\hat{D} = \frac{1}{1-i\zeta}\hat{B} + \frac{i\zeta}{1-i\zeta}\hat{C} + \epsilon\hat{E}\,, \tag{6d}$$

with $\epsilon = \sqrt{1-\left(1+|\zeta|\right)/|1-i\zeta|^2}$ [27] and $\epsilon_{\text{A}} = \sqrt{1-1/|\gamma|^2}$ [29]. These equations can be solved simultaneously for $\hat{A}$, $\hat{B}$, $\hat{C}$, and $\hat{D}$, and the solution used to evaluate the momentum diffusion constant, $\boldsymbol{D}$, defined as the two-time autocorrelation function of the force operator, to obtain

$$\begin{aligned}
\boldsymbol{D}\,\delta(t-t') = 2\epsilon_0 S\,\hbar k_0 \Big(& \big[\hat{A}(t),\hat{A}^\dagger(t')\big]|\mathcal{A}|^2 + \big[\hat{B}(t),\hat{B}^\dagger(t')\big]|\mathcal{B}|^2 \\
& + \big[\hat{C}(t),\hat{C}^\dagger(t')\big]|\mathcal{C}|^2 + \big[\hat{D}(t),\hat{D}^\dagger(t')\big]|\mathcal{D}|^2 \\
& + 2\operatorname{Re}\Big\{\big[\hat{A}(t),\hat{B}^\dagger(t')\big]\mathcal{A}^*\mathcal{B} - \big[\hat{A}(t),\hat{C}^\dagger(t')\big]\mathcal{A}^*\mathcal{C} - \big[\hat{A}(t),\hat{D}^\dagger(t')\big]\mathcal{A}^*\mathcal{D} \\
& \quad - \big[\hat{B}(t),\hat{C}^\dagger(t')\big]\mathcal{B}^*\mathcal{C} - \big[\hat{B}(t),\hat{D}^\dagger(t')\big]\mathcal{B}^*\mathcal{D} \\
& \quad + \big[\hat{C}(t),\hat{D}^\dagger(t')\big]\mathcal{C}^*\mathcal{D}\Big\}\Big)\,,
\end{aligned} \tag{7}$$

keeping in mind that most of the noise modes, as well as $\hat{B}_{\text{in}}$, obey the commutation relation $\big[\hat{E}(t),\hat{E}^\dagger(t')\big] = \hbar k_0/(2\epsilon_0 S)\,\delta(t-t')$. The sole exception is the noise introduced by the amplifier, $\hat{E}_{\text{A}}$, for which $\big[\hat{E}_{\text{A}}(t),\hat{E}_{\text{A}}^\dagger(t')\big] = -\hbar k_0/(2\epsilon_0 S)\,\delta(t-t')$; this is due to the model of the amplifier as a negative temperature heat-bath, whereby the creation and annihilation operators effectively switch rôles. Further discussion of this model can be found in Ref. [29, §7.2]. All the noise modes are independent from one another and from $\hat{B}_{\text{in}}$, which simplifies the expressions considerably.

Finally, the fluctuation–dissipation theorem [3] can be used in conjunction with Eqs. (5) and (7) to estimate the equilibrium temperature that the motion of the particle will tend to:

$$k_{\text{B}}T_{\text{A}} = \frac{\boldsymbol{D}}{-\boldsymbol{F}/v}\,, \tag{8}$$

where k_{B} is the Boltzmann constant.

2.1.   *The good-cavity limit as a simplified case*

Before discussing the result of Eqs. (5) and (7), cf. Section 3, we shall make several approxima-
tions to obtain a transparent set of equations to briefly explore the equilibrium behaviour of the
particle and to compare with a standard master equation approach. In particular, ζ is assumed
to be real, which is tantamount to assuming that the particle suffers no optical absorption, i.e.,
if it is an atom, that it is pumped far off-resonance. Moreover, the cavity is assumed to be very
good ($|t_{1,2,3}| \to 1$) and thus no gain medium is introduced in the cavity ($\gamma = 1$). With these
simplifications, Eq. (5) reduces to

$$\boldsymbol{F} \approx -8\hbar k_0^2 \frac{v}{c} \frac{\zeta^2}{|1-\alpha|^4} \operatorname{Re}\left\{ \left(1-\alpha^*\right)^2 \frac{\partial \alpha}{\partial k} \right\} \left|r_2 B_0\right|^2$$

$$\approx 16\hbar k_0^2 \zeta^2 v \frac{\kappa \Delta_{\mathrm{C}}}{\left(\Delta_{\mathrm{C}}^2 + \kappa^2\right)^2} \frac{1}{\tau} \left|r_2 B_0\right|^2 . \tag{9}$$

In the preceding equations, Δ_{C} is the detuning of the pump from cavity resonance, κ is the
HWHM cavity linewidth,

$$\kappa = \frac{1}{\tau} \frac{1 - |t_1 t_2 t_3|\gamma}{\sqrt{|t_1 t_2 t_3|\gamma}} , \tag{10}$$

and $\tau = L/c$ is the round-trip time. Using the same approximations as for Eq. (9), we also obtain
the diffusion constant

$$\boldsymbol{D} \approx 8\hbar^2 k_0^2 \zeta^2 \frac{\kappa}{\Delta_{\mathrm{C}}^2 + \kappa^2} \frac{1}{\tau} \left|r_2 B_0\right|^2 . \tag{11}$$

Note that $\gamma = 1$ here and therefore $\hat{E}_{\mathrm{A}}$ does not contribute to the diffusion constant. Eqs. (9)
and (11) hold for the case where $\Delta_{\mathrm{C}}/\kappa$ is not too large. The cavity can be fully described by
means of κ and the finesse $\mathcal{F} = \pi c/(2L\kappa)$. Let us now set $\Delta_{\mathrm{C}} = -\kappa$ in Eqs. (9) and (11), whereby

$$\boldsymbol{F} = -\tfrac{8}{\pi}\hbar k_0^2 \zeta^2 v \frac{\mathcal{F}}{\kappa} \left|r_2 B_0\right|^2, \text{ and } \boldsymbol{D} = \tfrac{8}{\pi}\hbar^2 k_0^2 \zeta^2 \mathcal{F} \left|r_2 B_0\right|^2 . \tag{12}$$

These two expressions have a readily-apparent physical significance; at a constant finesse, de-
creasing the cavity linewidth by making the cavity longer is equivalent to increasing the retar-
dation effects that underlie this cooling mechanism [30], leading to a stronger friction force. At
the same time, this has no effect on the intracavity field strength and therefore does not affect
the diffusion. On the other hand, improving the cavity finesse by reducing losses at the couplers
increases the intracavity intensity, thereby increasing both the friction force and the momentum
diffusion.

  Using Eq. (8) together with Eqs. (9) and (11) we obtain, for $\Delta_{\mathrm{C}} < 0$,

$$T_{\mathrm{A}} \approx \frac{\hbar}{k_{\mathrm{B}}} \left(\frac{|\Delta_{\mathrm{C}}|}{\kappa} + \frac{\kappa}{|\Delta_{\mathrm{C}}|} \right) \frac{\kappa}{2} \geq \frac{\hbar}{k_{\mathrm{B}}} \kappa , \tag{13}$$

with the minimum temperature occurring at $\Delta_{\mathrm{C}} = -\kappa$. One notes that this expression is identical
to the corresponding one for standard cavity–mediated cooling [12], and can be interpreted in a
similar light as the Doppler temperature, albeit with the energy dissipation process shifted from
the decay of the atomic excited state to the decay of the cavity field.

6
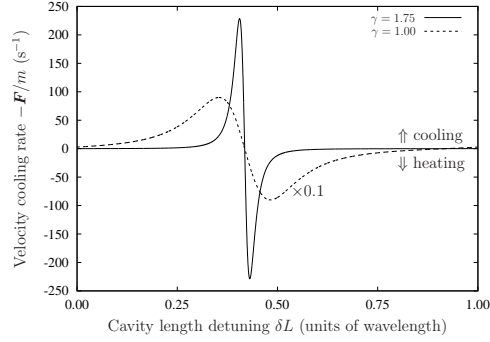
Figure 2.   Cooling rate $-(\mathrm{d}v/\mathrm{d}t)/v$ for ^{85}Rb pumped -10Γ from D$_2$ resonance inside a ring-cavity with a round-trip length $L = 300\,\mathrm{m}$, for two different values of the amplifier gain γ. Note that the curve for $\gamma = 1$, as drawn, is scaled *up* by a factor of 10. The cavity waist is taken to be $10\,\mu\mathrm{m}$. ($|t_1|^2 = |t_3|^2 = 0.5$, $|t_2|^2 = 0.99$, B_0 is chosen such as to give an atomic saturation $s = 0.1$.)

A particular feature to note in all the preceding expressions is that they are not spatial averages over the position of the particle, but they do not depend on this position either. As a result of this, the force, momentum diffusion and equilibrium temperature do not in any way depend on the position of the particle along the cavity field in a 1D model. The issue of sub-wavelength modulation of the friction force is a major limitation of cooling methods based on intracavity standing fields, in particular mirror–mediated cooling [28] and cavity–mediated cooling [13].

2.2.   *Comparison with a semiclassical model*

In the good-cavity limit and without gain our TMM model is equivalent to a standard master equation approach with the Hamiltonian

$$
\begin{aligned}
\hat{H} = {}& -\hbar\Delta_\mathrm{a}\hat{\sigma}^+\hat{\sigma}^- - \hbar\Delta_\mathrm{C}\hat{a}_\mathrm{C}^\dagger\hat{a}_\mathrm{C} \\
& + \hbar g\big(\hat{a}_\mathrm{C}^\dagger\hat{\sigma}^- e^{ik_0 x} + \hat{\sigma}^+\hat{a}_\mathrm{C} e^{-ik_0 x}\big) + \hbar g\big(a_\mathrm{P}^*\hat{\sigma}^- e^{-ik_0 x} + \hat{\sigma}^+ a_\mathrm{P} e^{ik_0 x}\big)\,,
\end{aligned} \tag{14}
$$

and the Liouvillian terms

$$
\mathcal{L}\hat{\rho} = -\Gamma\big(\hat{\sigma}^+\hat{\sigma}^-\hat{\rho} - 2\hat{\sigma}^-\hat{\rho}\hat{\sigma}^+ + \hat{\rho}\hat{\sigma}^+\hat{\sigma}^-\big) - \kappa\big(\hat{a}_\mathrm{C}^\dagger\hat{a}_\mathrm{C}\hat{\rho} - 2\hat{a}_\mathrm{C}\hat{\rho}\hat{a}_\mathrm{C}^\dagger + \hat{\rho}\hat{a}_\mathrm{C}^\dagger\hat{a}_\mathrm{C}\big)\,, \tag{15}
$$

as adapted from Ref. [14] and modified for a unidirectional cavity where only the unpumped mode is allowed to circulate. Here, $\hat{\rho}$ is the density matrix of the system, g the atom–field coupling strength, $\hat{a}_\mathrm{C}$ the annihilation operator of the cavity field, $\hat{\sigma}^+$ the atomic dipole raising operator, Δ_a the detuning from atomic resonance, Γ the atomic upper state HWHM linewidth, and x the coordinate of the atom inside the cavity. The pump field is assumed to be unperturbed by its interaction with the atom, and in the above is replaced by a c-number, a_P. Calculating the friction force form this model leads again to Eq. (9), thus confirming our TMM results by a more standard technique. The advantage of the TMM approach lies in the simplicity and generality of expressions such as Eq. (4), and the ease with which more optical elements can be introduced into the system. As shown above, Eq. (7), the momentum diffusion coefficient is easily calculated from the TMM.
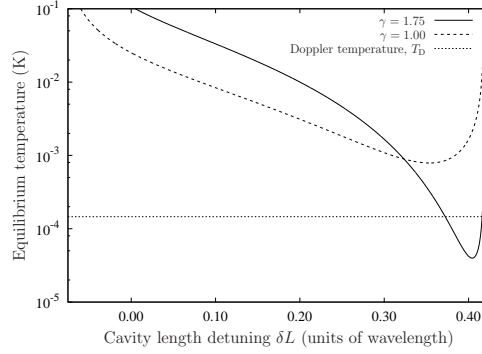
Figure 3. Equilibrium temperature predicted by the transfer matrix model for two values of the amplifier gain γ. The Doppler temperature for ^{85}Rb is also indicated. The horizontal axis differs from that in Fig. 2 mainly because the temperature is only well-defined for regions where the friction force promotes cooling. (Parameters are as in Fig. 2.)

3.   Numerical results and discussion

We can use the conversion factor $|B_0|^2 = P/(\hbar k_0 c)$, where P is the power of the input beam, to evaluate the above equations [notably Eqs. (5) and (7)] numerically in a physically meaningful way. Specifically, the particle is now assumed to be a (two–level) ^{85}Rb atom, pumped -10Γ from D$_2$ resonance, where $\Gamma = 2\pi \times 3.03$ MHz is the HWHM linewidth of this same transition at a wavelength of ca. 780 nm; because the detuning is much larger than the linewidth, we simplify the calculations by setting $\partial\zeta/\partial\omega = 0$. The beam waist where the particle interacts with the field is taken to be 10 μm. With the parameters in Fig. 2, the power is reduced by a factor of $1/|t_1 t_2 t_3|^2 = 4.04$ with each round-trip, in the presence of no gain in the amplifier. We shall compare this case to the low-gain case; the gain of the amplifier we consider is constrained to be small enough that $|\alpha|^2 = |t_1 t_2 t_3 \gamma|^2 < 1$. Under these conditions, there is no exponential build-up of intensity inside the cavity and the system is stable. A cavity with a large enough gain that $|\alpha|^2 > 1$ would effectively be a laser cavity. Such a system would have no stable state in our model, since we assume that the gain medium is not depleted, and will therefore not be considered further in this paper.

Fig. 2 shows the friction force acting on the particle, and Fig. 3 the equilibrium temperature, as the length of the cavity is tuned on the scale of one wavelength. In each of these two figures two cases are shown, one representing no gain in the amplifier ($\gamma = 1$) and one representing a low-gain amplifier ($\gamma = 1.75$); note that in both cases the condition $|\alpha|^2 < 1$ is satisfied.

In order to provide a fair comparison between these two cases, we choose the pump amplitude B_{in} such that the saturation of the particle is the same in the two cases. This ensures that any difference in cooling performance is not due to a simple increase in intensity. Since the TMM as presented here is based on a *linear* model of the particle, our results presented above are only valid in the limit of saturation parameter much smaller than 1. Thus, as a basis for the numerical comparisons between the two different cases, we choose to set the saturation parameter to 0.1. Fig. 2 shows that under these conditions the amplified system leads to a significant, approximately 25-fold, enhancement of the maximum friction force. This can therefore be attributed unambiguously to the effective enhancement of the cavity Q-factor by the amplifier.

However, for the parameters considered here, in particular for small particle polarisability ζ and for $|\alpha|^2 < 1$, the counterpropagating mode intensity is much smaller than that of the pumped mode, even if the former is amplified. Thus, the intracavity field is always dominated by the pump beam, whereas the friction force is mostly dependent on the Doppler-shifted reflection of the pump from the particle. Specifically, for the parameters used above we find that the total field intensity changes by less than 1% when the gain is increased from 1 to 1.75. Hence, similar results to those of Fig. 2 are obtained even *without* pump normalisation.

The steady-state temperature, obtained by the ratio of diffusion and friction, Eq. (8), is shown in Fig. 3 for the same parameters as above. We observe that the broader resonance in the friction as a function of cavity detuning (i.e., of cavity length), shown in Fig. 2, also leads to a wider range of lower temperatures compared to the amplified case. However, as expected, within the narrower resonance of the amplified system where the friction is significantly enhanced, the stationary temperature is also significantly reduced. We see that while the maximum friction force is increased by a factor of 25.4, the lowest achievable temperature is decreased by a factor of 19.9 when switching from $\gamma = 1$ to $\gamma = 1.75$. While the overall cavity intensity is dominated by the pump field, and is therefore hardly affected by the amplifier, the diffusion is actually dominated by the interaction of the weak counterpropagating field with the pump field. This can be seen most clearly by the strong detuning dependence of the analytic expression for $\boldsymbol{D}$ in the good-cavity limit, Eq. (11). As a consequence, the lowest achievable temperature is improved by a slightly smaller factor than the maximum friction coefficient. This is consistent with the idea that the amplifier not only increases the cavity lifetime, but also adds a small amount of additional noise into the system. Nevertheless, a strong enhancement of the cooling efficiency is observed in the presence of the amplifier.

4.   Conclusions and Outlook

We have presented a modified model for optomechanics inside ring cavities where *only one* of the counter-propagating fields in the cavity is allowed to circulate. By pumping the *other* mode and using a gain medium inside the cavity, one can greatly improve the optomechanical force acting on a polarisable particle inside the cavity, regardless of its energy level structure, without bringing about ill effects such as saturation or mirror burning. The conceptual introduction of a gain medium inside the cavity brings about several interesting possibilities. We have considered using this gain medium to offset losses inherent in the cavity, thereby improving its Q-factor significantly. This renders possible the use of optical fibres to build the cavity. One could also envisage using doped fibre amplifiers [31] to provide a distributed gain medium along the cavity. In this paper, we only considered low-gain media, such that the total losses in the cavity still exceeded the gain. Higher gains could be used to explore and exploit novel phenomena such as optomechanical interactions of weakly reflective micromirrors *inside laser cavities* and will be the subject of future work.

Acknowledgements

References

[1] S. Chu, L. Hollberg, J. E. Bjorkholm, *et al.*, Phys. Rev. Lett. **55** 48 (1985).
[2] S. Chu, Rev. Mod. Phys. **70** 685 (1998).
[3] H. J. Metcalf and P. van der Straten, J. Opt. Soc. Am. B **20** 887 (2003).
[4] J. Dalibard and C. Cohen-Tannoudji, J. Opt. Soc. Am. B **6** 2023 (1989).
[5] P. J. Ungar, D. S. Weiss, E. Riis, *et al.*, J. Opt. Soc. Am. B **6** 2058 (1989).
[6] M. Zeppenfeld, M. Motsch, P. W. H. Pinkse, *et al.*, Phys. Rev. A **80** 041401 (2009).
[7] E. S. Shuman, J. F. Barry and D. DeMille, Nature **467** 820 (2010).
[8] G. Hechenblaikner, M. Gangl, P. Horak, *et al.*, Phys. Rev. A **58** 3030 (1998).
[9] P. Maunz, T. Puppe, I. Schuster, *et al.*, Nature **428** 50 (2004).
[10] D. R. Leibrandt, J. Labaziewicz, V. Vuletić, *et al.*, Phys. Rev. Lett. **103** 103001 (2009).
[11] M. Koch, C. Sames, A. Kubanek, *et al.*, Phys. Rev. Lett. **105** 173003 (2010).

[12] P. Horak, G. Hechenblaikner, K. M. Gheri, *et al.*, Phys. Rev. Lett. **79** 4974 (1997).
[13] A. Xuereb, P. Domokos, P. Horak, *et al.*, submitted to Eur. Phys. J. D (2010).
[14] M. Gangl and H. Ritsch, Phys. Rev. A **61** 043405 (2000).
[15] T. Elsässer, B. Nagorny and A. Hemmerich, Phys. Rev. A **67** 051401 (2003).
[16] D. Kruse, M. Ruder, J. Benhelm, *et al.*, Phys. Rev. A **67** 051802 (2003).
[17] D. Nagy, J. K. Asbóth and P. Domokos, Acta Phys. Hung. B **26** 141 (2006).
[18] S. Slama, S. Bux, G. Krenz, *et al.*, Phys. Rev. Lett. **98** 053603 (2007).
[19] M. Hemmerling and G. R. M. Robb, Phys. Rev. A **82** 053420 (2010).
[20] R. J. Schulze, C. Genes and H. Ritsch, Phys. Rev. A **81** 063820 (2010).
[21] W. Niedenzu, R. Schulze, A. Vukics, *et al.*, Phys. Rev. A **82** 043605 (2010).
[22] V. Vuletić, *Laser Physics at the Limits* (Springer, 2001), chap. Cavity Cooling with a Hot Cavity, 67–74.
[23] T. Salzburger and H. Ritsch, Phys. Rev. A **74** 033806 (2006).
[24] S. Huang and G. S. Agarwal, Phys. Rev. A **79** 013821 (2009).
[25] T. Kumar, A. B. Bhattacherjee and Manmohan, Phys. Rev. A **81** 013835 (2010).
[26] R. Bonifacio, L. De Salvo, L. M. Narducci, *et al.*, Phys. Rev. A **50** 1716 (1994).
[27] A. Xuereb, P. Domokos, J. Asbóth, *et al.*, Phys. Rev. A **79** 053810 (2009).
[28] A. Xuereb, T. Freegarde, P. Horak, *et al.*, Phys. Rev. Lett. **105** 013602 (2010).
[29] C. W. Gardiner and P. Zoller, *Quantum Noise* (Springer, 2004).
[30] A. Xuereb, P. Horak and T. Freegarde, Phys. Rev. A **80** 013836 (2009).
[31] P. C. Becker, N. A. Olsson and J. R. Simpson, *Erbium-Doped Fiber Amplifiers: Fundamentals and Technology (Optics and Photonics)* (Academic Press, 1999).

Cavity cooling of atoms: Within and without a cavity

André Xuereb[1,2,a], Peter Domokos[3], Peter Horak[4], and Tim Freegarde[2]

[1] Max-Planck-Institut für Gravitationsphysik (Albert-Einstein-Institut) and Leibniz Universität Hannover, Callinstraße 38, D-30167 Hannover, Germany
[2] School of Physics and Astronomy, University of Southampton, Southampton SO17 1BJ, United Kingdom
[3] Research Institute of Solid State Physics and Optics, H-1525 Budapest P.O. Box 49, Hungary
[4] Optoelectronics Research Centre, University of Southampton, Southampton SO17 1BJ, United Kingdom

Abstract. We compare the efficiencies of two optical cooling schemes, where a single particle is either inside or outside an optical cavity, under experimentally-realisable conditions. We evaluate the cooling forces using the general solution of a transfer matrix method for a moving scatterer inside a general one-dimensional system composed of immobile optical elements. Assuming the same atomic saturation parameter, we find that the two cooling schemes provide cooling forces and equilibrium temperatures of comparable magnitude.

1 Introduction

'Traditional' laser cooling schemes, such as those applied to the alkali atoms [1,2] require a closed set of two [3] or more [4] energy levels within which the atom cycles. These schemes rely on the spontaneous atomic decay from the excited to the ground state to carry atomic translational energy away from the system. The requirement for a closed set of levels means that laser cooling has only been shown to be feasible for a small range of atomic species and for even fewer molecules [5,6].

Cavity cooling [7] switches the energy decay process from atomic spontaneous emission to the decay of a cavity field. Specifically, the motion of an atom is coupled to a cavity field, itself driven either directly or through scattering from the atom [8], and the decay of this field leads to damping of the atomic motion by a Sisyphus–like [9] mechanism. This mechanism inherently relies solely on the dipole force and should therefore be applicable to any scatterer that is subject to the dipole force [10]. This is the basis for recent investigations of cavity cooling of micromirrors [11] and dielectric spheres [12].

In a recent paper [13] we used a scattering theory [14] to examine the interaction between a particle and a 'generalised interferometer', and proposed an alternative to cavity cooling whereby the particle to be cooled is not inside the cavity, but outside it. By physically separating the atom from the cavity, one can use cavities that are of much higher optical quality, or even solid-state, rather than macroscopic, cavities, thereby rendering the apparatus simpler and more amenable to miniaturisation. How-

[a] Corresponding author. Electronic address: andre.xuereb@aei.mpg.de
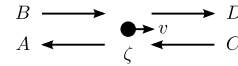
Fig. 1. A scatterer, characterised by its polarisability ζ and velocity v, interacting with the four field modes that surround it.

ever, by placing the atom outside the cavity, the atom–cavity coupling is reduced significantly. The important question is whether, in practical implementations, these two effects compensate for one another in such a way as to render the cooling forces experienced by an atom outside a cavity similar to those it experiences inside.

To answer this question we will first describe the two models, in Section 2.2 and Section 2.3, respectively, using realistic parameters for state-of-the-art optical devices. Taking into account saturation effects, it is seen that the two models result in similar cooling forces and equilibrium temperatures. An examination of scaling properties of the force acting on the atom in the two schemes then follows in Section 3, after which we conclude in Section 4.

2 Comparison of cavity cooling schemes

2.1 Generic scattering model

The two situations we describe will be discussed within the context of a scattering theory based on the transfer matrix method [14]. This scattering model can substitute the usual cavity QED calculations for these systems. At each point in a one-dimensional space, and at each frequency, the electric field is described by two complex amplitudes, representing two waves moving in opposite direc-

tions, cf. Fig. 1. The amplitudes A and B to the left of a generic scatterer, modelled through its polarisability ζ, are related to C and D to its right by means of a 2×2 matrix

$$\begin{pmatrix} A \\ B \end{pmatrix} = \begin{bmatrix} 1 + i\zeta & i\zeta \\ -i\zeta & 1 - i\zeta \end{bmatrix} \begin{pmatrix} C \\ D \end{pmatrix} . \tag{1}$$

For a two-level atom in the low-saturation limit, we can write

$$\zeta = -\frac{\sigma_{\mathrm{a}}}{2S} \frac{\Gamma}{\Delta + i\Gamma} , \tag{2}$$

where σ_{a} is the on-resonance scattering cross-section of the atom, S the mode area of the beam, Γ the HWHM linewidth of the transition, and Δ the detuning of the pump beam from resonance with the transition. In the case of a mirror, ζ is related to its macroscopic properties via its reflectivity $\mathfrak{r} = i\zeta/(1 - i\zeta)$ and its transmissivity $\mathfrak{t} = 1 + \mathfrak{r} = 1/(1 - i\zeta)$. Propagation of the electric field, having wavenumber k, over a distance x in free space is represented by the matrix

$$\begin{bmatrix} e^{ikx} & 0 \\ 0 & e^{-ikx} \end{bmatrix} . \tag{3}$$

In this model, complex optical systems can be built by multiplying the relevant matrices together, and the force acting on any single optical component is determined by the amplitudes of the fields interacting with it:

$$\boldsymbol{F}_{\mathrm{full}} = 2\epsilon_0 S \left(|A|^2 + |B|^2 - |C|^2 - |D|^2 \right) . \tag{4}$$

By accounting in the transfer matrix for the motion of the scatterer, following the process outlined in Ref. [14], the full velocity-dependent force can be calculated to first order in the scatterer velocity v and the friction force $\boldsymbol{F}_1$ then extracted.

A more rigorous model can be built that uses quantised fields rather than classical electromagnetic fields. In such a model, the transfer matrices operate on the respective annihilation operators, and a force operator can be defined in much the same way as the force in Eq. (4). The two-time autocorrelation function of this force operator can then be used to obtain the momentum diffusion $\boldsymbol{D}$ acting on the scatterer [14]. Finally, the fluctuation–dissipation theorem [15] gives the equilibrium temperature T that the motion of the scatterer will tend to:

$$k_{\mathrm{B}} T = -\frac{\boldsymbol{D}}{\boldsymbol{F}_1/v} , \tag{5}$$

which is only well-defined for a cooling force ($\boldsymbol{F}_1/v < 0$), and where k_{B} is the Boltzmann constant.

Further details of the calculations leading to the above expressions will not be presented in this paper. In the next two sections, the model is applied directly to investigate the nature of the cooling forces present in the two different configurations.

2.2 Cavity mediated cooling: Atom inside the cavity

Placing a scatterer—atom [7,16,17], micromirror [18,11], or 'point polarisable particle' [10]—inside a cavity has

(a)

(b)
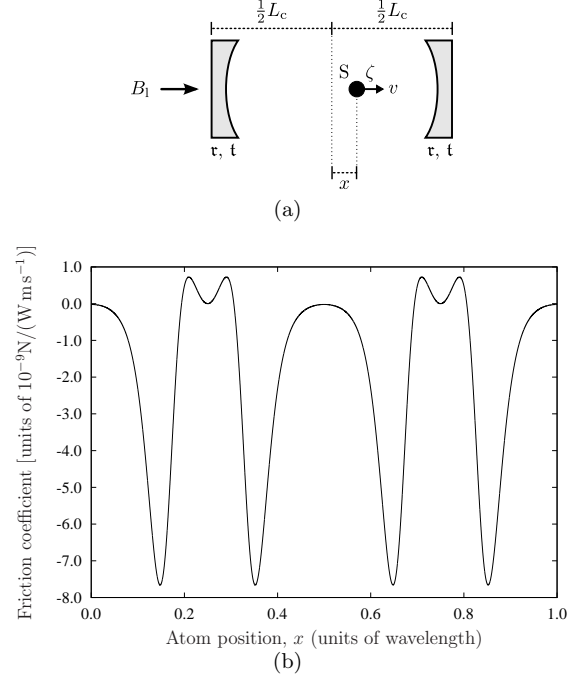
Fig. 2. (a) Model of a scatterer, S, inside a symmetrical Fabry–Pérot cavity of length L_{c}. The cavity mirrors have reflection and transmission coefficients, $\mathfrak{r}$ and $\mathfrak{t}$, and ζ is the polarisability of S. (b) Friction coefficient, per unit input power, experienced by the scatterer at different positions in the cavity, for realistic parameters (see text for details).

long been pointed out to be a powerful means of cooling the translational motion of that scatterer. Cooling of atoms inside resonators has been observed: first [16] as an increase in the storage time of atoms inside the cavity, and more directly in Ref. [17]. The layout of such an experiment is shown in Fig. 2(a). For our purposes, we place the scatterer inside a symmetrical Fabry–Pérot cavity of length L_{c}, which we pump from one side; the dominant field inside the cavity is a standing wave if the reflectivity of the mirrors, $\mathfrak{r}$, is sufficiently high. For a numerical example, we use the same cavity properties as Ref. [19]: finesse $\mathcal{F} = 56\,000$ modelled by using mirrors with $\mathfrak{t} = \mathfrak{r} + 1 = 1/(1 + 133.5i)$, cavity length $495\,\mu\mathrm{m}$, and mode waist $30\,\mu\mathrm{m}$; we use a wavelength $\lambda = 780\,\mathrm{nm}$. In contrast with Ref. [19], however, our cavity is pumped along its axis.

We also take the scatterer to be a two-level atom, with the cavity field detuned 10Γ to the red of the atomic transition frequency. Thus, the polarisability of the atom is $\zeta = 4.1 \times 10^{-5} + 4.1 \times 10^{-6}i$. The maximum friction coefficient is found at a detuning of $-2.6\,\kappa$ from the cavity resonance. As expected [10], the optimal friction coefficient occurs for a negative detuning, of the pump from the *bare* cavity resonance, but for a positive detuning from the dressed atom–cavity resonance.

The dependence of the friction force on the position of the scatterer, scanned over a wavelength, is shown in Fig. 2(b). The presence of the cavity manifests itself primarily through a strong enhancement of both the friction coefficient F_1/v and the intracavity field intensity over their bare field values. The scattering model explored above is only valid in the limit of small saturation; e.g., when power broadening of the atom is negligible and the linear polarisability ζ in Eq. (2) applies. For the ^{85}Rb D$_2$ transition, assuming that the beam is circularly polarised, the saturation intensity is $1.67\,\mathrm{mW\,cm^{-2}}$ [20]. In order to avoid saturation effects, we restrict the power input into the cavity to $2\,\mathrm{pW}$; this equates to an intracavity intensity of $23\,\mathrm{mW\,cm^{-2}}$ and hence a saturation parameter $s = 0.14$; this is because s is inversely proportional to the square of the detuning, -10Γ in this case, of the pump beam from resonance. In turn, this input power yields a maximal friction coefficient of $-1.5 \times 10^{-20}\,\mathrm{N/(m\,s^{-1})}$, which corresponds to a $1/e$ velocity cooling time of $9\,\mu\mathrm{s}$ for the same atom; averaging the friction force over a wavelength gives a cooling time of $37\,\mu\mathrm{s}$.

In the low-saturation regime, the friction force and momentum diffusion both scale linearly with input power; the equilibrium temperature is therefore independent of the pump power. For the parameters used above, the equilibrium temperature predicted for a scatterer at the point of maximum friction is $56\,\mu\mathrm{K}$; averaging the friction coefficient, as well as the diffusion coefficient, over a wavelength, gives a higher equilibrium temperature of $220\,\mu\mathrm{K}$.

2.3 External cavity cooling: Atom outside the cavity

More recently [13] it was proposed that even with the scatterer *outside* the cavity, the cavity's resonance can be exploited to enhance the optomechanical friction experienced by the scatterer over that in the standard optomechanical cooling setups [21,22,23], which place the scatterer in front of a single mirror. It is the aim of this section to explore this cooling mechanism, using experimental parameters similar to those in the previous section, and compare it with the cavity mediated cooling mechanism discussed there.

Our mathematical model, Fig. 3, represents the cavity as a standard, symmetrical Fabry–Pérot cavity. However, we emphasise that in principle what is required is simply an optical resonance: the cavity in the model can indeed be replaced by whispering gallery mode resonators [24] or even solid-state resonators. As a basis for numerical calculations, and to enable direct comparison, we model the same resonator as in the previous section. It is important to emphasise that the achievable quality factors of the resonators used for external cavity cooling can often be made larger than the ones in the previous section (see, e.g., Ref. [25]) because no optical or mechanical access inside the resonator itself is required.

The pump beam frequency is again taken to be detuned by 10Γ to the red of the atomic transition. By placing the atom outside the cavity, one is free to use high-numerical-aperture optics to produce a tighter focus

(a)

(b)
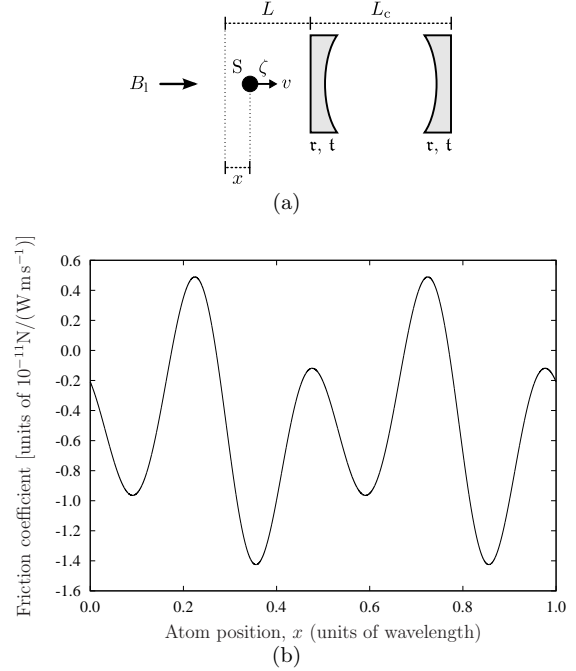
Fig. 3. External cavity cooling. (a) Model, similar to Fig. 2, but with the atom at a distance $L - x$ outside the cavity. (b) Friction coefficient per unit input power experienced by the scatterer as x is varied, for realistic parameters (see text for details). Note the change of scale, on the vertical axis, from Fig. 2(b).

than might be possible in a cavity with good optical and mechanical access. Having a tight focus strengthens the atom–field coupling because of the $1/w^2$ dependence of ζ on the beam waist w; whereas the friction force scales linearly with the input power, it also scales as $\zeta^2 \sim 1/w^4$ [13]. Focussing the beam therefore increases the atom–field coupling more than the local intensity. Thus, it is now assumed that the beam is focussed down to $1\,\mu\mathrm{m}$, which gives $\zeta = 3.7 \times 10^{-2} + 3.7 \times 10^{-3}i$.

In order to make a fair comparison between the two cases, we choose to set the saturation parameter $s = 0.14$, as in the previous section. The maximum achievable friction force coefficient is then $-2.9 \times 10^{-21}\,\mathrm{N/(m\,s^{-1})}$ for $200\,\mathrm{pW}$ of input power, which compares well with the previous result and leads to a $1/e$ velocity cooling time of $50\,\mu\mathrm{s}$ and an equilibrium temperature of $280\,\mu\mathrm{K}$. The magnitude of the force in this case results from the much smaller pumping beam mode waist, allowing the use of much higher powers and subsequently leading to a stronger atom–field interaction. With this beam waist and finesse we would be restricted to input powers several orders of magnitude smaller if the atom were inside such a cavity.

In summary, whereas the friction force inside a cavity is much stronger *per unit input power and for the same beam waist*, the restrictions imposed on the magnitude of these quantities when the atom is inside the cavity reduce
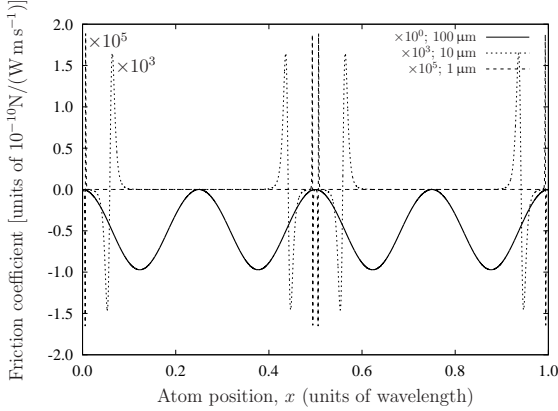
Fig. 4. Spatial dependence of the friction force acting on an atom *inside* a cavity with different mode waists but equal detuning from resonance, 10Γ to the red. The smaller the mode waist the stronger the friction force, by several orders of magnitude, but the more significant localisation becomes. (Parameters as in Section 2.2 but with $\partial\zeta/\partial k = 0$.)
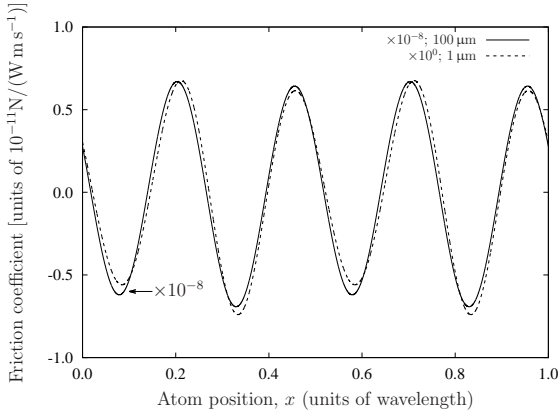
Fig. 5. Spatial dependence of the friction force acting on an atom *outside* a cavity, with different pumping field waists but equal detuning from resonance, 10Γ to the red. The friction force scales roughly as the inverse fourth power of the waist [26], but the length scale of the cooling and heating regions is unaffected. (Parameters as in Section 2.3 but with $\partial\zeta/\partial k = 0$.)

the maximally achievable friction force to a figure similar to when it lies outside the cavity.

3 Scaling properties of cavity cooling forces

3.1 Localisation

The broad nature of the spatial variations in the force shown in Fig. 2(b) is a consequence of the small polarisability of the atom in such a cavity. This is in sharp contrast to the case of large polarisability, achieved by an

atom at a tight beam focus or by a micromirror, as shown in Fig. 4. A scatterer of larger polarisability would experience extremely narrow peaks, of spatial extent $\ll \lambda$, in the friction force if it lies inside a cavity but not outside it.

Within the scattering model used in this paper, the atom–cavity coupling can be tuned by varying either the beam waist or the laser detuning from atomic resonance. Experimentally, however, atom–cavity coupling is rarely investigated close to resonance, in order to minimise the effects of atomic decoherence through spontaneous emission. In such cases, this coupling can be increased by operating a cavity with a small mode waist; this may in turn be detrimental to the performance of the system due to the strong sub-wavelength nature of the interaction, as explored in Fig. 4. The net effect of having a smaller mode waist is that this not only demands extremely good localisation but also tends to decrease the effective friction coefficient drastically—by up to several orders of magnitude—because of spatial averaging effects; this will be investigated in detail elsewhere.

In Section 2.3, no mention was made of the average friction force acting on the scatterer; indeed this average computes to approximately zero for any case involving far-detuned atoms, or other particles with an approximately constant polarisability, outside cavities. This, then, also demands localisation of the atom on a sub-wavelength scale; whilst experimentally challenging this disadvantage is somewhat mitigated by the easy mechanical and optical access afforded by external cavity cooling schemes. Moreover, Fig. 5 shows that spatial resonances are generally much wider here than in Fig. 4: the polarisability of the atom can be varied over a very wide range without affecting the length scale of the cooling and heating regions.

In contrast with the atomic situation, if the scatterer is a micromirror mounted on a cantilever, localisation does not present such a problem, since such micromirrors naturally undergo small oscillations and can be positioned with sub-nm accuracy.

3.2 Scaling with cavity finesse and linewidth

Cavity–mediated cooling mechanisms depend heavily on the physical properties of the cavity, namely its linewidth κ and finesse $\mathcal{F}$. These parameters can be tuned independently by changing the length of the cavity and the reflectivity of its mirrors. This section briefly explores how the mechanisms considered scale with κ and $\mathcal{F}$.

Expressions for the force acting on an atom inside a good cavity are not simple to write down. Nevertheless, in the good-cavity limit one may obtain an analytic formulation for the limiting temperature [7]:

$$T = \frac{\hbar\kappa}{k_{\mathrm{B}}}, \qquad (6)$$

i.e., making a cavity longer decreases the equilibrium temperature proportionally. This result can be understood by observing that whereas the diffusion constant depends
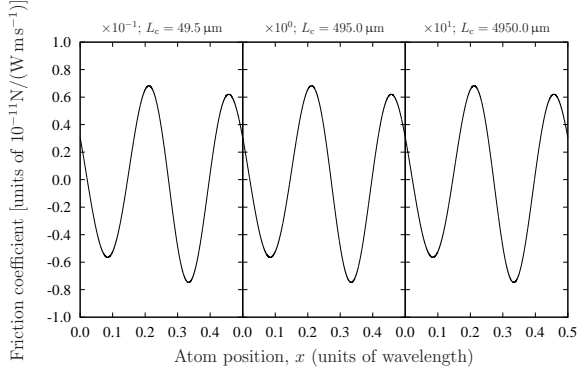
Fig. 6. Spatial dependence of the friction force acting on an atom *outside* a cavity, with detuning 10Γ to the red of resonance. Three different cavity lengths are shown; the friction force scales almost linearly with the cavity length. Note the different scaling factors and cavity lengths, given above each curve. (Parameters as in Section 2.3 but with $\partial\zeta/\partial k = 0$.)

only on the intensity inside the cavity ($\propto \mathcal{F}$), the friction force scales linearly with both the intensity and, if the intensity is kept constant, with the lifetime of the cavity field ($\propto 1/\kappa$). The friction force is therefore proportional to $\mathcal{F}/\kappa$, and the equilibrium temperature proportional to κ.

As is known from Ref. [13], the friction force ($\boldsymbol{F}_1$) acting on an atom outside a cavity scales approximately linearly with both the length and the finesse of the cavity. This is interpreted in terms of a 'distance folding' mechanism: the lifetime of the light inside a cavity scales inversely with its linewidth $\kappa \propto 1/(\mathcal{F}L_{\mathrm{C}})$ if all other parameters are kept fixed. One can see this behaviour reproduced in Fig. 6, where the friction coefficient for on an atom outside each of three cavities having different lengths is shown. This mechanism loses its importance if the atomic polarisability is too large, whereby the system behaves more like two coupled cavities, or if the cavity is too long. The momentum diffusion affecting the atom outside a cavity is essentially independent of the properties of a good cavity, since it depends on the local intensity surrounding the scatterer; putting these two results together, then, gives [13]

$$T \approx 1.9\frac{\hbar\kappa}{k_{\mathrm{B}}}, \tag{7}$$

in the limiting case of small polarisability and at the point of maximum friction; i.e., the temperature scales in the same way as for an atom inside the cavity. The numerical factor in the preceding equation depends on ζ and is larger for $\zeta \sim 1$.

The cavity linewidth also affects the velocity 'capture range' of the cooling mechanisms discussed in this text. In the case of cooling of atoms inside a cavity, it has been discussed in the literature [27,28] that the mechanism involved applies for atoms with a velocity $|v| < \kappa/k$. The theory described in this paper is correct only up to linear order in the velocity of the particle interacting with the cavity [14]; within this framework, it does not seem possible to make predictions for the capture range. However, the external cavity cooling mechanism is expected to operate as described in the regime where the motion of the atom determines the slowest time-scale of the system; for the good-cavity limit, this would necessitate $|v| < \kappa/k$.

4 Conclusions

We have used the solution for the friction force and diffusion constant experienced by a polarisable scatterer interacting with a general 1D optical system to compare two different 'cavity enhanced' cooling methods, where the scatterer is either inside or outside the cavity. It was found that, with state-of-the-art experimental parameters, the constraints imposed by the saturation of atomic transitions imply that the two mechanisms produce friction forces and lead to equilibrium temperatures that are of comparable magnitudes. The velocity capture range of both mechanisms scales linearly with the cavity linewidth, and is therefore expected to be similar in the two cases.

It was also shown that for weakly polarisable scatterers (e.g., atoms in the low-saturation regime), positioning requirements are stronger for external cavity cooling due to a net-zero spatially averaged friction force. This conclusion is reversed for strongly polarisable scatterers (e.g., micromirrors), in which case the friction force inside a cavity varies over a much shorter length-scale than that outside.

References

1. A. Ashkin, Phys. Rev. Lett. **40**(12), 729 (1978)
2. S. Chu, Rev. Mod. Phys. **70**(3), 685 (1998)
3. H.J. Metcalf, P. van der Straten, J. Opt. Soc. Am. B **20**(5), 887 (2003)
4. J. Dalibard, C. Cohen-Tannoudji, J. Opt. Soc. Am. B **6**(11), 2023 (1989)
5. M. Zeppenfeld, M. Motsch, P.W.H. Pinkse, G. Rempe, Phys. Rev. A **80**(4), 041401 (2009)
6. E.S. Shuman, J.F. Barry, D. DeMille, Nature **467**(7317), 820 (2010)
7. P. Horak, G. Hechenblaikner, K.M. Gheri, H. Stecher, H. Ritsch, Phys. Rev. Lett. **79**(25), 4974 (1997)
8. P. Domokos, H. Ritsch, Phys. Rev. Lett. **89**(25), 253003 (2002)
9. G. Hechenblaikner, M. Gangl, P. Horak, H. Ritsch, Phys. Rev. A **58**(4), 3030 (1998)
10. P. Domokos, H. Ritsch, J. Opt. Soc. Am. B **20**(5), 1098 (2003)

11. J.D. Thompson, B.M. Zwickl, A.M. Jayich, F. Marquardt, S.M. Girvin, J.G.E. Harris, Nature **452**(7183), 72 (2008)
12. P.F. Barker, M.N. Shneider, Phys. Rev. A **81**(2), 023826 (2010)
13. A. Xuereb, T. Freegarde, P. Horak, P. Domokos, Phys. Rev. Lett. **105**(1), 013602 (2010)
14. A. Xuereb, P. Domokos, J. Asbóth, P. Horak, T. Freegarde, Phys. Rev. A **79**(5), 053810 (2009)
15. J.P. Gordon, A. Ashkin, Phys. Rev. A **21**(5), 1606 (1980)
16. D.R. Leibrandt, J. Labaziewicz, V. Vuletić, I.L. Chuang, Phys. Rev. Lett. **103**(10), 103001 (2009)
17. M. Koch, C. Sames, A. Kubanek, M. Apel, M. Balbach, A. Ourjoumtsev, P.W.H. Pinkse, G. Rempe, Phys. Rev. Lett. **105**(17), 173003 (2010)
18. M. Bhattacharya, P. Meystre, Phys. Rev. Lett. **99**(7), 073601 (2007)
19. M. Mücke, E. Figueroa, J. Bochmann, C. Hahn, K. Murr, S. Ritter, C.J. Villas-Boas, G. Rempe, Nature **465**(7299), 755 (2010)
20. D.A. Steck (2008), Rubidium 85 D Line Data, `http://steck.us/alkalidata/rubidium85numbers.pdf`
21. V.B. Braginsky, A.B. Manukin, Soviet Physics JETP **25**(4), 653 (1967)
22. C.H. Metzger, K. Karrai, Nature **432**(7020), 1002 (2004)
23. S. Gröblacher, K. Hammerer, M.R. Vanner, M. Aspelmeyer, Nature **460**(7256), 724 (2009)
24. A. Schliesser, T.J. Kippenberg, arXiv e-prints (2010), `arXiv:1003.5922`
25. G. Rempe, R.J. Thompson, H.J. Kimble, R. Lalezari, Opt. Lett. **17**, 363 (1992)
26. A. Xuereb, P. Horak, T. Freegarde, Phys. Rev. A **80**(1), 013836 (2009)
27. P. Horak, H. Ritsch, Phys. Rev. A **64**(3), 033422 (2001)
28. P. Domokos, T. Salzburger, H. Ritsch, Phys. Rev. A **66**(4), 043406 (2002)

Appendix B

Posters and Presentations

B.1 Talks

Parts of this thesis were presented orally in the conferences and seminars listed below.

2010, INVITED *Cooling polarisable particles with an optical memory*; University of Malta (Malta, November)

2010, INVITED —; University of Hannover (Hannover, November)

2010, INVITED —; Institute for Quantum Optics and Quantum Information (IQOQI; Innsbruck, July)

2010, INVITED —; University of Vienna (Vienna, June)

2010 *Laser cooling using the dissipative dipole force*; University of Southampton School of Physics and Astronomy weekly QLM Seminar (Southampton, February)

2009 *Scattering theory of light–matter interactions*; 2nd UK Atom–Cavity Network Meeting (Leeds, December)

2009 *Scattering theory of cooling in optomechanical systems*; CMMC09 Workshop (Obergurgl, February)

2008 *Cooling of atoms using nanostructured surfaces*; University of Southampton School of Physics and Astronomy weekly QLM Seminar (Southampton, December)

B.2   Posters

A number of posters were also presented, both at specialist conferences and at research showcases aimed at a lay audience. These posters are listed below and reprinted over the next several pages.

2010 *Cooling atoms, particles and polarisable objects using the dissipative dipole force*; International Conference on Quantum Optics (Obergurgl, 2010), Final CMMC Meeting (Herrsching, 2010) and ICAP 2010 (Cairns, 2010)

2010 *Mirror-mediated cooling of a particle by coupling to its own reflection*; Final CMMC Meeting (Herrsching, 2010) and ICAP 2010 (Cairns, 2010)

2009 *Scattering theory of cooling in optomechanical systems*; ICOLS09 (Hokkaido, 2009)

2009 *Novel Optical Cooling Methods for Atoms and Molecules*; University of Southampton FESM Research Showcases 2009 and 2010 (Southampton, 2009 and 2010) and explains author's research to non-specialists

2008 *Novel Optical Cooling Methods for Atoms and Molecules*; Photon08 (Edinburgh, 2008) and Les Houches School (Les Houches, 2008)

2008 *Semiclassical Theory of Coherent Atom Cooling with a Single Mirror*; EuroQUAM Inaugural Conference (Barcelona, 2008)

FIGURE B.1: Explanation of the mirror-mediated cooling mechanism and some initial investigations into the model.

Novel optical cooling methods for atoms and molecules

André Xuereb[*,1], James Bateman[1], Peter Horak[2], Tim Freegarde[1]

[1]School of Physics and Astronomy, University of Southampton
[2]Optoelectronics Research Centre, University of Southampton

*E-mail address: andre.xuereb@soton.ac.uk

UNIVERSITY OF Southampton

Established optical cooling methods, employed in such situations as magneto-optical traps and optical molasses, work by means of a closed optical transition involving the absorption and spontaneous emission of large numbers of photons by each atom. This technique, therefore, cannot be extended to species—such as molecules—which, in general, do not have closed optical transitions.
Another way of introducing a viscous component to the force acting on an atom is to use the optical dipole force. Under the right conditions, this force causes one atom to be attracted to another similar atom or, by the use of a mirror, to its own reflection. The delay introduced by the light travelling from the atom to the mirror and back gives the required viscous component, always acting to slow the atom down. This effect can be augmented greatly by the use of a resonant cavity instead of a simple mirror. Having an array of these microscopic mirrors or cavities, with each imaging the atom onto itself, further increases the strength of this interaction. Better coupling of the atom to its reflection, and thus more efficient cooling, can be achieved by the use of evanescent waves or a dipole trap to confine the atom close to the surface.

Basic principles of the mechanism

Just as two separate particles in a light field may be **optically bound** [1], so can an atom be optically bound to its reflection in a mirror.

A **time delay** is introduced by this mechanism, resulting in a friction force which opposes the motion of the particle.

In effect, the atom can be seen as being optically bound **to itself at an earlier time.**
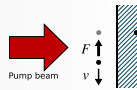
Disturbance in the electric field due to a refractive particle. Figure adapted from [1].
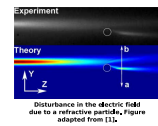
Fig. 1

Our model

Key components of the model:
- an **off-resonant** pump beam, interacting with
- an **atom** in front of
- a **single** mirror.

The force experienced by the atom is positive (heating) or negative (cooling) depending on the **distance** of the atom from the mirror (see Fig. 3).

We therefore need to introduce a **harmonic trap** to localise the atom inside the cooling region. This improves the cooling mechanism dramatically.

Theoretically, our model is very similar to **cavity-cooling mechanisms** [2].
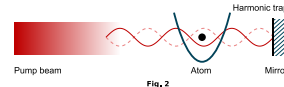
Fig. 2

Equations of motion

A **semiclassical** approach was followed [3], giving a set of coupled stochastic differential equations for the atom momentum and position, as well as the field mode amplitudes.

We considered only the interaction of a single atom with multiple field modes.

The resulting equations have correlated noise terms which lead to **momentum diffusion**:

$$dx = \frac{p}{m}dt$$
$$dp = [i\hbar(\mathcal{E}\frac{d}{dx}\mathcal{E}^* - \text{h.c.}) - U_0(\mathcal{E}^*\frac{d}{dx}\mathcal{E} + \text{h.c.})]dt + dP$$
$$d\alpha_k = i\Delta_k\alpha_k - (iU_0 + \gamma)\mathcal{E}f_k(x)dt + dA_k$$

The balance between the momentum diffusion and the cooling force gives rise to a **steady-state temperature.**

We may either perform a number of approximations and use a **perturbative** approach to derive an analytic solution to the atomic variables (see right); or we can **numerically** solve the equations via simulations (below).
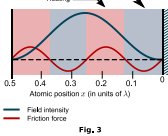
Fig. 3

Analytic solution

The equations of motion can be solved, **to lowest orders** in atomic speed and coupling constant.

This gives us the following expression for the **friction force**:

$$F = \left[\pi\hbar k^2 \frac{\sin(2\omega_r\tau)}{2\omega_r}|A|^2\left(\frac{gC}{\Delta}\right)^2 \sin(4k\tau c)\right]v$$

The perturbative solution thus obtained allows us to make a fair estimate of the friction force and its variation with several parameters.
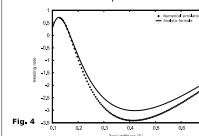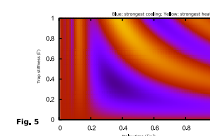
Fig. 4   Fig. 5

Numerical simulations

The coupled equations of motion were solved **numerically and non-perturbatively** for different atomic starting positions, initial momenta, etc.

One set of simulations was done with the noise terms **switched off**. This allowed us to compare the numerical results with the analytic (perturbative) solution. Fig. 6 shows one such comparison: the friction coefficient (heating rate) is plotted for several initial momenta. To a good approximation the two results **agree well**.

A second set of simulations was then performed using the **full equations of motion**. Diffusion introduces an approximately constant shift in the heating rates (see Fig. 7).
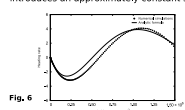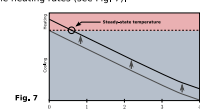
Fig. 6   Fig. 7

Capture range and steady-state temperature

The friction force is negative for a range of initial momenta (the **capture range**); see Fig. 6. The largest momentum that can be cooled corresponds to the **cutoff temperature.**

For shallow traps our analytic predictions match the simulations.

For stiffer traps, the mechanism has a **wider capture range** in the simulations (see Fig. 8).

Populations of atoms as hot as **−1 K** can therefore be cooled.

Fig. 8

The opposing mechanisms give rise to a temperature at which the cooling and heating effects balance; the **steady-state temperature:**

$$T = \frac{1}{4}\frac{\hbar}{k_B}\frac{\Gamma^2}{g^2}\frac{\omega_r}{\sin(2\omega_r\tau)}\frac{1-0.6\sin^2(4k\tau c)}{\sin(4k\tau c)}$$

This steady-state temperature attains a minimum of **0.5 mK.**

This is a decrease of just over **three orders of magnitude** from the cutoff temperature.

Fig. 9

Conclusions and future work

The next step would be to consider **cavities** rather than simple mirrors.

Polaritons and **evanescent waves** could be used to strengthen the interaction between the field and atom.

We also hope to **experimentally demonstrate** this cooling scheme (see diagrams to the right).

This mechanism has a number of distinct advantages over traditional ones:
- **no closed transition** is necessary; allowing it to be used for molecules;
- **applicability**; atom chips may easily cool and trap particles in this manner;
- **scalability**; several hundred microtraps using this scheme may be built on one single chip, further enhancing the cooling effect.

Fig. 10: The four stages in creating a nanotemplated surface.
Fig. 11: A schematic of the focus of our proposed experiments.
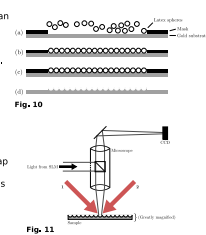
Fig. 10   Fig. 11

Literature

[1] N K Metzger, E M Wright, W Sibbet, K Dholakia, Opt. Expr, **14** (2006)

[2] G Hechenblaikner, M Gangl, P Horak, and H Ritsch, Phys. Rev. A, **58**, 4 (1998)

[3] P Horak, H Ritsch, Phys. Rev. A, **64**, 3 (2001);
P Domokos, P Horak, H Ritsch, J. Phys. B, **34**, 2 (2001)

[4] M Burns, J-M Fournier, J Golovchenko, Science, **249**, 4970 (1990)

[5] R Folman, et al., Phys. Rev. Lett, 84, **20** (2000).

[6] P Domokos, P Horak, H Ritsch, Fortschr. Phys. **49**, 10-11 (2001)

[7] J Eschner, Ch Raab, F Schmidt-Kaler, R Blatt, Nature, **413**, 6855 (2001)

[8] S A Tatarkova, A E Carruthers, K Dholakia, Phys. Rev. Lett, **89**, 28 (2002)

[9] H Melville, et al., Opt. Expr, **11**, 26 (2003)

[10] M A Wilson, et al., Phys. Rev. Lett, **91**, 21 (2003)

UNIVERSITY OF Southampton — School of Physics and Astronomy

Quantum Control Group
School of Physics and Astronomy
University of Southampton
Southampton SO17 1BJ
United Kingdom

EPSRC — Engineering and Physical Sciences Research Council

EUROPEAN SCIENCE FOUNDATION

Optoelectronics Research Centre
University of Southampton
Southampton SO17 1BJ
United Kingdom

Light

Figure B.2: A more in-depth treatment of mirror-mediated cooling and some speculation about possible experimental realisations.

FIGURE B.3: An explanation of laser cooling intended for a lay audience.

Scattering theory of cooling in optomechanical systems

André Xuereb*, Hamid Ohadi, James Bateman, Richard Murray,
Matthew Himsworth, Tim Freegarde[1],
Peter Domokos[2], Peter Horak[3]

*E-mail address: andre.xuereb@soton.ac.uk

[1]School of Physics and Astronomy, University of Southampton [2]Hungarian Academy of Sciences [3]Optoelectronics Research Centre, University of Southampton

UNIVERSITY OF
Southampton

We present a one-dimensional scattering theory describing from the optomechanical coupling of the motion of scatterers to the electromagnetic field. Multiple scattering to all orders is taken into account. The result is a versatile model that can be used to describe a wealth of effects, including optical molasses and novel interactions between atoms and cavities. This could potentially lead to optical cooling mechanisms applicable to a wide range of atomic and molecular species.
Our model is a generalisation of the transfer matrix approach in optics. The Lorentz boost and the Doppler shift are included in this generalised transfer matrix, and the approach can in principle be extended to describe two- or three-dimensional systems, as well as complex cascaded optical systems. In the simplest case of pumping at one frequency, the force and momentum diffusion acting on any component of the optical system can be calculated analytically.

Motivation

Light forces are now used to manipulate the motion of everything from **atoms** to **resonators**.

Several frameworks exist to describe these interactions between light and matter; but none addresses **the full range of interactions**: some are useful in discussing weak interactions, whereas others describe scatterers that act as boundary conditions on the electromagnetic field.

Our aim is a **single theoretical framework** that explains the optomechanical interactions between light and scatterers at all strengths of these interactions:

From   ●   **to**

Current theoretical frameworks cannot deal with the vast range of interaction strengths one is concerned with in experiments. These can range from a perturbative interaction with the field, as is the case with an atom interacting with its reflection in a mirror, to a moving boundary condition, as is the case in a Fabry-Perot cavity with one of its mirrors on a cantilever.

Introduction to matrix methods in 1D

The transfer matrix method is used in optics when dealing with **multi-element or multi-layer systems** (see Fig. 1).

The transfer matrix for the entire system is the product of the individual transfer matrices. Stacked systems, such as dielectric mirrors, are particularly simple to handle, requiring one to simply raise a 2-by-2 matrix to some integer power.

Each scatterer interacts with four light modes : two to the left and two to the right, as shown in Fig. 2. The transfer matrix represents the mixing among these four modes.

Complicated systems, made up of a number of optical elements, and their interactions with the light field can therefore be explored as easily as a single mirror.

Fig. 1: Multilayer dielectric mirrors are easily analysed by means of the transfer matrix method.

$\mathcal{A} \leftarrow$ **?** $\rightarrow \mathcal{C}$
$\mathcal{B} \rightarrow$ **?** $\leftarrow \mathcal{D}$

Fig. 2: The transfer matrix representing any particular element is calculated by working out the interaction among the four field modes surrounding the element.

Extension to moving scatterers

The transfer matrix of a static scatterer **is easily extended** to account for the motion of the scatterer. To perform this transformation we need to account for the **Lorentz boost** and the **Doppler shift** of the electromagnetic field.

For example (see figure to the right), field $\mathcal{A}$ interacts with a red-shifted field $\mathcal{B}$ and an unshifted field $\mathcal{C}$. The amplitude of field $\mathcal{B}$, as seen by field $\mathcal{A}$, is also modified; this is the Lorentz boost.

$\mathcal{A} \leftarrow$
$\mathcal{B} \rightarrow$ ● $\rightarrow v$ $\leftarrow \mathcal{C}$

The resulting transformation has a **wide applicability** and takes the form of a linear matrix transformation acting on the original transfer matrix:

$$M \rightarrow \begin{bmatrix} \left(1-\frac{v}{c}\right)\hat{P}_v & 0 \\ 0 & \left(1+\frac{v}{c}\right)\hat{P}_v^{-1} \end{bmatrix} \times M \times \begin{bmatrix} \left(1+\frac{v}{c}\right)\hat{P}_v^{-1} & 0 \\ 0 & \left(1-\frac{v}{c}\right)\hat{P}_v \end{bmatrix}$$

where $\hat{P}_v : f(k) \rightarrow f\left(k+2k\frac{v}{c}\right)$.

For example, suppose we characterise an atom by its polarizability, ζ. The transfer matrix for such an atom, assuming that it is not moving, is quite simple:

$$\begin{bmatrix} 1-i\zeta & -i\zeta \\ i\zeta & 1+i\zeta \end{bmatrix}$$

By applying the aforementioned transformation, we obtain the matrix for a **moving atom**, correct to first order in its velocity:

$$\begin{bmatrix} 1-i\zeta & -i\zeta\left(1-2\frac{v}{c}\right)\hat{P}_{2v} \\ i\zeta\left(1+2\frac{v}{c}\right)\hat{P}_{2v}^{-1} & 1+i\zeta \end{bmatrix}$$

Here, we have made the simplification that the polarizability is independent of frequency.

The variation of ζ with frequency, in fact, is what allows us to apply this method to explain such effects as **Doppler cooling** in 1D optical molasses [1].

Application: Cavity assisted cooling

We recently [2] proposed a novel cooling mechanism (mirror mediated cooling) that involves a particle interacting with its **own time-delayed reflection** in a distant mirror:

Heating   Cooling
— Field intensity
— Friction force
0.5 0.4 0.3 0.2 0.1 0
Atomic position (in units of λ)
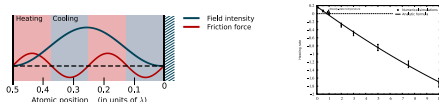
Using the transfer matrix method, we modelled this situation and obtained **the same results** as those obtained by means of a semiclassical theory. However, we can now go **beyond the small polarizability approximation** used in the semiclassical approach, allowing us to describe cooling of cantilevers [3, 4].

One drawback of mirror mediated cooling is the **large separation** (~3 m) required between the atom and the mirror.

By replacing the mirror with a cavity, as shown on the right, we can effectively **fold this distance** by making use of the multiple reflections in the cavity.

$\hat{M}_A$ M_P M_C
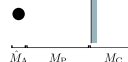
The new friction force depends crucially on the properties of the cavity, since the cooling mechanism arises from the decay of the cavity field, and allows us to **bring our atomic sample closer to the surface**.

Plotting the friction force experienced by the atom, we can see that it follows the amplitude of the intracavity field.

~3 m
~30 μm   ~1 mm
~30 μm
Near mirror transmissivity, $|t|$
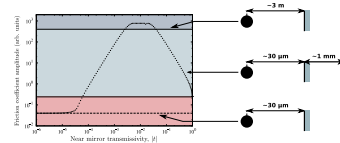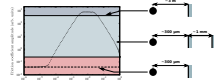
The above figure compares the cooling an atom by means of a single mirror (solid and dashed lines) to the **enhanced friction force** when using a second mirror (data points).

The enhancement is greatest when the **coupling into the cavity is optimised.** This occurs when the mirrors have equal (~0.01, in this case) transmissivities and at a cavity detuning that depends on the mirror reflectivities.

Conclusions and future work

We have extended the transfer matrix method to deal with **moving scatterers**, allowing us to deal with **the entire range** of interaction strengths.

We have therefore started to **bridge the gap** between theories explaining the range of interactions between light and matter.

A number of questions remain, however:
- Can we extend the matrix method to **two and three dimensions**?
- Can one account for **non-adiabatic effects** and explain sub-Doppler cooling mechanisms as well?

We have also proposed an extension to our mirror mediated cooling mechanism, which is in principle applicable to **any polarizable particle.** Our group is working towards demonstrating these cooling schemes **experimentally**.

Literature

[1] A Xuereb, *et al.*, Phys. Rev. A **79**, 053810 (2009).

[2] A Xuereb, P Horak, and T Freegarde, arXiv:0903.2945 (2009). Submitted.

[3] C H Metzger and K Karrai, Nature **432**, 1002 (2004).

[4] M Bhattacharya, H Uys, and P Meystre, Phys. Rev. A **77**, 033819 (2008).

[5] J K Asbóth, H Ritsch, and P Domokos, Phys. Rev. A **77**, 063424 (2008).

[6] P Horak, A Xuereb, and T Freegarde, arXiv:0904.3059 (2009). Submitted.

[7] P Horak, *et al.*, Phys. Rev. Lett. **79**, 4974 (1997).

FIGURE B.4: Introduction to our transfer matrix theory and its use in explaining both mirror-mediated cooling and external cavity cooling.

FIGURE B.5: An exploration of mirror-mediated cooling from the semi-classical and transfer matrix approaches, as well as external cavity cooling. Also some comments on the experimental apparatus used to conduct these investigations.

FIGURE B.6: Introduction of a classical, fully 3D and vectorial scattering theory to explain the interaction of a polarisable particle with its own reflection.

Bibliography

[1] Shapiro, J. A. Reminiscence on the birth of string theory. *arXiv e-prints* (2007). `arXiv:0711.3448`.

[2] Hudson, J. J., Sauer, B. E., Tarbutt, M. R. & Hinds, E. A. Measurement of the electron electric dipole moment using YbF molecules. *Phys. Rev. Lett.* **89**, 023003 (2002).

[3] Jones, K. M., Tiesinga, E., Lett, P. D. & Julienne, P. S. Ultracold photoassociation spectroscopy: Long-range molecules and atomic scattering. *Rev. Mod. Phys.* **78**, 483 (2006).

[4] Köhler, T., Góral, K. & Julienne, P. S. Production of cold molecules via magnetically tunable Feshbach resonances. *Rev. Mod. Phys.* **78**, 1311 (2006).

[5] Stuhl, B. K., Sawyer, B. C., Wang, D. & Ye, J. Magneto-optical trap for polar molecules. *Phys. Rev. Lett.* **101**, 243002 (2008).

[6] Zeppenfeld, M., Motsch, M., Pinkse, P. W. H. & Rempe, G. Optoelectrical cooling of polar molecules. *Phys. Rev. A* **80**, 041401 (2009).

[7] O'Connell, A. D., Hofheinz, M., Ansmann, M., Bialczak, R. C., Lenander, M., Lucero, E., Neeley, M., Sank, D., Wang, H., Weides, M., Wenner, J., Martinis, J. M. & Cleland, A. N. Quantum ground state and single-phonon control of a mechanical resonator. *Nature* **464**, 697 (2010).

[8] Gröblacher, S., Hammerer, K., Vanner, M. R. & Aspelmeyer, M. Observation of strong coupling between a micromechanical resonator and an optical cavity field. *Nature* **460**, 724 (2009).

[9] Schliesser, A., Arcizet, O., Rivière, R., Anetsberger, G. & Kippenberg, T. J. Resolved-sideband cooling and position measurement of a micromechanical oscillator close to the Heisenberg uncertainty limit. *Nat. Phys.* **5**, 509 (2009).

[10] Kippenberg, T. J. & Vahala, K. J. Cavity opto-mechanics. *Opt. Express* **15**, 17172 (2007).

[11] Ashkin, A. Acceleration and trapping of particles by radiation pressure. *Phys. Rev. Lett.* **24**, 156 (1970).

[12] Chu, S., Hollberg, L., Bjorkholm, J. E., Cable, A. & Ashkin, A. Three-dimensional viscous confinement and cooling of atoms by resonance radiation pressure. *Phys. Rev. Lett.* **55**, 48 (1985).

[13] Lett, P. D., Watts, R. N., Westbrook, C. I., Phillips, W. D., Gould, P. L. & Metcalf, H. J. Observation of Atoms Laser Cooled below the Doppler Limit. *Phys. Rev. Lett.* **61**, 169 (1988).

[14] Dalibard, J. & Cohen-Tannoudji, C. Laser cooling below the Doppler limit by polarization gradients: simple theoretical models. *J. Opt. Soc. Am. B* **6**, 2023 (1989).

[15] Ungar, P. J., Weiss, D. S., Riis, E. & Chu, S. Optical molasses and multilevel atoms: theory. *J. Opt. Soc. Am. B* **6**, 2058 (1989).

[16] Lu, Z. T., Corwin, K. L., Renn, M. J., Anderson, M. H., Cornell, E. A. & Wieman, C. E. Low-velocity intense source of atoms from a magneto-optical trap. *Phys. Rev. Lett.* **77** (1996).

[17] Chang, D. E., Regal, C. A., Papp, S. B., Wilson, D. J., Ye, J., Painter, O., Kimble, H. J. & Zoller, P. Cavity opto-mechanics using an optically levitated nanosphere. *Proc. Natl. Acad. Sci.* **107**, 1005 (2010).

[18] Li, T., Kheifets, S. & Raizen, M. G. Millikelvin cooling of an optically trapped microsphere in vacuum. *arXiv e-prints* (2011). `arXiv:1101.1283`.

[19] Horak, P., Hechenblaikner, G., Gheri, K. M., Stecher, H. & Ritsch, H. Cavity-induced atom cooling in the strong coupling regime. *Phys. Rev. Lett.* **79**, 4974 (1997).

[20] Leibrandt, D. R., Labaziewicz, J., Vuletić, V. & Chuang, I. L. Cavity sideband cooling of a single trapped ion. *Phys. Rev. Lett.* **103**, 103001 (2009).

[21] Koch, M., Sames, C., Kubanek, A., Apel, M., Balbach, M., Ourjoumtsev, A., Pinkse, P. W. H. & Rempe, G. Feedback cooling of a single neutral atom. *Phys. Rev. Lett.* **105**, 173003 (2010).

[22] Lewenstein, M. & Roso, L. Cooling of atoms in colored vacua. *Phys. Rev. A* **47**, 3385 (1993).

[23] Braginsky, V. B. & Manukin, A. B. Ponderomotive effects of electromagnetic radiation. *Sov. Phys. JETP* **25**, 653 (1967).

[24] Cohadon, P. F., Heidmann, A. & Pinard, M. Cooling of a mirror by radiation pressure. *Phys. Rev. Lett.* **83**, 3174 (1999).

[25] Arcizet, O., Cohadon, P. F., Briant, T., Pinard, M. & Heidmann, A. Radiation-pressure cooling and optomechanical instability of a micromirror. *Nature* **444**, 71 (2006).

[26] Gröblacher, S., Hertzberg, J. B., Vanner, M. R., Cole, G. D., Gigan, S., Schwab, K. C. & Aspelmeyer, M. Demonstration of an ultracold micro-optomechanical oscillator in a cryogenic cavity. *Nat Phys* **5**, 485 (2009).

[27] Cohen-Tannoudji, C., Diu, B. & Laloe, F. *Quantum Mechanics, Volume 1* (Wiley-Interscience, 1978).

[28] Cohen-Tannoudji, C. *Quantum Mechanics, Volume 2* (Wiley-Interscience, 1978).

[29] Shore, B. W. *The Theory of Coherent Atomic Excitation: Simple Atoms and Fields, Volume 1* (Wiley VCH, 1990).

[30] Shore, B. W. *The Theory of Coherent Atomic Excitation: Simple Atoms and Fields, Volume 2* (Wiley VCH, 1990).

[31] Woodgate, G. K. *Elemetary Atomic Structure* (Oxford University Press, 2000), seventh edn.

[32] Cohen-Tannoudji, C., Dupont-Roc, J. & Grynberg, G. *Atom–Photon Interactions: Basic Processes and Applications* (Wiley-Interscience, 1992).

[33] Foot, C. J. *Atomic Physics (Oxford Master Series in Atomic, Optical and Laser Physics)* (Oxford University Press, USA, 2005).

[34] Arimondo, E., Inguscio, M. & Violino, P. Experimental determinations of the hyperfine structure in the alkali atoms. *Rev. Mod. Phys.* **49**, 31 (1977).

[35] Steck, D. A. Rubidium 85 D Line Data (2008). URL `http://steck.us/alkalidata/rubidium85numbers.pdf`.

[36] Schrödinger, E. An undulatory theory of the mechanics of atoms and molecules. *Phys. Rev.* **28**, 1049 (1926).

[37] Gardiner, C. W. & Zoller, P. *Quantum Noise* (Springer, 2004), third edn.

[38] Lindblad, G. On the generators of quantum dynamical semigroups. *Commun. Math. Phys.* **48**, 119 (1976).

[39] Domokos, P., Horak, P. & Ritsch, H. Semiclassical theory of cavity-assisted atom cooling. *J. Phys. B* **34**, 187 (2001).

[40] Gardiner, C. W. *Handbook of stochastic methods: for physics, chemistry and the natural sciences* (Springer, 1996), 2 edn.

[41] Xuereb, A., Horak, P. & Freegarde, T. Atom cooling using the dipole force of a single retroflected laser beam. *Phys. Rev. A* **80**, 013836 (2009).

[42] Xuereb, A., Domokos, P., Asbóth, J., Horak, P. & Freegarde, T. Scattering theory of cooling and heating in optomechanical systems. *Phys. Rev. A* **79**, 053810 (2009).

[43] Gardiner, C. W. Adiabatic elimination in stochastic systems. I. Formulation of methods and application to few-variable systems. *Phys. Rev. A* **29**, 2814 (1984).

[44] Jackson, J. D. *Classical Electrodynamics* (Wiley, 1998), third edn.

[45] Hecht, E. *Optics* (Addison Wesley, 2001), 4th edn.

[46] *Springer Handbook of Atomic, Molecular, and Optical Physics* (Springer, 2005), 2nd edn.

[47] Deutsch, I. H., Spreeuw, R. J. C., Rolston, S. L. & Phillips, W. D. Photonic band gaps in optical lattices. *Phys. Rev. A* **52**, 1394 (1995).

[48] Tey, M. K., Maslennikov, G., Liew, T. C. H., Aljunid, S. A., Huber, F., Chng, B., Chen, Z., Scarani, V. & Kurtsiefer, C. Interfacing light and single atoms with a lens. *New J. Phys.* **11**, 043011 (2009).

[49] Toll, J. S. Causality and the dispersion relation: Logical foundations. *Phys. Rev.* **104**, 1760 (1956).

[50] Wang, D.-w., Li, A.-j., Wang, L.-g., Zhu, S.-y. & Zubairy, M. S. Effect of the counterrotating terms on polarizability in atom-field interactions. *Phys. Rev. A* **80**, 063826 (2009).

[51] Cohen-Tannoudji, C. Atomic motion in laser light. In Dalibard, J., Zinn-Justin, J. & Raimond, J. M. (eds.) *Fundamental Systems in Quantum Optics, Proceedings of the Les Houches Summer School, Session LIII* 1 (North Holland, 1992).

[52] Gordon, J. P. & Ashkin, A. Motion of atoms in a radiation trap. *Phys. Rev. A* **21**, 1606 (1980).

[53] Risken, H. *The Fokker-Planck Equation: Methods of Solutions and Applications.* Springer Series in Synergetics (Springer, 1996), third edn.

[54] Einstein, A. Über die von der molekularkinetischen Theorie der Wärme geforderte Bewegung von in ruhenden Flüssigkeiten suspendierten Teilchen. *Ann. Phys.* **322**, 549 (1905).

[55] Metcalf, H. J. & van der Straten, P. *Laser Cooling and Trapping* (Springer, 1999), first edn.

[56] Clerk, A. A., Devoret, M. H., Girvin, S. M., Marquardt, F. & Schoelkopf, R. J. Introduction to quantum noise, measurement, and amplification. *Rev. Mod. Phys.* **82**, 1155 (2010).

[57] Onsager, L. Reciprocal relations in irreversible processes. ii. *Phys. Rev.* **38**, 2265 (1931).

[58] Ford, G. W. & O'Connell, R. F. There is no quantum regression theorem. *Phys. Rev. Lett.* **77**, 798 (1996).

[59] Lax, M. The Lax–Onsager regression 'theorem' revisited. *Opt. Commun.* **179**, 463 (2000).

[60] Dalibard, J., Reynaud, S. & Cohen-Tannoudji, C. Potentialities of a new σ_+-σ_- laser configuration for radiative cooling and trapping. *J. Phys. B* **17**, 4577 (1984).

[61] Bateman, J., Xuereb, A. & Freegarde, T. Stimulated raman transitions via multiple atomic levels. *Phys. Rev. A* **81**, 043808 (2010).

[62] Kasevich, M. & Chu, S. Measurement of the gravitational acceleration of an atom with a light-pulse atom interferometer. *Applied Physics B: Lasers and Optics* **54**, 321 (1992).

[63] Freegarde, T. & Dholakia, K. Cavity-enhanced optical bottle beam as a mechanical amplifier. *Phys. Rev. A* **66**, 013413 (2002).

[64] Dumke, R., Volk, M., Müther, T., Buchkremer, F. B. J., Birkl, G. & Ertmer, W. Micro-optical realization of arrays of selectively addressable dipole traps: A scalable configuration for quantum computation with atomic qubits. *Phys. Rev. Lett.* **89**, 097903 (2002).

[65] Mücke, M., Figueroa, E., Bochmann, J., Hahn, C., Murr, K., Ritter, S., Villas-Boas, C. J. & Rempe, G. Electromagnetically induced transparency with single atoms in a cavity. *Nature* **465**, 755 (2010).

[66] Rodrigo, P. J., Perch-Nielsen, I. R., Alonzo, C. A. & Glückstad, J. GPC-based optical micromanipulation in 3D real-time using a single spatial light modulator. *Opt. Express* **14**, 13107 (2006).

[67] Ashkin, A. Optical trapping and manipulation of neutral particles using lasers. *Proc. Natl. Acad. Sci.* **94**, 4853 (1997).

[68] Barrett, M. D., Sauer, J. A. & Chapman, M. S. All-optical formation of an atomic Bose-Einstein condensate. *Phys. Rev. Lett.* **87**, 010404 (2001).

[69] Anderson, M. H., Ensher, J. R., Matthews, M. R., Wieman, C. E. & Cornell, E. A. Observation of Bose-Einstein condensation in a dilute atomic vapor. *Science* **269**, 198 (1995).

[70] Davis, K. B., Mewes, M. O., Andrews, M. R., van Druten, N. J., Durfee, D. S., Kurn, D. M. & Ketterle, W. Bose-Einstein condensation in a gas of sodium atoms. *Phys. Rev. Lett.* **75**, 3969 (1995).

[71] Aspect, A., Arimondo, E., Kaiser, R., Vansteenkiste, N. & Cohen-Tannoudji, C. Laser cooling below the one-photon recoil energy by velocity-selective coherent population trapping. *Phys. Rev. Lett.* **61**, 826 (1988).

[72] Leanhardt, A. E., Pasquini, T. A., Saba, M., Schirotzek, A., Shin, Y., Kielpinski, D., Pritchard, D. E. & Ketterle, W. Cooling Bose-Einstein condensates below 500 picokelvin. *Science* **301**, 1513 (2003).

[73] Braginsky, V. B. & Manukin, A. B. *Measurement of Weak Forces in Physics Experiments* (University of Chicago, 1977), 1st edn.

[74] Aspect, A., Dalibard, J., Heidmann, A., Salomon, C. & Cohen-Tannoudji, C. Cooling atoms with stimulated emission. *Phys. Rev. Lett.* **57**, 1688 (1986).

[75] Hechenblaikner, G., Gangl, M., Horak, P. & Ritsch, H. Cooling an atom in a weakly driven high-Q cavity. *Phys. Rev. A* **58**, 3030 (1998).

[76] Teo, C. & Scarani, V. Lenses as an atom-photon interface: A semiclassical model. *arXiv e-prints* (2010). `arXiv:1012.0630`.

[77] Purcell, E. M. Spontaneous emission probabilities at radio frequencies. *Phys. Rev.* **69**, 681 (1946).

[78] Cirac, J. I., Parkins, A. S., Blatt, R. & Zoller, P. Cooling of a trapped ion coupled strongly to a quantized cavity mode. *Opt. Commun.* **97**, 353 (1993).

[79] Barker, P. F. & Shneider, M. N. Cavity cooling of an optically trapped nanoparticle. *Phys. Rev. A* **81**, 023826 (2010).

[80] Romero-Isart, O., Pflanzer, A. C., Juan, M. L., Quidant, R., Kiesel, N., Aspelmeyer, M. & Cirac, J. I. Optically levitating dielectrics in the quantum regime: Theory and protocols. *Phys. Rev. A* **83**, 013803 (2011).

[81] Kippenberg, T. J. & Vahala, K. J. Cavity Optomechanics: Back-Action at the Mesoscale. *Science* **321**, 1172 (2008).

[82] Aspelmeyer, M., Gröblacher, S., Hammerer, K. & Kiesel, N. Quantum optomechanics—throwing a glance. *J. Opt. Soc. Am. B* **27**, A189 (2010).

[83] Gangl, M. & Ritsch, H. Cold atoms in a high-Q ring cavity. *Phys. Rev. A* **61**, 043405 (2000).

[84] Elsässer, T., Nagorny, B. & Hemmerich, A. Collective sideband cooling in an optical ring cavity. *Phys. Rev. A* **67**, 051401 (2003).

[85] Nagy, D., Asbóth, J. K. & Domokos, P. Collective cooling of atoms in a ring cavity. *Acta Physica Hungarica B* **26**, 141 (2006).

[86] Hemmerling, M. & Robb, G. R. M. Slowing atoms using optical cavities pumped by phase-modulated light. *Phys. Rev. A* **82**, 053420 (2010).

[87] Schulze, R. J., Genes, C. & Ritsch, H. Optomechanical approach to cooling of small polarizable particles in a strongly pumped ring cavity. *Phys. Rev. A* **81**, 063820 (2010).

[88] Niedenzu, W., Schulze, R., Vukics, A. & Ritsch, H. Microscopic dynamics of ultracold particles in a ring-cavity optical lattice. *Phys. Rev. A* **82**, 043605 (2010).

[89] Kruse, D., Ruder, M., Benhelm, J., von Cube, C., Zimmermann, C., Courteille, P. W., Elsässer, T., Nagorny, B. & Hemmerich, A. Cold atoms in a high-Q ring cavity. *Phys. Rev. A* **67**, 051802 (2003).

[90] Slama, S., Bux, S., Krenz, G., Zimmermann, C. & Courteille, P. W. Superradiant rayleigh scattering and collective atomic recoil lasing in a ring cavity. *Phys. Rev. Lett.* **98**, 053603 (2007).

[91] Vuletić, V. *Laser Physics at the Limits*, chap. Cavity Cooling with a Hot Cavity, 305 (Springer, 2001).

[92] Salzburger, T. & Ritsch, H. Lasing and cooling in a finite-temperature cavity. *Phys. Rev. A* **74**, 033806 (2006).

[93] Domokos, P. & Ritsch, H. Collective cooling and self-organization of atoms in a cavity. *Phys. Rev. Lett.* **89**, 253003 (2002).

[94] Baumann, K., Guerlin, C., Brennecke, F. & Esslinger, T. Dicke quantum phase transition with a superfluid gas in an optical cavity. *Nature* **464**, 1301 (2010).

[95] Bonifacio, R., De Salvo, L., Narducci, L. M. & D'Angelo, E. J. Exponential gain and self-bunching in a collective atomic recoil laser. *Phys. Rev. A* **50**, 1716 (1994).

[96] Zimmermann, C., Kruse, D., Cube, C. V., Slama, S., Deh, B. & Courteille, P. Collective atomic recoil lasing. *J. Mod. Opt.* **51**, 957 (2004).

[97] Horak, P., Xuereb, A. & Freegarde, T. Optical cooling of atoms in microtraps by time-delayed reflection. *J. Comput. Theor. Nanosci.* **7**, 1747 (September 2010).

[98] Aljunid, S. A., Tey, M. K., Chng, B., Chen, Z., Lee, J., Liew, T., Maslennikov, G., Scarani, V. & Kurtsiefer, C. Substantial scattering of a weak coherent beam by a single atom. In *2009 Conference on Lasers and Electro-Optics and the XIth European Quantum Electronics Conference (CLEO®/Europe-EQEC 2009), Munich, Germany*, 89 (IEEE, 2009).

[99] Gradshteyn, I. S. & Ryzhik, I. M. *Table of integrals, series and products* (Academic Press, 1994), fifth edn.

[100] Cook, R. J. Theory of resonance-radiation pressure. *Phys. Rev. A* **22**, 1078 (1980).

[101] Berg-Sørensen, K., Castin, Y., Bonderup, E. & Mølmer, K. Momentum diffusion of atoms moving in laser fields. *J. Phys. B* **25**, 4195 (1992).

[102] Horak, P. & Ritsch, H. Scaling properties of cavity-enhanced atom cooling. *Phys. Rev. A* **64**, 033422 (2001).

[103] Eschner, J., Raab, C., Schmidt-Kaler, F. & Blatt, R. Light interference from single atoms and their mirror images. *Nature* **413**, 495 (2001).

[104] Vuletić, V. & Chu, S. Laser cooling of atoms, ions, or molecules by coherent scattering. *Phys. Rev. Lett.* **84**, 3787 (2000).

[105] Maunz, P., Puppe, T., Schuster, I., Syassen, N., Pinkse, P. W. H. & Rempe, G. Cavity cooling of a single atom. *Nature* **428**, 50 (2004).

[106] Vilensky, M. Y., Prior, Y. & Averbukh, I. S. Cooling in a bistable optical cavity. *Phys. Rev. Lett.* **99**, 103002 (2007).

[107] Lev, B. L., Vukics, A., Hudson, E. R., Sawyer, B. C., Domokos, P., Ritsch, H. & Ye, J. Prospects for the cavity-assisted laser cooling of molecules. *Phys. Rev. A* **77**, 023402 (2008).

[108] Rempe, G., Thompson, R. J., Kimble, H. J. & Lalezari, R. Measurement of ultralow losses in an optical interferometer. *Opt. Lett.* **17**, 363 (1992).

[109] Mabuchi, H. & Kimble, H. J. Atom galleries for whispering atoms: binding atoms in stable orbits around an optical resonator. *Opt. Lett.* **19**, 749 (1994).

[110] Steck, D. A. Sodium D Line Data (2010). URL `http://steck.us/alkalidata/`
      `sodiumnumbers.pdf`.

[111] Steck, D. A. Rubidium 87 D Line Data (2010). URL `http://steck.us/`
      `alkalidata/rubidium87numbers.pdf`.

[112] Steck, D. A. Cesium D Line Data (2010). URL `http://steck.us/alkalidata/`
      `cesiumnumbers.pdf`.

[113] attocube systems AG. *ANSxy50 Data Sheet* (2010).

[114] Thompson, J. D., Zwickl, B. M., Jayich, A. M., Marquardt, F., Girvin, S. M. &
      Harris, J. G. E. Strong dispersive coupling of a high-finesse cavity to a microme-
      chanical membrane. *Nature* **452**, 72 (2008).

[115] Karásek, V., Dholakia, K. & Zemánek, P. Analysis of optical binding in one
      dimension. *Appl. Phys. B* **84**, 149 (2006).

[116] Asbóth, J. K., Ritsch, H. & Domokos, P. Optomechanical coupling in a one-
      dimensional optical lattice. *Phys. Rev. A* **77**, 063424 (2008).

[117] Wilson-Rae, I., Nooshi, N., Zwerger, W. & Kippenberg, T. J. Theory of ground
      state cooling of a mechanical oscillator using dynamical backaction. *Phys. Rev.
      Lett.* **99**, 093901 (2007).

[118] Marquardt, F., Chen, J. P., Clerk, A. A. & Girvin, S. M. Quantum theory of
      cavity-assisted sideband cooling of mechanical motion. *Phys. Rev. Lett.* **99** (2007).

[119] Genes, C., Vitali, D., Tombesi, P., Gigan, S. & Aspelmeyer, M. Ground-state
      cooling of a micromechanical oscillator: Comparing cold damping and cavity-
      assisted cooling schemes. *Phys. Rev. A* **77**, 033804 (2008).

[120] Bushev, P., Wilson, A., Eschner, J., Raab, C., Schmidt-Kaler, F., Becher, C. &
      Blatt, R. Forces between a single atom and its distant mirror image. *Phys. Rev.
      Lett.* **92**, 223602 (2004).

[121] Castin, Y. & Mølmer, K. Atomic momentum diffusion in a σ_+–σ_- laser configu-
      ration: influence of an internal sublevel structure. *J. Phys. B* **23**, 4101 (1990).

[122] Glauber, R. J. Coherent and incoherent states of the radiation field. *Phys. Rev.*
      131, 2766 (1963).

[123] Bhattacharya, M., Uys, H. & Meystre, P. Optomechanical trapping and cooling of partially reflective mirrors. *Phys. Rev. A* **77**, 033819 (2008).

[124] Metcalf, H. J. & van der Straten, P. Laser cooling and trapping of atoms. *J. Opt. Soc. Am. B* **20**, 887 (2003).

[125] Saulson, P. R. Thermal noise in mechanical experiments. *Phys. Rev. D* **42**, 2437 (1990).

[126] Courty, J. M., Heidmann, A. & Pinard, M. Quantum limits of cold damping with optomechanical coupling. *Eur. Phys. J. D* **17**, 399 (2001).

[127] Vitali, D., Mancini, S., Ribichini, L. & Tombesi, P. Macroscopic mechanical oscillators at the quantum limit through optomechanical coupling. *J. Opt. Soc. Am. B* **20**, 1054 (2003).

[128] Xuereb, A., Freegarde, T., Horak, P. & Domokos, P. Optomechanical cooling with generalized interferometers. *Phys. Rev. Lett.* **105**, 013602 (2010).

[129] Jayich, A. M., Sankey, J. C., Zwickl, B. M., Yang, C., Thompson, J. D., Girvin, S. M., Clerk, A. A., Marquardt, F. & Harris, J. G. E. Dispersive optomechanics: a membrane inside a cavity. *New J. Phys.* **10**, 095008 (2008).

[130] Bhattacharya, M. & Meystre, P. Trapping and cooling a mirror to its quantum mechanical ground state. *Phys. Rev. Lett.* **99**, 073601 (2007).

[131] Sankey, J. C., Yang, C., Zwickl, B. M., Jayich, A. M. & Harris, J. G. E. Strong and tunable nonlinear optomechanical coupling in a low-loss system. *Nat. Phys.* **6**, 707 (2010).

[132] Braginsky, V. Low quantum noise tranquilizer for Fabry–Perot interferometer. *Phys. Lett. A* **293**, 228 (2002).

[133] Nunnenkamp, A., Børkje, K., Harris, J. G. E. & Girvin, S. M. Cooling and squeezing via quadratic optomechanical coupling. *Phys. Rev. A* **82**, 021806 (2010).

[134] Clerk, A. A., Marquardt, F. & Harris, J. G. E. Quantum measurement of phonon shot noise. *Phys. Rev. Lett.* **104**, 213603 (2010).

[135] Xuereb, A., Domokos, P., Horak, P. & Freegarde, T. Scattering theory of multilevel atoms interacting with arbitrary radiation fields. *Phys. Scr.* **2010**, 014010 (2010).

[136] Spreeuw, R. J. C., Beijersbergen, M. W. & Woerdman, J. P. Optical ring cavities as tailored four-level systems: An application of the group U(2,2). *Phys. Rev. A* **45**, 1213 (1992).

[137] Cohen-Tannoudji, C. Atoms in strong resonant fields. In Balian, R., Haroche, S. & Liberman, S. (eds.) *Frontiers in laser spectroscopy, Proceedings of the Les Houches Summer School, Session XXVII* 1 (North Holland, 1977).

[138] Siegman, A. E. *Lasers* (University Science Books, Sausalito, CA, 1990).

[139] Metzger, C. H. & Karrai, K. Cavity cooling of a microlever. *Nature* **432**, 1002 (2004).

[140] Gigan, S., Bohm, H. R., Paternostro, M., Blaser, F., Langer, G., Hertzberg, J. B., Schwab, K. C., Bauerle, D., Aspelmeyer, M. & Zeilinger, A. Self-cooling of a micromirror by radiation pressure. *Nature* **444**, 67 (2006).

[141] Schliesser, A., Rivière, R., Anetsberger, G., Arcizet, O. & Kippenberg, T. J. Resolved-sideband cooling of a micromechanical oscillator. *Nat. Phys.* **4**, 415 (2008).

[142] Favero, I. & Karrai, K. Cavity cooling of a nanomechanical resonator by light scattering. *New J. Phys.* **10**, 095006 (2008).

[143] Domokos, P. & Ritsch, H. Mechanical effects of light in optical resonators. *J. Opt. Soc. Am. B* **20**, 1098 (2003).

[144] Schliesser, A. & Kippenberg, T. J. Cavity optomechanics with whispering-gallery-mode optical micro-resonators. *arXiv e-prints* (2010). `arXiv:1003.5922`.

[145] Huang, S. & Agarwal, G. S. Enhancement of cavity cooling of a micromechanical mirror using parametric interactions. *Phys. Rev. A* **79**, 013821 (2009).

[146] Kumar, T., Bhattacherjee, A. B. & ManMohan. Dynamics of a movable micromirror in a nonlinear optical cavity. *Phys. Rev. A* **81**, 013835 (2010).

[147] Dapasse, F. & Vigoureux, J.-M. Optical binding force between two Rayleigh particles. *J. Phys. D* **27**, 914 (1994).

[148] Levine, H. & Schwinger, J. On the theory of electromagnetic wave diffraction by an aperture in an infinite plane conducting screen. *Comm. Pure Appl. Math.* **3**, 355 (1950).

[149] Martin, O. J. F., Girard, C. & Dereux, A. Generalized field propagator for electromagnetic scattering and light confinement. *Phys. Rev. Lett.* **74**, 526 (1995).

[150] Burns, M. M., Fournier, J. M. & Golovchenko, J. A. Optical binding. *Phys. Rev. Lett.* **63**, 1233 (1989).

[151] Metzger, N. K., Wright, E. M., Sibbett, W. & Dholakia, K. Visualization of optical binding of microparticles using a femtosecond fiber optical trap. *Opt. Express* **14**, 3677 (2006).

[152] Clifford, M. A., Lancaster, G. P. T., Mitchell, R. H., Akerboom, F. & Dholakia, K. Realization of a mirror magneto-optical trap. *J. Mod. Opt.* **48**, 1123 (2001).

[153] Drexhage, K. H., Kuhn, H. & Schäfer, F. P. Variation of the fluorescence decay time of a molecule in front of a mirror. *Ber. Bunsen Phys. Chem.* **72**, 329 (1968).

[154] Bartlett, P. N., Birkin, P. R. & Ghanem, M. A. Electrochemical deposition of macroporous platinum, palladium and cobalt films using polystyrene latex sphere templates. *Chem. Commun.* 1671 (2000).

[155] Bartlett, P. N., Baumberg, J. J., Birkin, P. R., Ghanem, M. A. & Netti, M. C. Highly ordered macroporous gold and platinum films formed by electrochemical deposition through templates assembled from submicron diameter monodisperse polystyrene spheres. *Chem. Mater.* **14**, 2199 (2002).

[156] Casimir, H. B. G. & Polder, D. The Influence of Retardation on the London-van der Waals Forces. *Phys. Rev.* **73**, 360 (1948).

[157] Scheel, S. & Buhmann, S. Y. Casimir-polder forces on moving atoms. *Phys. Rev. A* **80**, 042902 (2009).

[158] Wilson, M. A., Bushev, P., Eschner, J., Kaler, S. F., Becher, C., Blatt, R. & Dorner, U. Vacuum-field level shifts in a single trapped ion mediated by a single distant mirror. *Phys. Rev. Lett.* **91**, 213602 (2003).

[159] Coyle, S., Netti, M. C., Baumberg, J. J., Ghanem, M. A., Birkin, P. R., Bartlett, P. N. & Whittaker, D. M. Confined plasmons in metallic nanocavities. *Phys. Rev. Lett.* **87**, 176801 (2001).

[160] Kimball Physics, inc. *Spherical Octagon Catalogue* (2010).

[161] Himsworth, M. *Coherent Manipulation of Ultracold Rubidium*. Ph.D. thesis, University of Southampton (2009).

[162] Ohadi, H., Himsworth, M., Xuereb, A. & Freegarde, T. Magneto-optical trapping and background-free imaging for atoms near nanostructured surfaces. *Opt. Express* **17**, 23003 (2009).

[163] Raab, E. L., Prentiss, M., Cable, A., Chu, S. & Pritchard, D. E. Trapping of neutral sodium atoms with radiation pressure. *Phys. Rev. Lett.* **59**, 2631 (1987).

[164] Shimizu, F., Shimizu, K. & Takuma, H. Four-beam laser trap of neutral atoms. *Opt. Lett.* **16**, 339 (1991).

[165] Emile, O., Bardou, F., Salomon, C., Laurent, P., Nadir, A. & Clairon, A. Observation of a new magneto-optical trap. *Europhys. Lett.* **20**, 687 (1992).

[166] Lee, K. I., Kim, J. A., Noh, H. R. & Jhe, W. Single-beam atom trap in a pyramidal and conical hollow mirror. *Opt. Lett.* **21**, 1177 (1996).

[167] Reichel, J., Hänsel, W. & Hänsch, T. W. Atomic micromanipulation with magnetic surface traps. *Phys. Rev. Lett.* **83**, 3398 (1999).

[168] Folman, R., Krüger, P., Cassettari, D., Hessmo, B., Maier, T. & Schmiedmayer, J. Controlling cold atoms using nanofabricated surfaces: Atom chips. *Phys. Rev. Lett.* **84**, 4749 (2000).

[169] Pollock, S., Cotter, J. P., Laliotis, A. & Hinds, E. A. Integrated magneto-optical traps on a chip using silicon pyramid structures. *Opt. Express* **17**, 14109 (2009).

[170] Nez, F. Optical frequency determination of the hyperfine components of the $5S_{1/2}$–$5D_{3/2}$ two-photon transitions in rubidium. *Opt. Commun.* **102**, 432 (1993).

[171] Ovchinnikov, Y. B., Shul'ga, S. V. & Balykin, V. I. An atomic trap based on evanescent light waves. *J. Phys. B* **24**, 3173 (1991).

[172] Schultz, B. E., Ming, H., Noble, G. A. & van Wijngaarden, W. A. Measurement of the Rb D2 transition linewidth at ultralow temperature. *Eur. Phys. J. D* **48**, 171 (2008).

[173] Corwin, K. L., Lu, Z. T., Hand, C. F., Epstein, R. J. & Wieman, C. E. Frequency-stabilized diode laser with the Zeeman shift in an atomic vapor. *Appl. Opt.* **37**, 3295 (1998).

[174] Sheludko, D. V., Bell, S. C., Anderson, R., Hofmann, C. S., Vredenbregt, E. J. D. & Scholten, R. E. State-selective imaging of cold atoms. *Phys. Rev. A* **77**, 033401 (2008).

[175] Vernier, A., Franke-Arnold, S., Riis, E. & Arnold, A. S. Enhanced frequency up-conversion inrb vapor. *Opt. Express* **18**, 17020 (2010).

[176] Wu, S., Plisson, T., Brown, R. C., Phillips, W. D. & Porto, J. V. Multiphoton magnetooptical trap. *Phys. Rev. Lett.* **103**, 173003 (2009).

[177] Autler, S. H. & Townes, C. H. Stark effect in rapidly varying fields. *Phys. Rev.* **100**, 703 (1955).

[178] Wohlleben, W., Chevy, F., Madison, K. & Dalibard, J. An atom faucet. *Eur. Phys. J. D* **15**, 237 (2001).

[179] Lewandowski, H. J., Harber, D. M., Whitaker, D. L. & Cornell, E. A. Simplified system for creating a Bose-Einstein condensate. *J. Low Temp. Phys.* **132**, 309 (2003).

[180] Herskind, P., Dantan, A., Langkilde-Lauesen, M., Mortensen, A., Sørensen, J. & Drewsen, M. Loading of large ion coulomb crystals into a linear paul trap incorporating an optical cavity. *Appl. Phys. B* **93**, 373 (2008).

[181] Hétet, G., Slodicka, L., Glätzle, A., Hennrich, M. & Blatt, R. QED with a spherical mirror. *Phys. Rev. A* **82**, 063812 (2010).

[182] Cirac, J. I. & Zoller, P. Quantum computations with cold trapped ions. *Phys. Rev. Lett.* **74**, 4091 (1995).

[183] Proite, N. A., Simmons, Z. J. & Yavuz, D. D. Observation of atomic localization using electromagnetically induced transparency. *arXiv e-prints* (2010). `arXiv: 1011.2754`.

[184] Karrai, K., Favero, I. & Metzger, C. Doppler optomechanics of a photonic crystal. *Phys. Rev. Lett.* **100**, 240801 (2008).

[185] Barker, P. F. Doppler cooling a microsphere. *Phys. Rev. Lett.* **105**, 073002 (2010).

[186] Beyer, O., Nee, I., Havermeyer, F. & Buse, K. Wavelength division multiplexing with Bragg gratings in poly (methyl methacrylate) (PMMA). In *Photorefractive Effects, Materials, and Devices*, 577 (Optical Society of America, 2003).

[187] Kruse, J., Gierl, C., Schlosser, M. & Birkl, G. Reconfigurable site-selective manipulation of atomic quantum systems in two-dimensional arrays of dipole traps. *Phys. Rev. A* **81**, 060308 (2010).

[188] Hannay, J. H. The Clausius-Mossotti equation: an alternative derivation. *Eur. J. Phys.* **4**, 141 (1983).

[189] Miller, K. J. Calculation of the molecular polarizability tensor. *J. Am. Chem. Soc.* **112**, 8543 (1990).

[190] Bartlett, P. N., Baumberg, J. J., Coyle, S. & Abdelsalam, M. E. Optical properties of nanostructured metal films. *Faraday Disc.* **125**, 117 (2004).

[191] Parsons, J., Burrows, C. P., Sambles, J. R. & Barnes, W. L. A comparison of techniques used to simulate the scattering of electromagnetic radiation by metallic nanostructures. *J. Mod. Opt.* **57**, 356 (2010).

[192] Oskooi, A. F., Roundy, D., Ibanescu, M., Bermel, P., Joannopoulos, J. D. & Johnson, S. G. MEEP: A flexible free-software package for electromagnetic simulations by the FDTD method. *Comput. Phys. Commun.* **181**, 687 (2010).

[193] Balian, R. & Bloch, C. Distribution of eigenfrequencies for the wave equation in a finite domain I. Three-dimensional problem with smooth boundary surface. *Ann. Phys.* **60**, 401 (1970).

[194] Balian, R. & Bloch, C. Distribution of eigenfrequencies for the wave equation in a finite domain. II. Electromagnetic field. Riemannian spaces. *Ann. Phys.* **64**, 271 (1971).

[195] Ohadi, H. *Single Ca^+ Ions in a Penning Trap for Applications in Quantum Information Processing.* Ph.D. thesis, Imperial College (2008).